

Mitteilung des Instituts
für Geomechanik und Geotechnik
Technische Universität Braunschweig
Heft Nr. 112



Stress state developments during the installation of pipe piles in sand and their influence on the lateral load-bearing behaviour

von
Philipp Stein

Braunschweig 2023

Herausgegeben von Univ.-Prof. Dr.-Ing. J. Stahlmann

Von der Fakultät Architektur, Bauingenieurwesen und Umweltwissenschaften
der Technischen Universität Carolo-Wilhelmina zu Braunschweig
zur Erlangung des Grades
eines Doktor-Ingenieurs (Dr.-Ing.)

genehmigte Dissertation.

Eingereicht am: 7. Juli 2022
Disputation am: 22. November 2022
Berichterstatter: Prof. Dr.-Ing. Joachim Stahlmann
Berichterstatterin: Prof. Dr.-Ing. Frank Rackwitz

Eigenverlag: Institut für Geomechanik und Geotechnik
Technische Universität Braunschweig
Beethovenstraße 51 b · 38106 Braunschweig
Telefon : (0531) 391-62000
Fax : (0531) 391-62040
E-Mail : igg@tu-bs.de
Internet : www.igg-tubs.de
ISBN : 978-3-948141-04-2

Druck: DruckVoll UG Anne Seckelmann
Weinbergweg 40 a · 38106 Braunschweig
Telefon : (0531) 390 679 64
Fax : (0531) 390 718 35
E-Mail : info@druckvoll-bs.de
Internet : www.druckvoll-bs.de

Druck auf chlorfrei gebleichtem Papier

**Stress state developments
during the installation of pipe piles in sand
and their influence on the lateral load-bearing behaviour**

Von der
Fakultät Architektur, Bauingenieurwesen und Umweltwissenschaften
der Technischen Universität Carolo-Wilhelmina
zu Braunschweig

zur Erlangung des Grades eines
Doktor-Ingenieurs (Dr.-Ing.)
genehmigte

Dissertation

von
Philipp Stein
geboren am 20.12.1985
aus Bremen

Eingereicht am 7. Juli 2022
Disputation am 22. November 2022
Berichterstatter Prof. Dr.-Ing. Joachim Stahlmann
Prof. Dr.-Ing. Frank Rackwitz

2023

"What we see depends mainly on what we look for."

(John Lubbock, 1834-1913)

Table of Contents

Table of Contents	i
Nomenclature	v
Chapter 1 Introduction.....	1
1.1 Motivation.....	1
1.2 Outline.....	2
Chapter 2 Geotechnical aspects on monopile foundations for offshore wind turbines.....	5
2.1 Overview	5
2.2 Pile installation effects.....	5
2.2.1 Pile capacity of driven piles.....	5
2.2.2 Impact pile driving.....	7
2.2.3 Vibratory pile installation	12
2.3 Lateral pile behaviour	19
2.3.1 Lateral bedding	19
2.3.2 Eigenfrequency	20
2.3.3 Non-linear soil springs (p-y approaches)	21
2.3.4 Influence of pile geometry	23
2.3.5 Soil stress state or depth dependency	25
2.3.6 Small strain stiffness	26
2.3.7 Cyclic effects	28
2.3.8 Influence of installation method	38
2.4 Interim conclusion.....	40
Chapter 3 Scope of work.....	43
3.1 State of the art	43
3.2 Research question.....	44

Table of Contents

3.3	Methodology	44
Chapter 4	Design of physical model	47
4.1	Generic OWT foundation.....	47
4.2	Scaling procedure	50
Chapter 5	Description of model tests	59
5.1	Model requirements and testing facilities.....	59
5.2	Model pile.....	61
5.3	Lateral loading	62
5.4	Model sand.....	63
5.4.1	Overview.....	63
5.4.2	Physical properties	63
5.4.3	Shear parameters	66
5.4.4	Dynamic stiffness	67
5.5	Pile installation equipment	68
5.6	Test program	71
5.6.1	Test stages.....	71
5.6.2	Test preparation.....	71
5.6.3	Pile installation.....	76
5.6.4	Cyclic lateral load test (CLLT)	79
5.7	Data processing.....	83
5.7.1	General objectives.....	83
5.7.2	pile driving monitoring (impact driving).....	84
5.7.3	pile driving monitoring (vibro driving).....	86
5.7.4	soil stress developments during pile installation.....	90
5.7.5	pile measurements during lateral loading	91
5.7.6	soil stress developments during lateral loading	93

5.7.7	eigenfrequency measurement.....	95
Chapter 6	Results of model tests	99
6.1	Overview	99
6.2	Pile installation	101
6.2.1	Evaluation scheme for pile installation processes	101
6.2.2	Impact driven piles	101
6.2.3	Vibratory driven piles.....	104
6.2.4	Soil stress developments during pile installation	110
6.2.5	Installation mode.....	114
6.2.6	Interim summary and discussion on pile installation processes	118
6.3	Monotonic lateral pile behaviour.....	123
6.3.1	Evaluation procedure for monotonic pile behaviour.....	123
6.3.2	Quasi-static load-deflection behaviour.....	124
6.3.3	Dynamic stiffness of pile-soil system after pile installation	129
6.3.4	Soil reaction due to quasi-static pile loading.....	130
6.3.5	Interim summary and discussion on monotonic lateral pile behaviour.....	133
6.4	Cyclic lateral pile behaviour due to unidirectional loading.....	135
6.4.1	Evaluation procedure for cyclic pile behaviour	135
6.4.2	Pile head displacement accumulation.....	135
6.4.3	Cyclic pile stiffness.....	142
6.4.4	Soil reaction to cyclic pile loading	146
6.4.5	Interim summary and discussion on cyclic lateral pile behaviour	153
6.5	Cyclic lateral pile behaviour due to changing loading direction.....	156
6.5.1	Pile head behaviour due to changing loading direction.....	156
6.5.2	Soil reaction due to changing loading direction.....	165

6.5.3	Interim summary and discussion on the influence of changing loading direction	
	171	
Chapter 7	Numerical simulations of the lateral pile behaviour using a one-dimensional bedded beam model.....	175
7.1	Overview	175
7.2	Static lateral pile behaviour	175
7.2.1	Numerical model for static calculations.....	175
7.2.2	Modifications on p-y approach based on offshore guidelines	176
7.2.3	Static calculation of scale model tests	182
7.2.4	Static calculations on offshore monopile foundations.....	184
7.3	Pile eigenfrequency	188
7.3.1	Numerical model for dynamic calculations.....	188
7.3.2	Theoretical influence of installation-induced soil stresses on the eigenfrequency of the model pile.....	189
7.3.3	Theoretical influence of accumulated soil stresses on the eigenfrequency of the model pile	191
7.4	Interim summary	192
Chapter 8	Résumé	195
References.....		201
Appendix A	Test program	219
Appendix B	Measurement equipment	221
Appendix C	Test preparation	225
Appendix D	Pile installation.....	227
Appendix E	Quasi-static lateral pile behaviour	247
Appendix F	Cyclic lateral pile behaviour	289
Appendix G	HCA model formulation and parameters	375
Appendix H	Numerical calculations.....	377

Nomenclature

Abbreviations

Symbol	Description
BAW	Federal Waterways Engineering and Research Institute (Bundesanstalt für Wasserbau)
BSH	Federal Maritime and Hydrographic Agency (Bundesamt für Seeschifffahrt und Hydrographie)
CEL	coupled Euler-Lagrange
CLLT	cyclic lateral load test
CNS	constant normal stiffness
CPT	cone penetration testing
DPM	dynamic probing medium
EoD	end of driving
FFT	Fast Fourier transform
FINO	research platforms in North Sea and Baltic Sea (Forschungsplattformen in Nord- und Ostsee)
HCA	high cycle accumulation model
IGG-TUBS	Institute for Geomechanics and Geotechnics of Technische Universität Braunschweig
INST	pile installation stage
LFRT	lateral frequency response test
OGL	offshore guidelines
OWF	offshore wind farm
OWT	offshore wind turbine
PREP	test preparation stage
PSS	primary stress state
PWP	pore water pressure
SRD	static resistance to driving
TP	transition piece
WIP	wished-in-place

Capital letters

Symbol	Unit	Description
A_{pile}	$[m^2]$	pile cross section
A_{pu}	[-]	empirical correction factor for ultimate bedding resistance
B_{Ni}	[-]	parameter describing cyclic behaviour
C_{Ni}	[-]	soil constants of HCA model describing cyclic behaviour depending on number of cycles
C_{amp}	[-]	soil constants of HCA model describing cyclic behaviour depending on strain amplitude
C_U	[-]	coefficient of uniformity
C_{ax}	$[kN \cdot s/m^3]$	damping constant
C		damping matrix
\hat{c}_{N1}	[-]	biased accumulation parameter
D	[-]	relative soil density (based on porosity n)
D_r	[-]	relative soil density (based on void ratio e)
D_{pile}	$[m]$	pile diameter
E	$[MN/m^2]$	modulus of elasticity
E_{base}	$[kN/m]$	lateral stiffness at pile base
E_{lat}	$[kN/m]$	lateral pile head stiffness
E_{inst}	$[kN/m]$	axial pile stiffness (pile installation)
E_{oed}	$[MN/m^2]$	oedometric modulus
E_{py}	$[kN/m^2]$	lateral bedding stiffness
E_{qs}	$[kN/m^3]$	axial pile-soil interface stiffness (pile installation)
EA	$[kN]$	normal stiffness
EI	$[kNm^2]$	bending stiffness

F	[kN]	axial force (pile installation)
F_c	[kN]	centrifugal force
F_{dyn}	[kN]	dynamic force
F_{in}	[kN]	inertia force
F_{line}	[kN]	line pull
F_r	[-]	normalised friction ratio (CPT)
F_{stat}	[kN]	static force
F_{bias}	[kN]	bias force (static surcharge force)
F_{str}	[kN]	pile force derived from strain measurements
G_{dyn}	[MN/m ²]	dynamic shear modulus
H	[kN]	lateral load
I_{pile}	[m ⁴]	pile's second moment of area
K		stiffness matrix
L	[m]	length
L_E	[m]	elastic length
L_{eq}	[m]	equivalent cantilever length
L_{free}	[m]	free pile length
L_{pen}	[m]	pile penetration
L_{pile}	[m]	pile length
L_{TP}	[m]	length of transition piece
M	[kNm]	bending moment
M_e	[kg·m]	eccentric moment
M		mass matrix

Nomenclature

N	[-]	cycle number
N _{reg}	[-]	cycle number (regular cycles)
N _{10,DPM}	[-]	number of blows for 10 cm penetration (dynamic probing)
N ₁₀₀	[-]	number of blows for 100 cm penetration (impact pile driving)
P		load vector
Q _{base}	[kN]	shear force at pile base
Q _t	[-]	normalised cone resistance (CPT)
R	[kN]	axial pile resistance or pile bearing capacity
R _{stat}	[kN]	displacement-dependent (static) pile resistance
R _{blow}	[kN]	total pile driving resistance per blow
R _{damp}	[kN]	velocity-dependent pile resistance (damping)
R _{in}	[kN]	acceleration-dependent pile resistance (inertia)
R ²	[-]	coefficient of determination
T _{cycl}	[s]	duration of load cycle
T _{s,50}	[s]	duration of significant wave with 50-year return period
T _{wave}	[s]	stress wave travel duration
V	[m ³]	volume
W	[kJ]	energy
W _{1s}	[kJ]	transferred energy over one second (vibratory driving)
W ₁₀₀	[kJ/m]	energy per 100 cm penetration (pile installation)
W _{blow}	[kJ]	energy per blow (impact driving)
W _{cycle}	[kJ]	energy per cycle (vibratory driving)
W _{set}	[kJ]	energy during penetrative motion (vibratory driving)

W_{\downarrow}	[k]	energy during downward motion (vibratory driving)
W_{rated}	[k]	rated impact hammer energy
Y		function describing average stress ratio
Y_c		function describing critical state stress ratio
\bar{Y}		function describing stress state with regard to critical state
Z_{pile}	[kN·s/m]	pile impedance

Small letters

Symbol	Unit	Description
a	[m/s ²]	acceleration
b	[-]	shape factor to describe shear stiffness reduction with strain level
b _{fluid}	[mm]	extent of fluidised zone around pile during vibratory driving
c _p , c _s	[m/s]	wave speed of primary (compression) waves and secondary (shear) waves in the soil
c _{pile}	[m/s]	stress wave speed in the pile
d	[mm]	grain size
d ₅₀	[mm]	mean grain size
e	[-]	void ratio
f	[Hz]	frequency
f _{0,lat}	[Hz]	first bending mode eigenfrequency of undamped system
f _{0,inst}	[Hz]	first eigenfrequency during pile installation
f _{D,lat}	[Hz]	first bending mode eigenfrequency of damped system
f _d	[Hz]	vibratory driving frequency
f _N	[-]	function describing cyclic behaviour depending on number of cycles
f _{ampl}	[-]	function describing cyclic behaviour depending on strain amplitude
f _p	[-]	function describing cyclic behaviour depending on mean effective stress level
f _γ	[-]	function describing cyclic behaviour depending on average stress ratio
f _e	[-]	function describing cyclic behaviour depending on void ratio
f _π	[-]	function describing cyclic behaviour depending on polarisation
f _s	[kPa]	measured sleeve friction (CPT)

g^A	[-]	soil state parameter describing cyclic history
h_H	[m]	lever arm
h_s	[m]	significant wave height
h_{WT}	[m]	height of water table above mudline
\hat{h}	[-]	transfer function
k	[-]	earth pressure coefficient
k_0	[-]	earth pressure at rest coefficient
k_1	[-]	earth pressure coefficient after soil compaction
k_p	[-]	passive earth pressure coefficient
m	[-]	flow rule
$m_{1,2}$	[kg]	point masses (dynamic pile system)
m_{dyn}	[kg]	dynamic mass of pile-vibro assembly
m_h	[kN/m ³]	gradient (versus depth) of horizontal subgrade reaction
m_{pile}	[kg]	pile mass
n	[-]	porosity
p	[kPa]	mean stress
p_{PWP}	[kPa]	pore water pressure
p_{py}	[kN/m]	lateral soil reaction
p_{ref}	[kPa]	reference (atmospheric) pressure ($p_{ref} = 100$ kPa)
p_u	[kN/m]	theoretical ultimate soil resistance
q	[kPa]	deviatoric stress
q_{stat}	[kN/m ²]	displacement-dependent (static) resistance (pile driving)
q_{damp}	[kN/m ²]	velocity-dependent (damping) resistance (pile driving)

Nomenclature

q_c	[MN/m ²]	measured cone resistance (CPT)
q_t	[MN/m ²]	corrected cone resistance (CPT)
r	[m]	radius (cylinder coordinate)
s	[m]	axial pile displacement
s_0	[m]	peak displacement amplitude
s_{set}	[m]	permanent penetration (set per cycle)
s_q	[m]	axial pile displacement at maximum static resistance ('quake')
t	[s]	time
t_{pile}	[m]	pile wall thickness
u	[m]	lateral pile head displacement
v	[m/s]	velocity
v_{pen}	[m/s]	pile penetration speed
y	[m]	lateral displacement
\mathbf{y}		deformation vector
z	[m]	depth (cylinder coordinate)
z_{eq}	[m]	equivalent depth

Greek letters

Symbol	Unit	Description
α_N	[-]	exponent describing cyclic behaviour depending on number of cycles
α_{pen}	[-]	exponent describing shape of soil resistance degradation factor
α_{damp}	[-]	exponent describing velocity-dependent damping
α_π	[°]	rotation of loading direction
β_z	[-]	soil resistance degradation factor
β_{res}	[-]	soil resistance reduction factor
β_{PSS}	[-]	reciprocal of PSS magnification factor (= soil resistance reduction factor)
γ	[-]	shear strain
γ'	[kN/m ³]	buoyant soil unit weight
γ_w	[kN/m ³]	water unit weight ($\gamma_w = 10 \text{ kN/m}^3$)
Δ		difference
δ	[°]	interface friction angle
ε	[-]	normal strain
η_{av}	[-]	average stress ratio
θ	[°]	direction (cylinder coordinate)
θ_H	[°]	loading direction
κ	[-]	exponent describing load-deflection behaviour
Λ	[-]	displacement amplification factor
λ	[-]	exponent describing dependence on parameters and their reference values
λ	[-]	scaling factor
ν	[-]	Poisson's ratio

Nomenclature

ξ_{σ}	[-]	factor to consider increase of soil stress due to cyclic loading
π	[-]	polarisation
ρ	[kg/m ³]	density
ρ_d	[kg/m ³]	dry soil density
ρ_s	[kg/m ³]	grain density
σ	[kN/m ²]	normal stress
σ_1, σ_3	[kN/m ²]	maximum and minimum principal stresses
σ_{rad}	[kN/m ²]	radial stress
σ_v	[kN/m ²]	vertical stress
σ_h	[kN/m ²]	horizontal stress
τ	[kN/m ²]	shear stress
τ_s	[kN/m ²]	interface shear strength
Φ	[-]	phase (frequency domain)
Φ_F	[-]	phase shift between rotation of vibro hammer eccentrics and oscillation of pile-vibro assembly
φ	[°]	soil friction angle
ψ	[°]	pile head inclination
ω	[1/s]	angular frequency
$\omega_{0,lat}$	[1/s]	first (angular) bending mode eigenfrequency
ω_d	[1/s]	vibratory driving (angular) frequency

Indices (subscripts, superscripts)

Symbol	Description
acc	accumulated value (cyclic loading)
ampl	amplitude (cyclic loading)
av	average value (cyclic loading)
base	pile base
deg	degraded value (bedding stiffness)
dyn	dynamic property or behaviour
exc	system excitation (frequency response test)
h	horizontal direction
impr	imprinted (soil stresses)
ini	initial value
load	loading
m	model (scaling)
max	maximum value (cyclic loading)
mdl	at mudline level
min	minimum value (cyclic loading)
mob	mobilised value
msrd	measured value
offset	offset value
p	prototype (scaling)
perm	permanent value (cyclic loading)
pen	pile penetration
pile	property or behaviour of pile

Nomenclature

PSS	primary stress state
rad	radial direction
res	residual value
resp	system response (frequency response test)
ref	reference value
s	pile shaft
sec	secant value (bedding stiffness)
set	penetrative motion (set per blow/cycle)
soil	property or behaviour of soil
stat	static property or behaviour
t	pile toe
toe	values at pile toe
top	values at pile top
unld	unloading
ult	ultimate value
v	vertical direction
'	effective (stress) / buoyant (unit weight)
*	dimensionless value
·	rate
↓	downward directed motion
↑	upward directed motion
⊥	transverse to loading direction
∥	in loading direction

Chapter 1 Introduction

1.1 Motivation

In the recent years, the importance of offshore wind energy production in Europe and other parts of the world has been steadily increasing. More powerful turbines are developed to increase the efficiency of offshore wind generation. To fix the offshore wind turbines (OWT) to the seabed, mainly monopile foundations are used in shallow and moderate water depths. These large diameter steel pipe piles make up a total share of 81.2% of total installed OWT and 80.5% of newly installed OWT in 2020 (Wind Europe 2021). They transfer the predominantly horizontal loads due to wind, wave and rotor excitation to the soil by means of lateral bedding. To install these foundations in the seabed, impact pile driving is used. A lot of experience with this method is present at contractors and consultants for installation and lateral design. However, impact pile driving leads to high underwater noise emissions, which have to be mitigated elaborately to reduce environmental impacts. Furthermore, impact pile driving is responsible for a considerable amount of fatigue during the lifetime of a monopile foundation. Lastly, the relatively long time needed to install a monopile including pile handling, pick-up of impact hammer and pure driving time is costly with regard to the immense logistical efforts in offshore projects.

As an alternative to impact pile driving, vibratory pile driving is known from onshore and nearshore pile and sheet pile installations in coarse-grained soil. Larger vibratory hammers have been developed which are suitable for monopile installation in very dense, overconsolidated sands, as has been shown in first commercial (FISCHER et al. 2013) and demonstration projects (CAPE Holland 2020). Regarding the lateral load bearing behaviour, however, very little experience exists with vibratory driven piles.

To close this gap and contribute to the a more systematic assessment of vibratory pile driving for the installation of monopile foundations for OWT, a comparative study on the installation effects of impact and vibratory driven piles and their effects on subsequent lateral loading is presented.

1.2 Outline

The evaluation of the relevant literature on pipe pile installation and the lateral behaviour of monopile foundations shows manifold studies on the effects of impact pile driving on the surrounding soil and also on the calculation methods to estimate the lateral load-bearing behaviour of monopile foundations for OWT. The research on the effects during vibratory driving is somewhat contradictory and does not focus on the influences on the subsoil. The largest share of investigations on the lateral behaviour of monopiles was conducted on small scale model investigations or numerical simulations without consideration of pile installation effects. Based on the current state of scientific knowledge, the research question about the influence of pile installation processes on the soil's stress state and lateral bedding is framed.

To examine the differences in the lateral behaviour of impact and vibratory driven monopiles, investigations were necessary focussing on the influence of the different installation methods on the surrounding soil, and on the behaviour of the driven piles under subsequent lateral loading. Scale model tests were chosen as they allow for a holistic exploration of geotechnical phenomena during pile installation and subsequent lateral loading. Scaling errors were kept small by use of a large testing facility. The focus was laid on subsoil conditions as present in the German North Sea and moderate loading conditions, including cyclic loading.

During impact and vibratory pile installation processes, dynamic force and motion characteristics of the pile, as well as the development of radial stresses in the soil were monitored and analysed. Soil stress developments known from impact pile driving with increased radial stresses at the pile toe were also found at vibratory installed piles with a specific 'mode' of vibratory driving. For the subsequent lateral loading, the load-displacement behaviour of the first cycle, the displacement accumulation, and the system stiffness development of further loading cycles and the corresponding soil stress developments were examined. Different lateral behaviour could be observed depending on the installation parameters. Certain vibratory driven piles showed similar behaviour to impact driven piles, while other vibratory driven piles showed larger pile head displacement under lateral loading. During cyclic loading from alternating directions, a recovery of accumulated pile head displacements and soil stress redistributions were observed.

Calculations of the static lateral pile behaviour with modified p-y curves considering pile installation effects showed good agreement with the first loading cycle of the model tests.

Furthermore, a notable effect of increased soil stresses near the pile toe on the lateral behaviour of large scale monopile foundations could be predicted. Also, for cyclic loading, a justification of reduced displacement accumulation in case of increased soil stresses was found. The activation of lateral resistance below the point of rotation ('toe kick') was found crucial for these effects.

Chapter 2 Geotechnical aspects on monopile foundations for offshore wind turbines

2.1 Overview

Different phenomena occurring during pile installation play an important role for the later load-bearing behaviour. In the context of driven piles in sand, this involves dynamic and cyclic effects on the soil state. In Section 2.2, some experiences regarding the influence of impact and vibratory installation on pile capacity shall be outlined. Known geotechnical phenomena and current research on the soil behaviour during impact and vibratory pile driving are summarised.

The lateral behaviour of offshore monopiles involves a wide range of topics that shall be presented in Section 2.3. First, the basic mechanisms of lateral bedding and the non-linearity of soil springs according to different p-y approaches will be described. The author will address major shortcomings of current offshore guidelines (OGL), especially when applied in the context of offshore wind, and some current works facing these issues. In the recent years, a large number of studies has been carried out on the behaviour of offshore monopile foundations under cyclic lateral loading. Within the framework of laterally loaded piles in sand, cyclic effects of the soil and the pile-soil system need to be discussed, including different methods to assess cyclic strain accumulation. Apart from static and cyclic behaviour, the dynamic response will be addressed. Finally, current knowledge about the influence of the installation method on lateral pile behaviour will be presented.

2.2 Pile installation effects

2.2.1 Pile capacity of driven piles

In engineering practice, the axial capacity of a vibratory driven pile is considered to be lower than that of an impact driven pile. A lot of research has been conducted on the comparison of the axial pile capacity of impact and vibratory driven piles (MOSHER 1987; LAMMERTZ & RICHWIEN 2006; HARTUNG 1994; BOREL et al. 2006; VIPULANANDAN et al. 1990; STAHLMANN et al. 2014). In most cases, the above statement regarding the comparative axial capacity of impact and vibratory driven piles is supported by test results. However, the axial capacity of vibratory driven piles is strongly influenced by installation parameters, e.g. driving frequency (HARTUNG

1994). In some cases, vibratory driven piles show even higher bearing capacities than impact driven piles. The following Figure 2-1 contrasts bearing capacities from vibratory driven piles R_{vibro} and impact driven piles R_{impact} . Markers in the upper-left part indicate higher bearing capacity of impact driven piles.

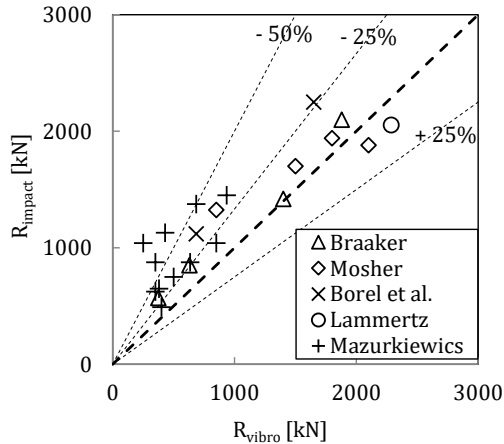


Figure 2-1: Comparison of (axial) resistance of vibratory and impact driven piles (FISCHER et al. 2013)

Explanation on the different pile bearing capacities is mostly given based on empirical relations, such as differing boundary conditions (e.g. relative soil density) or pile driving parameters (e.g. vibratory driving frequency) instead of geotechnical phenomenology. In the opinion of the author these generalised empirical-based findings should not be transferred to the lateral pile capacity without fully understanding the underlying soil mechanical phenomena.

Regarding the lateral bearing capacity, little research is available about differences between impact driven and vibratory driven piles. Within the 'VIBRO project' (GATTERMANN et al. 2015; MOORMANN et al. 2016; ACHMUS et al. 2020), comparative in-situ tests on three pairs of impact and vibratory driven monopiles showed lower or comparable lateral capacity and stiffness of the vibratory driven piles, depending on the penetration speed of the vibratory driven piles. One vibratory driven pile with rather low penetration speed showed almost the same lateral stiffness as the corresponding impact driven piles. LABENSKI (2018) carried out scale model tests on piles with different pile vibratory pile driving parameters resulting in 'cavity' and 'non-

'cavity' vibration modes (see section 2.2.3). Depending on the vibration mode, the lateral capacity of vibratory driven piles was similar to impact driven piles ('cavity' driven piles) or lower ('non-cavity' driven piles).

2.2.2 Impact pile driving

Regarding the soil behaviour due to pile installation processes, a lot of research focussing on axial pile bearing behaviour and driveability was carried out. Different authors used experimental setups with plane, half, and full model tests in combination with solid piles and pipe piles for their investigations. Numerical simulations which will be discussed later. It has to be noted that the penetration of unplugged pipe piles has less influence on the surrounding soil, especially on radial stresses, than the penetration of (partially) plugged pipe piles or even solid piles (WHITE et al. 2005).

The most common procedure to install prefabricated piles such as steel pipe piles is impact pile driving. Due to the impact loading of the soil around and especially underneath the pile, the soil state is affected (LINDER 1977). Figure 2-2 shows the principle of compaction zone under a closed or plugged pile toe and adjacent loosening zones.

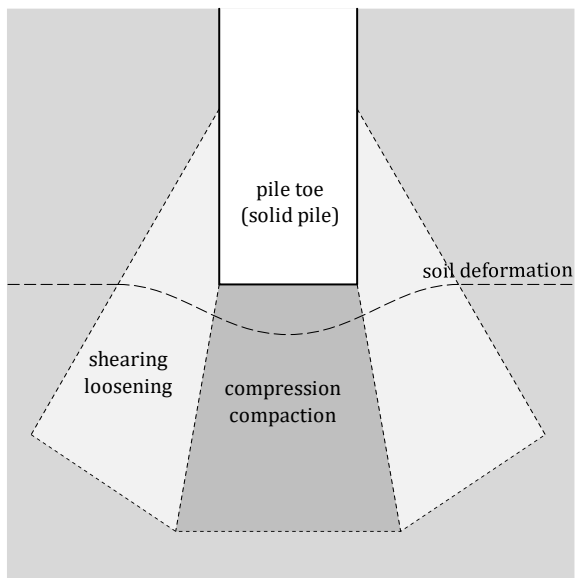


Figure 2-2: Soil compaction and loosening under driven pile (based on LINDER 1977)

To describe the pile driving process by means of wave equation analysis, much experience is available for impact pile driving. Linear-elastic/ideal-plastic and viscous mechanical models are used to describe static (frictional) and dynamic (damping) pile-soil interaction (SMITH 1960; MIDDENDORP 2004). The pile is considered as an elastic bar while the soil (or the pile-soil interaction) is modelled by spring and damper elements as depicted in Figure 2-3. Important model parameters are the maximum interface resistance and the related relative displacement as well as the damping coefficient for both pile shaft and pile toe. Each spring element has a yield strength q_{stat} representing the maximum static (or displacement-dependent) resistance and the corresponding displacement s_q (the so called 'quake'). The spring stiffness is defined as $E_{qs} = q_{stat}/s_q$. Different spring parameters for loading and unloading can be defined. Velocity-dependent resistance q_{damp} is calculated by the damping constant C_{ax} , velocity v and exponent α_{damp} . Spring and damping parameters for pile shaft and pile toe are denoted with indices s and t . Furthermore, acceleration-dependent inertia forces acting on the pile have to be considered (SMITH 1960; JONKER 1987; MIDDENDORP 2004; RAUSCHE 2002). Static, damping and inertia resistance yield

$$q_{stat} = E_{qs} \cdot s \tag{2-1}$$

$$q_{damp} = C_{ax} \cdot v^{\alpha_{damp}} \tag{2-2}$$

$$R_{in} = m_{pile} \cdot a \tag{2-3}$$

Equations (2-1) and (2-2) can be formulated on stress level (as given) or on force level if integrated over the according surfaces (pile shaft, pile toe).

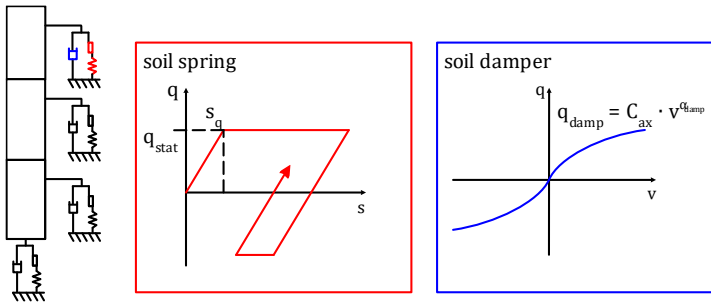


Figure 2-3: 1D model for pile installation

The maximum static pile shaft resistance $q_{s,stat}$ [kN/m^2] of a soil element at a given depth z [m] can be interpreted as interface shear strength τ_s which depends on the normal (= radial) soil stress σ'_{rad} [kN/m^2] acting on the pile shaft (cf. Figure 2-4):

$$q_{s,stat}(z) = \tau_s(z) = \sigma'_{rad}(z) \cdot \tan(\delta) = \gamma' \cdot z \cdot k_0 \cdot \tan(\delta) \quad (2-4)$$

with the effective unit weight of the soil γ' [kN/m^3], the earth pressure coefficient k_0 [-] and the friction coefficient $\tan(\delta)$ [-] (STEVENS et al. 1982). Instead of the definition as stress in [kN/m^2], q_s is often given as line load in [kN/m], acting over the circumference of the pile. Instead of the geostatic approach, the shaft resistance is mostly correlated to cone penetration testing (CPT) readings in practice (TOOLAN & FOX 1977; JARDINE et al. 2005).

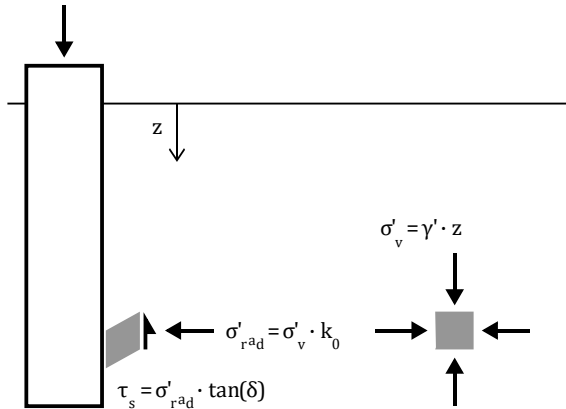
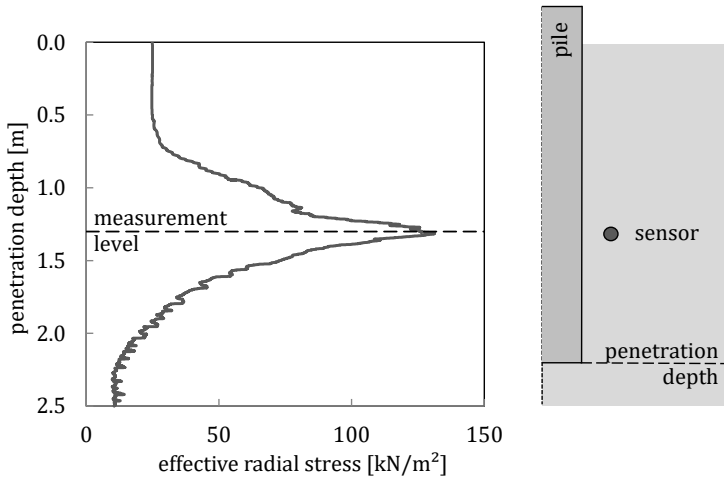


Figure 2-4: Shear stress on pile wall

For a driven pile, VESIĆ (1970) reported a reduction of the local shaft friction $q_s(z)$ with pile penetration L_{pen} [m]. HEEREMA (1978) used the concept of 'friction fatigue' to describe the reduction of the initial local shaft resistance a residual value based on the distance between soil element and pile toe $L_{pen} - z$. Soil stress measurements showed that actually an increase of soil stresses can be observed as the pile toe approaches measuring section, which can be explained by the soil compaction described above (Figure 2-2). The maximum value of soil stresses in the vicinity of the pile is reached shortly before the pile toe reaches the soil element in focus. Afterwards, the soil stresses decrease approximately to initial values (before pile installation) (ALLARD 1990; GAVIN & LEHANE 2003; WITZEL 2004; LÜKING 2010), as shown in Figure 2-5:



**Figure 2-5: Development of radial effective soil stress over pile penetration
(based on FISCHER 2021)**

The height of the non-dimensional (normalized by the overburden pressure $\gamma \cdot z$) soil stress peaks due to pile driving is independent of the depth and decays with increasing distance from the pile in hyperbolic shape (ALLARD 1990). Model tests by FISCHER (2021) revealed that this development is valid for both radial and tangential stresses in the vicinity of the pile.

Another soil mechanical analogy to the reduction of local shaft friction can be given by direct shear tests or interface shear tests where the maximum shear strength is mobilised due to a certain shear displacement and then drops to a residual value due to further shearing. To consider the quasi-cyclic nature of pile penetration due to impact driving, cyclic constant normal stiffness (CNS) shear tests can be used, which show a decrease of normal stress with number of load cycles due to cyclic shearing (FISCHER 2021).

For pile driving simulations, the maximum soil resistance available when the pile toe reaches a soil element is denoted as 'initial' value (even though the 'initial' stress state is already influenced by the approaching pile) and falls to a 'residual' value. According to FISCHER (2021) and ALM & HAMRE (2002), the local static resistance to driving (SRD) of a soil element $q_{s,SRD}$ can be described as function of the distance between the soil element and the pile toe penetration

$$L_{pen} - z.$$

$$q_{s,SRD} = q_{s,res}(z) + \left(q_{s,ini}(z) - q_{s,res}(z) \right) \cdot \beta_z(L_{pen} - z) \quad (2-5)$$

The residual soil resistance is defined as a fraction of the initial soil resistance

$$q_{s,res} = q_{s,ini} \cdot \beta_{res} \quad (2-6)$$

with $\beta_{res,A\&H} = 0.2$ (ALM & HAMRE 2002) and $\beta_{res,Fi} = 0.16$ (FISCHER 2021). The resistance degradation during pile penetration is described by the factor

$$\beta_z = e^{\alpha_{pen} \cdot (L_{pen} - z)} \quad (2-7)$$

with shape factor

$$\alpha_{pen,A\&H} = \frac{\sqrt{q_c / \sigma'_v}}{80} \quad (2-8)$$

according to ALM & HAMRE (2002) for different soil conditions or

$$\alpha_{pen,Fi} = 4.2 - 1.4 \cdot D \quad (2-9)$$

according to FISCHER (2021) (for saturated sand) depending on the soil density D [-]¹:

$$D = \frac{\max n - n}{\max n - \min n} = \frac{\rho_d - \min \rho_d}{\max \rho_d - \min \rho_d} - \frac{1 + \min e}{1 + e} \cdot D_r \quad (2-10)$$

Figure 2-6 shows the degradation factors β_z proposed by FISCHER (2021) and ALM & HAMRE (2002) over the distance between soil element and penetration depth $L_{pen} - z$.

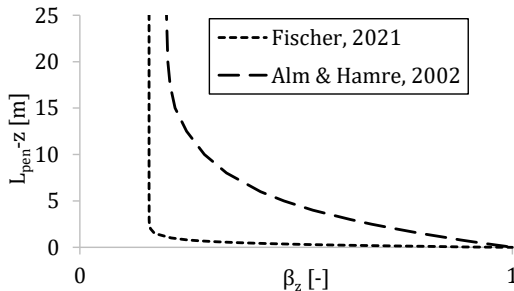


Figure 2-6: Shaft friction degradation factors β_z for offshore conditions

¹ D is a dimensionless measure for the soil density based on maximum, minimum and actual porosity n . D is used as an alternative to the relative density D_r which is based on the void ratio e .

The plot can be interpreted as a reduction factor for the (initial) soil resistance at end of pile driving (EoD). The approach of FISCHER shows a more pronounced decay of pile resistance compared to the approach of ALM & HAMRE.

2.2.3 Vibratory pile installation

General/installation method

Vibratory pile driving is an installation method commonly used for pipe piles, steel profiles and sheet piles in sand. Fundamentals of the vibratory driving method have been described by VIKING (2006), MASSARSCH et al. (2017), and many other authors. Here, the most important installation parameters and known soil mechanical phenomena shall be described.

For vibratory pile installation, a sinusoidal centrifugal force F_c [kN] over time t [s] which depends on the eccentric moment M_e [kg·m] and the angular driving frequency ω_d [rad/s] is applied at the pile head. The driving frequency f_d can also be given in [Hz], the corresponding cycle period is $1/f_d$ [s]

$$F_c(t) = M_e \cdot \omega_d^2 \cdot \sin(\omega_d \cdot t) \quad (2-11)$$

$$\omega_d = f_d \cdot 2\pi \quad (2-12)$$

A static surcharge or bias force F_{bias} [kN] is given by the deadweight of the system and may be increased by a pushing apparatus or lowered by line pull of a crane. The centrifugal force results in pile vibration that may be described as acceleration a [m/s²], velocity v [m/s] and displacement s [m] over time t [s]. Figure 2-7 (left) shows the vertical position z [m] of a vibratory driven pile over time. The pile penetration L_{pen} [m] is overlaid by the dynamic pile displacement s . The penetration speed v_{pen} [m/s] is the gradient of the pile penetration L_{pen} and must not be confused with the vibration velocity v . On the right side of the figure, the velocity v is plotted over the dynamic pile movement $L_{\text{pen}} + s$. All parameters are defined positive downwards (in direction of pile penetration).

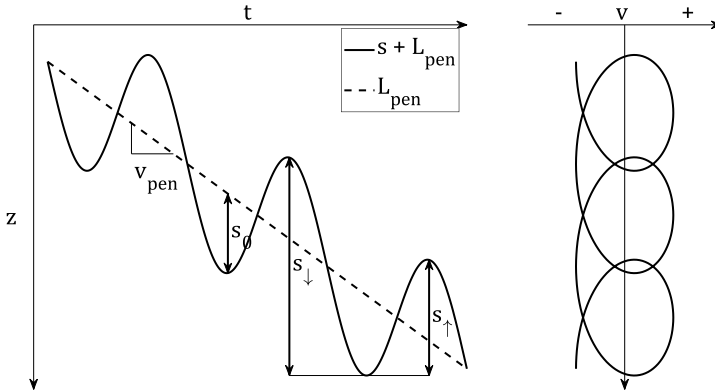


Figure 2-7: Pile movement during vibratory driving

The theoretical peak displacement amplitude s_0 [m] depends on the eccentric moment of the vibratory hammer M_e [kg·m] and the dynamic mass m_{dyn} [kg], which is the sum of all moving parts of pile and hammer (pile, clamps, gearbox, not suppressor).

$$s_0 = M_e / m_{dyn} \quad (2-13)$$

To describe the driving mode (see below), the upwards and downwards directed pile displacements per cycle s_{\uparrow} and s_{\downarrow} can be characterised as central parameters. The permanent penetration or set per cycle s_{set} can be calculated as

$$s_{set} = s_{\downarrow} - s_{\uparrow} = v_{pen} / f_d \quad (2-14)$$

Rigid body assumption

For long piles, the propagation of the sinusoidal force through the pile can be regarded as a wave propagation problem described by stress wave theory, as commonly applied for impact driven piles (see Section 2.2.2). Due to the long period $1/f_d$ compared to the contact time of an impact hammer, the problem may be simplified by considering the pile as a rigid body (VIKING 2002). Based on the driving frequency f_d [Hz] and wave travel time T_{wave} [s], this is valid if

$$\frac{1}{f_d} \gg \frac{2 \cdot L_{pile}}{c_{pile}} = T_{wave} \quad (2-15)$$

with

$$c_{\text{pile}} = \sqrt{E/\rho} \quad (2-16)$$

holds true. The wave travel time T_{wave} is defined by twice (upwards and downwards travelling wave) the pile length L_{pile} [m] divided by the wave speed in the pile c_{pile} [m/s], which depends on the modulus of elasticity E [N/m²] and the density ρ [kg/m³] of the pile material (EA-Pfähle 2012).

Pile-soil behaviour during vibratory driving

As a result of the dynamic motion of the pile, the soil particles in the vicinity of the pile along the pile shaft are excited and reach a state of free fall, resulting in a severe reduction of the effective normal stresses acting on the pile shaft. This 'cyclic mobility' (VIKING 2006) may be supported by soil liquefaction due to excess pore water pressures in case of saturated soil conditions. As a consequence, the pile shaft resistance is drastically reduced. This behaviour is often termed 'fluidisation' or 'pseudo-liquefaction'. The pile-soil interaction at the pile shaft can then be described as viscous (RODGER & LITTLEJOHN 1980). Thus, the pile toe resistance is dominant for vibratory driving in granular soils (MASSARSCH et al. 2022).

Regarding the behaviour of the soil beneath the pile toe, different explanations can be found in the literature. RODGER & LITTLEJOHN (1980) distinguish 'viscous' and 'impact' vibratory driving modes². 'Viscous' vibratory driving mode is expected to occur in loose cohesionless soils and for piles with low toe resistance. The soil underneath the pile toe is excited and fluidised. The pile toe always has contact to the surrounding soil. For penetration, the pile-vibro assembly has to overcome the reduced resistance of the fluidised soil. The degree of reduction of soil resistance due to fluidisation depends on driving frequency and acceleration amplitude. For the static load-displacement relationship given in Figure 2-3, the pile resistance q_s (or shear strength τ_s) is reduced depending on the acceleration amplitude as shown in Figure 2-8.

In 'impact' vibratory driving mode, the soil beneath the pile toe shows elasto-plastic behaviour with equal loading and unloading stiffness. The maximum pile toe resistance is mobilised during downwards movement of the pile for penetrative motion of the pile. During upward

² 'Viscous' and 'impact' vibratory driving were also called 'fast' and 'slow' vibratory driving, respectively. The first-mentioned terms are used here to avoid confusion with 'cavity' and 'non-cavity' vibratory driving.

motion of the pile-vibro assembly, the pile toe loses contact with the soil ('out-of-contact motion').

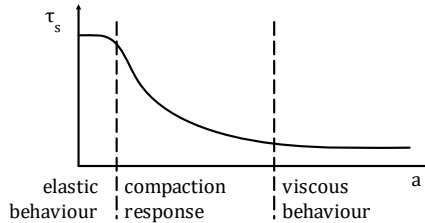


Figure 2-8: Relationship between shear strength τ_s and acceleration amplitude a (based on RODGER & LITTLEJOHN 1980)

(DIERSSEN 1994) distinguished between 'cavity' and 'non-cavity' vibratory driving³, depending on whether or not the pile toe loses contact to the underlying soil during upwards motion. Both modes are subtypes of 'impact' vibratory driving according to RODGER & LITTLEJOHN (1980). Looking at the soil displacements, VOGELSANG (2017) found out that no actual 'cavity' is produced underneath the pile toe but probably a liquified soil-water mixture is pumped into this region and pumped out again. The development of pile toe resistance during cyclic movement is depicted in Figure 2-9. The main difference between 'cavity' (left) and 'non-cavity' (right) installation originates from a rotation of primary stresses (change of polarisation) during 'out-of-contact' motion (phase II) of 'cavity' driving. This causes a 'swept-out-of-memory' effect and thus a soil stiffness similar to that of an unloaded sample. Similar behaviour can be observed in drained triaxial shear tests with two-way loading (compression and extension) (CUDMANI 2001).

The development of 'cavity' or 'non-cavity' driving mode depends on vibration parameters driving frequency f_d , eccentric moment M_e and bias force F_{bias} as well as the soil state parameters density D_r and mean stress p' . 'Cavity' driving mode is encountered in dense sand using high eccentric moment and high driving frequency while 'non-cavity' driving is expected in loose sand with low eccentric moment and large surcharge force (CUDMANI 2001). VOGELSANG

³ 'Cavity' and 'non-cavity' vibratory driving were originally called 'slow' and 'fast' vibratory driving as well. Here, the nomenclature used by CUDMANI 2001 is used to avoid confusion with 'viscous' and 'impact' vibratory driving modes.

(2017) observed an influence of the magnitude and relation of upwards and downwards directed movements per cycle s_U and s_D on the installation mode. Smaller displacement amplitudes with small upwards motion led to 'non-cavity' mode installation processes with maximum mobilised pile toe forces equal to those mobilised by a monotonic (jacked) installed pile. Large displacement amplitudes with large upwards motions led to 'cavity' mode installation processes with lower mobilised pile toe resistance. Cavity mode "is considered (...) the most widely encountered case" (MASSARSCH et al. 2022).

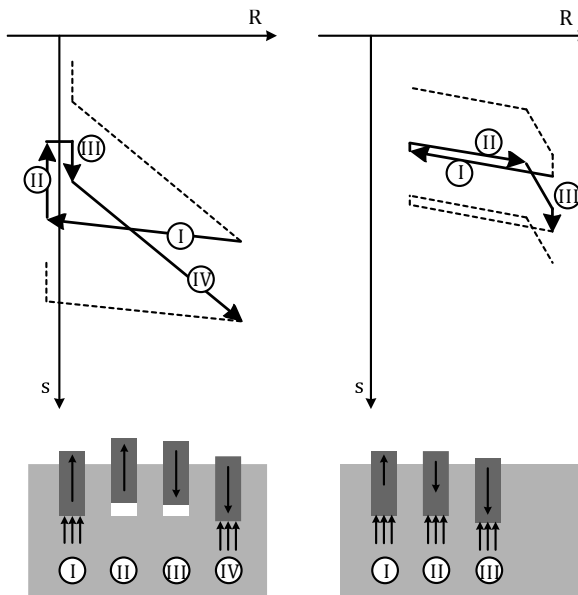


Figure 2-9: Pile toe behaviour during 'cavity' (left) and 'non-cavity' (right) vibratory pile driving

Without actual considering the vibratory driving modes, the soil models and wave equation analysis developed for impact driving described in section 2.2.2 have successfully been used to model vibratory pile driving (MIDDENDORP & JONKER 1988; RAUSCHE 2002; STEIN 2018). The reduction of the soil resistance due to any effects of vibratory driving is considered by global β -factors (JONKER 1987), comparable to the reduction of local shaft friction used to model impact pile driving (cf. Section 2.2.2). MORIYASU et al. (2018) detected a reduction of local shaft friction

(friction fatigue) also in the context of vibratory pile installation by means of strain measurements along the shaft of vibro-driven piles.

Effects on soil state

Experimental half-model tests (REMSPECHER et al. 2019a) and numerical simulations (DARYAEI et al. 2018; CHRISOPOULOS et al. 2017) showed the development of a loosening zone in the vicinity of the pile (wall) and a compaction zone in further distance. According to REMSPECHER et al. (2019a), this effect can be traced to the pile toe penetration and is not influenced by further penetration and passing of the pile shaft. DARYAEI et al. (2018) showed influences of the driving frequency on the extent of loosening and compaction zone. Similar effects also occur due to impact pile driving (DARYAEI et al. 2019; STAUBACH et al. 2020).

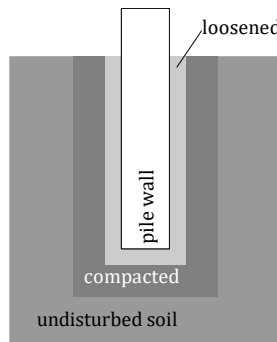


Figure 2-10: Soil state changes due to pile driving

Numerical simulations showed a severe reduction of effective soil stresses indicating soil liquefaction in the vicinity of the pile, even in sand with high permeability (CHRISOPOULOS et al. 2017). Measurements by FISCHER et al. (2013) in 0.1 m distance to a vibrated and an impact driven model pile ($D_{\text{pile}} = 0.36$ m) showed no obvious pore water pressure build-ups. In case of the impact driven pile, a development of effective soil stresses over pile penetration was observed fitting into the framework of friction fatigue (FISCHER 2021, see section 2.2.2). During vibratory driving, the stress state remained more or less unchanged. DARYAEI et al. (2018) also detected soil stress concentrations under the pile toe of low-frequency vibrated piles. This behaviour is widely known for impact driven piles, as shown above in Figure 2-2 (LINDER 1977).

MASSARSCH et al. (2017) and MASSARSCH et al. (2020) presented a variety of field measurements and theoretical considerations on vibratory pile installation and vibratory compaction projects. As the dynamic change of soil stresses is linked to the particle velocity of the soil (MASSARSCH et al. 2022) they concluded that horizontal ground vibrations indicate stress waves which lead to a permanent increase of lateral earth pressure around vibratory driven piles. Stress ratios ($k_i = \sigma_h / \sigma_v$) estimated based on CPT readings and dilatometer measurements were shown to increase due to vibratory compaction. The change of stress ratio from k_0 (earth pressure at rest) towards k_p (passive earth pressure) with a final value of k_1 (earth pressure after compaction) is interpreted as overconsolidation, advancing with the number of loading cycles. In most cases the ratio of stress ratios lay in a range of $k_1/k_0 \approx 1 \dots 4$ with higher values for soils with lower cone resistances. It has to be admitted that the majority of cases dealt with in MASSARSCH et al. (2017) and MASSARSCH et al. (2020) were compaction projects where the initial soil density can be considered rather loose, especially in relation to offshore conditions with dense, already overconsolidated sand.

Effects of vibratory driving frequency

The vibration frequency f_d has a great influence on vibratory pile installation. MASSARSCH et al. (2017) and MASSARSCH et al. (2022) distinguish between driving at low frequency (at and below the system's resonance frequency ($f_d \leq f_{0,inst}$) and high frequency ($f_d > 1.5 \cdot f_{0,inst}$). The resonance frequency of the vibro-pile-soil system $f_{0,inst}$ is not a soil parameter but depends on parameters such as dynamic mass and pile penetration (MASSARSCH et al. 2022). At system resonance, pile and soil move in phase leading to little relative displacements and thus elastic soil behaviour. The pile penetration speed is reduced when driving near system resonance (MASSARSCH et al. 2022) while faster pile penetration can be achieved when driving above system resonance (HARTUNG 1994). This can be explained by a reduced driving resistance along the pile shaft of the plastified soil (about 10% of static shaft resistance) when driving above system resonance ($f_d > 1.5 \cdot f_{0,inst}$) and a high shaft resistance of the almost elastic soil (about 100% of static shaft resistance) at system resonance (MASSARSCH et al. 2021).

The displacement amplitude is amplified at system resonance and the energy transmission between pile and soil is optimal (MASSARSCH et al. 2022). The ground vibrations increase (MASSARSCH et al. 2021) which leads to soil compaction around the pile. Above system resonance, an arching zone is formed which leads to a reduction of soil stresses around the pile

(MASSARSCH et al. 2022). As a consequence, the resulting axial pile bearing capacity, especially the toe resistance, is high for piles driven at system resonance (MASSARSCH et al. 2022) and reduces with increasing driving frequency (HARTUNG 1994).

2.3 Lateral pile behaviour

2.3.1 Lateral bedding

The lateral behaviour of a buried pile can be treated as the load-deflection behaviour of a bedded beam which can be described by the equation

$$\mathbf{P} = \mathbf{K} \cdot \mathbf{y} = (\mathbf{K}_{\text{pile}} + \mathbf{K}_{\text{soil}}) \cdot \mathbf{y} \quad (2-17)$$

with the load vector \mathbf{P} , the stiffness matrices \mathbf{K} for pile and soil and the deformation vector \mathbf{y} . The loading vector may consist of a horizontal force and moment at the mudline. The pile stiffness matrix is commonly known and elastic behaviour is assumed for the pile material. The formulation of the soil stiffness will be discussed in the following sections. In case of a linear soil behaviour, the pile deflection and stress resultants can easily be determined. For non-linear soil behaviour, an iterative approach is necessary.

The lateral bedding of vertical members in soil is commonly described as the relationship between the soil reaction, defined as line load p_{py} [kN/m] and lateral deflection y [m]. The bedding stiffness E_{py} is defined as

$$E_{py} = \frac{p_{py}}{y} \quad (2-18)$$

This approach can be traced to WINKLER (1867), who used linear elastic springs for bedded beams to determine internal forces and deflections. TERZAGHI (1955) defined the spring stiffness of the soil as coefficient of horizontal subgrade reaction⁴ E_{py} . Based on elasticity theory, the following relation between spring stiffness and oedometric stiffness E_{oed} is proposed:

$$E_{py} = \frac{E_{oed}}{1.35} \quad (2-19)$$

⁴ The original formulation of TERZAGHI is based on the subgrade reaction as force per unit area. Here, the subgrade reaction is defined as line load (force per unit length) and the corresponding stiffness as force per unit area.

TERZAGHI (1955) assumed linear behaviour of the soil for soil reactions $p_{py} < 0.5 \cdot p_{py,ult}$. The main soil strains arise within a pressure bulb whose horizontal extent depends on the pile diameter (approximately $3 \cdot D_{pile}$ around the pile axis).

2.3.2 Eigenfrequency

The eigenfrequency of OWT structures, and therefore the dynamic stiffness of the foundation, is one key parameter for the design of OWT (ARANY et al. 2017). The eigenfrequency of a single pile can be estimated by analogy to a simple cantilever or a linear-elastically bedded beam (ACHMUS 2011). For accurate calculation of the dynamic response of a bedded beam, stiffness, damping, and mass parameters are necessary. Equation (2-20) shows the general form of the differential equation for a dynamic system with the load vector \mathbf{P} , stiffness, damping and mass matrices \mathbf{K} , \mathbf{C} , and \mathbf{M} and the deflection vector \mathbf{y} over time t .

$$\mathbf{P}(t) = \mathbf{K} \cdot \mathbf{y}(t) + \mathbf{C} \cdot \dot{\mathbf{y}}(t) + \mathbf{M} \cdot \ddot{\mathbf{y}}(t) \quad (2-20)$$

For an offshore monopile modelled as an elastically bedded beam, stiffness and mass of the pile are known. The soil stiffness can be taken as initial or secant stiffness of appropriate p-y curves. Based on measurements from offshore structures, KALLEHAVE et al. (2012) and TODO BOM et al. (2020) showed that the eigenfrequency estimation using initial spring stiffness $E_{py,ini}$ according to offshore guidelines (see Section 2.3.3) underestimates the dynamic stiffness of the soil. Small-strain stiffness parameters (e.g. dynamic shear modulus G_{dyn}) are suggested to be used for eigenfrequency estimation.

Regarding soil damping, radiation damping (resulting from wave radiation) and material damping (resulting from hysteretic energy loss) need to be distinguished (CARSWELL et al. 2015; DAMGAARD et al. 2014). Radiation damping can be neglected at frequencies below 1 Hz (SHIRZADEH et al. 2013). Material damping can be described by viscous dashpots.

PRENDERGAST & GAVIN (2016) used a number of different formulations to determine the dynamic spring stiffness for a bedded Winkler beam from small-strain soil stiffness. Eigenfrequency and damping of the pile-soil system were calculated, e.g. to investigate the effect of scour on natural frequency of offshore monopiles (PRENDERGAST et al. 2015) or for back-analysis of dynamic soil parameters (model fitting by changing mass and stiffness) (PRENDERGAST et al. 2019). The small strain shear stiffness of the soil G_{dyn} was obtained from correlations with CPT readings (PRENDERGAST et al. 2014). Damping parameters were obtained as linear combination of system

stiffness and mass (Rayleigh approach). Alternatively, the approach of LEE et al. (1988) can be used to estimate soil damping, as shown in (STEIN 2020).

2.3.3 Non-linear soil springs (p-y approaches)

Most p-y approaches use non-linear p-y springs defined by an initial soil (spring) stiffness $E_{py,ini}$ and an ultimate soil reaction $p_{py,ult}$. Figure 2-11 shows the general shape of p-y curves for the static and cyclic loading case.

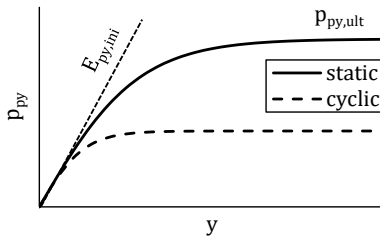


Figure 2-11: General static and cyclic p-y curves

Current offshore guidelines (OGL, e.g. DNV-OS-J101; API RP 2GEO) use a hyperbolic tangent function based on MURCHISON & O'NEILL (1984) to describe the non-linear behaviour of the soil springs. The initial soil spring stiffness $E_{py,ini}$ is increasing linearly with depth.

$$p_{py}(y) = p_{py,ult} \cdot \tanh\left(\frac{E_{py,ini}}{p_{py,ult}} \cdot y\right) \quad (2-21)$$

$$E_{py,ini} = m_h \cdot z \quad (2-22)$$

$$m_h \left[\frac{\text{MN}}{\text{m}^3} \right] = 0.1589 \cdot e^{0.1411 \cdot \varphi' [^\circ]} \quad (2-23)$$

For sand, the gradient of the initial soil stiffness m_h is a function of the relative soil density D_r or the soil friction angle φ . OGL give tabulated values for m_h based on soil friction angle. Figure 2-12 shows the values given in API RP 2GEO (OGL) as well as a power law found in the literature (THIEKEN et al. 2015) and a best fit using an exponential law (Equation (2-23)).

The ultimate bedding resistance $p_{py,ult} = A_{pu} \cdot p_u$ is derived from theoretical assumptions regarding soil mechanical failure modes (see REESE et al. 1974) and an empirical correction factor A_{pu} .

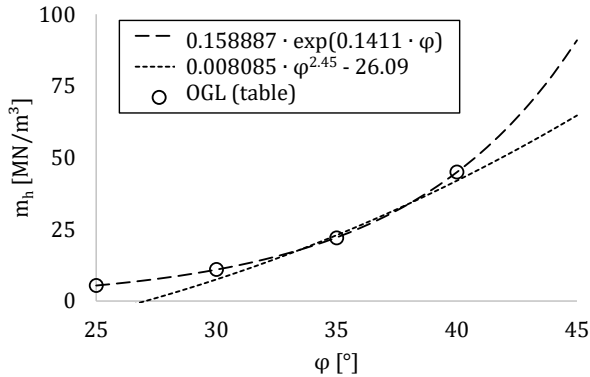


Figure 2-12: Gradient of initial lateral soil stiffness as function of soil friction angle

The p-y approach developed by MURCHISON & O'NEILL (1984), which is used in the OGL, is a modification of an earlier approach by REESE et al. (1974) which is based on lateral load tests carried out on Mustang Island (COX et al. 1974). For details on the p-y formulation, see API RP 2GEO or REESE et al. (1974).

The Mustang Island tests (Cox et al. 1974) were executed on slender piles which are not comparable to monopiles used in offshore wind farms. Cyclic p-y curves were also established based on test results with up to 200 load cycles. These cyclic curves, however, simply consider the reduced bearing capacity after a number of cycles. The hysteretic behaviour of the soil due to repeated loading cannot be described by the model.

Regarding the suitability to describe the load-displacement behaviour of monopile foundations, the p-y method used in the OGL has some major shortcoming which are still current topics in research:

1) pile geometry

Monopiles used in current offshore wind projects have diameters far greater than those used in the oil and gas industry which was the background for the development of the p-y curves presented in current OGL. Ultimate bearing capacities according to classical p-y approaches lead to unrealistic values and an overestimation of the lateral bearing capacity of monopiles (ACHMUS 2011). Apart from that, monopiles have much

higher bending stiffness and relatively short embedment lengths, leading to a 'toe kick' instead of a vertical bending line at the pile toe (ACHMUS 2009).

2) soil stiffness

The initial stiffness does not represent the soil stiffness for small strains, which leads to an underestimation of the initial pile stiffness and thus to an underestimation of the structure's eigenfrequency (KIRSCH et al. 2014). Apart from that, the soil stress state (linear according to current OGL) is not depicted correctly, as it is better described by an exponential law (increasing under-linear with depth) (KALLEHAVE et al. 2012).

3) cyclic behaviour

Cyclic p-y curves with reduced ultimate bearing capacity (but unaltered initial stiffness) are used to account for soil degradation due to cyclic loading. The load-displacement behaviour described by these 'cyclic' curves has no physical meaning referring to cyclic/hysterical soil behaviour. Some outdated OGLs (GL IV-2) additionally demanded a vertical bending line at the pile toe as a design criterion to ensure beneficial behaviour under cyclic loading though the meaningfulness of this requirement is questionable (ACHMUS 2009).

4) installation effects

The pile installation procedure has not been specifically considered in the design codes. However, the Mustang Island test piles (Cox et al. 1974) as well as the majority of all recent offshore monopiles were installed using impact driving. Therefore, one may assume that modifications of the original p-y formulations which are based on experiences in offshore practice are applicable to impact driven piles. p-y formulations based on 3D numerical simulations can be assumed not to be biased by the installation method as the installation processes and their influence on the surrounding soil cannot (yet) be accurately modelled by numerical methods.

2.3.4 Influence of pile geometry

The influence of the pile diameter on the lateral soil stiffness and ultimate capacity (the so called 'diameter effect') has been addressed by several authors. KALLEHAVE et al. (2012) proposed an increase of the initial stiffness of the p-y curves for large pile diameters due to the decrease of shear strain in a pressure bulb whose extension depends on the pile diameter. (KIRSCH et al.

2014) suggested to use a reduced friction angle for large pile diameters, resulting in reduced lateral soil stiffness and capacity.

Apart from that, the flexural stiffness of monopiles is much higher than that of slender piles. Flexible and rigid piles can be distinguished based on their flexural stiffness EI [kNm^2], the oedometric soil stiffness E_{oed} [kN/m^3] and the pile's embedment length L_{pen} [m]. POULOS & HULL (1989) use a relation which is here reformulated to a dimensionless bending stiffness EI^* to distinguish between rigid and flexible piles. For a uniform soil profile ($E_{\text{oed}}(z) = \text{const.}$), the dimensionless stiffness is

$$\frac{1}{EI^*} = \frac{E_{\text{oed}} \cdot L_{\text{pen}}^4}{EI} \quad (2-24)$$

and for a soil profile where the soil stiffness increases linearly with depth EI^* yields

$$\frac{1}{EI^*} = \frac{\delta E_{\text{oed}} \cdot L_{\text{pen}}^5}{\delta z \cdot EI} \quad (2-25)$$

Table 2-1 gives reciprocal values of the dimensionless stiffness $1/EI^*$ for rigid and stiff piles in uniform and linear soil profiles. Piles with a dimensionless stiffness in between cannot be considered perfectly rigid nor flexible.

Table 2-1: Pile stiffness distinction according to (POULOS & HULL 1989)

	rigid pile	flexible pile
soil profile	$1/EI^*$	
uniform	< 4.8	> 390
linear	< 1.6	

Another important difference between rigid and flexible piles regarding soil reaction is the pile toe deflection or 'toe kick'. Flexible/slender piles show zero deflection and rotation at the pile toe and can be considered as a clamped cantilever. In this case, an increase of the pile length has no influence on the pile head deflection at a given load level. Laterally loaded, rigid piles, on the contrary, can be characterised by a point of rotation and a so called 'toe kick'. Figure 2-13 shows sketches of a flexible (left) and a rigid (right) pile subjected to combined lateral force and moment loading and their bedding resistances.

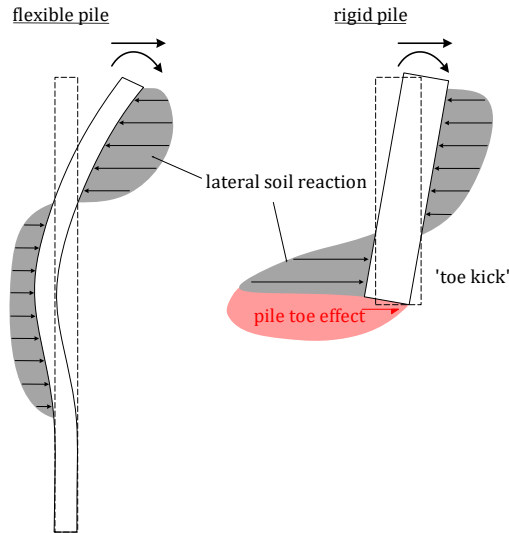


Figure 2-13: Lateral bedding behaviour of flexible (left) and rigid (right) piles

The mobilisation of soil resistances along the pile shaft (grey shaded areas) depends on soil stiffness and pile deflection. In case of the flexible pile, deflection and rotation at the pile toe are zero, so no soil resistances are mobilised here. The rigid pile shows a constant rotation over the pile length and a 'toe kick'. The grey shaded area indicates the soil reaction according to the Winkler approach. Apart from that, spatial bedding resistance underneath the pile toe level (red shaded area) and/or shear stresses at the pile toe (red arrow) may be mobilised. BURD et al. (2017) and ZHANG & ANDERSEN (2019) introduce (among other features) an additional non-linear spring at the pile toe to consider the lateral resistance mobilised by the shearing of the pile base. According to FU et al. (2020), the pile base resistance can be determined in analogy to the soil behaviour direct simple shear tests. THIEKEN et al. (2015) introduced a stretching factor to modify the springs close to the pile toe and increase the local stiffness and ultimate bedding resistance depending on the distance from the pile toe.

2.3.5 Soil stress state or depth dependency

In the original formulation of the p-y curves by REESE et al. (1974) (see Equations (2-21) and (2-22)), the term $m_h \cdot z$ displays the linear depth-dependency of the (initial) bedding stiffness.

As the soil stiffness depends on the soil material and stress level ($\sigma' \sim \gamma' \cdot z$), GEORGIADIS (1983) introduced an equivalent depth z_{eq} to account for different soil stiffnesses and unit weights in layered soils. However, even in a homogenous soil, the assumption of a linear increase of the bedding stiffness with stress level or depth is doubtful. A power law with exponent < 1 is often used to describe the stress dependency of the soil stiffness (OHDE 1939). The oedometric soil stiffness E_{oed} [kN/m²], for example, can be calculated by

$$E_{oed} = E_{oed,ref} \cdot p_{ref} \cdot \left(\frac{p'}{p_{ref}} \right)^{\lambda_{E_{oed}}} \quad (2-26)$$

with the reference pressure $p_{ref} = 100$ kN/m², the oedometric stiffness at reference pressure $E_{oed,ref}$ [kN/m²] and an exponent $\lambda_{E_{oed}} < 1$.

WIEMANN (2007) and KALLEHAVE et al. (2012) used this approach for a better representation of the soil stiffness profile. Equation (2-27) gives the initial bedding stiffness $E_{py,ini}$ [kN/m²] over depth z [m] according to the modification of KALLEHAVE et al. (2012). m_h [kN/m³] is the gradient of initial subgrade reaction according to API RP 2GEO, $z_{ref} = 2.5$ m is the reference depth and the exponent $\lambda_z = 0.6$ was proposed by KALLEHAVE et al. (2012).

$$E_{py,ini} = m_h \cdot z_{ref} \cdot \left(\frac{z}{z_{ref}} \right)^{\lambda_z} \quad (2-27)$$

2.3.6 Small strain stiffness

Offshore guidelines describe the initial soil stiffness $E_{py,ini}$ as function of soil friction angle, which is a shear strength parameter. For dynamic problems, such as eigenfrequency estimations, dynamic soil properties (e.g. dynamic stiffness) should be used (PRENDERGAST et al. 2015). Even though eigenfrequency analysis and load-deflection behaviour are normally treated separately, the dynamic soil stiffness, which is considered to be equal to the small strain stiffness, may be relevant for the deflection at small load levels as well. The applicability of dynamic versus static soil parameters may be distinguished based on the strain level (EA Baugruddynamik 2019). The following Figure 2-14 shows the qualitative decrease of the dynamic shear stress G_{dyn} normalised by the maximum value $G_{dyn,max}$ with shear strain γ in the form

$$\frac{G_{dyn}}{G_{dyn,max}} = \frac{1}{1 + \gamma^b \cdot 10^3} \quad (2-28)$$

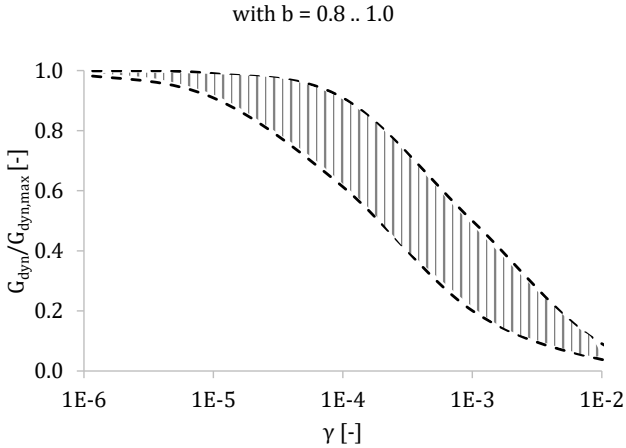


Figure 2-14: Decrease of dynamic shear modulus with shear strain

A more sophisticated approach derived from a large database of dynamic soil tests with different sands and at different stress levels was developed by OZTOPRAK & BOLTON (2013).

A formulation of the soil stiffness as function of strain level is used by KIRSCH et al. (2014), THIEKEN et al. (2015), and SURYASENTANA & LEHANE (2016) to include the dynamic soil stiffness as initial stiffness into the p-y curves and get a smooth transition to the soil stiffness for the static case. According to KIRSCH et al. (2014), the relation between dynamic and static oedometric soil stiffness yields

$$\frac{E_{\text{oed,dyn}}}{E_{\text{oed,stat}}} = 10^{-0.42 \cdot \log(0.0006 \cdot E_{\text{oed,stat}})} \quad (2-29)$$

with the static oedometric modulus $E_{\text{oed,stat}}$ in $[\text{MN}/\text{m}^2]$.

As the main part of soil strain arises within a lateral extent of about $3 \cdot D_{\text{pile}}$ around the pile axis (see Section 2.3.1), larger pile diameters D_{pile} lead to a reduced strain level at equal pile deflection y . KALLEHAVE et al. (2012) account for the resulting increased soil stiffness by adding another pile diameter term to Equation (2-27):

$$E_{\text{py,ini}} = m_h \cdot z_{\text{ref}} \cdot \left(\frac{z}{z_{\text{ref}}} \right)^{\lambda_z} \cdot \left(\frac{D_{\text{pile}}}{D_{\text{pile,ref}}} \right)^{\lambda_D} \quad (2-30)$$

with $D_{\text{pile,ref}} = 0.61 \text{ m}$ and $\lambda_D = 0.5$.

2.3.7 Cyclic effects

Definition of cyclic loading

Cyclic loading is defined as repeated loading and unloading processes of a material or structure with a loading rate small enough to exclude dynamic effects such as inertia forces. Thus, even though present in impact and vibratory pile driving, these processes cannot be described solely by cyclic loading effects. Cyclic loading is characterised by an average load level X^{av} and a loading amplitude X^{ampl} , resulting in min and max values $X^{max} = X^{av} + X^{ampl}$ and $X^{min} = X^{av} - X^{ampl}$ where X may be any loading property, e.g. force, moment, stress, or, in case of deflection controlled cyclic loading, displacement or strain. Regular cyclic loading is characterised by packages of load cycles with equal mean value and amplitude. Definitions are given in Figure 2-15 which shows force-controlled one-way cyclic loading. In the upper part of the figure, the force H is plotted over time t or number of cycles N . As the loading rate has no influence on the system behaviour, the relation between N and t (the loading frequency) is of no importance. This is an important difference between cyclic and dynamic effects! In the lower part of the figure, the deflection u is plotted over time or number of cycles.

In the literature, different counting methods for the cycle number N exist. Traditionally, for one-way loading, the first cycle ends after one loading and full unloading process, as indicated by the blue labels in Figure 2-15. A displacement offset u_{offset} can be defined at the point where the minimum load level is reached the first time. Other conventions exist for symmetric or asymmetric two-way loading. NIEMUNIS et al. (2005) developed a high cyclic accumulation (HCA) model which describes the cyclic soil behaviour at average stress/strain level after the first (= 'irregular') cycle. Thus, the cycle count of the HCA model starts with $N_{reg} = 0$ at $X = X^{av}$ during the loading phase after the first ('irregular') cycle, indicated by green labels in Figure 2-15.

The load or deflection resulting from cyclic loading may be described by a permanent value X^{perm} , describing the state after N cycles at full unloading, or an accumulated value X^{acc} , describing the state at average level during cycle N_{reg} .

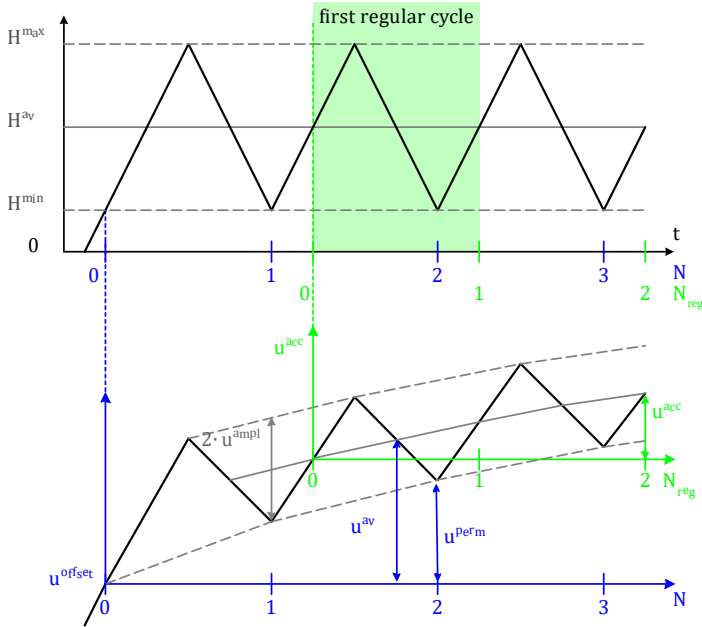


Figure 2-15: Definition of cyclic loading parameters and cycle count

Material behaviour of sand due to cyclic loading

Prior to cyclic laterally loaded piles, the behaviour of granular soils due to cyclic loading shall be addressed. In case of regular cyclic loading at a load level of below about 70% to 80% of the failure load, the strain accumulation can be described by a function f_N [-] which is the relation between the permanent strain after the N^{th} cycle $\varepsilon(N)$ [-] and the strain after the first cycle $\varepsilon(N=1)$ [-]:

$$\varepsilon(N) = \varepsilon(1) \cdot f_N(N) \quad (2-31)$$

Rather simple logarithmic or power laws may be used to define f_N for a limited number of cycles (see below). A more sophisticated method to predict cyclic behaviour of granular soil is the explicit HCA model by NIEMUNIS et al. (2005). The accumulated strain ε^{acc} (after the first, irregular cycle, see Figure 2-15) is described by the flow rule m multiplied with a number of empirical functions:

$$\varepsilon^{\text{acc}}(N_{\text{reg}}) = m \cdot f_{\text{ampl}} \cdot f_p \cdot f_Y \cdot f_e \cdot f_\pi \cdot f_N \quad (2-32)$$

These functions describe the influence of the number of cycles N_{reg} (f_N), the strain amplitude $\varepsilon^{\text{ampl}}$ (f_{ampl}), the void ratio e (f_e), the average mean effective stress p^{av} (f_p) the average stress ratio $q^{\text{av}}/p^{\text{av}}$ (f_r) and the loading polarisation π (f_π). Definitions of the functions and parameters are listed in Appendix G. For instance,

- a higher average pressure level p^{av} leads to a lower strain accumulation rate $\dot{\varepsilon}^{\text{acc}}$ at constant stress ratio $q^{\text{av}}/p^{\text{av}}$,
- a higher stress ratio $q^{\text{av}}/p^{\text{av}}$ leads to a higher strain accumulation rate $\dot{\varepsilon}^{\text{acc}}$ at constant average stress level p^{av} , and
- the cyclic preloading history depends on the number N_{reg} and amplitude $\varepsilon^{\text{ampl}}$ of prior cycles (WICHTMANN 2016).

In contrast to the formulations of HETTLER (1981), STEWART (1986), and others, the HCA model does not consider the first cycle of cyclic loading but starts at the second cycle with $N_{\text{reg}} = 0$. As explained above, the first cycle is regarded as an irregular cycle, showing a very different load-bearing behaviour than the subsequent cycles. As shown in Figure 2-15, an additional amount of loading has to be applied to reach the average loading level of the subsequent cycles. When using the HCA model, the irregular cycle has to be computed separately using an implicit soil model.

WICHTMANN et al. (2004) and LE (2015) investigated the influence of polarisation changes in cyclic laboratory tests on sand. 'Polarisation' is defined as the direction of the oscillation of cyclic loading (in the stress plane). The term 'multidirectional' with regard to stress amplitudes is explained by a cyclic triaxial test where the stress components σ_1 and σ_3 oscillate in different phases (out-of-phases cycling according to NIEMUNIS et al. (2005)).

Figure 2-16 (a) shows stress paths with different slopes in the p-q plane, defined as 'polarisation'. Cyclic triaxial tests carried out by WICHTMANN et al. (2004) showed that with decreasing slope of the stress path (increasing influence of volumetric stress due to increasing amplitude of minimum principal stress σ_3), at constant deviatoric stress amplitude q^{ampl} , the total strain accumulation increases. Figure 2-16 (b) shows strain path of 'multidirectional' cyclic triaxial tests, resulting from principal stresses σ_1 and σ_3 oscillating in different phases.

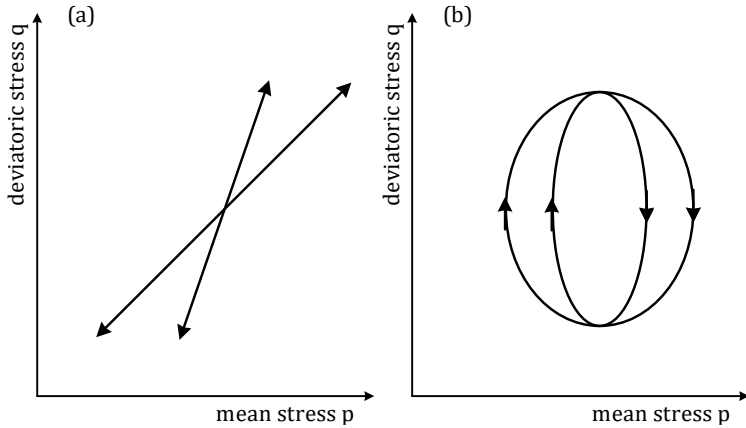


Figure 2-16: Definition of 'polarisation' (a) and 'multidirectional' triaxial tests (b)

In simple shear tests (WICHTMANN et al. 2004; LE 2015) polarisation changes were realised by changing the direction of shearing. After a change of the shearing direction, the rate of cyclic strain accumulation $\dot{\epsilon}^{acc}$ sharply increased and decreased towards the 'average' strain rate afterwards (see Figure 2-17).

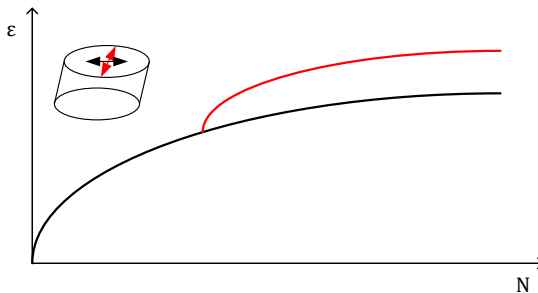


Figure 2-17: Strain accumulation in direct shear test due to polarisation change (based on LE 2015)

The height of the sudden increase and the duration for recovery ('back polarisation') of the strain rate (only) depended on the rotation angle $\sin(\alpha_{\pi})$. The explanation for this phenomenon is given on a granular basis: A chaotic arrangement of the soil grains is assumed before the first cycle. Within a certain number of cycles, the soil grains are arranged according to the polarisation of the cyclic loading, leading to a reduced strain rate. Due to a change in the

polarisation of the cyclic loading, the arrangement of the soil grains does not fit to the loading polarisation anymore. As a result, the cyclic strain rate increases until the arrangement of the grains corresponds to the polarisation of the cyclic loading again after a certain number of cycles.

Cyclic laterally loaded piles

Generally, there are many parallels between the cyclic behaviour of sand samples and that of laterally loaded piles. Thus, some of the formulations given in the previous part of this section may be applicable to pile-soil systems, either. In that case, parameters need to be replaced accordingly, e.g. strain ϵ by pile deflection u or stress σ by lateral pile head loading H . The topic of cyclic laterally load piles in general has been addressed by several authors (HETTLER 1981, 1986; LITTLE & BRIAUD 1988; LONG & VANNESTE 1994; LIN & LIAO 1999, and others).

HETTLER (1981) used the logarithmic law

$$f_{N,\log} = 1 + B_N \cdot \ln N \quad (2-33)$$

with the soil constant B_N to predict the accumulated pile deflection due to cyclic loading while LITTLE & BRIAUD (1988) used the power-law

$$f_{N,pwr} = N^{\alpha_N} \quad (2-34)$$

with the soil constant α_N . This approach was confirmed by LEBLANC et al. (2010) and NICOLAI & IBSEN (2014) and the soil constant α_N was found to depend on the relative soil density as well as the ratios of minimum to maximum cyclic loading M_{\min}/M_{\max} and of maximum cyclic loading to ultimate static loading M_{\max}/M_{ult} (moment loading). The beforementioned authors, however, formulated the accumulation functions f_N based on pile head rotation rather than lateral pile head displacement. In contrast to the displacement accumulation, the pile head secant stiffness during one cycle $E_{py,\text{sec}}$ (see below) increased logarithmically with N . Likewise, the lateral pile capacity of a cyclically loaded pile was higher than that of a previously unloaded system. This increase in soil stiffness and strength may be explained by soil densification. Model tests were carried out with rather loose sand (LEBLANC et al. 2010) and dense sand (NICOLAI & IBSEN 2014). The comparability of the two studies however, is doubtful as LEBLANC et al. (2010) installed the model pile by means of impact driving while NICOLAI & IBSEN (2014) reported jacking (= static pushing) of the pile.

PERALTA (2010) stated, based on model tests, that the logarithmic approach in Equation (2-33) is valid for flexible piles while the power-law in Equation (2-34) should be used for rigid piles. DÜHRKOP (2009) proposed a linear-logarithmic approach

$$f_{N,\log\text{-lin}} = 1 + B_{N1} \cdot [\ln(B_{N2} \cdot N + 1) + B_{N3} \cdot N] \quad (2-35)$$

with three soil constants B_{N1} , B_{N2} , B_{N3} . The constant B_{N3} is relevant for large number of cycles ($N > 100,000$) only. According to the model tests of DÜHRKOP (2009), B_{N2} and B_{N3} may be soil constants while B_{N1} depends on the cyclic loading ratio. CUÉLLAR (2011) further modified this approach for very large cycle numbers ($N > 10^6$) to account for a decrease of the accumulation rate. He explained the transition from logarithmic to linear accumulation law by a phase of soil densification (logarithmic accumulation) which is completed as the maximum soil density is reached. The assumption of soil densification was supported by the observation of a cone of subsidence around the pile at mudline level whose volume agreed with the change in soil volume due to densification to maximum density (see Figure 2-18).

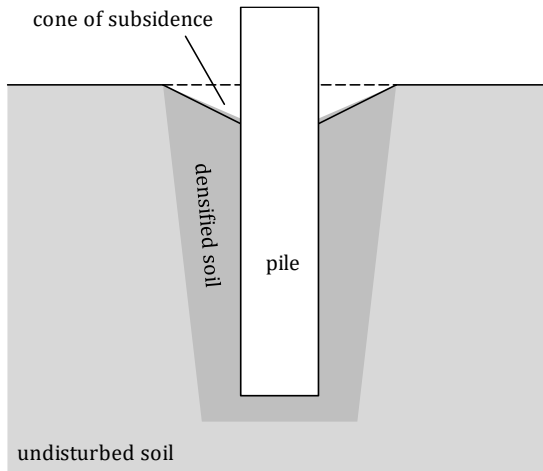


Figure 2-18: Soil densification and particle convection due to cyclic lateral loading (based on CUÉLLAR 2011)

It has to be emphasized that the cyclic accumulation approaches presented above define a function to be multiplied with the deflection due to the first cycle (see Equation (2-31)). Thus, different absolute displacements after N cycles may also be due to different (static) load-displacement behaviour in the first cycle.

Cyclic stiffness

The initial stiffness of the soil springs $E_{py,ini}$ is an important parameter to describe the p-y curves, e.g. according to current OGL. The secant stiffness of a load cycle $E_{py,sec}$ is given as the slope between the origin of the cycle and the displacement at the maximum load. The degraded stiffness $E_{py,deg}$ can be calculated as the slope between the origin of the first cycle ($p = 0, y = 0$) and the maximum load and displacement of a specific cycle (LITTLE & BRIAUD 1988). This parameter $E_{py,deg}$ is not a stiffness in the physical meaning, but may be used to calculate the displacement at a certain load level after N cycles. This approach is used by 'cyclic' p-y curves (API RP 2GEO; KIRSCH et al. 2014) as well as the stiffness degradation method (SDM, ACHMUS et al. 2009). From the Mustang Island tests (COX et al. 1974), for example, cyclic (= degraded) p-y curves were deduced which are actually validated for not more than 200 cycles. For the definition of $E_{py,ini}$, $E_{py,sec}$ and $E_{py,deg}$, see Figure 2-19.

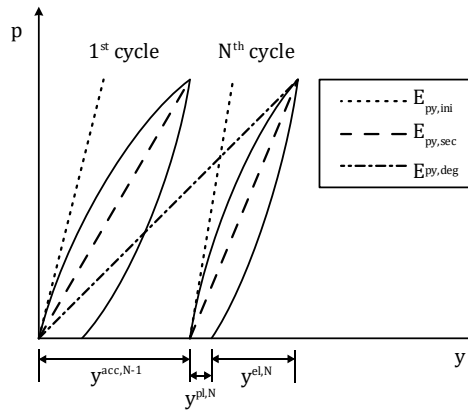


Figure 2-19: Definition of stiffness for cyclic loading

Since the calculation of the degraded stiffness $E_{py,deg}$ at the N^{th} cycle includes the accumulated deformation due to cyclic loading y^{acc} , $E_{py,deg}$ will decrease with the number of cycles N. The initial stiffness $E_{py,ini}$ and secant stiffness $E_{py,sec}$ are expected to increase with number of cycles N in analogy to the soil's unloading/reloading modulus, as reported by DÜHRKOP (2009), LEBLANC et al. (2010), NICOLAI & IBSEN (2014), and STEIN et al. (2019b). Likewise, NICOLAI et al. (2017) observed that the static capacity of pre-cycled piles can be much higher than that of primary loaded piles.

'Healing' effect

SOLF (2012) discovered 'healing' effects of cyclic lateral loading to pre-loaded piles. Piles that had experienced permanent deflection from single extreme events or large-amplitude cyclic loading were subjected to small-amplitude cyclic loading afterwards, as illustrated in Figure 2-20. Low-amplitude cyclic loading leads to a certain displacement accumulation (I). A single event with high load leads to large elastic and plastic deformations (II). The plastic deformations partly recover due to subsequent low-amplitude cyclic loading (III).

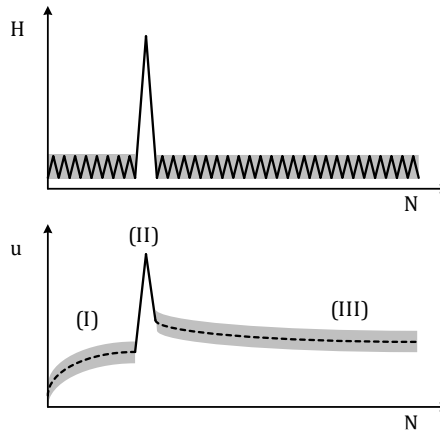


Figure 2-20: 'Healing' effect due to low-amplitude cyclic loading after single event with high load amplitude

For piles with sufficient flexural stiffness and a certain degree of toe clamping, a recovery of pile head deflection was observed. Closer examinations by ZACHERT (2015) showed that the recovery is predominant in the upper soil layers. The deflection of the pile toe experienced less or even no recovery. During regular cyclic loading, the pile bending moment at the instant of minimum load during one cycle increased with number of cycles, indicating a compression imprinted to the soil and a pre-tension of the pile. This pre-tension was considered the reason for the recovery of permanent pile deflections.

Loading direction

The behaviour of laterally loaded piles due to cyclic loading with varying loading direction has been investigated by several authors with different methods (DÜHRKOP & GRABE 2008; PERALTA

2010; SU 2012; RUDOLPH & GRABE 2013; RUDOLPH et al. 2014; LE et al. 2017; RICHARDS et al. 2020). The results are not comparable because the variation of loading direction was executed differently.

DÜHRKOP & GRABE (2008) and RUDOLPH & GRABE (2013) carried out 1g scale model tests with one-way cyclic lateral loading. The angle of loading direction in the horizontal (x-y) plane was varied continuously and swept an angle from 0° (unidirectional) to 120° (multidirectional). RUDOLPH et al. (2014) carried out very similar investigations in the centrifuge. The model tests performed by SU (2012) where displacement controlled and rather multi-stage than cyclic tests (4 loading-unloading cycles in 4 directions). RICHARDS et al. (2020) carried out scale model tests with unidirectional and multidirectional cyclic loading with a constant average loading H^{av} overlaid by a cyclic loading with amplitude H^{ampl} . Multidirectional loading covered fan-type loading as described above as well as L-shape and T-shape loading. L-shape and T-shape multidirectional loading refer to the directions of H^{av} and H^{ampl} in the horizontal (x-y) plane (Figure 2-21, left).

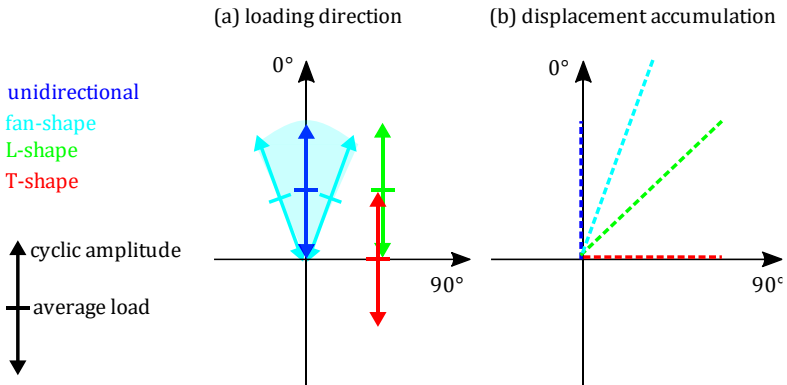


Figure 2-21: Schematic illustration of multi-directional pile loading (left) and resulting pile head deflection accumulation (right)

The resulting accumulation of pile head displacement/rotation is shown on the right side of the figure. For unidirectional loading (blue), pile head accumulation evolves in the direction of loading, as expected. Fan-shape multidirectional loading (cyan) results in higher accumulated deflections (approximately by factor 2, but with high deviations depending on loading regime and other factors) compared to unidirectional loading with a pile drift towards initial loading

direction. This was explained by loosening of the soil due to shearing in transverse direction to the loading direction and a propagation of pile deflection towards the direction of least soil resistance (DÜHRKOP & GRABE 2008). RUDOLPH et al. (2014) reported back-accumulation of the accumulated pile head displacement during loading in transverse direction. In Case of L-shape loading (red) loads to deflection accumulations in direction of the average load H^{av} . Very similar accumulation rates and total accumulations as in case of unidirectional loading were encountered if H^{av} and H^{amp} were kept constant, even though H^{av} and H^{amp} were not aligned. T-shape loading (green) caused similar deflection accumulations, but in both direction of average loading H^{av} and cyclic amplitude H^{amp} .

LE et al. (2017) carried out numerical simulations where the direction of H^{av} was kept constant while the direction of H^{amp} was changed rapidly by a certain angle after a certain number of cycles (change from unidirectional loading to L-shape multidirectional loading). This led to further deflection accumulation in direction of H^{av} with increasing or decreasing rate, depending on the average loading H^{av} and the variation of the direction of cyclic loading H^{amp} . Similiar to the observations of RICHARDS et al. (2020), deflection accumulation was observed in direction of the H^{av} .

PERALTA (2010) carried out scale model tests with one-way cyclic lateral loading. Here, the angle of loading direction (both average loading and cyclic amplitude) was changed by $+90^\circ$ several times after a certain number of cycles for more than one 'full rotation' of the loading direction. The resulting pile head deflections were limited to the "first quadrant of the initial loading direction" (PERALTA 2010). Figure 2-22 shows exemplary results of a flexible pile in medium dense sand from the abovementioned study.

The possible recovery of permanent pile head deflections from extreme events due to subsequent small-amplitude loading discovered by SOLF (2012) (see Figure 2-20) was noticed to be faster after changing the loading direction (KUDELLA & SOLF 2012).

SU (2012) reported an influence of initial lateral loading on the effects of subsequent transverse displacement-controlled loading. This was explained by asymmetric pile-soil interaction for the subsequent transverse loading cycle and the enforced displacement direction.

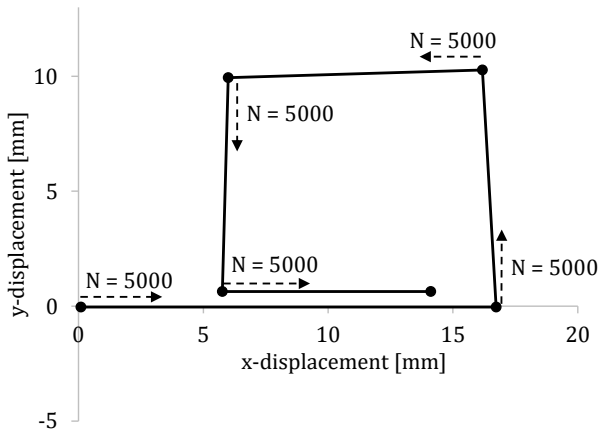


Figure 2-22: Pile head deflections due to cyclic loading from alternating loading directions (based on PERALTA 2010)

2.3.8 Influence of installation method

In offshore practice, impact driving and vibratory driving are common or promising dynamic piling techniques with advantages and disadvantages regarding the available experiences of designers and piling contractors, logistic requirements, economic feasibility and environmental impacts (see Chapter 1). Jacking as well as wished-in-place are merely academic variants used in physical and numerical modelling. These variants may be used due to shortcomings of testing facilities or numerical methods but may also give insight into the influences of dynamic effects if compared to corresponding investigations.

LABENSKI (2018) examined the influence of vibratory driving on the static lateral pile capacity. In scale model tests, piles were installed with different vibration parameters (resulting in vibratory driving modes interpreted as cavity and non-cavity pile driving according to VOGELSANG (2017)) and by means of static jacking as reference. The lowest lateral bearing capacity resulted from non-cavity vibratory driven piles and was found to be comparable to that of a jacked pile while the highest bearing capacity was encountered for cavity driven piles. The lateral pile behaviour of cavity-vibrated piles was even stiffer than predicted by current p-y approaches (LABENSKI & MOORMANN 2018). Based on these findings, LABENSKI (2019)

proposed a modification of the initial stiffness of the p-y curves to account for the vibratory driving mode.

LE et al. (2019) carried out numerical investigations based on scale model tests by REMSPECHER et al. (2019b). The pile installation was considered by defining a loosening zone directly at the pile shaft and a compaction zone in further distance (see section 2.2.3) based on results from the scale model tests. LE et al. (2019) could show that especially the narrow loosening zone alongside the pile shaft leads to a higher cyclic deflection accumulation. The cyclic lateral pile behaviour of impact driven piles was not explored. STAUBACH et al. (2020) and STAUBACH et al. (2021) used a similar approach by simulating the pile installation (impact driving and jacking) through a coupled Euler-Lagrange (CEL) method using the hypoplastic and Sanisand constitutive soil models. Impact driving and jacking resulted in very similar changes of the soil state (effective stresses and relative density) (STAUBACH et al. 2020). Based on the soil state at the end of the CEL calculations, the pile behaviour under static (STAUBACH et al. 2021) and cyclic lateral loading (STAUBACH et al. 2020) was investigated. For cyclic loading, the HCA approach was used. Simulations with consideration of installation effects were compared to simulations with wished-in-place (WIP) piles. In case of static loading, the consideration of the pile installation process (impact driving) lead to a stiffer pile head behaviour. In case of cyclic loading, the consideration of the pile installation process (both impact driving and jacking) in medium-dense sand lead to a lower rate of horizontal displacement accumulation compared to a WIP pile. In dense sand, however, the accumulation rate of the WIP pile was lower than that of the installed piles. At high cycle numbers ($N = 5 \cdot 10^6$), the soil state of installed and WIP piles "equalizes" (STAUBACH et al. 2020).

ACHMUS et al. (2020) studied results from in-situ lateral pile tests and CPT readings taken prior and after pile installation by means of impact and vibratory driving into dense sand (VIBRO project). Depending on the vibratory parameters, load level and loading/unloading/reloading scenario, vibratory driven piles showed softer but also similar and even higher lateral stiffness than impact driven piles. In all cases (vibratory and impact driven piles), an overall decrease of CPT values was encountered, interpreted as loosening of the soil. The decrease in soil density was more pronounced for two of the three vibratory driven piles while one vibratory driven pile with lower driving frequency and lower penetration speed even showed higher CPT readings at certain depths.

2.4 Interim conclusion

Pile toe effect due to impact pile driving

In the literature addressing pile resistance during impact driving, the initial shaft resistance $q_{s,ini}$ can be taken as the maximum resistance, occurring when the pile toe reaches a soil element. This shaft resistance is then continuously reduced towards the residual shaft resistance $q_{s,res}$ as the pile passes the soil element. However, since the 'initial' soil resistance is caused by an increase of horizontal stresses during pile driving and the 'residual' soil resistance is caused by a stress state similar to the primary stress state (PSS, before pile driving), the indices 'ini' and 'res' may be misleading and will be replaced by 'z=pen' and 'PSS' to highlight the corresponding stage of the pile installation:

$$q_{s,PSS} = q_{s,z=pen} \cdot \beta_{PSS} \quad (2-36)$$

Furthermore, instead of 'friction fatigue', which points towards the reduction of the pile shaft resistance, the term 'pile toe effect' will be used to emphasize the influence of phenomena at the pile toe on the soil behaviour. By substituting q_s according to Equation (2-4) and the pile installation effect according to Equations (2-6) and (2-7), the horizontal earth pressure during pile driving can be described as

$$\sigma'_{rad}(L_{pen}, z) = \sigma'_{rad,PSS}(z) \cdot \left[1 + \left(\frac{1}{\beta_{PSS}} - 1 \right) \cdot e^{\alpha_{pen} \cdot (L_{pen} - z)} \right] \quad (2-37)$$

Vibratory driving modes

Along the pile shaft, soil fluidisation can be assumed to take place during vibratory pile driving (RODGER & LITTLEJOHN 1980; VIKING 2006). Regarding the pile toe behaviour, different concepts exist which distinguish between different vibratory driving modes. It has to be stated that, despite sometimes being used synonymously, the concepts of 'impact/viscous' vibratory driving and 'cavity/non-cavity' vibratory driving are not fully compatible (DIERSSEN 1994): 'Impact' and 'viscous' vibratory driving (RODGER & LITTLEJOHN 1980) mainly differ regarding elasto-plastic and viscous pile toe behaviour while 'cavity' and 'non-cavity' vibratory driving (CUDMANI 2001) differ regarding the development of a gap underneath the pile toe during upward motion and resulting loading and unloading stiffness, and the magnitude of mobilised pile toe resistance.

Pile installations in coarse-grained soil have a severe impact on the soil state, namely void ratio and stress state. Both impact and vibratory pile driving result in a narrow loosening zone in the vicinity of the pile wall and a compaction zone in further distance to the pile. Due to impact pile driving, stress concentrations have been observed underneath the pile toe. In case of vibratory pile driving, the occurrence and extent of the loosening and compaction zone as well as the development of soil stress concentrations depend on relative soil density and vibratory driving parameters. Thus, it seems to be possible to achieve similar soil states by vibratory pile driving compared to impact pile driving. This hypothesis is supported by the fact that equal axial pile capacities of vibratory driven piles compared to impact driven piles were reported using certain installation parameters in certain soil conditions.

Lateral behaviour of monopile foundations

Concerning the applicability of calculation methods for laterally loaded piles to offshore monopile foundations, the boundary conditions have to be regarded carefully. Much knowledge, including current offshore guidelines, is based on a limited number of field tests with mainly impact driven, slender piles that show zero pile displacement and inclination at the pile toe. Offshore monopiles, in contrast, are large diameter, stiff piles that produce a toe kick under lateral loading. Thus, the soil state at the pile toe must be considered to assess the lateral pile behaviour. For impact driven piles, this includes increased soil stresses near the pile toe, as described in Section 2.2.2.

Regarding the cyclic behaviour, the following aspects taken from current research, which are partly in contradiction to guidelines, seem to be meaningful for offshore wind foundations:

- no degradation (but rather strengthening): lateral stiffness and capacity of pile-soil system increases due to cyclic lateral loading
- healing effect: small-amplitude cyclic lateral loading lead to recovery of deformed system
- loading direction: changing wind/wave directions need to be expected but no clear/uniform results how this effects cyclic accumulation

Only little research is available on the effect of installation methods on laterally loaded piles. Concerning the static lateral pile capacity and stiffness, in-situ tests and scale model investigations imply that impact driving tends to result in higher stiffness and capacity of the

pile-soil system. By variation of vibratory driving parameters, however, similar (or in single cases even higher) stiffness and capacity were observed. Stiffness and capacity of vibratory driven piles seems to be linked to pile driving modes, pile penetration speed and/or driving frequency. Due to the complex interactions between these and other pile driving parameters, a thorough descriptions of these effects is not yet available.

Chapter 3 Scope of work

3.1 State of the art

Impact driven monopiles are the preferred foundation type for offshore wind turbines in water depths of up to 40 m. Most important aspects in geotechnical design are the dynamic stiffness (eigenfrequency of the structure), limitation of inclination and possible cyclic degradation effects. Apart from that, other aspects such as pile drivability, fatigue, and noise emissions will influence planning and design as well. Especially for the latter subjects, vibratory pile installation is a highly promising alternative.

To assess the lateral load-displacement behaviour of piles, a variety of methods does exist. Different approaches may be used for different problems, ranging from elastic beam theory with linear or non-linear bedding to 3D numerical methods with implicit cyclic soil models. Current offshore guidelines recommend the use of the elastic beam theory with non-linear bedding that is described by p-y curves to assess the monotonic load-bearing behaviour. As the p-y curves in the offshore guidelines were developed for typical cases in the oil and gas industry, they apply for slender piles. p-y curves considering cyclic loading are validated for a limited number of cycles only. Research for offshore wind resulted (and still results) in modified or completely new p-y formulations considering large pile diameters, base shearing, small strain stiffness and CPT based soil parameters. The influence of cyclic loading can be described based on the explicit HCA model which may also be implemented into bedded beam approaches.

Numerous researchers have investigated the influence of dynamic pile installation processes (impact and vibratory pile driving) on the soil state with different methods. Influences of pile installation methods and parameters on the axial load-displacement behaviour are mostly described purely empirical. Effects of the pile installation process on the lateral load-displacement behaviour are not explicitly included in the available calculation methods. As the p-y curves used for this purpose can be traced back to experiences with impact driven piles, an implicit consideration of effects from impact driving can be assumed. As these experiences were made with mostly slender piles, however, their applicability to monopiles is questionable. Especially the combination of increased soil stresses at the pile toe of impact driven piles (Figure 2-6) and a toe kick of stiff monopiles (Figure 2-13) may lead to different lateral pile behaviour.

3.2 Research question

The state of knowledge described above leads to the following question:

Which are the geotechnical mechanisms during different 'modes' of pile driving, how do they effect the surrounding soil, and what is their influence on the lateral bedding?

During vibratory pile driving, pseudo-fluidisation is likely to occur along the pile shaft. In case of impact driving, soil compaction and increasing soil stresses due to the installation process are expected. This may lead to very different geotechnical phenomena during pile installation. In case of vibratory pile driving, especially the 'driving mode' (e.g. cavity/non-cavity or impact/viscous modes) needs to be examined as this decides about the soil behaviour underneath the pile toe. Therefore, pile forces and motions as well as the resulting soil response need to be studied.

The lateral bedding generally depends on the state of the surrounding soil and thus on effects from the pile installation process. During lateral loading, yielding of the soil at shallow depth is expected. Resulting stress-redistributions which may influence the pile-soil behaviour of subsequent load cycles and the cyclic displacement accumulation. In deeper soil layers, a toe kick can be expected due to the high bending stiffness of monopiles. Here, differences between impact and vibratory driven piles are very likely.

The current knowledge about installation effects on the soil's stress state, lateral bedding of monopiles and stress-dependency of the mechanical behaviour of sand (both monotonic and cyclic) lead to the following hypothesis:

Different pile installation methods induce different soil stresses in the surrounding soil. Regarding lateral bedding under monotonic loading, the pile installation process can be considered by means of stress-dependent p - y curves. In case of cyclic behaviour, installation-induced soil stresses are meaningful for strain accumulations as they affect the stress level and stress ratio.

3.3 Methodology

Scale model investigations were chosen to investigate the questions outlined above. In physical experiments using real soil, different aspects of the soil behaviour (compression, extension, shearing) and problems (static, dynamic, cyclic) can be modelled. Thus, the effects of pile

installation and subsequent lateral loading on the system can be investigated in the same experimental setup in the 'natural' order.

As the effort for the preparation and execution of scale model tests is quite high, the number of investigated variations is limited. As the scope of this research is the influence of the pile installation process, only installation methods and parameters will be varied. Soil conditions, pile properties and loading scenario will be chosen to represent offshore conditions and not varied.

Pile, soil and load parameters will be chosen to represent conditions for OWT in the German North Sea. Regarding vibratory installation, different variations shall be investigated to give hints on preferable vibratory driving parameters.

Chapter 4 Design of physical model

4.1 Generic OWT foundation

The model foundation investigated within this thesis was designed based on typical current monopile foundations used for offshore wind farms (OWF) in the German North Sea with the following main characteristics:

- pile diameter $D_{\text{pile}} \leq 8 \text{ m}$
- penetration length ratio $L_{\text{pen}}/D_{\text{pile}} \approx 4$
- dense to very dense saturated sand with $\gamma' \approx 11 \text{ kN/m}^3$
- cyclic loading due to wind and waves
- installation by means of impact and vibratory driving

While the structural properties (geometry, stiffness) and external loading (force, moment) of both offshore and model piles can be assessed quite precisely, the mechanical properties of the soil are hard to determine. Therefore, the pile itself is sized down to model scale based on similarity laws while the soil properties are chosen based on geotechnical experience.

Pile properties

Based on the properties given above, a generic OWT was created. Table 4-1 shows structural properties for the generic offshore monopile, a scaled monopile according to similarity laws and the actual model pile. The evolution of the scaled monopile and the actual model will be explained later.

The wall thickness (*) of the offshore pile was considered constant over the pile with minimum wall thickness according to API RP 2A-WSD:

$$t_{\text{pile}} [\text{mm}] = 6.35 + \frac{D_{\text{pile}} [\text{mm}]}{100} \quad (4-1)$$

The lateral force and moment load at mudline level (***) were taken from current offshore projects.

Table 4-1: Generic OWT

parameter		unit	offshore monopile	scaled monopile	actual model pile	comments
<i>pile properties</i>						
material	--	--	S355	--	1.4301	
diameter	D_{pile}	[m]	7.8	0.61	0.61	
penetration	L_{pen}	[m]	31	2.42	2.4	
wall thickness	t_{pile}	[mm]	84	0.525	3.0	<i>offshore pile: mean value (*) model pile: based on bending stiffness and availability</i>
bending stiffness	EI	[MN·m ²]	$3.20 \cdot 10^6$	9.35	52.7	<i>scaling laws could not be met</i>
elastic length	L_E	[m]	55.3	4.33	6.68	<i>Eq. (4-9) with $\gamma' = 11 \text{ kN/m}^3$</i>
<i>loading properties</i>						
lateral load	H	[kN]	10,000	4.8	15	<i>at mudline level (**)</i>
moment	M_{mdl}	[kNm]	400,000	11.2	30	
lever arm	h_H	[m]	40	2.34	2	<i>= M_{mdl}/H</i>

Soil properties

The mechanical properties of sand depend on strength parameters such as friction angle φ' and stiffness parameters such as oedometric soil stiffness E_{oed} . These values depend on physical properties such as grain size distribution, state parameters such as relative density D_r or stress state σ and the stress history of the soil, e.g. glacial preloading. In offshore practice, the actual mechanical properties cannot be determined in-situ, the extraction of undisturbed samples for laboratory tests is difficult, either. Physical properties of the soil can be received from disturbed samples. Indirect soil investigation methods such as CPT or geophysical methods are used to

gather information about the subsoil. From these explorations, information about soil properties or pile resistances are deducted based on empirical relationships.

To model the offshore soil conditions in the German North Sea, sand was emplaced and compacted layer wise to achieve a dense packing. Due to the compaction procedure in the limited volume of the test pits, a stress state with $k_0 \approx 1$ was produced resembling glacial preloaded (over consolidated) sand (cf. Section 5.6.2).

Loads on offshore monopile foundations

Looking at the different numbers of cycles and variation of loading directions used in prior research (see section 2.3.7) a loading scenario representing offshore conditions (here: German North Sea) is wanted. BSH (2012) defined a standard storm event for the design of OWT with a duration of 35 hrs. Wind and waves are aligned, their magnitude is increasing to a maximum value after 17.5 hrs and then decreasing again. Wind speed and significant wave height with a 50-year return period shall be used to calculate the maximum wind and wave loads.

With a wave period of $T_{s,50} = 10.5$ s (RICHWIEN & LESNY 2004), a total number of about 12,000 waves or loading cycles occurs within 35 hours. Measurements from research platforms FINO1 and FINO 3 in the German Bight (BSH 2010) show that prevailing wind and wave directions are varying between Southwest and Northwest with highest occurrences at these two orthogonal directions. Figure 4-1 shows the cumulated significant wave heights of all waves higher than one meter measured at FINO 1 (left) and FINO 3 (right) over a period of about 7 years (2010 to 2017) and classified in directions with a spread of 5° . For both locations, two main wind/wave directions with a relative angle of about 90° can be identified.

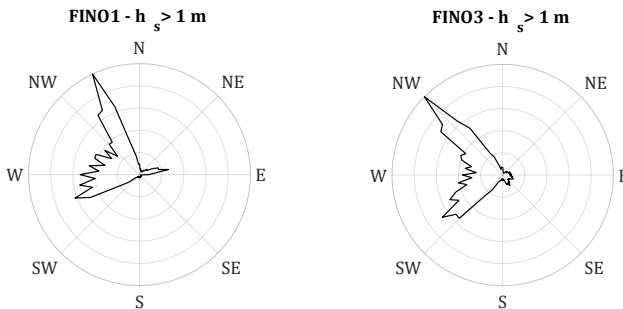


Figure 4-1: Wave directions measured at FINO 1 (left) and FINO 3 (right) (data from BSH 2010)

For the model design, constant values of maximum lateral loads were assumed. For the geometry of the offshore pile presented above, characteristic loads of $M_{mdl} = 400 \text{ MNm}$, $H = 10 \text{ MN}$ at mudline level were assessed based on data from different OWF. A wave period of $T_{s,50} = 10.5 \text{ s}$ was used to calculate a number of $N = 12,000$ cycles within a standard storm event of 35 hours. Two main wind/wave directions with a relative angle of about 90° (see above) were taken.

4.2 Scaling procedure

Physical models suffer from scaling effects which can be kept small if the model dimensions are close to the prototype. The available facilities at the author's institution allow for comparably large pile models and thus little scaling effects. To transfer the generic OWT to a (smaller) scale model while obtaining its main characteristics, similarity laws had to be applied. For scaling an offshore monopile to model scale, dimensional analysis was carried out. Shortcomings in scaling were met by using dimensionless parameters to scale lateral loading. The subsoil was not scaled but appropriate model sand and compaction procedures were found to produce a model soil with satisfactory properties.

Dimensional analysis

The relation between offshore pile (index p for 'prototype') and model quantities (index m) is given by scaling factors λ (e.g. length $L_m = L_p/\lambda_L$). All prototype parameters have to be formulated in fundamental physical parameters (e.g. length L, force F, density ρ). Scaling factors for a number of parameters (e.g. $\lambda_L = 10$ based on geometric constraints, $\lambda_a = \lambda_\rho = 1$ in an 1g model) are defined and the remaining scaling factors can be derived by algebraic operations (BUCKINGHAM 1914):

$$\text{volume:} \quad V = L^3 \rightarrow \lambda_V = \lambda_L^3 \quad (4-2)$$

$$\text{mass:} \quad m = \rho \cdot V \rightarrow \lambda_m = \lambda_\rho \cdot \lambda_V \quad (4-3)$$

$$\text{force:} \quad F = m \cdot a \rightarrow \lambda_F = \lambda_m \cdot \lambda_a \quad (4-4)$$

$$\text{moment:} \quad M = F \cdot L \rightarrow \lambda_M = \lambda_F \cdot \lambda_L \quad (4-5)$$

Dimensionless parameters

Physical parameters are made dimensionless by division/multiplication with other physical parameters of the problem. Dimensionless parameters must be equal for offshore pile and model pile. Different approaches may lead to the same dimensionless parameter, as shown in the following equations for the dimensionless force H^* to scale the horizontal force acting on the pile at mudline level H [kN]:

$$\text{(LABENSKI \& MOORMANN 2018)} \quad H^* = \frac{H}{\gamma' \cdot D_{\text{pile}}^3 \cdot k_p} \quad (4-6)$$

$$\text{(LEBLANC et al. 2010)} \quad H^* = \frac{H}{\gamma' \cdot D_{\text{pile}}^2 \cdot L_{\text{pen}}} \quad (4-7)$$

$$\begin{array}{l} \text{(HETTLER 1981)} \\ \text{(DÜHRKOP \& GRABE 2008)} \end{array} \quad H^* = \frac{H}{\gamma' \cdot L_{\text{pen}}^2 \cdot L_E} \quad (4-8)$$

$$L_E = \sqrt[4]{\frac{EI}{\gamma' \cdot L_{\text{pen}}}} \quad (4-9)$$

All approaches are using the soil unit weight γ' [kN/m³] and a number of length units (pile diameter D_{pile} [m], pile penetration L_{pen} [m], elastic length L_E [m]) in the denominator. Equation (4-6) uses the pile diameter with the power of three, thus the dimensionless force will not be affected by pile penetration. On the other hand, Equation (4-8) is independent of the pile diameter D_{pile} . Both assumptions are worth discussing. However, as long as the ratio $L_{\text{pen}}/D_{\text{pile}}$ is also considered as a dimensionless parameter and kept constant, either D_{pile} or L_{pen} may be used. In Equation (4-6), the (dimensionless) earth pressure coefficient k_p is also used to consider the soil strength, Equation (4-8) considers the pile bending stiffness EI in the elastic length L_E .

Time and frequencies

The following rule of thumb can be used to assess whether inertia effects need to be considered (EA-Pfähle 2012):

$$m[\text{t}] \cdot \left(\omega \left[\frac{1}{\text{s}} \right] \right)^2 < 0.1 \cdot E_{\text{lat}} \left[\frac{\text{kN}}{\text{m}} \right] \quad (4-10)$$

$$\omega = 2 \cdot \pi / T_{\text{cycl}} \quad (4-11)$$

If the product of the mass of the system m and the square of the angular loading frequency ω is small compared to the (in this case lateral) pile stiffness E_{lat} , inertia effects do not influence the system behaviour.

Deduction of model parameters

The design of the scaled model was carried out by the following steps:

- 1) Tests were carried out at earth gravity (1g tests). Thus, all acceleration quantities in the model (including gravity) had to be equal to the corresponding acceleration quantities under offshore conditions. This implied that densities (e.g. soil unit weight γ') had equal sizes in the model and in situ. Dimensionless parameters generally need not to be scaled, either. This applies for relative quantities like earth pressure coefficients $k = \sigma_3/\sigma_1$ or friction coefficients $\tau/\sigma = \tan(\varphi')$ and thus the friction angle φ' itself.
- 2) The diameter of the model pile was chosen as large as possible to limit scaling errors. With 4 m diameter of the test pit (Figure 5-2) and a minimum distance between pile axis and boundary of $3 \cdot D_{pile}$ (EA-Pfähle 2012), $D_{pile} = 0.61$ m was chosen. Compared to the offshore pile, this leads to a scaling factor for length units of $\lambda_L \approx 12.8$.
- 3) To deduct scaling laws for further quantities, dimensional analyses (Equations (4-2) to (4-5)) and dimensionless parameters were used (see above).
- 4) The amplitude of the lateral load applied to the model is taken from current offshore projects and made dimensionless by a measure for the soil resistance of the pile-soil system and the pile's resistance to bending. The loading regime is developed based on a design storm event according to BSH (2012).

The resulting model parameters can be found in Table 4-1. Perfect model characteristics cannot be met for all parameters due to practical reasons. The actual model parameters are also given. The scaling laws for the pile's bending stiffness cannot be met with a steel pile because the required wall thickness (≈ 0.4 mm) might not withstand buckling. Alternative materials may be damaged during pile driving. Steel was used as pile material to account for high loads during pile driving.

Model soil

Regarding the model soil, it was intended to use sand with typical offshore conditions. To represent offshore soil conditions, fine sand was installed and compacted in layers of 0.2 m and saturated by flooding the test pit from bottom to top. By this procedure, a density in the range of $\rho_d \approx 1700 \dots 1750 \text{ kg/m}^3$ was achieved. This is equivalent to a submerged soil unit weight of $\gamma' \approx 10.4 \dots 10.7 \text{ kN/m}^3$, a relative density of $D_r \approx 0.72 \dots 0.87$ and an internal friction angle of $\varphi' \approx 37 \dots 40^\circ$. More details about the soil characteristics based on laboratory tests can be found in Section 5.4. Pre-tests with different layer thickness and compaction procedures are documented in STEIN et al. (2020).

It has to be admitted that a very dense packing and resulting stiffness and strength parameters could not be achieved with the layer-wise sand installation technique. Higher soil densities may be realised by pluviation of dry sand. This method was used by several authors for laboratory (WICHTMANN 2016) and small scale model tests (PERALTA 2010). Drying the amount of sand needed for the large-scale model tests used in this research (approx. 50 m^3), however, was not feasible.

Regarding the soil conditions based on CPT data, several current CPT readings taken for the Federal Maritime and Hydrographic Agency (BSH) in the German Bight were used as reference. Figure 4-2 shows measured cone resistance q_c taken from offshore readings (left) and in the model tests (centre, cf. Section 5.6.2, Figure 5-12). The right part of the figure shows a comparison of normalised cone resistance Q_t [-] (ROBERTSON 1990; LUNNE et al. 2014)

$$Q_t = \frac{q_t - \sigma_v}{\sigma'_v} \quad (4-12)$$

$$F_r = \frac{f_s}{q_t - \sigma_v} \cdot 100\% \quad (4-13)$$

with the (theoretical) total and effective vertical stresses σ_v and σ'_v .

All data is plotted towards a depth of one pile penetration which is 2.4 m for the scale model and assumed to be about 32 m for current offshore monopiles. CPT data from offshore locations in the German North Sea obviously show a certain scatter while the reproducibility of the model soil was quite satisfactory. Comparing normalised cone resistance Q_t towards a depth of $z = L_{pen}$ shows that the soil 'strength' in the model tests seems to be even higher than offshore, even

though the relative density is probably lower. An overview over the actual soil conditions in the tests and its variations based on CPT and DPM readings can be found in Section 5.6.2.

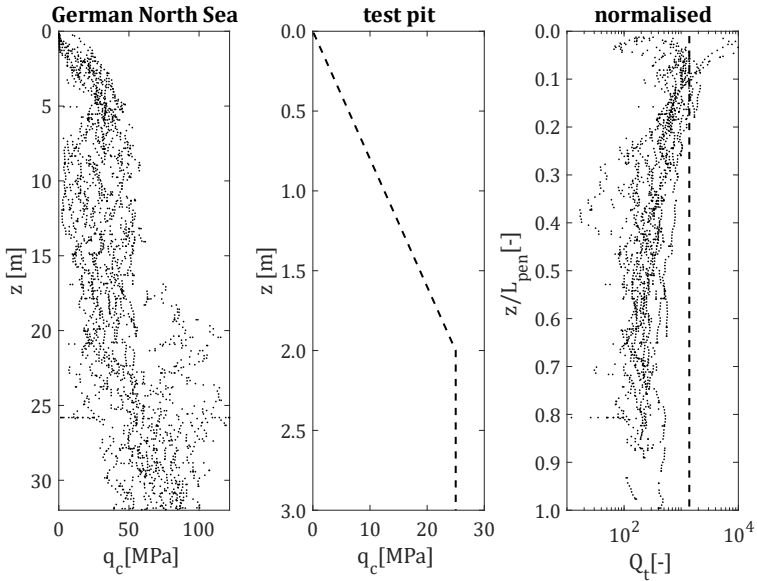


Figure 4-2: CPT readings from the German North Sea⁵ (data from BSH 2019, left), from test pit (centre), and comparison of normalised cone resistance (right)

Taking into the account the somewhat lower relative density and the somewhat higher normalised cone resistance of the model soil compared to in-situ conditions, the chosen filling strategy of the model sand and the characteristics of the model soil are regarded suitable for the model tests.

Vibratory hammer

Looking at the vibro hammer, some vibratory driving parameters from offshore monopile installations and prototype tests are published (FISCHER et al. 2013; ACHMUS et al. 2020). Eccentric moment M_e , dynamic mass m_{dyn} , displacement amplitude s_0 and ranges of used driving frequencies f_d and centrifugal forces F_c are given in the following Table 4-2. For a

⁵ CPT data from areas N-3.5, N-3.6, N-3.7, and N-3.8 (see BSH 2019) was used.

comparison to the parameters used in the model tests (cf. Sections 5.5 and 6.2.3), the centrifugal force F_c is normalised by the dynamic mass m_{dyn} and the gravity g . The bias force F_{bias} (= dead weight - line pull) is normalised by the centrifugal force F_c .

Table 4-2: Vibratory driving parameters for monopile installation

parameter			VIBRO test	OWP Riffgat	model tests		comments
reference			(ACHMUS et al. 2020)	(FISCHER et al. 2013)	Sections 5.2, 5.5, 6.2.3		
pile diameter	D_{pile}	[m]	4.3	5.7 6.5	0.61		
pile penetration	L_{pen}	[m]	21	16 22	2.4		
vibratory hammer			PVE 500M	APE 600b Quad	APE J&M Model 23 Model 23A		
eccentric moment	M_e	[kg·m]	500	920	2.33	1.36	
driving frequency	f_d	[Hz]	12 23	16 19	12 27	15 34	
centrifugal force	F_c	[kN]	2,800 10,000	10,000 13,000	13 67	12 62	$F_c = M_e \cdot (2\pi \cdot f_d)^2$
total dynamic mass	m_{dyn}	[kg]	138,000	564,000 804,000	689		
displacement amplitude	s_0	[mm]	3.6	1.6	3.4	2.0	$s_0 = M_e / m_{dyn}$
dimensionless measures	$\frac{F_{bias}}{F_c}$	[-]	0.14 0.50	0.52 0.92	0.14 0.73	0.16 0.80	
	$\frac{F_c}{m_{dyn} \cdot g}$	[-]	2.10 7.70	1.28 2.41	1.96 9.93	1.79 9.19	

The displacement amplitude and the dimensionless parameters for the centrifugal force are in the same ranges for the published prototype tests and the model tests. The displacement amplitude s_0 is a dimensioned value and was not scaled. The relevance of the displacement amplitude for phenomena during vibratory installation may be assessed based on the pile-soil interaction. The pile-soil interaction can be described by the rheological model described in Figure 2-3 where the pile displacement determines the mobilisation of static soil resistance. As the model soil is similar to (unscaled) offshore conditions (see above), it seems reasonable to use a vibratory hammer with similar displacement amplitude.

Magnitude of lateral loading

For the load amplitude several scaling approaches are mentioned in the literature to normalize lateral loads (see above). With respect to the scaling errors discussed above (pile and soil stiffness) it seems to be appropriate to take these parameters into account. For the soil stiffness, however, it is difficult to determine precise data for the relevant stress level, especially for offshore conditions. Thus, it was decided to rely on pile stiffness ($E \cdot I$) and soil strength (φ' , k_p) data, which are regarded more reliable. For the underlying offshore and model conditions/properties, see sections 4.1, 5.2 and 5.4.

A new scaling law for the lateral load was established, including pile diameter and penetration length (even though their relation is equal for offshore pile and model pile) as well as soil unit weight and passive earth pressure coefficient:

$$H^* = \frac{H}{D_{\text{pile}} \cdot L_{\text{pen}}^2 \cdot \gamma' \cdot k_p} \quad (4-14)$$

with

$$k_p = \tan^2 \left(45 + \frac{\varphi}{2} \right) \quad (4-15)$$

For soil unit weight and soil friction angle, $\gamma_m' = 10.4 \text{ kN/m}^3$ and $\gamma_p' = 11 \text{ kN/m}^3$ and $\varphi_m = \varphi_p = 40^\circ$ were assumed. Using this scaling approach, a lateral force of $H_m = 4.4 \text{ kN}$ in the model would be similar to a lateral force $H_p = 10 \text{ MN}$ on an offshore pile.

Scaling the pile loading solely based on the similarity of the lateral force may not represent a similar pile bending behaviour if pile bending stiffness and/or moment loading cannot be accurately scaled. In this case, the pile bending stiffness of the model pile was much higher than it should have been according to scaling laws (see Table 4-1).

Regarding the pile deflection due to bending moment, one can define the elastic strain in the pile wall due to moment loading as dimensionless measure for the moment loading M^* [-]. The moment at mudline level M_{mdl} [kNm] can be influenced either by the magnitude of the lateral force or the point of force application (= length of the cantilever); the strain further depends on the pile diameter D_{pile} [m] and the bending stiffness EI [kNm²]:

$$M^* = \frac{M_{\text{mdl}} \cdot D_{\text{pile}}}{EI} = \frac{H \cdot h_H \cdot D_{\text{pile}}}{EI} \quad (4-16)$$

Due to the design of the testing facilities (cf. Section 5.1), only a limited lever arm of the applied lateral force of $h_{H,m} \leq 2$ m was possible in the model. Using this scaling approach for the lateral load a moment load at mudline level of $M_{\text{mdl},m} = 84$ kNm (corresponding to a lateral load of $H_m = 42$ kN with a cantilever of $h_{H,m} = 2$ m) would be similar to offshore conditions with $M_{\text{mdl},p} = 400$ MNm.

The quality of a certain scaling law can be quantified by dividing the dimensionless load quantities (H^* , M^*) of the model by the corresponding dimensionless load of the offshore pile. In case of a perfect model, the outcome would be equal to one. To find a good compromise between the two scaling approaches for lateral force and mudline moment described above, the two quality measures for H^* and M^* were multiplied. Figure 4-3 shows the quality measures for H^* (dashed line) and M^* (dotted lines) as well as the combined measure (solid line) for different lateral loads in the model. A good compromise can be found for $H_m = 13.7$ kN.

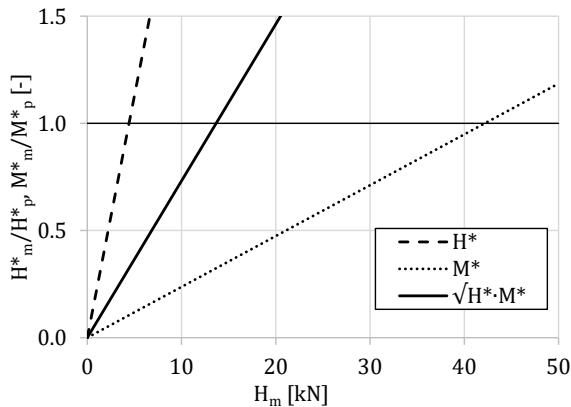


Figure 4-3: 'Quality' of load scaling

From the above considerations, a combined scaling law for the lateral load (H), including lateral soil resistance (γ' , K_p , L_{pen}), pile bending stiffness (EI) and lever arm (h_H), can be deduced:

$$\begin{aligned}
 H^* &= \frac{H}{\sqrt{(\gamma' \cdot k_p \cdot L_{pen}^2 \cdot D_{pile}) \cdot \left(\frac{EI}{D_{pile} \cdot h_H}\right)}} \\
 &= \frac{H}{\sqrt{\gamma' \cdot K_p \cdot L_{pen}^2 \cdot EI/h_H}}
 \end{aligned}
 \tag{4-17}$$

Chapter 5 Description of model tests

5.1 Model requirements and testing facilities

All measures in a physical model have to be captured by means of measurements that involve the use of appropriate sensors. Measurements should have as little influence on the physical properties they are aimed at as possible. This poses a challenge on the real-time assessment of soil properties and soil state parameters during pile installation and during lateral loading. Description of the installation process will focus on dynamic pile forces and pile motion during pile driving. Regarding lateral pile behaviour, the design drivers described above, namely (quasi-)static load-displacement behaviour, lateral eigenfrequency and cyclic degradation shall be investigated. Therefore, the lateral load and pile deflection need to be continuously monitored. The dynamic response of the systems is required to assess its eigenfrequency. To get an insight into the soil behaviour itself, information about soil stress developments during both pile installation and lateral loading is crucial.

The geotechnical test pits at IGG-TUBS with their infrastructure served as testing facility for the scale model tests. Regarding the model parameters, the dimensions of the two identical cylindrical buckets are decisive for the model dimensions (cf. Section 4.2). Figure 5-1 shows an aerial view of the testing facility during the installation of a model pile.



Figure 5-1: Geotechnical test pits and infrastructure at IGG-TUBS during installation of model pile (test Z03, pile installation)

Figure 5-2 shows cross section and top view of the test pit with model pile at final penetration and the cylindrical coordinates z , r and θ used to describe geometries (e.g. sensor locations, loading direction) in the test setup.

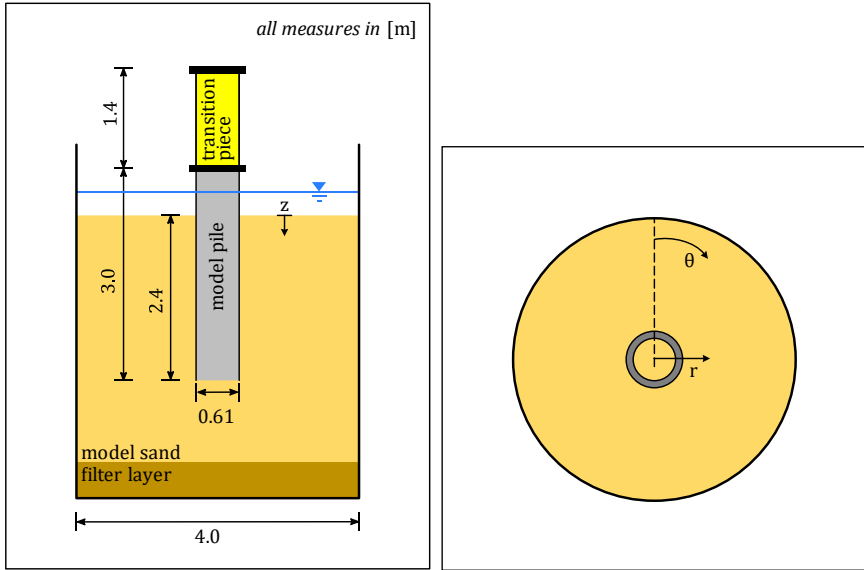


Figure 5-2: Scale model in test pit

A stainless-steel tube was used as model pile. Section 5.2 describes the model pile and section 5.3 addresses the loading scenario.

A fine silica sand which was emplaced and compacted layer wise was used as model soil. Pre-tests were carried out to identify an appropriate combination of layer thickness and number of compaction passages (STEIN et al. 2020). Section 5.4 gives the physical and mechanical properties of the sand while Section 5.6.2 describes the procedure to install the model soil.

Pile installation was performed by impact driving, vibro driving and static pushing/jacking. The utilised equipment is presented in Section 5.5, the installation procedures are described in Section 5.6.3.

5.2 Model pile

A stainless-steel tube (1.4301, DN600) with a flange to connect pile helmet, vibro hammer and transition piece was used as model pile. For the transition piece, the same kind of tube was used. The properties of the model pile and transition piece are given in Table 5-1. At the pile top and both ends of the transition piece, welded flanges (type 11, PN10, DIN EN 1092-1) were attached. At the top of the transition piece, two smooth flanges (type 01, PN10, DIN EN 1092-1) were attached as additional mass.

Table 5-1: Model pile and transition piece

parameter		unit	value	comments	
penetration length	L_{pen}	[m]	2.4	<i>target penetration</i>	
pile length	L_{pile}	[m]	3.0		
length transition piece	L_{TP}	[m]	1.4		
diameter	D_{pile}	[m]	0.61	<i>pile and transition piece</i>	
wall thickness	t_{pile}	[mm]	3		
cross section	A_{pile}	[m ²]	0.0057		
moment of inertia	I_{pile}	[m ⁴]	$264 \cdot 10^{-6}$		
modulus of elasticity	$E_{1.4301}$	[MN/m ²]	200,000		
density	$\rho_{1.4301}$	[kg/m ³]	7850		
bending stiffness	EI	[MNm ²]	52.7		
normal stiffness	EA	[MN]	1150		
axial wave velocity	C_{pile}	[m/s]	5048		$\sqrt{E/\rho}$

Equation (2-24) was used to evaluate the flexural stiffness of the pile. High soil stiffness tends towards a more flexible behaviour of the pile. The evaluation of Equation (2-24) highly depends on the estimated soil stiffness, which depends on the stress state (depth) and load level. A stress (or depth)-dependent soil stiffness according to OHDE (1939) with reference stiffness $E_{oed,ref} = 300$ kPa, stiffness exponent $\lambda = 0.6$ for fine sand (cf. ENGEL & SOOS 2017) and soil unit weight of $\gamma' = 11$ kN/m³ was assumed. This results in a stiffness ratio of $1/EI^* \approx 5.3$ when using

the averaged oedometric soil stiffness (from mudline level to pile toe level) and $1/EI^* \approx 8.5$ when using the (max) soil stiffness at pile toe level. Both values are close to the limit for a rigid pile with uniform soil profile according to POULOS & HULL (1989). Table 5-2 shows a comparison of relative pile rigidity $1/EI^*$ for different cases, including the 'generic' offshore monopile described in section 4.1 with an average oedometric stiffness $E_{oed} = 50$ MPa and limiting values for rigid and flexible piles.

Table 5-2: Pile rigidity

case	E_{oed} [MPa]	$1/EI^*$ [-]	
model pile	8.4	5.3	<i>average soil stiffness</i>
	13.5	8.5	<i>max soil stiffness ($z = L_{pen}$)</i>
offshore monopile	50	14.5	<i>see Table 4-1</i>
rigid pile	--	< 4.8	<i>uniform soil profile (POULOS & HULL 1989)</i>
flexible pile	--	> 390	

5.3 Lateral loading

To represent wind and wave conditions during several storm events in the Germany North Sea, five loading phases with varying loading directions were defined (see Table 5-3). The number of cycles per phase was taken from the BSH standard storm event. The two orthogonal loading directions θ_H were chosen based on the FINO measurements (see section 4.1). For the loading quantity, a lateral load of $H = 15$ kN with a lever arm of $h_H = 2$ m was chosen for phases 1, 2, 3 and 5, based on the scaling laws described in Section 4.2. For phase 4, an even higher maximum lateral load of $H = 20$ kN was chosen to represent an extreme storm event (e.g. 50 year storm).

Table 5-3: Generic loading scenario for model pile

phase	H [kN]	θ_H [°]	N [-]	comments
1	1 .. 15	0	12,000	
2	1 .. 15	90	12,000	

3	1 .. 15	0	12,000	<i>pre-loading for phase 4</i>
4	5 .. 20	0	12,000	
5	1 .. 15	90	12,000	
4/5 ext			12,000+	<i>extension of phase 4 or 5</i>

In some tests, the phases 4 and/or 5 were extended to up to 140.000 cycles to investigate high cycle behaviour. The full test program is given in 0.

5.4 Model sand

5.4.1 Overview

To install a model soil with soil properties similar to offshore conditions, sand was used which was commercially available from Schlingmeier Quarzsand GmbH & Co. KG (Schwülper/ Braunschweig, Germany) labelled 'G 0.1-1.2T' and shall be referred to as 'Braunschweig sand'. Physical and mechanical properties have been investigated in the laboratories of IGG-TUBS and the Federal Waterways Engineering and Research Institute (BAW).

5.4.2 Physical properties

The material consists of silica sand and can be classified as poorly graded sand (SP) according to DIN 18196/ASTM D-2487 and coarse sandy, slightly fine sandy medium sand (mSa, csa, fsa') according to DIN EN ISO 14688-1. The grains show compact, round shape. Figure 5-3 shows the grain size distribution, Figure 5-4 shows photos of the grains in macroscopic and microscopic view,

Table 5-4 shows the grain parameters of the model sand. Grain size distributions were taken from the data sheet of the supplier (Schlingmeier), sievings at the IGG-TUBS lab and optical analysis using a CamSizer at the geotechnical lab of BAW.

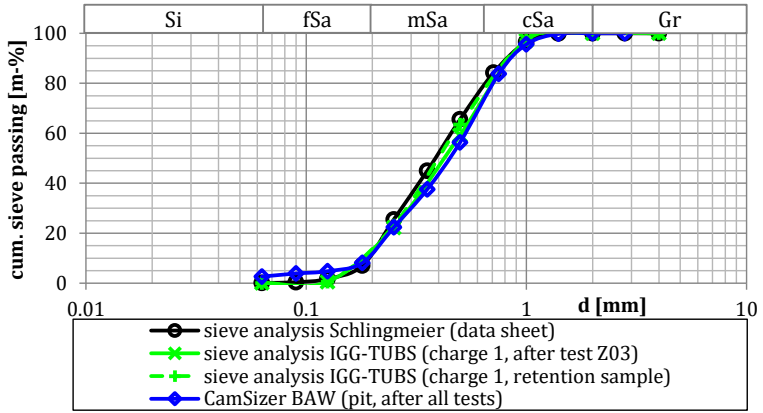


Figure 5-3: Grain size distribution



Figure 5-4: Macroscopic (left) and microscopic (middle, right) view of model sand

Table 5-4: Grain parameters of model sand

parameter		dimension	value	comments
mean grain size	d_{50}	[mm]	0.39	
coefficient of uniformity	C_U	[-]	2.4	
grain density	ρ_s	[kg/m ³]	2650	
roundness		[-]	0.61	mean values of all grain fractions
sphericity		[-]	0.69	

With the CamSizer in the BAW lab, also grain shape properties roundness and sphericity were determined. For the definitions of these parameters refer to Vos (2014). CamSizer evaluations give good agreement with DIN EN ISO 13503-2. The found grain shapes are illustrated in

Figure 5-5.

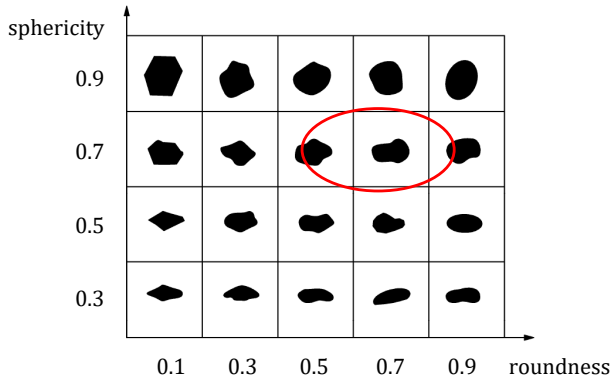


Figure 5-5: Grain shape according to DIN EN ISO 13503-2

Soil parameters like stiffness and soil strength play an important role for pile installation process and lateral load displacement behaviour. These quantities depend on the soil density and stress state. While an equal stress state could not be realised in the 1g model, a dense packing was targeted. Minimum and maximum soil density were determined according to DIN 18126. Table 5-5 shows the different density parameters for minimum and maximum soil density, the parameter ranges for dense and very dense sand and the mean values of the density parameters of the model soil as used in the model tests. A dense packing can be assumed for the model soil.

Table 5-5: Absolute and relative density of model sand

packing	ρ_d [kg/m ³]	D_r [-]	e [-]
min	1.492	0	0.476
max	1.796	1	0.776
dense	1.644 .. 1.735	0.65 .. 0.85	0.581 .. 0.521
very dense	1.735 .. 1.796	0.85 .. 1.00	0.521 .. 0.476
model soil	1.707	0.74	0.552

5.4.3 Shear parameters

Direct shear tests according to DIN EN ISO 17892-10 and triaxial shear tests according to DIN EN ISO 17892-9 were carried out on dry sand to determine the internal angle of soil friction φ' . To account for the low stress state in 1g model tests, the vertical stress was set to $\sigma'_v = 25, 50$ and 100 kPa. Samples with different void ratio e were tested to evaluate the influence of the compactness of the soil. The following figure shows the relation between relative density D_r and soil friction angle φ' (cf. SCHULTZE 1968):

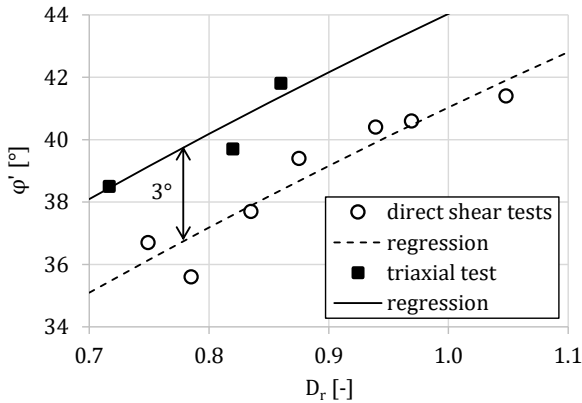


Figure 5-6: Soil friction angle versus relative density

Triaxial tests showed about 3° higher soil friction angles as the direct shear tests. This is in good agreement with ROWE (1969) who found that the peak soil friction angle φ' from (direct) shear box tests underestimates the peak angle in plane strain or triaxial compression by about $\Delta\varphi' \approx 4^\circ$. The relation between relative density and peak friction angle in direct shear tests can be formulated by

$$\tan \varphi' = 0.56 \cdot D_r + 0.31 \tag{5-1}$$

For the target density of $D_r = 0.74$ a soil friction angle of $\varphi' \approx 36^\circ$ (direct shear) or $\varphi' \approx 39^\circ$ (triaxial) can be assumed.

The critical friction angle φ_c was assumed to be equal to the angle of repose. By means of the fixed-funnel method, an angle of repose of 32.2° was determined.

5.4.4 Dynamic stiffness

Seismic tests (see EA Baugruddynamik 2019) were carried out to determine dynamic soil stiffness parameters. Therefore, compression waves and shear waves were sent through a dense dry sand probe ($\rho_d = 1717 \text{ kg/m}^3$; $D_r = 0.77$) in a triaxial cell. Compression wave velocity c_p and shear wave velocity c_s [m/s] were determined from wave travel time. Poisson's ratio ν [-], dynamic shear modulus G_{dyn} and dynamic oedometric modulus $E_{\text{oed,dyn}}$ can be derived from the measurements using the following relations (EA Baugruddynamik 2019):

$$\nu = (c_p^2 - 2c_s^2) / 2(c_p^2 - c_s^2) \quad (5-2)$$

$$c_s = \sqrt{G_{\text{dyn}} / \rho} \rightarrow G_{\text{dyn}} = c_s^2 \cdot \rho \quad (5-3)$$

$$c_p = \sqrt{E_{\text{oed,dyn}} / \rho} \rightarrow E_{\text{oed,dyn}} = c_p^2 \cdot \rho \quad (5-4)$$

For increasing cell pressure $p = \sigma_1 = \sigma_3$ (isotropic stress state), several measurements were taken to investigate the pressure dependency of the dynamic soil stiffness. The resulting soil consolidation affected the soil density negligibly (from $D_r = 0.770$ at $p = 10$ kPa to $D_r = 0.774$ at $p = 100$ kPa). Figure 5-7 shows discrete values for derived dynamic soil stiffness $E_{\text{oed,dyn}}$ (red) and dynamic shear modulus G_{dyn} (blue), as well as power law approximations of the soil stiffness (coloured lines) in the form

$$E = E_{\text{ref}} \cdot p_{\text{ref}} \left(\frac{p}{p_{\text{ref}}} \right)^\lambda \quad (5-5)$$

$$p_{\text{ref}} = 100 \text{ kPa}$$

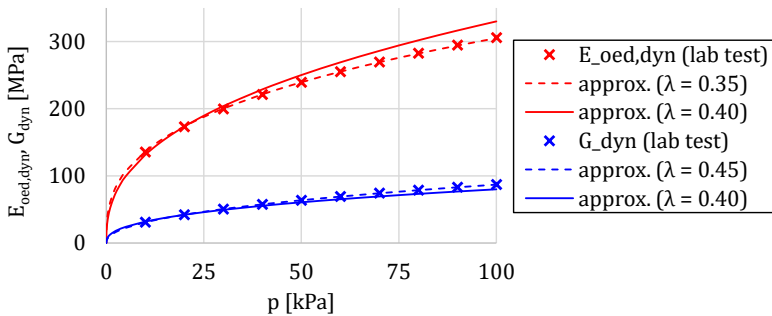


Figure 5-7: Dynamic soil stiffness of model sand

The dashed lines indicate best-fit approximations, resulting in different exponents λ_E and λ_G while the solid lines indicate fits with $\lambda_E = \lambda_G = 0.4$. For the model sand, the parameters to approximate the dynamic soil stiffness $E_{oed,dyn}$ and dynamic shear modulus G_{dyn} are given in Table 5-6.

Table 5-6: Dynamic soil parameters

parameter	unit	best fit	uniform λ
$E_{oed,dyn,ref}$	[kPa]	3,050	3,300
λ_E	[-]	0.35	0.40
$G_{dyn,ref}$	[kPa]	870	800
λ_G	[-]	0.45	0.40

5.5 Pile installation equipment

The test pile was installed either by impact or vibratory driving. In each case, a cap (type 05, PN10, DIN EN 1092-1) was connected to the flange at the top of the pile on which either the impact hammer was placed or to which the vibro hammer was mounted.

Impact pile driving

For impact pile driving, a Diesel hammer type Delmag D2 (Figure 5-8, left) with a maximum rated energy of $W_{rated} = 2.8$ kJ per blow was used. The hammer was guided by a leader mounted to a wheel loader. The fuel valve was controlled manually to achieve maximum hammer energy.

Vibratory pile driving

For vibratory pile driving, a hydraulic hammer type APE J&M Model 23 was used (Figure 5-8, middle). Free riding and crane guided vibratory installations were carried out. The driving frequency f_d could be regulated by the hydraulic flow. For crane-guided installation, a load cell and a damper were attached between the suppressor of the vibratory hammer and the crane hook (Figure 5-8, right). The penetration speed v_{pen} could be controlled by the crane in two stages (~ 20 mm/s and ~ 70 mm/s).



**Figure 5-8: D2 Diesel hammer (left)
and Model 23 vibro hammer during pile installation (middle)
and detail of crane suspension (right)**

For variations of the installation process, the eccentrics of the hammer were modified to produce a lower eccentric moment M_e . Figure 5-9 gives the relationship between driving frequency f_d and centrifugal force F_c for the unmodified (Model 23, blue) and modified (Model 23A, red) vibro hammers. The dashed lines indicate that driving frequencies of 26 Hz and 34 Hz, respectively, lead to a centrifugal force of 62 kN (cf. Section 5.6.3).

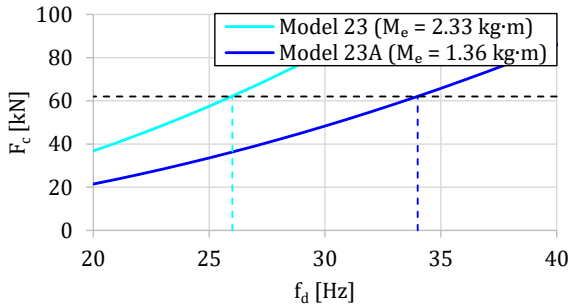


**Figure 5-9: Centrifugal force over driving frequency for the Model 23 vibratory hammer
with different eccentric moments**

For pile extraction, a smaller vibro hammer, type APE Model 3, was used. The following table gives the main parameters of the vibratory hammers.

Table 5-7: Vibratory hammer parameters

parameter	unit	APE J&M Model 23	APE J&M Model 23A	APE Model 3	comments
M_e	[kg·m]	2.33	1.36	0.35	
m_{dyn}	[kg]	685	685	324	<i>including all moving parts*</i>
s_0	[mm]	3.9	1.9	1.1	<i>see Equation (2-13)</i>
$f_{d,max}$	[Hz]	27	34	38	
$F_{c,max}$	[kN]	62.1	67.1	19.7	<i>see Equations (2-11) and (2-12)</i>

* the dynamic mass m_{dyn} comprises all moving parts of the hammer-pile system: gearbox, connection plate, pile flange, pile

Regarding the rigid body assumption during vibratory pile driving, Equation (2-15) is applied to the pile and vibro parameters (Table 5-1 and Table 5-7). Due to the short pile length L_{pile} and the high longitudinal wave velocity c_{pile} , the pile can be considered a rigid body during vibratory driving (not for impact driving!). The following equations show the comparison of wave travel time T_{wave} with the shortest possible vibratory cycle period based on the maximum vibration frequency $f_{d,max}$. $T_{wave} \ll 1/f_{d,max}$, thus the rigid body assumption is valid for vibratory pile installation within the model tests.

$$T_{wave} = \frac{2 \cdot L_{pile}}{c_{pile}} \ll \frac{1}{f_{d,max}} \quad (5-6)$$

$$\frac{2 \cdot 3 \text{ m}}{5048 \text{ m/s}} = 1.2 \cdot 10^{-3} \text{ s} \ll 26 \cdot 10^{-3} \text{ s} = \frac{1}{38 \text{ Hz}}$$

$$c_{pile} = \sqrt{E/\rho} = \sqrt{200 \cdot 10^9 / 7850} = 5048 \text{ m/s} \quad (5-7)$$

5.6 Test program

5.6.1 Test stages

To investigate the influence of the installation method on the behaviour of cyclic laterally loaded piles, impact driven, vibratory driven and jacked piles were investigated. Apart from the installation method, test parameters were not changed. Each test can be subdivided into the following stages, which are briefly described in the following sections:

- test preparation (PREP)
- pile installation (INST)
- cyclic lateral load test (CLLT)

5.6.2 Test preparation

Before each test, the test pit was prepared by layer-wise filling and compaction of the model sand. Since two test pits were available, the sand could be taken from the pit where the prior test had been executed. Both pits were drained, the model sand had a natural water content of approximately 3 %. The soil was replaced to a depth of 3 m ($\approx L_{pen} + D_{pile}$). The model sand was installed in 15 layers of 0.2 m (target layer thickness after compaction) using a crane mounted clamshell and shovels to spread the sand. Afterwards, the soil was densified using a vibratory plate with a centrifugal force of 50 kN, acting on an area of 0.64 m² (type Wacker DPU 5045H). The mass of the (wet) sand of each layer was recorded as well as the actual layer height before and after compaction (levelled at nine points on the sand surface). On different soil levels, sensors (total earth pressure, pore water pressure, temperature, acceleration) were installed. Earth pressure spades to measure horizontal earth pressure were pushed into the soil from the current layer with orientation of the sensor plane towards the centre of the test pit. All other sensors were placed on top of the current layer. Figure 5-10 shows earth pressure transducers on top of a compacted sand layer. Following sand placement till target level, the pit was flooded using the drainage at the bottom of the pit.



Figure 5-10: Earth pressure sensors in the test pit (left) and detail of earth pressure spade ① pore water pressure transducer ② and earth pressure pad ③ (right, by courtesy of Glötzl)

To verify the reproducibility and evenness of the sand installation, dynamic probing (DPM) according to DIN EN ISO 22476-2 and cone penetration testing (CPT) according to DIN EN ISO 22476-1 were carried out after sand installation (= prior to pile installation). DPM soundings were done at each test and CPT were conducted at most tests from test Z08 onwards. From DPM the blow count $N_{10,DPM}$ and from CPT the cone resistance q_c were used as a measure for the sand installation quality. A correction of the measured cone resistance q_c was ignored due to the small hydrostatic pressure compared to the cone resistance.

DPM and CPT readings

Soundings were taken at different positions within the test pit defined by the radial distance from the centre of the pit r and the angle versus north θ . Figure 5-11 shows DPM results from test Z07 (left) and CPT results from tests Z11 (right). Dark lines indicate probing locations close to the centre of the pit while light lines indicate locations closer to the walls.

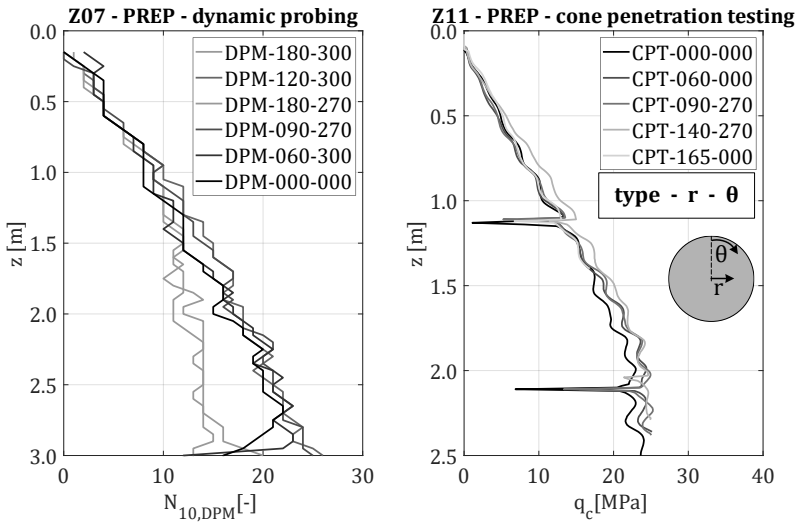


Figure 5-11: DPM readings from test Z07 (left) and CPT readings from test Z11 (right) at different locations within the test pit

Lower DPM blow counts at locations close to the walls of the test pit can be noticed. This may be due to pit wall friction, taking some of soil's dead weight thus reducing soil stresses and therefore soil resistance. For the cone resistance of the CPT such behaviour could not be recognised. Due to the geometry of the CPT device, however, no CPT measurements could be executed closer than 1.65 m to the pit wall. As measure for the soil resistance of each test, mean gradients of the DPM and CPT readings over depth were taken. For DPM only locations with a certain distance to the pit walls ($r \leq 1.5$ m) were considered.

Correlations between results of cone penetration tests, dynamic probing and geotechnical parameters are available (e.g. MAHLER & SZENDEFY 2009; ROBERTSON 2010; ALAM et al. 2014; DIN 4094-1). However, these experiences have to be treated with great caution, especially in the environment of scale model investigations in a test pit with low stress state and compacted sand. Thus, the results of the CPT and DPM soundings shall be considered for quality control and proof of reproducible test preparation only. Therefore, DPM soundings taken within a radius of 1.5 m from the centre of the test pit and all CPTs of each test are given in Figure 5-12. In Table C-1, the mean trends $\delta N_{10,DPM}/\delta z$ and $\delta q_c/\delta z$ are given for each test to compare the quality of the sand preparation by a single number.

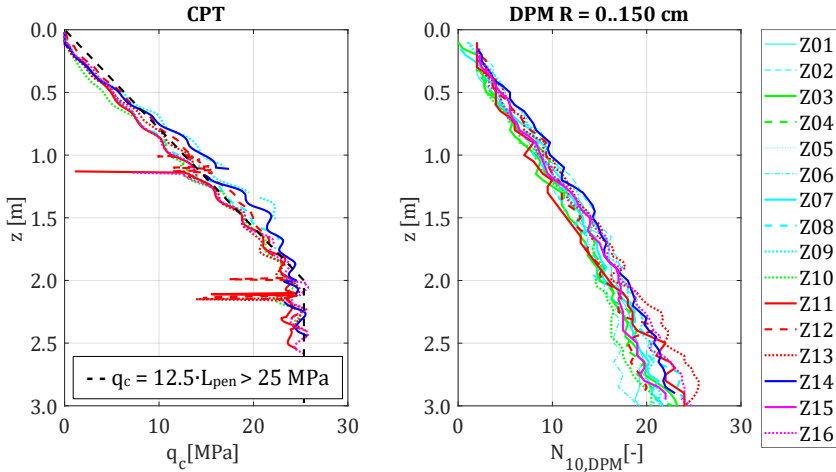


Figure 5-12: CPT (left) and DPM (right) readings for all tests after preparation

Both DPM and CPT readings show a good reproducibility of the filling of the test pits in the different tests. It may also be noticed that q_c values of about 25 MPa in a depth of about 2 m are quite high. A reason for this may be given by the overconsolidation due to dynamic compaction, as stated below.

Soil mass and volume

The soil density after soil installation can be estimated by the total mass of the installed soil and the volume of the test pit ($D_{r,pit}$). However, this method may lead to considerable errors, mainly due to the soil's water content which was not determined with the required precision during sand placement. After some of the tests, cylindrical soil samples were taken to determine the actual soil density according to DIN 18125-2 ($D_{r,sample}$). To avoid influences of the pile installation and pile loading as well as the boundary of the pit, the samples were taken at a radius of 1 m from the centre of the pit. Relative densities from samples and gradients of DPM and CPT readings are given in 0, Table C-1. As average value, a relative density of $D_r = 0.74$ is assumed for the model sand in the test pit.

Primary stress state

The primary stress state in the sand filled pit has already been investigated by FISCHER (2021), who used the same facilities and filling procedures for his tests. Silo theory (DIN 4085) was not applicable since the diameter of the pit is similar to the depth of the pit and a reduction of the earth pressure was not observed. On the contrary, an increase of horizontal earth pressure due to the compaction procedure (DIN 4085) was noticed. Figure 5-13 shows the profiles of measured effective horizontal soil stresses σ'_h after sand placement over depth z for all tests (coloured lines) and the theoretical overburden pressure $\gamma \cdot z$ (black dashed line). Obviously, a stress state with $k_0 \geq 1$ is present, probably caused by the soil compaction.

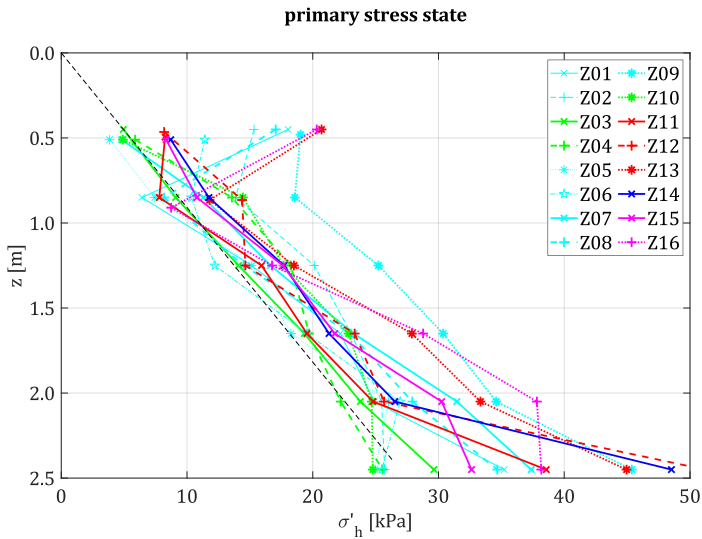


Figure 5-13: Horizontal soil stresses after sand placement

As justified by FORAY et al. (1998), higher horizontal earth pressure coefficients may represent the behaviour of overconsolidated soils as to be found in the German North Sea. FORAY et al. (1998) also observed higher CPT readings in overconsolidated sand compared to normally consolidated sand, which fits well with the somewhat surprisingly high CPT values shown above.

5.6.3 Pile installation

Three different installation methods were used. Regarding the vibratory installation technique, installation parameters were varied as well:

- impact driving
- vibratory driving
 - o crane-guided/free-riding
 - o different eccentric moments

Before installation, the pile was placed in the centre of the test pit and held in place using rollers on a pile guiding frame which rested on the walls of the test pit. The pile was installed to penetration depth of about 1 m. The installation process was interrupted and the rollers were loosened and pulled back to allow the flange to pass. Afterwards, the installation was continued to target penetration depth. Figure 5-14 shows the pile after upending (left) and during impact (middle) and vibratory pile driving (right).



Figure 5-14: Pile before installation (left), during impact driving (middle) and during vibratory driving (right)

Impact pile driving

For impact pile driving, the Delmag D2 Diesel hammer, carried by a wheel loader, was used. The hammer was operated close to maximum energy. Pile driving measurements (EA-Pfähle 2012) using two pairs of strain and acceleration sensors (mounted in opposite directions of the pile, 47 cm below the pile top) and the Allnamics PDR data acquisition unit were carried out. Pile penetration was recorded visually using a video camera and a measure drawn over the pile length and later synchronised with the pile driving records acquired with the PDR. Soil stresses were measured using the earth pressure and pore water pressure transducers and the National Instruments SCXI data acquisition unit. PDR records and soil stresses were later synchronised manually.

Vibratory pile driving

For vibratory pile driving, the APE J&M Model 23 vibratory hammer (with varying eccentrics) was rigidly attached to the model pile. Pile driving measurements at the pile head and measurements of the soil stresses were done as described above. Additionally, the following measurements were taken and acquired using the Dewesoft DW43 data acquisition unit:

- acceleration at the pile head (measured on the mounting plate)
- strains in two measuring sections
(45 cm below the pile head and 10 cm above the pile toe)
- actual pile penetration (using the cable transducer between mounting plate and crane)
- soil accelerations
- line pull (crane-guided installation only)

The measurement setup is drawn in Figure 5-15.

Driving frequency (from the acceleration measurement), pile toe penetration and line pull (for crane-guided installation) from the DW43 system were displayed in real time and used to control the installation process.

For a crane-guided pile installation the vibratory hammer (rigidly attached to the model pile) was fastened at the crane hook via a rubber damper to reduce vibrations on the crane and a load cell. The hammer frequency f_d was adjusted with a throttle regulating the hydraulic flow. The pile was lowered into the soil with a constant penetration speed v_{pen} and at constant driving

frequency f_a . The driving frequency was adjusted to achieve a similar centrifugal force with the different vibro hammers (cf. Figure 5-9 and Equation (2-11)).

For free-riding pile installation, the vibratory hammer was not fastened to the crane. The driving frequency was increased subsequently using the throttle to provide a more or less constant, continuous penetration. Depending on the manual control of the driving frequency, 'aggressive' and 'moderate' installations can be distinguished: In case of 'aggressive' frequency control, the throttle to regulate the hydraulic flow was opened faster to aim at a constant and swift pile penetration. In case of 'moderate' frequency control, the throttle was opened more slowly, resulting in situations where the pile was close to a 'refusal' (= no/little further penetration).

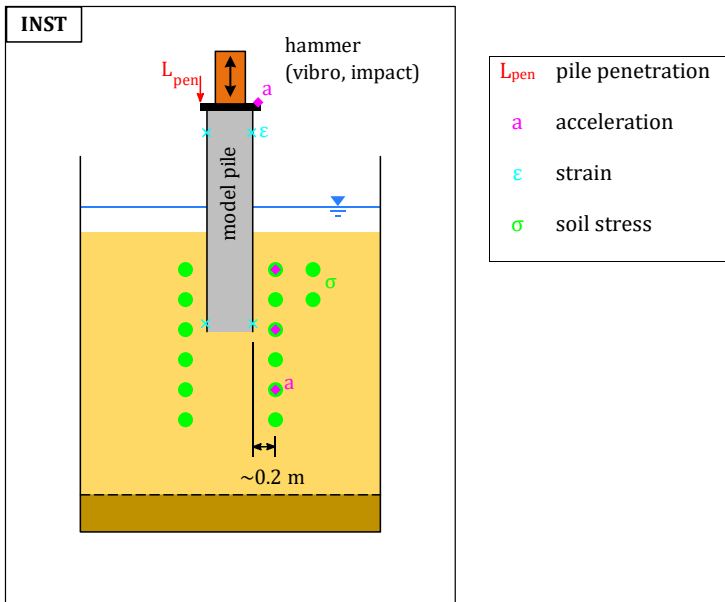


Figure 5-15: Measures taken during pile installation

5.6.4 Cyclic lateral load test (CLLT)

After pile installation the transition piece was mounted on top of the pile. The system's bending mode eigenfrequency after pile installation was determined by means of a lateral frequency response test (LFRT) (see below). The actual pile penetration was measured with the upper edge of the test pit as reference. The guiding frame was aligned with the loading direction to serve as support for the displacement transducers. Displacement transducers and inclinometer were installed. The system was left unloaded for about 72 hours to allow for pile setup and relaxation of possible pore water build-ups.

Figure 5-16 shows the pile with loading device and all measuring equipment for cyclic lateral load testing (left) and the pile with detached loading device and measuring equipment for lateral frequency response testing (right).

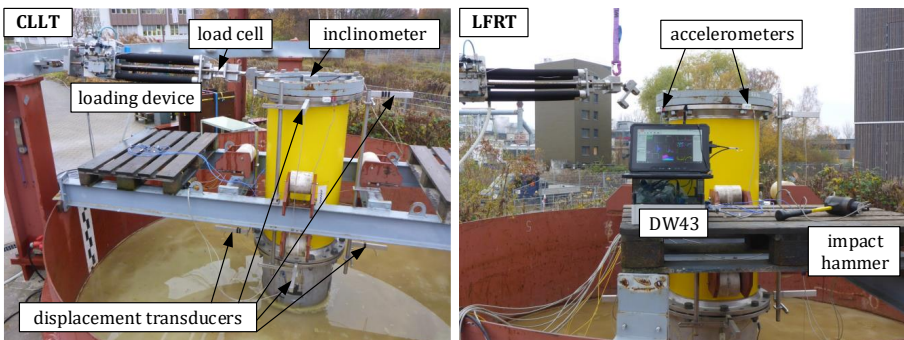


Figure 5-16: Pile with measurement equipment and loading device prepared for CLLT (left) and pile detached from loading device for LFRT (right)

Figure 5-17 shows the measured quantities and corresponding sensors used during cyclic lateral loading (CLLT) and for eigenfrequency measurements (LFRT).

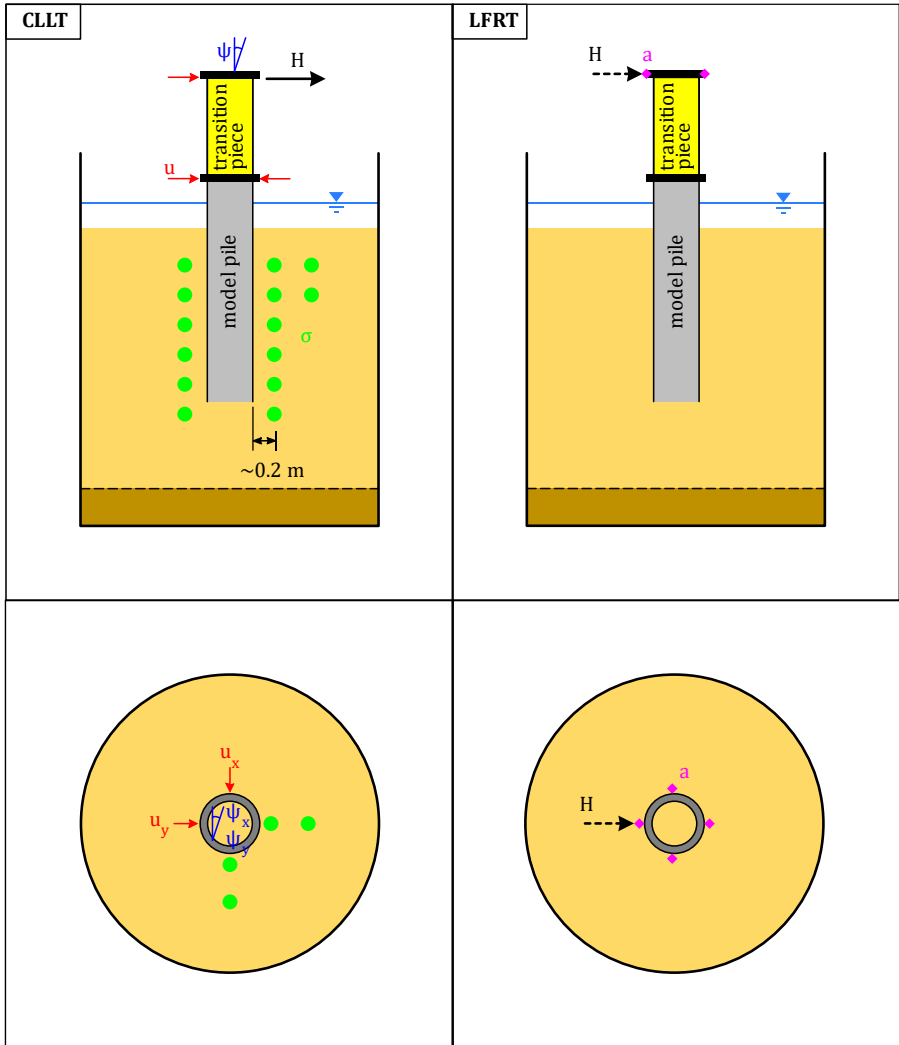


Figure 5-17: Measurement setup for cyclic lateral load testing (left) and lateral frequency response test (right)

Cyclic lateral loading was carried out in several phases. Directly before each phase of the cyclic lateral load test, the loading device was attached. Directly before each loading phase, a pre-tension of 50% of the minimum lateral load ($H = 2.5$ kN for phase 4 and 1 kN otherwise) was

applied. The pre-tension was necessary to assure a permanent pulling load applied to the pneumatic muscle used in the loading device. Figure 5-18 shows the force signal (top left) and displacement signal (bottom left) of the start of phase 4 of test Z14. A phase offset of $u \approx 4.5$ mm can be seen in displacement signals which originates from transducer offset and displacement of previous loading phases. This offset is later subtracted from the measurement signal. At about $t \approx 3 \dots 4.5$ min, the pre-tension of about $H \approx 2.5$ kN is applied, resulting in an increase in pile head displacement of about $\Delta u \approx 0.2$ mm. Afterwards, cyclic loading with normally 12,000 cycles and consequently cyclic pile head movements start. The pile response to cyclic loading, which was described exemplary for the pile head displacement u , also applies for pile deflection in general and soil stresses. In all cases, phase offsets were determined to evaluate system performance during specific loading phases.

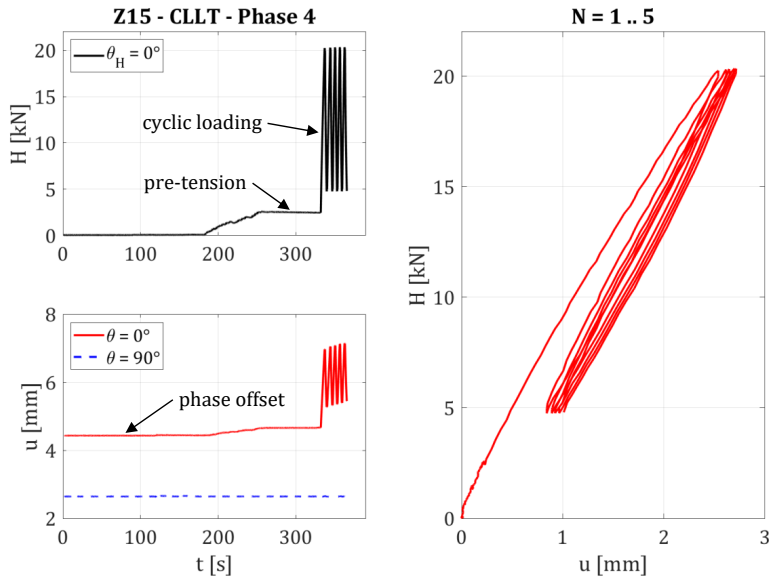


Figure 5-18: Exemplary force (top left) and displacement (bottom left) signals and load-displacement curves (right) for start of cyclic lateral loading

After each phase, the system was completely unloaded and the loading device was detached to execute a frequency response test and to change the loading direction.

In each test, the loading scenario described in Table 5-3 was executed at least until phase 4 ($H = 5..20$ kN). Within some tests, phases 4 or 5 were extended to up to 140,000 cycles to investigate high cycle behaviour. After phase 4 or 5, phases with different loading scenarios (e.g. different load ranges H_{mdl} , different angles θ_H) were executed. Cycle period was adjusted to $T_{cycl} \approx 5$ s for phases with a maximum load of 15 kN and $T_{cycl} \approx 7$ s for phases with a higher maximum load. A detailed list of all tests can be found in 0.

Load-deflection measurements

While cyclic loading, the following measurements were taken with a frequency of 100 Hz (resulting in 500 to 700 samples per cycle):

- lateral force H [kN] at the top of the TP
- pile displacement u [mm] at different directions and levels
- pile inclination ψ [°] at the top of the TP
- total soil stresses σ_v , σ_{rad} [kPa] in vertical and radial directions as well as pore water pressure p_{PWP} [kPa] at different positions

The positions of the sensors are sketched in Figure 5-17 (left).

Eigenfrequency measurements

To investigate the change of the pile's lateral dynamic behaviour, the bending mode eigenfrequency was determined by means of lateral frequency response tests at various stages before, during and after cyclic lateral loading. Therefore, an impact excitation and the pile's response had to be measured. High sensitivity accelerometers were mounted to the top of the transition piece. An instrumented impact hammer was used for the excitation. Details on eigenfrequency determination are given in (STEIN 2020).

Between the load phases, lateral frequency response tests were executed to measure the system's eigenfrequency. Therefore, high sensitivity accelerometers were mounted to the top of the transition piece. The system was dynamically excited at the top of the transition piece using an equipped impact hammer. The sensor and excitation positions are drawn in Figure 5-17 (right).

Mudline elevation measurements

Before the first phase and after each phase of cyclic loading, the actual pile penetration and the mudline elevation around and in the pile were measured. The pile penetration was measured the same way as after pile installation. The mudline elevation around the pile was measured using scaling labels fixed to the pile wall at mudline level in eight directions with a reading accuracy of 5 mm (see Figure 5-19). The mudline elevation inside the pile was measured at three points inside the pile using a levelling arm from the upper edge of the transition piece.

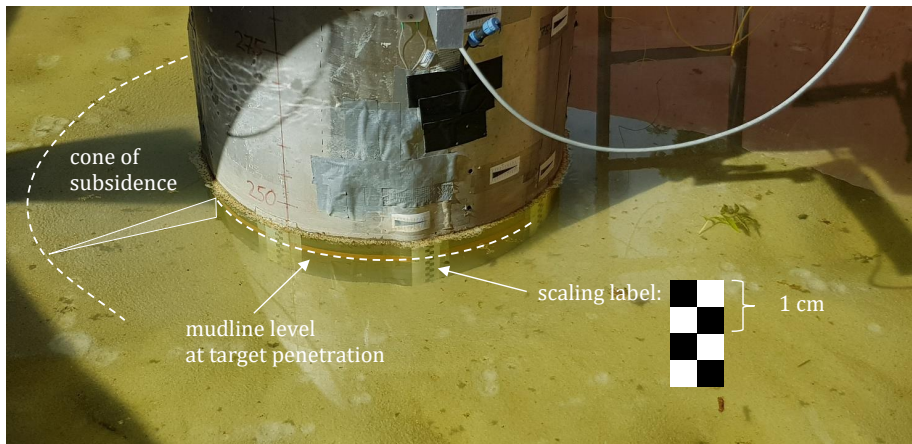


Figure 5-19: Soil subsidence around pile

5.7 Data processing

5.7.1 General objectives

To analyse the pile behaviour due to cyclic lateral loading, the following information had to be extracted from the measurements:

- load deflection behaviour
- deflection accumulation law
- soil stiffness development
- soil stress development

Therefore, load and deflection quantities at different pile sections had to be calculated and load cycles had to be identified from the continuous measurements. The determination of the pile's eigenfrequency is an independent topic.

To investigate possible installation effects on the pile and soil behaviour, the pile installation process had to be described. For vibratory installation, the following parameters were analysed:

- driving frequency
- pile motions (acceleration, velocity, displacement, penetration speed)
- pile forces and external forces
- soil stresses

For impact driving, the following parameters were analysed:

- impact energy
- blow count
- soil stresses

5.7.2 pile driving monitoring (impact driving)

From the strain and acceleration measurements logged by the PDR and the penetration records from the accompanying videos, blow counts per 100 cm penetration N_{100} [-], total driving resistance per blow R_{blow} [kN] and driving energy per blow W_{blow} [kJ] over penetration depth L_{pen} [m] were evaluated.

The blow count N_{100} is defined as the number of hammer blows for an increase of pile penetration of 100 cm. For the driving resistance and driving energy, the measured strain and acceleration signals were evaluated. Pile force F_{str} [kN] was calculated from the measured strain ε [-] and axial pile stiffness EA [kN], velocity v [m/s] was derived from measured acceleration a [m/s^2] by integration over time t [s]:

$$F_{\text{str}}(t) = \varepsilon(t) \cdot EA \quad (5-8)$$

$$v(t) = \int a(t) dt \quad (5-9)$$

The energy induced into the pile $W(t)$ [kJ] can be calculated as integral of the product of force and velocity over time (EA-Pfähle 2012):

$$W(t) = \int F_{\text{str}}(t) \cdot v(t) dt \quad (5-10)$$

The energy per blow or driving energy W_{blow} is the energy at the end of the blow. The penetration specific energy W_{100} [kJ/m] is the energy per blow multiplied with the number of blows per 1 m penetration:

$$W_{100} = W_{\text{blow}} \cdot N_{100} \quad (5-11)$$

Additionally, the total driving resistance per blow R_{blow} can be calculated from force and velocity signals and the dynamic stiffness or pile impedance Z_{pile} , as described in (EA-Pfähle 2012). This is performed by default during pile driving monitoring. Further analysis of the force and velocity signals are possible to estimate static pile resistance, e.g. by wave equation analysis and signal matching.

The following Figure 5-20 shows typical force and velocity signals of one hammer blow during impact pile driving. Pile force from measured strain and pile stiffness F_{str} and pile force from integrated acceleration and pile impedance $v \cdot Z_{\text{pile}}$ are given in [kJ], transferred energy W is given in [kJ]. Parallel to the time t , the pile length coordinate $L = t \cdot c_{\text{pile}}$ is plotted on the abscissa. Zero of time and length is defined at the start of the blow.

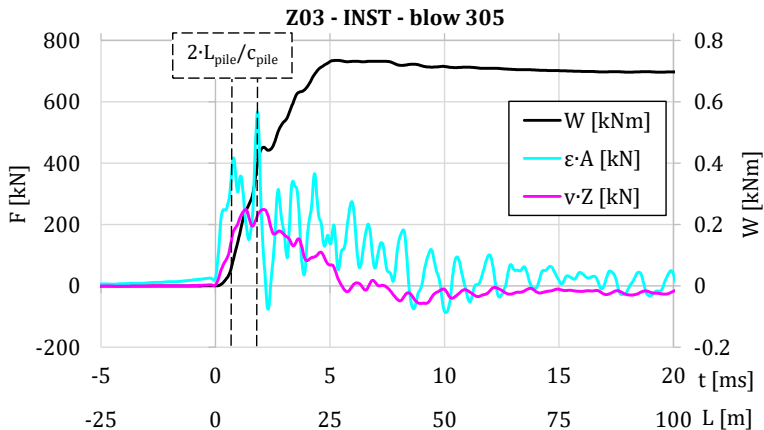


Figure 5-20: Typical pile signal from hammer blow

Before the start of the blow, an increase in the force signal was detected which is usual for Diesel hammers and indicates the compression of the fuel in the combustion chamber. The hammer blows were long compared to pile length, measuring 2.55 m from the sensor level to the pile toe. Due to the length of the impact compared to the pile length, the analysis of the pile signals as usual in pile driving analysis or dynamic pile testing may not be appropriate. However, the evaluation of the measured energy is considered a valid method to assess the driving energy and thus the comparability and repeatability of the tests.

5.7.3 pile driving monitoring (vibro driving)

To describe the pile motion during vibratory driving, time signals and derived vibro parameters are distinguished. Time signals were captured for pile penetration $L_{pen}(t)$ [m], pile head acceleration $a(t)$ [m/s^2], pile strain $\varepsilon(t)$ [-] and line pull $F_{line}(t)$ [kN]. Pile penetration speed v_{pen} [m/s] was defined as the gradient of the pile penetration. Velocity signal $v(t)$ [m/s] and displacement signal $s(t)$ [m] were integrated from acceleration signal, integration errors were corrected by the measured pile penetration speed v_{pen} and pile penetration L_{pen} . Force signals $F_{str,top}(t)$ and $F_{str,toe}(t)$ were calculated from dynamic strain measurements (after deduction of strain offset) and pile stiffness (Equation (5-8)). The centrifugal force $F_c(t)$ was calculated from driving frequency and eccentric moment, the inertia force $F_{in}(t)$ was calculated from the pile acceleration $a(t)$ and dynamic mass m_{dyn} . The dynamic force $F_{dyn}(t)$ is defined as the sum of inertia force $F_{in}(t)$ and centrifugal force $F_c(t)$:

$$F_{in}(t) = a(t) \cdot m_{dyn} \quad (5-12)$$

$$F_c(t) = M_e \cdot \omega_d^2 \cdot \sin(\omega_d \cdot t + \Phi_F) \quad (5-13)$$

$$F_{dyn}(t) = F_{in}(t) + F_c(t) \quad (5-14)$$

The phase Φ_F was not measured.

For further evaluation of measured pile forces, the system above the strain sensors at the pile head is depicted in Figure 5-21. For the free vibrated piles, only the dynamic force F_{dyn} acts on the system above the measurement level which is equal to the offset-corrected measured force $F_{str,top}$:

$$\begin{aligned} F_c(t) + F_{in}(t) &= M_e \cdot \omega_d^2 \cdot \sin(\omega_d \cdot t + \Phi_F) + a(t) \cdot m_{dyn} \\ &= \varepsilon(t) \cdot EA = F_{str,top}(t) \end{aligned} \quad (5-15)$$

For the validity of Equation (5-15), the correct mass m_{dyn} (i.e. including the pile section until the measurement level) and the correct phase Φ_F have to be considered. Φ_F is the phase shift between the rotation of the eccentrics of the vibro hammer and the oscillation of the pile-vibro assembly and varies between 0 and π (NENDZA 2007). As the phase Φ_F was not measured directly (e.g. from the position of the eccentrics), it was recursively estimated from the measured forces $F_{str,top}$, F_{in} and F_c . Therefore, Φ_F was varied between 0 and π and the value with the smallest integral over time of the difference between $F_{str,top}$ and $F_{in} + F_c$ was taken.

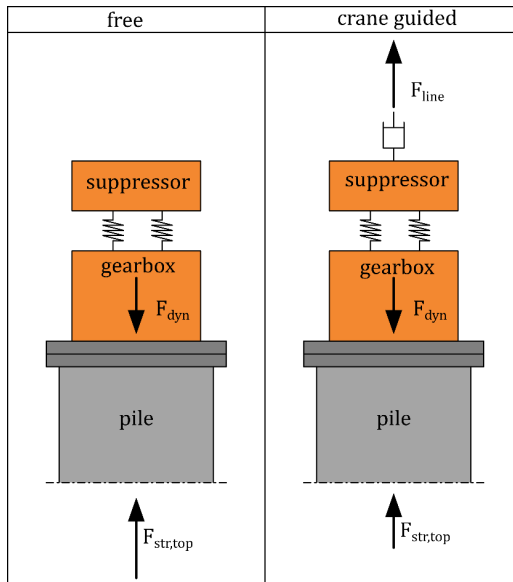


Figure 5-21: Forces acting on the pile head and vibro above upper strain sensor level

In case of crane-guided vibratory driving, additional line pull and growing influence of the suppressor make it difficult to evaluate the system's dynamics.

Vibratory driving energy

The energy W_{1s} [kJ] was calculated similar to Equation (5-10) over the period of one second and divided by the driving frequency f_d [Hz] (= number of vibration cycles per second) to get the energy per cycle W_{cycle} [kJ]. To get penetration specific energy W_{100} [kJ/m], the energy W_{1s} was divided by the penetration speed v_{pen} [m/s]:

$$W_{100} = W_{1s}/v_{pen} \quad (5-16)$$

Integration of $F \cdot v$ over time according to Equation (5-10) gives the total energy acting on the pile-soil system. To get a better understanding of energy-dependence on the pile penetration, two distinctions were made:

- The energy during downward-directed pile movement W_{\downarrow} was calculated considering only energy induced when $v > 0$.
- The energy during irreversible penetrative pile movement W_{set} was calculated considering only energy induced when $v > 0$ and the pile toe reached a penetration that had not been reached before, as proposed by SCHÖNIT & REUSCH (2008).

Static and dynamic pile forces

Pile forces were derived from measured strain F_{str} and acceleration and eccentric moment F_{dyn} as described above. These forces are in equilibrium with static and dynamic pile resistances. $R_{stat}(s)$ describes the static, displacement-dependent soil resistance, $R_{damp}(v)$ describes the velocity-dependent damping and $R_{in}(a)$ describes the acceleration dependent inertia force acting on the pile. Definitions of R_{stat} , R_{damp} and R_{in} can be taken from Figure 2-3 and Equations(2-1), (2-2) and (2-3). Static pile resistance and damping were estimated by the following procedure:

- For dynamic mass m_{dyn} , the pile mass below the measuring section in focus was taken without any attached soil body. Thus, R_{in} is known from measured acceleration.
- It was assumed that $R_{stat}(s=0) = 0$; the dynamic part of the displacement (without overlying pile penetration speed) was taken for s . So $R_{damp}(s=0)$ is the measured force minus inertia force at $s = 0$.
- A linear relationship between R_{damp} and v was assumed ($\alpha_{damp} = 1$ in Equation (2-2)), thus the damping constant can be calculated by

$$C_{ax} \cdot L_{pen} \cdot 2 \cdot \pi \cdot D_{pile} = R_{damp}(s=0)/v(s=0),^6$$

⁶ The 'circumference' of the pile shaft of an open-ended pipe pile is approximated by $2 \cdot \pi \cdot D_{pile}$ (outer + inner pile shaft) as the wall thickness is small compared to the diameter.

- With known damping constant C_{ax} and 'inertia constant' m , R_{damp} and R_{in} can be calculated at any timestamp and R_{stat} can be calculated from the measured force by subtracting R_{damp} and R_{in} .

From the time signals, statistical values (min, mean, max, peak-to-peak) were calculated over a period of three cycles to be plotted in penetration records. The driving frequency f_d was calculated from acceleration measurements at pile head using moving-window FFT algorithm with a window length of one second. The following Figure 5-22 shows exemplary force and motion signals over three vibration cycles.

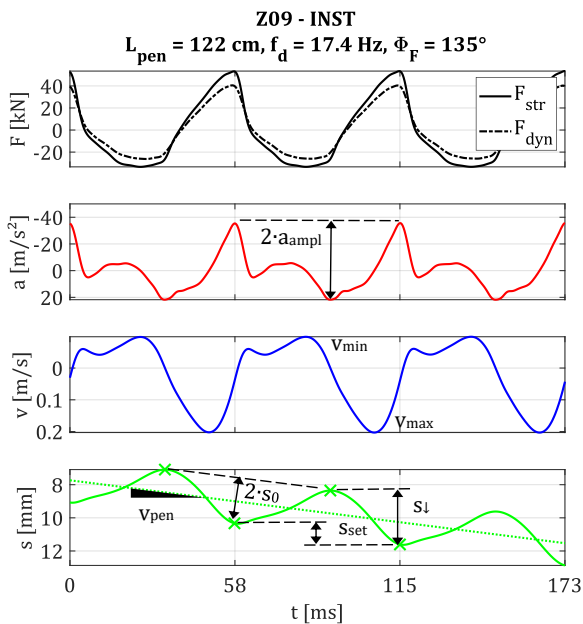


Figure 5-22: Pile signals from vibratory driving measurements and exemplary derived vibro parameters

Pile force signals (top) are drawn in black. The solid line indicates the pile force from measured strain F_{str} , the dashed line shows pile force F_{dyn} from measured acceleration (inertia force) F_{in} plus the sinusoidal course of the centrifugal force F_c . Pile motion signals are drawn in different colours. The straight dashed green line (bottom) describes the pile penetration measured with the wire transducer which was used to correct the displacement and velocity signals. The slope

of this line is the penetration speed v_{pen} . The peak oscillation amplitude s_0 , set per cycle s_{set} , and downward displacement s_d were extracted from the displacement signal (= double integrated acceleration signal). Acceleration amplitude a_{ampl} as well as largest upwards and downwards directed velocities v_{min} and v_{max} are also meaningful parameters to describe vibro pile driving, as will be shown in Section 6.2.3.

5.7.4 soil stress developments during pile installation

During all pile installations, independent of the installation method, total soil stresses in vertical and radial direction σ_v and σ_{rad} and pore water pressures p_{PWP} were measured. From the measured total stresses σ_v and σ_{rad} , the pore water pressure p_{PWP} was subtracted to get the effective soil stresses σ'_v and σ'_{rad} . The pore water pressure at any point in the test pit (i.e. at any sensor location) was considered equal to the hydrostatic pressure $\gamma_w \cdot (z+h_{WT})$, while the actual water table h_{WT} above mudline was gotten from the actual pore water pressure measured at different locations to account for fluctuations in the water table over time (e.g. due to evaporation or rain).

$$\sigma' = \sigma - p_{PWP} \quad (5-17)$$

$$p_{PWP} = \gamma_w \cdot (h_{WT} + z) \quad (5-18)$$

$$h_{WT} = \frac{p_{PWP,msrd}}{\gamma_w} - z \quad (5-19)$$

PWP measurements in the vicinity of the pile are used to investigate possible effects of PWP build-ups. Figure 5-23 shows measurement signals of the effective horizontal stress (top) and pore water pressure (middle) as well as the pile toe penetration (bottom). The timestamps where the pile toe reaches the measurement level of the earth pressure spade ($z \approx 2.05$ m) and the PWP sensor ($z \approx 2.2$ m) are marked with solid and dashed lines, respectively.

The effective horizontal soil stress (Figure 5-23, top) oscillates with an amplitude of over 50 kPa and its mean value increases by about 50 kPa as the pile toe approaches the measurement section. This phenomenon will be discussed in Section 6.2. At the same time, the measured PWP shows an oscillation amplitude of way below 1 kPa and an overall increase of about 1 kPa, both negligible for the evaluation of the effective earth pressure.

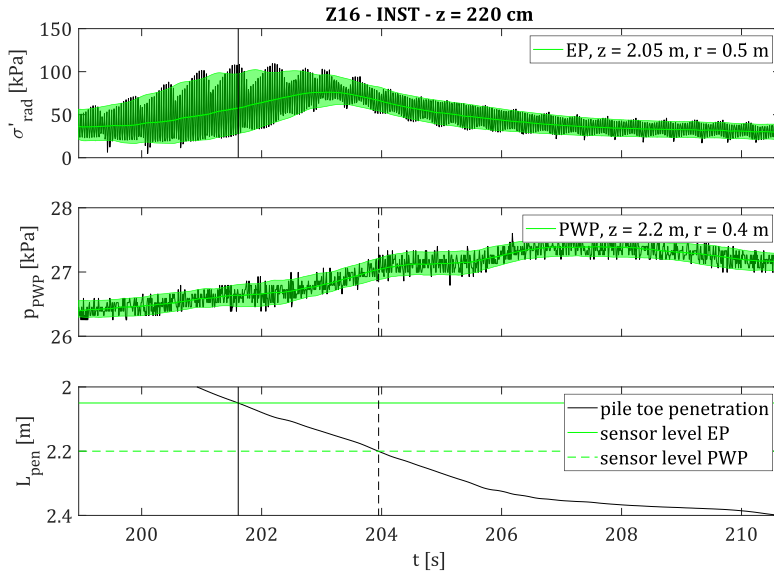


Figure 5-23: Exemplary development of soil stresses in the vicinity of the pile during vibratory driving

For further analysis, statistical values (min, max, mean, median) of the effective stress signals over a period of one second were taken and matched to the pile penetration to describe stress amplitudes and overall trends.

5.7.5 pile measurements during lateral loading

Horizontal displacement and inclination of the pile were measured in two directions. The lateral displacement was measured at the top and bottom of the transition piece while the inclination was measured at the top of the transition piece only. The lateral load applied at the top of the transition piece was measured in loading direction (cf. Section 5.6.4). All signals were captured at a sampling frequency of 100 Hz and filtered using a moving median filter with a window length of 10 samples; the inclinometer signals were filtered using a moving median filter with a window length of 30 samples. Figure 5-24 shows an exemplary plot of the measured lateral load H (top), displacement at pile head u (middle) and inclination at the TP ψ (bottom) for the first two cycles of test Z09. The plots on the right show zoomed signals. The

filtering procedure was especially necessary for smoothing of the inclination signals (bottom). The accelerometer-based inclinometers were affected by the sudden pulling and releasing of the loading device.

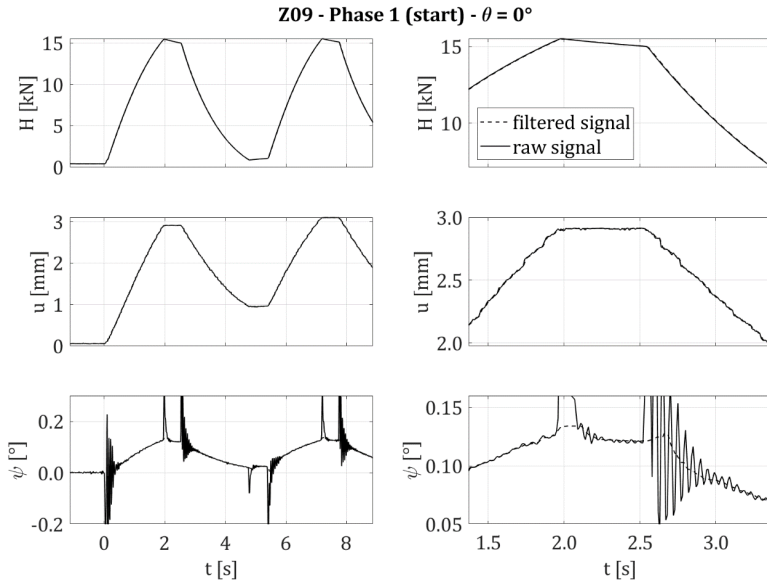


Figure 5-24: Exemplary raw and filtered signals from cyclic lateral loading

From the measured lateral force H , cycles were isolated and timestamps for the beginning and end of each loading and unloading phase were detected. Pile deflections were picked at the timestamps. Figure 5-25 (left) shows the procedure for the first cycle of phase 1 of test Z14. A load level of $H = 1.15$ kN is used to determine the cycles. Lateral load H is drawn in the upper left graph and the corresponding horizontal pile displacement at pile head level u is drawn in the bottom left graph. The resulting load displacement curve is drawn in the top right graph. An anelastic behaviour can be recognised. Between the points $u(H)$ of the particular load levels during the loading and unloading periods, the loading and unloading secant stiffness $E_{lat,load}$ and $E_{lat,unld}$ can be determined. As expected, the unloading stiffness of the first cycle is much higher than the loading stiffness.

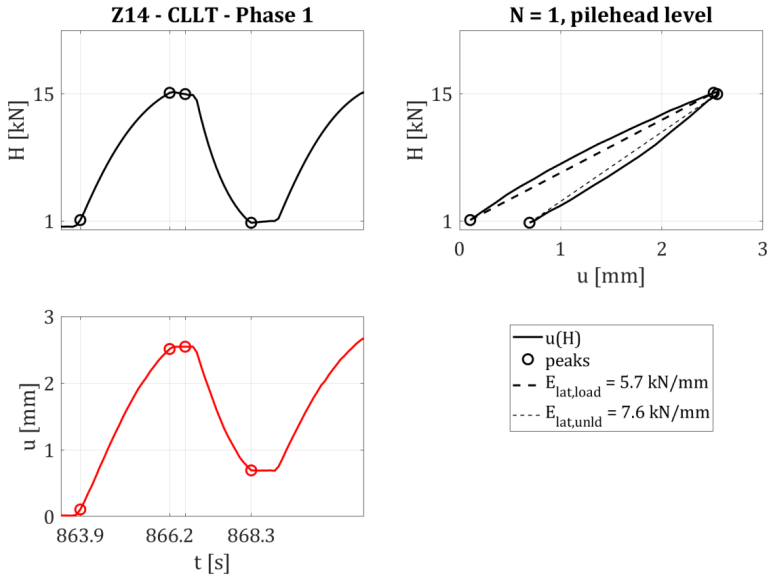


Figure 5-25: Example of detection of cycles (left) and calculation of secant stiffness (right)

5.7.6 soil stress developments during lateral loading

Effective soil stresses were calculated from measured total stresses and pore water pressures as described in Section 5.7.4. To investigate possible PWP accumulation, PWP transducers were placed in a distance of about 10 cm to the pile wall ($r \approx 40$ m) at depths and directions with highest expected soil stresses ($z \approx 20, 60$ cm in downwind direction and $z \approx 220$ cm in upwind direction; Figure 5-26, middle) for some tests. Figure 5-26 shows exemplary PWP signals for phase 1 of test Z13. During cyclic lateral loading of about 18 hours, no PWP build-up was measured (Figure 5-26, left). The maximum differences from the mean PWP were far below 1 kPa (Figure 5-26, middle) and does not have a severe influence on the effective soil stress σ' .

As the PWP sensors were placed in a distance of 10 cm to the pile wall, PWP accumulation at closer distance to the pile cannot be excluded by these measurements. PWP build-ups at the locations of the earth pressure spades with a distance of about 20 cm to the pile wall ($r \approx 50$ m) and thus an influence on the effective earth pressure (Equations (5-17) to (5-19)), however, can be excluded.

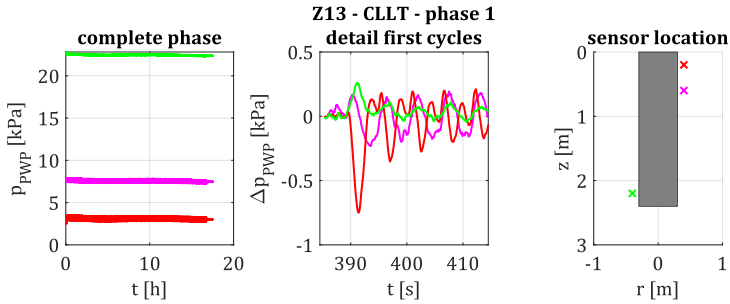


Figure 5-26: Exemplary PWP development in the vicinity of the pile due to lateral loading

Regarding the fluctuation of the PWP during the first cycles (Figure 5-26, middle) it is notable that the measured PWP at the uppermost sensor location (red) drops during initial loading and has a phase shift with respect to the other two PWP measurements (magenta, green). An increase of PWP with soil loading would be expected as the pore water takes a (here little) part of the load acting on the soil matrix. A possible explanation for the unsuspected behaviour can be given considering dilatant soil behaviour:

- At shallow depth, overburden pressure $\sigma'_v = \gamma' \cdot z$ and thus shear strength $\tau_s = \sigma'_v \cdot \tan(\varphi)$ is low, leading to dilatant soil behaviour and early soil failure together with an increase of the pore volume. This causes the decrease of the PWP.
- In deeper soil layers, overburden pressure and shear strength are higher so that the increase of pore volume due to dilatant soil behaviour is less severe.

To analyse changes due to cyclic loading, the difference of soil stresses $\Delta\sigma'$ with respect to a certain stage of the tests (e.g. the start of a loading phase) was calculated by subtracting a certain offset. The same procedure is illustrated in Figure 5-18 for the pile head displacement. The phase offset for example was taken as mean value over several seconds before pre-tension was applied to the loading device.

$$\Delta\sigma'_{\text{phase}} = \sigma' - \sigma'_{\text{offset,phase}} \quad (5-20)$$

The soil stresses at different positions within the test pit were sampled synchronous to the pile measurements. Thus, the soil stresses (and derived measures, e.g. changes in effective soil stresses) at certain load cycles (min and max values) can be given by the same time stamps as selected for the pile deflections. Thus, soil stress developments over load cycles $\sigma(N)$ can be

given for certain sensors or soil stress distribution over depth $\sigma(z)$ can be given for certain load cycles.

5.7.7 eigenfrequency measurement

For the eigenfrequency measurements mentioned in Section 5.6.4, two signals were obtained: The excitation signal measured by an accelerometer mounted to the impact hammer $a_{\text{exc}}(t)$, which can be scaled to a force signal $H_{\text{exc}}(t)$, and the lateral pile response measured by the accelerometers mounted to the transition pieces, $a_{\text{resp}}(t)$. As shown in Figure 5-17, four accelerometers were mounted to the top flange of the transition piece in directions of $\theta = 0^\circ, 90^\circ, 180^\circ$ and 270° . For the examination of the system's bending mode eigenfrequency, only those signals measured by the sensors aligned with the direction of the hammer impact were evaluated. Measurements at opposite sides of the transition piece were intended to be taken for redundancy but could also be used to distinguish between cantilever and ring oscillations as described in STEIN (2020).

In modal analysis, the eigenfrequencies of a system are identified by means of the transfer function $\hat{h}(f)$ which is the relation between system excitation and system response in the frequency domain:

$$\hat{h}(f) = \frac{a_{\text{resp}}(f)}{a_{\text{exc}}(f)} = \frac{\text{FFT}(a_{\text{resp}}(t))}{\text{FFT}(a_{\text{exc}}(t))} \quad (5-21)$$

The excitation and response in the frequency domain can be obtained from the time domain signals by a Fast Fourier Transformation (FFT). The resulting FFTs of the system excitation, system response and the system's transfer function consist of a real part describing the amplitude of system acceleration at different frequencies and an imaginary part describing the phase. System eigenfrequencies can be assumed where the real part of the transfer function has a local maximum and the phase shows a turning point (= local extrema of the derivate of the phase).

Figure 5-27 shows excitation (black) and response (blue) signals in the time domain (top left) with a sharp impact and decay of the response signal over about 300 ms. In the frequency domain (top right), the response has peaks at about 21 Hz, 288 Hz, and 410 Hz while the excitation (= hammer impact) shows a constant course over the plotted frequency range. Thus, the shape of the amplitude transfer function is similar to the response spectrum and not plotted

here. The phase Φ of the transfer function (bottom right, green) shows continuous values between $-\pi$ and π . Turning points can be found at the abovementioned frequencies, so they all are candidates for the pile's bending mode eigenfrequency.

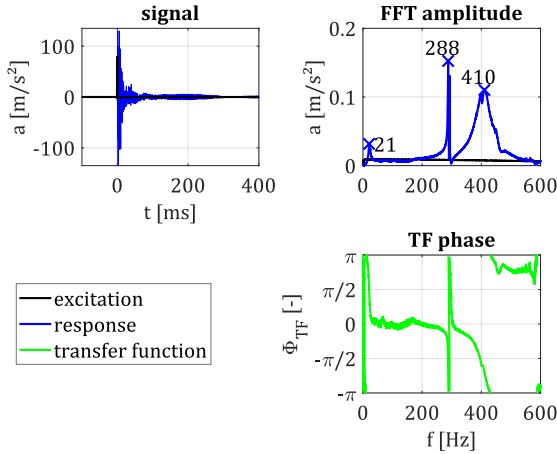


Figure 5-27: Measured signals (top left), frequency spectra (top right) and phase of transfer function (bottom right) from LFRT

The bending mode eigenfrequency $f_{0,lat}$ [Hz] of a simple cantilever (see Figure 5-28, right) can be estimated used an analytical cantilever model (DEN HARTOG & MESMER 1952):

$$f_{0,lat} = \frac{1}{2 \cdot \pi} \cdot \sqrt{\frac{3 \cdot EI}{L_{eq}^3 \cdot (m_1 + 0.23 \cdot \rho \cdot A \cdot L_{eq})}} \quad (5-22)$$

EI [kNm^2] is the pile bending stiffness, m_1 [kg] is a point mass at the free end of the cantilever, and $\rho \cdot A$ [kg/m] is the mass of the pile per unit length. L_{eq} [m] is the equivalent length of the cantilever, which is in the range between the total length of the pile and transition piece $L_{pile} + L_{TP}$ and the free length of the transition piece and the pile above the mudline L_{free} , depending on the soil bedding. The model pile and the equivalent system are shown in Figure 5-28. Here, the mass of the flange connection between pile and TP is distributed over the equivalent pile length $(\rho \cdot A + m_2/L_{eq})$:

physical model idealised system

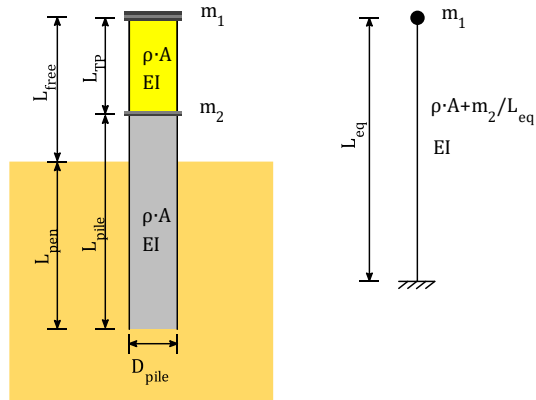


Figure 5-28: Physical pile model (left) and equivalent clamped cantilever (right)

Using the equivalent cantilever system, the system's eigenfrequency is estimated between 14 Hz and 48 Hz (STEIN 2020), thus the excitation is suited for modal analysis of the pile-soil system.

Referring to the signal analysis, 21 Hz indicates the first fundamental of the bedded beam. Further evaluation of the acceleration signals revealed that the higher frequencies may belong to annular oscillations of the upper flange (STEIN 2020). Therefore, the peaks in the frequency spectra around 21 Hz are considered as bending mode eigenfrequencies. Their differences and developments will be analysed, among other subjects, in the subsequent chapter.

Time

Time and loading frequency of the cyclic lateral loading tests are not scaled because velocity dependent damping and inertia effects and are considered negligible for loading frequencies smaller than 1 Hz. Cycle times of $T_{cycl} \approx 5 \dots 7$ s were chosen to conduct one phase with 12,000 cycles from one working day to the other. The mass of the foundation (including model pile, transition piece (TP), flanges and saturated soil within the pile) is about $m \approx 2,000$ kg. A loading duration of $T_{cycl} = 5$ s, results in an angular frequency of $\omega \approx 1.3$ 1/s. The initial lateral secant stiffness of the pile at 0.6 m above the mudline was about $E_{lat,sec} \approx 6.3$ kN/mm for the first cycle and increasing with further cycles (STEIN et al. 2019a). Equation (4-10) then yields:

$$m [t] \cdot \omega [1/s] = 3.16 \ll 630 = 0.1 \cdot E_{iat} [kN/m]$$

Thus, inertia effects can be neglected and the loading frequency varied within a certain range without influencing the model.

Based on the generic OWT, scaling laws and practical constraints, the model with the parameters given in Table 4-1 was set up in the geotechnical test pit at the Institute for Geomechanics and Geotechnics of Technische Universität Braunschweig (IGG-TUBS).

Chapter 6 Results of model tests

6.1 Overview

In this chapter, the results of the model tests described in the previous chapter shall be presented and discussed. Table 6-1 gives an overview over all tests with the main characteristics of the installation process and a set of colours, markers, and line styles to be used for each test when comparing results of different tests. The installation equipment is specified in Section 5.5. Regarding free and guided vibratory installation refer to Section 5.6.3. Eccentric moment M_e and driving frequency f_d can be regarded as control parameters for all vibratory installations. For the crane-guided installations, the penetration speed v_{pen} is another control parameter while for free installation, the penetration speed is a part of the response of the dynamic system. Tests with vibratory pile installation are grouped regarding free/crane-guided installation and the control parameters M_e and f_d . For tests of one group, the same colour is used. The group of tests with free vibratory installation and high eccentric moment is subdivided into a 'moderate' (thin lines) and a more 'aggressive' (bold lines) manual control of the driving frequency (cf. Section 5.6.3). Crane-guided vibratory driven piles were installed with a 'fixed' driving frequency.

The evaluation of the model tests is structured as follows:

- Section 6.2 dynamic response of pile and soil during pile installation with respect to different installation methods/parameters
- Section 6.3 monotonic response of pile and soil to lateral loading with respect to different installation methods/parameters (first cycles of cyclic lateral load tests)
- Section 6.4 cyclic response of pile and soil to uni-directional lateral loading with respect to different installation methods/parameters (first phases of cyclic lateral load tests)
- Section 6.5 cyclic response of pile and soil response to multi-directional lateral loading (all phases of cyclic lateral load tests)

Table 6-1: Pile installation parameters

test	installation method	M_e [kg·m]	f_d [Hz]	v_{pen} [mm/s]	group [v_{pen} - M_e - f_d]	line marker	line style
Z01	vibro	2.33	13.8 .. 22.2	variable	free-hi-mod	×	—
Z02	vibro	2.33	11.1 .. 25.3	variable	free-hi-mod	+	- -
Z03	impact	--	--	--	--	×	—
Z04	impact	--	--	--	--	+	- -
Z05	vibro	2.33	12.0 .. 22.2	variable	free-hi-mod	*	...
Z06	vibro	2.33	12.0 .. 23.9	variable	free-hi-mod	*	..
Z07	vibro	2.33	11.7 .. 26.1	variable	free-hi-aggr	×	—
Z08	vibro	2.33	14.1 .. 27.9	variable	free-hi-aggr	+	- -
Z09	vibro	2.33	14.0 .. 29.6	variable	free-hi-aggr	*	...
Z10	impact	--	--	--	--	*	...
Z11	vibro	1.36	34.3	20	guided-hi-fix	×	—
Z12	vibro	1.36	34.4	20	guided-hi-fix	+	- -
Z13	vibro	1.36	34.4	70	guided-hi-fix	*	...
Z14	vibro	1.36	16.1 .. 30.8	variable	free-lo	×	—
Z15	vibro	2.33	25.8	20	guided-lo-fix	×	—
Z16	vibro	2.33	26.0	70	guided-lo-fix	+	- -

6.2 Pile installation

6.2.1 Evaluation scheme for pile installation processes

In this section, soil installation processes are investigated. They are described by means of pile driving monitoring data over penetration depth. This is quite compact for impact driven piles but elaborate for vibratory driven piles. In the latter case, pile motions and the mobilisation of pile resistances are analysed in detail. Soil stress developments over penetration depth for different sensor levels as well as comparisons to corresponding pile driving parameters are used to examine influences of the installation process on the soil's stress state.

6.2.2 Impact driven piles

For the three impact driven piles Z03, Z04 and Z10, pile driving records showing blow count per 1 m pile penetration N_{100} , total driving resistance per blow R_{blow} and energy per 1 m penetration W_{100} over pile penetration L_{pen} are given in Figure 6-1.

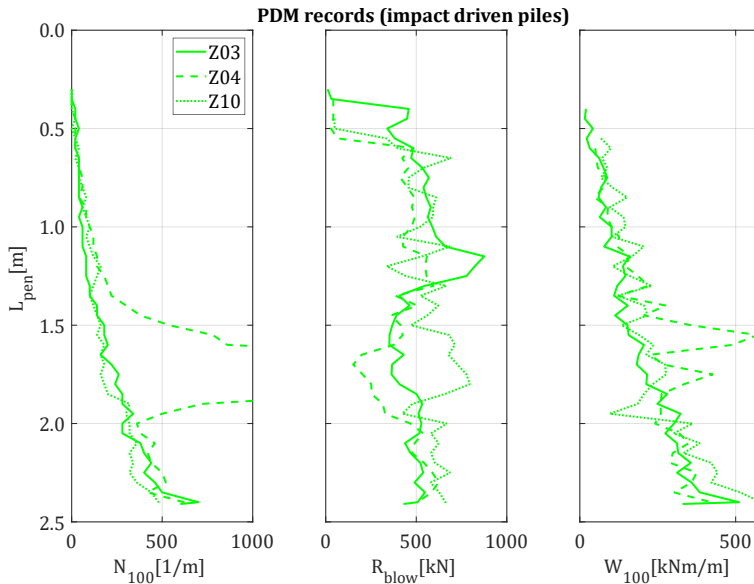


Figure 6-1: Impact pile driving installation records

As mentioned in Section 5.7.2, the measured driving resistance has to be treated with caution due to the long duration of the impact compared to the short pile length. Pile Z04 shows very high blow counts at a penetration depth between 1.3 m and 2.0 m (actually up to 3,900 blows per meter pile penetration). During this test, a malfunction of the Diesel hammer occurred leading to blows with low energy and thus low penetration per blow in the mentioned penetration interval. The integral energy per 1 m penetration W_{100} , however, shows good agreement for all tests with some deviations.

To investigate the soil response to impact pile driving, the development of the measured horizontal stresses over pile penetration was evaluated. Figure 6-2 shows the development of radial soil stresses measured in a distance of about 20 cm to the pile shaft in different depths (cf. Figure 5-15).

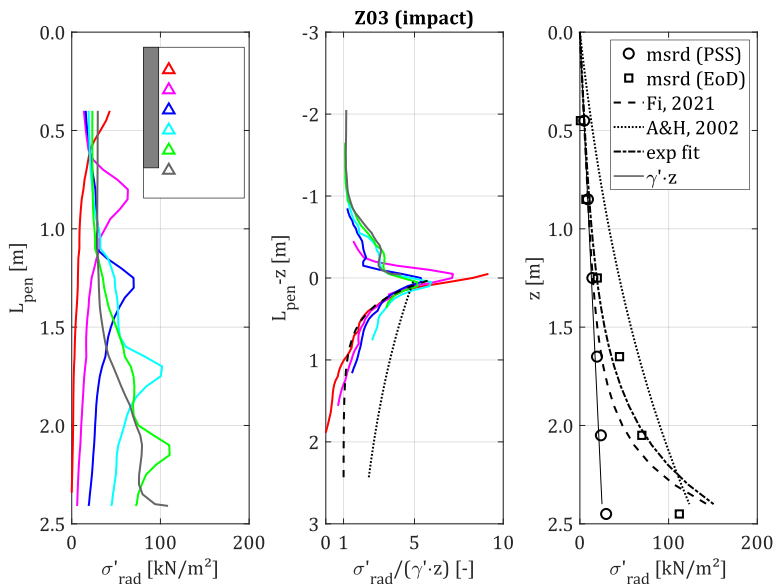


Figure 6-2: Soil stress developments due to installation of pile Z03 (impact driven)

The left diagram shows the development of the absolute effective soil stresses over pile penetration. Stress measurements in different depths are drawn in different colours. The sensor locations are marked in the pictogram. The radial soil stresses increase as the pile toe

approaches the sensor level and decrease afterwards. The diagram in the middle shows the normalised soil stresses (divided by the overburden pressure with $\gamma' = 11 \text{ kN/m}^3$) versus distance between pile toe and sensor level as well as the corresponding curves according to the approaches of FISCHER (2021) (F_i , - -) and ALM & HAMRE (2002) (A&H, ...), which are described in Section 2.2.2. The right diagram shows measured soil stresses before pile installation (primary stress state, PSS, \circ) and after pile installation (end of driving, EoD, \square) as well as the theoretical horizontal stresses with an earth pressure coefficient $k_0 = 1$ ($\gamma' \cdot z \cdot k_0$, -), the soil stresses due to pile installation effects according to FISCHER (2021) and ALM & HAMRE (2002) (see above) and an exponential fit (- \cdot).

The measured radial stresses before pile installation (PSS) show good agreement with the theoretical overburden pressure which indicates an earth pressure coefficient of $k_0 = 1$. The reason for these high horizontal stresses is the soil compaction during filling of the test pits, as described in Section 5.6.2.

The courses of the normalised soil stresses during approach of the pile toe and passing of the pile shaft is similar for all sensor levels. The peak height shows some deviations and in the upper soil elements the soil stresses eventually decrease to residual values below the primary stress state. Similar observations were made by FISCHER (2021) who argued that the compaction effects from the sand placement may be undone by the pile installation and thus the horizontal stresses are adjusted according to classical theory with $k_0 = 1 - \sin(\varphi')$. The shape of the soil stress reduction after passing of the pile toe is similar to that formulated by FISCHER (2021).

The horizontal stresses after pile installation (EoD) can also be approximated by the approach presented by FISCHER (2021). The measured horizontal stress at the deepest sensor presented in Figure 6-2 needs to be interpreted with caution. The sensor was buried below the pile's final penetration. Thus, the pile toe has not reached the sensor level. Looking at the grey line in the left diagram, the stress in this sensor level is supposed to increase with further driving progress. Looking at the normalised courses in the middle diagram, the maximum stresses according to the approach of FISCHER (2021) were reached when the pile toe approached the corresponding measuring sections.

Looking at the other impact driven piles Z04 and Z10 (Appendix D), the general observations made at pile Z03 are valid as well. However, for the installation of pile Z10, the soil stress

development according to FISCHER (2021) fits less good to the measurements. The peak soil stresses are higher and the residual stresses do not fall below the primary stress state for all but the uppermost sensor level.

6.2.3 Vibratory driven piles

To get an impression about similarities and differences between installation procedures of the vibratory driven piles, Figure 6-3 shows vibratory driving records containing control and response parameters. Tests Z07, Z11, Z14 and Z15 are selected exemplarily for the different vibration variants. Installation records of all tests, grouped by installation variant, are given in Appendix D. From given installation frequency f_d and eccentric moment M_e , the centrifugal force F_c was calculated according to Equation (2-11). The measured displacement amplitude s_0 and the acceleration amplitude a_{ampl} can be regarded as two of many system response parameters. The penetration speed v_{pen} can be regarded as control parameter in case of crane-guided pile installation and as system response parameter in case of free vibratory driving; the bias force F_{bias} (= dead weight of the pile-vibro assembly $G_{\text{pile+vibro}}$ - line pull F_{line}) vice versa.

For the crane-guided installations of piles Z11 (red lines) and Z15 (magenta lines), the centrifugal force F_c is constant due to a constant vibration frequency f_d and equal due to an appropriate adjustment of f_d and M_e (see Section 5.5). The penetration speed v_{pen} is almost constant as the penetration speed is limited by the crane. The theoretical value of the displacement amplitude s_0 is different for different eccentric moments (cf. Equation (2-13) and Table 5-7). The acceleration amplitude a_{ampl} shows a stable course as well. The bias force F_{bias} is also stable indicating that the portion of the dead weight $G_{\text{pile+vibro}}$ carried by the soil resistance does not change.

For the free installations of piles Z07 (cyan lines) and Z14 (blue line), the centrifugal force F_c increases with penetration as the driving frequency f_d is increased. However, the penetration speed v_{pen} decreases with pile penetration. The static surcharge force $F_{\text{bias}} = G_{\text{pile+vibro}}$ is constant as line pull F_{line} is zero. For the vibro hammer with high eccentric moment (cyan lines) the development of the displacement amplitude s_0 , which theoretically should be unaffected by the driving frequency f_d , shows large fluctuations and predominantly lower values than in case of the guided pile installations (magenta lines). In case of the vibro hammer with small eccentric moment, the displacement amplitudes of free vibratory driven pile (blue) is close to that of the crane-guided (red) installations. Theoretical values of the displacement amplitude s_0 are

1.9 mm in case of the low eccentric moment (blue, red) and 3.9 mm in case of the high eccentric moment (cyan, magenta; see Table 5-7). The acceleration amplitude a_{ampl} shows high fluctuations compared to the crane-guided installations.

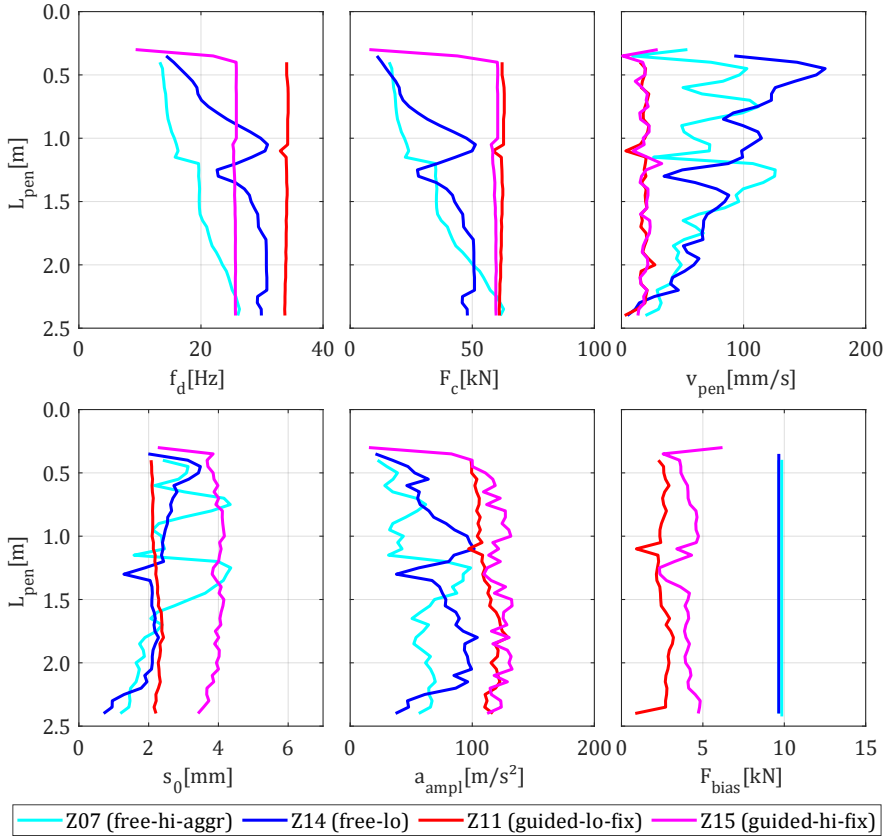


Figure 6-3: Vibratory pile driving installation records

A closer look at the force and motion signals reveals fundamental difference between different vibratory driven piles. For comparison of free and guided vibratory driven piles with high and low eccentric moment, piles Z02, Z07, Z11, Z14 and Z15 were chosen as exemplary tests for the following installation parameters:

Z02: free vibratory driving, high eccentric moment, moderate frequency control

Z07: free vibratory driving, high eccentric moment, aggressive frequency control

Z14: free vibratory driving, low eccentric moment

Z15: crane-guided vibratory driving, high eccentric moment

Z11: crane-guided vibratory driving, low eccentric moment

Figure 6-4 and Figure 6-5 show time signals of pile displacement s and velocity v of the above-mentioned tests for different penetration depths. Positive motion directs downwards and is visualised accordingly. In the displacement signals, dotted lines denote penetrative motion ($v > 0 \wedge s > s_{max}$). Same scaling of the motion amplitudes was chosen for all tests. Three full vibration cycles were plotted regardless of the vibration frequency f_d .

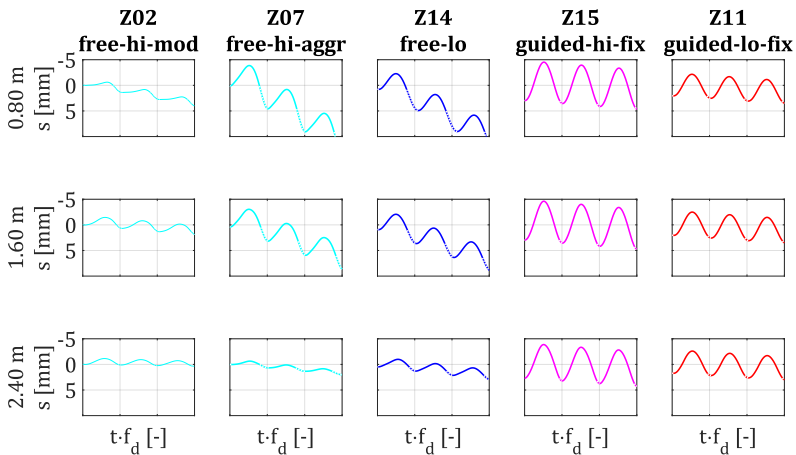
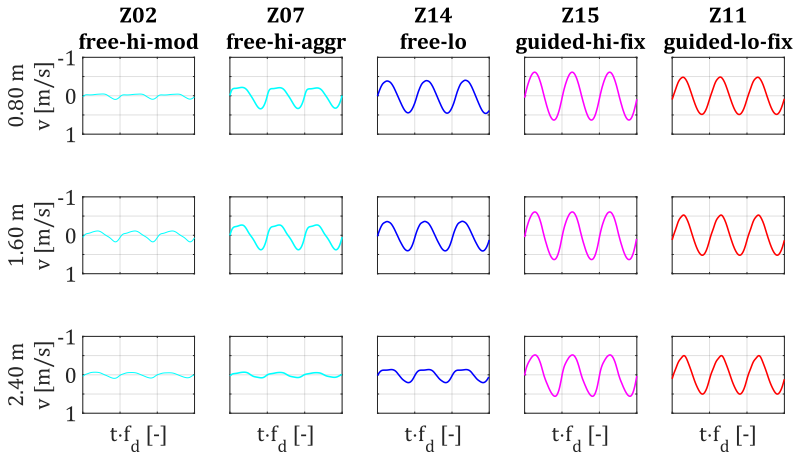


Figure 6-4: Displacement signals of vibratory driven piles for different tests (columns) at different penetration depths (rows)

The displacement signals show a much higher penetration speed (= general course of the displacement signal) of the free vibratory driven piles until a certain penetration depth. The low penetration speed of the crane-guided vibratory driven piles results in low amount of penetrative motion during one vibration cycle. A similar behaviour can be observed for the free vibratory driven piles at high penetration depth and for the free vibratory driven pile with moderate frequency control for medium and high penetration depth.



**Figure 6-5: Velocity signals of vibratory driven piles
for different tests (columns) at different penetration depths (rows)**

The velocity signals of free and guided vibratory driven piles differ in amplitude and shape. Free vibratory driven piles show lower velocity amplitudes and an asymmetry between downward and upward directed velocities while guided vibratory driven piles show more or less harmonic (sinusoidal) velocity signals. In case of the free vibratory driven piles, the upwards directed velocity shows a flat top with a lower absolute peak value compared to the downwards directed velocity with a more pronounced and higher peak. This qualitative difference can be quantified by a velocity asymmetry $v_{\max}/-v_{\min}$ with $v_{\max}/-v_{\min} \approx 1$ for guided pile installation and $v_{\max}/-v_{\min} > 1$ for free vibratory driving.

Comparing the piles motions (both displacement and velocity) at different depth, the crane-guided vibratory driven piles show very similar signals in shape and amplitude regardless of the pile penetration. The behaviour of the free vibratory driven piles, on the contrary, is affected by the penetration depth. Especially at high penetration depth, the motion amplitudes decrease even though the driving frequency and thus centrifugal force are steadily increased (cf. s_0 , f_d and F_c in Figure 6-3).

Additionally, the force-motion relationship of the exemplary tests and penetration depths were analysed. Figure 6-6 shows the mobilised static pile resistance⁷ R_{stat} versus pile displacement s . Three full cycles are plotted for each test/depth; horizontal grid lines are spaced at 1 mm. On the right side of Figure 6-6, the idealised load-displacement behaviour of 'cavity' vibratory driving according to CUDMANI (2001) is shown (cf. Figure 2-9).

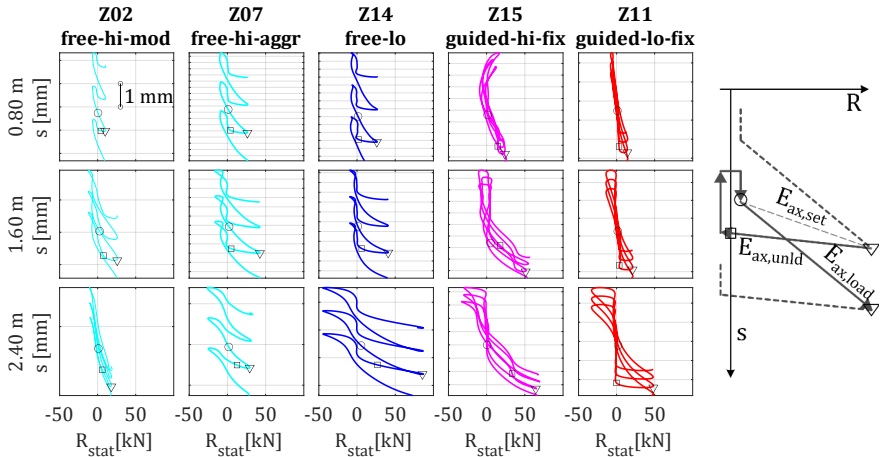


Figure 6-6: Force-displacement signals of vibratory driven piles for different tests (columns) at different penetration depths (rows)

The force-displacement curves of subsequent cycles of the guided vibratory driven piles Z11 and Z15 are overlapping, resulting from the low penetration speed. Especially at deeper pile penetration, considerable negative (pulling) forces are mobilised during upward motion of the pile. This can be explained by downward directed shaft friction during upward directed motion. Taking this into consideration, the shape of the load-displacement curves resembles 'cavity' mode vibratory driving in the most cases. This classification is mainly based on the following conditions:

⁷ i.e. the measured force at the pile head $F_{str,top}$, corrected for the dynamic influences: inertia force $F_{in} = m \cdot a$ and velocity depending pile resistance R_{damp} . For the calculation of damping force, refer to Section 5.7.3.

- The mobilised (static) pile resistance shows an increase with downward directed pile motion, so the maximum soil resistance is probably not mobilised.
- During initial upward pile motion, the pile resistance vanishes and upward motion continues with zero load, so a gap or 'cavity' underneath the pile toe can be assumed.

Resonance effects on pile-soil system during vibratory driving

The undamped axial eigenfrequency $f_{0,inst}$ of the vibro-pile-soil system during pile installation can be estimated by

$$f_{0,inst} = \frac{1}{2\pi} \cdot \sqrt{E_{inst}/m_{dyn}} \quad (6-1)$$

where m_{dyn} is the dynamic mass of the system and E_{inst} is the integral pile-soil interface stiffness of the pile shaft and pile toe. As the pile penetration and thus the total interface stiffness increases over the installation process, the eigenfrequency is not a fixed system parameter (MASSARSCH et al. 2022) but increases with pile penetration. This was also observed when determining the systems axial eigenfrequency at different penetration depths (see Appendix D).

To investigate possible resonance effects during vibratory pile driving, the displacement amplitude s_0 was looked at. Theoretical, the displacement amplitude yields $s_{0,theor} = M_e/m_{dyn}$ (Equation (2-13)). The actual displacement amplitude $s_{0,msrd}$ was taken from double integration of acceleration measurement (see section 5.7.3). The relation of the actual displacement amplitude to the theoretical displacement amplitude can be interpreted as amplification factor $\Lambda = s_{0,msrd}/s_{0,theor}$. According to MASSARSCH et al. (2022), a high displacement amplification indicates pile driving near system resonance.

The following Figure 6-7 shows the influence of resonance effects on the vibratory installation process. The pile penetration speed v_{pen} (left) and acceleration amplitude a_{ampl} (right) are plotted over the amplification factor Λ . Different markers and colours indicate different tests and vibratory driving variants (see Table 6-1). Each marker shows the mean values of the corresponding vibratory driving parameters over a penetration depth of 30 cm.

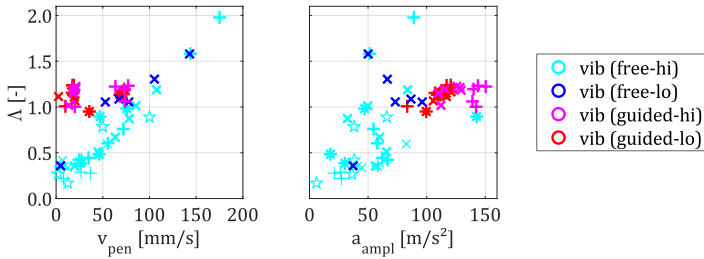


Figure 6-7: Influence of resonance effects on pile installation

A clear positive linear influence of the amplification factor Λ on the penetration speed v_{pen} can be seen in case of the free vibratory driven piles (cyan, blue). This is surprising as the pile penetration is expected to slow down near system resonance (MASSARSCH et al. 2022). In case of the crane-guided piles (magenta, red), the penetration speed is controlled by the crane and thus independent of resonance effects. The acceleration amplitude a_{ampl} increases with increasing displacement amplification Λ . Here, also the crane guided vibratory piles, which generally show higher acceleration amplitudes, do fit in the picture.

6.2.4 Soil stress developments during pile installation

Effects on the soil state are investigated based on soil stress measurements as described in Section 5.7.4. Figure 6-8 shows the development of soil stresses over pile penetration for four vibratory driven piles with different installation parameters. The impact driven pile Z03, which has been discussed in Section 6.2.1., is given as comparison. The plots for each test have the same arrangement as in Figure 6-2 (left). Plots of all tests are given in Appendix D.

For test Z08 (free vibratory installation, high eccentric moment) an increase of the horizontal soil stresses as the pile toe approaches the sensor levels and a decrease of soil stresses as the pile shaft passes the sensor levels can be seen equal to test Z03 (impact driven). The installation of pile Z14 (free vibratory installation, low eccentric moment) shows very similar behaviour but with lower maximum soil stresses in the deeper sensor levels. During the installation of piles Z11 and Z15 (both crane-guided vibratory driven with different eccentric moments), no such behaviour can be observed. The horizontal soil stresses remain more or less stable as the pile toe approaches and passes the sensor levels. Only in the courses of the two uppermost sensor levels slight buckles can be seen.

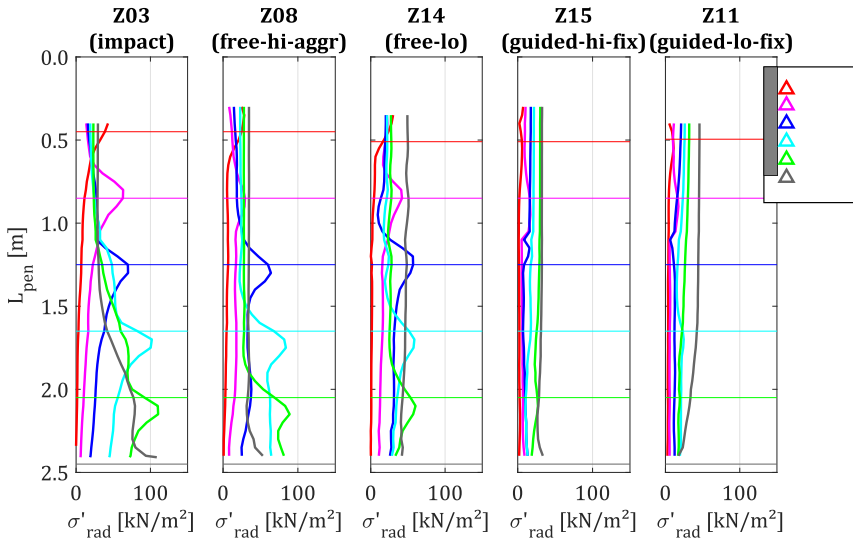


Figure 6-8: Development of mean soil stresses over pile penetration

Similar behaviour can be noted for the other installation processes with corresponding installation parameters (see Appendix D). Piles with free vibratory installation and high eccentric moment but lower driving frequency and penetration speed (Z01, Z02, Z05, Z06) show minor effects on soil stresses compared to the reference case Z08. Piles with crane-guided vibratory installation and higher (crane-controlled) penetration speed (Z13, Z16) show some effects in contrast to the reference cases (Z11, Z15), but very low effects compared to the free vibro driven piles.

The soil stress state after pile installation (EoD, end of driving) is decisive for the lateral load bearing behaviour of the model pile, as will be shown in Section 6.3.2. The following Figure 6-9 shows radial effective stresses σ'_{rad} for all tests after pile installation (EoD). Measured values at the distinct sensor levels are given by markers. Exponential fits according to Equation (2-37), which is repeated below, have been deduced from the measured soil stresses and are drawn with coloured lines. Only measuring levels that were reached until final pile penetration were considered. The overburden stress $\gamma \cdot z$ is given for orientation.

$$\sigma'_{rad}(L_{pen}, z) = \sigma'_{rad,PSS}(z) \cdot \left[1 + \left(\frac{1}{\beta_{PSS}} - 1 \right) \cdot e^{-\alpha_{pen} \cdot (L_{pen} - z)} \right] \quad (6-2)$$

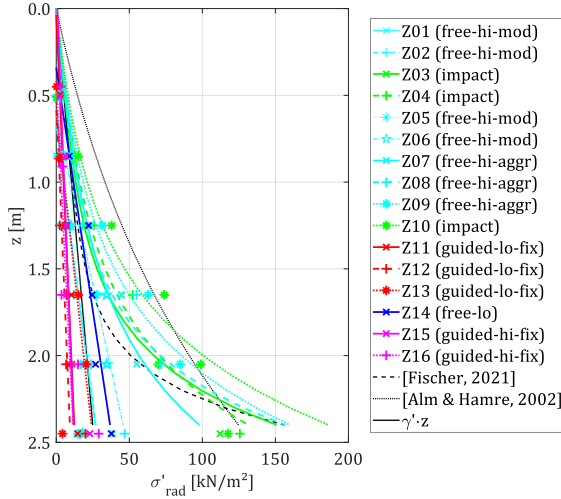


Figure 6-9: Fit of horizontal effective soil stresses over depths after pile installation

Table 6-2 gives fitted parameters α_{pen} and $1/\beta_{PSS}$ for the effective radial soil stress over depth after pile installation for the impact and free vibratory driven piles. Values of $1/\beta_{PSS} > 1$ indicate an increase of soil stresses due to pile installation; values of $\alpha_{pen} \gg 0$ indicate an exponential decay of this effect with further pile penetration. Vibratory pile installations with values of $\alpha_{pen} \ll 0$ (see Appendix D) indicate that the approach according to Equation (2-37) is not suitable.

For the impact driven piles and for the vibro driven piles with high eccentric moment, high frequency/penetration speed and no penetration guidance (free), an equal effect of soil stress developments could be monitored. An increase of horizontal stresses by a factor of $1/\beta_{PSS} \approx 5$ at the pile toe with an exponential decay of $\alpha_{pen} \approx 1.6$ towards the mudline, equal to the concept of friction fatigue, were encountered. The shape factor according to Equation (2-9) after FISCHER

(2021) yields $\alpha_{\text{pen}} = 4.2 - 1.4 \cdot D = 3.22$ with density $D = 0.70$ which corresponds to $D_r = 0.74$. The shape factor according to Equation (2-8) after ALM & HAMRE (2002) yields⁸ $\alpha_{\text{pen}} = 0.42$.

Table 6-2: Soil stress state after EoD

test	installation method	group [Me-fd-v _{pen}]	α_{pen} [-]	$1/\beta_{\text{PSS}}$ [-]	R^2 [-]	line style
Z03	impact	--	2.06	6.38	0.79	—
Z04	impact	--	1.46	5.33	0.73	- -
Z07	vibro	hi-hi-free	1.33	3.97	0.72	- -
Z08	vibro	hi-hi-free	1.94	6.46	0.72	• • •
Z09	vibro	hi-hi-free	1.39	6.41	0.81	- •
Z10	impact	--	1.31	7.68	0.76	• • •
Z14	vibro	lo-hi-free	1.48	1.72	0.13	—
FISCHER (2021)	impact	--	3.22	6.25	--	- -
ALM & HAMRE (2002)	impact	--	0.42	5.0	--	• • •

The extreme values of the soil stresses, however, uncover a significant difference between impact driven and free vibratory driving pile installation. Figure 6-10 shows the development of minimum and maximum effective radial soil stresses (shaded areas) around the mean effective horizontal soil stresses (thick lines) over penetration (cf. Figure 5-23). The curves are plotted for the same piles as in Figure 6-8. For the sake of clarity, only the sensor levels at $z = 1.25$ m and 2.05 m are shown here. The scaling of the soil stresses is different for impact and vibratory driven piles. The soil stresses due to impact driven pile installation (Z03) show high amplitudes of compression stresses ($\Delta\sigma'_{\text{rad}} \gg 100$ kN/m² in the deeper sensor location) in addition to the mean stress level. The soil stresses due to vibrators pile driving show a much smaller range ($\Delta\sigma'_{\text{rad}} < 50$ kN/m²) around the mean effective radial soil stress.

⁸ The shape factor according to ALM & HAMRE is a function of the overburden pressure and the CPT cone resistance. With a more or less linear increase of both cone resistance and overburden pressure, the value stated above is calculated.

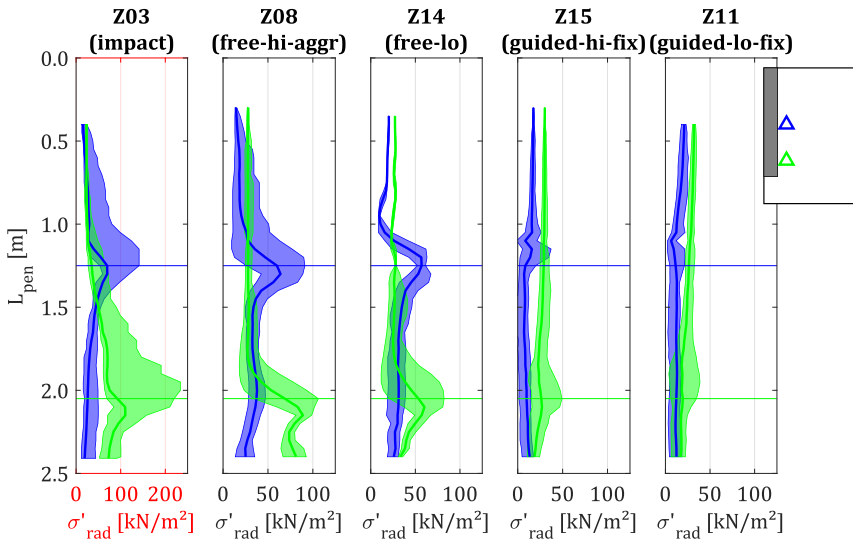


Figure 6-10: Development of soil stresses ranges over pile penetration

6.2.5 Installation mode

After observing different soil stress developments during impact and vibratory pile installation, the question arises which pile installation parameters exist to determine or even to control soil stress development. First of all, interrelations between the different soil stresses described above need to be investigated. The following Figure 6-11 visualises the definitions of imprinted soil stresses and soil stress amplitudes measured during vibratory pile driving (harmonic signal, left) and impact pile driving (transient signal, middle). In case of vibratory driving, mean values of the signals are assumed to represent the imprinted soil stresses. In case of impact pile driving, there is little difference between mean values, median values and min values. Here, median values were assumed to represent the imprinted soil stresses. Imprinted soil stresses were calculated over a penetration depth of 30 cm (15 cm above and below sensor level) as depicted on the right side of Figure 6-11. The maximum values were taken over the complete pile installation, assuming that they represent the stress state when the pile toe reaches the sensor level (cf. Figure 6-8).

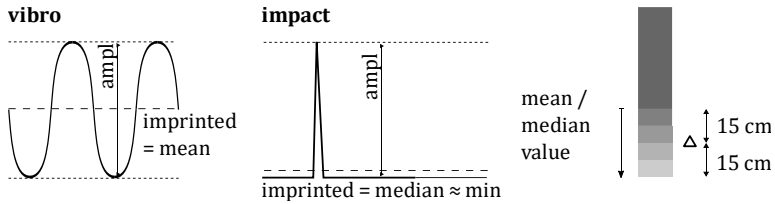


Figure 6-11: Definition of imprinted soil stresses and stress amplitudes during vibratory (left) and impact driving (middle) and penetration range for the calculation of mean values (right)

Figure 6-12 shows combinations of radial stress amplitudes $\sigma'_{rad,ampl}$ and imprinted radial stresses $\sigma'_{rad,impr}$. In the left diagram, absolute values are given, in the right diagram, values are normalised by the overburden pressure $\gamma' \cdot z$. Different markers and colours indicate different tests and vibratory driving variants (see Table 6-1).

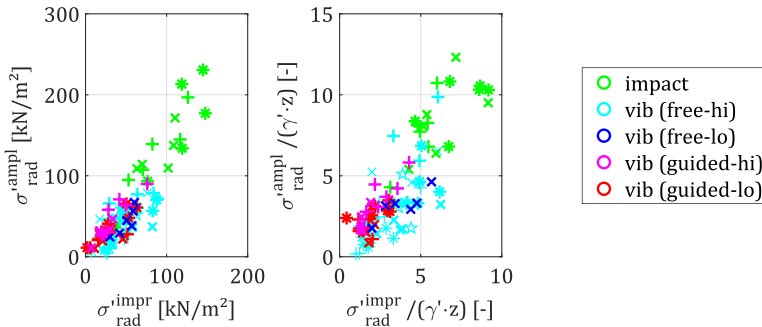


Figure 6-12: Comparison of soil stress amplitudes and imprinted soil stresses during pile installation

Obviously higher dynamic stress amplitudes correlate with higher imprinted soil stresses; a linear relation exists between $\sigma'_{rad,ampl}$ and $\sigma'_{rad,impr}$. Highest soil stresses occur due to impact pile driving (green) whereas crane-guided vibratory driving (red, magenta) results in lowest soil stresses. The dimensionless diagram (right) shows that the relationship between stress amplitude and imprinted soil stress is not substantially biased by the general increase of stress state with depth. For further interpretations of the influence of pile driving parameters on radial stress state, the imprinted soil stresses are considered.

Regarding pile driving parameters, the focus was laid on pile motion (displacement, velocity, acceleration), pile forces and energy. Following the findings of VOGELSANG (2017), upwards and downwards directed motion and forces were treated separately. For definitions of the utilised motion, force, and energy quantities, refer to Section 5.7.3 and Figure 5-22.

The following Figure 6-13 shows diagrams of the normalised imprinted radial soil stresses versus dimensionless measures of penetration per cycle (a), velocity symmetry (b), acceleration amplitude (c), bias force (d) and penetrative energy (e). In (a), the net penetrative displacement s_{set} (set per cycle) is related to total downward directed displacement s_{\downarrow} . In (b), the max upwards directed velocity ($-v_{min}$) is related to the max downwards directed velocity (v_{max}). In (c), the acceleration amplitude a_{ampl} , is corrected for resonance effects by the amplification Λ and made dimensionless by earth gravity g . In (d), the bias force F_{bias} (dead weight minus line pull) is divided by the frequency-dependent centrifugal force F_c . In (e), the energy consumed during penetrative motion W_{set} is related to the total energy per cycle W_{cycle} .

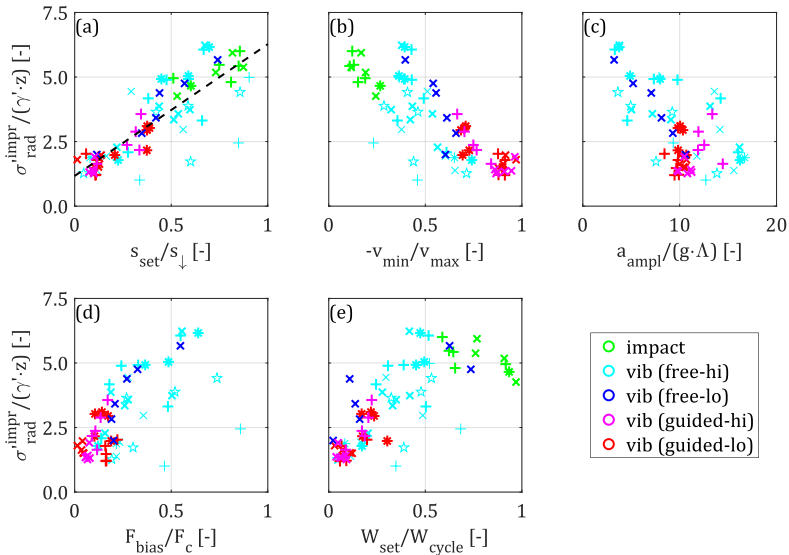


Figure 6-13: Influence of pile forces, energy, and motion on imprinted soil stresses at pile toe level

Where possible, installation processes with impact driven piles were also considered. All values were derived by taking the mean of the measurements taken while the pile toe was situated in a range of 15 cm above and below the sensor levels (= over a length of 30 cm). Colours and markers were chosen according to installation parameters and tests (see Table 6-1).

The motion signals of crane-guided vibratory driven piles (cf. Figure 6-4, Figure 6-5) show very similar upwards and downwards directed motion amplitudes (displacement and velocity) thus $S_{set}/s_{\downarrow} \rightarrow 0$ (cf. Figure 6-13 (a), reddish markers) and $-v_{min}/v_{max} \rightarrow 1$ (b). Free vibratory driving, in contrast, may be characterised by larger penetration per cycle and large downward directed velocity compared to upwards directed velocity, thus $S_{set}/s_{\downarrow} \gg 0$ (cf. Figure 6-13 (a), blueish markers) and $-v_{min}/v_{max} \ll 1$ (b). All these measures can also be deducted from the motion signals of impact driven piles. High values of S_{set}/s_{\downarrow} (cf. Figure 6-13 (a), green markers), for example, result from the relatively small upward motion (rebound) of the pile after hammer blows. Low velocity symmetry $-v_{min}/v_{max} \ll 1$ (b) can also be seen in the pile's forces signal (cf. Figure 5-20, $v \cdot Z$ with constant pile impedance Z).

- Figure 6-13 (a) shows a linear relation between normalised imprinted radial soil stress $\sigma'_{rad, impr}/(\gamma' \cdot z)$ and pile penetration per cycle normalised by downward direction motion S_{set}/s_{\downarrow} which can be described by

$$\frac{\sigma'_{rad, mean}}{\gamma' \cdot z} = 5.1 \cdot \frac{S_{set}}{s_{\downarrow}} + 1.2 \quad (6-3)$$

- Figure 6-13 (b) also shows a negative correlation between imprinted soil stresses and velocity symmetry.
- Figure 6-13 (c) shows that low acceleration amplitudes lead to high imprinted soil stresses. High acceleration amplitudes are dominant for the crane-guided vibratory driven piles. In this case, the amplification factor Λ is necessary to correct the acceleration amplitude for resonance effects and get a good correlation to the imprinted soil stresses.
- From Figure 6-13 (d) follows that high bias forces F_{bias} or low centrifugal forces F_c lead to high imprinted soil stresses. Small values for F_{bias}/F_c apply for crane-guided vibratory driven piles as the bias force is reduced by the line pull and the centrifugal force is comparably high over the whole installation process (cf. Figure 6-3).

- Figure 6-13 (d) shows that penetrative energy is also a driver for the occurrence of imprinted soil stresses.
- Resonance effects, expressed by the displacement amplification Λ (see above) did not show any correlation with the induced soil stresses. The same applies for the upward directed displacement s_{\uparrow} .

6.2.6 Interim summary and discussion on pile installation processes

First of all, it has to be emphasised that vibratory pile installation processes are complex with a certain number of control parameters and an even larger number of system response parameters. Resonance effects have a great impact on pile motion (acceleration and displacement amplitude) and in case of free vibratory driving also determine the installation speed.

Pile driving modes

Crane-guided vibratory driven piles show harmonic pile motion (displacement and velocity) which is unaffected by the pile penetration. Free vibratory driven piles show 'asymmetric' motion and a decrease of motion amplitudes with higher penetration depth. The installation variants can be distinguished based on the set per cycle in relation to the downward directed pile motion s_{set}/s_{\downarrow} which can also be evaluated for impact driven piles.

VOGELSANG (2017) distinguished pile driving modes based on the upwards and downwards motion during one cycle s_{\uparrow} and s_{\downarrow} . The main reason for the distinction between 'cavity' and 'non-cavity' installation was seen in the magnitude of upward motion (VOGELSANG 2017). For a comparison with the results presented here, the upwards directed motion is substituted by $s_{\uparrow} = s_{\downarrow} - s_{set}$. In quasi-static model tests, 'cavity' mode was achieved with $s_{set}/s_{\downarrow} = 6 \text{ mm}/10 \text{ mm} = 0.6$ while a motion cycle with $s_{set}/s_{\downarrow} = 4 \text{ mm}/5 \text{ mm} = 0.8$ resulted in 'non-cavity' mode. During vibratory pile installations carried out in the framework of this thesis, values of s_{set}/s_{\downarrow} in a much larger range between 0 and 1 were observed. Crane-guided vibratory driving resulted in values of $s_{set}/s_{\downarrow} < 0.5$, impact driving lead to $s_{set}/s_{\downarrow} > 0.5$ and during free vibratory driving the whole range $0 < s_{set}/s_{\downarrow} < 1$ was covered.

LABENSKI (2020) investigated predominantly vibratory driven piles where 'cavity' mode was detected. Even though the model was smaller compared to the one used here, substantial ratios such as the centrifugal force related to bias force F_c/F_{bias} and eccentric moment related to

dynamic mass $M_e/m_{\text{dyn}} = s_0$ are in similar ranges. During crane-guided vibratory driving, LABENSKI (2020) observed a "higher degree of cavity"⁹ compared to free vibratory driven piles. This was explained by the free upward directed but restricted downward directed pile motion and thus large values of s_1 (VOGELSANG 2017, see above). Regarding the observed values of s_{set}/s_1 , the findings of LABENSKI (2020) concerning the effects of crane-guided vibratory driving on system response are in contradiction to the observations presented here.

Furthermore, a distinction of installation modes can be made based on the amplitude of harmonic accelerations with high values for crane-guided vibratory driven piles and low values for free vibratory driven piles. As the acceleration signal of impact driven piles is transient, this installation method is related to zero harmonic acceleration. It is reasonable to assume that pile acceleration is linked to the acceleration of the surrounding soil. As illustrated by RODGER & LITTLEJOHN (1980), high acceleration leads to viscous soil behaviour while lower acceleration causes soil compaction (cf. Figure 2-8). Thus, the differences in vibratory pile driving modes of the free and crane-guided installed piles shown above probably resemble the concepts of 'impact' and 'viscous' mode according to RODGER & LITTLEJOHN (1980).

Soil reaction

Generally, any dynamic pile installation procedure (impact/vibratory driving) results in stress wave propagation (MASSARSCH et al. 2017) which was proven here by the measurements of oscillating radial soil stresses for all installation procedures (see Figure 6-10). An increase of imprinted (= mean or median) soil stresses was observed as the pile toe approaches a measuring level during impact pile driving and free vibratory pile driving, especially with high eccentric moment. Crane-guided vibratory pile driving did not cause enhanced stresses imprinted into the soil (Figure 6-8 and Figure 6-9). For impact driving, similar effects were shown in numerical simulations by STAUBACH et al. (2021).

MASSARSCH et al. (2020) describe stress wave propagations and increased lateral soil stresses due to horizontal ground vibrations in rather loose to medium dense sand in the framework of vibratory soil compaction. Here, similar effects were observed due to predominantly vertical

⁹ LABENSKI used the parameter $\kappa = s_1/(s_1-s_0)$ as measure for cavity driving with low κ values indicating a high degree of "cavity". Values of $\kappa \approx 0.5 \dots 2.5$ in a depth of $2 \cdot D_{\text{pile}}$ were observed. The relation between the value κ and the relation used in this Thesis is $s_{\text{set}}/s_1 = 1/(\kappa+1)$, so $\kappa \approx 0.5 \dots 2.5 \leftrightarrow s_{\text{set}}/s_1 \approx 0.7 \dots 0.3$.

vibrations on dense, overconsolidated sand in the framework of pile driving. After passage of the pile toe, the enhanced soil stresses decayed in analogy to the concept of friction fatigue according to Equation (2-37):

$$\sigma'_{\text{rad}}(L_{\text{pen}}, z) = \sigma'_{\text{rad,PSS}}(z) \cdot \left[1 + \left(\frac{1}{\beta_{\text{PSS}}} - 1 \right) \cdot e^{\alpha \cdot (L_{\text{pen}} - z)} \right]$$

After reaching target penetration, this leads to increased soil stresses near the pile toe only.

In field tests, pile installation effects on the soil state may be derived from CPTs conducted before and after pile driving. ACHMUS et al. (2020) present such data for impact and free vibratory driven piles in sand. All cases show a decrease of cone resistance due to the pile installation over the complete pile length. Unfortunately, only little information about CPT readings below final penetration depth was published.

In the model tests, imprinted soil stresses and stress amplitudes measured during passage of the pile toe show a good correlation. The normalised imprinted soil stresses show a linear increase with the ratio of downward directed displacement s_1 and penetrative displacement s_{set} (Equation (6-3)). The acceleration amplitude a_{ampl} , on the contrary, shows a negative correlation with the imprinted soil stresses. Resonance effects do not directly influence soil stress developments.

Crane-guided vibratory driven piles are installed in 'viscous' mode and do not induce increased soil stresses whereas impact driven piles evoke imprinted soil stresses. Free vibratory driven piles may, under certain conditions, be installed in 'impact' mode and induce increased soil stresses comparable to impact driven piles.

Soil mechanical interpretation of phenomena during pile installation

The following paragraphs give a description of the assumed soil mechanical phenomena occurring during 'impact' and 'viscous' pile installation modes. The mentioned installation modes are illustrated in Figure 6-14.

- A phase transition of the soil from granular to fluid behaviour ('fluidisation') in the vicinity of the pile wall is assumed during vibratory pile driving due to oscillating motion of the pile (cf. Section 2.2.3). Only oscillating pile motions with a continuous change of sign of the pile acceleration (as shown in Figure 5-22) leads to fluidisation! Impact pile

driving with very high acceleration amplitudes but transient motion signals will not evoke that effect.

- The degree and extent of fluidisation depends on the amplitude of harmonic pile acceleration. Along the pile shaft, the extension of the 'vicinity' in radial direction is irrelevant. At the pile toe, the fluidised zone extends underneath the pile toe by the length b_{fluid} (Figure 6-14).
- In any case, the vertical oscillation of the pile with the amplitude s_0 (see Figure 5-22) causes stress waves that are transferred from the fluidised zone to the granular zone. Stress waves propagate through the elastic half space of the granular zone of the soil.
- If the oscillating pile stays within the fluidised zone ($s_0 < b_{\text{fluid}}$), the granular zone of the soil is not affected by the pile installation (except for the abovementioned stress-wave propagation; Figure 6-14, left).
- If the pile toe leaves the fluidised zone during one vibration cycle ($s_0 > b_{\text{fluid}}$), the pile toe penetrates into the granular zone similar to impact driving, resulting in the mobilisation of quasi-static pile toe resistance and a compaction of the affected soil in a certain range (Figure 6-14, right). This also gives an explanation why s_0 is more or less affected by different pile installations (Figure 6-3) and why velocity signals may become asymmetric (Figure 6-5): in case of 'impact' mode, the downward directed pile movement is hindered in the granular zone. The acceleration amplitude decreases at a certain pile penetration ($L_{\text{pen}} > 1.5 \text{ m} \rightarrow a_{\text{ampl}} < 10 \cdot g$; Figure 6-3) and thus even a rather small displacement amplitude is sufficient to surpass the fluidised soil domain ($b_{\text{fluid}} < s_0 < 2 \text{ mm}$).
- The pile-soil system behaves equally due to single impacts (impact driving): no soil 'fluidisation' occurs ($b_{\text{fluid}} = 0$) as there is no opportunity for the soil underneath the pile toe to change its phase before pile penetration starts. After each impact (hammer blow), the soil recovers to its initial, granular phase. The arrangement of the grains, however, may be changed.
- The pile-soil system behaves differently in case of 'viscous' mode: the pile is surrounded by a completely fluidised soil domain and oscillates harmonically (Figure 6-5). Due to high acceleration amplitudes ($a_{\text{ampl}} > 10 \cdot g$; Figure 6-3), the extent of fluidisation

underneath the pile toe is greater than the displacement amplitude ($b_{fluid} \geq s_0$; $s_0 \approx 2$ mm or 4 mm, depending of the eccentric moment).

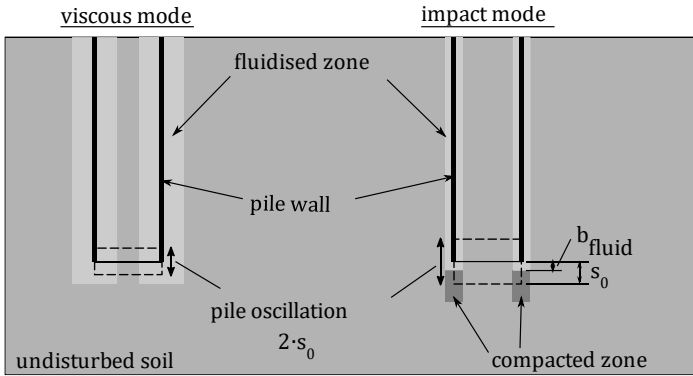


Figure 6-14: Supposed phenomena underneath the pile toe depending on pile installation mode

According to this explanation, 'viscous' mode and 'impact' mode can be distinguished based on the acceleration amplitude a_{ampl} and the displacement amplitude s_0 or set per cycle s_{set} . The following Figure 6-15 shows all observations (cf. Figure 6-11) of vibratory pile installations in the plane $a_{ampl}/\Lambda - s_{set}$. On the left side of the figure, each observation is indicated by the marker of the corresponding test (cf. Table 6-1). On the right side, the observations are coloured according to the magnification of imprinted radial soil stresses with respect to the theoretical overburden pressure

$$\sigma_{rad}^{* impr} = \frac{\sigma_{rad}^{impr}}{\gamma' \cdot z} \tag{6-4}$$

Blue markers indicate imprinted radial soil stresses in the same magnitude as the overburden pressure while red markers direct to radial soil stresses magnified by a factor of 6 or greater. Based on the soil stress magnification, observations can be assigned to 'viscous' or 'impact' vibratory driving modes.

Treating the set per cycle s_{set} and the amplification-adjusted acceleration amplitude a_{ampl}/Λ as predictor variables, the following effects on the radial soil stresses can be stated, which agree with the supposed phenomena visualised in Figure 6-14:

- (A) larger acceleration amplitudes lead to lower imprinted soil stresses due to higher degree of pseudo-fluidisation
- (B) larger sets per cycle lead to higher imprinted soil stresses due to greater penetration into non-fluidised soil

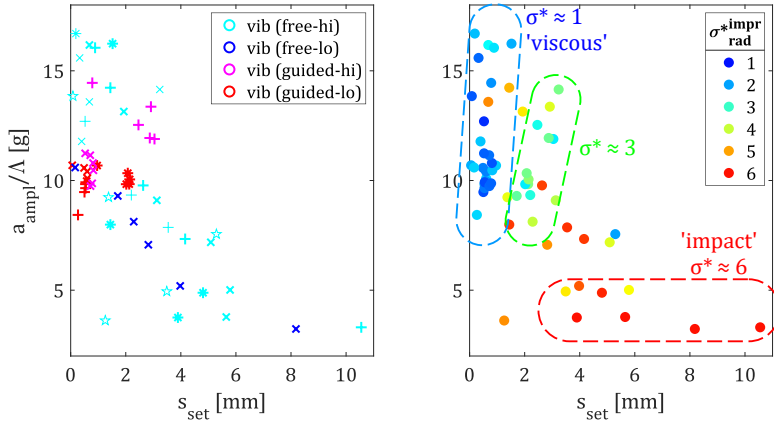


Figure 6-15: Observations of different tests (left) and resulting imprinted soil stresses (right) in the acceleration amplitude-displacement amplitude plane

The explanation presented above is not compatible with the concept of cavity/non-cavity driven piles (DIERSSEN 1994; CUDMANI 2001; VOGELSSANG 2017; LABENSKI 2020) but merely follows the concept of RODGER & LITTLEJOHN (1980).

6.3 Monotonic lateral pile behaviour

6.3.1 Evaluation procedure for monotonic pile behaviour

To investigate the quasi-static lateral pile behaviour, the data of the first cycle of different phases of the cyclic lateral load tests was used. The first cycle of phase 1 represents an undisturbed system; phases 2 and 3 represent a preloaded system where inhomogeneities from test preparation but also installation effects may be reduced. Phase 4 represents a preloaded system with higher load amplitude. Developments of the pile or soil behaviour over the phases are addressed in Sections 6.4 and 6.5.

Concerning the load-displacement behaviour, measurements at the pile head were evaluated. For the dynamic stiffness, measurements of the bending mode eigenfrequency after pile installation and before start of the cyclic loading were also taken into account. Soil stress measurements at different load levels were evaluated to investigate the soil behaviour.

6.3.2 Quasi-static load-deflection behaviour

For the sake of comparability of the different tests with slightly different penetration depths L_{pen} [m], the pile head deflection u [m] (measured at pile head level, approx. $1 \cdot D_{pile}$ over mudline) and the lateral force H [kN] (acting on top of the transition piece) were transferred to dimensionless values

$$u^* = u/L_{pile} \tag{6-5}$$

and

$$H^* = \frac{H}{\gamma' \cdot D_{pile} \cdot L_{pen}^2} \tag{6-6}$$

using the pile length L_{pile} [m], the soil unit weight γ' [kN/m²], the pile diameter D_{pile} [m] and the embedment length L_{pen} [m] shown in Figure 6-16.

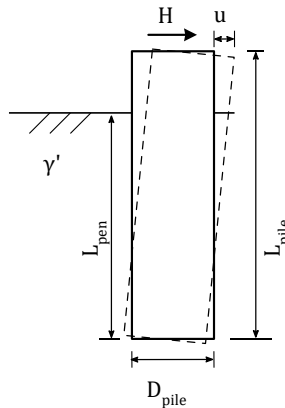


Figure 6-16: System parameters for the lateral pile analysis

The load-displacement behaviour of the first cycle was approximated by a power law of the type

$$u^* = u_{\text{ref}}^* \cdot H^{*\kappa} + u_{\text{offset}}^* \quad (6-7)$$

as proposed by HETTLER (1981). The factor $u_{\text{ref}}^* [-]$ can be interpreted as the dimensionless displacement due to a reference load of $H_{\text{ref}}^* = 1$, the exponent $\kappa [-]$ determines the curvature of the function, and $u_{\text{offset}}^* [-]$ is the displacement offset. Figure 6-17 shows the load-displacement behaviour of the impact driven pile Z03, the free vibratory driven pile Z07 and the crane-guided vibratory driven pile Z12. Measurement data is plotted by coloured markers, power fits according to Equation (6-7) are shown as coloured lines. Good fits can be found for both loading and unloading phase.

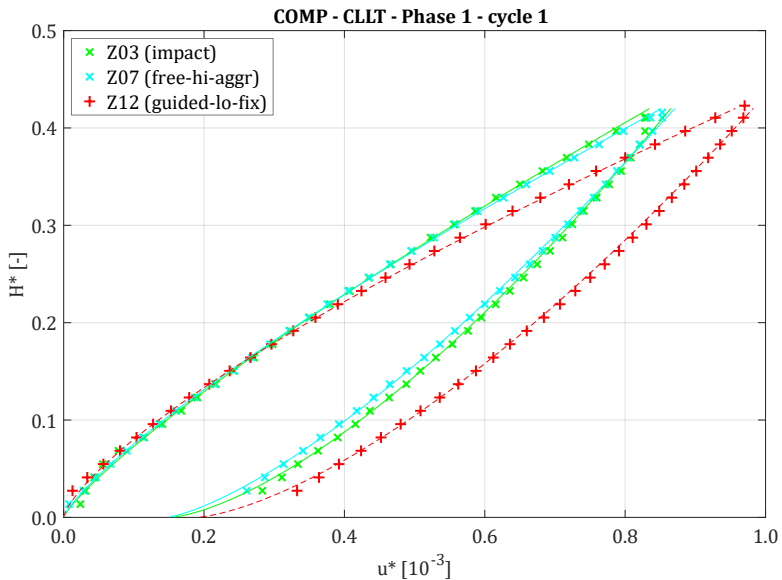


Figure 6-17: Exemplary plot of load-displacement measurements (coloured markers) and power fit (coloured lines)

For the loading phase starting with $H^* = 0$ the displacement offset is set to $u_{\text{offset}}^* = 0$. At the end of the first unloading phase, the horizontal force H^* does not go back to zero. The fitted data can be used to estimate the permanent deformation of the system at $H^* = 0$, expressed by $u_{\text{perm}}^* = u_{\text{offset}}^* > 0$.

Referring to the exemplary load-displacement curves in Figure 6-17 it is obvious that, especially at higher load level, the crane-guided vibratory driven pile Z12 behaves softer and shows higher permanent displacements than the free vibratory driven pile Z07 and the impact driven pile Z03.

As described in Section 6.1, the piles were grouped according to the installation parameters (hammer type, crane-guidance). Figure 6-18 shows fitted load-displacement functions of the first loading phase for each test in the test groups (coloured lines) together with mean fits for the corresponding groups (black lines) and a comparison of the mean fits of all groups (bottom left, coloured lines).

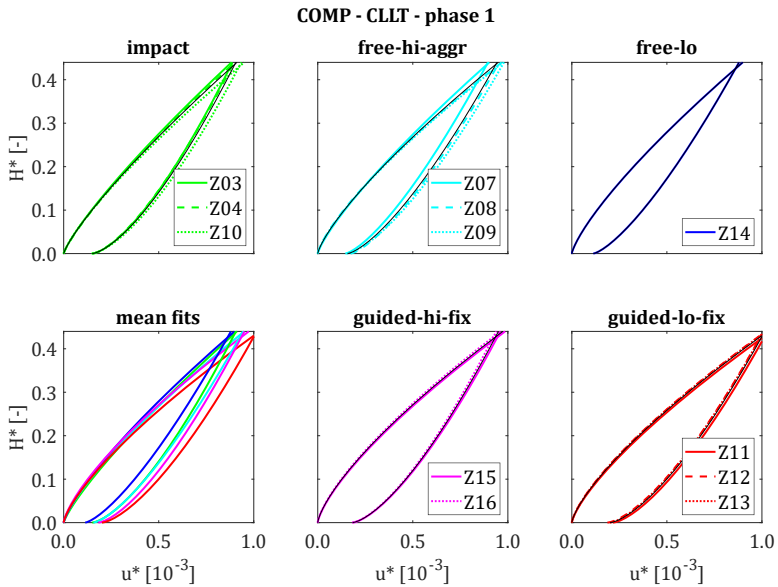


Figure 6-18: Load-displacement behaviour of tests (phase 1, cycle 1) grouped by installation parameters

The groups show different deviations. While the load-displacement curves of the crane-guided vibratory driven piles are very similar, those of the free vibratory driven piles with the high eccentric moment have certain differences. This may be because, in case of crane-guided installation, the driving frequency (and thus the centrifugal force) was set prior to the start of the pile penetration and remained constant afterwards. In case of the free vibratory pile driving,

on the contrary, the driving frequency was increased manually as the pile penetrated into the soil, resulting in certain deviations of the system dynamics over penetration depth and between the different tests (see Section 6.2.3). The result of the pile installed by free vibratory driving with low eccentric moment has to be treated with caution as only one test with this configuration (Z14) was carried out and minor variations may result in similar differences as produced by the free vibratory pile installation with the high eccentric moment (Z07, Z08, Z09). At high load level, the impact driven piles and the free vibratory driven pile with low eccentric moment (Z14) show the least pile head displacement while the crane-guided vibratory driven piles show the highest pile head displacement. Table 6-3 shows fitting parameters to describe the lateral load-displacement behaviour of the model pile due to different installation procedures. For each group, mean values of all tests from that group were taken for each parameter. Detailed results of each test are given in 0.

Table 6-3: Fitted parameters for load-displacement curves (test groups, CLLT, phase 1, cycle 1)

group	loading		unloading		
	u^{*ref} [10 ⁻³]	κ [-]	u^{*ref} [10 ⁻³]	κ [-]	u^{*perm} [-]
impact	2.49	1.22	1.32	0.67	0.15
vibro (free-hi-aggr)	2.75	1.29	1.41	0.71	0.16
vibro (free-lo)	2.59	1.29	1.40	0.73	0.11
vibro (guided-hi-fix)	3.02	1.38	1.34	0.68	0.18
vibro (guided-lo-fix)	3.14	1.36	1.42	0.68	0.20

Plotting the power law parameters u^{*ref} over κ for all tests shows that the parameters have a linear relationship and are grouped for the different installation methods. Figure 6-19 shows parameter combinations for single tests and also the mean fitting parameters of each group. Different colours indicate different installation parameters and different markers distinguish the unique tests (cf. Table 6-1). Circles (o) are used to indicate the mean values of the test groups. Tests Z01 and Z02 are not included as they were identified as outliers.

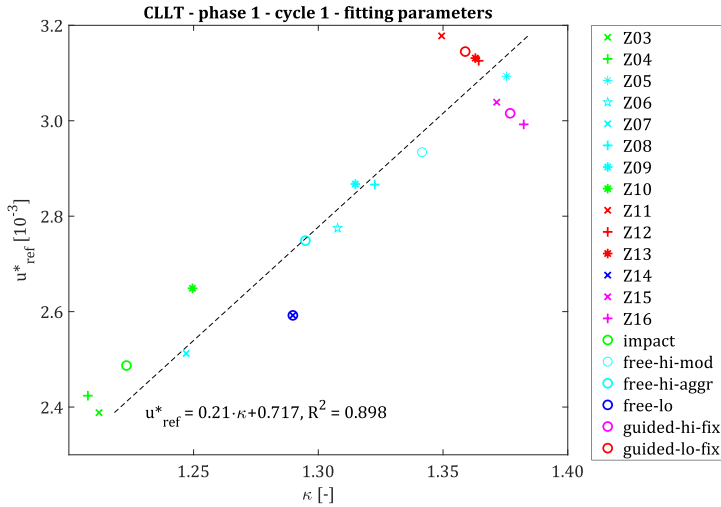


**Figure 6-19: Fitted parameters for load-displacement curves
(all tests and test groups, CLLT, phase 1, cycle 1)**

The load-displacement behaviour of impact driven piles can be described by lower values for the function u^*_{ref} and curvature κ compared to crane-guided vibratory driven piles. The parameters of free vibratory driven piles lie in between with notable deviations in case of the vibratory hammer with high eccentric moment (free-hi) and only one test with the low eccentric moment (free-lo). For test phases 1 to 3 of the cyclic lateral load tests, a linear relationship between u^*_{ref} and κ could be found. Still, the tendency of low u^*_{ref} and κ values for the impact driven piles and free vibratory driven piles remains but the differences between vibratory driven piles are blurring. Data of other phases is given in 0.

Over the loading phases, the variation of the tests regarding initial stiffness and displacement at maximum load level declines. This can also be visualised by means of histogram plots of the parameters κ and u^*_{ref} , as shown in Figure 6-20. The distributions of the parameters get narrower from phase to phase.

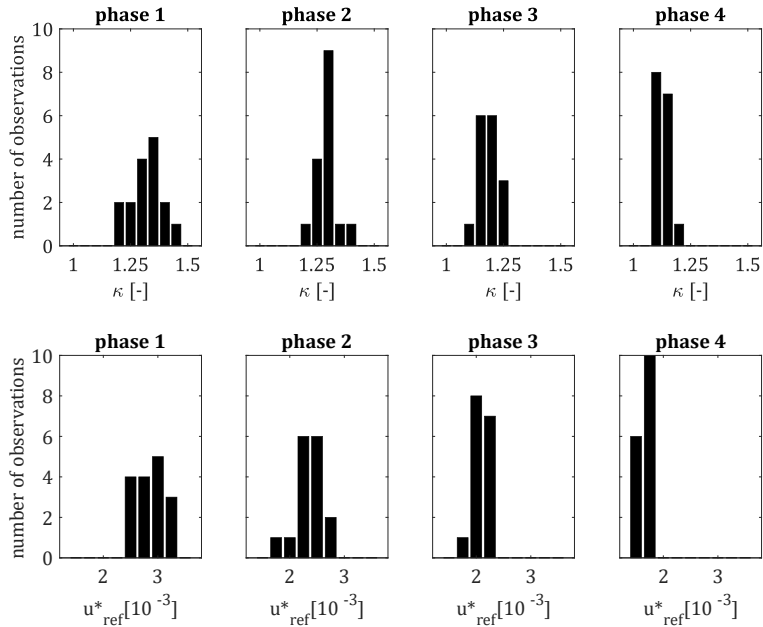


Figure 6-20: Variation of fitting parameters for monotonic loading

6.3.3 Dynamic stiffness of pile-soil system after pile installation

The bending mode eigenfrequency of the pile-soil system $f_{0,lat}$ was determined at several instances of the different tests in two directions (0° , 90°). To estimate the eigenfrequency of the undisturbed system, the measurements taken directly after pile installation (end of driving, EoD) were assessed. Ranges of the measured frequencies are shown in Figure 6-21.

The results show median values of the eigenfrequencies of each group (◆) from 19.5 Hz to 20.8 Hz or a range of 1.3 Hz. The different measurements taken at one pile (different directions) show similar variations, some were even bigger. Thus, the measured eigenfrequency seems not to be a reliable indicator to evaluate installation effects in the model tests.

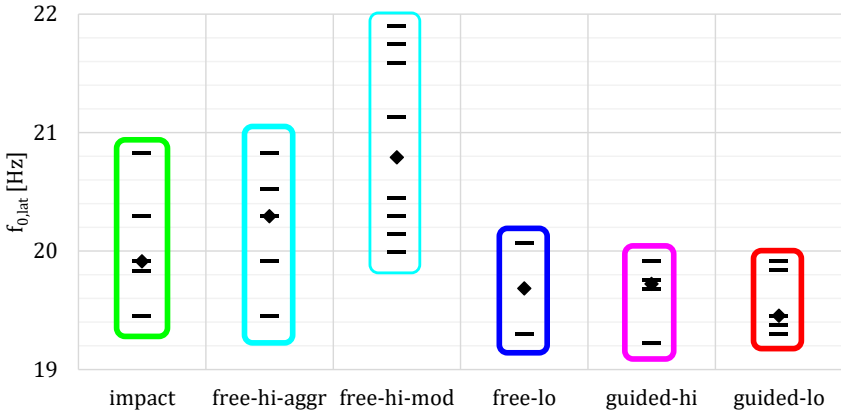


Figure 6-21: Measured bending mode eigenfrequencies after pile installation (EoD) and before lateral loading (N=0)

6.3.4 Soil reaction due to quasi-static pile loading

To analyse the bedding reaction to lateral pile loading, the effective horizontal soil stresses were evaluated. Measurements are available for different discrete depths z , distances from the pile axis r and angles θ (cf. Figure 5-17, left). Here, measurements in a distance of $r = 0.5$ m to the pile axis or 0.2 m from the pile wall and in depths from $z \approx 0.45$ m (which was the uppermost sensor layer) to $z \approx 2.45$ m (which already is about 0.05 m below the pile toe) are shown. The soil stresses measured in loading direction are labelled 'downwind', soil stresses measured on the opposite side of the pile are labelled 'upwind'. The difference between the two measurements is the 'resultant' soil stress. Soil reaction during first cycle's loading phase

Figure 6-22 shows the effective radial soil stresses σ'_{rad} over depth z for different load levels H during the first cycle of the phase 1 of test Z03 (impact driven). Darker lines indicate higher loads with a load interval of 2 kN between two lines. On the left-hand side and in the middle, the stresses in upwind and downwind direction are plotted, on the right the resultant (= downwind - upwind) is shown. Generally, the absolute soil stresses in both upwind and downwind direction grow towards the pile toe which is a result from the pile installation process (cf. Section 6.2).

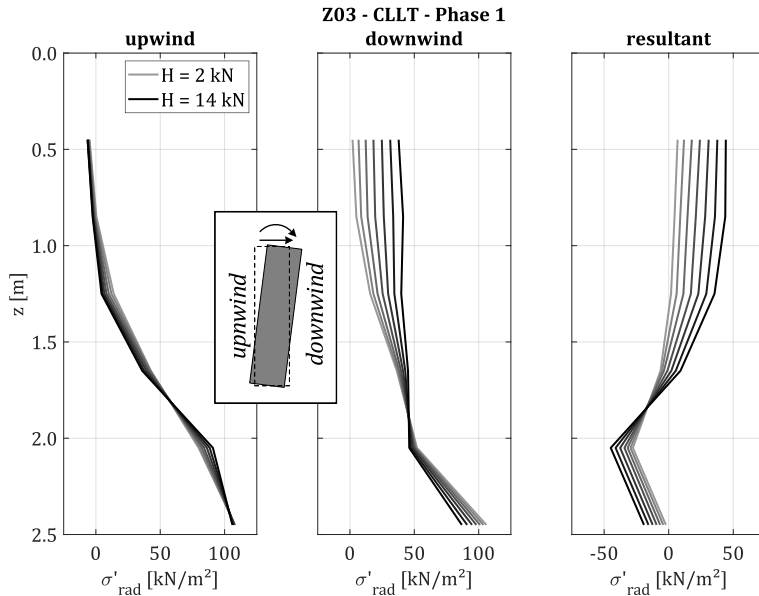


Figure 6-22: Soil stress development over first loading phase

With increasing lateral load, higher soil stresses develop on the downwind side in depth above approx. 1.65 m as the pile is pushed against the soil. Below approx. 2.05 m, soil stresses are reduced on the downwind side as the soil is unloaded. Thus, a rotation point can be expected somewhere around $z \approx 1.85$ m. The exact depth cannot be given due to the resolution of the discrete measuring points. On the upwind side, only minor soil stress changes occur. The soil is unloaded in the upper soil layers and loaded below the rotation point. A similar behaviour was observed at all piles. 0 shows the corresponding graphs of $\Delta\sigma'(z)$ to illustrate the soil stress changes due to cyclic lateral loading rather than the absolute values.

Looking at the soil stresses in downwind direction above the rotation point, soil stresses increase more or less steadily, indicated by equally spaced iso-load lines. Yielding of the soil cannot be discovered, as this would not allow further mobilisation of soil reaction and thus an increase of horizontal stresses.

This interpretation needs to be examined more closely as the boundary conditions of the test pit may impede failure. To disprove this, the failure mechanism according to classic earth pressure theory is used: According to REESE et al. (1974), the ultimate bedding resistance in

shallow depth is described by spatial passive earth pressure. At failure, a wedge is formed with the slope $45^\circ + \varphi'/2$. With the geometries of model pile and test pit and a soil friction angle of $\varphi' = 40^\circ$ this leads to a depth of $z \leq 0.79$ m unto which possible soil failure is unaffected by the boundaries of the test pit, as can be seen in Figure 6-23. Thus, the uppermost sensor level in the vicinity of the pile ($z \approx 0.45$ m, $r \approx 0.2$ m) is unaffected while in the next sensor level ($z \approx 0.85$ m) a possible soil failure may be impeded by the pit walls. However, the (theoretical) failure load $p_{py,ult}$ increases with depth z and the issue addressed above should not arise in deeper soil layers.

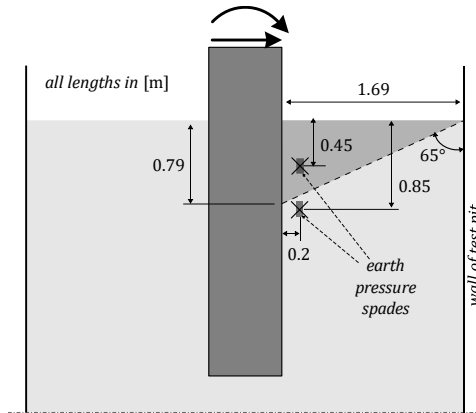


Figure 6-23: Influence of boundary on failure mechanism and soil stress measurements

With an increase of soil stresses of about 50 kN/m^2 at maximum load, the soil reaction due to lateral loading can be considered moderate compared to the soil stress developments during pile installation (cf. Figure 6-10 and Figure 6-12) with effective soil stress amplitudes of $\Delta\sigma'_{rad} \approx 100 \dots 200 \text{ kN/m}^2$ for impact driven piles and $\Delta\sigma'_{rad} \approx 50 \dots 100 \text{ kN/m}^2$ for free vibratory driven piles.

Imprinted soil stresses after first cycle

To investigate the soil behaviour due to unloading of the pile, soil stress profiles in upwind direction, downwind direction, and resultant (from left to right) at low ($H = 1 \text{ kN}$), medium ($H = 7 \text{ kN}$) and high ($H = 14 \text{ kN}$) load levels of both loading (solid lines) and unloading (dashed lines) phase of the first cycle were investigated. The following Figure 6-24 shows exemplary soil stress profiles from phase 1 of test Z03 (impact driven).

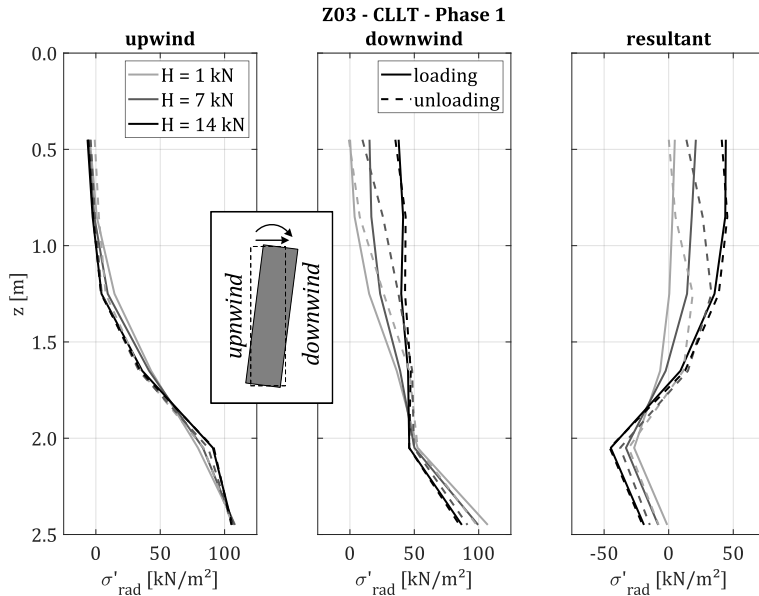


Figure 6-24: Soil stress development during first loading and unloading cycle

In deeper soil layers ($z > 1$ m), especially in downwind direction, the soil stresses do not return to the initial values when the pile is unloaded. Instead, higher stresses are imprinted into the soil. This can be seen by the light-grey and grey ($H = 1..7$ kN), dashed (unloading) lines in the right diagram (resultant) showing higher soil stresses compared to the corresponding solid (loading) lines between $z = 1$ m and $z = 2$ m. These imprinted soil stresses are the result of the first loading/unloading cycle and describe the stress state for the subsequent cycle(s) (see Section 6.4.4).

6.3.5 Interim summary and discussion on monotonic lateral pile behaviour

The quasi-static load-deflection behaviour at the pile head can be described by a power law of the type $u^*(H^*) = u^*_{ref} \cdot H^{*\kappa} + u^*_{offset}$ for both loading and unloading phases. For the loading phase, the different installation variants can be distinguished based on the parameters u^*_{ref} and κ . Impact driven piles show least pile head displacement at maximum load level, followed by free vibratory driven piles. Crane-guided vibratory driven piles show the highest pile head displacement at maximum load level. This generally confirms the numerical simulations of

(STAUBACH et al. 2021) which show an increase of lateral pile stiffness due to impact driving compared with wished-in-place (WIP) piles.

Evidently, the lateral bearing behaviour is linked to the pile installation effect and the imprinted radial soil stresses. Increased soil stresses lead to increased soil stiffness and thus increased lateral bedding stiffness. As pile installation effects on soil stresses decay with pile penetration ('friction fatigue'), the differences in the soil's stress state will eventually be manifested near the pile toe. Thus, the pile installation effect observed due to impact and free vibratory pile driving will affect the lateral pile behaviour especially if a toe kick occurs. This applies to short piles with high flexural stiffness, e.g. monopiles.

LABENSKI (2020) investigated the static pile behaviour of vibratory driven piles at a load level of about $H^* \leq 2.5$ while the maximum load levels during the tests presented here was limited to about $H^* \leq 0.5$ (according to the definition of H^* given in Equation (6-6)). According to LABENSKI (2020) the lateral stiffness correlates with the ratio s_{set}/s_{\downarrow} which is reduced by limited penetration speed, and correlates inversely with the ratio F_{bias}/F_c , which is reduced by the line pull in case of crane-guided vibratory driving. In case of guided vibratory pile driving, the model tests carried out by LABENSKI (2020) revealed much higher static lateral bedding stiffnesses compared to free vibratory driving. These findings are partly in contradiction to the observations made during the model tests presented in this thesis: Here, pile installation effects and thus increased bedding stiffness were observed for large values of s_{set}/s_{\downarrow} and high values of F_{bias}/F_c . (cf. Figure 6-13). Crane-guided vibratory driven piles showed a considerably lower pile head stiffness (cf. Figure 6-18). This agrees with MASSARSCH et al. (2022), who state that a line pull at the end of vibratory pile installation may have a negative effect on the soil stiffness below the pile toe.

The dynamic response of the pile-soil system shows a certain scatter. The measured reproducibility of the system response seems to be below possible influences of increased soil stresses on the dynamic pile bedding stiffness (= small strain stiffness). This may be explained by the marginal pile deflections at the pile toe occurring during dynamic excitation. The pile's eigenfrequency is mainly driven by the soil characteristics and state at shallow depth.

6.4 Cyclic lateral pile behaviour due to unidirectional loading

6.4.1 Evaluation procedure for cyclic pile behaviour

Regarding cyclic behaviour, two topics are of main interest for monopile design: Accumulations of pile head displacement or inclination for serviceability and the change of the foundation stiffness for fatigue calculations. The following Figure 6-25 shows exemplary pile head behaviour due to cycles $N = 1; 10; 100; 1,000$ and $10,000$. The measured loading/unloading-displacement loops are drawn by lines and the lateral pile head secant stiffness E_{lat} was calculated between load levels of kN and $5 kN$ (\circ).

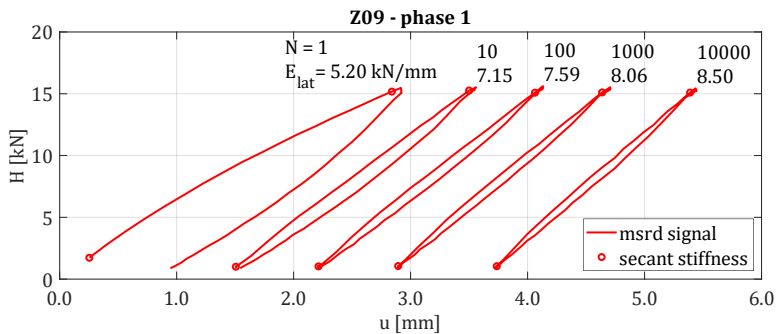


Figure 6-25: Hysteresis loops of loading-unloading cycles

A notable portion of permanent displacement can be seen in the first cycle which drastically decreases with cycle count but still contributes to displacement accumulation. The secant stiffness declines with number of load cycles. Both phenomena will be further analysed in the following sections.

6.4.2 Pile head displacement accumulation

As described in Section 2.3.7, different approaches exist to describe cyclic strain (or displacement) accumulation. Accumulation function of the form $f_N = u(N)/u(N=1)$ describe the accumulated displacement in relation to the displacement during or after the first cycle (= monotonic behaviour). This may be useful when comparing tests of different geometries or in different soils. In case of different installation methods, the quasi-static (monotonic) behaviour showed differences as shown in Section 6.3. So, the use of an accumulation function as defined above may be misleading as information about the absolute value of displacement

accumulation is lost. Still, the accumulation function can be used to describe the shape of the accumulation behaviour (log, log-linear, power law).

The course of absolute displacement (e.g. permanent displacement u_{perm}) is biased by an offset (displacement of the first cycle) and thus is also not suitable to analyse accumulation behaviour. Instead, the convention of the HCA model shall be used to analyse the accumulation behaviour due to cyclic lateral loading: The first 'irregular' cycle is ignored and the strain accumulation is described during the subsequent 'regular' cycles only. The course of the accumulated displacement (after the first, 'irregular' cycle) u_{acc} can be made dimensionless by division by the pile length L_{pile} [m]:

$$\gamma = u^* = u/L_{pile} \tag{6-8}$$

The resulting inclination can be interpreted as shear strain γ [-] (see Figure 6-26):

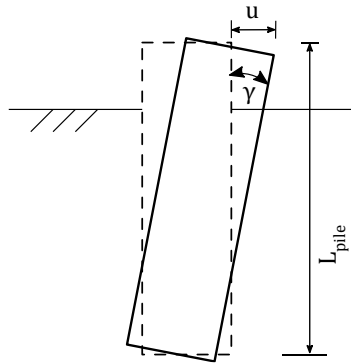


Figure 6-26: Fictional shear strain γ due to pile head displacement u

A measure of 'fictional' strain was calculated for the accumulated displacement u_{acc} and the displacement amplitude u_{ampl} . For the definition of cycle count and strain quantities, refer to Figure 2-15 (Section 2.3.7).

The formulation of the HCA model (NIEMUNIS et al. 2005) for the accumulated strain γ_{acc} is given by multiplication of the flow rule m with the amplitude function f_{ampl} , the stress state function f_p , the stress ratio function f_r , the void ratio function f_e , the polarisation function f_n and the cycle function f_N .

$$\gamma_{acc}(N_{reg}) = m \cdot f_{ampl} \cdot f_p \cdot f_Y \cdot f_e \cdot f_{\pi} \cdot f_N \quad (6-9)$$

or

$$\gamma_{acc}(N_{reg}) = m \cdot f_{ampl} \cdot f_p \cdot f_Y \cdot f_e \cdot f_{\pi} \cdot C_{N1} \cdot [\ln(C_{N2} \cdot (N_{reg}) + 1) + C_{N3} \cdot N_{reg}] \quad (6-10)$$

The given formulation for f_N is only valid for constant loading amplitudes. From Equation (6-10) follows that the shape of the accumulation curve is determined by the constants of the cycle function C_{N2} and C_{N3} while the constant C_{N1} as well as all other functions are needed for scaling purpose only, as long as they are not updated during cyclic loading. The possibility to update the amplitude function and the void ratio function of the HCA model is mentioned by (NIEMUNIS et al. 2005), but (WICHTMANN & TRIANTAFYLIDIS 2011) report that mean values of strain amplitude and void ratio are used to calculate f_{ampl} and f_e for calibration of the model.

As shown above, the displacement accumulation is linked to the displacement amplitude. In analogy to the HCA model of (NIEMUNIS et al. 2005), this effect shall be considered by the amplitude function f_{ampl} . From the mean value of the fictional shear strain amplitude $\gamma_{ampl,mean}$, the amplitude function f_{ampl} [-] was calculated by

$$f_{ampl} = \left(\frac{\gamma_{ampl,mean}}{\gamma_{ref}} \right)^{C_{ampl}} \quad (6-11)$$

with the reference strain $\gamma_{ref} = 10^{-4}$ and the constant $C_{ampl} = 1.7$ taken from (WICHTMANN & TRIANTAFYLIDIS 2011).

Figure 6-27 shows the resulting courses (fitted to the measurements; see below) of the accumulated strain γ_{acc} during test phase 1, corrected by the amplitude function f_{ampl} .

Again, notable deviation can be observed for the free vibratory driven piles with high eccentric moment (cyan). The accumulated strain after the first 'irregular' cycles shows clear differences between impact driven and free vibratory driven piles on the one hand and crane-guided vibratory driven piles on the other hand. The observation that the free vibratory driven pile with low eccentric moment (test Z14, blue) shows the least accumulated strain has to be treated with caution as only one test is available with this installation variant. Crane-guided vibratory driven piles show the highest accumulated strain. The 'order' of the amount of accumulation regarding installation method is less pronounced for the subsequent phases (see Appendix F).

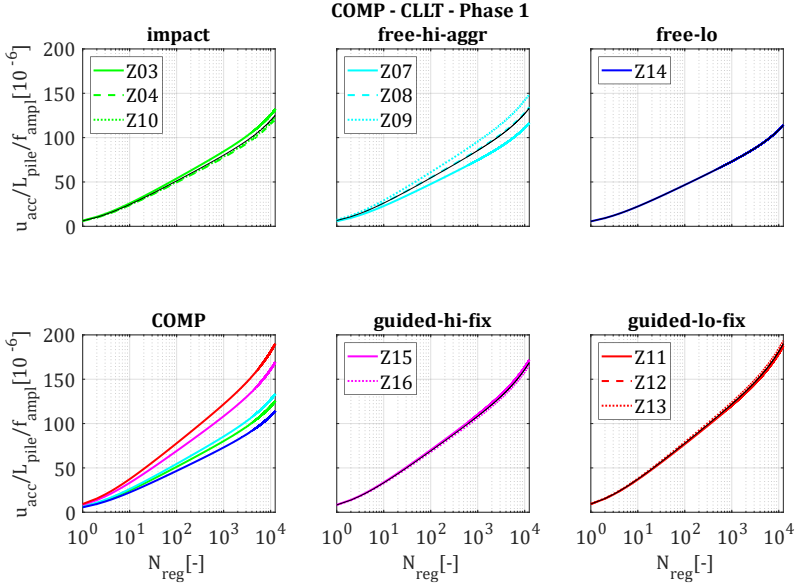


Figure 6-27: Fitted strain accumulation for HCA model

Influences of the first cycle's (permanent) strain are not considered in the HCA model by definition. Influences of the strain amplitude have been considered by the amplitude function f_{ampl} , but seem to be limited (see below). Further influences on the accumulation behaviour may be considered by the stress state function f_p , the loading ratio function f_Y , the void ratio function f_e and the polarisation function f_π . As these functions are unknown (even though $f_\pi = 1$ can be assumed as polarisation changes do not occur during the first loading phase), they were included into a 'biased' accumulation parameter

$$\hat{C}_{N1} = m \cdot f_p \cdot f_Y \cdot f_e \cdot f_\pi \cdot C_{N1} \tag{6-12}$$

which will be used for further analysis.

The accumulation curves presented above show fits between the measured strain accumulation, corrected by the amplitude function, and the modified accumulation function

$$\gamma_{acc}(N_{reg})/f_{ampl} = \hat{C}_{N1} \cdot [\ln(C_{N2} \cdot (N_{reg}) + 1) + C_{N3} \cdot N_{reg}] \tag{6-13}$$

Fits were performed in Matlab (MathWorks 2020). Good agreement could be achieved by treating the parameters $C_{N2} = 0.65$ and $C_{N3} = 10^{-4}$ as soil constants, leading to the following values for \hat{C}_{N1} for phase 1 of the CLLT, plotted over the first cycle's permanent fictional strain $\gamma_{perm,N=1} = u_{perm,N=1}/L_{pile}$:

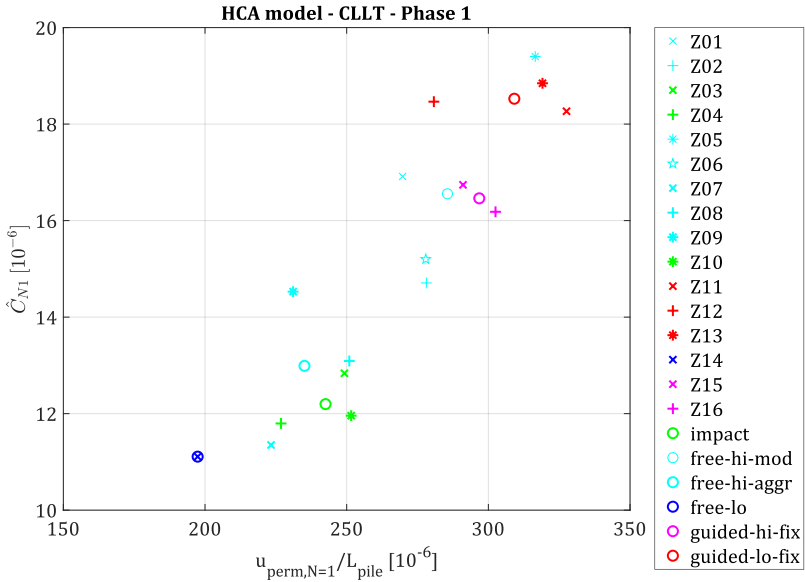


Figure 6-28: Biased cyclic accumulation parameter \hat{C}_{N1} (with $C_{N2} = 0.65$, $C_{N3} = 10^{-4}$) vs. first cycle permanent strain $u_{perm,N=1}/L_{pile}$ for tests and test groups

Figure 6-28 shows a linear correlation between the biased cyclic accumulation parameter \hat{C}_{N1} and the permanent fictional strain of the first cycle $u_{perm,N=1}/L_{pile}$. Lower combinations of both parameters can be observed for impact driven and free vibratory driven piles with 'aggressive' penetration control while higher values apply for crane-guided vibratory driven piles and free vibratory driven piles with a more moderate frequency control.

The variance in accumulation behaviour of the free vibratory driven piles can be seen in the following Figure 6-29. All free vibratory driven piles with high eccentric moment (cyan) are shown, together with the impact driven pile Z04 (green) and the crane-guided vibratory driven pile Z12 (red). The installation of the free vibratory driven piles shown here differ only in the manual frequency control (cf. Sections 6.1 and 6.2.3).

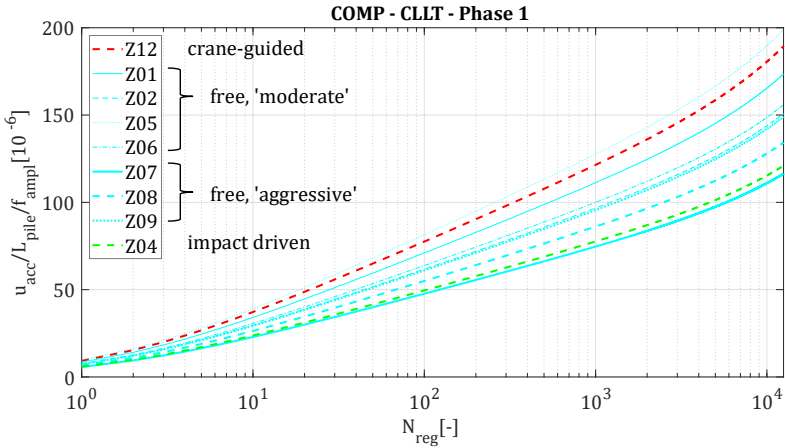


Figure 6-29: Fitted strain accumulation for free vibratory driven piles

The accumulation behaviour of the free vibratory driven piles is spread over the whole range between the abovementioned 'boundary values'. Free vibratory driven piles with a more 'aggressive' frequency control (thick lines: Z07, Z08, Z09) show lower strain accumulation compared to those with a more 'moderate' frequency control (thin lines: Z01, Z02, Z05 Z06).

Further test phases 2, 3 and 5 gave also good agreement between measured accumulation and Equation (6-10) with the same constants $C_{N2} = 0.65$ and $C_{N3} = 10^{-4}$. The resulting biased constants \hat{C}_{N1} are given in Table 6-4 as mean values for the groups of tests with same installation method. Parameters for all tests are given in Appendix F.

Table 6-4: Mean fitted 'biased' accumulation parameter for HCA model accumulation law (test groups, CLLT, phases 1, 2 and 3)

group	$\hat{C}_{N1} [10^{-6}]$		
	phase 1	phase 2	phase 3
impact	12.2	11.9	8.9
vibro (free-hi-aggr)	13.0	15.9	10.0
vibro (free-lo)	11.1	15.0	9.0
vibro (guided-hi-fix)	16.5	16.5	11.9
vibro (guided-lo-fix)	18.5	22.9	13.1

** for phase 5 only a limited number of tests was available*

Phases 1 and 2 show similar or increasing accumulation behaviour. Phase 3 always shows the lowest accumulation behaviour. These results indicate that phases 1, 2 and 3 can be regarded as independent concerning cyclic pre-loading. Different accumulation behaviour results in different scaling only, which can be explained by changes of the void ratio or stress state. The loading history, however, is erased by the changing loading direction (cf. Section 6.5).

For phase 4, the accumulation behaviour showed a different shape and less good agreement was found for parameters $C_{N2} = 0.65$ and $C_{N3} = 10^{-4}$. Better agreements were found using different cyclic parameters C_{N2} and C_{N3} . However, this violates the HCA model assumptions according to which C_{N2} and C_{N3} are soil constants. As a different horizontal force was applied (namely $H = 5..20$ kN in phase 4 in contrast to $H = 1..15$ kN in phases 1, 2 and 3), the flow rule m and the functions f_Y and f_P will probably change. This, however, will only result in different scaling of the accumulation curve and not change its shape. Since the cyclic loading during phase 4 was conducted in the same direction as during phase 3, a pre-loaded system may be assumed. On the other hand, (WICHTMANN 2016) found out that due to an increase of the average load level (equal to monotonic loading), the 'cyclic memory' of the soil may be partly or fully erased. In case of the transition from phase 3 to phase 4, the average load level is raised from $H_{av} = 8$ kN to 12.5 kN. Due to the first ('irregular') cycle of phase 4, effects of the cyclic preloading during phase 3 on the behaviour during phase 4 may be partly or fully removed.

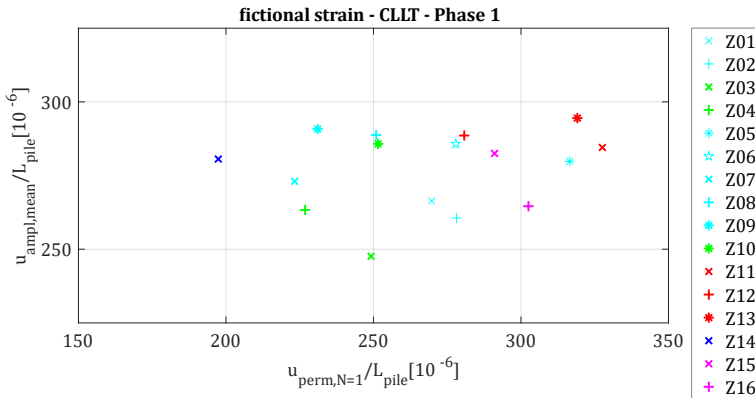


Figure 6-30: Ranges of mean strain amplitude $\gamma_{amp,mean}$ and first cycle's permanent strain amplitude $\gamma_{perm,N=1}$

Figure 6-30 shows the combinations of $\gamma_{\text{ampl,mean}} = u_{\text{ampl,mean}}/L_{\text{pile}}$ (used to normalise the strain accumulation in the HCA model) and $\gamma_{\text{perm,N=1}} = u_{\text{perm,N=1}}/L_{\text{pile}}$ (used to normalise the accumulation in 'classical' accumulation functions) for all tests. The range of $\gamma_{\text{ampl,mean}}$ is quite small in comparison to that of $\gamma_{\text{perm,N=1}}$. Thus, in this case, the influence of the amplitude function on the strain accumulation is merely a scaling issue.

6.4.3 Cyclic pile stiffness

Development of quasi-static lateral secant stiffness during cyclic loading

From the lateral force H [kN] and the pile head displacement u [mm] measured during cyclic lateral loading, the lateral pile head stiffness E_{lat} [kN/mm] can be calculated as

$$E_{\text{lat}} = \Delta H / \Delta u \quad (6-14)$$

The secant stiffness between minimum and maximum load is defined as shown in Figure 2-19 and was evaluated for both loading and unloading of each cycle. As the maximum and minimum load, and therefore the load difference ΔH , were kept constant by the loading device, the secant stiffness E_{lat} is directly proportional to the displacement amplitude $u_{\text{ampl}} = \Delta u / 2$.

The following Figure 6-31 shows exemplary plots of the development of secant stiffness over cycles for tests Z03, phase 2 and Z15, phase 1. The coloured lines show measured secant stiffness where the upper lines indicate unloading stiffness while the lower ones indicate loading stiffness. The curves show some fluctuations which can be explained by small magnitude of Δu (in the region of 2 mm) which is influenced by the resolution of the measurement devices. In case of the measurement of the accumulated displacement this effect does not play an important role.

The behaviour of the first loading cycle differs greatly from the further cycles. The unloading stiffness decreases during the first cycles. For cycle numbers $N > 20$, loading and unloading stiffness converge. For 'regular' cycles ($N \geq 2$), the loading stiffness shows a linear course in half-logarithmic scale.

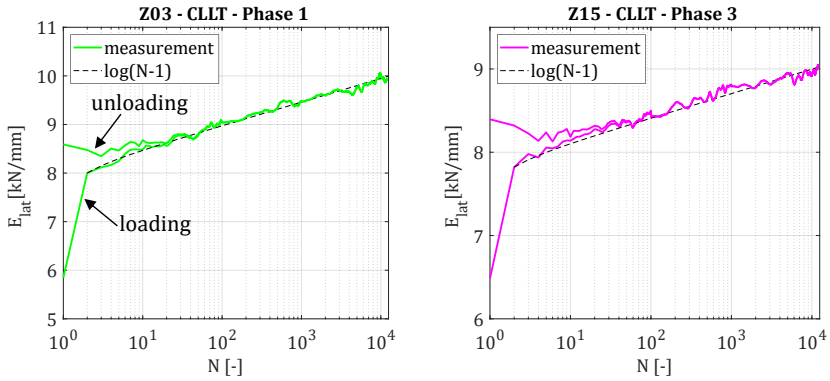


Figure 6-31: Development of measured lateral pile head secant stiffness during cyclic loading

Figure 6-32 shows an overview of the pile head secant stiffness of the loading cycles for all tests and test groups in the familiar manner.

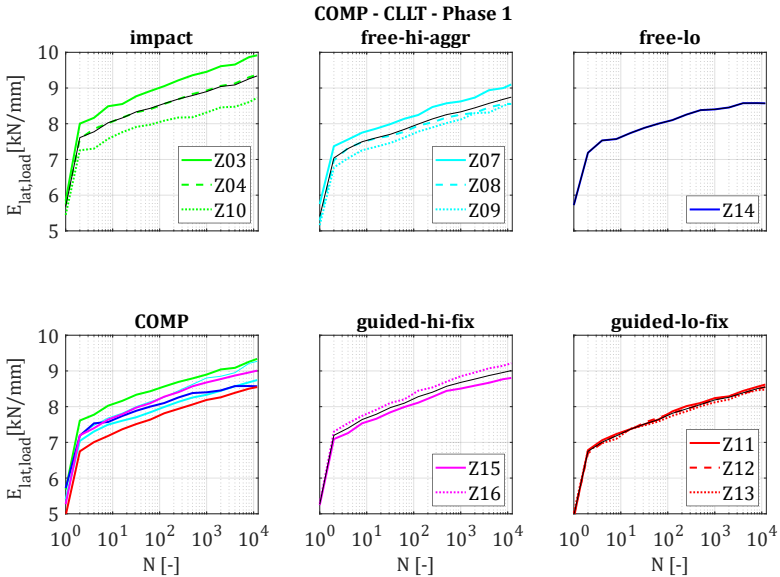


Figure 6-32: Development of pile head secant loading stiffness over cycle count

Most important to notice is a severe increase in pile head stiffness of 26% to 41% (mean value 34%) due to the first cycle and another 19% to 33% (mean 25%) due to the subsequent 12,000 cycles.

Figure 6-33 shows the course of the secant stiffness of the unloading cycles for different test groups. The curves are smoothed for better readability; the qualitative shape is similar for all tests.

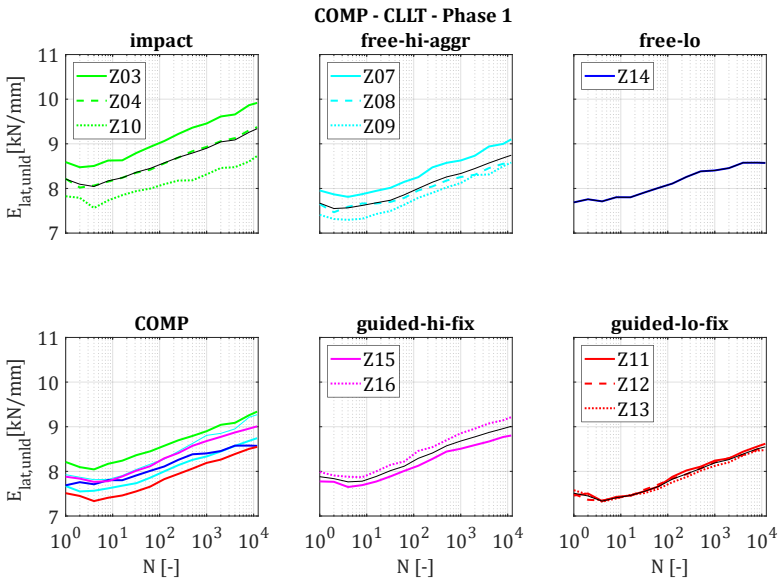


Figure 6-33: Development of pile head secant unloading stiffness over cycle count

Impact driven piles show the highest mean courses of both loading and unloading stiffness, but also a large variation between the tests (Z03, Z04, Z10). Crane-guided vibratory driven piles show the lowest secant stiffness and a very good reproducibility.

Development of dynamic stiffness during cyclic loading

During the tests Z07, Z10 and Z15, lateral frequency response tests were carried out before start of the cyclic lateral loading ($N = 0$), after $N = 1; 10; 100$ and $1,000$ cycles and after the end of each cyclic loading phase ($N = 12,000$). Figure 6-34 shows the development of the eigenfrequencies $f_{0,lat}$ [Hz] measured in loading direction after the above-mentioned cycle

counts in relation to the eigenfrequencies measured before lateral loading ($N = 0$). Higher eigenfrequencies indicate a stiffer system.

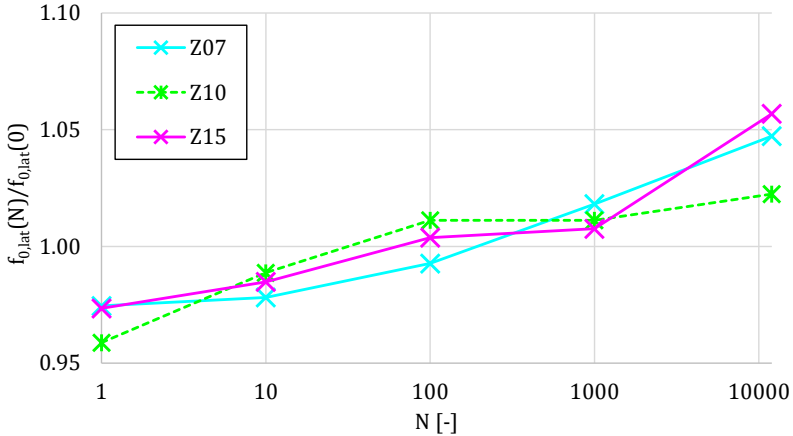


Figure 6-34: Development of lateral pile eigenfrequency during cyclic loading

For all three tests, a softening of the system can be observed due to the first loading/unloading cycle as $f_{0,lat}(N=1)/f_{0,lat}(N=0) < 1$. The stiffness recovers after about 100 cycles and after end of cyclic loading the eigenfrequency reaches about 102% to 106% of the initial value. Based on only three tests with different pile installation procedures, a discussion of the course of $f_{0,lat}$ over N seems not well founded.

For a comparison of the dynamic stiffness with the cyclic secant stiffness, the measured stiffnesses of tests Z07, Z10 and Z15 were used. It has to be taken into account that each loading cycle has a considerable impact on the soil behaviour for following unloading and loading cycles, especially during the first cycles (cf. Figure 6-31). The lateral frequency response test, on the other hand, can be considered as non-destructive testing method with very little influence on the soil behaviour. This has two implications:

- Relative stiffnesses from (non-destructive) eigenfrequency measurements should be compared to relative secant stiffnesses of the preceding unloading cycle.
- No static (secant) stiffness is available for $N = 0$, thus all measurements have to be related to the respective measurements of the first cycle $N = 1$.

The following Figure 6-35 show the outlined comparison of quasi-static and dynamic pile stiffness.

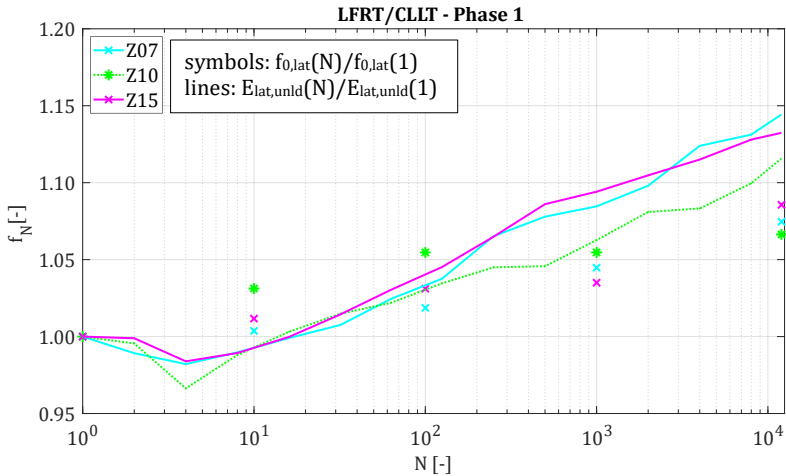


Figure 6-35: Comparison of measured pile head unloading secant stiffness (lines) and measured eigenfrequency (markers) over cyclic loading

In general, a similar behaviour can be observed from both dynamic and static stiffness. A quantitative match between the two measures for the pile stiffness, however, is not obvious. One reason for the quantitative differences may be the fact that the (quasi-)static lateral stiffness was deduced from measurements at the pile head (approx. 60 cm above mudline) while the dynamic stiffness (pile eigenfrequency) was measured at the top of the transition piece. The stiffness of the transition piece itself (which is not affected by cyclic loading) influences the dynamic stiffness but not the (quasi-)static stiffness. Thus, the dynamic stiffness shows less influence of cyclic effects compared to the quasi-static stiffness.

6.4.4 Soil reaction to cyclic pile loading

Soil stress developments due to cyclic loading

To investigate the soil stress development during cyclic loading, the changes of effective radial soil stresses (compared to the effective radial stress after pile installation, N = 0) are plotted for an increasing number of cycles. Figure 6-36 shows exemplary results from pile Z05. Different

diagrams show soil stress developments in upwind direction, downwind direction and for stress resultants (from left to right). Soil stress profiles for maximum lateral load level (solid lines) and after subsequent unloading (dashed lines) are plotted for $N = 1; 10; 100; 1,000$ and $10,000$ cycles (with growing darkness).

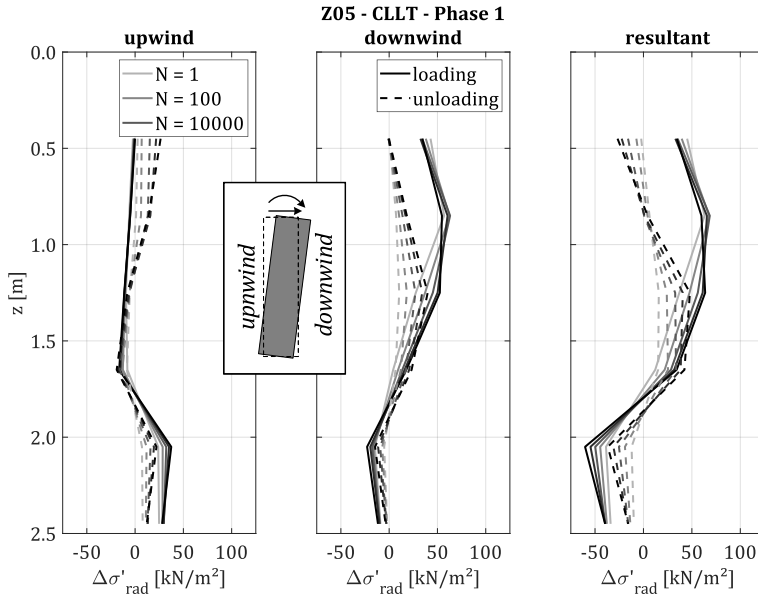


Figure 6-36: Upwind, downwind and resultant soil stress profiles at maximum and minimum load level for different number of cycles

The behaviour of the soil can be roughly divided into three layers:

1) Shallow depth ($z < 1$ m)

In downwind direction, soil resistance is mobilised due to lateral loading. Soil stresses go back to initial values after unloading. Soil stresses remain stable during cyclic loading.

In upwind direction, soil stresses stay at initial values during loading (when the pile is pulled away from the soil) and increase during unloading (as the pile moves towards the soil). With increasing number of cycles, soil stresses accumulate in upwind direction.

2) Intermediate depth ($1 \text{ m} < z < 1.8 \text{ m}$)

In downwind direction, soil stresses grow due to lateral loading. Increased radial stresses remain imprinted in the soil after unloading. Thus, stresses grow due to cyclic loading. The stress amplitude (difference between maximum stresses during loading and minimum stresses after unloading) decreases with depth and becomes zeros around $z \approx 1.8 \text{ m}$ where the point of zero deflection can be assumed.

In upwind direction, only minor changes of soil stresses can be witnessed.

3) Toe kick ($z > 1.8 \text{ m}$)

Below the assumed point of zero deflection, the 'toe kick' leads to stress reductions in downwind direction during loading. Absolute values of soil stress reduction grow with number of cycles and the soil stresses during unloading 'follow' this trend.

In upwind direction, an increase of soil stresses with number of cycles was measured by the two lowermost sensor levels. Higher stresses during loading partly remain imprinted in the soil after unloading.

Figure 6-37 shows a detailed analysis of the development of soil stresses over displacement cycles. The changes of radial effective soil stresses with respect to the stress state after pile installation (EoD, end of driving)

$$\Delta\sigma'_{\text{rad}} = \sigma'_{\text{rad}} - \sigma'_{\text{rad,EoD}} \quad (6-15)$$

divided by the overburden pressure $\gamma \cdot z$ at different sensors locations is given over the pile head displacement in loading direction u_{0° (not the local pile displacement at measurement level!). The diagrams are arranged according to the sensor location (left/right: upwind/downwind θ ; vertical: depth z). Exemplary data of the first phase of the cyclic lateral load test of pile Z07 was used. Single cycles are drawn with increasing darkness according to the cycle number. The start (\triangleright) and end (\triangleleft) of each drawn cycle is labelled by markers.

For all sensor layers, but especially those at intermediate depth and those below the rotation point, it has to be kept in mind that the actual pile displacement in the respective depth is smaller than the pile head displacement at the measurement level ($\approx 0.6 \text{ m}$ above mudline). The normalisation of the soil stress changes allows a comparison of the different sensor layers. Obviously, highest amplitudes of normalised stresses can be observed at shallow depths.

Z07 - CLLT - phase 1 ($\theta_H = 0^\circ$)

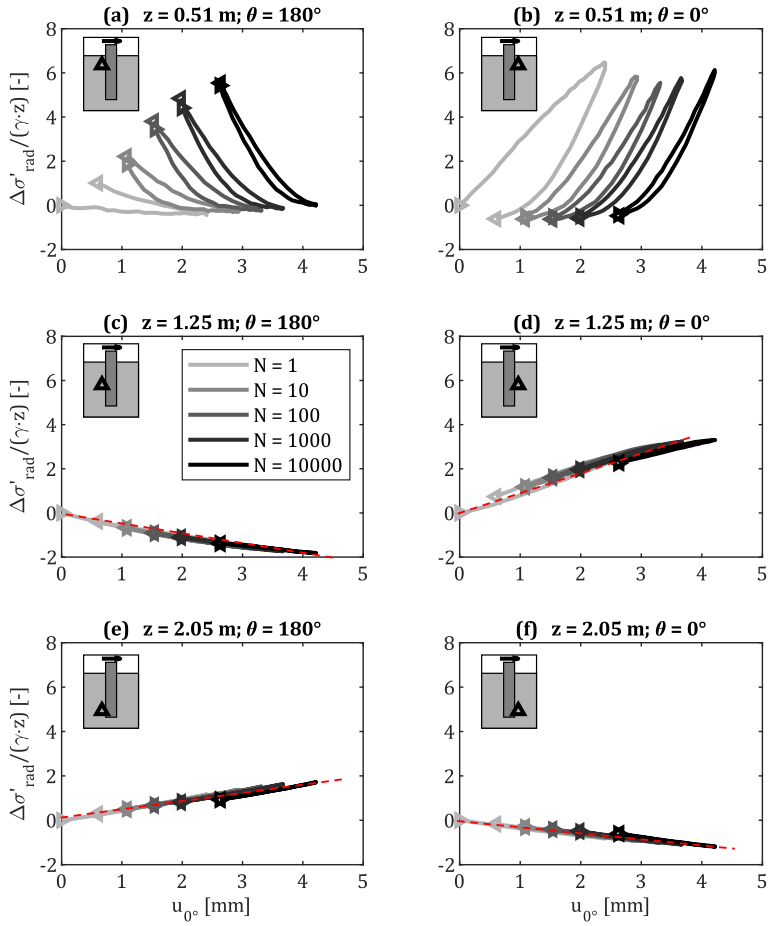


Figure 6-37: Development of soil stresses over displacement cycles

- (a) For the sensor at shallow depth in upwind direction, the soil stress does not change when the pile is pulled away from the soil during the first loading cycle but increases as the pile is allowed to move towards the sensor again during the first unloading cycle. During subsequent loading cycles, the soil stress decreases towards the initial values ($\Delta\sigma'_{\text{rad}}/(\gamma \cdot z) \approx 0$) and increase towards continuously growing values during unloading. The shape of the soil stresses over pile head deflection becomes steeper with increasing cycle number.
- (b) In downwind direction, soil stresses increase to similar values during each loading cycle and decrease below the initial values ($\Delta\sigma'_{\text{rad}}/(\gamma \cdot z) < 0$) during unloading. The shape of the soil stresses over pile head deflection is approximately parallel except for the first loading cycle.
- (a, b) At the sensor levels in shallow depth, the soil stress change over pile head displacement shows a loop-like shape, indicating a hysteretic behaviour and plastic behaviour (ratcheting) due to cyclic effects.
- (e, f) Due to the toe kick, as expected, sensors below the rotation point show an increase of soil stresses in upwind direction (e) and a decrease of soil stresses in downwind direction (f) during loading cycles and vice versa during unloading cycles.
- (c - f) At the sensor levels in and below intermediate depth, the changes in soil stresses over pile head displacement move on a more or less straight line during subsequent loading and unloading cycles (red dashed lines). This indicates linear elastic behaviour of the soil in the emerging stress range. Deviations from the linear-elastic behaviour can be observed in downwind direction at intermediate depth (d) and in upwind direction below the rotation point (e), indicating ratcheting behaviour.

The soil behaviour in shallow and intermediate depth can be explained by the model drawn in Figure 6-38:

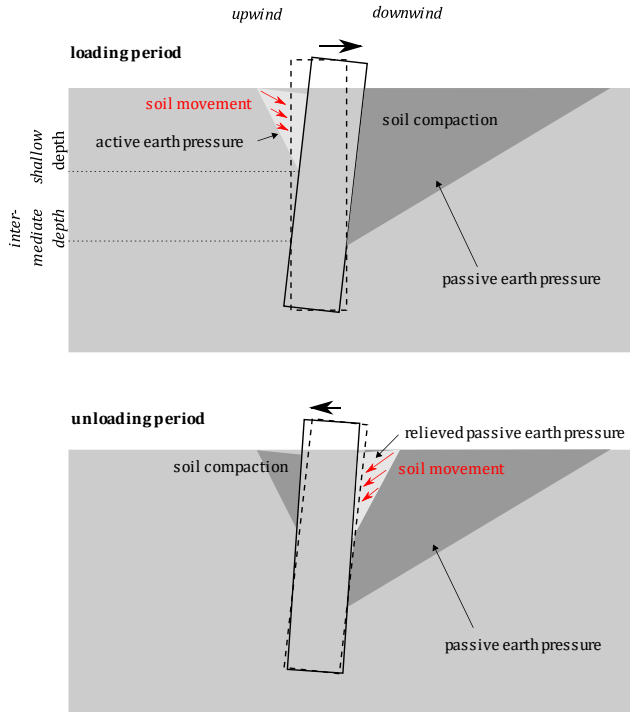


Figure 6-38: Soil reaction during loading (top) and unloading period (bottom)

1) Shallow depth ($z < 1 \text{ m}$)

In upwind direction, a 'gap' is formed during loading and material is transported into that gap. In downwind direction, passive earth pressure is mobilised. During unloading, the passive earth pressure pushes the pile back towards its original position. The additional material in the upwind direction is compacted, acts as a shifted support and evokes increased radial soil stresses. The pile deflection during unloading is large enough to relieve the passive earth pressure.

2) Intermediate depth ($1 \text{ m} < z < 1.8 \text{ m}$)

No 'gap' is formed between pile and soil in upwind direction during loading. In downwind direction, bedding resistance is mobilised during loading. During unloading, the soil reaction 'pushes' the pile back towards its original position. The pile deflection

during unloading is not large enough to fully relieve the soil reaction, so increased radial stresses remain imprinted in the soil in downwind direction. Likewise, in upwind direction, soil stresses decrease during loading and partly recover due to partly back movement of the pile.

3) Toe kick ($z > 1.8$ m)

The mechanisms below the rotation point are the same as at intermediate depth, but with opposite sign: The pile deflections are small and the soil behaves elastic. Stress accumulations during cyclic loading are merely an effect of accumulated pile deflections.

Effects on soil density

Caused by the recurrent processes of soil compaction and soil movement towards the pile, the soil around the pile is densified and soil volume is reduced. Even though soil deformations were not measured directly, observations of the mudline around the pile (cf. Figure 5-19) reveal such developments. The following Figure 6-39 shows exemplary plots of the depth of soil subsidence Δz_0 observed around the pile, measured directly at the pile shaft after phase 1 of different tests. Cones with depths of 2 cm to 4 cm with a more or less uniform expansion around the pile circumference were detected.

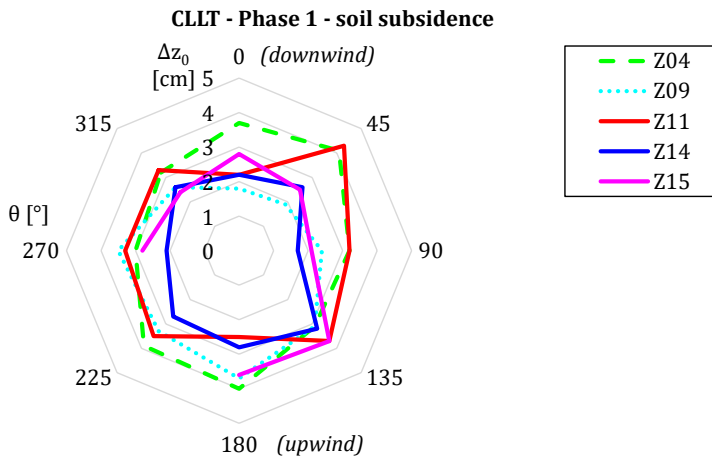


Figure 6-39: Exemplary plots of soil subsidence around model after cyclic loading phase 1

As outlined by (CUÉLLAR 2011), the change of volume given by the mudline subsidence indicates a change of soil density along the pile (cf. Figure 2-18). As the measurements of mudline were quite inaccurate and limited to the depth of the subsidence at the pile wall, a quantification of soil compaction similar to the above cited work was not carried out here.

6.4.5 Interim summary and discussion on cyclic lateral pile behaviour

The displacement accumulation of laterally loaded piles can be described by the HCA model on system level. The HCA model reveals accumulation behaviour unbiased by the monotonic behaviour of the first, 'irregular' cycle. Especially the shape of the displacement accumulation during test phases 1, 2, 3 and 5 shows good agreement with the log-linear formulation of the HCA model. These test phases have a load level of $H = 1 \dots 15$ kN and can be considered independent of their preceding phases due to change in loading direction. The shape of the displacement accumulation during test phase 4 can be better described by a power law. This test phase has a higher load level of $H = 5 \dots 20$ kN and can be considered preloaded by the preceding phase 3 which is loaded in the same direction.

The installation variants can be distinguished based on the 'biased' accumulation parameter \hat{C}_{N1} (accumulation intensity). Impact driven and free vibratory driven piles show lower displacement accumulation compared to the crane-guided vibratory driven piles. This is partly in contradiction with numerical simulations of (STAUBACH et al. 2021) which showed lower accumulation rates of impact driven piles compared to WIP (unaffected by any installation processes) piles in dense sand.

The pile head secant stiffness due to cyclic loading shows a linear increase with the logarithm of the 'regular' cycles. The monotonic stiffness of the first, 'irregular' cycle is considerably lower than that of the subsequent cycles. The unloading stiffness is larger than the loading stiffness during the first cycles and later approximates the loading stiffness. The dynamic stiffness shows a similar development based on a limited number of measurements.

Due to first loading/unloading cycle, soil stresses are imprinted to the soil, especially at shallow and intermediate depth above the rotation point ($z < 1.8$ m). Further increase of soil stresses is observed due to cyclic loading together with a densification of the soil around the pile, revealed by a cone of subsidence at the mudline. At shallow depth, high normalised soil stresses induce strain ratcheting and stress accumulation. At and below intermediate depth, comparably low

normalised soil stresses occur and the soil behaves elastically with the unloading path following the loading path back.

On the influence of the soil's stress state on the accumulation behaviour

Following the HCA model and treating C_{N1} as a soil constant (as C_{N2} and C_{N3}), the different accumulation behaviour of the piles has to be explained by differences in stress state (f_p), loading ratio (f_r) or void ratio (f_e). Larger values of the beforementioned functions indicate a greater amount of accumulation. Details on the HCA model and the definition of its different functions can be found in (NIEMUNIS et al. 2005; WICHTMANN & TRIANTAFYLIDIS 2011; WICHTMANN 2016). A description of the functions and estimated parameters used in this thesis is given in Appendix G. From the functional formulation of f_p and f_r it is evident that the strain accumulation

- decreases with increasing average mean stress p_{av} , and
- increases with increasing average stress ratio q_{av}/p_{av} .

To quantify the possible effect of the installation-induced stress changes on the cyclic accumulation, the functions f_p and f_r were calculated for two scenarios. Figure 6-40 (left) gives the mean pressure p for the primary stress state (PSS, dashed line) and considering an installation effect according to Equation (2-37) (INST, solid line). For the primary stress state, the effective radial stress σ'_{rad} can be treated as mean effective pressure p as the dynamic compaction during sand placement leads to $k_0 \approx 1$ (cf. Section 5.6.2). In case of the stress state after pile installation, however, the soil stress profile according to Equation (2-37) is only validated for the radial stresses acting on the pile. Therefore, the mean value of the overburden pressure $\gamma' \cdot z$ and σ'_{rad} according to Equation (2-37) with $\alpha = -1.6$ and $1/\beta_{PSS} = 5$ was taken for p .

Figure 6-40 (middle) shows the resulting course of f_p over depth for the primary stress state and the stress state with installation effect. The function of the HCA model considering the average mean stress yields

$$f_p = \exp \left[-C_p \cdot \left(\frac{p_{av}}{p_{ref}} - 1 \right) \right] \quad (6-16)$$

with the atmospheric pressure $p_{ref} = 100$ kPa and

$$C_p = 0.41 \cdot [1 - 0.34 \cdot (d_{50} - 0.6)] = 0.44 \quad (6-17)$$

based on a mean grain size of $d_{50} = 0.39$ mm (cf. Table 5-4). The greatest deviation of f_p is of course observed at the pile toe where values for f_p are 1.40 for the primary stress state and 1.12 for the installation effected stress state. The mean values are 1.49 and 1.42, respectively.

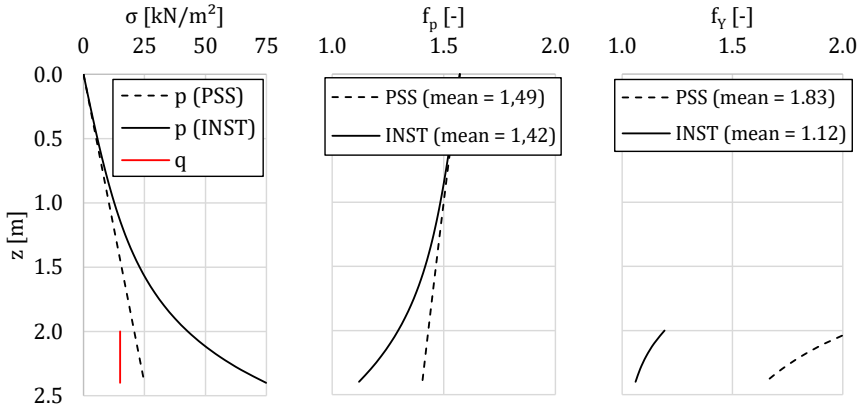


Figure 6-40: Stresses p and q (left), functions f_p (middle) and f_Y (right) over depth for PSS conditions (dashed lines) and due to pile installation effect (solid lines)

Likewise, values for the loading ratio function f_Y were estimated for the two scenarios. The function of the HCA model considering the average stress ratio

$$f_Y = \exp[C_Y \cdot \bar{Y}] \quad (6-18)$$

with

$$C_Y = 2.60 \cdot \left[1 + 0.12 \cdot \ln \left(\frac{d_{50}}{0.6} \right) \right] = 2.47 \quad (6-19)$$

is somewhat less simple with

$$\bar{Y} = \frac{Y - 9}{Y_c - 9} \quad (6-20)$$

$$Y = \frac{27 \cdot (3 + \eta_{av})}{(3 + 2\eta_{av})(3 - \eta_{av})} \quad (6-21)$$

$$\eta_{av} = q_{av}/p_{av} \quad (6-22)$$

$$Y_c = \frac{9 - \sin^2 \varphi_c}{1 - \sin^2 \varphi_c} \quad (6-23)$$

with $\varphi_c = 32,2^\circ$ (cf. Section 5.4.3). The focus was set on the toe kick as here the differences in the stress state p are most obvious. For the average deviatoric stress q_{av} , the measured stress difference at the two lowermost sensor levels at average load level $\Delta\sigma'_{rad,av} \approx 15 \text{ kN/m}^2$ (cf. Figure 6-36, left) was taken. From the stress ratio q_{av}/p_{av} the stress ratio function f_Y was calculated. Figure 6-40 (right) shows the resulting course of f_Y in the region of the toe kick and the mean values of 1.83 for the primary stress state and 1.12 with consideration of installation effects.

Thus, smaller values of f_p and f_Y due to imprinted soil stresses as a result of pile installation effects explain the lesser accumulation of pile head displacements of the impact driven and free vibratory driven piles compared to the crane-guided vibratory driven piles.

6.5 Cyclic lateral pile behaviour due to changing loading direction

6.5.1 Pile head behaviour due to changing loading direction

As described before, the direction of lateral loading was altered by 90° back and forth between phases with 12,000 cycles each. Displacement accumulations and changes in lateral stiffness in loading direction were discussed in section 6.4. Apart from that, a back-accumulation due to subsequent transverse loading was observed. This phenomenon as well as changes in the system's stiffness in different directions shall be discussed here.

Back-accumulation

Back-accumulation can be visualised in a comprehensive manner by tracking the pile head displacement in the horizontal plane. The following Figure 6-41 shows the trace of the pile head of test Z09. Each symbol represents the pile head displacement in directions 0° and 90° after $N = 0; 1; 10; 100; 1,000$ and $10,000$ cycles of phases 1 to 5, starting with $N = 0$ of phase 1 at the origin ($u_0 = u_{90} = 0 \text{ mm}$). The arrows at the markers representing $N = 0$ indicate the loading direction during the individual phases.

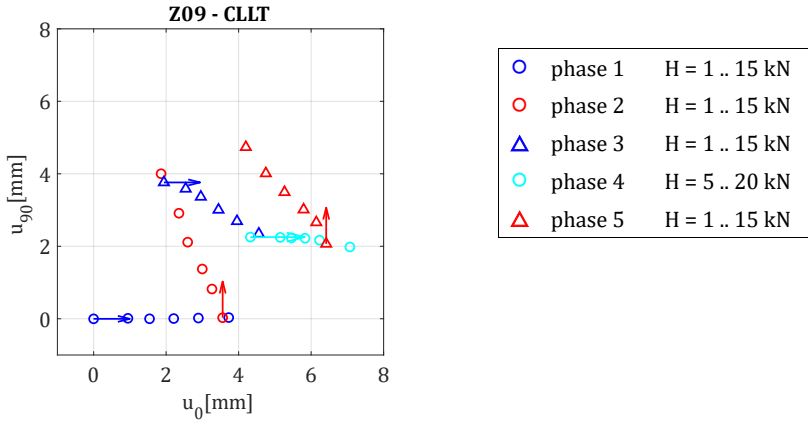


Figure 6-41: Exemplary track of pile head displacement in horizontal plane during cyclic lateral loading from varying directions

Similar behaviour occurred in all tests whose traces are given in Appendix F.

- (i) During phase 1, pile head displacements accumulate in loading direction (0°). Similar spacings between markers point towards approximately logarithmic accumulation law (see also Figure 6-42; detailed analysis in Section 6.4.2). During phase 2, displacements accumulate in loading direction (90°) again with very similar rate.
- (ii) Simultaneously, considerable back-accumulation in transverse direction (0°) can be witnessed which eats up about one half of the accumulated displacements from phase 1 until the end of phase 2. Similar behaviour takes place during phase 3 regarding the accumulated displacements from phase 2. The rate of the back-accumulation (spacing transverse to loading direction) again shows an approximately logarithmic course with number of cycles, as can also be seen in Figure 6-42
- (iii) Furthermore, the displacement accumulation (in loading direction) during phase 3 is somewhat slower compared to phase 1 (both 0° , blue). The same applies for phases 5 and 2 (both 90° , red).

- (iv) Due to (ii) and (iii), the total accumulated displacement accumulation at the end of phases 3 and 5 is only slightly greater than at the end of phases 1 and 2, respectively.
- (v) The behaviour in connection with phase 4 (cyan) needs to be examined separately as there is no change of loading direction between phases 3 and 4 and the mean load level of phase 4 is larger than that of the other phases. In phase 4, there is less back-accumulation, possibly because a great portion of the accumulated displacements from phase 2 has already been depleted during phase 3. The back-accumulation during phase 5 should be compared to the sum of displacement accumulation from preceding phases 3 and 4 (both 0°). Here again, almost half of the accumulated displacements were eaten up.

Table 6-5 gives the portion of permanent back-accumulation $u_{\perp,perm}$ during phases 2 to 5 referred to the accumulated permanent displacements $u_{||,perm}$ from preceding phase(s) with transverse loading direction for all tests. For phase 5, the accumulated displacements from phases 3 and 4 are used as reference, as described above. Except for phase 4 (where the amount of back-accumulation is probably limited due to the preceding phase 3 with same loading direction), the portion of back accumulation lies between 30% and 50% in all tests.

In analogy to the accumulation function of the HCA model, a function with the same mathematical structure can be used to describe the back-accumulation. The amplitude function f_{ampl} to scale the back-accumulation was determined based on the mean displacement amplitude in loading direction. For the back-accumulation as well, the cyclic parameters $C_{N2} = 0.65$ and $C_{N3} = 10^{-4}$ were found suitable to fit the measurement data. Figure 6-42 shows exemplary plots of the accumulation in loading direction ($u_{||}$) and the back-accumulation in transverse direction (u_{\perp}) during phase 2 of tests Z03, Z09 and Z11.

Table 6-5: Portion of back-accumulation due to transverse loading

Test	Phase 2	Phase 3	Phase 4	Phase 5
	$\theta_H = 90^\circ$	$\theta_H = 0^\circ$	$\theta_H = 0^\circ$	$\theta_H = 90^\circ$
	$\frac{-u_{\perp perm,i}}{u_{\parallel perm,i-1}}$ [-]	$\frac{-u_{\perp perm,i}}{u_{\parallel perm,i-1}}$ [-]	$\frac{-u_{\perp perm,i}}{u_{\parallel perm,i-2}}$ [-]	$\frac{-u_{\perp perm,i}}{u_{\parallel perm,i-1} + u_{\parallel perm,i-2}}$ [-]
Z01	48%	38%	5%	47%
Z02	47%	35%	6%	
Z03	45%	40%	10%	49%
Z04	33%	34%	-2%	48%
Z05	35%	33%	4%	
Z06	34%	33%	2%	42%
Z07	44%	33%	5%	
Z08	43%	34%	4%	
Z09	51%	37%	5%	48%
Z10	45%	51%	11%	
Z11	39%	30%	6%	
Z12	47%	33%	5%	44%
Z13	43%	31%	6%	
Z14	45%	39%	8%	
Z15	36%	31%	3%	42%
Z16	49%	42%	9%	45%
mean	43%	36%	5%	46%

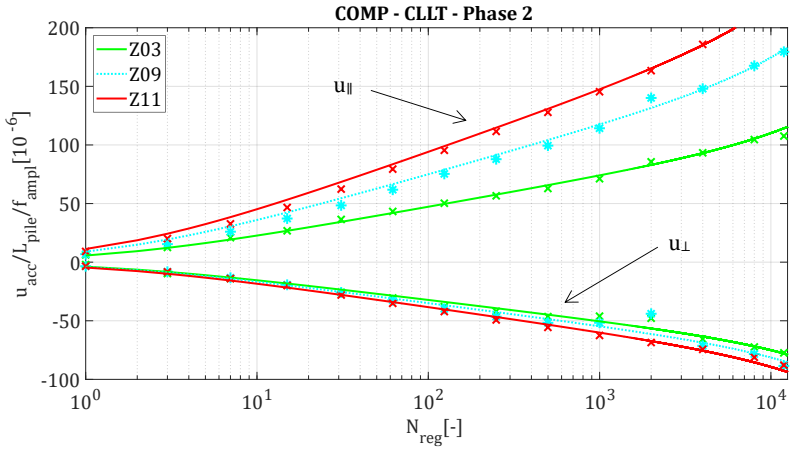


Figure 6-42: Displacement accumulation in loading direction and back-accumulation in transverse direction

The biased parameter \hat{C}_{N1} consequently depends on the corresponding accumulation parameter of the preceding phase and has a negative sign. Figure 6-43 shows back accumulation parameters $\hat{C}_{N1,\perp}$ of phase 3 versus accumulation parameters $\hat{C}_{N1,||}$ of preceding phase 2 of all tests.

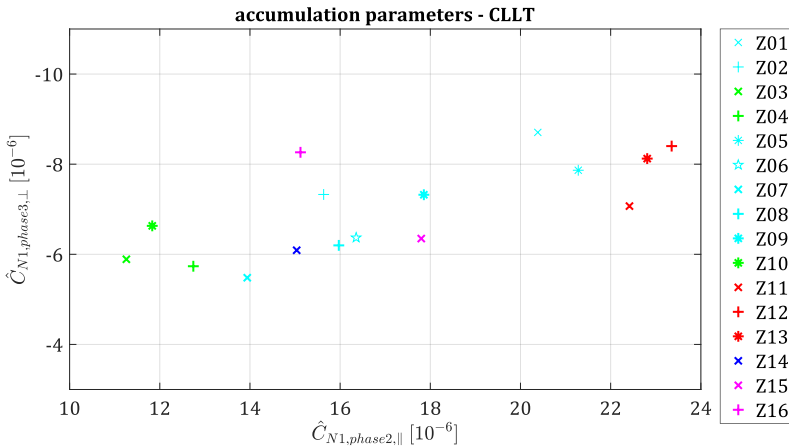


Figure 6-43: Comparison of back-accumulation parameters to accumulation parameters of preceding phase

Parameters are grouped in the shown plane according to the installation method. The accumulation parameter $\hat{C}_{N1,\parallel}$ has a larger span than the back-accumulation parameter $\hat{C}_{N1,\perp}$ but still a slight linear trend between both parameters can be suspected.

A detailed view on the load-displacement behaviour on individual cycle level is shown in Figure 6-44 for phases 2 ($\theta_H = 90^\circ$, left) and phase 3 ($\theta_H = 0^\circ$, right) of test Z08. The upper diagrams show the familiar hysteresis loops while the lower diagrams show the pile head movement in the horizontal plane (= top view). u_{\parallel} indicates the pile head displacement in direction of the applied lateral force H while u_{\perp} specifies transverse displacement. Only a limited number of cycles with logarithmic spacing was plotted for the sake of clarity.

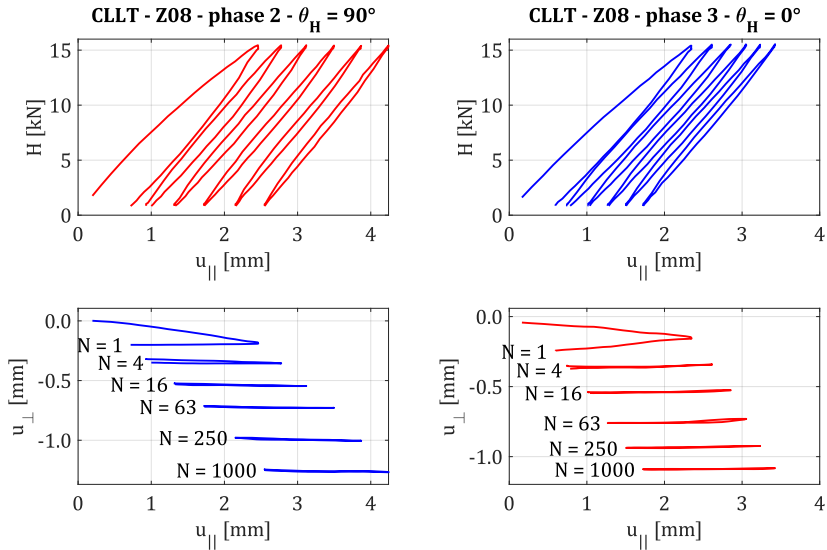


Figure 6-44: Hysteresis loops (top) and pile head movement on cycle level (bottom)

The bottom diagrams show how the pile head moves in transverse direction u_{\perp} as it is deflected in loading direction u_{\parallel} . A permanent displacement in both directions (u_{\parallel} and u_{\perp}) between cycle start and end is only visible in the very first cycles. The first cycle shows a somewhat different behaviour in phases 2 and 3. In phase 2, the main part of the transverse displacement u_{\perp} occurs during loading period (as the pile is pulled into loading direction) without further transverse displacement during unloading. In phase 3, approximately the same amount of transverse

displacement takes place during loading and unloading periods. A similar behaviour could be witnessed in most tests. In phase 4, no clear curves of transverse movement can be generated as the amount of back-accumulation is very low (cf. Table 6-5). Phase 5 behaved similar to phase 2 in most cases.

Change in lateral pile head stiffness

The pile head secant stiffness deducted from load and displacement measurements gives limited information on the influence of transverse loading as lateral force was only applied in loading direction. However, the secant stiffness at the beginning of a cyclic loading phase can be compared to the secant stiffness at the end of a preceding phase with the same loading direction. The following Figure 6-45 shows the secant stiffnesses of all tests over all phases, divided into loading directions of 0° (top) and 90° (bottom). The loading secant stiffness is used and the first 'irregular' cycle of each phase is not shown as its behaviour differs significantly from the further cycles (cf. Figure 6-31 in Section 6.4.3). For each phase, cycle counts are scaled logarithmically.

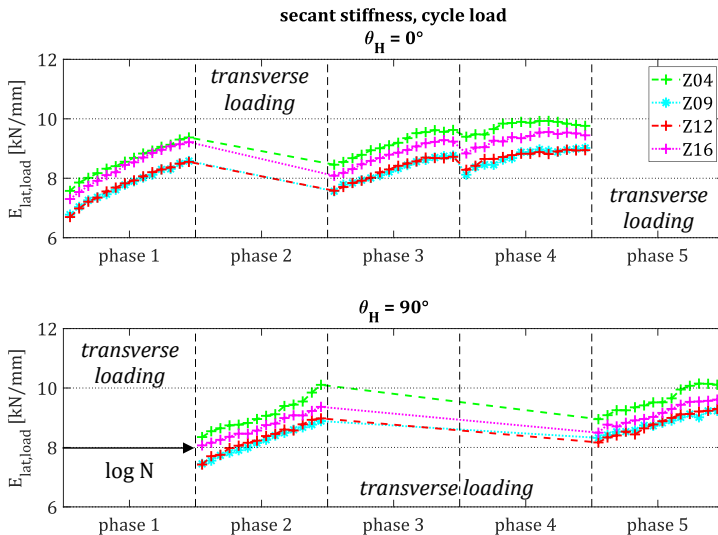


Figure 6-45: Loading cycle secant stiffnesses of all tests over all phases for 0° (top) and 90° (bottom) loading direction

The influence of transverse loading in direction of $\theta_H = 90^\circ$ on pile head secant stiffness in direction of 0° becomes visible between phases 1 and 3. The secant stiffness in the direction of 0° decreases from the end of phase 1 to the beginning of phase 3 (top diagram) while the secant stiffness in the direction of 90° (bottom diagram) steadily increases during phase 2. A contrary development can be seen during phases 3 and 4.

Better insight into that phenomenon can be gained from the pile's bending mode eigenfrequency which was determined before and after each cyclic loading phase in two directions ($0^\circ, 90^\circ$; in and transverse to lateral loading) by default. Figure 6-46 shows the pile's bending mode eigenfrequency measured in the direction of 90° after each loading phase for selected tests. Values were normalised by the corresponding value after pile installation and before the first loading phase ($N=0$).

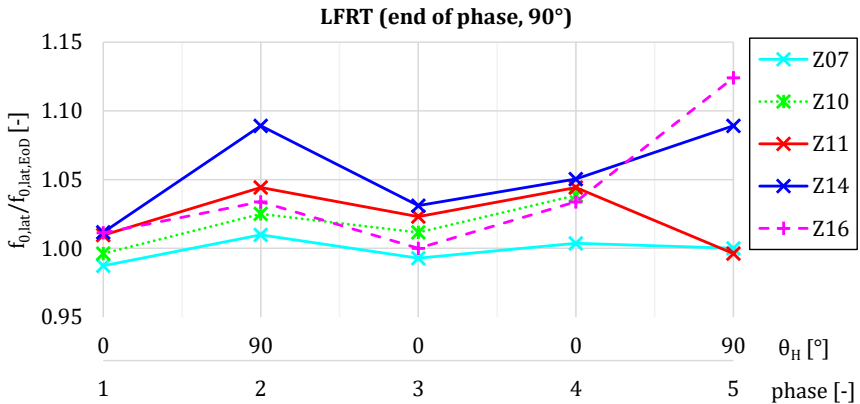


Figure 6-46: Development of pile's bending mode eigenfrequency over loading phases measured in direction of 90°

The first loading phase 1 (loading direction 0°) has limited influence on the pile eigenfrequency in transverse direction (90°) as $f_{0,lat}/f_{0,lat,N=0} \approx 1$ with some eigenfrequencies lying above and others below the value before cyclic loading. Due to cyclic loading in phase 2 (90°), eigenfrequency in loading direction increases and decreases again due to transverse loading in subsequent phase 3. In phase 4 (loading direction still 0° and transverse to shown eigenfrequency measurements) the eigenfrequency increases again. For phase 5 (loading direction and eigenfrequency measurement aligned in 90°) most of the tests (except for Z11)

show a further increase of the pile's bending mode eigenfrequency. Similar courses can be seen for all tests and opposite trends for measurements taken in 0°. Related figures grouped by installation method and measurement direction are given in Appendix F.

A close look on the development of the dynamic stiffness is possible for tests Z07, Z10 and Z15. As mentioned before, the pile's dynamic stiffness was assessed after N = 1; 10; 100; 1,000 and 12,000 cycles during these tests (cf. Figure 6-34). Figure 6-47 shows the development of the measured eigenfrequency in (top) and transverse to loading direction (bottom) for different test phases. All measurements were normalised by measured eigenfrequency before start of the corresponding phase (N = 0).

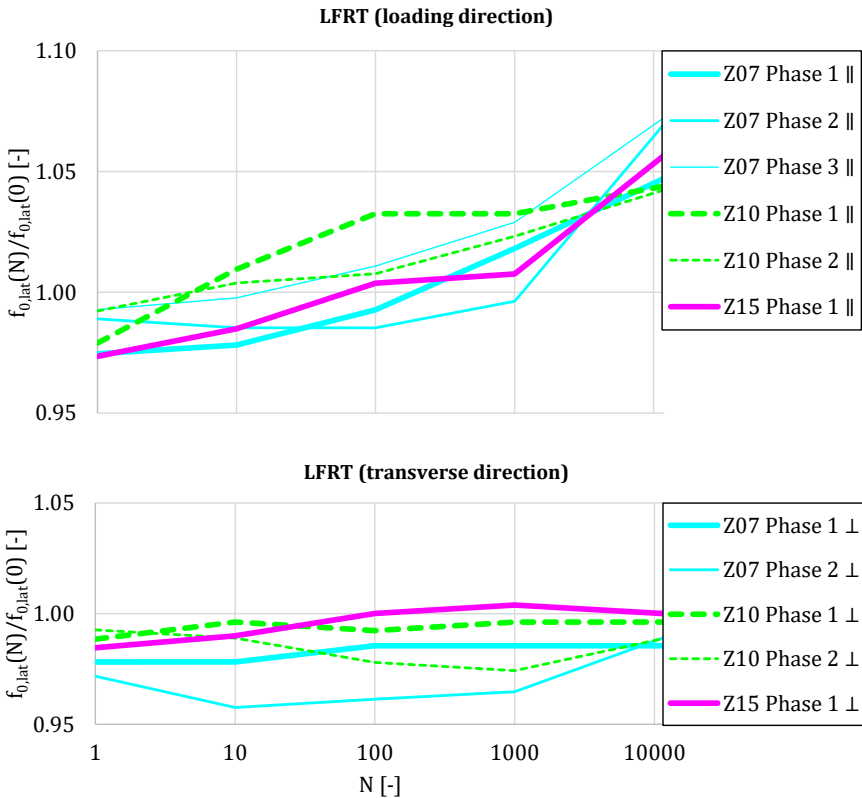


Figure 6-47: Development of pile's bending mode eigenfrequency during cyclic loading in loading direction (top) and in transverse direction (bottom)

In loading direction, the eigenfrequency decreases during the first cycle(s) ($f_{0,lat}(N)/f_{0,lat}(N) < 1$) and then increases. In transverse direction, the eigenfrequency also decreases during the first cycle(s) but then stays more or less constant (in contrast to the behaviour in loading direction).

It is remarkable that the decrease of the pile's eigenfrequency transverse to the loading direction can also be observed at the 'undisturbed' system in phase 1. Together with the following constant course, this indicates that the development of the pile's eigenfrequency transverse to loading direction may not be linked to the back-accumulation. During phase 2 of tests Z07 and Z10 (thin lines), no steady decrease of the eigenfrequency over number of cycles can be witnessed as might be expected in analogy to the back-accumulation behaviour. The dynamic stiffness seems to be 'reset' by the monotonic loading of the first, 'irregular' cycle.

6.5.2 Soil reaction due to changing loading direction

Regarding the possible implications of increased soil stresses near the pile on lateral pile behaviour, it is of great interest whether these imprinted stresses remain due to multiple phases of cyclic lateral loading from changing directions. To address this question, soil stresses measured before (pre) and after (post) each loading phase were analysed. Figure 6-48 shows measured effective radial stresses σ'_{rad} over depth z in the main loading direction $\theta = 0^\circ$ (right) and in opposite direction 180° (left). Different colours denote different phases where blueish lines indicate the main loading direction of $\theta_H = 0^\circ$ (aligned with the soil stresses in focus) while reddish lines signify the minor loading direction $\theta_H = 90^\circ$. Dashed lines show radial stresses before cyclic loading in the corresponding phase (pre) whereas solid lines indicate the stress state at the end of the phase (post). For instance, the dashed blue line (phase 1, pre) specifies the soil stresses before cyclic loading. The black dotted line gives the theoretical overburden stress $\gamma \cdot z$ for orientation. Tests Z03 (impact driven) and Z12 (crane-guided vibratory driven) were chosen as exemplary cases because they show a very different stress state after pile driving due to the installation effects described in Section 6.2.

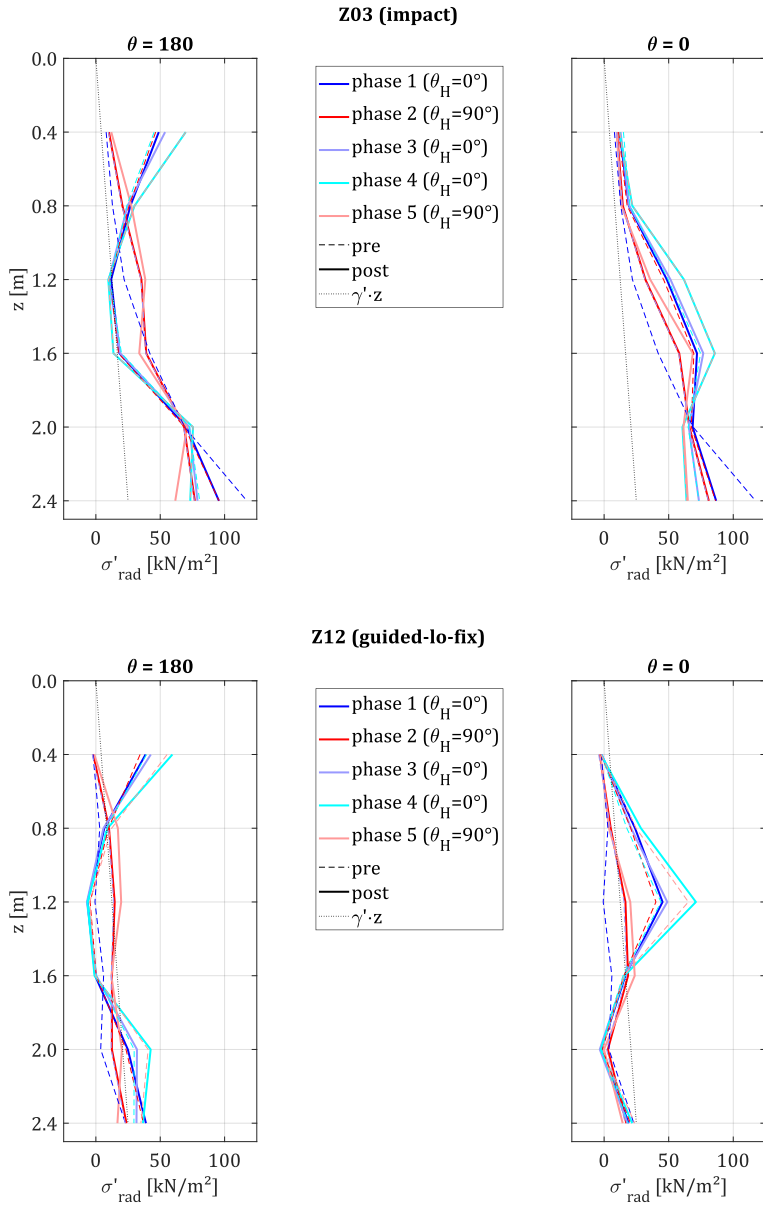


Figure 6-48: Soil stress developments due to changing loading directions

The course of the soil stresses at the beginning of one phase is almost identical to that at the end of the preceding phase in all cases (e.g. red dashed line and blue solid line). This was expected since there is no serious action on the pile between the loading phases. Execution of the lateral frequency response test (LFRT, cf. Section 5.7.7) including manual detachment and attachment of the loading mechanism and dynamic excitation with the impact hammer obviously did not have a severe impact on the soil's stress state. It is also remarkable that the radial soil stresses measured after phases 1 and 3 (solid blue and light blue lines) are almost identical. The same applies for phases 2 and 5 (solid red and light red lines).

Looking at the blueish solid lines (post cyclic loading in direction of $\theta_H = 0^\circ$) reveals an increase of soil stresses on the load-facing side ($\theta = 0^\circ$, right) in a depth of about $z = 0.8$ m to 1.8 m and a decrease on the opposite side. At the uppermost sensor level ($z = 0.4$ m) a severe increase of soil stresses in the unloading direction can be witnessed, as discussed in Section 6.4.3. These changes in soil stresses are more or less erased or at least diminished due to transverse loading, as can be seen by the solid reddish lines (post cyclic loading in direction of $\theta_H = 90^\circ$). The described behaviour applies for both tests shown in Figure 6-48 (Z03 and Z12) and all other tests (see Appendix F).

Near the pile toe, a certain decrease of soil stresses can be observed in the direction of $\theta = 0^\circ$ where the soil is unloaded by the toe kick (cf. Section 6.4.3). Further relaxation occurs during transverse loading but a considerable portion of the imprinted soil stresses due to pile installation effects remains. Impact driven and free vibratory driven piles still show radial stresses in depth of $z \approx 2.0 \dots 2.5$ m ($\sigma'_{rad} \approx 50 \dots 100$ kN/m²) way above the theoretical overburden pressure ($\gamma' \cdot z \approx 20 \dots 25$ kN/m²).

Having in mind the steady back-accumulation of the pile head displacement due to transverse cyclic loading and the more abrupt change of the eigenfrequency due to transverse monotonic loading, the question arises when the recovery of soil stresses takes place. Therefore, soil stress profiles in upwind and downwind direction of the preceding test phase are evaluated. The following Figure 6-49 shows the effective radial soil stresses measured during the first cycle of phase 5 of test Z04 in upwind and downwind direction of the preceding phase 4 and the corresponding resultant (= downwind – upwind). Soil stress profiles are plotted for load levels of $H = 1; 7$ and 14 kN (with increasing darkness) for loading period (solid lines) and unloading period (dashed lines) of the first cycle.

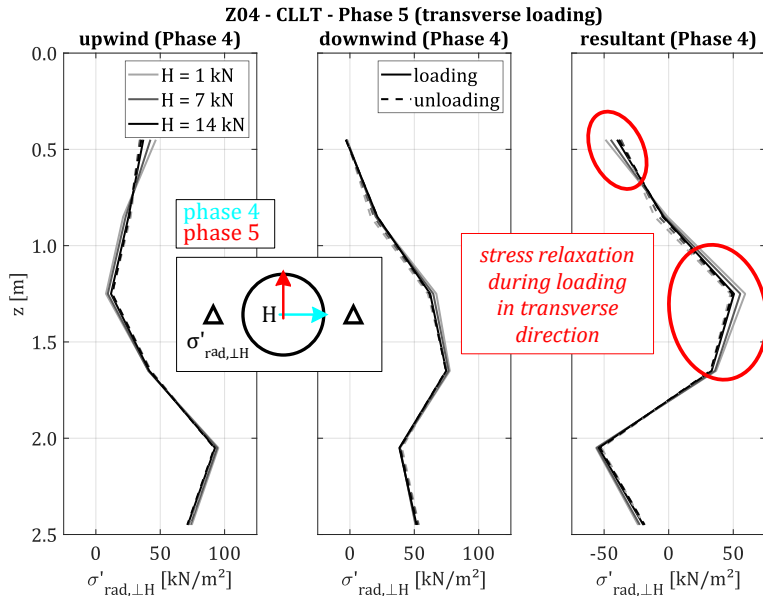
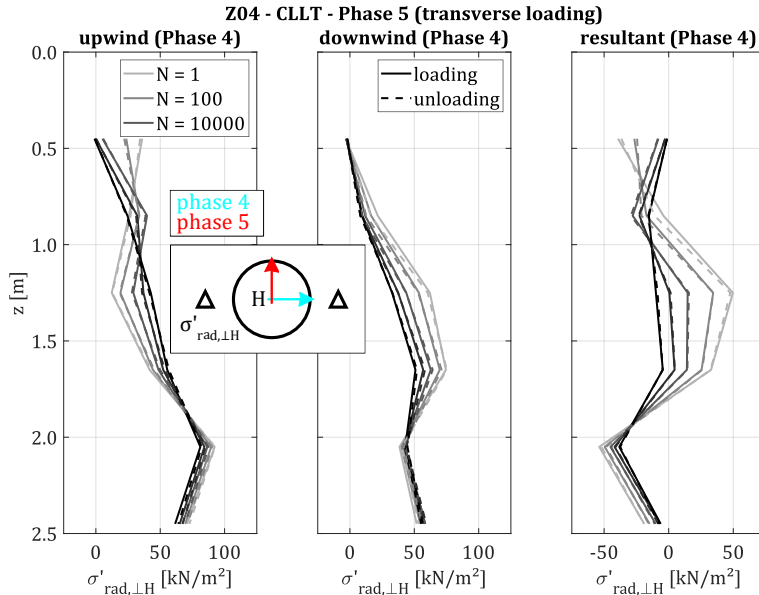


Figure 6-49: Soil stress development during first loading and unloading cycle in loading direction of preceding test phase

Only marginal changes in the soil stress profiles due to the first cycle in transverse direction to the stress measurements can be seen. Some decrease of the stress resultant in shallow and intermediate depth is visible, occurring mainly during loading period.

In analogy to the soil stress development during the first cycle shown above, Figure 6-50 shows the effective radial soil stresses measured during cyclic loading of phase 5 of test Z04 in upwind and downwind direction of the preceding phase 4 and the corresponding resultant. Soil stress profiles are plotted for cycles $N = 1; 10; 100; 1,000$ and $10,000$ (with increasing darkness) for maximum (solid lines) and minimum load level (dashed lines).

Soil stress relaxations can be observed at shallow depth in upwind direction of the preceding test phase and at intermediate depth in downwind direction of the preceding phase. Stresses grow at intermediate depth in upwind direction. Stress redistribution proceeds steadily over cyclic loading but the rate (with logarithm of cycle count; indicated by the distance between the stress profiles) decreases with the logarithm of cycles.



**Figure 6-50: Soil stress development during cyclic loading
in loading direction of preceding test phase**

To give a deeper insight into the effect of transverse loading, soil stresses in different depths are plotted over transverse displacement cycles in analogy to Figure 6-37. Exemplary, data of phase 2 of the cyclic lateral load test of pile Z09 is shown in Figure 6-51. Soil stresses were analysed in direction of loading of the preceding phase 1, thus the soil elements looked at are subject to shearing during the loading phase in focus. The changes of radial effective stresses $\Delta\sigma'_{rad}$ are taken with respect to the initial values before the start of phase 1 (after pile installation). Consequently, the recovery of imprinted soil stresses (cf. Section 6.4.4) of a pre-loaded system is inspected here. The changes of soil stresses $\Delta\sigma'_{rad}$ are divided by the overburden pressure $\gamma \cdot z$ at different sensors locations. The pile head deflection u_{90° (again not local pile deflection at sensor level!) used in the below diagrams is the displacement in direction of loading during phase 2 and therefore transverse to the location and orientation of the considered stress transducers in the soil. The start (\triangleright) and end (\triangleleft) of the cycles is labelled by markers.

Z09 - CLLT - phase 2 ($\theta_H = 90^\circ$)

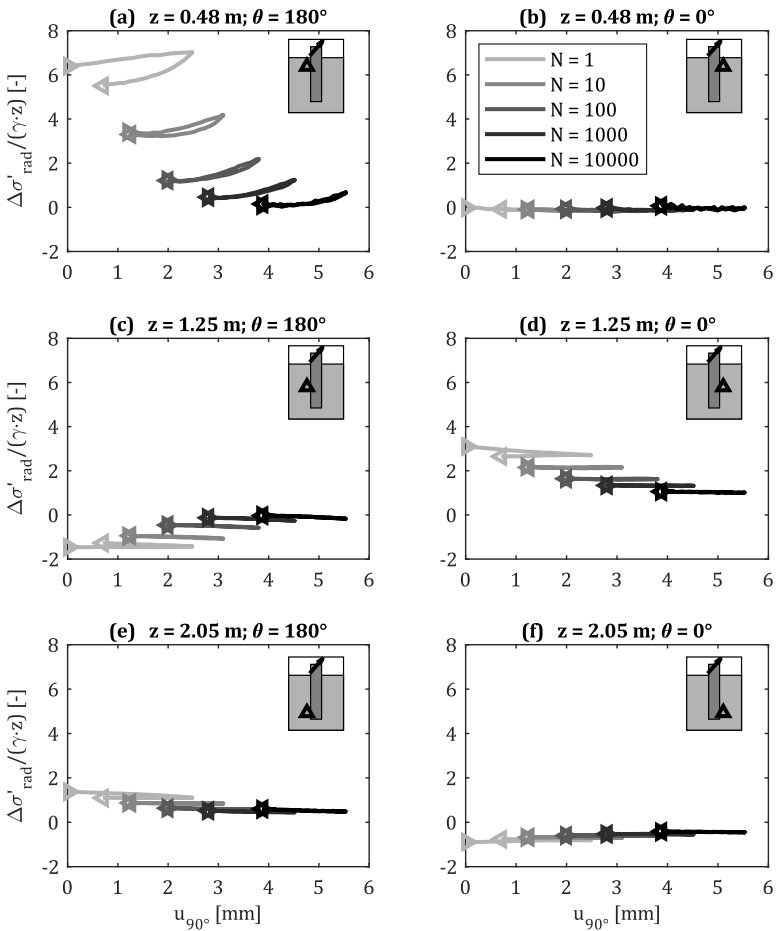


Figure 6-51: Recovery of soil stresses over transverse displacement cycles

Especially in upwind direction of the preceding phase at shallow depth (a) and at intermediate depth (c, d), a severe recovery of radial soil stresses towards the initial values ($\Delta\sigma'_{rad} \rightarrow 0$) can be observed. These are the regions with highest changes of soil stresses during phase 1 (see

Figure 6-48). In contrast to phase 1 (see Figure 6-37), also in intermediate and deep depths ratcheting can be witnessed.

6.5.3 Interim summary and discussion on the influence of changing loading direction

Cyclic lateral loading in transverse direction to preceding phases of cyclic lateral loading leads to notable recovery in the range of about 40% of preceding displacement accumulation. This back-accumulation occurs steadily during cyclic loading and can be described by same mathematical formulation as accumulation and with the same soil constants C_{N2} and C_{N3} from the HCA model. As mentioned in Section 2.3.7, the different concepts of 'multidirectional' loading given in the literature make it difficult to compare different studies. Regarding the loading scenario with unidirectional loading packages from changing directions, the model tests presented in this thesis are comparable only to the experiments carried out by (PERALTA 2010) for the first two loading packages. In contrast to the strong back-accumulation due to transverse loading witnessed in this research (see Figure 6-41), (PERALTA 2010) did not mention this effect even though her results show marginal amounts of back-accumulation (see Figure 2-22). Studies on other types of multidirectional loading (fan-shape, T-shape, L-shape; see Figure 2-21) have shown higher or at least similar total pile head displacements compared to unidirectional loading.

Pile head secant stiffness and dynamic system stiffness decrease due to transverse loading. Based on eigenfrequency measurements, this seems to be an effect of the first, 'irregular' cycle in transverse direction. Thus, this behaviour may not be linked to back-accumulation.

The redistribution of soil stresses (from intermediate depth in upwind direction towards intermediate depth in downwind direction and shallow depth in upwind direction) which has taken place during preceding phases of cyclic lateral loading is partly reverted during cyclic lateral loading in transverse direction. Stress redistributions occur steadily during cyclic loading and thus are probably linked to the back-accumulation phenomenon. The imprinted soil stresses near the pile toe due to pile installation remain during/after several phases of cyclic lateral loading from changing directions.

Soil mechanical interpretation of phenomena during cyclic loading from alternating directions

Lateral bedding resistance of a tubular pile comprises of additional radial compressive stresses acting predominantly from the load-opposing direction and shearing stresses acting predominantly on the transverse flanks of the pile, as sketched in Figure 6-52.

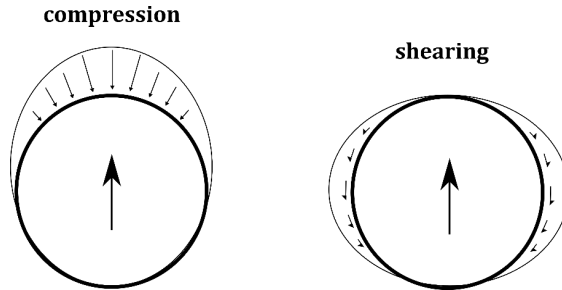


Figure 6-52: Schematic bedding resistance distribution around circumference of tubular piles

Note that due to the 'toe kick', the compressed zone is on the opposite side below the rotation point (cf. Figure 2-13).

Due to cyclic lateral loading from one direction, the soil in the compressed zone is densified while the soil on the opposite side is loosened (Figure 6-52, left). During subsequent transverse loading, the zones addressed above are subject to shearing. The soil in the densified zone behaves dilatant, leading to an increase of volume while the soil in the loosened zone reacts contracting, leading to a reduction of volume (Figure 6-52, right).

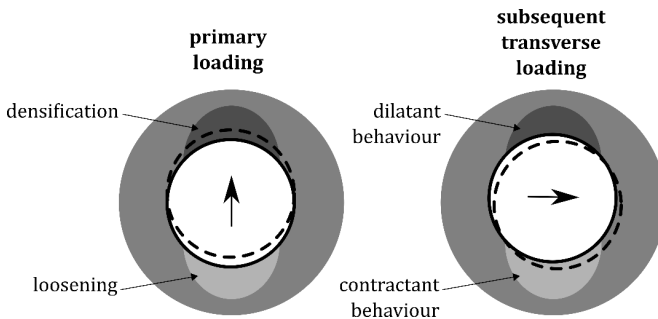


Figure 6-53: Schematic soil reaction due to primary (left) and subsequent transverse (right) loading (horizontal section)

The volume changes on opposing sides and in different depths lead to a back-rotation of the pile (Figure 6-54, right) which result in the observed back-accumulation of pile head displacements.

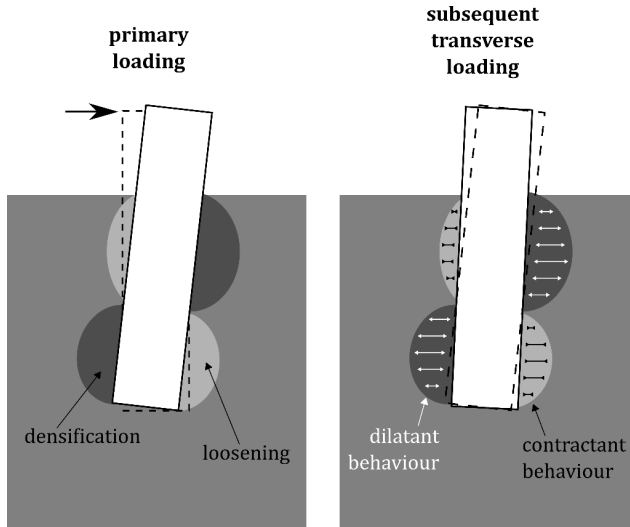


Figure 6-54: Soil reaction due to primary (left) and subsequent transverse (right) loading (cross section)

The unlike cyclic behaviour of dynamic stiffness and back-accumulation can be explained by the concepts of 'polarisation' (cf. Figure 2-17) and 'accumulation' (cf. Figure 2-15), which are described in Section 2.3.7. In case of a laterally loaded pile, the surrounding soil has a certain loading history from the pile installation process (mainly shearing) but can be considered unpolarised regarding compression. Due to cyclic lateral loading, the soil in the dark shaded areas of Figure 6-54 (left) is polarised. With each loading cycle, a certain amount of displacement is accumulated and the soil reacts stiffer (cf. Section 6.4). From the distinction between the first 'irregular' and the following 'regular' cycles (cf. Figure 6-31) it can be concluded that a large portion of polarisation occurs during the first loading cycle.

During the first cycle of subsequent transverse loading, the previously compressed soil is subject to shearing and the polarisation of the soil changes rapidly. This leads to an immediate softening of the system in the primary loading direction which is manifested in the decrease of the system's eigenfrequency (Figure 6-47, bottom). During the following cycles, the further

polarisation of the soil is only marginal. However, the cyclic shearing of the soil leads to continues accumulation of volumetric strain: In the formerly compressed zones, the soil dilates (Figure 6-54, left, dark shaded areas) while in the formerly relieved zones, the soil contracts (light shaded areas). This is expressed by the back-accumulation of the pile head displacement due to cyclic loading in transverse direction (Figure 6-42, bottom graphs).

Chapter 7 Numerical simulations of the lateral pile behaviour using a one-dimensional bedded beam model

7.1 Overview

In this chapter, numerical simulations of the static and dynamic pile behaviour are shown. Therefore, a simple one-dimensional bedded beam model, also known as Winkler method, is used. This simple approach cannot wholly represent the complex spatial soil behaviour witnessed in the model tests. It was chosen as it is the common approach to calculate lateral pile behaviour in offshore practice (probably due to its simplicity), so a lot of experience exists. Modifications of the method have been developed to account for topics such as hysteretic behaviour (HOULSBY et al. 2017), pile base resistance (FU et al. 2020), cyclic lateral behaviour (TRIANTAFYLIDIS & CHRISOPOULOS 2016), and multi-directional loading (LOVERA et al. 2021).

For the static pile behaviour (Section 7.2), non-linear springs (p-y curves) describe the pile-soil interaction. For the dynamic behaviour (Section 7.3), linear soil stiffness and viscous soil damping are considered. The influence of the installation induced soil stresses on the static and dynamic pile behaviour witnessed in the scale model tests shall be reproduced by applying appropriate soil springs. These soil springs will then be used to investigate installation effects on a large scale monopile foundation.

7.2 Static lateral pile behaviour

7.2.1 Numerical model for static calculations

To calculate the static lateral pile-soil behaviour, the pile-soil system is transformed to the one-dimensional mechanical system shown in Figure 7-1. This system can be mathematical formulated by Equation (2-17) which is repeated here:

$$\mathbf{P} = \mathbf{K} \cdot \mathbf{y} = (\mathbf{K}_{\text{pile}} + \mathbf{K}_{\text{soil}}) \cdot \mathbf{y} \quad (7-1)$$

The load vector \mathbf{P} consists of the horizontal load H and the moment load M applied at mudline level. The stiffness matrix \mathbf{K} is composed of pile and soil stiffness. The pile is modelled as a Bernoulli beam with linear-elastic material behaviour. Soil bedding is described by non-linear p-y curves. Therefore, Equation (7-1) has to be solved iteratively. The bedding stiffness $E_{p,y,sec}$ at each node is updated based on the local pile deflection y and the corresponding mobilised

bedding resistance p of the previous iteration step. As a first estimate, the initial bedding stiffness $E_{py,ini}$ is used.

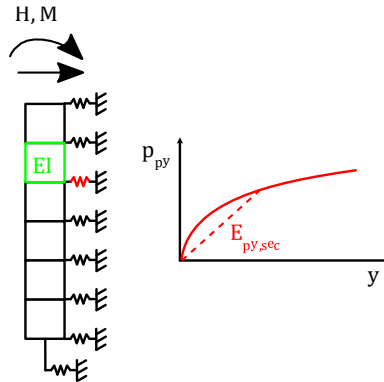


Figure 7-1: 1D static pile-soil model

The mathematical problem is established and solved in Matlab (MathWorks 2020) and consists of 100 elements. Further information on the numerical model can be found in Appendix H.

7.2.2 Modifications on p-y approach based on offshore guidelines

Static p-y curves according to offshore guidelines (API RP 2GEO) with a hyperbolic formulation according to MURCHISON & O'NEILL (1984) (see Equations (2-21) ff.) and an adjustment of the initial stiffness $E_{py,ini}$ as proposed by KALLEHAVE et al. (2012) to account for non-linear relation between soil stiffness and depth (see Equation (2-27)) were used as basis for the calculations. Further modifications were implemented to account for higher soil stiffness at small strain level, additional lateral soil resistance at the pile toe, and increased stress level due to pile installation.

Small strain stiffness

Based on the p-y formulation of KALLEHAVE et al. (2012), the initial bedding stiffness is calculated based on the soil friction angle and depth. The effect of the pile diameter on the strain level and therefore the bedding stiffness (Equation (2-30)) was not considered as the effect of the strain level will be included in the small strain stiffness. Equation (2-29) according to KIRSCH et al. (2014) is used to calculate the relation between static and dynamic oedometric soil stiffness.

The reduction of the soil secant stiffness over strain is depicted in Figure 2-14 and can be described by

$$p_{py}(y < y_{small}) = E_{py,dyn} \cdot \frac{1}{1 + \epsilon_{av}^{0.7} \cdot 10^3} \cdot y \quad (7-2)$$

The average strain level ϵ_{av} is calculated over 2.5 pile diameters (KALLEHAVE et al. 2012; KIRSCH et al. 2014):

$$\epsilon_{av} = \frac{y}{2.5 \cdot D_{pile}} \quad (7-3)$$

To calculate the pile bedding stiffness from the oedometric soil stiffness and vice versa, Equation (2-19) according to TERZAGHI (1955) is used. The flow chart in Figure 7-2 shows the schematic sequence and parameters for the construction of the p-y curves.

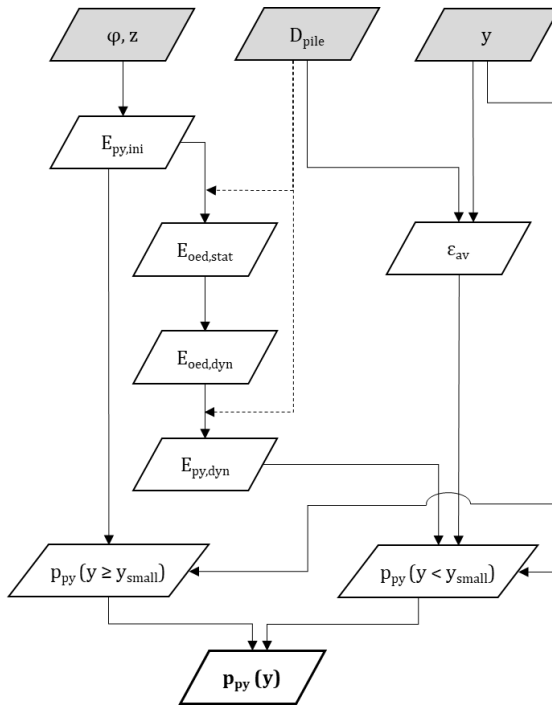


Figure 7-2: Flowchart for the construction of p-y curves with small strain stiffness

The pile displacement y_{small} is defined by the load level at which the tangent stiffness of the dynamic p-y curve according to Equation (7-2) and the tangent stiffness of the static p-y curve according to KALLEHAVE et al. (2012) are equal. For higher bedding resistances, the p-y curves according to KALLEHAVE et al. (2012) are used and 'shifted' parallel to the displacement coordinate y towards y_{small} . The top diagram of Figure 7-3 shows the original p-y curves according to KALLEHAVE et al. (2012) (black) and the modified p-y curves with consideration of the small strain stiffness (red). In the lower diagram, the bedding stiffness E_{py} is plotted over the average strain level ϵ_{av} . Both curves are established for the conditions in the model tests at a depth of $z = 1$ m.

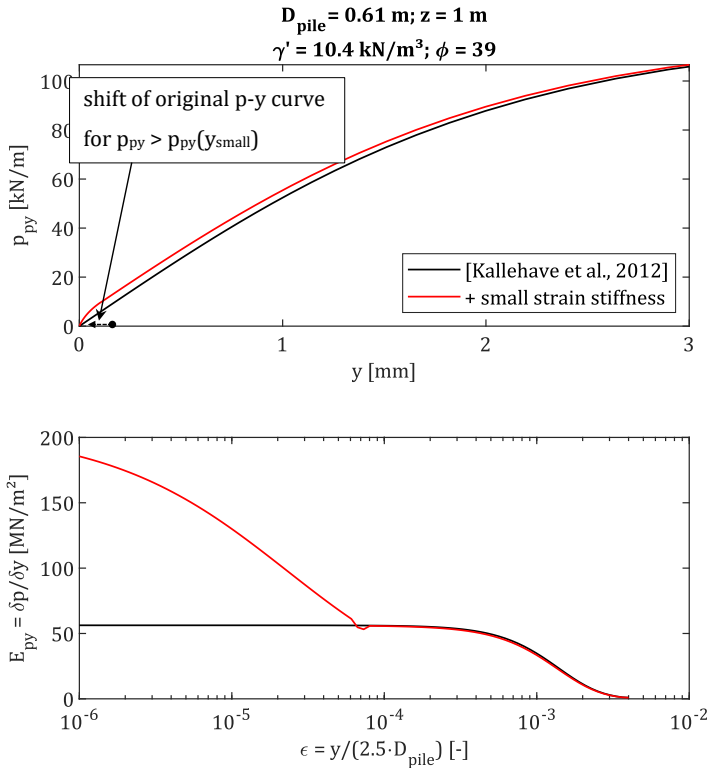


Figure 7-3: Exemplary p-y curves (top) according to (KALLEHAVE et al. 2012) (black) and modified curves with consideration of small strain stiffness (red) and corresponding bedding stiffness (bottom)

The small strain stiffness is effective for average strain levels $\varepsilon < 10^{-4}$ and, in this case, leads to a higher bedding stiffness for small pile displacements of $y \ll 0.1$ mm.

Pile installation effect

The p-y formulation according to KALLEHAVE et al. (2012) already includes an under-linear relation between initial bedding stiffness and depth (see Equation (2-27)) which can also be interpreted as an interrelation between bedding stiffness and stress state. This requires a linear increase of stress level (overburden pressure or earth pressure at rest) with depth, thus a constant soil unit weight.

The installation-induced, increased radial soil stresses due to impact pile driving and certain variants of vibratory pile driving (see Section 6.2) can be considered by a slight modification of the depth-term in the p-y approach by KALLEHAVE et al. (2012). As shown in Equations (7-4) and (7-5), the initial stiffness $E_{py,ini}$ [kN/m²] depends on an equivalent depth z_{eq} [m] which is defined by the lateral stress σ'_{rad} [kN/m²].

$$E_{py,ini} = m_h \cdot z_{ref} \cdot \left(\frac{z_{eq}}{z_{ref}} \right)^{\lambda_z} \quad (7-4)$$

$$z_{eq} = \sigma'_{rad}(z) / \gamma' \quad (7-5)$$

The lateral stress can be assessed by the approaches of FISCHER (2021) or ALM & HAMRE (2002) (see Section 2.2.2). This leads to an increased initial bedding stiffness near the pile toe. If $z_{eq} = z$ is used, (7-4) describes the p-y approach according to KALLEHAVE et al. (2012) without any installation effects.

Additional lateral resistance at the pile toe

As mentioned in Section 2.3.4, additional lateral pile resistance is mobilised at the pile toe of rigid piles. This can be expected for offshore monopiles and for the model piles. To account for this, an additional base shear spring is added to the lowermost pile element. The proposed base shear formulation corresponds to a shear box test. Figure 7-4 shows results of shear box tests (cf. Section 5.4.3), executed with a relative density of $D_r = 0.75$ at three different constant normal load (CNL) levels:

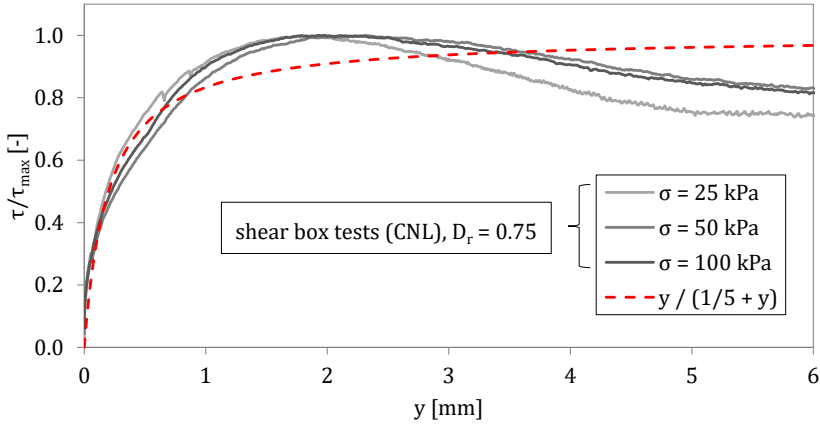


Figure 7-4: Relative shear resistance over shear displacement

The displacement dependent shear resistance is normalised by its ultimate value $\tau_{\max} = \sigma'_v \cdot \tan \varphi'$. The course of the normalised shear stress over shear displacement can be approximated by a hyperbolical relation, even though the peak and residual strength of dense sand cannot be reproduced:

$$\tau/\tau_{\max} = \frac{y \text{ [mm]}}{\frac{1}{5} + y \text{ [mm]}} \quad (7-6)$$

Based on Equation (7-6), the displacement-dependent base shear resistance $Q_{\text{base}}(y)$ [kN] is described by

$$Q_{\text{base}}(y) = \frac{y \cdot 1000}{\frac{1}{E_{\text{base,ini}}} + \frac{y \cdot 1000}{Q_{\text{base,ult}}}} \quad (7-7)$$

Good agreement with the direct shear tests could be achieved by setting the initial stiffness of the shear spring $E_{\text{base,ini}}$ [kN/m] to five times the ultimate shear resistance $Q_{\text{base,ult}}$ [kN]:

$$E_{\text{base,ini}} \text{ [kN/m]} = 5 \cdot Q_{\text{base,ult}} \text{ [kN]} \quad (7-8)$$

The ultimate shear resistance is derived from the vertical soil stress σ'_v , and the soil friction angle φ' . To convert Q_{base} to force dimension, the cross section of the pile base $\pi \cdot D_{\text{pile}}^2/4$ is taken:

$$Q_{\text{base,ult}} = \pi \cdot \frac{D_{\text{pile}}^2}{4} \cdot \sigma'_v \cdot \tan(\varphi') \quad (7-9)$$

For the sake of simplicity and consistency, $\sigma'_v = \sigma'_{\text{rad}}$ is assumed in case of increased soil stresses due to pile installation effects, as measured by FISCHER (2021). Otherwise, the overburden stress can be taken.

Sensitivity of the p-y approach to soil friction angle

The ultimate bedding resistance $p_{\text{py,ult}}$ and the initial stiffness of the p-y curves $E_{\text{py,ini}}$ are both functions of the internal friction angle of the soil φ' . According to API RP 2GEO, φ' may be determined by drained triaxial tests or shear box tests. As the resulting soil friction angles from the two laboratory tests at a given stress level and soil density differ by about 3° (cf. Figure 5-6), p-y calculations of the model tests were carried out with $\varphi' = 36^\circ$ (shear box tests) and $\varphi' = 39^\circ$ (triaxial tests) to check the sensitivity of the method. The p-y approach of MURCHISON & O'NEILL (1984) with the modification of KALLEHAVE et al. (2012) was used; small strain stiffness, pile installation effects and additional pile toe resistance were not considered.

The following Figure 7-5 shows the resulting pile head displacement u over the lateral load H as applied in the model tests. The mean course of the measurements of the free vibratory driven piles (cyan) is plotted for orientation.

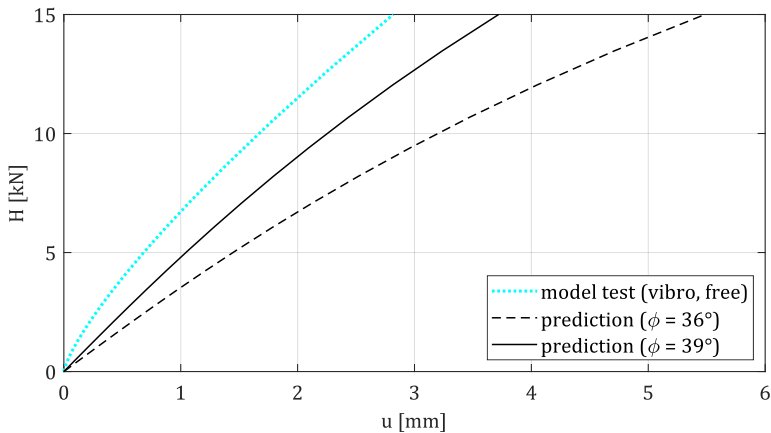


Figure 7-5: Simulated (black) and measured (cyan) load-displacement behaviour of model pile

The simulation of the lateral load-bearing behaviour shows a high sensitivity to the soil friction angle: A decrease of $\Delta\varphi' = -3^\circ$ leads to an increase of pile head displacement of over 45% at maximum load level. In case of an offshore monopile, the sensitivity is somewhat lower but still leads an increase of pile head displacement by about 25% (see Figure H-4 in Appendix H). The lateral stiffness measured during the model tests is severely underestimated, especially at small load level. This agrees with the concept of small strain stiffness which is not included in the p-y curves used here (MURCHISON & O'NEILL 1984; KALLEHAVE et al. 2012).

7.2.3 Static calculation of scale model tests

To calculate the lateral behaviour of the model piles under quasi-static loading, the p-y curves according to MURCHISON & O'NEILL (1984) and KALLEHAVE et al. (2012) with the modifications described above and the following parameters are used:

- initial soil stiffness according to Equations (2-22) and (2-23) with buoyant unit weight of $\gamma' = 10.4 \text{ kN/m}^3$ and a soil friction angle of $\varphi' = 39^\circ$
- increased bedding stiffness at small average strain according to Equations (2-29) and (7-2)
- base shear spring according to Equation (7-7) at the lowermost pile element
- variant with increased stress state due to pile installation described by Equation (2-37) with parameters $1/\beta_{\text{PSS}} = 5$ and $\alpha = -1.6$

The predicted pile head behaviour is plotted in Figure 7-6, together with fitted results of the scale model tests. The top diagram shows the load-displacement curve at measurement level (0.6 m above mudline), the bottom diagram shows the corresponding pile head stiffness. The black dashed lines depict the predicted pile head behaviour without installation effect while the solid lines show the pile head behaviour with consideration of increased soil stresses. The coloured lines show the mean courses of impact driven (green) and crane-guided vibratory driven piles (red; cf. Table 6-3).

The prediction considering installation effects (black solid line) shows very good agreement with the measured pile head behaviour of the impact drive piles (green). The prediction without consideration of installation effects (black dashed line) shows reasonable agreement with the measured pile head displacement of the crane-guided vibratory driven piles. Here, the pile head

stiffness is slightly underestimated, resulting in an overestimation of the pile head displacement.

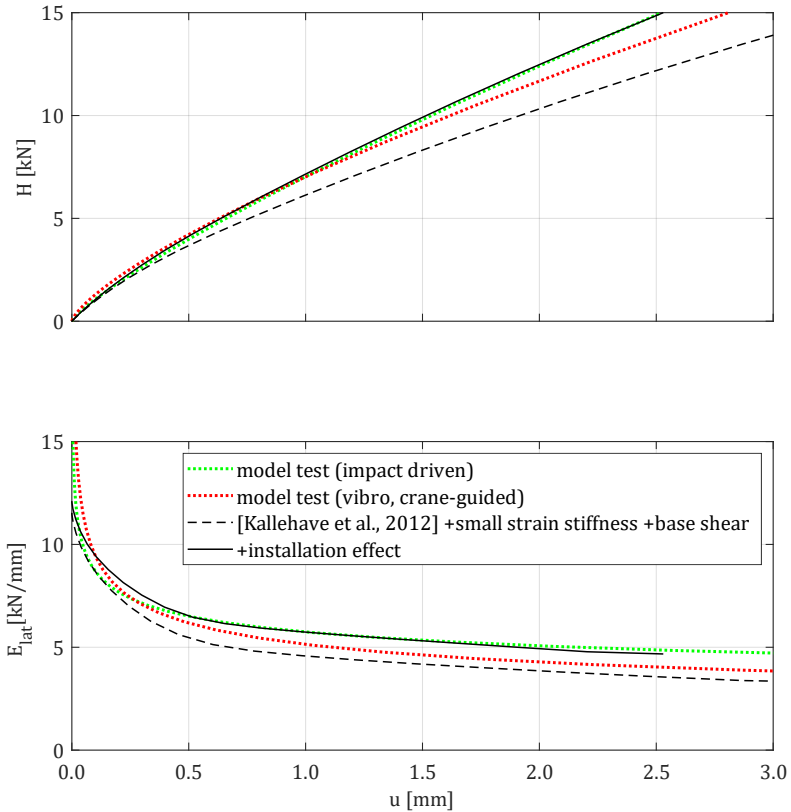


Figure 7-6: Predicted (black) and measured (coloured) pile head behaviour of model pile

Figure 7-7 shows the predicted pile behaviour over depth, namely bending $y(z)$ line, mobilised soil resistance $p_{py}(z)$, and the underlying soil stress profile $\sigma'_{rad}(z)$. The mobilised resistance of the base shear spring is divided by the element length and added to the lateral resistance acting on the lowermost pile element, resulting in increased soil resistance at that element.

The variant with increased stress state (solid lines) shows considerably smaller deflections, especially at the pile toe. Despite the small displacements below the point of rotation, higher bedding stiffness allows for the mobilisation of considerable bedding resistance.

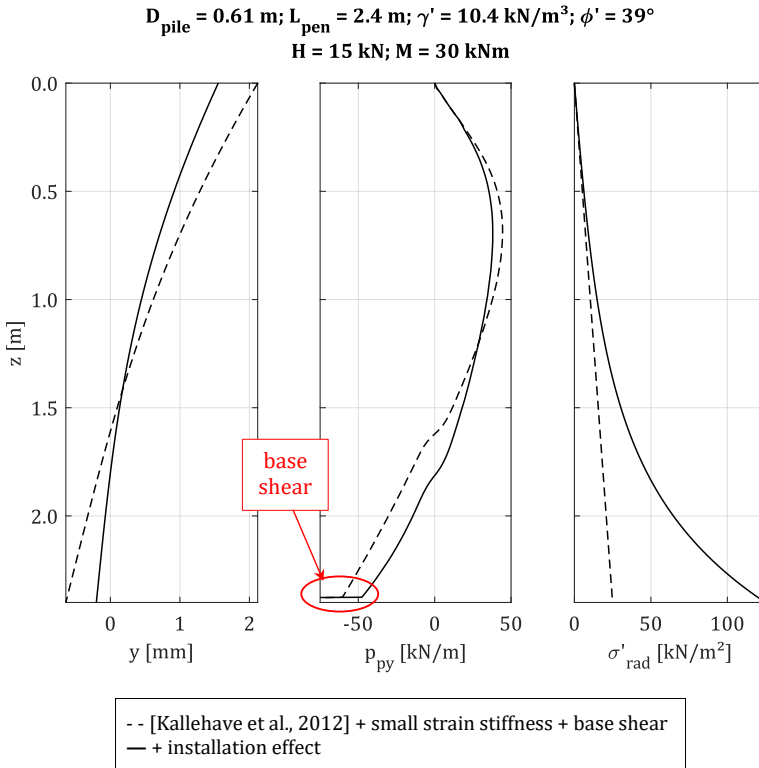


Figure 7-7: Predicted pile behaviour over depth

7.2.4 Static calculations on offshore monopile foundations

To assess the influence of pile installation effects on offshore monopile foundations, predictions with the p-y formulation described in Section 7.2.2 are carried out for the generic monopile foundation described in Section 4.1 ($D_{\text{pile}} = 7.8 \text{ m}; L_{\text{pen}} = 31 \text{ m}; H = 10 \text{ MN}; M = 400 \text{ MNm}$). The soil parameters are assumed to be similar to the model tests ($\gamma' = 11 \text{ kN/m}^3; \phi' = 39^\circ$), which is typical for the German North Sea. The increased soil stiffness at small strain level is not used here as the effect of small strain stiffness is limited for the given pile dimension and stress level.

Instead, the increased initial p-y stiffness for large pile diameters to account for the reduced strain level according to Equation (2-30) after KALLEHAVE et al. (2012) is used.

Regarding possible installation effects, the radial stresses over depth are calculated according to Equation (2-37). Two different methods are used to determine the shape parameter α_{pen} :

- The approach of FISCHER (2021) shows good agreement with the scale model tests. A soil density of $D = 1.0$ (very dense) is assumed and Equation (2-9) yields $\alpha_{pen,Fi} = 2.8$.
- The approach of ALM & HAMRE (2002) was validated for offshore conditions by a back-calculation of mostly jacket piles. Here, a CPT value of $q_c \leq 80$ MPa (cf. Figure 4-2) is assumed, leading to a value of $\alpha_{pen,A\&H} \approx 0.2$ (cf. Equation (2-8)) for the relevant depths¹⁰.

Calculations with the parameters outlined above, however, show hardly any influence of the pile installation effect on the lateral pile behaviour. As shown in the top part of Figure 7-8, the bending lines (left) of the three variants with and without increased soil stresses (right) are identical. The mobilised bedding resistances (middle) show little differences below the rotation point. The fact that the pile toe displacement is approximately zero indicates that the utilisation of the system is low.

Therefore, the design of the monopile is 'optimised' to a pile diameter of $D_{pile} = 5$ m. The pile penetration is set to $L_{pen} = 4 \cdot D_{pile} = 20$ m and the wall thickness was calculated according to Equation (4-1). All other parameters including lateral loading remain unchanged. The results of the updated calculations are shown in bottom part of Figure 7-8. The variant without pile installation effect (dotted line) shows the highest deflections, both at the pile head and the pile toe. The variant with the installation effect after FISCHER (2021) shows a considerably lower pile head displacement, even though the increased soil stresses decay rapidly within only about 1 m depth. In case of the installation effect according to the approach of ALM & HAMRE (2002) the decay of the installation induced stresses is much slower. This causes the least pile deflection of all three variants. Even though the pile deflection is very low near the pile toe, the increased bedding stiffness, evoked by the high soil stresses, allows for the mobilisation of high bedding resistance.

¹⁰ The sensitivity of the shape factor according to ALM & HAMRE is actually low, as shown in Figure H-8.

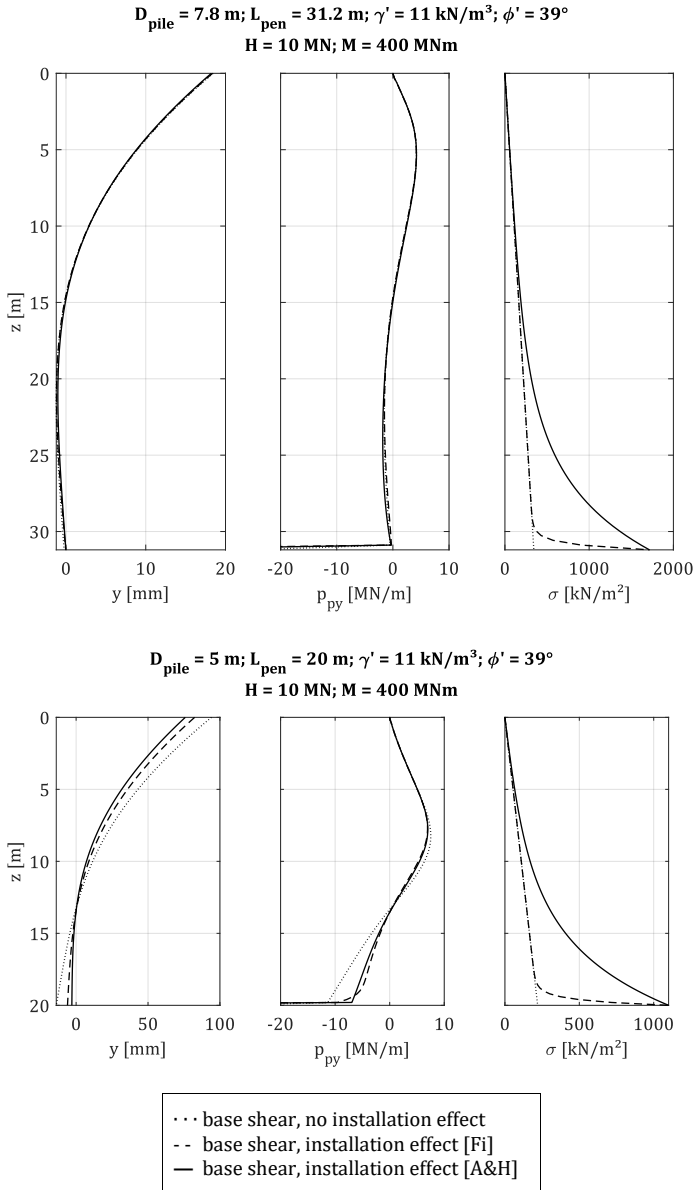


**Figure 7-8: Bending line and stress resultants of generic monopile foundations
 due to lateral loading**

Looking at the integral mobilised bedding resistances of the 5 m pile, especially below the rotation point, the question arises where the difference in 'negative' bedding resistances between the variant without installation effect and the variants with installation effects has gone. The answer lies in the mobilised base shear force, which depends on the vertical stress acting on the shear band (Equation (7-9)). In the implementation of the base shear spring, the vertical stress is assumed to be equal to the (increased) radial stress at pile toe level. This assumption is justifiable because the vertical stresses are also heavily affected by the pile installation, as shown by FISCHER (2021).

The upper part of Table 7-1 shows absolute and relative pile head displacements of the three variants and the mobilised base shear forces $Q_{\text{base,mob}}$ at maximum load level. In this scenario, the pile head displacement is reduced by about 10% to 20%, depending on the approach to assess the installation effect on the soil stress state. Mobilised base shear resistance increases massively when pile installation effects are considered. The lower part of the table shows results of analogous calculations without consideration of lateral resistance at the pile base ($Q_{\text{base,mob}} = 0$; see Figure H-7 in Appendix H). As expected, absolute pile head displacements are somewhat larger. The comparison of the two scenario shows that especially the installation effect after FISCHER (2021) benefits from additional base shearing resistance.

Table 7-1: Pile head displacements and mobilised base shear forces for 5 m monopile

variant	u [mm]	u/max u [-]	$Q_{\text{base,mob}}$ [MN]
<i>with base shear</i>			
no installation effect	94.1	1.00	-3.4
installation effect (FISCHER 2021)	82.4	0.88	-16.9
installation effect (ALM & HAMRE 2002)	75.9	0.81	-16.4
<i>without base shear</i>			
no installation effect	97.3	1.00	0
installation effect (FISCHER 2021)	94.3	0.97	0
installation effect (ALM & HAMRE 2002)	82.3	0.85	0

More extensive results from lateral calculations (stress resultants and pile head behaviour) can be found in Appendix H.

The influence of base shear resistance on lateral pile behaviour can also explain findings by LI et al. (2018) regarding the effect of vertical pile load on lateral pile capacity: Vertical loading evokes pile toe resistance which acts as vertical stress on the shear band at the pile base. Thus, higher shear resistance at the pile base can be mobilised.

7.3 Pile eigenfrequency

7.3.1 Numerical model for dynamic calculations

As shown in STEIN (2020), the measured system dynamics show good agreement with a one-dimensional numerical model with depth-dependent interface stiffness and damping based on the stress-dependent dynamic soil stiffness, as shown in Figure 7-9.

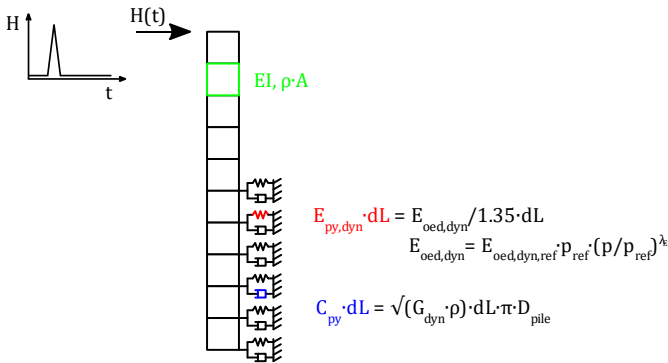


Figure 7-9: 1D dynamic pile-soil model

The mathematical formulation of the pile-soil system was given in Equation (2-20):

$$\mathbf{P}(t) = \mathbf{K} \cdot \mathbf{y}(t) + \mathbf{C} \cdot \dot{\mathbf{y}}(t) + \mathbf{M} \cdot \ddot{\mathbf{y}}(t)$$

K, **C** and **M** are the stiffness, damping and mass matrices of the system. The system matrices are composed of the pile and soil matrices, e.g. $\mathbf{K} = \mathbf{K}_{\text{pile}} + \mathbf{K}_{\text{soil}}$. $\mathbf{y}(t)$ is the deformation vector and $\mathbf{P}(t)$ is the load vector. In case of an excitation with a hammer blow at the top of the TP, only the first entry of the load vector is occupied:

$$\mathbf{P}(t) = \begin{pmatrix} H(t) \\ 0 \\ \vdots \\ 0 \end{pmatrix} \quad (7-10)$$

Pile stiffness and pile mass can be derived from geometry and material properties, pile damping is neglected. For the pile stiffness, a Bernoulli beam is used. For the soil, the stress-dependent dynamic stiffness according to Figure 5-7 is taken to calculate depth-dependent dynamic soil stiffness $E_{py,dyn}$ and soil damping C_{py} (STEIN 2020). An added soil mass can be included as well, e.g. based on the soil density and the soil volume inside the pile.

With an excitation function $H(t)$, the system response can be simulated by means of numerical integration (e.g. Newmark-beta method, NEWMARK 1959). For $H(t)$, the measured excitation of the actual frequency response test or a generic signal (e.g. $1 - \cos(t)$) may be used. The eigenfrequency of the numerical model may be estimated in the same manner as from measured signals taken acquired during lateral frequency response test (see Section 5.7.7).

Alternatively, the eigenfrequencies and mode shapes of the undamped systems (thus neglecting soil damping) can be determined by solving the differential equation

$$(\mathbf{K} - \omega_{0,lat}^2 \cdot \mathbf{M}) \cdot \mathbf{y} = 0 \quad (7-11)$$

for the eigenvalues $\omega_{0,lat} = f_{0,lat} \cdot 2\pi$ (eigenfrequencies) and the eigenvectors \mathbf{y} (mode shapes) (GASCH et al. 2012).

7.3.2 Theoretical influence of installation-induced soil stresses on the eigenfrequency of the model pile

To assess the theoretical influence of the imprinted soil stresses due to pile installation effects, eigenfrequency calculations and numerical simulations were carried out using two different soil stress profiles.

Figure 7-10 (left) shows a linear soil stress profile $\sigma' = \gamma' \cdot z$, describing the stress state without installation effects (red) and another profile with enhanced soil stresses near the pile toe according to Equation (2-37) and parameters $1/\beta_{PSS} = 5$ and $\alpha_{pen} = 1.6$, representing the stress state after impact driving or free vibratory driving (cf. Figure 6-9). In the middle part of the figure, the resulting spring stiffness of the pile-soil interface according to Equations (5-5) and (2-19) is drawn. The right diagram shows the first eigenfrequencies and corresponding mode shapes of the undamped system according to Equation (7-11).

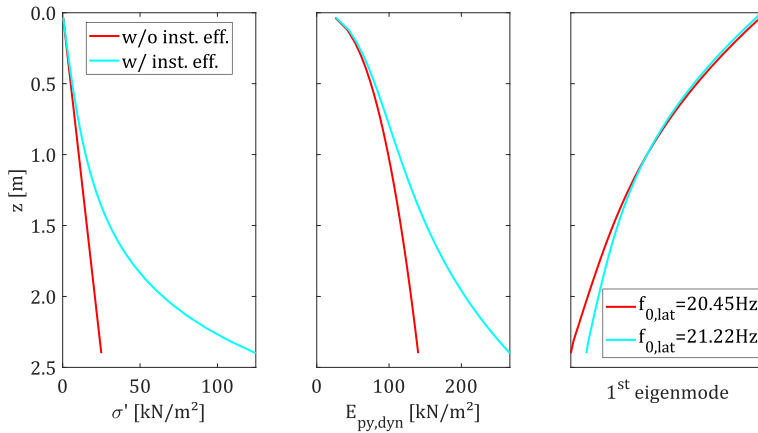


Figure 7-10: Soil stress profile (left), resulting soil stiffness profile (centre) and calculated mode shape (right) for test pile with (cyan) and without (red) consideration of installation effect on soil stress state

The influence of the pile installation effect near the pile toe is mitigated by the under-linear relation between soil stiffness and soil stress. The consequence for the first eigenfrequency $f_{0,lat}$ is below 1 Hz and thus in the range of the reproducibility of the tests (e.g. 19 Hz to 21.5 Hz in case of the impact driven piles; see Figure 6-21). The mode shapes show small differences near the pile toe which are plausible as a higher spring stiffness near the pile toe will lead to a higher degree of clamping.

Figure 7-11 shows results of numerical simulations using the same soil profiles (cyan, red) as shown in Figure 7-10 compared to the measured pile response (black) before the start of cyclic lateral loading ($N = 0$) at pile Z07 (free vibratory driven). The measured excitation signal of the impact hammer is shown in the upper left diagram and was also used as excitation signal for the simulation. The middle and lower left diagrams show response signals filtered by a low pass filter (filtering higher order eigenfrequencies and noise > 200 Hz) and a band pass filter (isolating the first eigenfrequency). The right diagram shows the FFTs of the low pass filtered signals. Resonance frequencies of the damped system $f_{D,lat}$ and damping factors D are given for all systems.

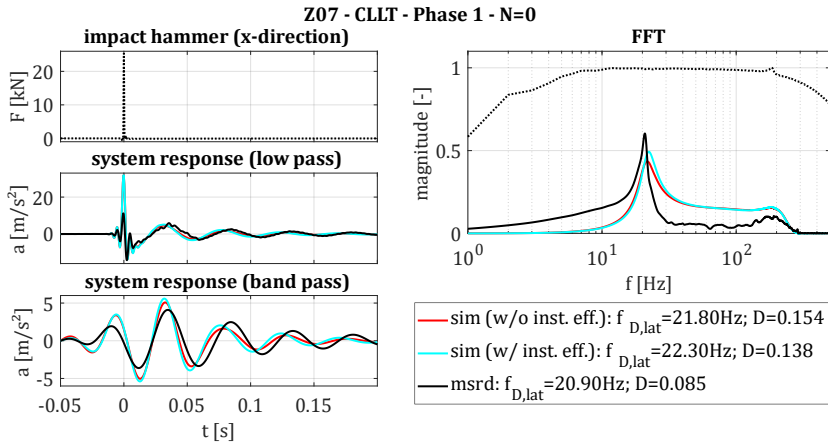


Figure 7-11: Measured (black) and simulated (red, cyan) system response in time domain (left) and frequency domain (right)

Measurement and simulations show good agreement regarding the first eigenfrequency. Damping is overestimated in the simulation but good agreement can be achieved if the damping constant is globally reduced by 50%. The influences of the installation effect on the resonance frequency are again very limited with less than 1 Hz.

7.3.3 Theoretical influence of accumulated soil stresses on the eigenfrequency of the model pile

In analogy to the procedure described in Section 7.3.2, the possible influence of increased soil stresses at shallow and intermediate depths due to cyclic loading is evaluated by means of the one-dimensional numerical model without damping effects. At shallow depth ($z < 1$ m), increased soil stresses after unloading were measured in the upwind direction. At intermediate depth ($1 \text{ m} < z < 1.8$ m) increased soil stresses after unloading were measured in the downwind direction (see Section 6.4.4). The cyclic effects are considered by multiplying the soil stress used to calculate the dynamic soil stiffness with a factor of $\xi_{\sigma}(z)$, varying with depth. That soil stress factor is set to $\xi_{\sigma} = 1.5$ at the mudline ($z = 0$; increase of soil stresses of 50%) and is linearly decreasing to $\xi_{\sigma} = 1.0$ until $z = 1.8$ m (no increase of soil stresses). Compared to the pile installation effect (Figure 7-10), this means a moderate increase of soil stresses and thus soil stiffness, but at lower depths (Figure 7-12):

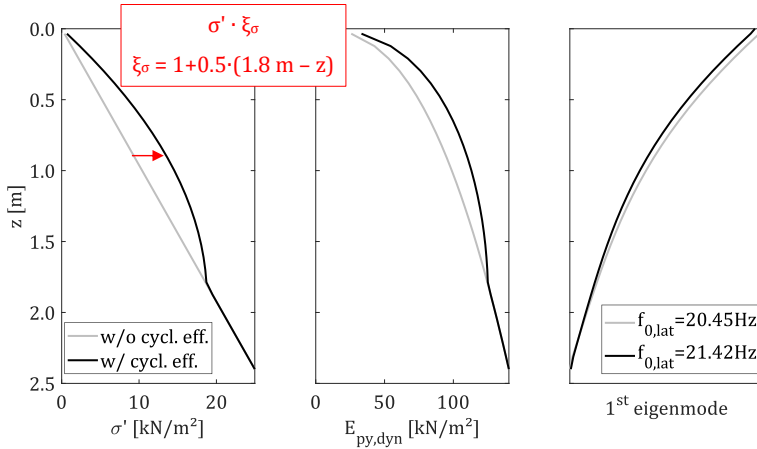


Figure 7-12: Soil stress profile (left), resulting soil stiffness profile (centre) and calculated mode shape (right) for test pile with (black) and without (grey) consideration of cyclic effects on soil stress state

The increase of the resulting undamped bending mode eigenfrequency of about 5% lies in the same range as the increase of the measured bending mode eigenfrequencies due to cyclic lateral loading (2% to 6%; see Figure 6-34). This emphasises the influence of the upper soil layers on the system dynamics.

7.4 Interim summary

A simple one-dimensional bedded beam model is suitable to predict the lateral behaviour of the model piles. For the static case, non-linear p-y curves after MURCHISON & O'NEILL (1984) and KALLEHAVE et al. (2012) with further adjustments to account for small strain stiffness and lateral resistance at the pile base give reasonable agreement with model tests. However, the soil friction angle has an enormous impact on the outcome of the calculations and has to be chosen carefully.

The consideration of increased soil stresses due to pile installation results in a good fit with the measurements of impact driven piles. Thus, a modification of the p-y curves was developed which is suitable to take into account pile installation effects. This approach can be transferred to offshore monopile foundations. A notable reduction of pile deflection and especially a higher

degree of clamping is achieved when the utilisation of the pile is high enough. This shows opportunities to optimize pile design when considering pile installation effects.

The modification of the initial p-y stiffness $E_{py,ini}$ based on the ratio of installation-induced soil stresses to the overburden pressure may also be applied to other formulations of the p-y curves. The ultimate bedding resistance $p_{py,ult}$ is not changed by the proposed method.

For the dynamic case, good agreement between calculation and model tests is achieved using dynamic soil properties from laboratory tests. Influences of increased soil stresses due to pile installation on the system's eigenfrequency are predicted, but lie within the variance of the model tests. Dynamic calculation on large scale monopile foundations were not conducted as this requires extensive knowledge of the dynamics of the superstructure (tower and rotor-nacelle assembly).

Chapter 8 Résumé

A large portion of knowledge on geotechnical problems of offshore pile foundations was based on experience and research in the field of the oil and gas industry. In the last two decades, attention has shifted towards the offshore wind industry in general and large diameter monopile foundations in particular. Due to predominantly lateral, high cyclic loading conditions and stiff piles, the calculation methods used so far were questioned and a lot of research was conducted on novel approaches for lateral pile design and driveability predictions. Vibratory pile driving became more popular in recent years due to positive environmental and possibly economic effects. In the offshore industry, however, experience with vibratory driven piles is still small and little research is available on the effects on lateral pile behaviour. This led to the development of this research project.

A comparative study on impact and vibratory driven piles was carried out by means of scale model investigations with a scaling factor of about 1:13. Dense, over-consolidated, and water saturated sand was used as model soil, resembling offshore conditions in the German North Sea. During the installation of impact driven and certain vibratory driven piles, a massive increase and subsequent decay of radial effective soil stresses was witnessed, resulting in high imprinted soil stresses at the pile toe after pile installation. For impact driven piles, this phenomenon is known as 'friction fatigue'. For vibratory driven piles, the degree of this 'installation effect' depends the response of the pile-vibro-soil system:

- Low acceleration amplitudes,
- large penetration per vibration cycle, and
- an asymmetry of the pile motion (upwards/downwards directed velocity)

lead to high soil stresses. This can be explained by a low range of soil fluidisation at low acceleration amplitudes and an elasto-plastic behaviour of the subjacent soil, which is compacted at sufficing penetration per cycle. Such installation behaviour could be reproduced by free vibratory driving and a frequency control leading to quick and continuous pile penetration (here also termed 'aggressive' frequency control). By means of free vibratory pile driving, similar imprinted soil stresses could be generated as by impact pile driving! On the contrary, crane-guided vibratory installation with holding back the pile did not lead to increased soil stresses. This is explained by viscous soil behaviour underneath the pile toe of an extent larger than the pile oscillation amplitude.

Subsequent lateral loading to service load level showed lower pile head deflections of impact driven and free vibratory driven piles with 'aggressive' frequency control compared to the crane-guided vibratory driven piles. This leads to the suggestion that the lateral bedding stiffness is enhanced by the imprinted soil stresses. This effect can be included into the formulation of the p-y curves according to KALLEHAVE et al. (2012) by increasing the initial bedding stiffness $E_{py,ini}$ depending on the radial soil stress, expressed by an equivalent depth z_{eq} (Equations (7-4) and (7-5)):

$$E_{py,ini} = m_h \cdot z_{ref} \cdot \left(\frac{z_{eq}}{z_{ref}} \right)^{\lambda_z}$$

$$z_{eq} = \sigma'_{rad}(z) / \gamma'$$

Evidently, increased soil stresses near the pile toe only affect the lateral pile behaviour if the pile resistance at that depth (the 'toe kick') is mobilised. This can be expected for stiff piles as the model piles and current offshore monopiles, but not for flexible ones as jacket piles. Thus, the modification of the p-y curves can be used to calculate offshore monopile foundations and reveals certain potential for optimisation of foundation design. Therefore, the extent of imprinted radial soil stresses has to be predicted accurately.

Regarding the occurrence of pile installation effects during offshore pile driving by means of vibratory hammers, a validation is necessary. The determination of the dynamic response of the soil-pile-vibro system can be done based on vibratory driving monitoring (VDM) which is standard in the offshore industry. The in-situ measurement of soil stress is much more elaborate and may be substituted by indirect measurements such as CPTs or pressuremeter soundings.

To assess the decay of increased soil stresses along the pile length different approaches to describe the 'friction fatigue' effect for drivability studies can be used. They have been calibrated by actual soil stress measurements in scale model tests (FISCHER 2021) or by back-calculation of offshore piling projects (ALM & HAMRE 2002).

In addition to the monotonic behaviour of differently driven piles, the displacement accumulation and the development of the system stiffness under cyclic lateral loading with 12,000 cycles were investigated. Again, impact driven and free vibratory driven piles with 'aggressive' frequency control show considerably lower displacement accumulations compared to crane-guided vibratory driven piles. Operable calculations on the cyclic lateral pile

behaviour were not conducted. However, a variant analysis of the relevant parameters of the high cyclic accumulation (HCA) model according to NIEMUNIS et al. (2005) can explain the lower displacement accumulation in case of an increased stress state near the pile toe.

After unidirectional cyclic lateral loading, the loading direction was alternated several times by 90°. Along with the expected displacement accumulation in loading direction, a considerable amount (30% to 50%) of back-accumulation of the previously accumulated pile head displacement was witnessed transverse to the loading direction. Likewise, the system stiffness decreased. Detailed analysis of bending mode eigenfrequency measurements carried out at different cycles in and transverse to the direction of lateral loading reveal that the dynamic system stiffness decreases after only one transverse load cycle. The back-accumulation, in contrast, takes place continuously over transverse cyclic loading and has the same shape as the previous accumulation, but with lower intensity. This discrepancy is explained by the different soil mechanical concepts of accumulation and polarisation: Continuous strain accumulation due to soil shearing during transverse loading is responsible for the back-rotation of the pile while the instant polarisation of the soil determines the stiffness of the system.

Cyclic lateral loading also induces notable stress rearrangements along the pile, especially at shallow and intermediate depth. During transverse cyclic loading, the initial soil stress profiles in the previous loading direction were restored. Imprinted radial stresses near the pile toe due to pile installation effects partly decreased slightly over several cycle packages from alternating directions but remained massively enhanced compared to the primary stress state.

In a nutshell,

- impact pile driving induces imprinted soil stresses near the pile toe,
- vibratory pile driving may evoke similar soil stresses, depending on the installation mode,
- those imprinted soil stresses lead to increased lateral bedding reaction around the toe of stiff monopiles,
- that increased lateral bedding is favourable for the static and cyclic lateral pile behaviour, and
- the imprinted soil stresses are robust against cyclic loading from alternating directions.

Additionally,

- cyclic lateral loading leads to an increase of lateral system stiffness, and
- transverse lateral loading leads to notable back-rotation of previously accumulated pile head displacement.

All these topics may be considered in the geotechnical design of offshore monopile foundations and show potential for optimisation. However, validation by preferably full-scale tests is necessary.

Installation effects on the soil stress state as known from impact driving as well as a similar lateral behaviour were encountered at certain free vibratory driven piles. It has to be emphasised that free vibratory pile driving is not a sufficient condition to achieve imprinted soil stresses and corresponding lateral behaviour, as shown on free vibratory driven piles with no or little pile installation effects and softer lateral behaviour! The effect on the soil stresses is merely linked to the vibration characteristics.

The different 'modes' of vibratory driving encountered in the scale model tests, particularly evoked by free and crane-guided installation, raise questions regarding the soil models used for vibratory pile driving simulations. Pile driveability studies play an important role in the planning of offshore projects. Their results are crucial for fatigue analyses and the plain decision on the right installation equipment. In commercially available driving prediction software the same soil models are used for vibro driveability studies as for impact driving. These soil models do not distinguish between vibratory driving modes, such as 'cavity/non-cavity' or 'viscous/impact' modes. The latter was used here to explain the phenomena witnessed in the scale model tests. A corresponding soil model with acceleration-dependent fluidisation or a displacement-dependent distinction between elasto-plastic and viscous soil behaviour underneath the pile toe is not known to the author. Such a model may facilitate more accurate vibratory driving predictions and even allow for a prediction of increased soil stresses, which may then be applied in the pile design.

Due to the setup of the scale model tests, suggestions on the favourable impact of pile installation effects on the load bearing behaviour is limited to piles in dense sand under lateral loading at moderate load level. It is reasonable to assume that increased soil stresses around the pile toe may also increase the ultimate bedding resistance, and thus the lateral pile capacity, as well as the axial pile stiffness and capacity. This may be validated by appropriate model test.

Vibratory installation in medium dense sand may even lead to more favourable results due to possible compaction effects.

References

Literature

- Achmus, Martin (2009): Bemessung von Gründungselemente für Offshorewindenergieanlagen. Stand des Wissens und offene Fragen. In Forschungszentrum Küste (Ed.): 7. FZK-Kolloquium. Potenziale für die Maritime Wirtschaft. Forschungszentrum Küste. Available online at http://www.fzk.uni-hannover.de/uploads/tx_tkpublikationen/3_02_Achmus.pdf, checked on 6/3/2013.
- Achmus, Martin (2011): Bemessung von Monopiles für die Gründung von Offshore-Windenergieanlagen. Konzepte und offene Fragen. In *Bautechnik* 88 (9), pp. 602–616. DOI: 10.1002/bate.201101503.
- Achmus, Martin; Kuo, Yu-Shu; Abdel-Rahman, Khalid (2009): Behavior of monopile foundations under cyclic lateral load. In *Computers and Geotechnics* 36 (5), pp. 725–735. DOI: 10.1016/j.compgeo.2008.12.003.
- Achmus, Martin; Schmoor, Kirill Alexander; Herwig, Volker; Matlock, Benjamin (2020): Lateral bearing behaviour of vibro-driven and impact-driven large diameter foundation piles in dense sand. In *geotechnik*. DOI: 10.1002/gete.202000006.
- Alam, Jahangir; Hossain, Mohammad Shahadat; Azad, Abul Kalam (2014): Development of correlation between dynamic cone resistance and relative density of sand. In *Journal of Civil Engineering, Institute of Engineers, Bangladesh (IEB)* 42 (1), pp. 63–76.
- Allard, Marie-Agnès (1990): Soil stress field around driven piles. Dissertation. California Institute of Technology, Pasadena, CA.
- Alm, Torstein & Hamre, Liv (2002): Soil model for pile driveability predictions based on CPT interpretations. In : Proceedings of the 15th International Conference on Soil Mechanics and Geotechnical Engineering. International Conference on Soil Mechanics and Geotechnical Engineering. Istanbul, Turkey, 27-31 August 2001. ISSMGE. Lisse: Balkema, pp. 1297–1302.
- Arany, Laszlo; Bhattacharya, Subhamoy; Macdonald, John H.G.; Hogan, S. John (2017): Design of monopiles for offshore wind turbines in 10 steps. In *Soil Dynamics and Earthquake Engineering* 92, pp. 126–152. DOI: 10.1016/j.soildyn.2016.09.024.

- Borel, Serge; Bustamente, Michel; Rocher-Lacoste, Frédéric (2006): The comparative bearing capacity of vibratory and impact driven piles. In Henri Gonin, Alain E. Holeyman, Frédéric Rocher-Lacoste (Eds.): *TransVib 2006. International Symposium on vibratory pile driving & deep soil vibratory compaction*. Paris, 21./22. September 2006. Laboratoire central des ponts et chaussées. Paris (Actes des journées scientifiques du LCPC), pp. 277–284.
- Buckingham, E. (1914): On Physically Similar Systems. Illustrations of the use of dimensional equations. In *Physical Review* 4 (4), pp. 345–376, checked on 5/23/2013.
- Bundesamt für Seeschifffahrt und Hydrographie (Ed.) (2010): FINO database. FINO 1 and FINO 3 wave data. Available online at fino.bsh.de, checked on 26.11.2020.
- Bundesamt für Seeschifffahrt und Hydrographie (Ed.) (2019): Datenportal Flächen-vor-unter-suchung. Drucksondierungen (CPT) (N-3.5, N-3.6, N-3.7, N-3.8). Available online at <https://pinta.bsh.de/>, checked on 5/4/2022.
- Bundesamt für Seeschifffahrt und Hydrographie (BSH) (2012): Anwendungshinweise für den Standard „Konstruktive Ausführung von Offshore-Windenergieanlagen“ des BSH (aktualisierte Fassung). Geotechnische Sicherheitsnachweise für Gründungselemente.
- Burd, Harvey; Byrne, Byron W.; MacAdam, Ross; Houlsby, Guy T.; Martin, Chris; Beuckelaers, William et al. (2017): Design aspects for monopile foundations. In Woojin Lee (Ed.): *Proceedings of the 19th International Conference on Soil Mechanics and Geotechnical Engineering*. 19th International Conference on Soil Mechanics and Geotechnical Engineering. Seoul. Seoul: Korea Geotechnical Society, 35-44.
- CAPE Holland (2020): Vibro driving: the next chapter in offshore wind. Available online at <https://capeholland.com/news/vibro-driving-the-next-chapter-in-offshore-wind/>, updated on 6/5/2020, checked on 3/31/2022.
- Carswell, W.; Johansson, J.; Løvholt, F.; Arwade, S. R.; Madshus, C.; DeGroot, D. J.; Myers, A. T. (2015): Foundation damping and the dynamics of offshore wind turbine monopiles. In *Renewable Energy* 80, pp. 724–736. DOI: 10.1016/j.renene.2015.02.058.
- Chrisopoulos, Stylianos; Vogelsang, Jakob; Triantafyllidis, Theodoros (2017): FE Simulation of Model Tests on Vibratory Pile Driving in Saturated Sand. In Theodoros Triantafyllidis (Ed.): *Holistic Simulation of Geotechnical Installation Processes*, vol. 82. Cham: Springer International Publishing (82), pp. 124–149.

- Cox, William R.; Reese, Lymon C.; Grubbs, Berry R. (1974): Field Testing of Laterally Loaded Piles in Sand. In : Offshore Technology Conference 1974. Sixth Annual Offshore Technology Conference 1974. Houston/Texas, USA, May 6-8, 1974. OTC, OTC 2079.
- Cudmani, Roberto O. (2001): Statische, alternierende und dynamische Penetration in nichtbindigen Böden. Zugl.: Karlsruhe, Univ., Diss., 2000. Karlsruhe: Inst. für Bodenmechanik und Felsmechanik (Veröffentlichungen des Institutes für Bodenmechanik und Felsmechanik der Universität Fridericiana in Karlsruhe, 152).
- Cuéllar, Pablo (2011): Pile Foundations for Offshore Wind Turbines: Numerical and Experimental Investigations on the Behaviour under Short-Term and Long-Term Cyclic Loading. Dissertation. Technische Universität Berlin, Berlin, checked on 6/7/2013.
- Damgaard, M.; Zania, Varvara; Andersen, L.V.; Ibsen, Lars Bo (2014): Effects of soil–structure interaction on real time dynamic response of offshore wind turbines on monopiles. In *Engineering Structures* 75, pp. 388–401. DOI: 10.1016/j.engstruct.2014.06.006.
- Daryaei, Reza; Bakroon, Montaser; Aubram, Daniel; Rackwitz, Frank (2018): Numerical Investigation of the Frequency Influence on Soil Characteristics During Vibratory Driving of Tubular Piles. With assistance of Technische Universität Berlin.
- Daryaei, Reza; Bakroon, Montaser; Aubram, Daniel; Rackwitz, Frank (2019): Numerical evaluation of the soil behavior during impact driving of pipe-piles. With assistance of Technische Universität Berlin.
- Den Hartog, J. P. & Mesmer, Gustav (1952): *Mechanische Schwingungen*. Berlin, Heidelberg: Springer Berlin Heidelberg.
- Diessen, Guillermo (1994): Ein bodenmechanisches Modell zur Beschreibung des Vibrationsrammens in körnigen Böden. Dissertation. Universität Fridericiana, Karlsruhe. Institut für Bodenmechanik und Felsmechanik.
- Dührkop, Jan (2009): Zum Einfluss von Aufweitungen und zyklischen Lasten auf das Verformungsverhalten lateral beanspruchter Pfähle im Sand. Dissertation. Technische Universität Hamburg-Harburg, Institut für Geotechnik und Baubetrieb, Hamburg.
- Dührkop, Jan & Grabe, Jürgen (2008): Monopilegründungen von Offshore-Windenergieanlagen – Zum Einfluss einer veränderlichen zyklischen Lastangriffsrichtung. In *Bautechnik* 85 (5), pp. 317–321. DOI: 10.1002/bate.200810024.

- EA Baugrunderdynamik. Empfehlungen des Arbeitskreises Baugrunderdynamik (2019). 2. Auflage. Berlin: Ernst & Sohn.
- EA-Pfähle. Empfehlungen des Arbeitskreises "Phähle (2012). With assistance of Hans-Georg Kempfert. Berlin: Ernst & Sohn.
- Engel, Jens & Soos, Paul von (2017): Eigenschaften von Boden und Fels - ihre Ermittlung im Labor. In Karl Josef Witt (Ed.): Grundbau-Taschenbuch. 8. Auflage. Berlin: Ernst & Sohn.
- Fischer, Jan (2021): Ramminduzierte Spannungsfeldänderungen im Nahbereich von Rohrprofilen großen Durchmessers. Dissertation. Technische Universität Braunschweig, Braunschweig. Institut für Geomechanik und Geotechnik.
- Fischer, Jan; Sychla, Hauke; Bakker, Joost; Neef, Laurens de; Stahlmann, Joachim (2013): A comparison between impact driven and vibratory driven steel piles in the German North Sea. In Jürgen Grabe (Ed.): Proceedings of the Conference on Maritime Energy, COME 2013. Conference on Maritime Energy, COME 2013. Hamburg, May 21-22, 2013., Technische Universität Hamburg-Harburg, Institut für Geotechnik und Baubetrieb. Hamburg (Veröffentlichungen des Instituts für Geotechnik und Baubetrieb, 26), pp. 361–380.
- Foray, P.; Balachowski, L.; Colliat, J-L (1998): Bearing capacity of model piles driven into dense overconsolidated sands. In *Can. Geotech. J.* 35 (2), pp. 374–385. DOI: 10.1139/t97-082.
- Fu, Dengfeng; Zhang, Youhu; Aamodt, Kristoffer Knoph; Yan, Yue (2020): A multi-spring model for monopile analysis in soft clays. In *Marine Structures* 72, p. 102768. DOI: 10.1016/j.marstruc.2020.102768.
- Gasch, Robert; Knothe, Klaus; Liebich, Robert (2012): Strukturdynamik. Berlin, Heidelberg: Springer Berlin Heidelberg.
- Gattermann, Jörg; Herwig, Volker; Moormann, Christian (2015): VIBRO Project - Vergleich des lateralen Tragverhaltens von vibrierten und geschlagenen Stahlrohrpfählen in sandigen Böden. In Hafentechnische Gesellschaft e.V. (Ed.): HTG-Kongress 2015. HTG-Kongress 2015. Bremen, 09.-11.11.2015. Hafentechnische Gesellschaft e.V., pp. 173–184.
- Gavin, Kenneth G. & Lehane, Barry M. (2003): The shaft capacity of pipe piles in sand. In *Can. Geotech. J.* 40 (1), pp. 36–45. DOI: 10.1139/T02-093.

- Georgiadis, Michael (1983): Development of P-Y Curves for Layered Soils. In Stephen Gailord Wright (Ed.): Proceedings of the Conference on Geotechnical Practice in Offshore Engineering. Conference on Geotechnical Practice in Offshore Engineering. University of Texas at Austin, Austin, Texas, April 27-29, 1983. American Society of Civil Engineers. New York, N.Y: The Society.
- Hartung, Michael (1994): Einflüsse der Herstellung auf die Pfahltragfähigkeit in Sand. Dissertation. Technische Universität Braunschweig, Braunschweig.
- Heerema, Edward P. (1978): Predicting Pile Driveability: Heather As An Illustration Of The "Friction Fatigue" Theory. In : SPE European Petroleum Conference. SPE European Petroleum Conference. London, United Kingdom, 1978-10-24: Society of Petroleum Engineers.
- Hettler, Achim (1981): Verschiebungen starrer und elastischer Gründungskörper in Sand bei monotoner und zyklischer Belastung.
- Hettler, Achim (1986): Horizontal belastete Pfähle mit nichtlinearer Bettung in körnigen Böden. Zugl.: Karlsruhe, Univ., Habil.-Schr. Karlsruhe: Institut für Bodenmechanik und Felsmechanik der Univ. Fridericiana (Veröffentlichungen des Institutes für Bodenmechanik und Felsmechanik der Universität Fridericiana in Karlsruhe, 102).
- Houlsby, G. T.; Abadie, C. N.; Beuckelaers, W.J.A.P.; Byrne, B. W. (2017): A model for nonlinear hysteretic and ratcheting behaviour. In *International Journal of Solids and Structures* 120, pp. 67–80. DOI: 10.1016/j.ijsolstr.2017.04.031.
- Jardine, Richard J.; Chow, Fiona; Overy, Robert; Standing, Jamie (2005): ICP design methods for driven piles in sands and clays. London: Thomas Telford.
- Jonker, G. (1987): vibratory pile driving hammers for pile installations and soil improvement projects. OTC 5422. In : Offshore Technology Conference 1987. 19th Annual Offshore Technology Conference 1987. Houston/Texas, USA, April 27-30, 1987. OTC, pp. 549–559.
- Kallehave, Dan; Thilsted, C. Le; Liingaard, M. A. (2012): Modification of the api p-y formulation of initial stiffness of sand. In *Offshore Site Investigation and Geotechnics 2012: Integrated Technologies - Present and Future, OSIG 2012*, pp. 465–472.
- Kirsch, Fabian; Richter, Thomas; Coronel, Maria (2014): Geotechnische Aspekte bei der Gründungsbemessung von Offshore-Windenergieanlagen auf Monopfählen mit sehr großen Durchmesser. In *Stahlbau* 83 (S2), pp. 61–67. DOI: 10.1002/stab.201430008.

Kudella, Peter & Solf, Oksana (2012): Untersuchungen zur Verformungsakkumulation bei zyklisch horizontal beanspruchten Offshore-Monopiles. In Stavros A. Savidis (Ed.): Vorträge zum Workshop "Gründungen von Offshore-Windenergieanlagen". Workshop Gründung von Offshore-Windenergieanlagen. Aachen: Shaker (Veröffentlichungen des Grundbauinstitutes der Technischen Universität Berlin, Heft 56), pp. 89–105.

Labenski, Johannes (2018): Experimentelle Untersuchungen zum lateralen Tragverhalten einvibrierter offener Stahlrohrpfähle. In Deutsche Gesellschaft für Geotechnik (Ed.): 35. Baugrundtagung. Beiträge der Spezialsitzung. 35. Baugrundtagung. Stuttgart, 26.09.2018, pp. 163–172.

Labenski, Johannes (2019): Untersuchungen zum statisch lateralen Tragverhalten von in nichtbindigen Böden einvibrierten Monopiles: Vorstellung eines modifizierten p-y Ansatzes. In Joachim Stahlmann (Ed.): Pfahl-Symposium 2019. With assistance of Nils Hinzmann, Philipp Stein. Pfahl-Symposium 2019. Braunschweig, 21.-22.02.2019. Institut für Grundbau und Bodenmechanik, Technische Universität Braunschweig, pp. 75–88.

Labenski, Johannes (2020): Untersuchungen zum Einbringverhalten und dem lateralen Tragverhalten unter monotoner Einwirkung von in nichtbindigen Böden vibrierend installierten Monopiles. Dissertation. Universität Stuttgart, Stuttgart. Institut für Geotechnik.

Labenski, Johannes & Moormann, Christian (2018): Experimental Investigations on the Lateral Bearing Behaviour of Vibratory-Driven Open Steel Pipe Piles. In Deep Foundations Institute (Ed.): Proceeding of the 2018 DFI-EFFC International Conference on Deep Foundations and Ground Improvement. International Conference on Deep Foundations and Ground Improvement (DFI-EFFC). Rome, Italy, 05.06.2018 - 07.06.2018. Deep Foundations Institute, pp. 170–179.

Lammertz, Patrick & Richwien, Werner (2006): Bearing capacity of open ended steel pipe piles vibrated in sand. In Henri Gonin, Alain E. Holeyman, Frédéric Rocher-Lacoste (Eds.): TransVib 2006. International Symposium on vibratory pile driving & deep soil vibratory compaction. Paris, 21./22. September 2006. Laboratoire central des ponts et chaussées. Paris (Actes des journées scientifiques du LCPC), pp. 295–304.

Le, Viet Hung (2015): Zum Verhalten von Sand unter zyklischer Beanspruchung mit Polarisationswechsel im Einzelscherversuch. With assistance of Technische Universität Berlin, Stavros A. Savidis: Shaker Verlag.

- Le, Viet Hung; Rackwitz, Frank; Savidis, Stavros A. (2017): Verformungsakkumulation bei Monopilegründungen in Sand mit Lastrichtungswechseln. In *Bauingenieur* 92 (6), pp. 263–270.
- Le, Viet Hung; Remspecher, Fabian; Rackwitz, Frank (2019): Numerical Investigation of Installation Effects on the Cyclic Behaviour of Monopile Foundation Under Horizontal Loading. In M.F Randolph, Dinh Hong Doan, Anh Minh Tang, Man Bui, Van Nguyen Dinh (Eds.): *Proceedings of the 1st Vietnam Symposium on Advances in Offshore Engineering*, vol. 18. Singapore: Springer Singapore (Lecture Notes in Civil Engineering), pp. 389–394.
- LeBlanc, Christian; Byrne, Byron W.; Houlsby, Guy T. (2010): Response of stiff piles in sand to long-term cyclic lateral loading. In *Geotechnique* 60 (2), pp. 79–90. DOI: 10.1680/geot.7.00196.
- Lee, S. L.; Chow, Y. K.; Karunaratne, G. P.; Wong, K. Y. (1988): Rational wave equation model for pile-driving analysis. In *J. Geotech. Engrg.* 114 (3), pp. 306–325. DOI: 10.1061/(ASCE)0733-9410(1988)114:3(306).
- Li, Q.; Prendergast, L. J.; Askarinejad, A.; Gavin, K. (2018): Effect of scour on the behavior of a combined loaded monopile in sand. In António S. Cardoso, José L. Borges, Pedro A. Costa, António T. Gomes, José C. Marques, Castorina S. Vieira (Eds.): *Numerical Methods in Geotechnical Engineering IX*: CRC Press, pp. 1529–1534.
- Lin, San-Shyan & Liao, Jen-Cheng (1999): Permanent Strains of Piles in Sand due to Cyclic Lateral Loads. In *Journal of Geotechnical and Geoenvironmental Engineering* 125 (9), pp. 798–802. DOI: 10.1061/(ASCE)1090-0241(1999)125:9(798).
- Linder, Wolf-Rüdiger (1977): Zum Eindring- und Tragverhalten von Pfählen in Sand. Dissertation. Technische Universität Berlin, Berlin.
- Little, Robert Lewis & Briaud, J.-L (1988): Full scale cyclic lateral load tests on six single piles in sand. [Vicksburg, Miss., [Springfield, Va.]: U.S. Army Engineer Waterways Experiment Station]; [Available from National Technical Information Service] (Miscellaneous paper, GL-88-27).
- Long, J. H. & Vanneste, Geert (1994): Effects of Cyclic Lateral Loads on Piles in Sand. In *Journal of Geotechnical Engineering* 120 (1), pp. 225–244. DOI: 10.1061/(ASCE)0733-9410(1994)120:1(225).

- Lovera, Anaïs; Ghabezloo, Siavash; Sulem, Jean; Randolph, Mark F.; Kham, Marc; Palix, Elisabeth (2021): Pile response to multi-directional lateral loading using P–y curves approach. In *Geotechnique* 71 (4), pp. 288–298. DOI: 10.1680/jgeot.18.P.297.
- Lüking, Jan (2010): Tragverhalten von offenen Verdrängungspfählen unter Berücksichtigung der Pfropfenbildung in nichtbindigen Böden. Dissertation. Universität Kassel, Kassel, checked on 6/17/2013.
- Lunne, T.; Powell, J. J. M.; Robertson, P. K. (2014): Cone Penetration Testing in Geotechnical Practice. First edition. Boca Raton, FL: CRC Press.
- Mahler, András & Szendefy, János (2009): Estimation of CPT resistance based on DPH results. In *Per. Pol. Civil Eng.* 53 (2), p. 101. DOI: 10.3311/pp.ci.2009-2.06.
- Massarsch, K. Rainer; Fellenius, Bengt H.; Bodare, Anders (2017): Fundamentals of the vibratory driving of piles and sheet piles. In *geotechnik* 40 (2), pp. 126–141. DOI: 10.1002/gete.201600018.
- Massarsch, K. Rainer; Wersäll, Carl; Fellenius, Bengt H. (2020): Horizontal stress increase induced by deep vibratory compaction. In *Proceedings of the Institution of Civil Engineers - Geotechnical Engineering* 173 (3), pp. 228–253. DOI: 10.1680/jgeen.19.00040.
- Massarsch, K. Rainer; Wersäll, Carl; Fellenius, Bengt H. (2022): Vibratory driving of piles and sheet piles – state of practice. In *Proceedings of the Institution of Civil Engineers - Geotechnical Engineering* 175 (1), pp. 31–48. DOI: 10.1680/jgeen.20.00127.
- Massarsch, Karl Rainer; Wersäll, Carl; Fellenius, Bengt H.; Ehrmanntraut, Editha (2021): Bedeutung der Frequenz für das Vibrationsrammen von Spundbohlen. In *Bautechnik* 98 (6), pp. 410–422. DOI: 10.1002/bate.202000070.
- Middendorp, Peter (2004): Thirty years of experience with the wave equation solution based on the method of characteristics. In : Proceedings of the Seventh International Conference on the Application of Stresswave Theory to Piles 2004. Seventh International Conference on the Application of Stresswave Theory to Piles. Kuala Lumpur, Malaysia, 9-11 August 2004.
- Middendorp, Peter & Jonker, G. (1988): Prediction of Vibratory Hammer Performance by Stress Wave Analysis. In Bengt H. Fellenius (Ed.): Application of Stress-Wave Theory to Piles. Third international conference. Third International Conference on Application of Stress-Wave Theory to Piles. Ottawa, Canada, May 25-27, 1988. Vancouver: BiTech.

- Moormann, Christian; Kirsch, Fabian; Herwig, Volker (2016): Vergleich des axialen und lateralen Tragverhaltens von vibrierten und gerammten Stahlrohrpfählen. In Deutsche Gesellschaft für Geotechnik (Ed.): 34. Baugrundtagung. 34. Baugrundtagung. Bielefeld, 14.-17.09.2016.
- Moriyasu, Shunsuke; Kobayashi, Shun-ichi; Matsumoto, Tatsunori (2018): Experimental study on friction fatigue of vibratory driven piles by in situ model tests. In *Soils and Foundations* 58 (4), pp. 853–865. DOI: 10.1016/j.sandf.2018.03.010.
- Mosher, Reed L. (1987): Comparison of axial capacity of vibratory-driven piles to impact-driven piles. Vicksburg, Mississippi (Technical report).
- Murchison, Jack M. & O'Neill, Michael W. (1984): Evaluation of p-y-Relationship in Cohesionless Soils. In : Analysis and design of pile foundations, pp. 174–191.
- Nawabi, Orhan (2021): Ermittlung von Bodenparametern für das HCA-Modell für Braunschweiger Sand. Masterarbeit. Technische Universität Braunschweig. Institut für Geomachanik und Geotechnik.
- Nendza, Matthias (2007): Untersuchungen zu den Mechanismen der dynamischen Bodenverdichtung bei Anwendung des Rütteldruckverfahrens. Dissertation. Technische Universität Braunschweig, Braunschweig.
- Newmark, Nathan M. (1959): A Method of Computation for Structural Dynamics. In *J. Engrg. Mech. Div.* 85 (3), pp. 67–94. DOI: 10.1061/JMCEA3.0000098.
- Nicolai, G.; Ibsen, L. B.; O'Loughlin, C. D.; White, D. J. (2017): Quantifying the increase in lateral capacity of monopiles in sand due to cyclic loading. In *Géotechnique Letters* 7 (3), pp. 245–252. DOI: 10.1680/jgele.16.00187.
- Nicolai, Giulio & Ibsen, Lars Bo (2014): Small-Scale Testing of Cyclic Laterally Loaded Monopiles in Dense Saturated Sand. In *Journal of Ocean and Wind Energy* 1 (4), pp. 240–245.
- Niemunis, Andrzej; Wichtmann, Torsten; Triantafyllidis, Theodoros (2005): A high-cycle accumulation model for sand. In *Computers and Geotechnics* 32 (4), pp. 245–263. DOI: 10.1016/j.compgeo.2005.03.002.
- Ohde, Johannes (1939): Zur Theorie der Druckverteilung im Baugrund. In *Der Bauingenieur*, pp. 451–459.

- Oztoprak, S. & Bolton, M. D. (2013): Stiffness of sands through a laboratory test database. In *Geotechnique* 63 (1), pp. 54–70. DOI: 10.1680/geot.10.P.078.
- Peralta, Proserpine (2010): Investigations on the Behavior of Large Diameter Piles under Long-Term Lateral Cyclic Loading in Cohesionless Soil. Dissertation. Leibniz Universität Hannover, Hannover. Institut für Geomechanik, checked on 5/23/2013.
- Poulos, Harry G. & Hull, Tim S. (1989): The role of analytical geomechanics in foundation engineering. [Place of publication not identified]: [publisher not identified].
- Prendergast, Luke J. & Gavin, Kenneth G. (2016): A comparison of initial stiffness formulations for small-strain soil–pile dynamic Winkler modelling. In *Soil Dynamics and Earthquake Engineering* 81, pp. 27–41. DOI: 10.1016/j.soildyn.2015.11.006.
- Prendergast, Luke J.; Gavin, Kenneth G.; Doherty, Paul (2015): An investigation into the effect of scour on the natural frequency of an offshore wind turbine. In *Ocean Engineering* 101, pp. 1–11. DOI: 10.1016/j.oceaneng.2015.04.017.
- Prendergast, Luke J.; Gavin, Kenneth G.; Igoe, David (2014): Dynamic soil-structure interaction modeling using stiffness derived from in-situ Cone Penetration Tests. In : 3rd International Symposium on Cone Penetration Testing. 3rd International Symposium on Cone Penetration Testing. Las Vegas, USA, 12-14 May, 2014. Available online at <http://hdl.handle.net/10197/7189>.
- Prendergast, Luke J.; Wu, W. H.; Gavin, Kenneth G. (2019): Experimental application of FRF-based model updating approach to estimate soil mass and stiffness mobilised under pile impact tests. In *Soil Dynamics and Earthquake Engineering* 123, pp. 1–15. DOI: 10.1016/j.soildyn.2019.04.027.
- Rausche, Frank (2002): Modeling of vibratory pile driving. In Alain E. Holeyman (Ed.): Proceedings of the International Conference on Vibratory Pile Driving and Deep Soil Compaction. TRANSVIB 2002. International Conference on Vibratory Pile Driving and Deep Soil Compaction, TRANSVIB 2002. Louvain-la-Neuve, Belgium, 9-10 September 2002. Lisse: Balkema, pp. 21–32.
- Reese, Lymon C.; Cox, Willam R.; Koop, Francis D. (1974): Analysis of Laterally Loaded Piles in Sand. In : Offshore Technology Conference 1974. Sixth Annual Offshore Technology Conference 1974. Houston/Texas, USA, May 6-8, 1974. OTC, OTC 2080.

- Remspecher, Fabian; Le, Viet Hung; Rackwitz, Frank; Herwig, Volker (2019a): Einfluss der Vibrationspfahleinbringung auf das Last-Verformungsverhalten eines offenen Stahlrohrpfahls unter lateraler zyklischer Belastung. In Joachim Stahlmann (Ed.): Pfahl-Symposium 2019. With assistance of Nils Hinzmann, Philipp Stein. Pfahl-Symposium 2019. Braunschweig, 21.-22.02.2019. Institut für Grundbau und Bodenmechanik, Technische Universität Braunschweig, pp. 137–155.
- Remspecher, Fabian; Le, Viet Hung; Rackwitz, Frank; Herwig, Volker; Matlock, Benjamin (2019b): Vibratory Driven Installation of Monopiles – An Experimental Investigation of the Soil-Pile Interaction. In M.F Randolph, Dinh Hong Doan, Anh Minh Tang, Man Bui, Van Nguyen Dinh (Eds.): Proceedings of the 1st Vietnam Symposium on Advances in Offshore Engineering, vol. 18. Singapore: Springer Singapore (Lecture Notes in Civil Engineering), pp. 171–176.
- Richards, Iona A.; Byrne, Byron W.; Houlsby, Guy T. (2020): Monopile rotation under complex cyclic lateral loading in sand. In *Geotechnique* 70 (10), pp. 916–930. DOI: 10.1680/jgeot.18.P.302.
- Richwien, Werner & Lesny, Kerstin (2004): Windfarmen in der Nordsee. Fundamente für Windmühlen auf hoher See. In *Unikate: Berichte aus Forschung und Lehre* (23), pp. 60–69.
- Robertson, P. K. (1990): Soil classification using the cone penetration test. In *Can. Geotech. J.* 27 (1), pp. 151–158. DOI: 10.1139/t90-014.
- Robertson, P. K. (2010): Estimating in-situ state parameter and friction angle in sandy soils from CPT. In : 2nd International Symposium on Cone Penetration Testing. Huntington Beach/CA, USA.
- Rodger, A. A. & Littlejohn, G. S. (1980): A study of vibratory driving in granular soils. In *Geotechnique* 30 (3), pp. 269–293.
- Rowe, P. W. (1969): The Relation Between the Shear Strength of Sands in Triaxial Compression, Plane Strain and Direct. In *Geotechnique* 19 (1), pp. 75–86.
- Rudolph, Christina; Bienen, Britta; Grabe, Jürgen (2014): Effect of variation of the loading direction on the displacement accumulation of large-diameter piles under cyclic lateral loading in sand. In *Can. Geotech. J.* 51 (10), pp. 1196–1206. DOI: 10.1139/cgj-2013-0438.

- Rudolph, Christina & Grabe, Jürgen (2013): Untersuchungen zu zyklisch horizontal belasteten Pfählen bei veränderlicher Lastrichtung. In *geotechnik* 36 (2), pp. 90–95. DOI: 10.1002/gete.201200025.
- Schönit, Markus & Reusch, Dirk (2008): Online-estimation of vibratory driven pile bearing capacity. In Edmundas Kazimieras Zavadskas, A. Kaklauskas, M. J. Skibniewski (Eds.): 25th International Symposium on Automation and Robotics in Construction. ISARC-2008. 25th International Symposium on Automation and Robotics in Construction. Vilnius, June 26-29, 2008. Vilnius: Vilnius Gediminas Technical University, pp. 119–128.
- Schultze, Edgar (1968): Der Reibungswinkel nichtbindiger Böden. In *Der Bauingenieur* 43 (9), pp. 313–320.
- Shirzadeh, R.; Devriendt, C.; Bidakhvidi, M. A.; Guillaume, P. (2013): Experimental and computational damping estimation of an offshore wind turbine on a monopile foundation. In *Journal of Wind Engineering and Industrial Aerodynamics* 120, pp. 96–106. DOI: 10.1016/j.jweia.2013.07.004.
- Smith, E. (1960): Pile driving analysis by the wave equation. In *Proceedings of the ASCE, Journal of the Soil Mechanics and Foundation Division*, pp. 35–61.
- Solf, Oksana (2012): Zum mechanischen Verhalten von zyklisch belasteten Offshore-Gründungen. Dissertation. Karlsruher Institut für Technologie (KIT), Karlsruhe.
- Stahlmann, Joachim; Sychla, Hauke; Stein, Philipp; Fischer, Jan (2014): Tragfähigkeit vibrierter und gerammter Stahlpfähle - ein experimenteller Vergleich. In Hafentechnische Gesellschaft e.V. (Ed.): HTG-Kongress 2014. 100 Jahre HTG. HTG-Kongress 2014. Berlin, 21.-23. Mai 2014. Hafentechnische Gesellschaft e.V., pp. 239–251.
- Staubach, P.; Macháček, J.; Moscoso, M. C.; Wichtmann, T. (2020): Impact of the installation on the long-term cyclic behaviour of piles in sand: A numerical study. In *Soil Dynamics and Earthquake Engineering* 138, p. 106223. DOI: 10.1016/j.soildyn.2020.106223.
- Staubach, Patrick; Macháček, Jan; Wichtmann, Torsten (2021): Large-deformation analysis of pile installation with subsequent lateral loading: Sanisand vs. Hypoplasticity. In *Soil Dynamics and Earthquake Engineering* 151, p. 106964. DOI: 10.1016/j.soildyn.2021.106964.

- Stein, Philipp (2018): Modellversuche zur Vibrationsrammung offener Stahlrohrpfähle. In Deutsche Gesellschaft für Geotechnik (Ed.): 35. Baugrundtagung. Beiträge der Spezialsitzung. 35. Baugrundtagung. Stuttgart, 26.09.2018, pp. 173–182.
- Stein, Philipp (2020): Messung und Simulation der Biegeeigenfrequenz eines lateral gebetteten Stahlrohrpfahls. In Joachim Stahlmann (Ed.): Messen in der Geotechnik 2020. Fachseminar am 20./21. Februar 2020. With assistance of Universitätsbibliothek Braunschweig. Messen in der Geotechnik 2020. Braunschweig, 20.-21.02.2020. Institut für Geomechanik und Geotechnik. Braunschweig.
- Stein, Philipp; Gattermann, Jörg; Daumlechner, Eugen; Hinzmann, Nils; Stahlmann, Joachim (2020): ZykLaMP. Großmaßstäbliche Modellversuche zur lateralen Tragfähigkeit offener Stahlrohrpfähle unter zyklischer Belastung bei verschiedenen Einbringungsverfahren. Institut für Geomechanik und Geotechnik, Technische Universität Braunschweig. Braunschweig (FKZ 0324133).
- Stein, Philipp; Hinzmann, Nils; Gattermann, Jörg; Stahlmann, Joachim (2019a): Experimentelle Versuche zur Steifigkeitsänderung von Monopfahlgründungen unter zyklisch lateraler Belastung. In Joachim Stahlmann (Ed.): Pfahl-Symposium 2019. With assistance of Nils Hinzmann, Philipp Stein. Pfahl-Symposium 2019. Braunschweig, 21.-22.02.2019. Institut für Grundbau und Bodenmechanik, Technische Universität Braunschweig, pp. 115–133.
- Stein, Philipp; Hinzmann, Nils; Gattermann, Jörg; Stahlmann, Joachim (2019b): Experimentelle Versuche zur Steifigkeitsänderung von Monopfahlgründungen unter zyklisch lateraler Belastung. In Joachim Stahlmann (Ed.): Pfahl-Symposium 2019. With assistance of Nils Hinzmann, Philipp Stein. Pfahl-Symposium 2019. Braunschweig, 21.-22.02.2019. Institut für Grundbau und Bodenmechanik, Technische Universität Braunschweig, pp. 115–136.
- Stevens, Robert S.; Wiltsie, Edward A.; Turton, Thomas H. (1982): Evaluating Pile Drivability for Hard Clay, Very Dense Sand, and Rock. OTC 4205. In : Offshore Technology Conference 1982. 14th Annual Offshore Technology Conference 1982. Houston/Texas, USA, May 3-6, 1982. OTC.
- Stewart, Harry E. (1986): Permanent Strains from Cyclic Variable-Amplitude Loadings. In *J. Geotech. Engrg.* 112 (6), pp. 646–660. DOI: 10.1061/(ASCE)0733-9410(1986)112:6(646).

- Su, D. (2012): Resistance of Short, Stiff Piles to Multidirectional Lateral Loadings. In *Geotech. Test. J.* 35 (2). DOI: 10.1520/GTJ103840.
- Suryasentana, S. K. & Lehane, Barry M. (2016): Updated CPT-based p-y formulation for laterally loaded piles in cohesionless soil under static loading. In *Geotechnique* 66 (6), pp. 445–453. DOI: 10.1680/jgeot.14.P.156.
- Terzaghi, Karl (1955): Evaluation of Coefficients of Subgrade Reaction. In *Geotechnique* 5 (4), pp. 297–326. DOI: 10.1680/geot.1955.5.4.297.
- Thieken, Klaus; Achmus, Martin; Lemke, Katrin (2015): A new static p-y approach for piles with arbitrary dimensions in sand. In *geotechnik* 38 (4), pp. 267–288. DOI: 10.1002/gete.201400036.
- Todo Bom, Luis Berenguer; Siedler, Simon Scott; Tautz-Weinert, Jannis (2020): Validation of CPT-based initial soil stiffness in sand for offshore wind jacket piles. In Joachim Stahlmann (Ed.): *Messen in der Geotechnik 2020. Fachseminar am 20./21. Februar 2020*. With assistance of Universitätsbibliothek Braunschweig. *Messen in der Geotechnik 2020*. Braunschweig, 20.-21.02.2020. Institut für Geomechanik und Geotechnik. Braunschweig.
- Toolan, F. & Fox, D. (1977): Geotechnical planning of piled foundations for offshore platforms. In *Proceedings of the Institution of Civil Engineers* 62 (2), pp. 221–244. DOI: 10.1680/iicep.1977.3224.
- Triantafyllidis, Theodoros & Chrisopoulos, Stylianos (2016): Ein Modell zur Berechnung des Verformungsverhaltens von horizontal hochzyklisch beanspruchten Pfählen. In *Bautechnik* 93 (9), pp. 605–627. DOI: 10.1002/bate.201600036.
- Vesić, Aleksander Sedmak (1970): Tests on instrumented piles, Ogeechee river site. Durham, NC: Duke Univ (Soil mechanics series, 22).
- Viking, Kenneth (2002): Vibro-driveability. A field study of vibratory driven sheet piles in non-cohesive soils. Doctoral thesis. Royal Institute of Technology (KTH), Stockholm.
- Viking, Kenneth (2006): The vibratory pile installation technique. In Henri Gonin, Alain E. Holeyman, Frédéric Rocher-Lacoste (Eds.): *TransVib 2006. International Symposium on vibratory pile driving & deep soil vibratory compaction*. Paris, 21./22. September 2006. Laboratoire central des ponts et chaussées. Paris (Actes des journées scientifiques du LCPC), pp. 65–82.

- Vipulanandan, Cumaraswamy; Wong, Daniel; O'Neill, Michael W. (1990): Behavior of Vibro-Driven Piles in Sand. In *J. Geotech. Engrg.* 116 (8), pp. 1211–1230. DOI: 10.1061/(ASCE)0733-9410(1990)116:8(1211).
- Vogelsang, Jakob (2017): Untersuchungen zu den Mechanismen der Pfahlrammung. Dissertation.
- Vos, Koen (2014): Particle shape evaluation: A new objective approach using DIA applied to the frac sand industry. Extractive Industry Geology (EIG) Conference. St. Andrews, Scotland, 6/12/2014.
- White, David; Schneider, J. A.; Lehane, Barry M. (2005): The influence of effective area ratio on shaft friction of displacement piles in sand. In Susan Gourvenec (Ed.): *Frontiers in offshore geotechnics. Proceedings of the first International Symposium on Frontiers in Offshore Geotechnics*, University of Western Australia, Perth, 19-21 september 2005. International Symposium on Frontiers in Offshore Geotechnics. Perth. London: Taylor & Francis (Balkema: Proceedings and monographs in engineering, water and earth sciences).
- Wichtmann, Torsten (2016): Soil behaviour under cyclic loading. Experimental observations, constitutive description and applications (Veröffentlichungen des Institutes für Bodenmechanik und Felsmechanik am Karlsruher Institut für Technologie (KIT)).
- Wichtmann, Torsten; Niemunis, Andrzej; Triantafyllidis, Theodoros (2004): The effect of volumetric and out-of-phase cyclic loading on strain accumulation. In Theodoros Triantafyllidis (Ed.): *Proceedings of the International Conference on Cyclic Behaviour of Soils and Liquefaction Phenomena*. International Conference on Cyclic Behaviour of Soils and Liquefaction Phenomena. Bochum, 31.03.2004-02.04.2004.
- Wichtmann, Torsten & Triantafyllidis, Theodoros (2011): Prognose der Langzeitverformungen für Gründungen von Offshore-Windenergieanlagen mit einem Akkumulationsmodell. In *Bautechnik* 88 (11), pp. 765–781. DOI: 10.1002/bate.201101519.
- Wiemann, Jens (2007): Bemessungsverfahren für horizontal belastete Pfähle. Untersuchungen zur Anwendbarkeit der p-y Methode. Essen: VGE-Verlag (Mitteilungen aus dem Fachgebiet Grundbau und Bodenmechanik, 33).
- Wind Europe (2021): Offshore Wind in Europe. Key trends and statistics 2020. With assistance of Lizet Ramirez, Daniel Fraile, Guy Brindley, Rory O'Sullivan. Available online at

https://proceedings.windeurope.org/biplatform/rails/active_storage/blobs/eyJfcmFpbHMiOnsibWVzc2FnZSI6IkJBaHBBCDhDIiwIZXhwIjpudWxsLCJwdXliOiJibG9iX2lkIn19--652a2d205034a95011d035451622eca84378db37/WindEurope-Offshore-wind-in-Europe-statistics-2020.pdf, checked on 3/31/2022.

Winkler, Emil (1867): Die Lehre von der Elasticitaet und Festigkeit. Mit besonderer Rücksicht auf ihre Anwendung in der Technik; für polytechnische Schulen, Bauakademien, Ingenieure, Maschinenbauer, Architekten, etc. Prag: Dominicus.

Witzel, Melanie (2004): Zur Tragfähigkeit und Gebrauchstauglichkeit von vorgefertigten Verdrängungspfählen in bindigen und nichtbindigen Böden. Dissertation. Kassel Univ. Press, Kassel.

Zachert, Hauke (2015): Zur Gebrauchstauglichkeit von Gründungen für Offshore-Windenergieanlagen. Dissertation. Karlsruher Institut für Technologie (KIT), Karlsruhe.

Zhang, Youhu & Andersen, Knut H. (2019): Soil reaction curves for monopiles in clay. In *Marine Structures* 65, pp. 94–113. DOI: 10.1016/j.marstruc.2018.12.009.

Standards and Guidelines

DIN 4094-1, 2002: Baugrund Felduntersuchungen.

DIN 4085, 2017: Baugrund, Berechnung des Erddrucks.

DIN 18126, 1996: Baugrund, Untersuchung von Bodenproben.

DIN 18125-2, 2011: Baugrund, Untersuchung von Bodenproben – Bestimmung der Dichte des Bodens.

DNV-OS-J101, 2013: Design of Offshore Wind Turbine Structures, checked on 6/3/2013.

DIN 18196, 2011: Erd- und Grundbau – Bodenklassifikation für bautechnische Zwecke.

DIN EN ISO 13503-2, 2020: Erdöl- und Erdgasindustrie – Komplettierungsflüssigkeiten und -materialien – Teil 2: Messung der Eigenschaften von Stützmaterialien zum Einsatz bei hydraulischen Fraktionierungs- und in Kiespackungsvorgängen.

DIN EN 1092-1, 2018: Flansche und ihre Verbindungen.

API RP 2GEO, 2014: Geotechnical and foundation design considerations.

DIN EN ISO 14688-1, 2020: Geotechnische Erkundung und Untersuchung - Benennung, Beschreibung und Klassifizierung von Boden - Teil 1: Benennung und Beschreibung.

DIN EN ISO 22476-1, 2013: Geotechnische Erkundung und Untersuchung – Felduntersuchungen.

DIN EN ISO 22476-2, 2012: Geotechnische Erkundung und Untersuchung – Felduntersuchungen.

DIN EN ISO 17892-10, 2019: Geotechnische Erkundung und Untersuchung – Laborversuche an Bodenproben.

DIN EN ISO 17892-9, 2018: Geotechnische Erkundung und Untersuchung – Laborversuche an Bodenproben.

API RP 2A-WSD, 2014: Planning, designing, and constructing fixed offshore platforms - working stress design.

GL IV-2, 2012: Rules and Guidelines, Chapter IV Industrial Service, Part 2 Guidelines for the Certification of Offshore Wind Turbines.

ASTM D-2487, 2006: Standard Practice for Classification of Soils for Engineering Purposes (Unified Soil Classification System).

Software

MathWorks (2020): MATLAB. Version R2020a. 64 bit.

Appendix A Test program

The following Table A-1 shows an overview over all tests executed within the research project. Details about the installation method are given in Table 6-1. Regarding the direction and loading amplitude of the different phases refer to Table 5-3.

Table A-1: Test program

test	installation method		phases	comments
Z01	vibro	free-hi-mod	6	phase 1: measurement of pile head displacement not redundant phase 4, first cycle: max H \approx 23 kN phase 5: 6,740 cycles phase 6: 1,006 cycles
Z02	vibro	free-hi-mod	4	phase 1: failure of DAQ during first 250 cycles; load control operable phase 3: interruption for about 6 hrs phase 4: interruption for about 10 hrs
Z03	impact		5	
Z04	impact		5	installation: malfunction of diesel hammer with low energy and penetration per blow from 1.3 m to 2.0 m penetration
Z05	vibro	free-hi-mod	4	phase 4: measurement of pile head displacement not redundant during first 500 cycles; phase extended to 144,000 cycles
Z06	vibro	free-hi-mod	5	phase 1: failure of DAQ during cycles 1,011 to 11,725; but load control operable
Z07	vibro	free-hi-aggr	4	all phases: LFRT after cycles 1; 10; 100; 1,000 phase 4: extended to 96,000 cycles
Z08	vibro	free-hi-aggr	5	phase 1: interruption after 5,505 cycles phase 5: extended to 82,166 cycles; LFRT after cycles 1; 10; 1,000; 43,000; 82,166
Z09	vibro	free-hi-aggr	5	
Z10	impact		4	phases 1 and 2: LFRT after cycles 1; 10; 100; 1,000 phase 4: extended to 83,550 cycles
Z11	vibro	guided-hi-fix	5	phase 5: extended to 47,000 cycles
Z12	vibro	guided-hi-fix	5	phase 5: extended
Z13	vibro	guided-hi-fix	4	phase 4: extended to 45,000 cycles
Z14	vibro	free-lo	5	
Z15	vibro	guided-lo-fix	5	phase 1: LFRT after cycles 1; 10; 100; 1,000 phase 5: extended to 46,000 cycles
Z16	vibro	guided-lo-fix	5	phase 5: extended to 46,000 cycles

Appendix B Measurement equipment

Table B-1 shows the data acquisition equipment and Table B-2 the sensors used in the model tests.

Table B-1: Data acquisition units

manufacturer	type	measuring range	sample rate	resolution	accuracy
Allnamics	PDR	± 0.1 V	50 kHz	24 bit	0.2 %
National Instruments	SCXI	± 10 V	200 kHz	16 bit	0.1 %
Dewesoft	DW43	$\pm 0.01 .. 10$ V $\pm 10 .. 1000$ mV/V 4 .. 20 mA	200 kHz	24 bit	0.1 %

The Allnamics PDR was used to measure pile forces and motions during pile installations. The National Instruments SCXI System was used to measure soil stresses during preparation of the model soil, pile installation and cyclic lateral load tests as well as lateral loading and pile head displacements during cyclic lateral loading. The Dewesoft DW43 Unit was used for redundant pile force and motion measurements during pile installations and for the lateral frequency response tests.

Table B-2: Sensors

sensor	manufacturer	type	measuring range	frequency range	non-linearity
<i>PDR sensors (pile installation, sampled with Allnamics PDR)</i>					
accelerometer (impact)	Measurement Specialties	EGCS-S055B-5000	$\pm 50,000 \text{ m/s}^2$	DC .. 2,100 Hz	1 %
accelerometer (vibro)	Measurement Specialties	EGCS-S055B-500	$\pm 5,000 \text{ m/s}^2$	DC .. 1,000 Hz	1 %
strain sensor	TLM, Allnamics	FLA-2-350-23 (full bridge)	$\pm 4,000 \text{ }\mu\text{m/m}$	n.a.	1 %
<i>PDM sensors (pile installation, sampled with Dewesoft DW43)</i>					
accelerometer (vibro)	PCB	M353B18	$\pm 5,000 \text{ m/s}^2$	1.0 .. 10 kHz	$\leq 1\% \text{ FS}$
accelerometer (impact)	PCB	M350B04	$\pm 50,000 \text{ m/s}^2$	0.4 .. 10 kHz	$\leq 2\% \text{ FS}$
accelerometer (soil)	Analog Devices	ADXL335	$\pm 36 \text{ m/s}^2$	DC .. 550 Hz	0.3 %
strain gauge	HBM	LY61-10/350	$\pm 1,000 \text{ }\mu\text{m/m}$	n.a.	$\leq 1\%$
cable transducer	Baumer	GCA5	0 .. 4.7 m	n.a.	$\leq 2\% \text{ FS}$
load cell (line pull)	MecSense	T20	0 .. 20 kN	n.a.	0.03 %
<i>dynamic excitation and response sensors (lateral frequency response test, sampled with DW43)</i>					
accelerometer	PCB	3741B1210G	$\pm 100 \text{ m/s}^2$	DC..1,000 Hz	$\leq 1\% \text{ FS}$
impact hammer	PDI	7 lb	n.a.	n.a.	n.a.

Table B-2: Sensors (continued)

<i>pile head sensors (cyclic lateral load testing, sampled with National Instruments SCXI)</i>					
displacement transducer	novotechnik	LS1	0 .. 50 mm 0 .. 100 mm	< 50 Hz	≤ 0.15 % FS
inclinometer	AMOS	AIM 72	±3°	DC .. 3 Hz	0.05 % FS
load cell	HBM	S9M	±50 kN	n.a.	0.02 % FS
measuring amplifier (load cell)	Soemer	DAD 141.1	±3 mV/V	n.a.	≤ 0.03 % resolution 200,000 digits
<i>soil stresses and pore water pressures (preparation of model soil, pile installation, and cyclic lateral load testing, sampled with SCXI)</i>					
earth pressure pad	Glötzl	E10 AU	0 .. 5 bar	< 1 kHz	≤ 0.5 % FS
earth pressure spade	Glötzl	E7/14 AU	0 .. 5 bar	< 1 kHz	≤ 0.5 % FS
pore water pressure transducer	Glötzl	PP3 RS	0 .. 5 bar	< 1 kHz	≤ 0.5 % FS
<i>dynamic excitation and response sensors (lateral frequency response test, sampled with DW43)</i>					
accelerometer	PCB	3741B1210G	±100 m/s ²	DC..1,000 Hz	≤ 1% FS
impact hammer	PDI	7 lb	n.a.	n.a.	n.a.

The load cell used for the cyclic lateral load tests (HBM S9M) was connected to a measuring amplifier (Soemer DAD 141.1) which also served as part of the control unit for the loading device. The amplifier also converted the signal from the load cell (full bridge, [mV/V]) to a voltage signal which was sampled by the National Instruments SCXI data acquisition unit.

Appendix C Test preparation

The following figures show mean values of CPT and DPM readings taken after sand placement of the different tests. CPT readings are available only for tests Z08 and later. Table C-1 shows the gradients of DPM and CPT readings as well as determined relative density D_r where available.

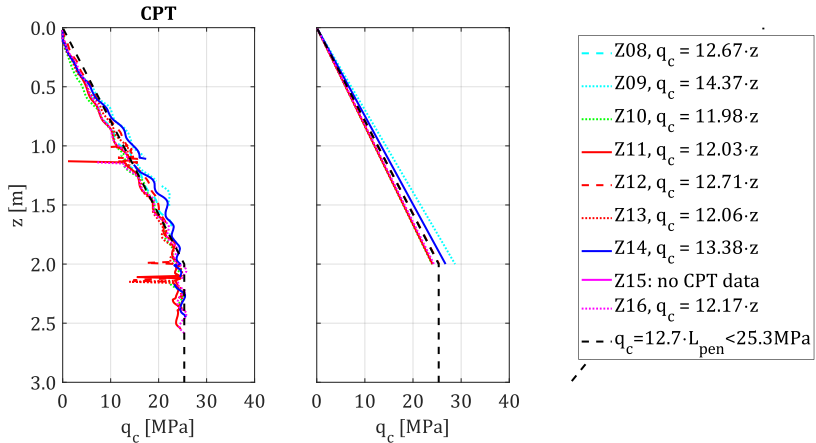


Figure C-1: Mean q_c values from CPT readings (left) and linear regressions (right)

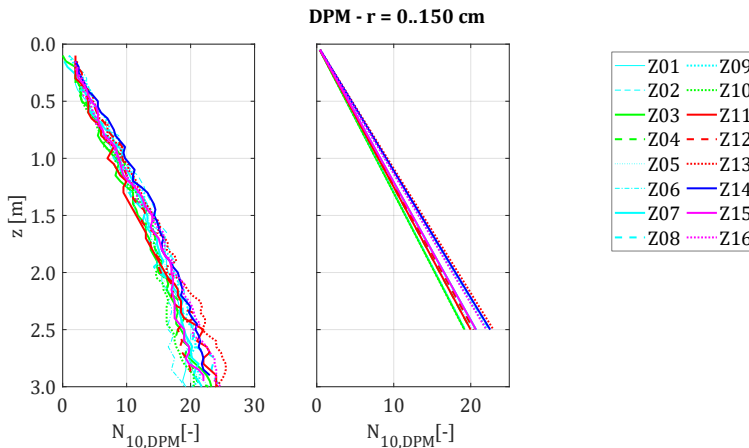


Figure C-2: Mean N_{10} values from DPM soundings (left) and linear regressions (right)

Table C-1: Sand installation quality

test	$D_{r,sample}$ [-]	$\delta N_{10,DPM}/\delta z$ [1/m]	$\delta q_c/\delta z$ [MPa/m]
Z01	0.762	8.31	--
Z02	0.739	8.95	--
Z03	0.742	7.68	--
Z04	--	7.99	--
Z05	--	8.12	--
Z06	--	8.39	--
Z07	--	8.73	--
Z08	--	8.75	12.7
Z09	0.701	9.19	14.4
Z10	--	8.03	12.0
Z11	--	7.99	12.0
Z12	--	9.12	12.7
Z13	--	9.18	12.1
Z14	--	9.40	13.4
Z15	--	8.62	--
Z16	--	8.81	12.2
mean	0.736	8.65	12.7

Appendix D Pile installation

Vibratory installation records

The following figures show installation records of vibratory pile installations, grouped by installation variant, in analogy to Figure 6-3.

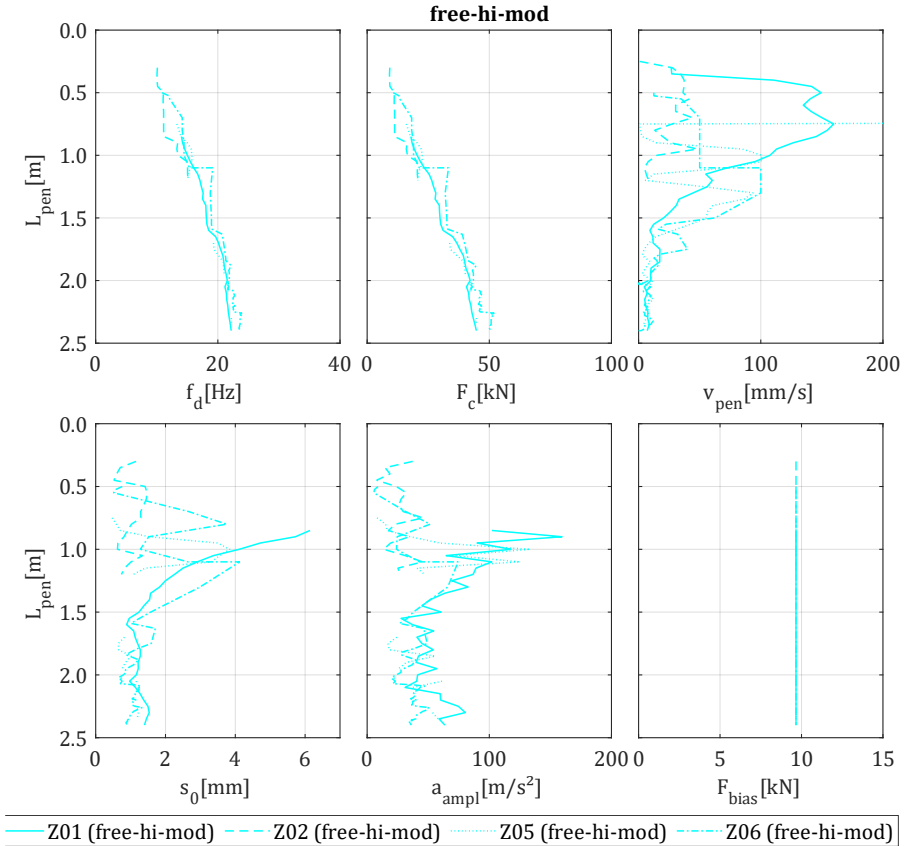


Figure D-1: Installation records of free vibratory driven piles with high eccentric moment and moderate frequency control

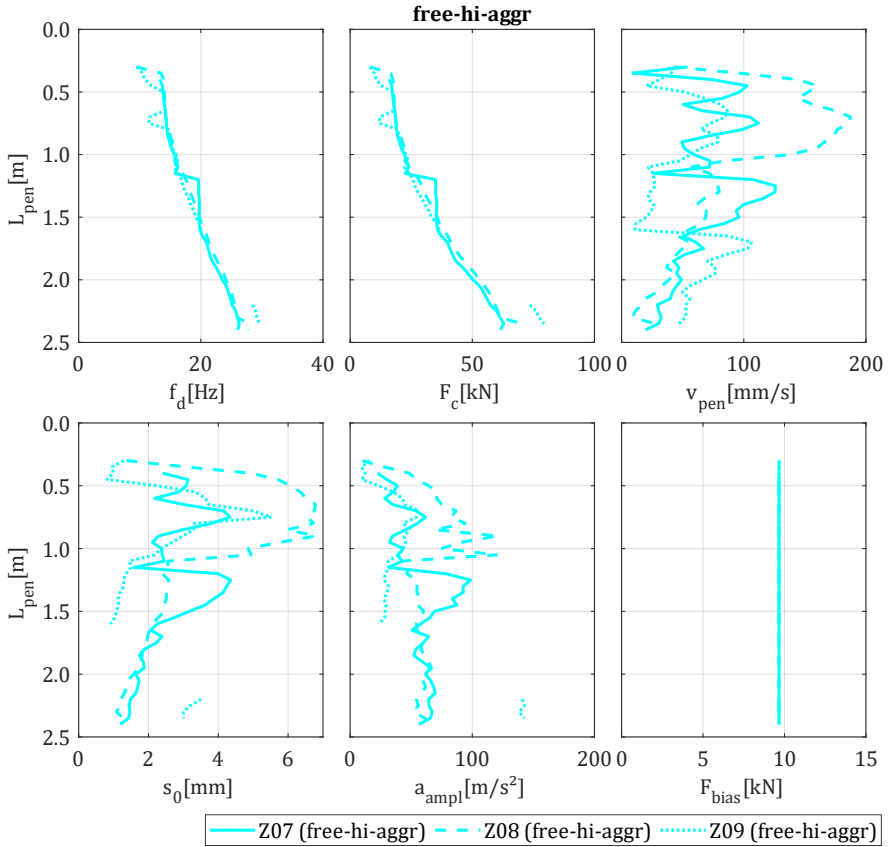
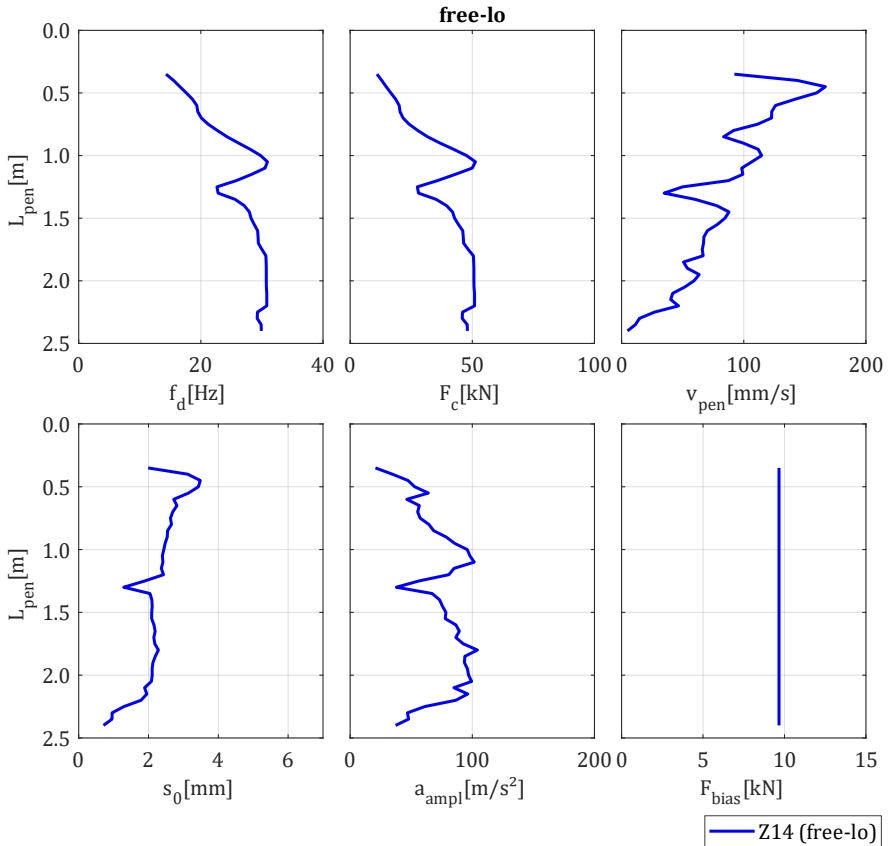


Figure D-2: Installation records of free vibratory driven piles with high eccentric moment and aggressive frequency control



**Figure D-3: Installation record of free vibratory driven pile
with low eccentric moment**

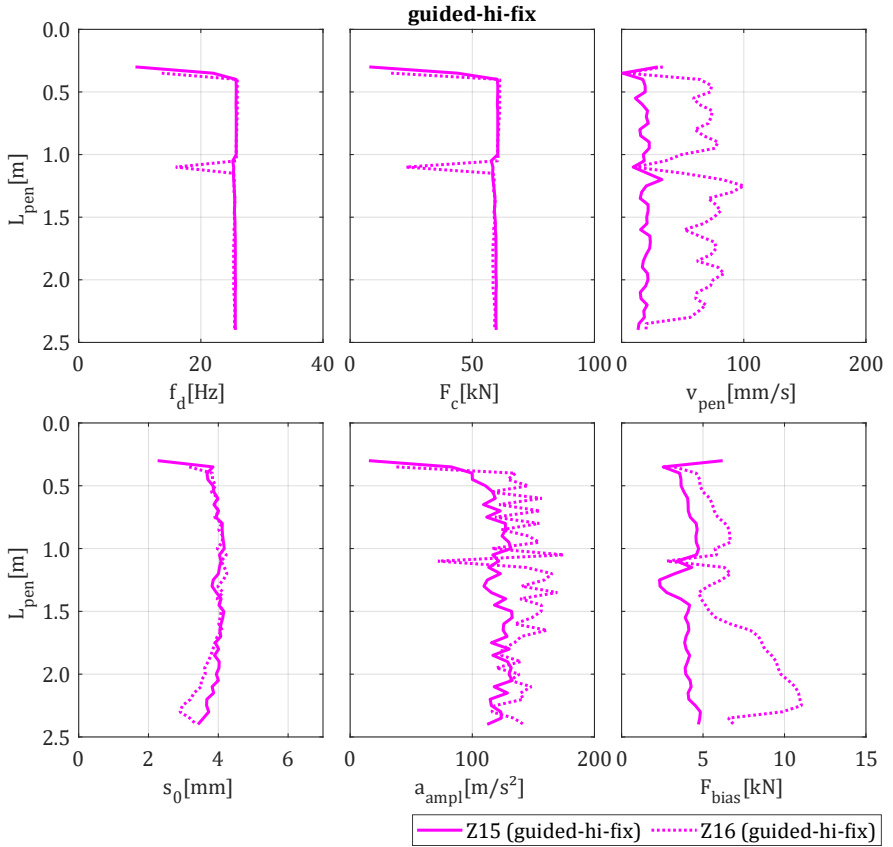


Figure D-4: Installation records of crane-guided vibratory driven piles with high eccentric moment

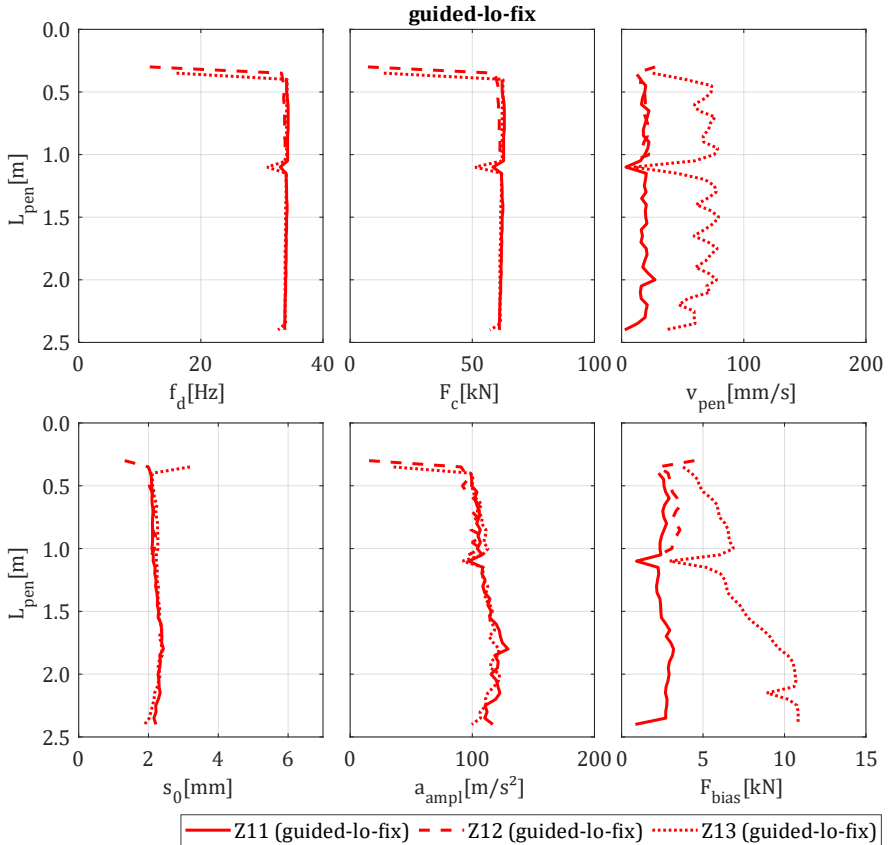


Figure D-5: Installation records of crane-guided vibratory driven piles with low eccentric moment

The penetration speed v_{pen} of crane guided piles (Z11, Z12, Z13, Z15, Z16) is almost constant as the penetration speed is limited by the crane. Note that piles Z13 and Z16 were intentionally installed with higher crane speed. For these piles, the bias force F_{bias} increases with pile penetration as an increasing portion of the dead weight $G_{pile+vibro}$ is carried by the soil resistance and the line pull F_{line} decreases.

Soil stress development

The following figures show the development of effective radial soil stresses σ'_{rad} measured at different levels over pile penetration L_{pen} during pile installation processes of all tests in analogy to Figure 6-2.

During the installation of pile Z02, a malfunction of the cable transducer measuring the pile penetration occurred. Due to an unfortunate positioning of the camera, the pile and soil measurements could only be matched very roughly with the pile penetration.

For the installation of pile Z05, the synchronisation of pile and soil measurements was not satisfactory.

During the installation of pile Z07 ($L_{pen} < 1.6$ m), the sample rate of the soil stress measurements was accidentally set to 1 Hz instead of 100 Hz, so the resolution in this part are very low.

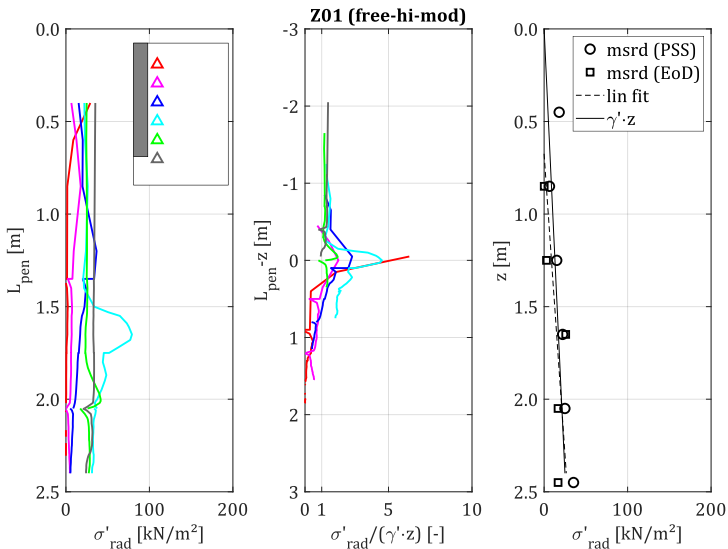


Figure D-6: Soil stress development due to vibratory driving of pile Z01

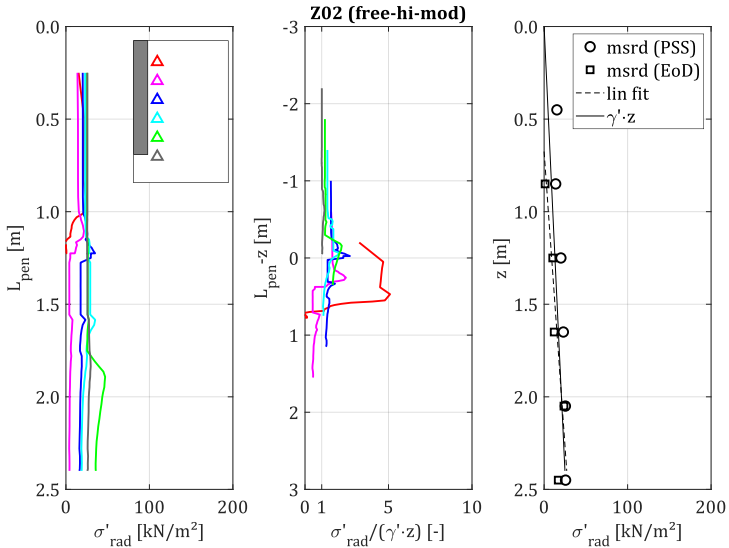


Figure D-7: Soil stress development due to vibratory driving of pile Z02

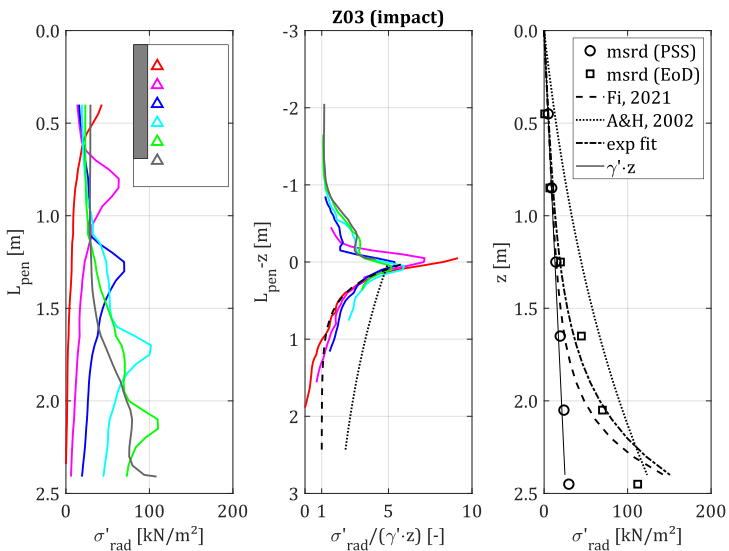


Figure D-8: Soil stress development due to impact driving of pile Z03

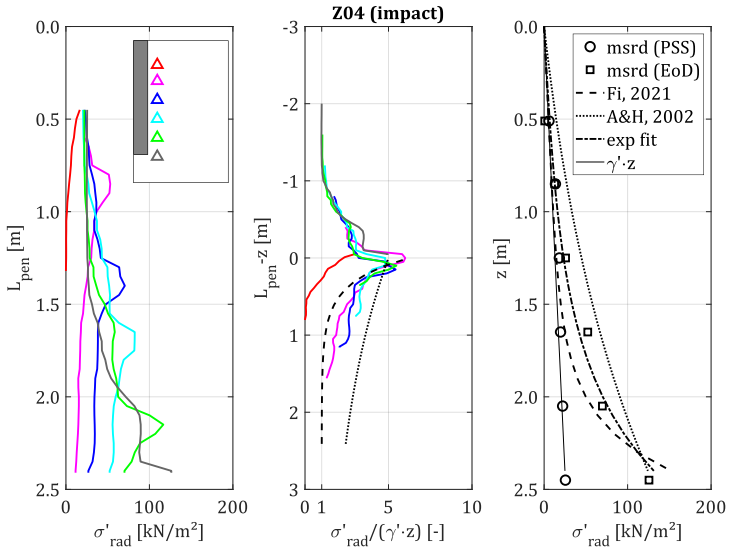


Figure D-9: Soil stress development due to impact driving of pile Z04

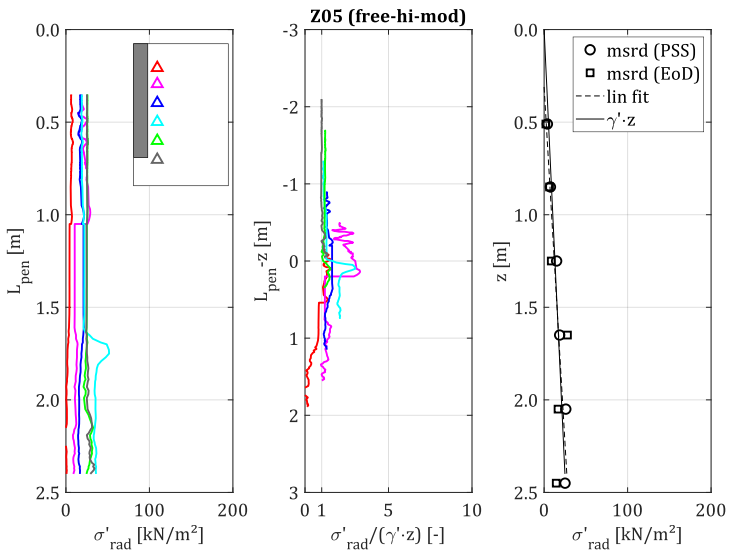


Figure D-10: Soil stress development due to vibratory driving of pile Z05

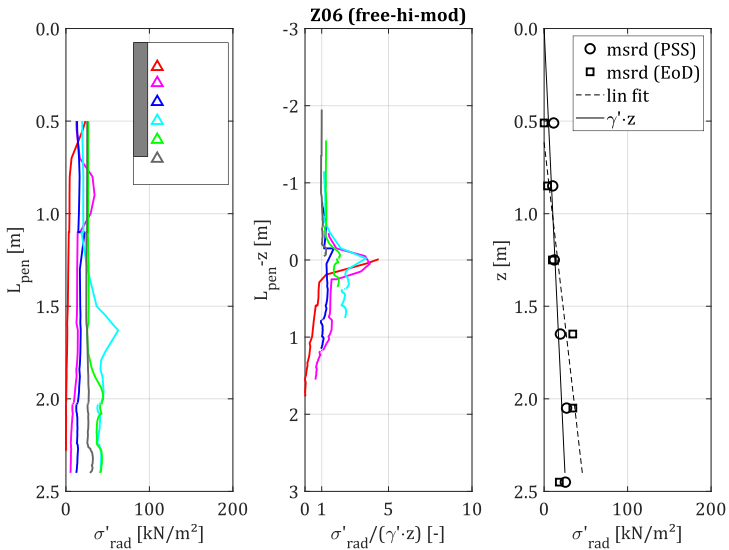


Figure D-11: Soil stress development due to vibratory driving of pile Z06

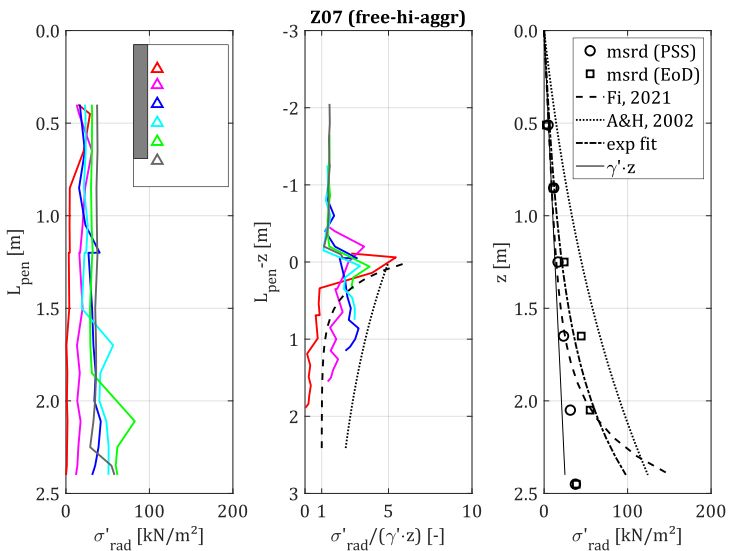


Figure D-12: Soil stress development due to vibratory driving of pile Z07

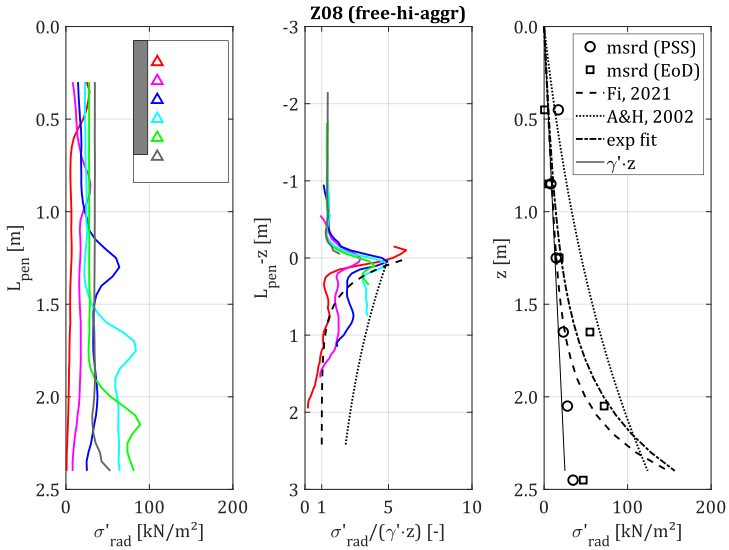


Figure D-13: Soil stress development due to vibratory driving of pile Z08

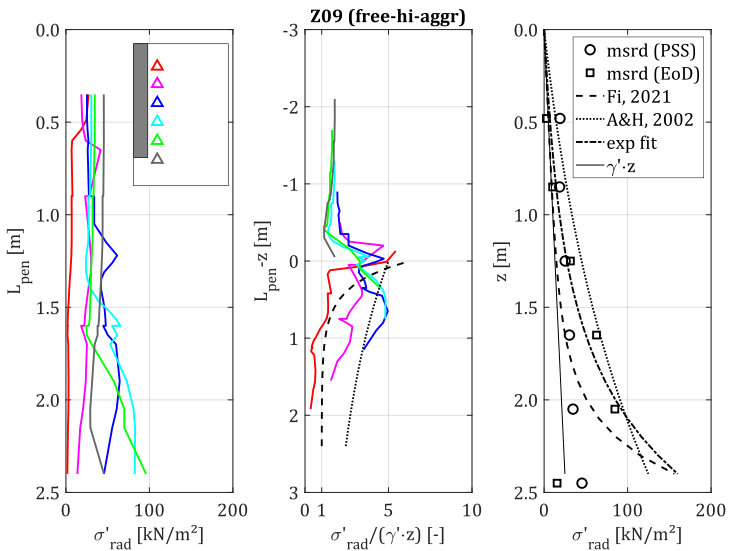


Figure D-14: Soil Stress development due to vibratory driving of pile Z09

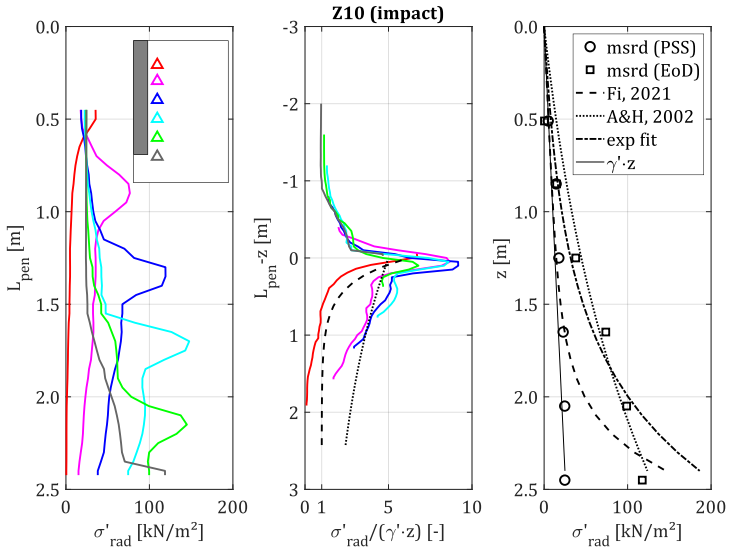


Figure D-15: Soil stress development due to impact driving of pile Z10

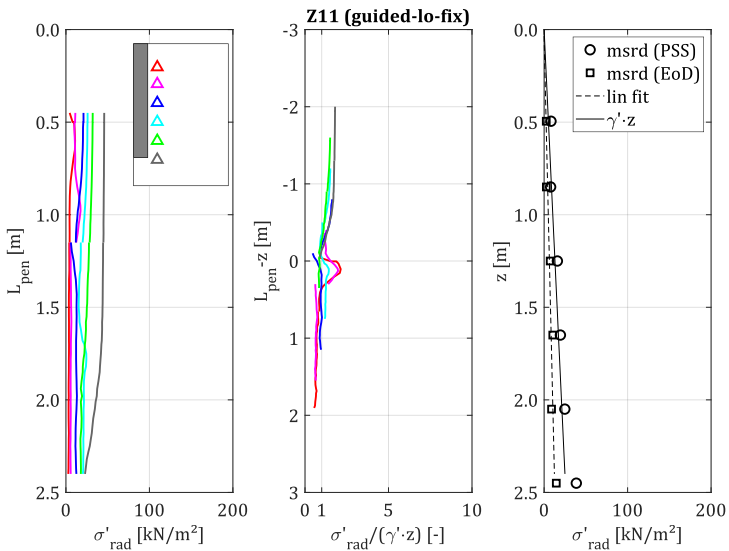


Figure D-16: Soil Stress development due to vibratory driving of pile Z11

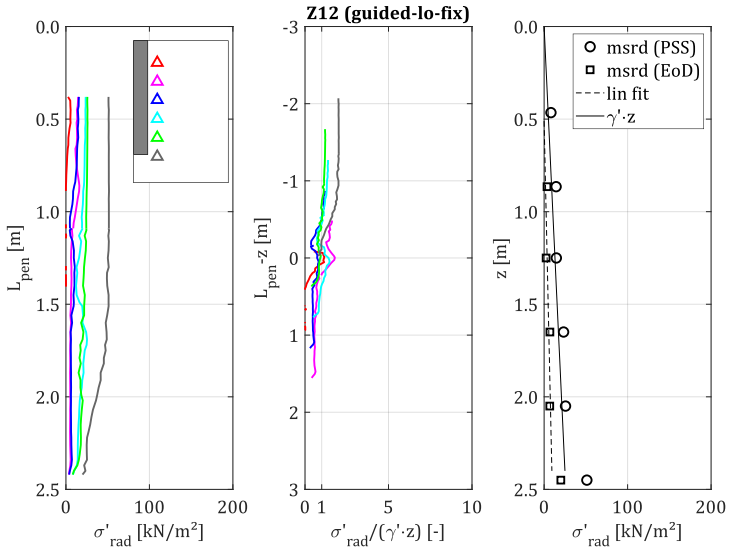


Figure D-17: Soil stress development due to vibratory driving of pile Z12

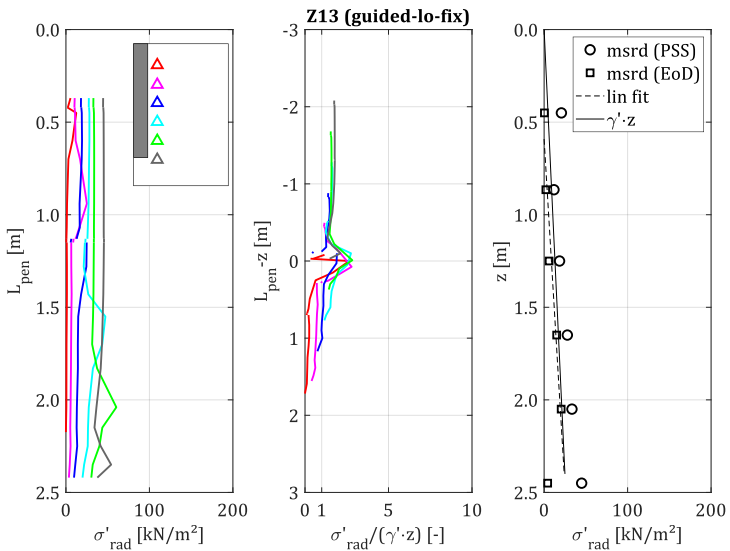


Figure D-18: Soil stress development due to vibratory driving of pile Z13

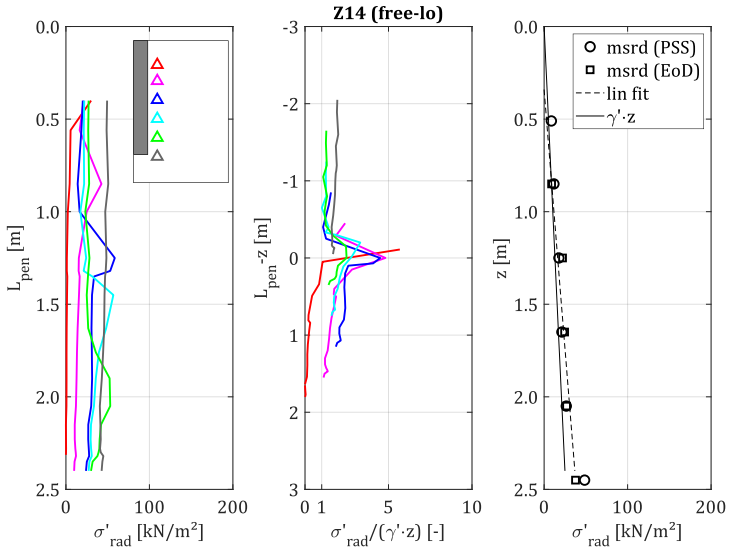


Figure D-19: Soil stress development due to vibratory driving of pile Z14

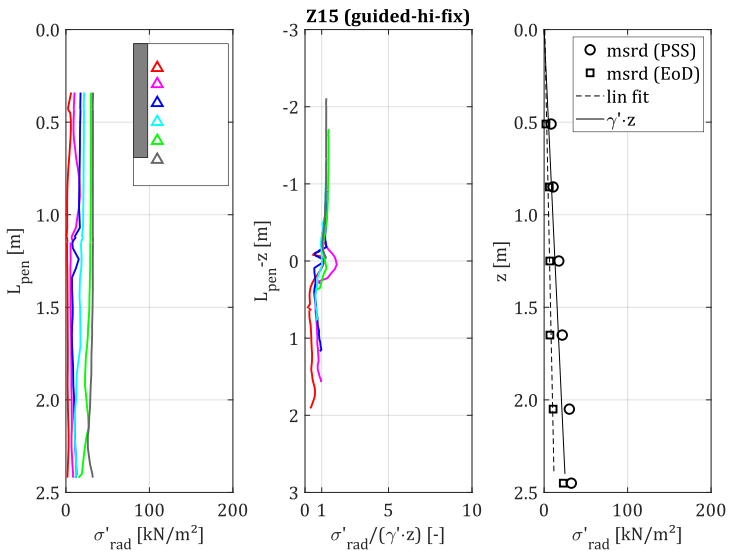


Figure D-20: Soil stress development due to vibratory driving of pile Z15

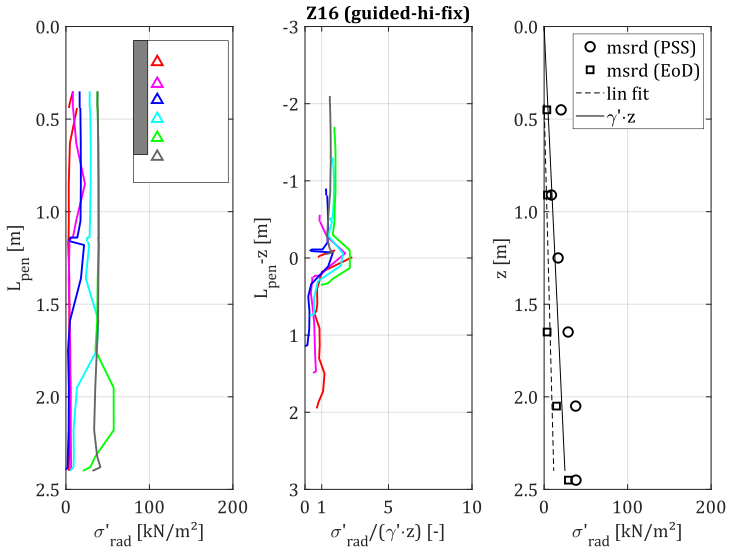


Figure D-21: Soil stress development due to vibratory driving of pile Z16

Imprinted soil stresses after pile installation

The following table shows regression parameters α_{pen} and β_{PSS} according to Equation (6-2), describing the shape of the soil stress profile after pile installation:

Table D-1: Soil stress state after pile installation

test	installation method	group [$M_e \cdot f_d \cdot v_{\text{pen}}$]	α_{pen} [-]	$1/\beta_{\text{PSS}}$ [-]	R^2 [-]	line style
Z01	vibro	hi-lo-free	-1.49	0.92	0.63	—
Z02	vibro	hi-lo-free	-1.85	0.96	0.94	- -
Z03	impact		2.06	6.38	0.79	—
Z04	impact		1.46	5.33	0.73	- -
Z05	vibro	hi-lo-free	-2.73	1.00	0.37	...
Z06	vibro	hi-lo-free	-3.36	1.00	0.45	- .
Z07	vibro	hi-hi-free	1.33	3.97	0.72	—
Z08	vibro	hi-hi-free	1.94	6.46	0.72	- -
Z09	vibro	hi-hi-free	1.39	6.41	0.81	...
Z10	impact		1.31	7.68	0.76	...
Z11	vibro	lo-hi-guided	-0.07	0.52	0.04	—
Z12	vibro	lo-hi-guided	-0.44	0.54	0.53	- -
Z13	vibro	lo-hi-guided	-1.12	0.89	0.87	...
Z14	vibro	lo-hi-free	1.48	1.72	0.13	—
Z15	vibro	hi-lo-guided	0.06	0.47	0.02	—
Z16	vibro	hi-lo-guided	0.06	0.34	0.01	- -

Eigenfrequency determination

To estimate the axial eigenfrequency of the pile-soil system analytically, the one-dimensional model (Figure 2-3) is further simplified to a single-element model. As justified before, the pile can be regarded as a rigid body for vibratory driving (not for impact driving!). The mass of the pile can be concentrated in a single point mass. To deal with possible yielding of the soil springs (cf. Figure 2-3) the following approach was used: In case of displacement amplitudes $s_0 = M_e/m_{dyn} \leq s_q$, a linear elastic spring with spring stiffness $E_{qs} = R_{stat}/s_q$ was used. In case of higher displacement amplitudes $s_0 > s_q$, the secant stiffness $E_{qs,sec} = R_{stat}/s_0$ was used as modified spring stiffness. This procedure leads to softer springs and is applicable at low penetration depths (where s_q has low values) and for vibro hammers with high eccentric moments (where s_0 has large values). The left diagrams in Figure D-22 show the soil spring stiffness at the pile shaft $E_{qs,s}$ over depth z . The black lines depict the basic soil model parameters, while the coloured lines show the modified spring stiffness for the different vibro hammers.

The soil springs are combined to one linear-elastic spring with the spring stiffness E_{inst} . Crane support and soil damping is neglected. Thus, the eigenfrequencies of the undamped systems $f_{0,inst}$ yield

$$f_{0,inst} = \frac{1}{2\pi} \cdot \sqrt{E_{inst}/m_{dyn}} \tag{D-1}$$

$$E_{inst} = \int E_{qs} dz \tag{D-2}$$

with different dynamic masses of the system for the M3 and M23/M23A vibratory hammers.

Since the (total) spring stiffnesses increase with pile penetration, the eigenfrequencies of the pile-soil systems change likewise, as shown in Figure D-22:

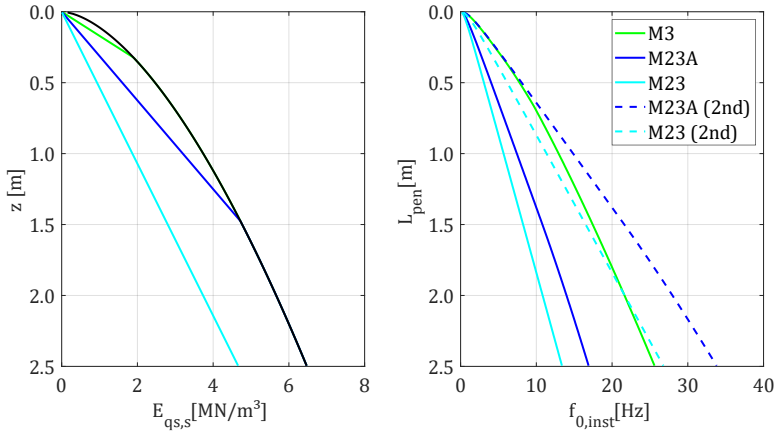


Figure D-22: Spring stiffness of the soil model (left) and eigenfrequencies of the vibro-pile-soil system (right) over penetration depth for different vibro hammers

The estimated eigenfrequencies are of course sensitive to the chosen soil model. Details of the soil model can be found in STEIN (2018) For the interface stiffness $E_{q,s}$, a stress dependent soil stiffness according to OHDE (1939) was used:

$$E_{oed} = E_{oed,ref} \cdot p_{ref} \cdot \left(\frac{\gamma' \cdot z}{p_{ref}} \right)^{\lambda_{Eoed}} \quad (D-3)$$

with $E_{oed,ref} = 300 \text{ kPa}$; $\lambda_{Eoed} = 0.6$

With respect to the frequency ranges of the used vibratory hammers (cf. Table 5-7) it is likely that vibratory driving may take place at the 2nd harmonic ($\approx 2 \cdot f_{0,inst}$). It should also be considered that damping effects leads to lower eigenfrequencies.

For an experimental estimation of the system's eigenfrequency, pile extractions after tests Z06, Z09 and Z10 were carried out. The hammer frequency was varied over a wide range (sweep) while the pile was held at a constant penetration depth by the crane. The excitation of the pile and the hammer as well as the response of the soil were measured using accelerometers mounted at the pile head and embedded in the sand in different depths ($z = 0.4 \text{ m}, 1.2 \text{ m}, 2.0 \text{ m}$). The sweeps were divided into windows of one second and analysed in the frequency domain using a fast Fourier transform to find acceleration magnitudes for different excitation

frequencies. As the magnitude of the hammer and pile excitation a_{pile} depends on the driving frequency f_d (Equation (2-11)), the magnitude of the response a_{soil} is expected to be influenced likewise. Therefore, the measured soil acceleration was divided by the pile acceleration. The following Figure D-23 shows the normalised soil response $a_{\text{soil}}/a_{\text{pile}}$ over the frequency range of the sweeps f_d for different sensor depths during the extraction of the model pile after test Z09 using the APE Model 3 vibratory hammer at a pile penetration of $L_{\text{pen}} \approx 2$ m.

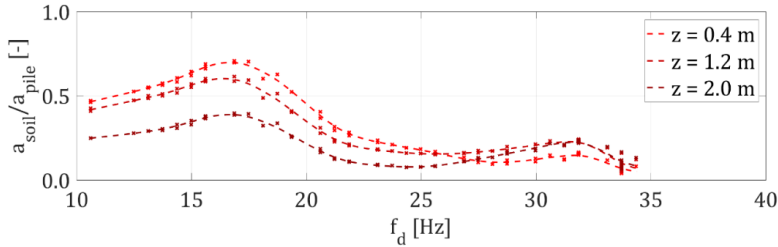


Figure D-23: Normalised soil acceleration over excitation frequency

A local maximum of the soil response spectra can be found for an excitation frequency of about 17 Hz. Sweeps in different depths were analysed the same way but it has to be admitted that the plots were not always as clear as shown in Figure D-23. Additionally, during free pile installation using the unmodified Model 23 vibratory hammer, possible resonance effects were experienced at certain combinations of pile penetration and driving frequency. The whole test pit seemed to shake for some seconds which could later be retraced by videos of the installation process.

Figure D-24 shows the resonance frequencies observed during pile extractions (void shapes) and installations (other markers); colours indicate the used vibro hammers. For the extraction of tests Z06 and Z09 with the Model 3 hammer (green) as well as for the installations of tests Z07, Z08 and Z09 with the Model 23 hammer (cyan) good agreements can be seen. Data from one extraction and one installation with the modified hammer Model 23A from tests Z10 and Z14 is available as well (blue). The resonance observed during the installation of test Z14 ($L_{\text{pen}} = 1.4$ m, $f_d = 28$ Hz, Model 23A) is about twice as high compared to the resonance during the extraction of test Z10 ($L_{\text{pen}} = 1.6$ m, $f_d = 14$ Hz, Model 23A). Maybe the resonance observed at 28 Hz was the 2nd harmonic, thus the first harmonic would lie close to one half of 28 Hz which would fit good to the data from Z10.

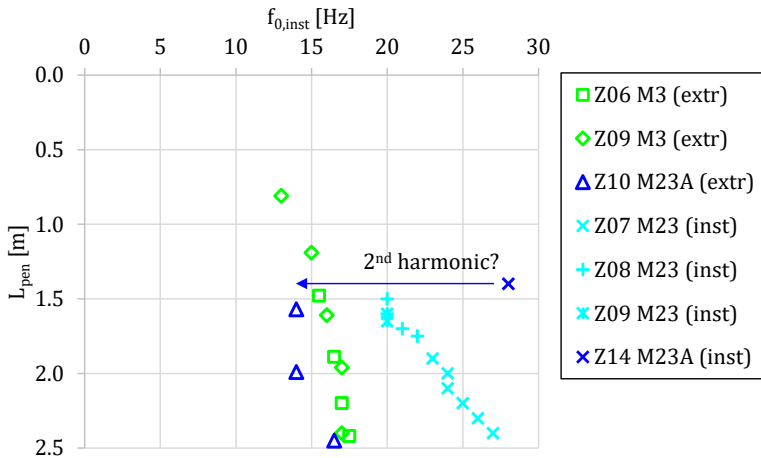


Figure D-24: Evaluation of pile-soil response over depth

The vibro hammers show different resonance profiles over depth which can be explained by different oscillation amplitudes caused by the eccentric moment (see Equation (2-13)) and different dynamic masses of the vibratory hammers. Similar to the analytical courses (Figure D-22), an increase of the eigenfrequencies $f_{0,inst}$ with depth can be seen.

A quantitative comparison of the observed resonances (Figure D-24) with the theoretical natural frequencies (Figure D-22) gives poor agreement. The most striking deviation is the fact that the dynamic system with the Model 23 hammer has the lowest theoretical eigenfrequency (due to the high eccentric moment M_e , thus a high displacement amplitude s_0 and a modification of the spring stiffness E_{qs}) while the highest resonant frequencies were observed. As with the resonance encountered during the installation of test Z14, the resonances observed during installation with the Model 23 vibro hammer shown in Figure D-24 may be higher harmonics, which would give reasonable fit with the simulated eigenfrequencies.

Due to the large discrepancies and uncertainties the experimental and analytical courses of the systems' eigenfrequencies seem not be suited for further evaluation. However, a major influence of penetration depth and vibratory equipment is unquestionable. Thus, the declaration of one fixed value for the soil or system eigenfrequency is not justified. It seems to be more reasonable to use the phase shift Φ_F as indicator for the proximity to resonance.

Appendix E Quasi-static lateral pile behaviour

Lateral pile head displacement

The following figures show the load-displacement behaviour of the first loading period of each test of the different test groups. Measured values are donated as markers, fitted curves are drawn as lines.

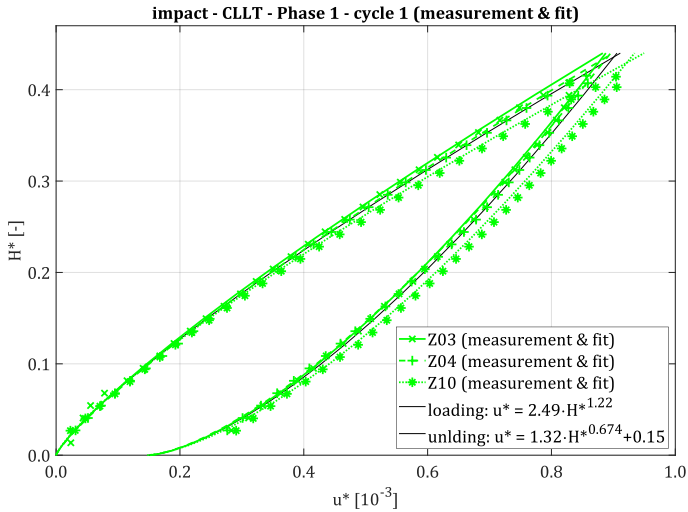


Figure E-1: Quasi-static load displacement behaviour of impact driven piles at beginning of phase 1

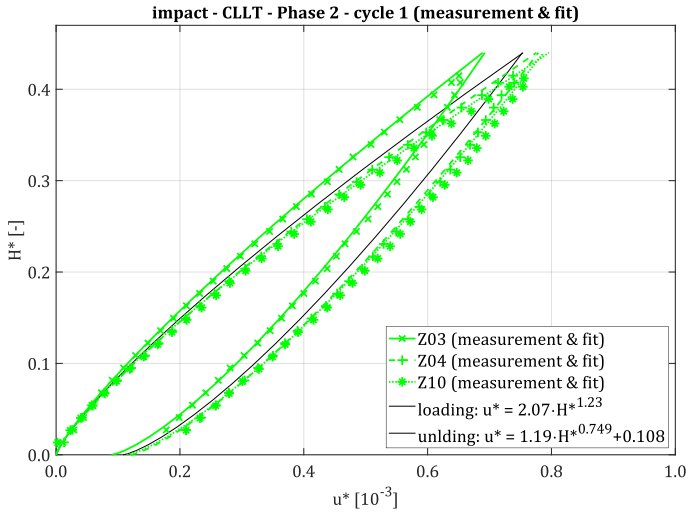


Figure E-2: Quasi-static load displacement behaviour of impact driven piles at beginning of phase 2

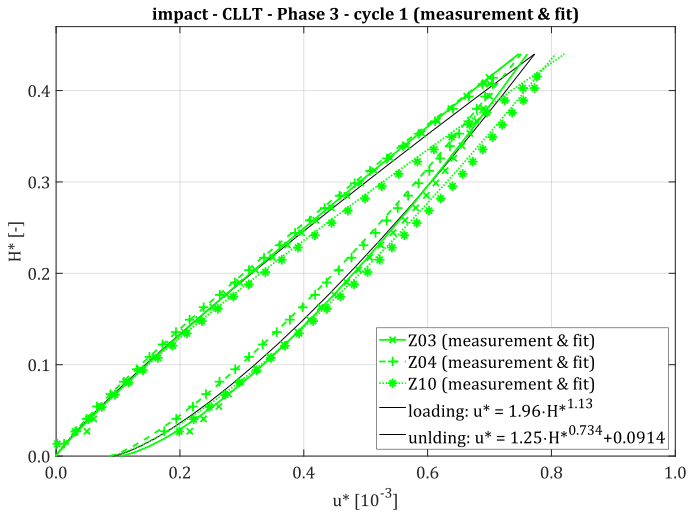


Figure E-3: Quasi-static load displacement behaviour of impact driven piles at beginning of phase 3

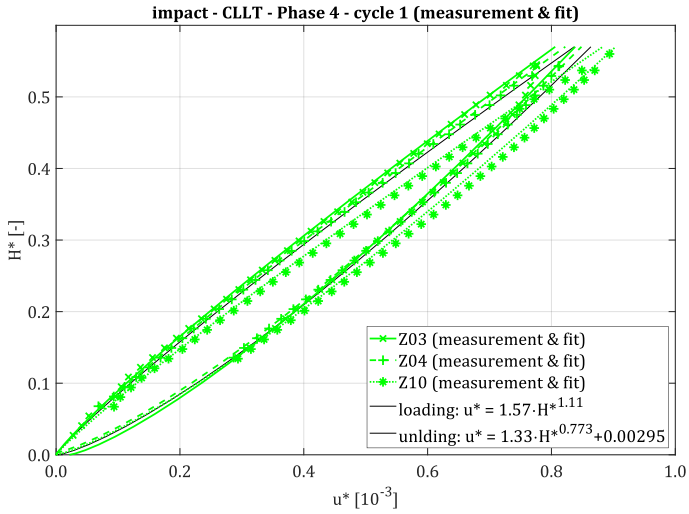


Figure E-4: Quasi-static load displacement behaviour of impact driven piles at beginning of phase 4

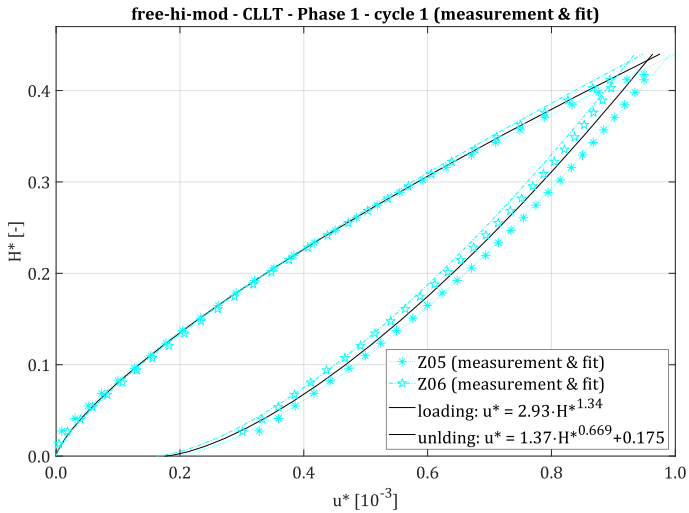


Figure E-5: Quasi-static load displacement behaviour of free vibratory driven piles with high eccentric moment and 'moderate' frequency control at beginning of phase 1

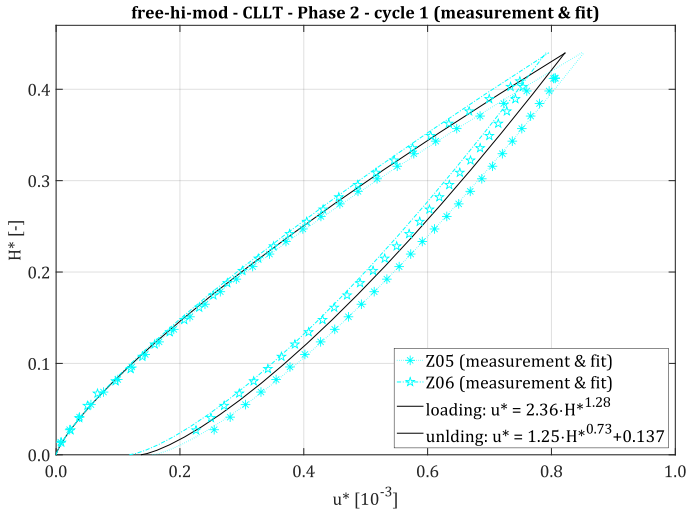


Figure E-6: Quasi-static load displacement behaviour of free vibratory driven piles with high eccentric moment and 'moderate' frequency control at beginning of phase 2

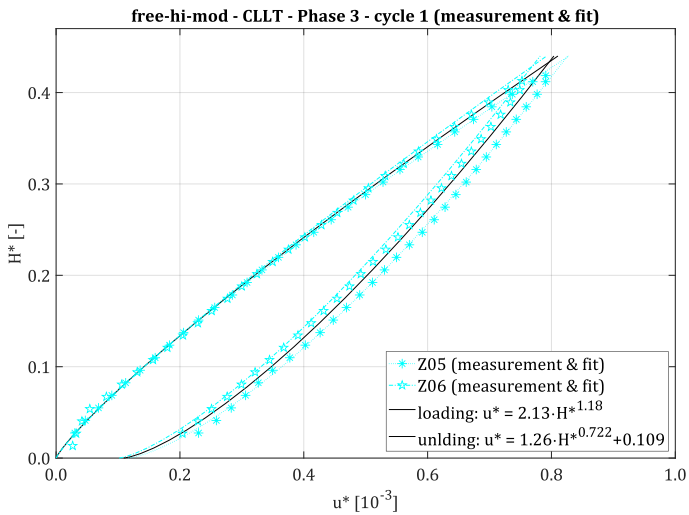


Figure E-7: Quasi-static load displacement behaviour of free vibratory driven piles with high eccentric moment and 'moderate' frequency control at beginning of phase 3

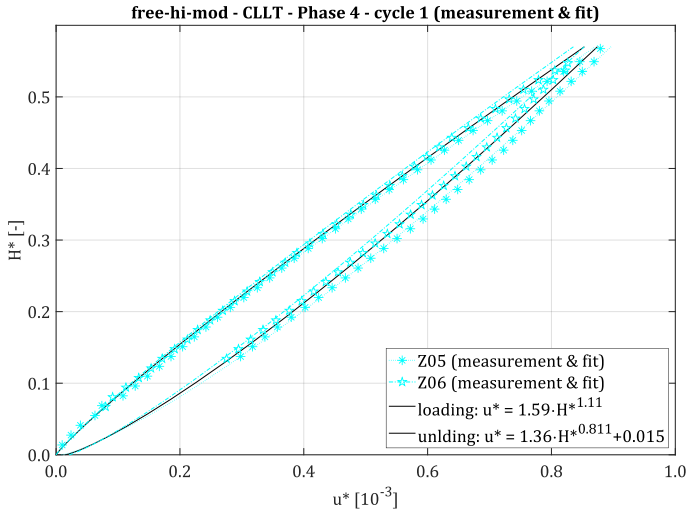


Figure E-8: Quasi-static load displacement behaviour of free vibratory driven piles with high eccentric moment and 'moderate' frequency control at beginning of phase 4

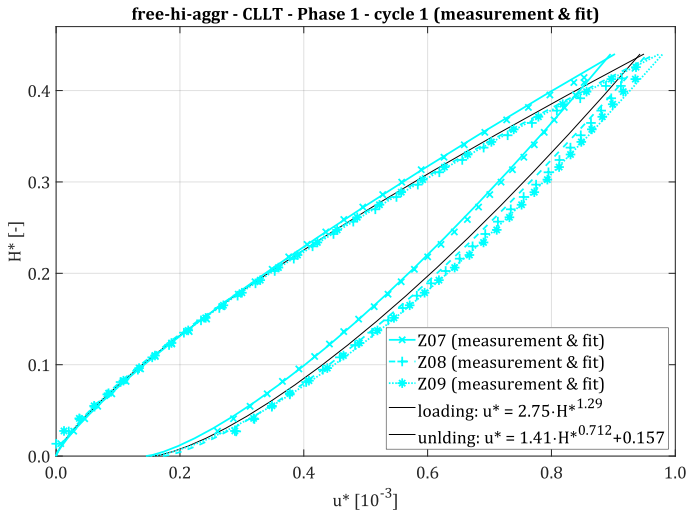


Figure E-9: Quasi-static load displacement behaviour of free vibratory driven piles with high eccentric moment and 'aggressive' frequency control at beginning of phase 1

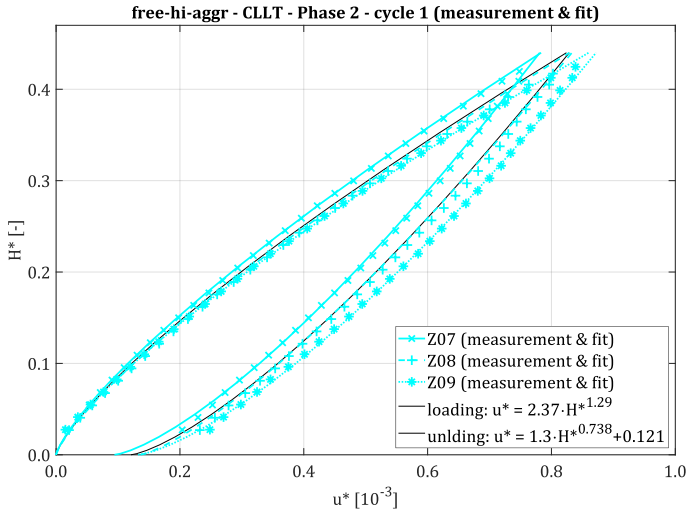


Figure E-10: Quasi-static load displacement behaviour of free vibratory driven piles with high eccentric moment and 'aggressive' frequency control at beginning of phase 2

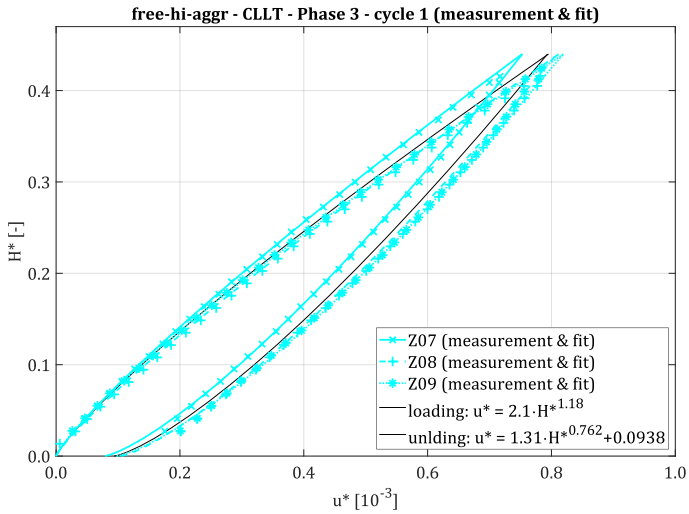


Figure E-11: Quasi-static load displacement behaviour of free vibratory driven piles with high eccentric moment and 'aggressive' frequency control at beginning of phase 3

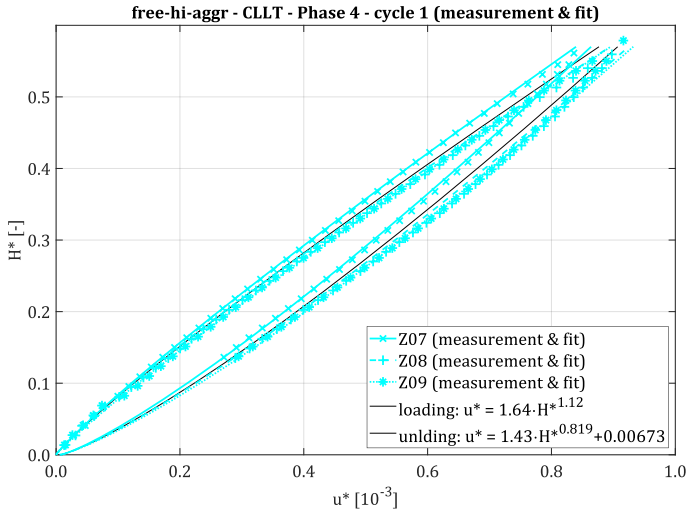


Figure E-12: Quasi-static load displacement behaviour of free vibratory driven piles with high eccentric moment and 'aggressive' frequency control at beginning of phase 4

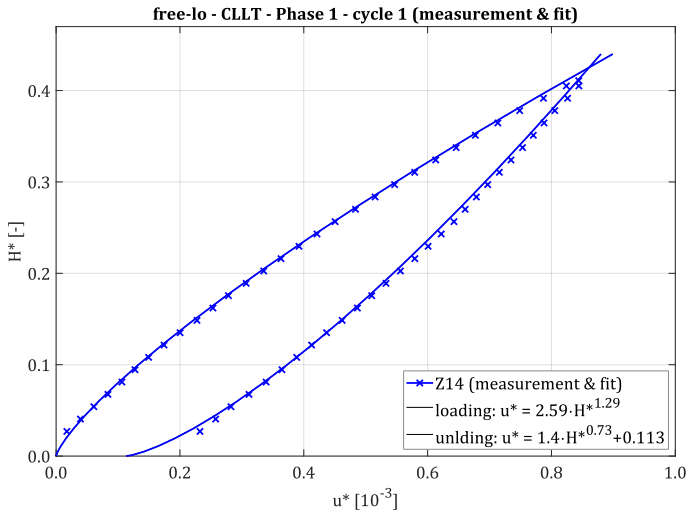


Figure E-13: Quasi-static load displacement behaviour of free vibratory driven pile with low eccentric moment at beginning of phase 1

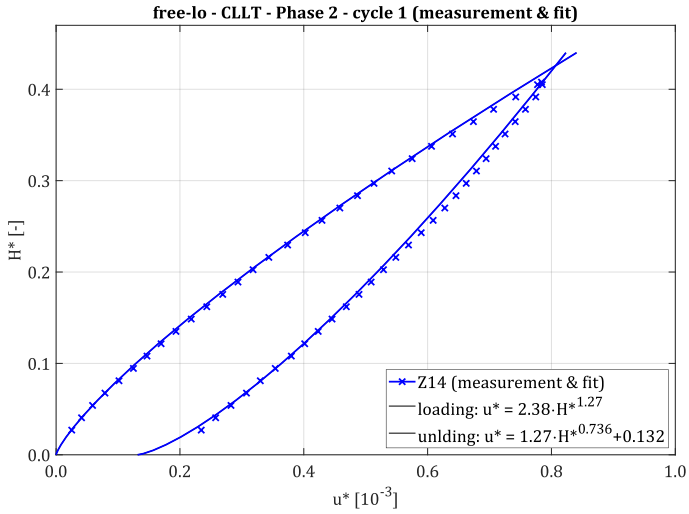


Figure E-14: Quasi-static load displacement behaviour of free vibratory driven pile with low eccentric moment at beginning of phase 2

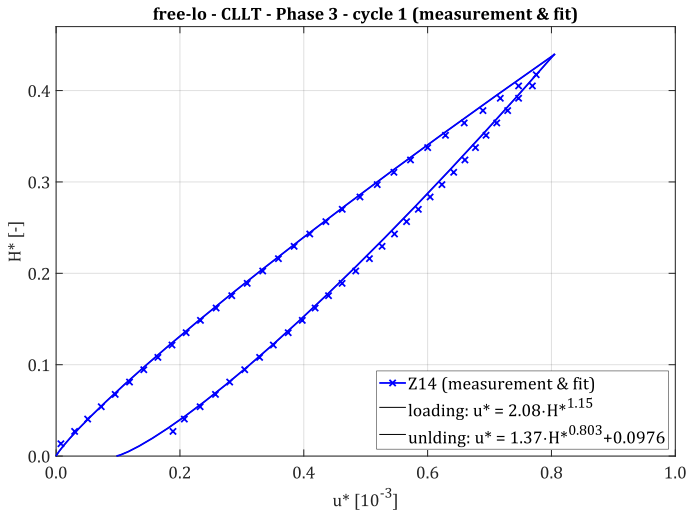


Figure E-15: Quasi-static load displacement behaviour of free vibratory driven pile with low eccentric moment at beginning of phase 3

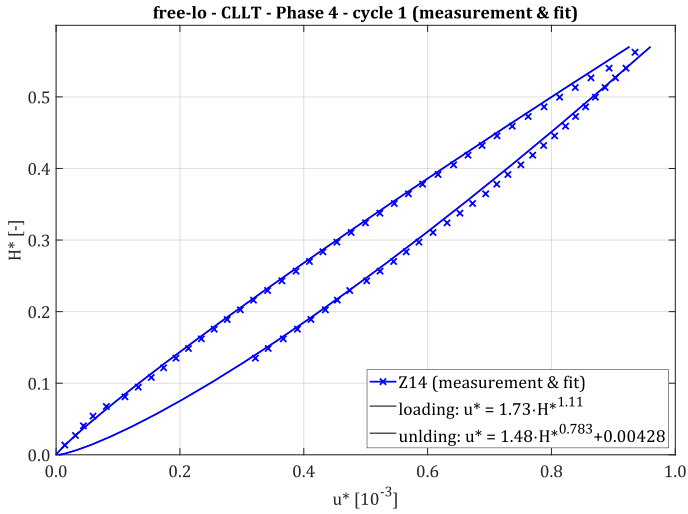


Figure E-16: Quasi-static load displacement behaviour of free vibratory driven pile with low eccentric moment at beginning of phase 4

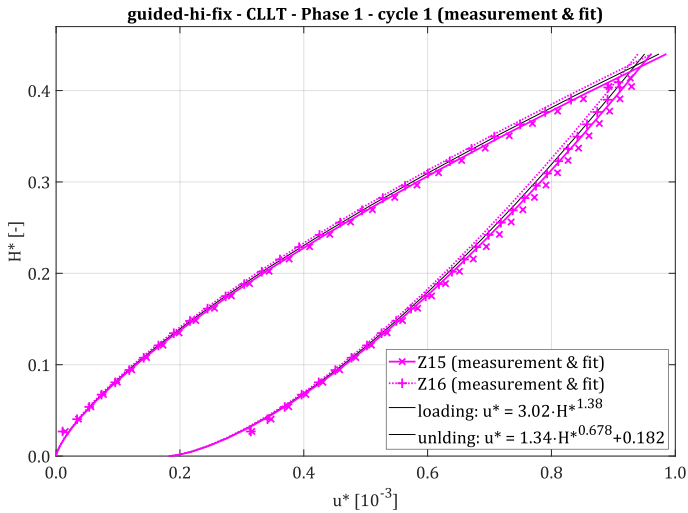


Figure E-17: Quasi-static load displacement behaviour of guided vibratory driven piles with high eccentric moment at beginning of phase 1

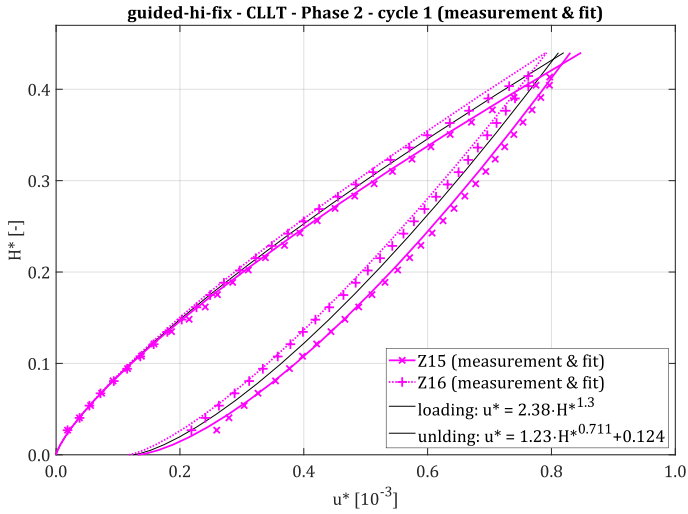


Figure E-18: Quasi-static load displacement behaviour of guided vibratory driven piles with high eccentric moment at beginning of phase 2

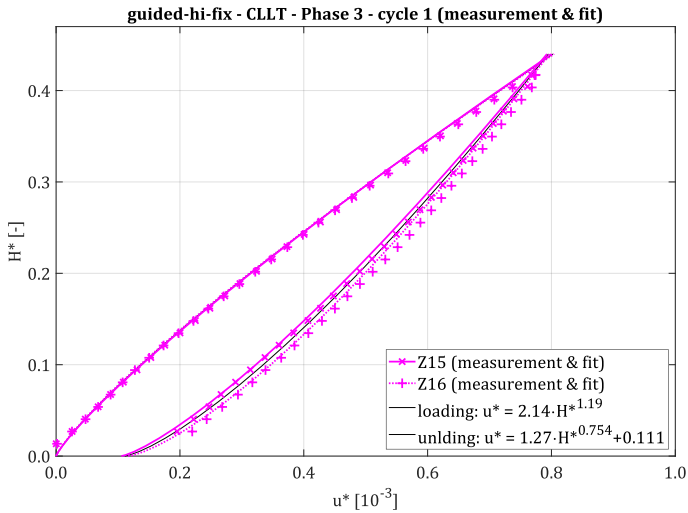


Figure E-19: Quasi-static load displacement behaviour of guided vibratory driven piles with high eccentric moment at beginning of phase 3

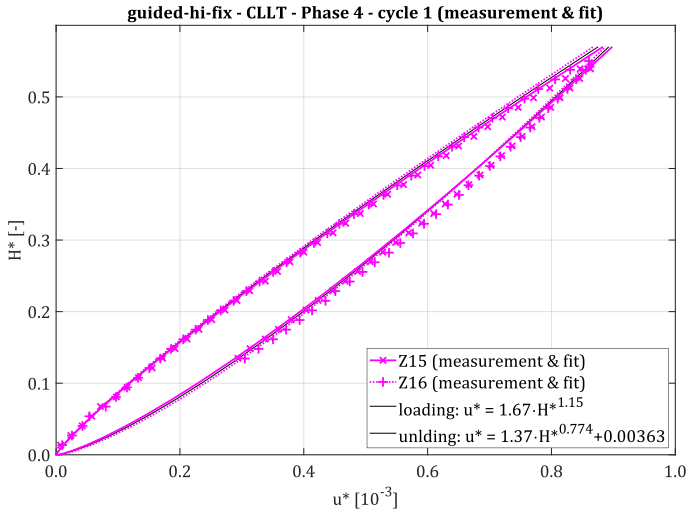


Figure E-20: Quasi-static load displacement behaviour of guided vibratory driven piles with high eccentric moment at beginning of phase 4

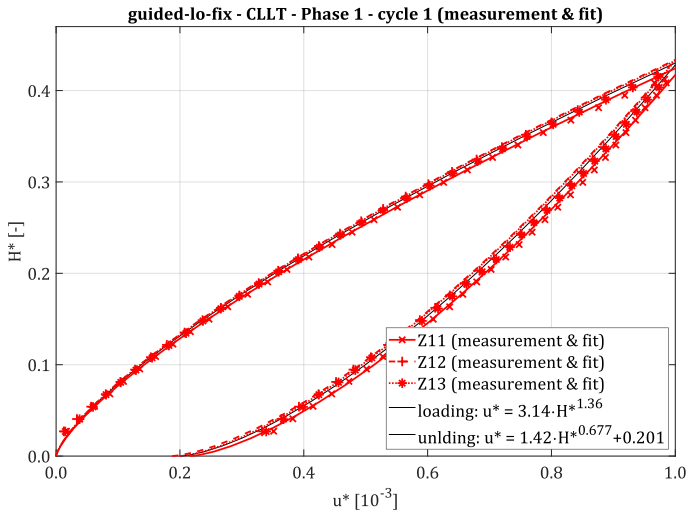


Figure E-21: Quasi-static load displacement behaviour of guided vibratory driven piles with low eccentric moment at beginning of phase 1

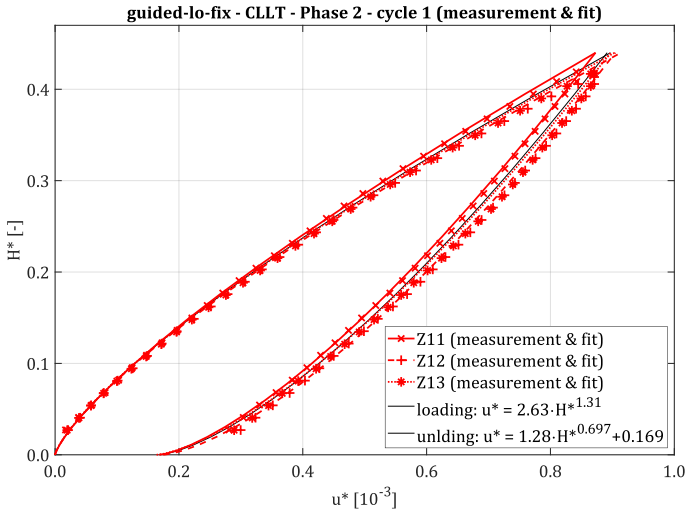


Figure E-22: Quasi-static load displacement behaviour of guided vibratory driven piles with low eccentric moment at beginning of phase 2

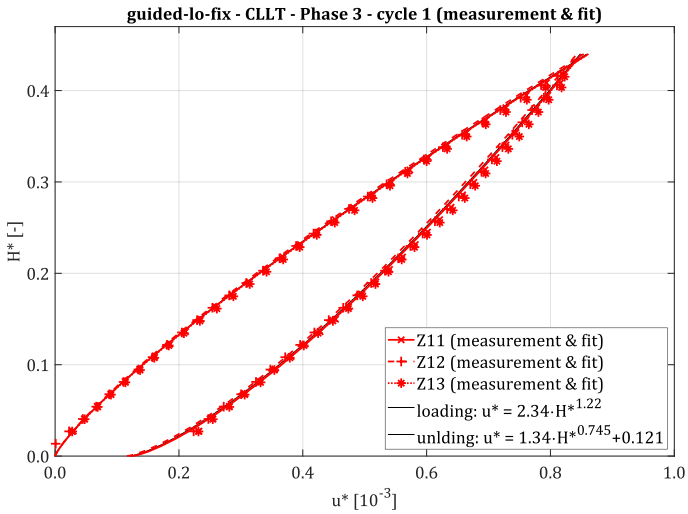


Figure E-23: Quasi-static load displacement behaviour of guided vibratory driven piles with low eccentric moment at beginning of phase 3

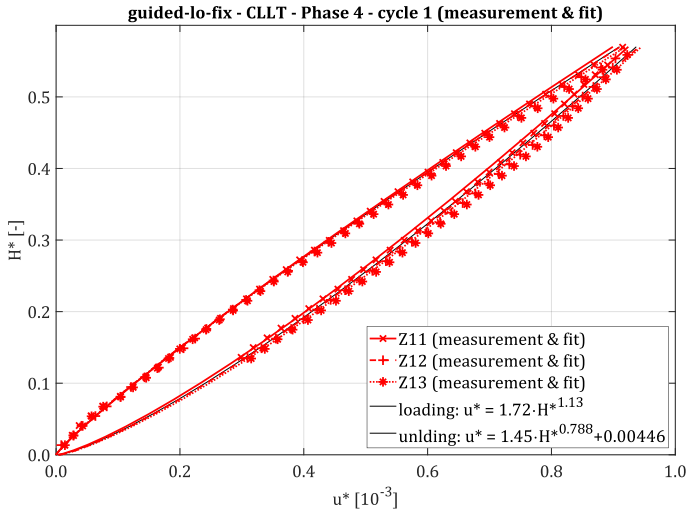


Figure E-24: Quasi-static load displacement behaviour of guided vibratory driven piles with low eccentric moment at beginning of phase 4

The following table gives the corresponding fitting parameters for all tests.

Table E-1: Fitted parameters for load-displacement curves (all tests, CLLT, phases 1-4, cycle 1)

	phase 1				phase 2				phase 3				phase 4							
	loading		unloading		loading		unloading		loading		unloading		loading		unloading					
	u_{ref}^* [10 ⁻³]	κ [-]	u_{perm}^* [10 ⁻³]	κ [-]	u_{ref}^* [10 ⁻³]	κ [-]	u_{perm}^* [10 ⁻³]	κ [-]	u_{ref}^* [10 ⁻³]	κ [-]	u_{perm}^* [10 ⁻³]	κ [-]	u_{ref}^* [10 ⁻³]	κ [-]	u_{perm}^* [10 ⁻³]	κ [-]				
Z01	2.97	1.45	1.36	0.66	1.14	2.50	1.41	1.31	0.82	0.16	2.18	1.26	1.27	0.77	0.10	1.50	1.14	1.40	0.86	0.07
Z02	2.98	1.34	1.39	0.61	1.14	2.23	1.33	1.17	0.71	0.09	2.05	1.23	1.22	0.76	0.10	1.55	1.20	1.32	0.71	-0.07
Z03	2.39	1.21	1.28	0.67	1.15	1.85	1.21	1.10	0.74	0.09	1.84	1.10	1.17	0.70	0.10	1.52	1.13	1.26	0.77	0.02
Z04	2.42	1.21	1.31	0.69	1.15	2.12	1.23	1.23	0.76	0.12	1.92	1.15	1.25	0.77	0.09	1.54	1.12	1.32	0.76	-0.01
Z05	3.09	1.38	1.40	0.67	1.19	2.46	1.29	1.28	0.74	0.16	2.21	1.19	1.27	0.71	0.12	1.63	1.11	1.38	0.79	0.01
Z06	2.78	1.31	1.33	0.66	1.16	2.26	1.27	1.22	0.72	0.12	2.05	1.16	1.24	0.73	0.10	1.56	1.11	1.33	0.84	0.02
Z07	2.51	1.25	1.36	0.72	1.15	2.26	1.29	1.25	0.73	0.09	1.96	1.17	1.26	0.76	0.08	1.57	1.11	1.36	0.82	0.01
Z08	2.87	1.32	1.42	0.72	1.17	2.36	1.28	1.31	0.77	0.14	2.12	1.17	1.32	0.77	0.10	1.70	1.14	1.46	0.82	0.01
Z09	2.87	1.31	1.46	0.69	1.15	2.50	1.30	1.34	0.72	0.13	2.21	1.21	1.34	0.75	0.10	1.66	1.10	1.46	0.81	0.01
Z10	2.65	1.25	1.36	0.66	1.15	2.22	1.25	1.25	0.75	0.11	2.12	1.15	1.31	0.73	0.09	1.64	1.10	1.41	0.79	0.00
Z11	3.18	1.35	1.42	0.68	1.22	2.52	1.29	1.26	0.71	0.17	2.34	1.22	1.34	0.74	0.13	1.69	1.12	1.44	0.80	0.00
Z12	3.13	1.36	1.42	0.67	1.19	2.69	1.32	1.28	0.69	0.17	2.33	1.23	1.34	0.74	0.12	1.72	1.14	1.46	0.79	0.01
Z13	3.13	1.36	1.42	0.68	1.20	2.66	1.32	1.30	0.69	0.16	2.34	1.22	1.35	0.75	0.12	1.75	1.14	1.46	0.78	0.00
Z14	2.59	1.29	1.40	0.73	1.11	2.38	1.27	1.27	0.74	0.13	2.08	1.15	1.37	0.80	0.10	1.73	1.11	1.48	0.78	0.00
Z15	3.04	1.37	1.36	0.68	1.18	2.49	1.31	1.22	0.68	0.13	2.12	1.19	1.30	0.78	0.11	1.69	1.15	1.40	0.79	0.00
Z16	2.99	1.38	1.32	0.68	1.18	2.26	1.28	1.24	0.74	0.12	2.16	1.20	1.24	0.73	0.12	1.66	1.15	1.35	0.76	0.00
impact	2.49	1.22	1.32	0.67	1.15	2.07	1.23	1.19	0.75	0.11	1.96	1.13	1.25	0.73	0.09	1.57	1.11	1.33	0.77	0.00
free-hi-aggr	2.75	1.29	1.41	0.71	1.16	2.37	1.29	1.30	0.74	0.12	2.10	1.18	1.31	0.76	0.09	1.64	1.12	1.43	0.82	0.01
free-lo	2.59	1.29	1.40	0.73	1.11	2.38	1.27	1.27	0.74	0.13	2.08	1.15	1.37	0.80	0.10	1.73	1.11	1.48	0.78	0.00
guided-hi-fix	3.02	1.38	1.34	0.68	1.18	2.38	1.30	1.23	0.71	0.12	2.14	1.19	1.27	0.75	0.11	1.67	1.15	1.37	0.77	0.00
guided-lo-fix	3.14	1.36	1.42	0.68	1.20	2.63	1.31	1.28	0.70	0.17	2.34	1.22	1.34	0.75	0.12	1.72	1.13	1.45	0.79	0.00

The following figures show diagrams of the parameters u^*_{ref} and κ for the loading phase of the first cycle of phases 1, 2, and 3.

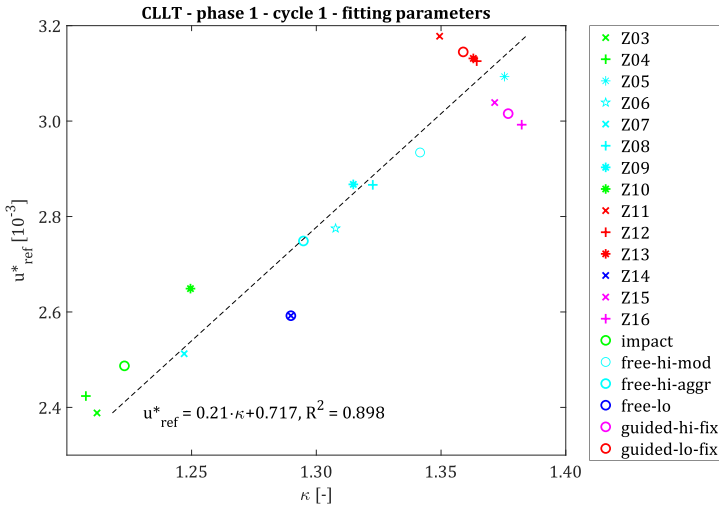


**Figure E-25: Fitted parameters for load-displacement curves
(all tests and test groups, CLLT, phase 1, cycle 1)**

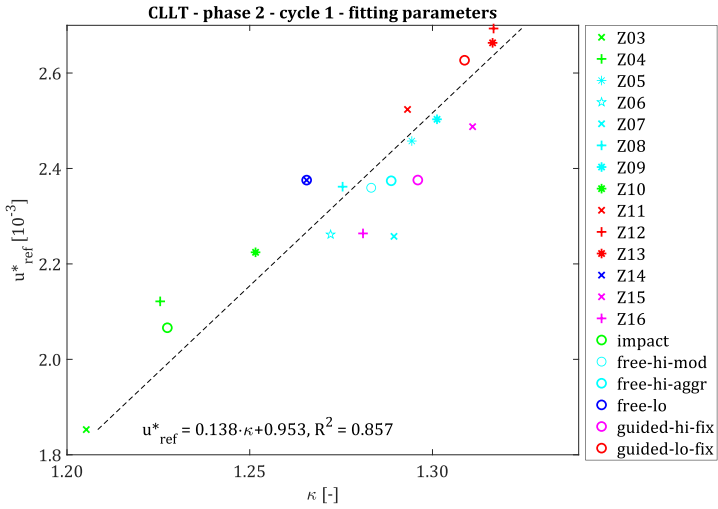


**Figure E-26: Fitted parameters for load-displacement curves
(all tests and test groups, CLLT, phase 2, cycle 1)**

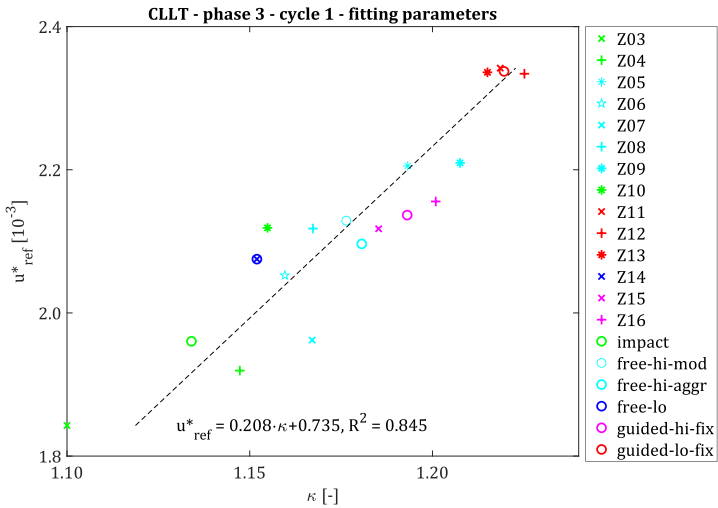


**Figure E-27: Fitted parameters for load-displacement curves
(all tests and test groups, CLLT, phase 3, cycle 1)**

Maximum soil reaction

The following figures show the soil reaction profile over depth at maximum load level of the first cycle of phases 1, 3 and 4. Differences of the measured effective soil stresses $\Delta\sigma'$ compared to the stress state before loading ($H = 0$) are plotted. Soil stresses in upwind direction, downwind direction and resultants are shown from left to right. Each figure shows one test group. Phases 2 and 5 are not shown as not enough sensor levels are available in the corresponding loading direction.

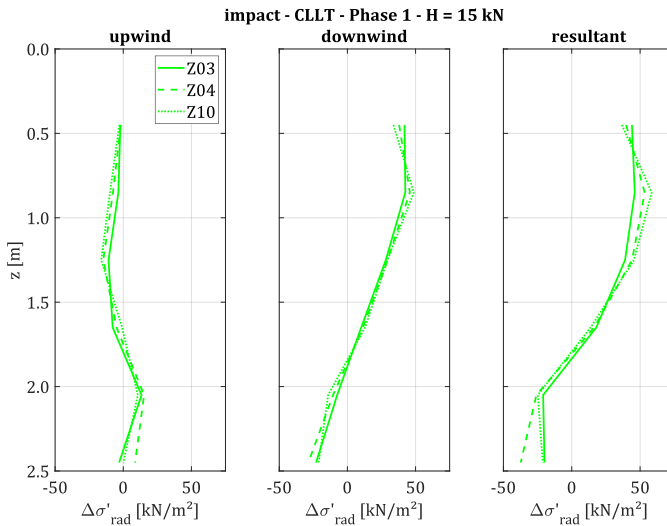
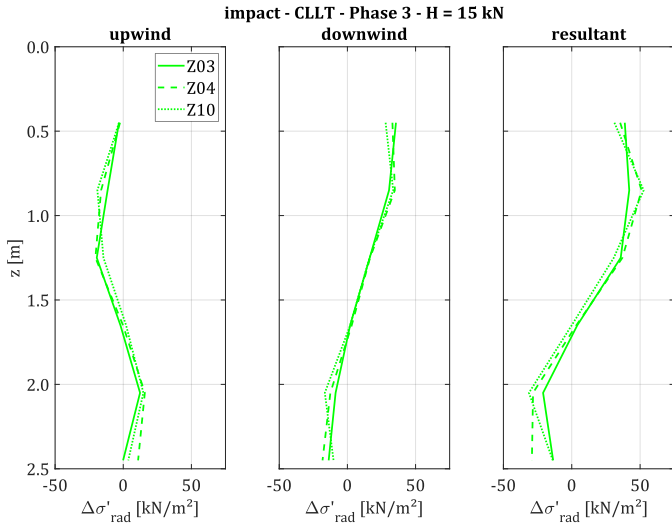
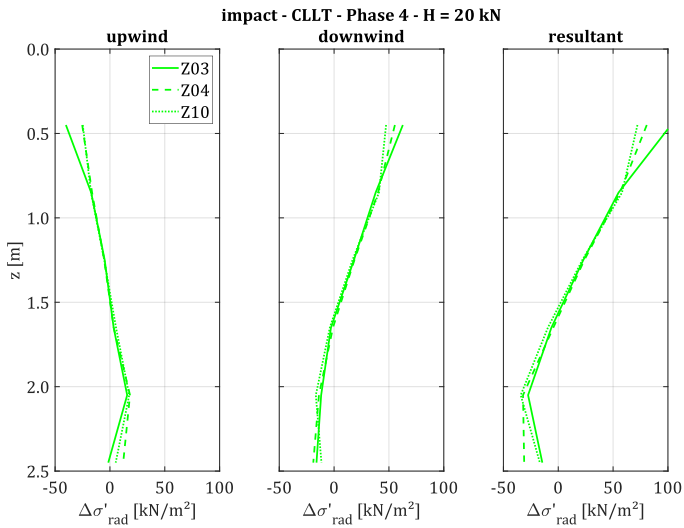


Figure E-28: Soil reaction of impact driven piles at maximum load level of the first loading cycle of phase 1



**Figure E-29: Soil reaction of impact driven piles
at maximum load level of the first loading cycle of phase 3**



**Figure E-30: Soil reaction of impact driven piles
at maximum load level of the first loading cycle of phase 4**

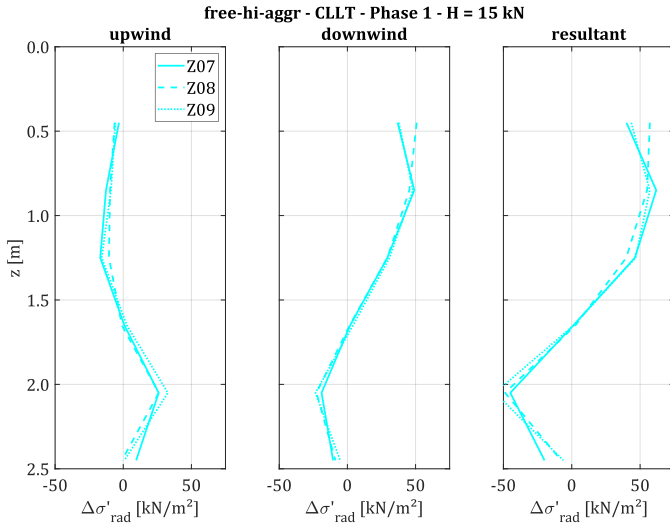


Figure E-31: Soil reaction of free vibratory driven piles with high eccentric moment and 'aggressive' frequency control at maximum load level of the first loading cycle of phase 1

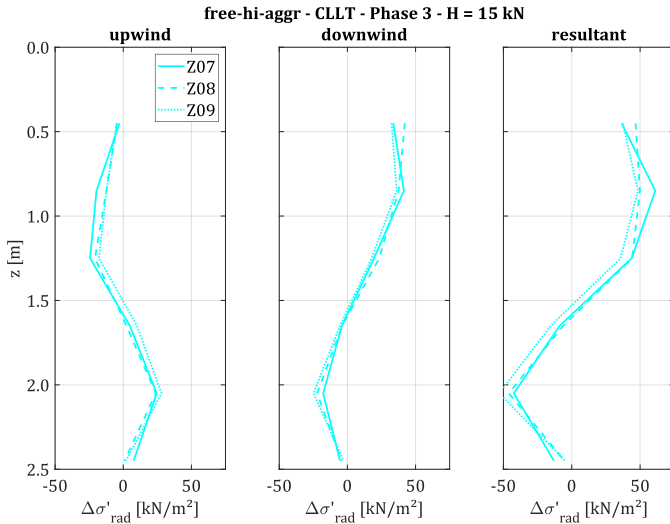


Figure E-32: Soil reaction of free vibratory driven piles with high eccentric moment and 'aggressive' frequency control at maximum load level of the first loading cycle of phase 3

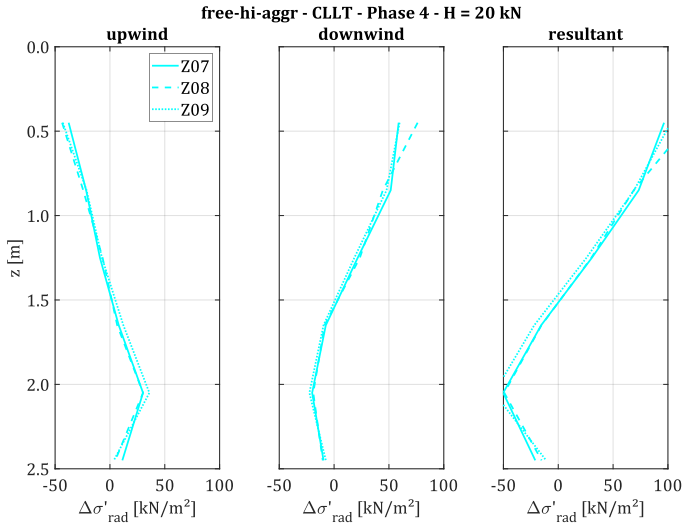


Figure E-33: Soil reaction of free vibratory driven piles with high eccentric moment and 'aggressive' frequency control at maximum load level of the first loading cycle of phase 4

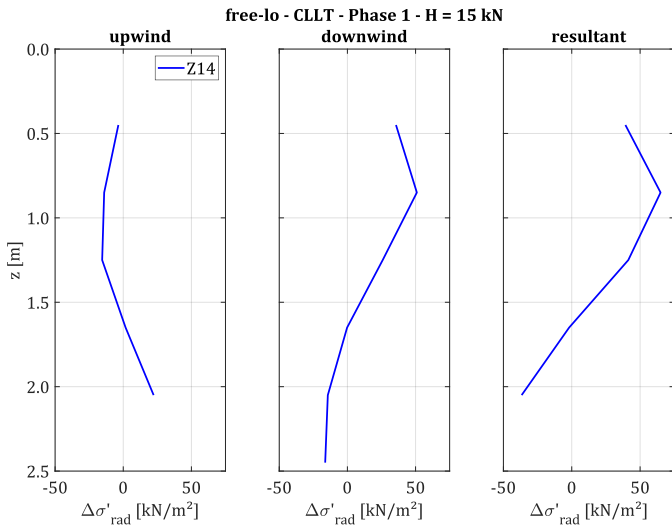


Figure E-34: Soil reaction of free vibratory driven pile with low eccentric moment at maximum load level of the first loading cycle of phase 1

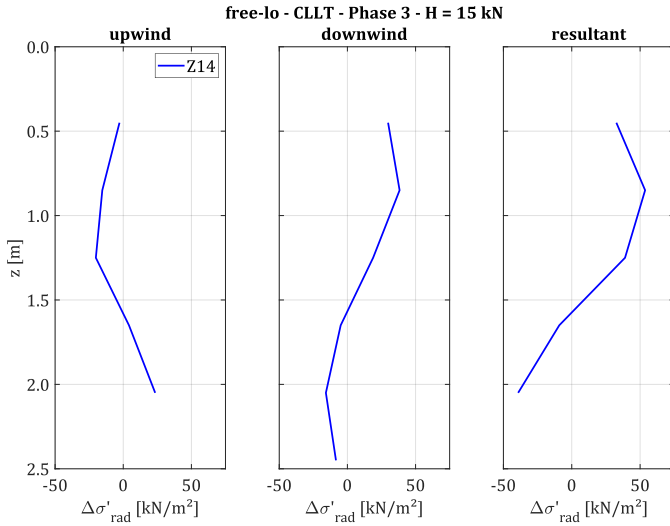


Figure E-35: Soil reaction of free vibratory driven pile with low eccentric moment at maximum load level of the first loading cycle of phase 3

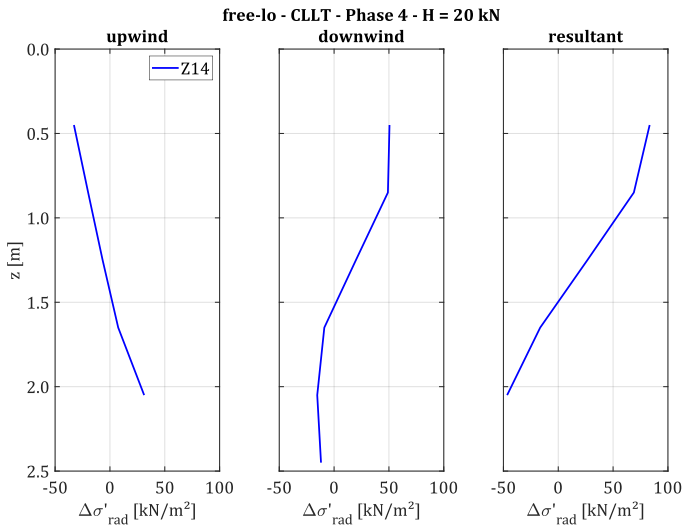


Figure E-36: Soil reaction of free vibratory driven pile with low eccentric moment at maximum load level of the first loading cycle of phase 4

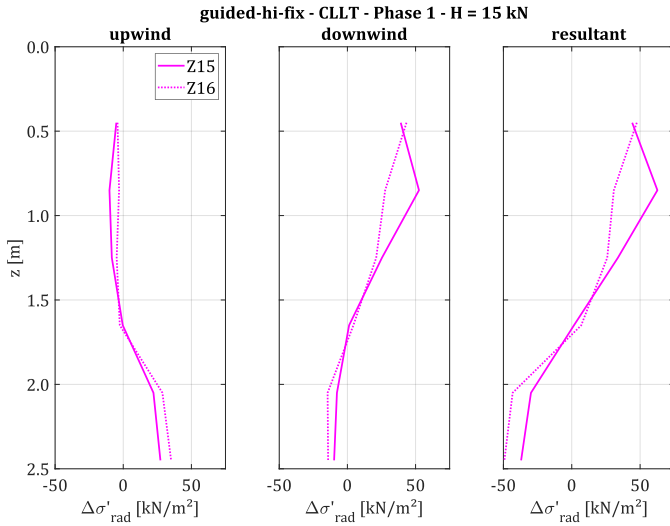


Figure E-37: Soil reaction of crane-guided vibratory driven piles with high eccentric moment at maximum load level of the first loading cycle of phase 1

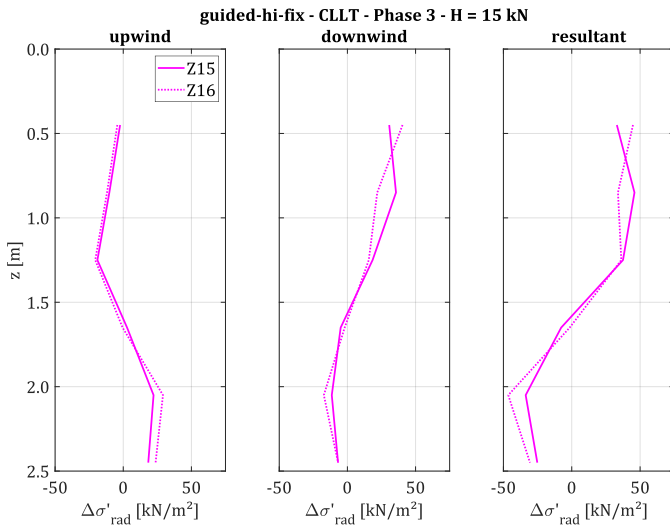


Figure E-38: Soil reaction of crane-guided vibratory driven piles with high eccentric moment at maximum load level of the first loading cycle of phase 3

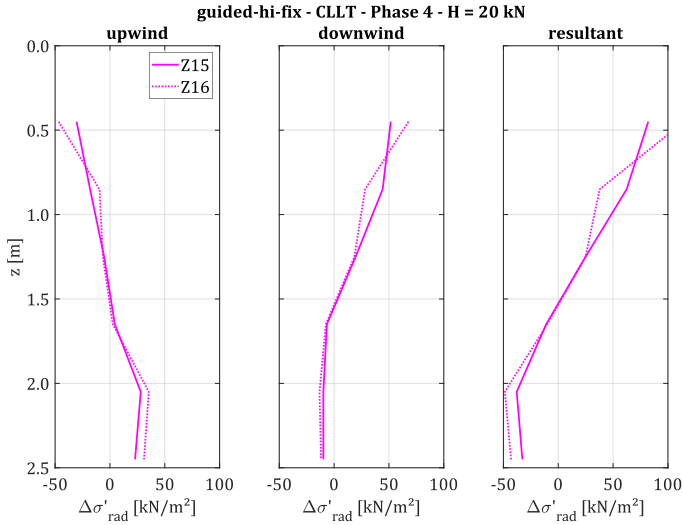


Figure E-39: Soil reaction of crane-guided vibratory driven piles with high eccentric moment at maximum load level of the first loading cycle of phase 4

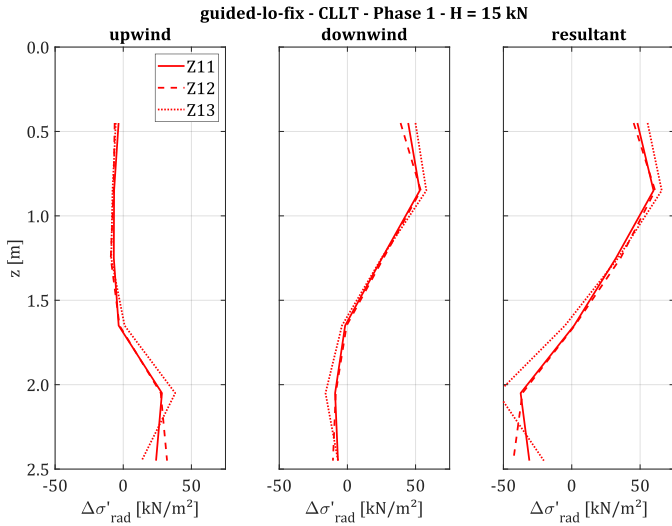


Figure E-40: Soil reaction of crane-guided vibratory driven piles with low eccentric moment at maximum load level of the first loading cycle of phase 1

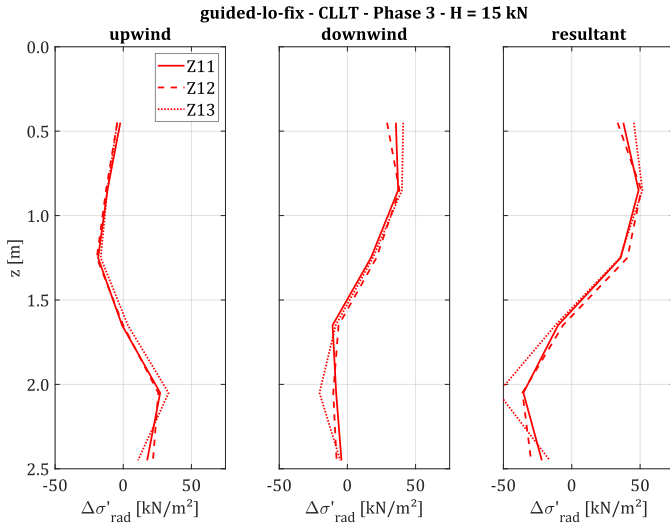


Figure E-41: Soil reaction of crane-guided vibratory driven piles with low eccentric moment at maximum load level of the first loading cycle of phase 3

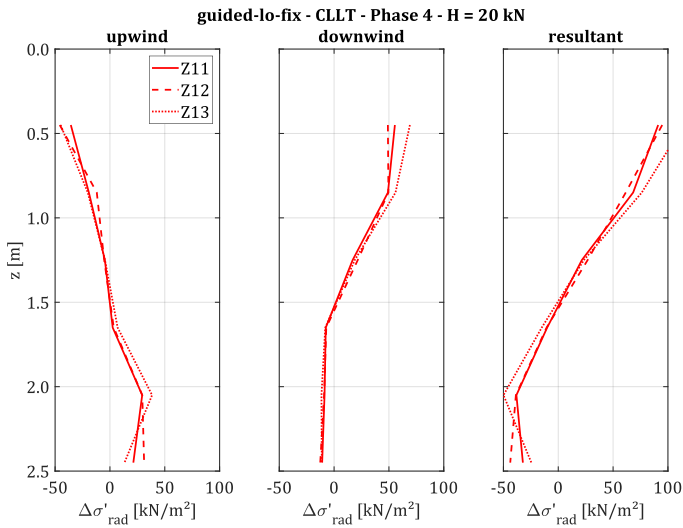


Figure E-42: Soil reaction of crane-guided vibratory driven piles with low eccentric moment at maximum load level of the first loading cycle of phase 4

Development of soil reaction during increasing lateral loading

The following figures show the soil reaction during loading period of the first cycle of phase 1 of all tests. Differences of the measured effective soil stresses $\Delta\sigma'$ compared to the stress state before loading ($H = 0$) are plotted. Soil stresses in upwind direction, downwind direction and resultants are shown from left to right. Darker lines indicate a higher lateral load H .

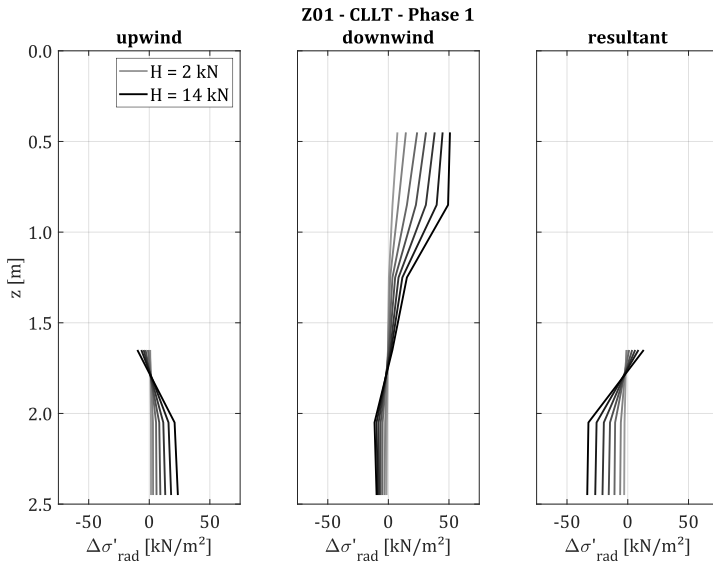


Figure E-43: Changes of effective radial soil stresses due to the first loading period of test Z01

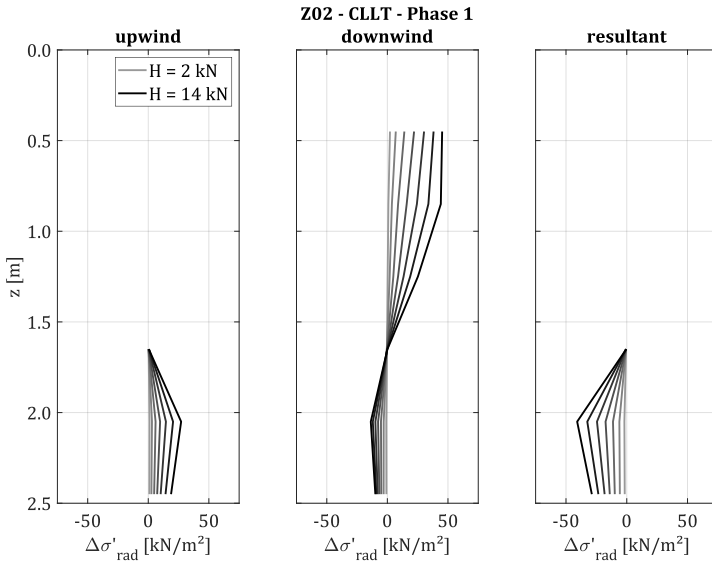


Figure E-44: Changes of effective radial soil stresses due to the first loading period of test Z02

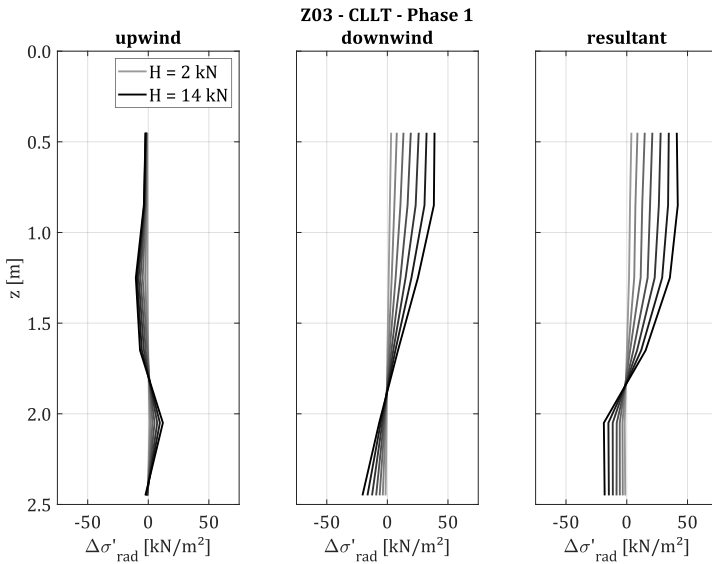


Figure E-45: Changes of effective radial soil stresses due to the first loading period of test Z03

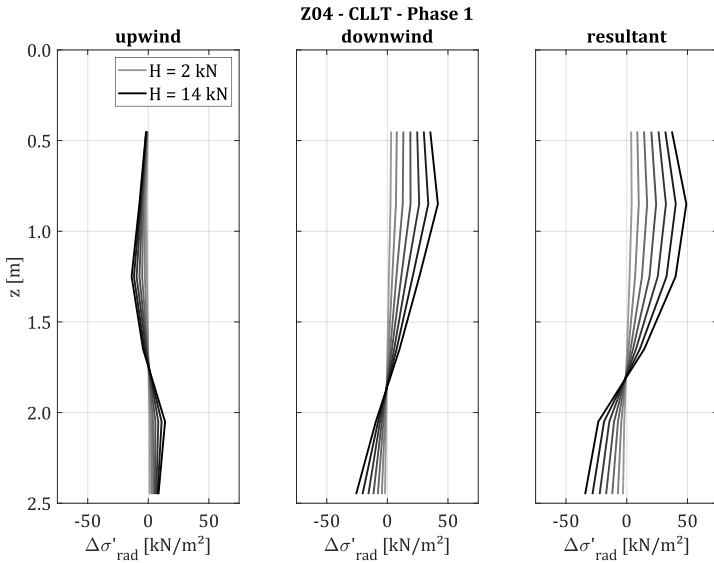


Figure E-46: Changes of effective radial soil stresses due to the first loading period of test Z04

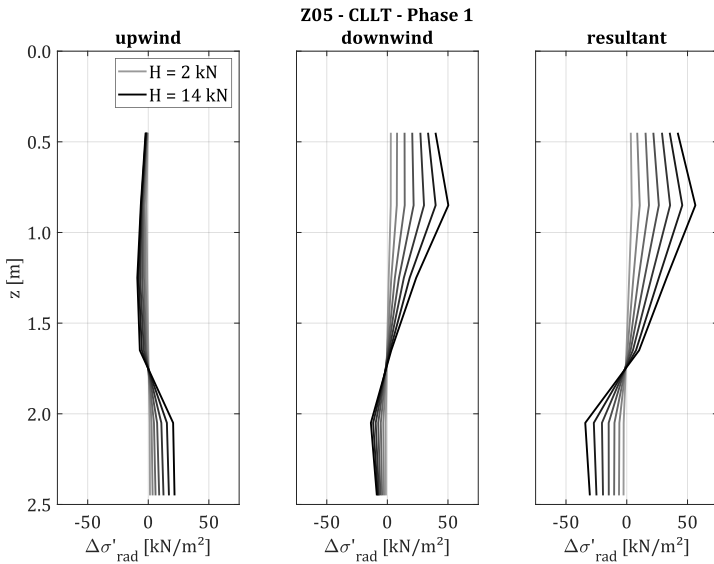


Figure E-47: Changes of effective radial soil stresses due to the first loading period of test Z05

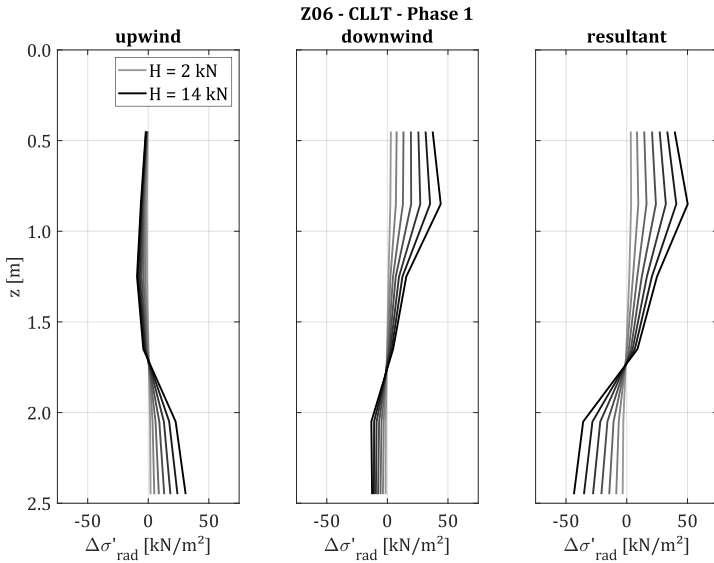


Figure E-48: Changes of effective radial soil stresses due to the first loading period of test Z06

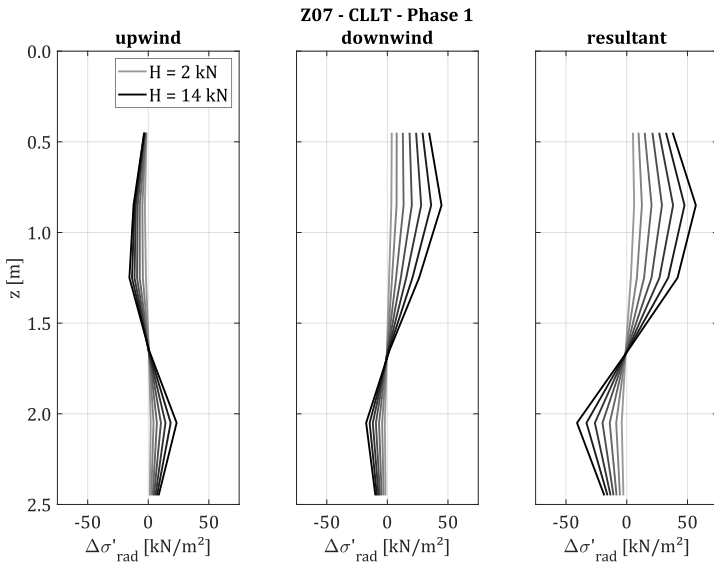


Figure E-49: Changes of effective radial soil stresses due to the first loading period of test Z07

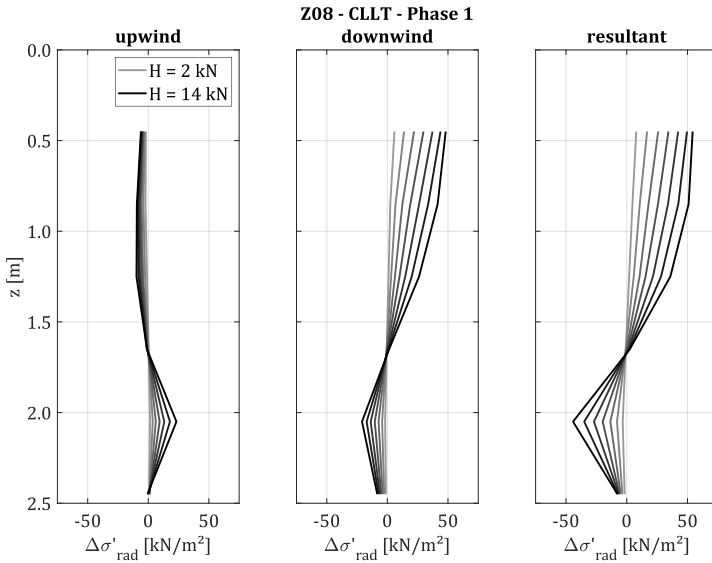


Figure E-50: Changes of effective radial soil stresses due to the first loading period of test Z08

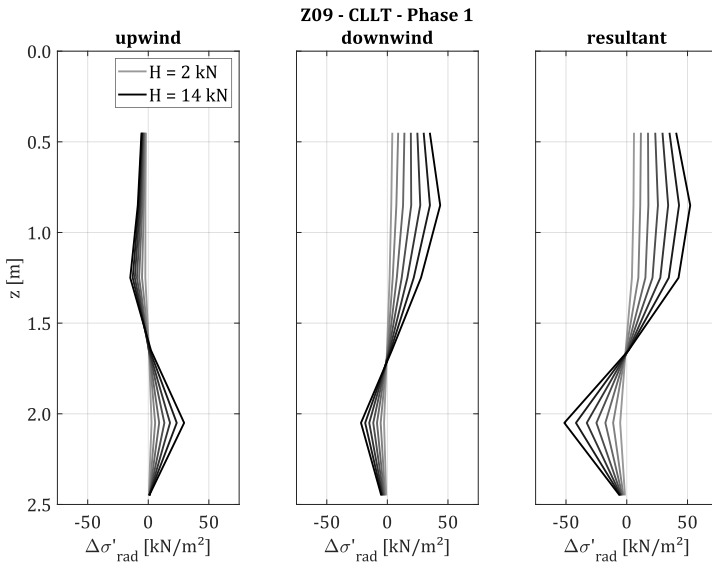


Figure E-51: Changes of effective radial soil stresses due to the first loading period of test Z09

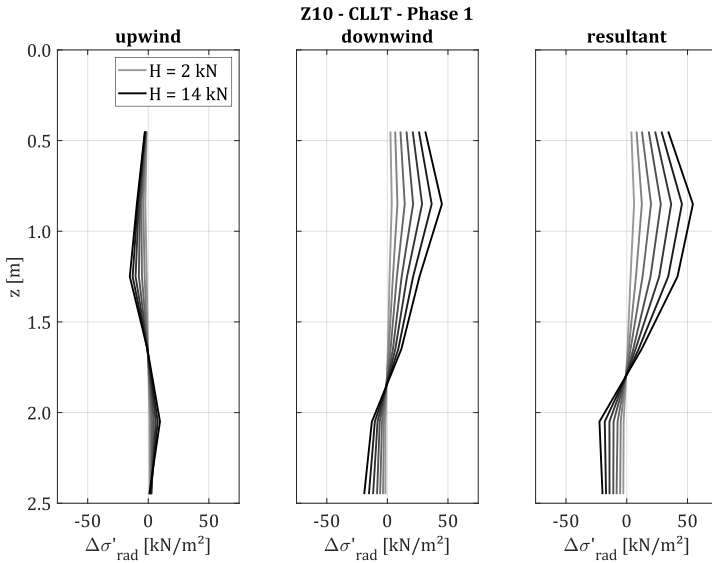


Figure E-52: Changes of effective radial soil stresses due to the first loading period of test Z10

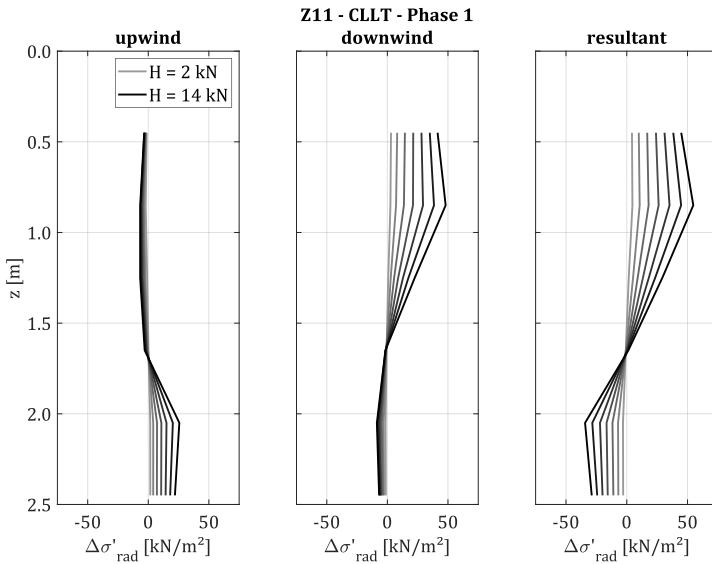


Figure E-53: Changes of effective radial soil stresses due to the first loading period of test Z11

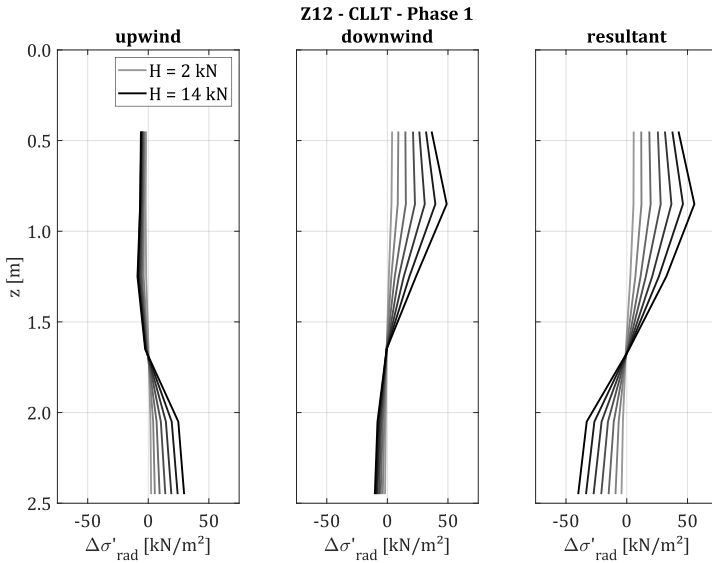


Figure E-54: Changes of effective radial soil stresses due to the first loading period of test Z12

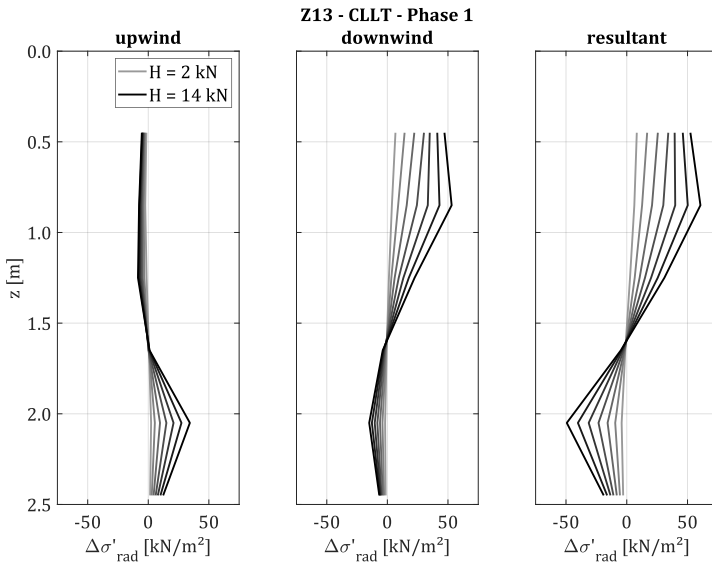


Figure E-55: Changes of effective radial soil stresses due to the first loading period of test Z13

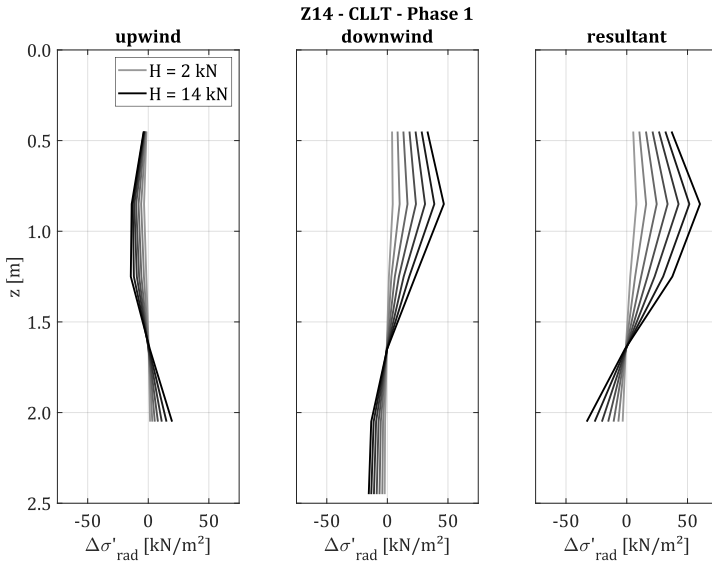


Figure E-56: Changes of effective radial soil stresses due to the first loading period of test Z14

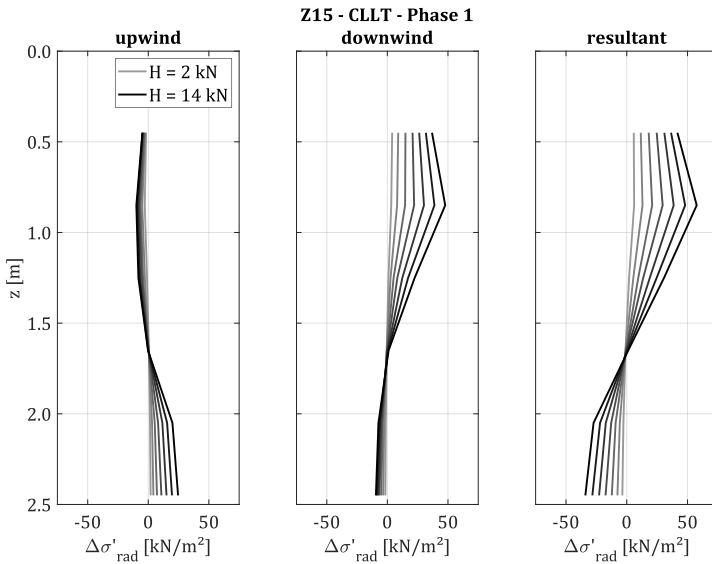


Figure E-57: Changes of effective radial soil stresses due to the first loading period of test Z15

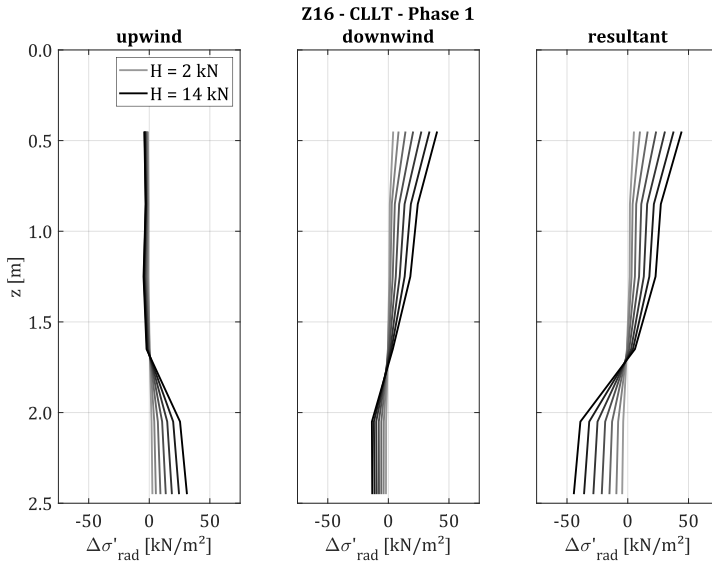


Figure E-58: Changes of effective radial soil stresses due to the first loading period of test Z16

Development of soil reaction during first loading and unloading cycle

The following figures show the soil reaction during loading and unloading of the first cycle of phase 1 of all tests. The measured effective radial soil stresses σ'_{rad} are plotted over depth z . Soil stresses in upwind direction, downwind direction and resultants are shown from left to right. Solid lines show stresses during loading while dashed lines show stresses during unloading half cycles. Darker lines indicate a higher lateral load H .

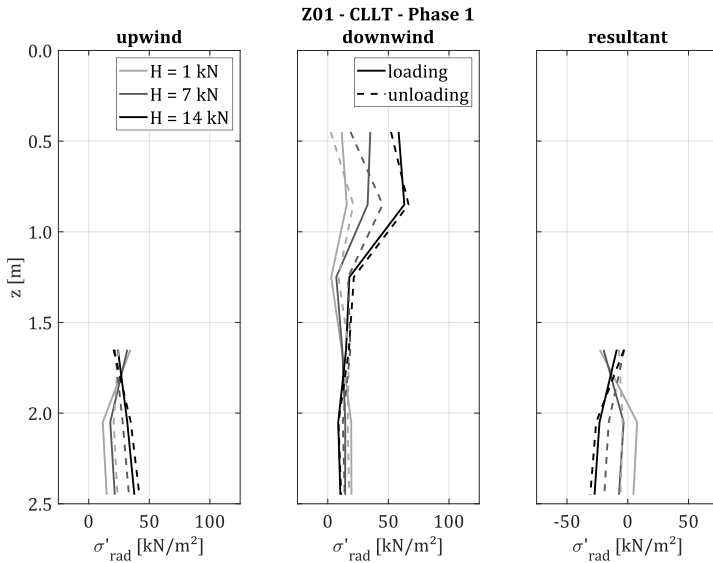


Figure E-59: Effective radial soil stresses due to first loading/unloading of test Z01

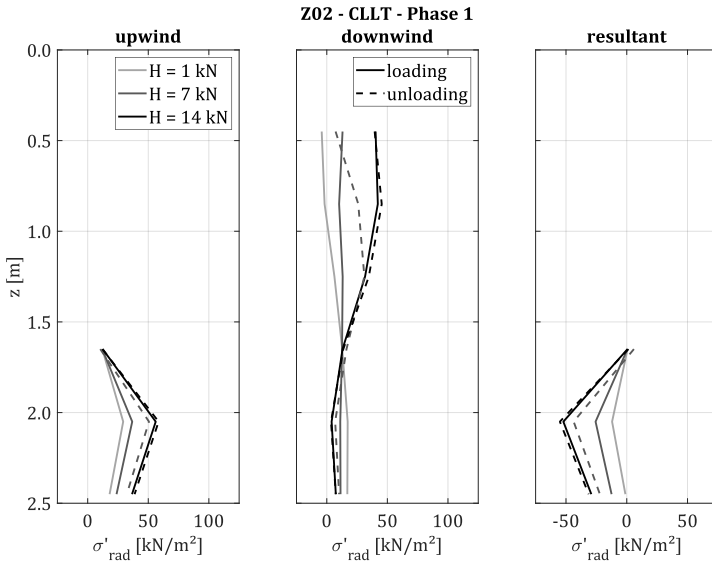


Figure E-60: Effective radial soil stresses due to first loading/unloading of test Z02

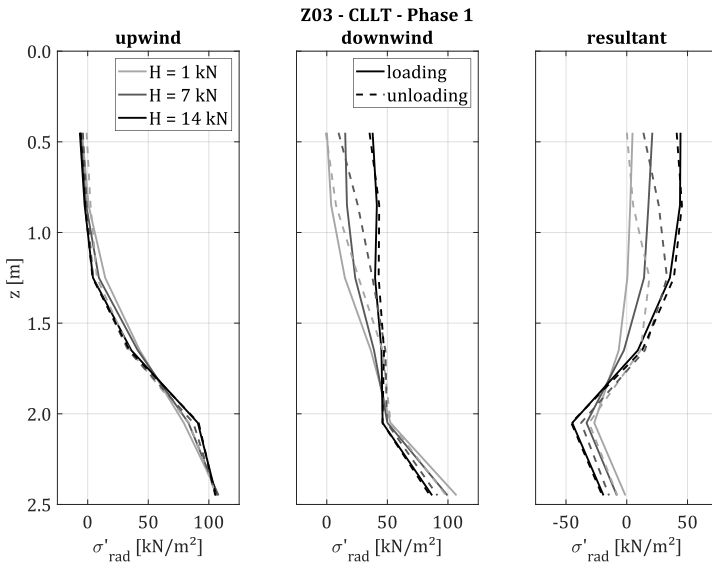


Figure E-61: Effective radial soil stresses due to first loading/unloading of test Z03

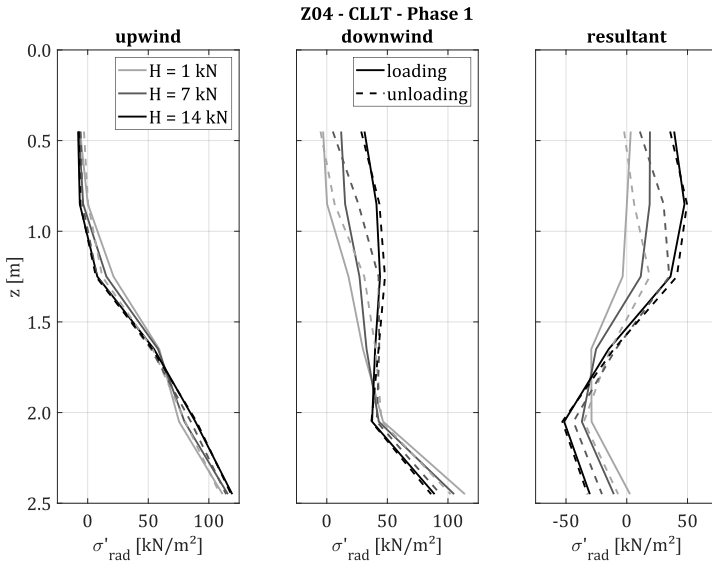


Figure E-62: Effective radial soil stresses due to first loading/unloading of test Z04

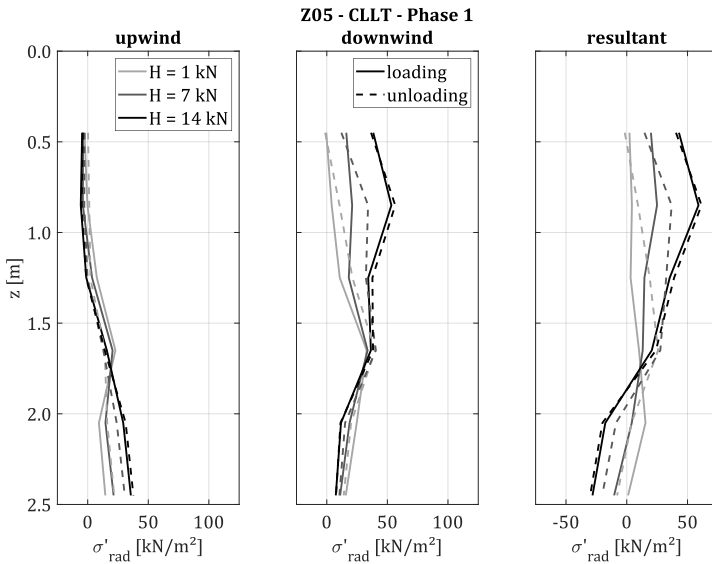


Figure E-63: Effective radial soil stresses due to first loading/unloading of test Z05

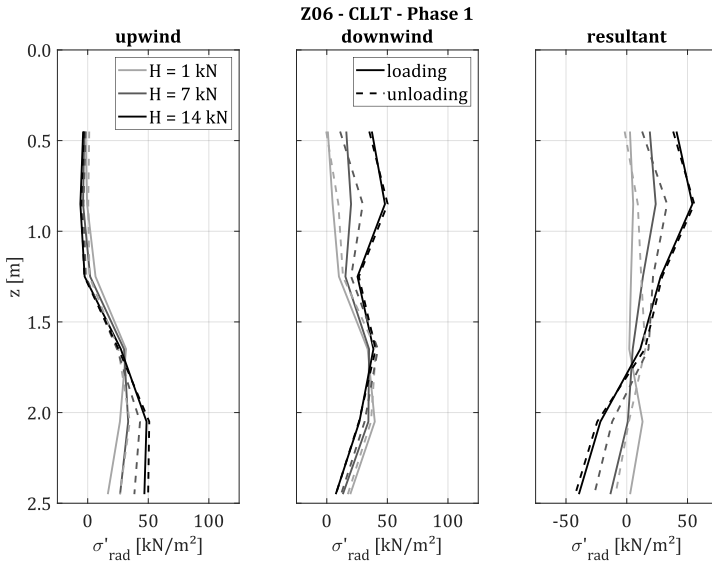


Figure E-64: Effective radial soil stresses due to first loading/unloading of test Z06

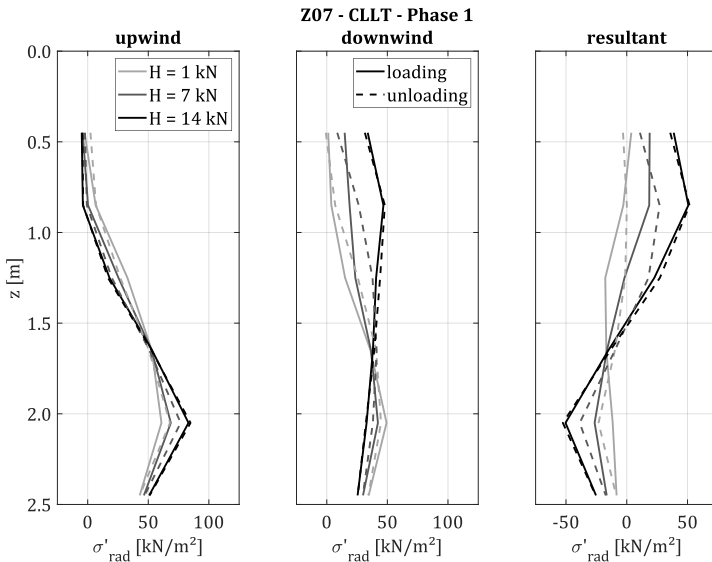


Figure E-65: Effective radial soil stresses due to first loading/unloading of test Z07

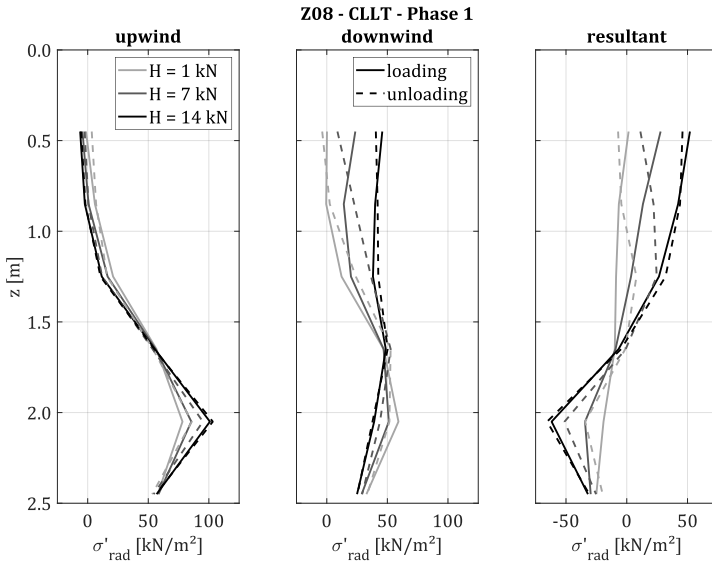


Figure E-66: Effective radial soil stresses due to first loading/unloading of test Z08

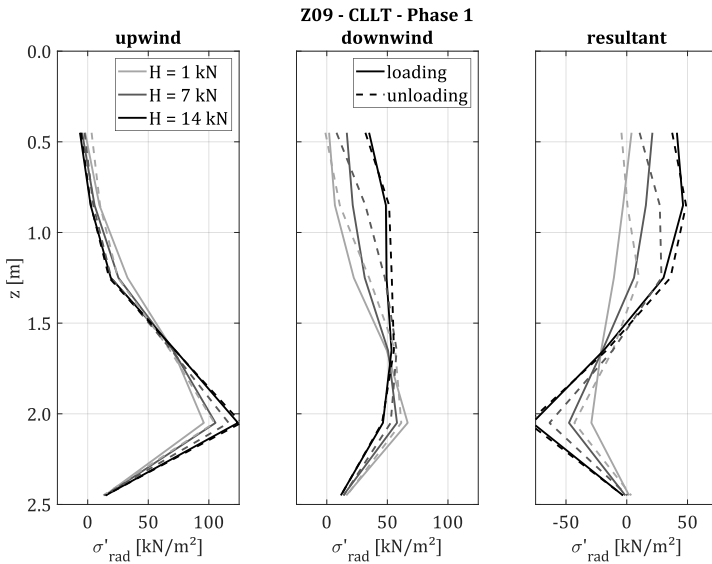


Figure E-67: Effective radial soil stresses due to first loading/unloading of test Z09

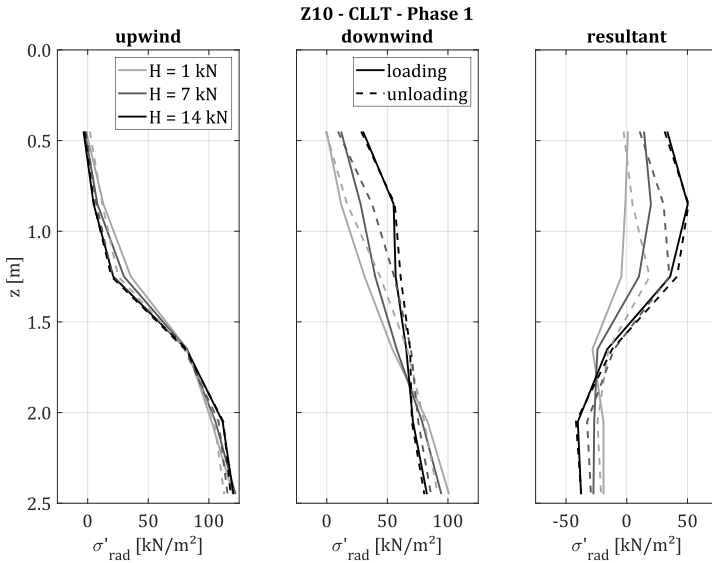


Figure E-68: Effective radial soil stresses due to first loading/unloading of test Z10

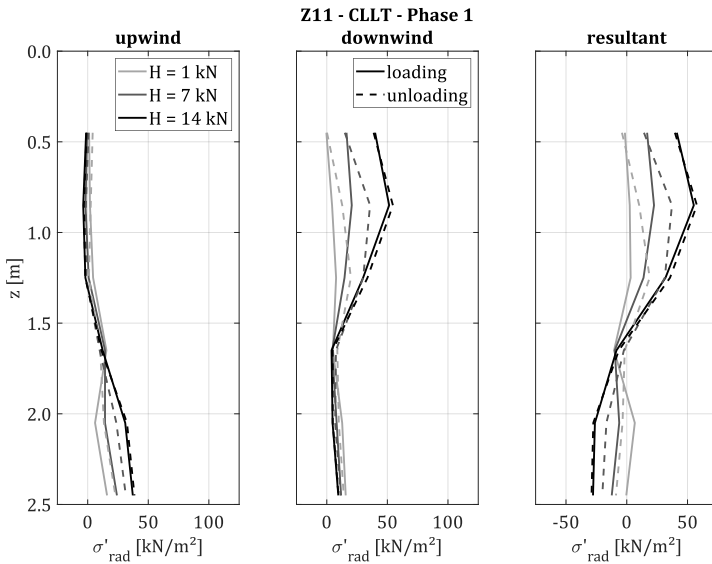


Figure E-69: Effective radial soil stresses due to first loading/unloading of test Z11

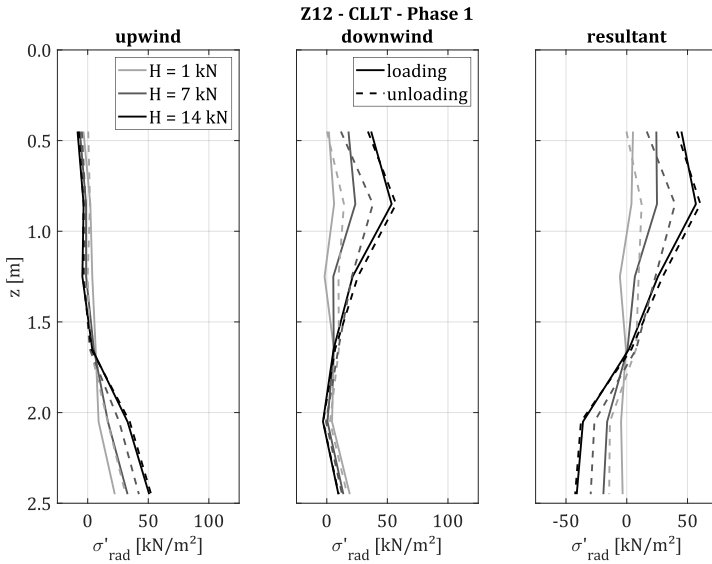


Figure E-70: Effective radial soil stresses due to first loading/unloading of test Z12

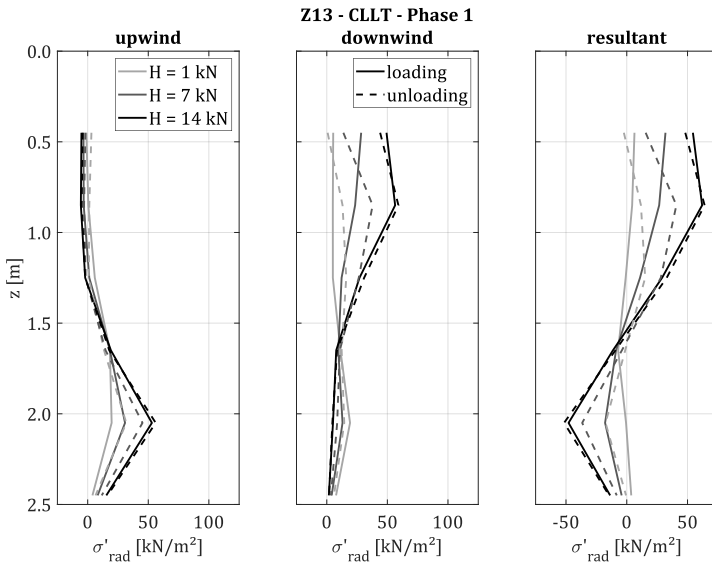


Figure E-71: Effective radial soil stresses due to first loading/unloading of test Z13

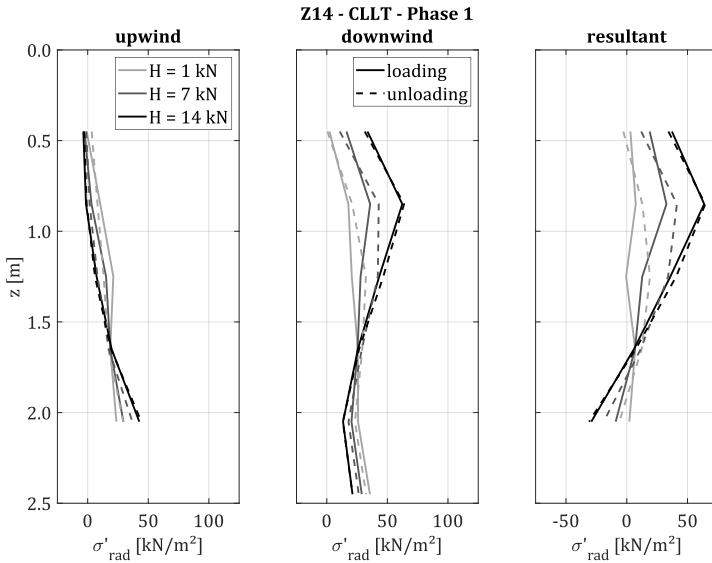


Figure E-72: Effective radial soil stresses due to first loading/unloading of test Z14

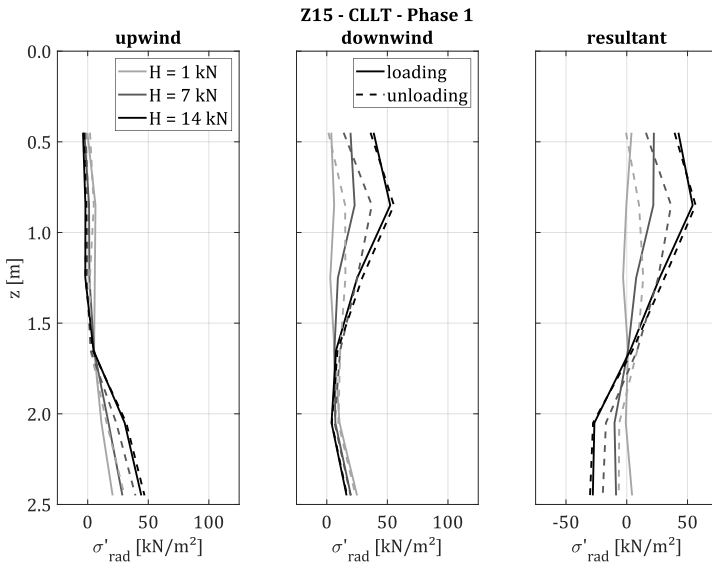


Figure E-73: Effective radial soil stresses due to first loading/unloading of test Z15

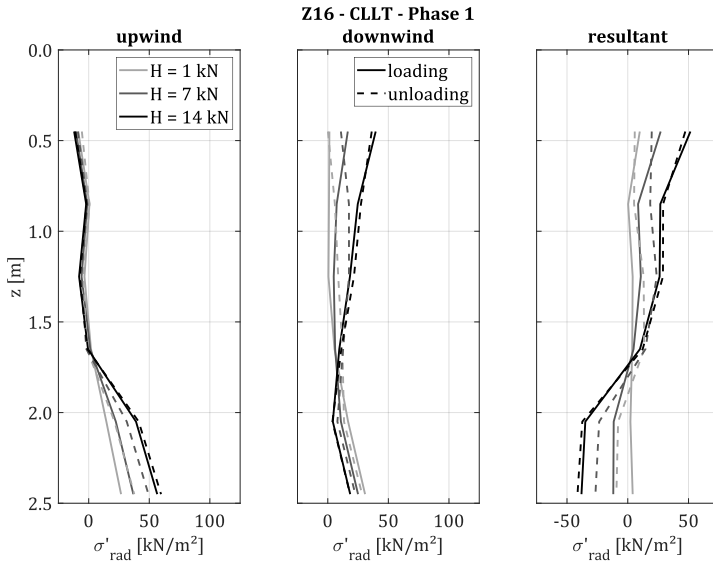


Figure E-74: Effective radial soil stresses due to first loading/unloading of test Z16

Appendix F Cyclic lateral pile behaviour**Pile head traces in horizontal plane**

The following figures show the traces of the pile head in the horizontal plane. Each symbol represents the pile head displacement in directions 0° and 90° after $N = 0, 1, 10, 100, 1,000$ and $10,000$ cycles of phases 1 to 5. The arrows at the markers representing $N = 0$ indicate the loading direction during the individual phases.

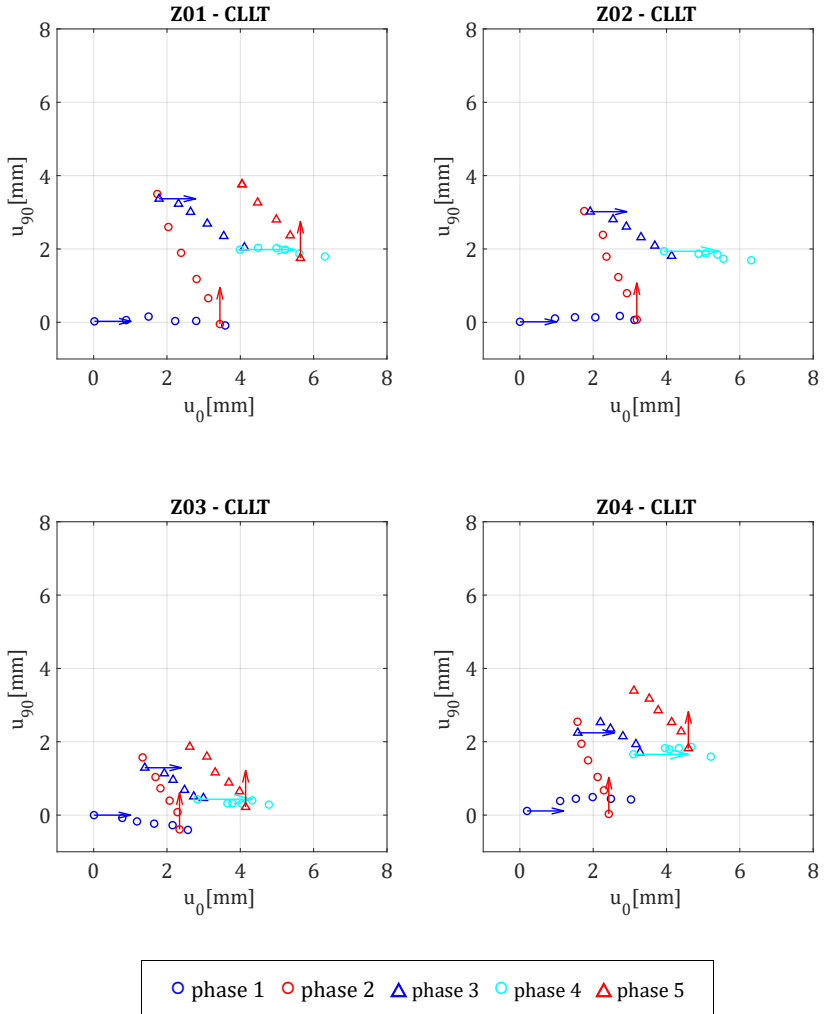


Figure F-1: Track of pile head displacement in horizontal plane during cyclic lateral loading from varying directions for tests Z01, Z02, Z03 and Z04

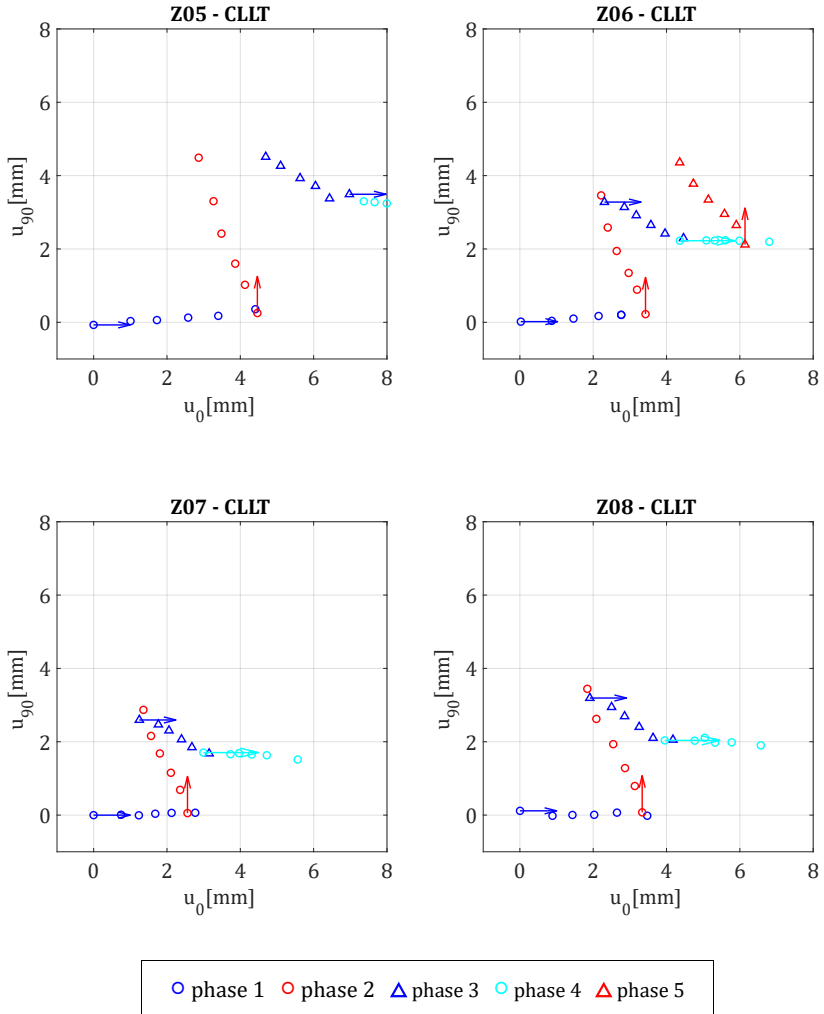


Figure F-2: Track of pile head displacement in horizontal plane during cyclic lateral loading from varying directions for tests Z05, Z06, Z07 and Z08

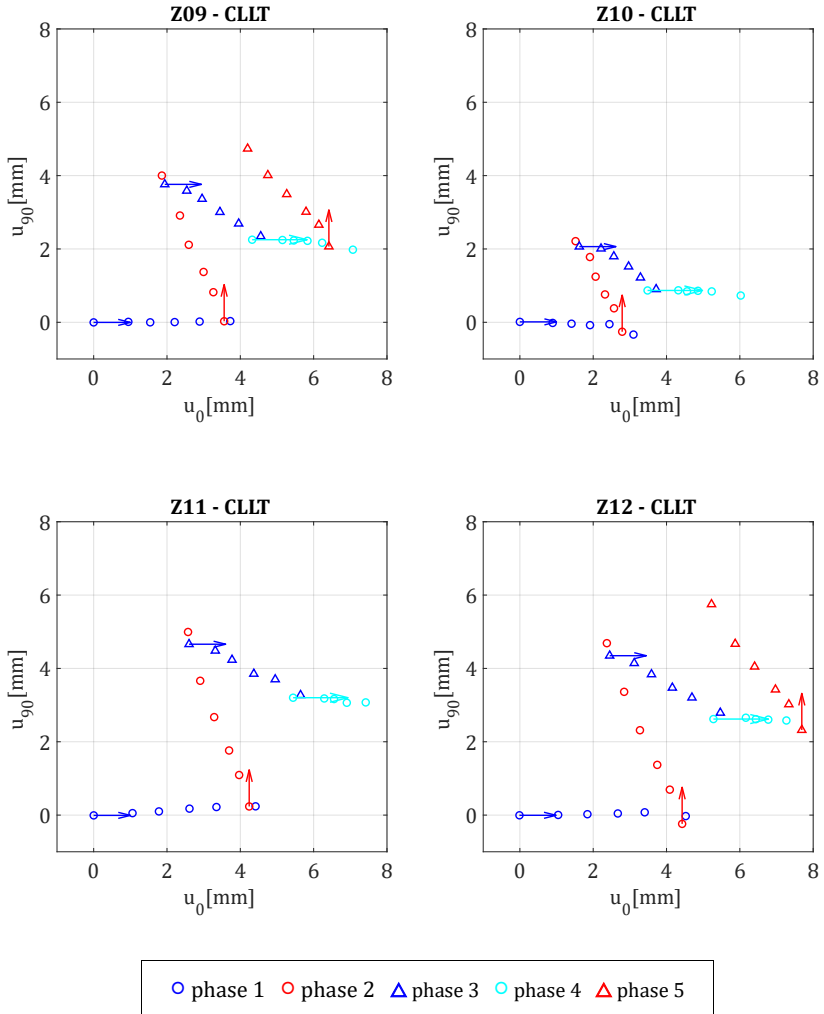


Figure F-3: Track of pile head displacement in horizontal plane during cyclic lateral loading from varying directions for tests Z09, Z10, Z11 and Z12

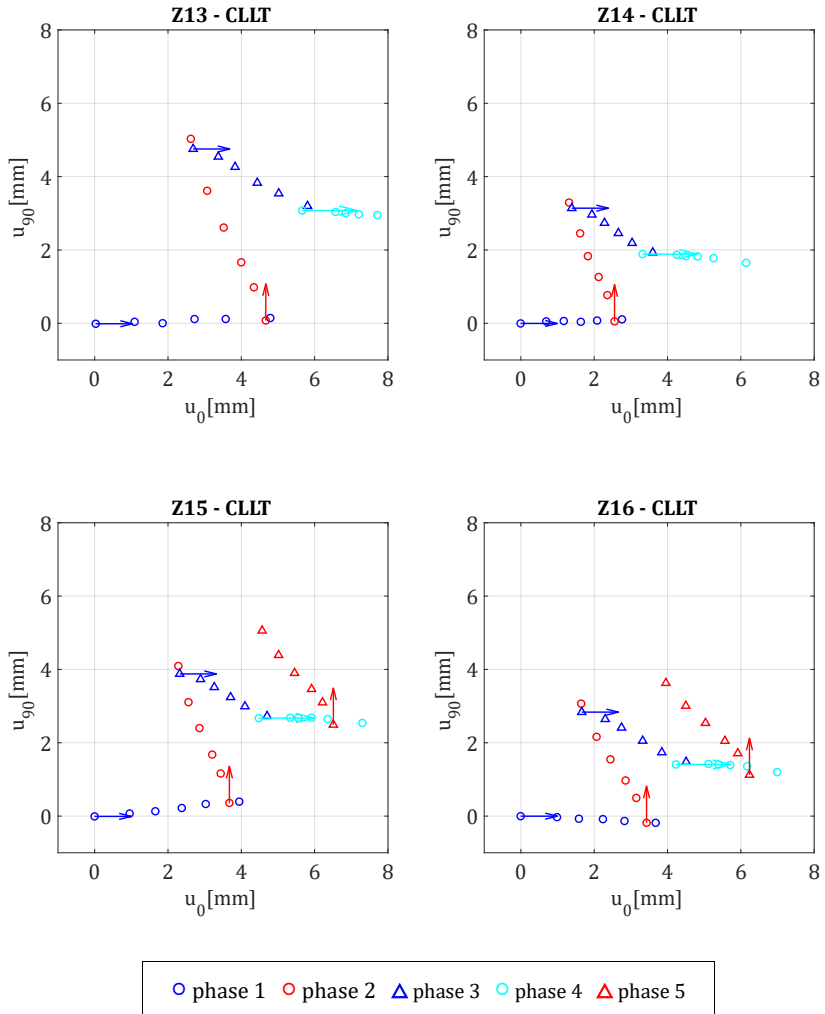


Figure F-4: Track of pile head displacement in horizontal plane during cyclic lateral loading from varying directions for tests Z13, Z14, Z15 and Z16

Pile head displacement accumulation (HCA formulation)

The following diagrams show the fictional strain $\gamma_{acc} = u_{acc}/L_{pile}$ accumulated after the first, 'irregular' cycle related to the amplitude function f_{ampl} for all pile groups. Markers indicate measured values, lines indicate fits according to Equation (6-13). The increasing courses in the positive domain show the accumulation in loading direction (\parallel). The decreasing courses in the negative domain show back-accumulation in direction transverse to the loading direction (\perp). For accumulation in both loading and unloading direction, the amplitude function $f_{ampl} = (\gamma_{ampl,\parallel,mean}/\gamma_{ref})^{C_{ampl}}$ referring to the strain amplitude in loading direction (\parallel) is used to scale the accumulated strain.

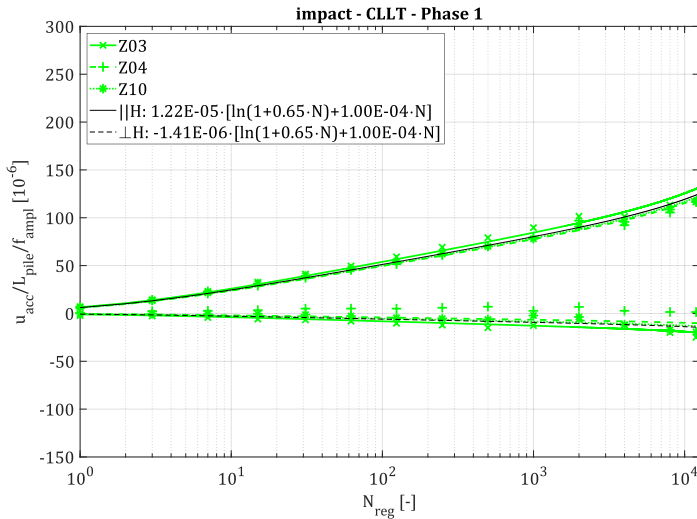


Figure F-5: Pile head displacement accumulation after first ('irregular') cycle of impact driven piles during phase 1

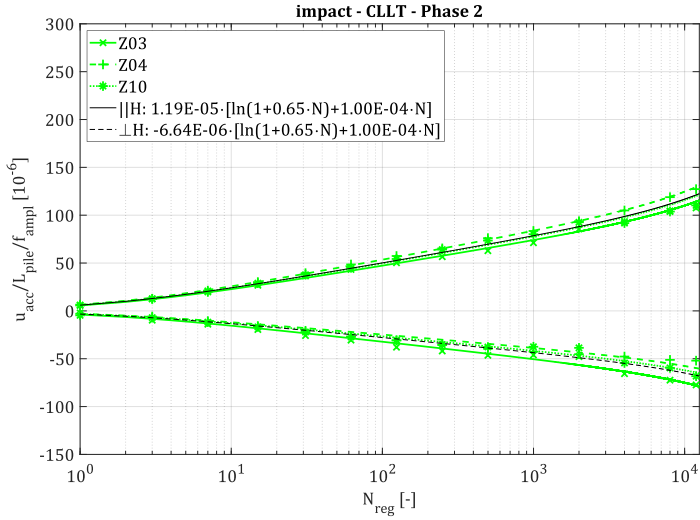


Figure F-6: Pile head displacement accumulation after first ('irregular') cycle of impact driven piles during phase 2

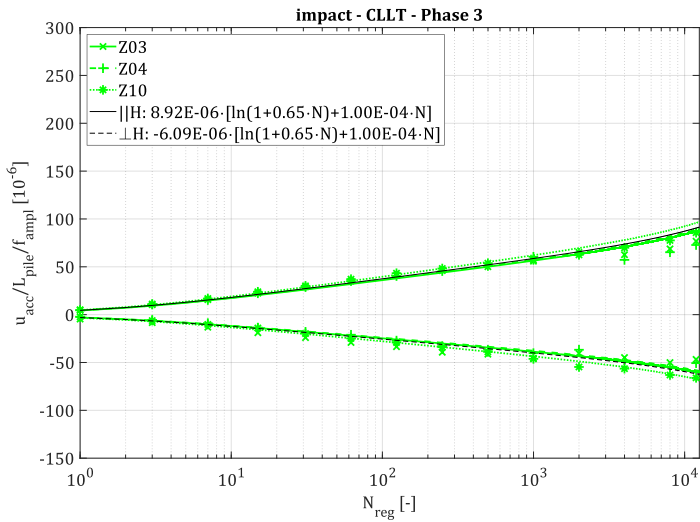


Figure F-7: Pile head displacement accumulation after first ('irregular') cycle of impact driven piles during phase 3

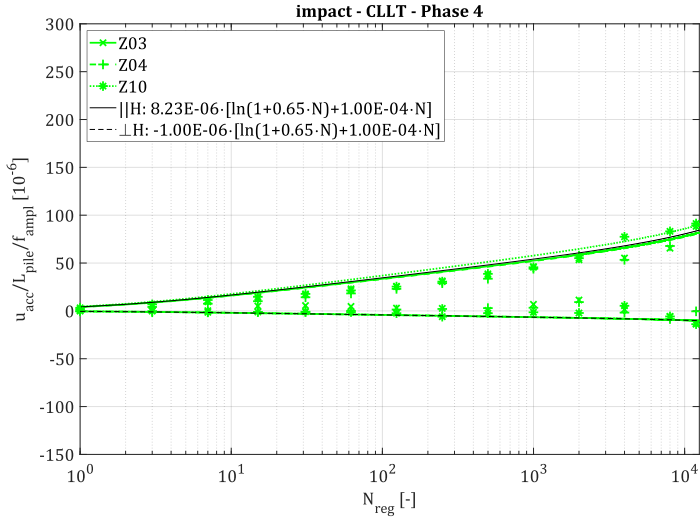


Figure F-8: Pile head displacement accumulation after first ('irregular') cycle of impact driven piles during phase 4

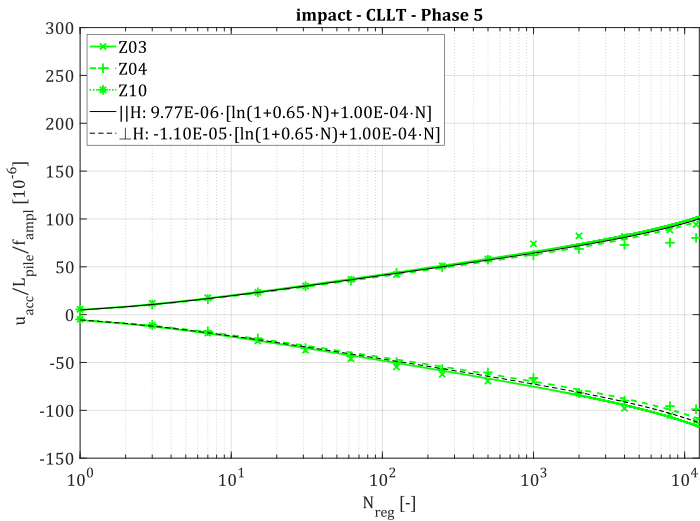


Figure F-9: Pile head displacement accumulation after first ('irregular') cycle of impact driven piles during phase 5

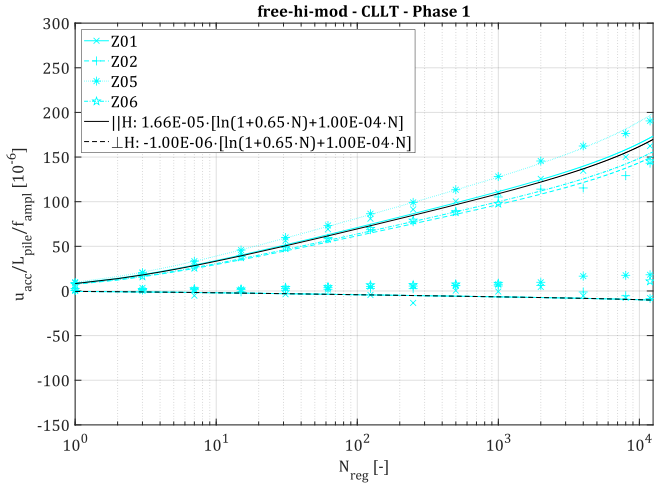


Figure F-10: Pile head displacement accumulation after first ('irregular') cycle of free vibratory driven piles with high eccentric moment and 'moderate' frequency control during phase 1

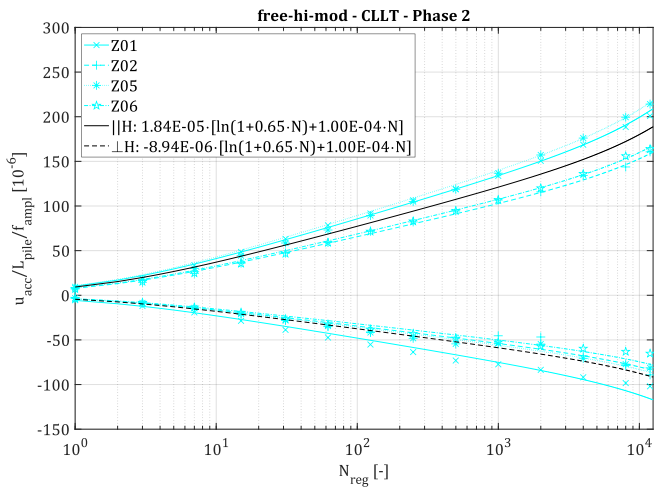


Figure F-11: Pile head displacement accumulation after first ('irregular') cycle of free vibratory driven piles with high eccentric moment and 'moderate' frequency control during phase 2

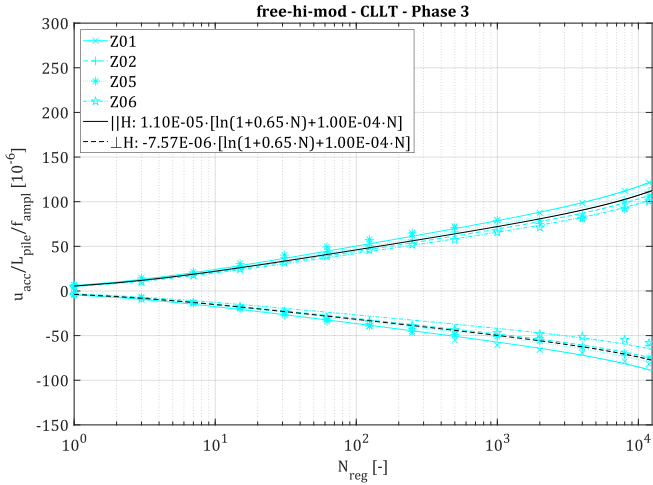


Figure F-12: Pile head displacement accumulation after first ('irregular') cycle of free vibratory driven piles with high eccentric moment and 'moderate' frequency control during phase 3

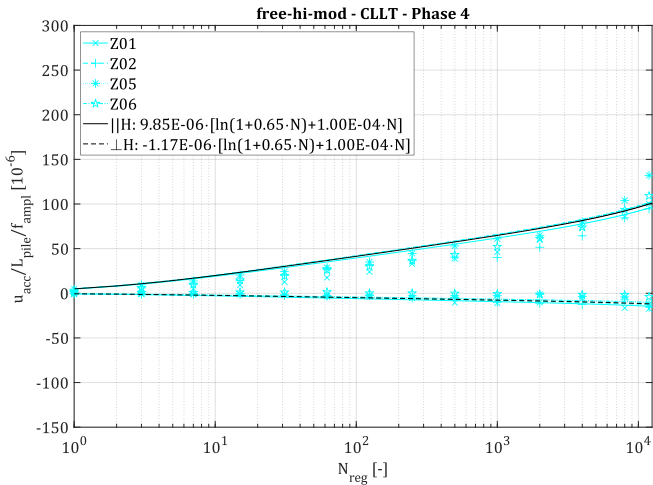


Figure F-13: Pile head displacement accumulation after first ('irregular') cycle of free vibratory driven piles with high eccentric moment and 'moderate' frequency control during phase 4

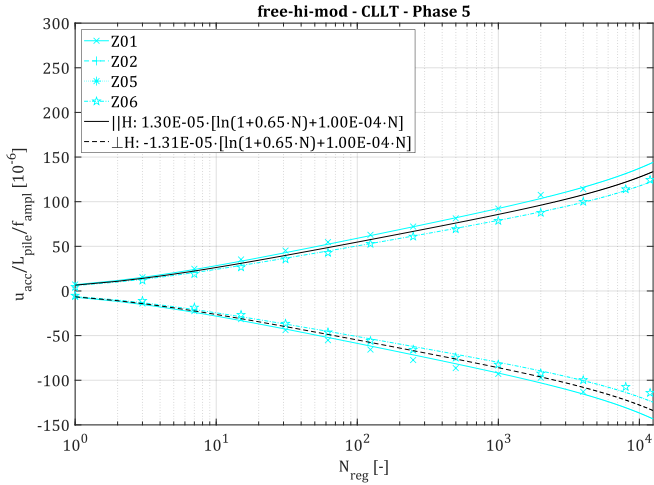


Figure F-14: Pile head displacement accumulation after first ('irregular') cycle of free vibratory driven piles with high eccentric moment and 'moderate' frequency control during phase 5

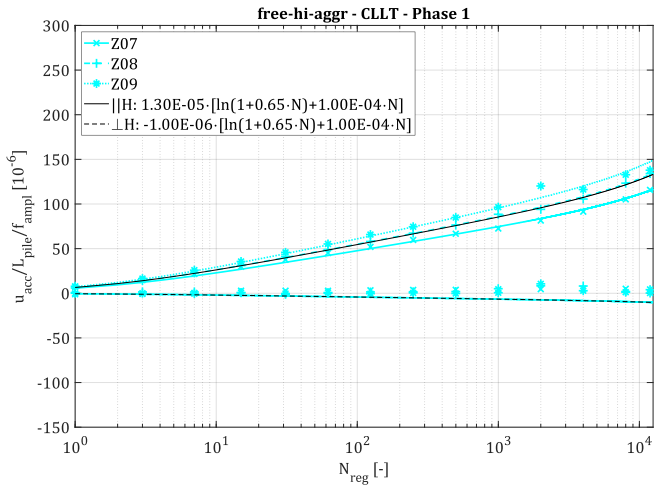


Figure F-15: Pile head displacement accumulation after first ('irregular') cycle of free vibratory driven piles with high eccentric moment and 'aggressive' frequency control during phase 1

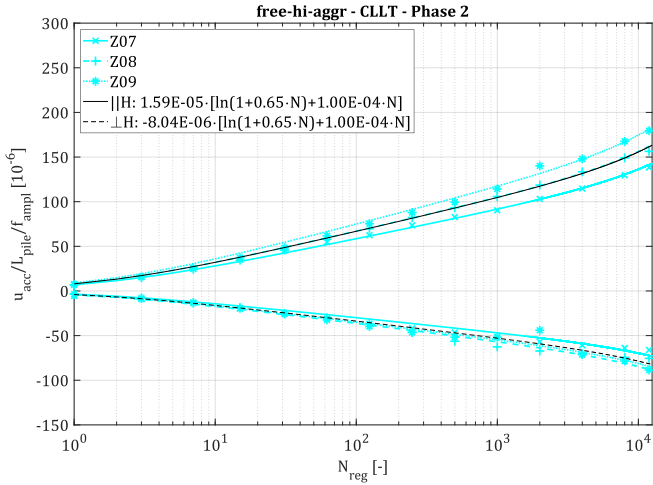


Figure F-16: Pile head displacement accumulation after first ('irregular') cycle of free vibratory driven piles with high eccentric moment and 'aggressive' frequency control during phase 2

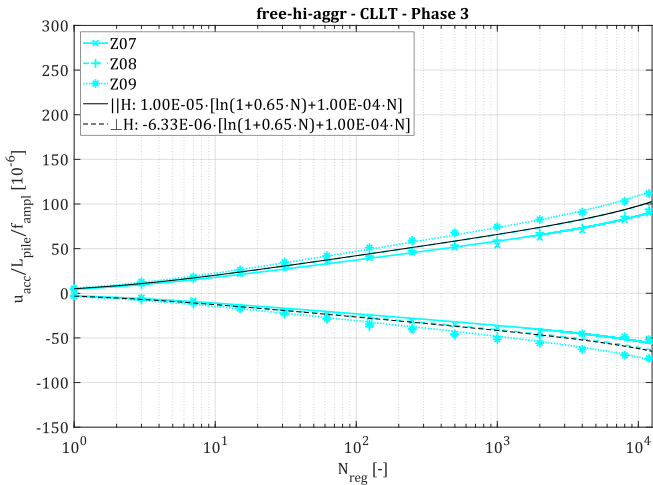


Figure F-17: Pile head displacement accumulation after first ('irregular') cycle of free vibratory driven piles with high eccentric moment and 'aggressive' frequency control during phase 3

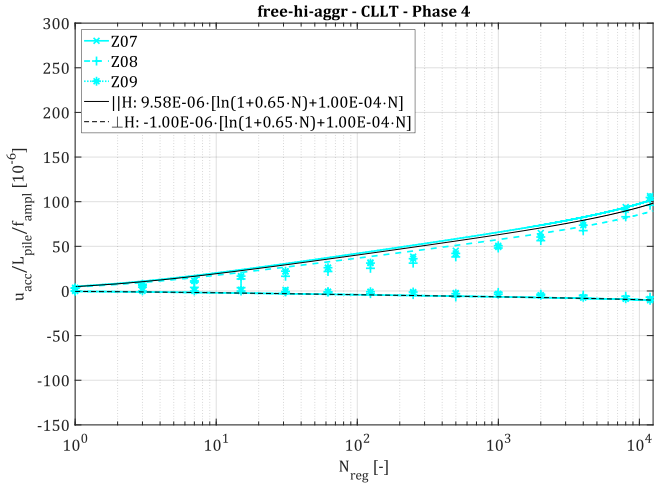


Figure F-18: Pile head displacement accumulation after first ('irregular') cycle of free vibratory driven piles with high eccentric moment and 'aggressive' frequency control during phase 4

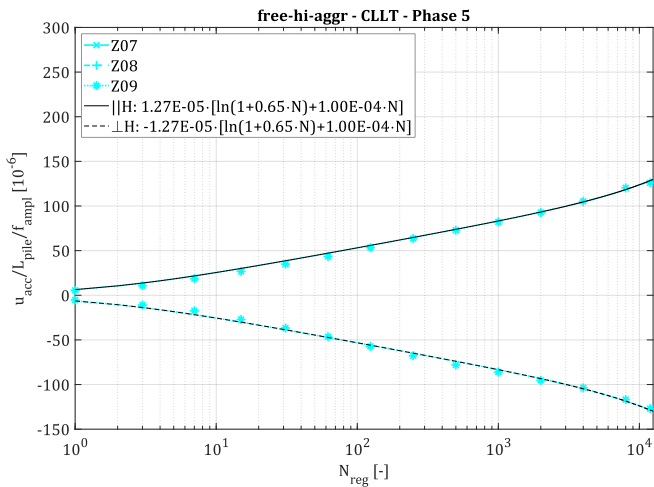


Figure F-19: Pile head displacement accumulation after first ('irregular') cycle of free vibratory driven piles with high eccentric moment and 'aggressive' frequency control during phase 5

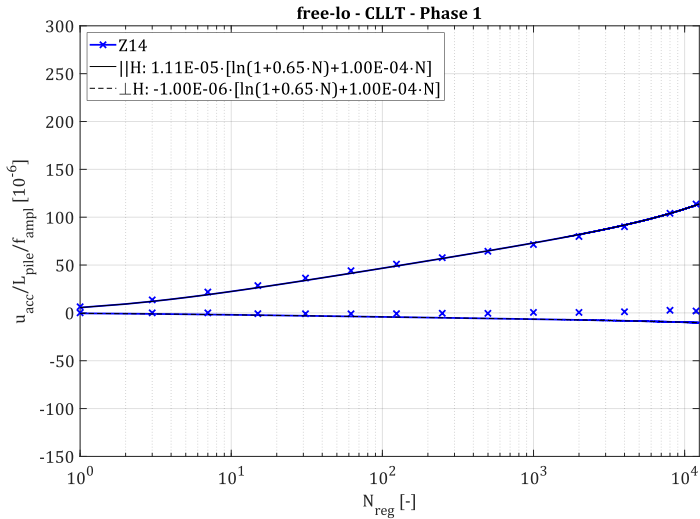


Figure F-20: Pile head displacement accumulation after first ('irregular') cycle of free vibratory driven piles with low eccentric moment during phase 1

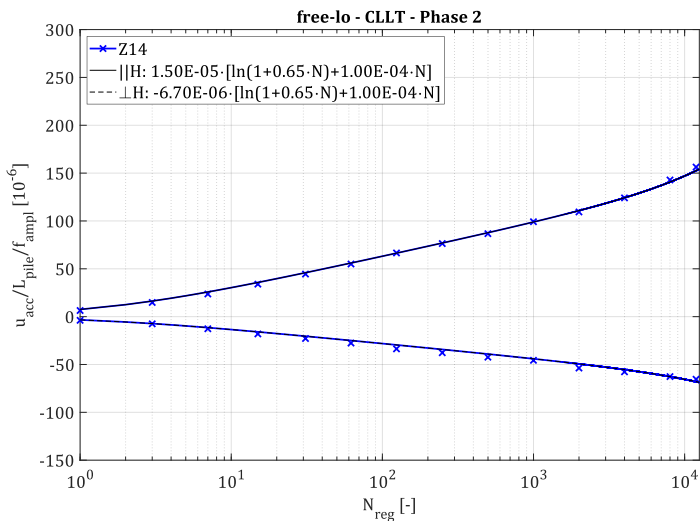


Figure F-21: Pile head displacement accumulation after first ('irregular') cycle of free vibratory driven piles with low eccentric moment during phase 2

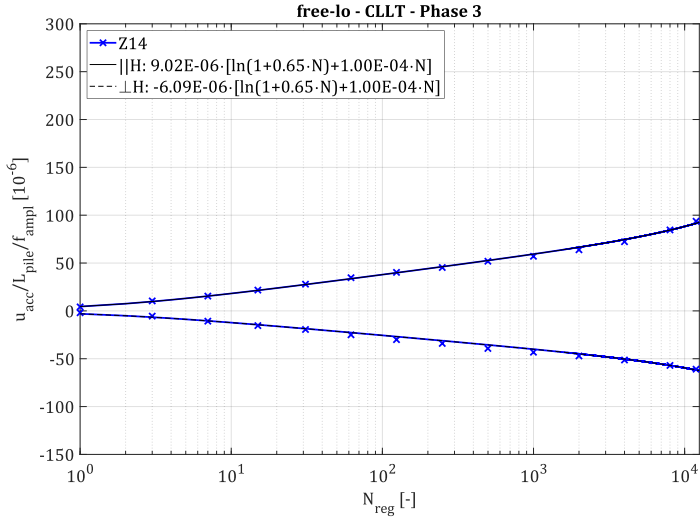


Figure F-22: Pile head displacement accumulation after first ('irregular') cycle of free vibratory driven piles with low eccentric moment during phase 3

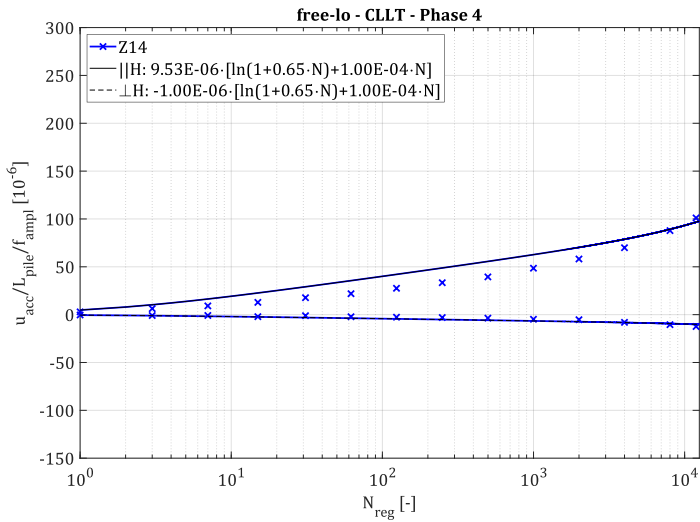


Figure F-23: Pile head displacement accumulation after first ('irregular') cycle of free vibratory driven piles with low eccentric moment during phase 4

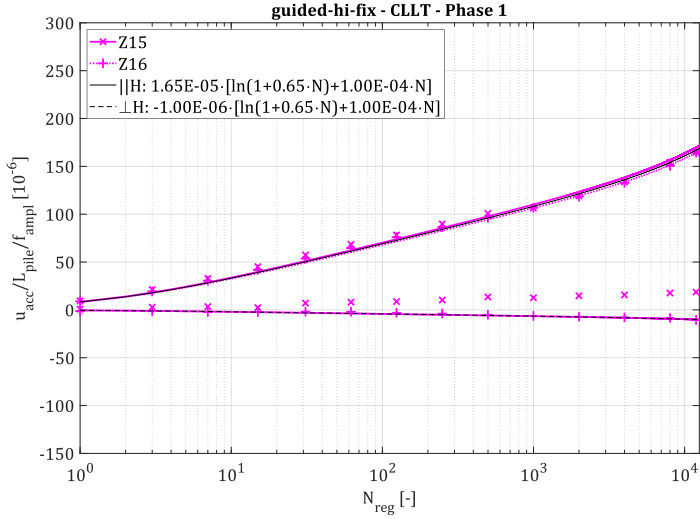


Figure F-24: Pile head displacement accumulation after first ('irregular') cycle of crane-guided vibratory driven piles with high eccentric moment during phase 1

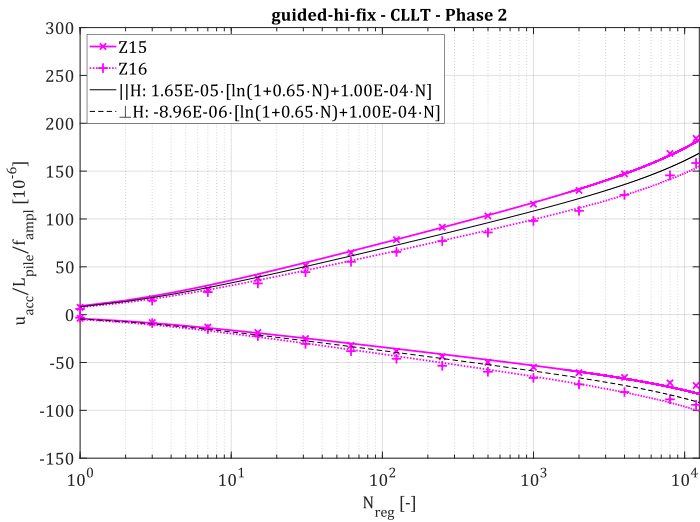


Figure F-25: Pile head displacement accumulation after first ('irregular') cycle of crane-guided vibratory driven piles with high eccentric moment during phase 2

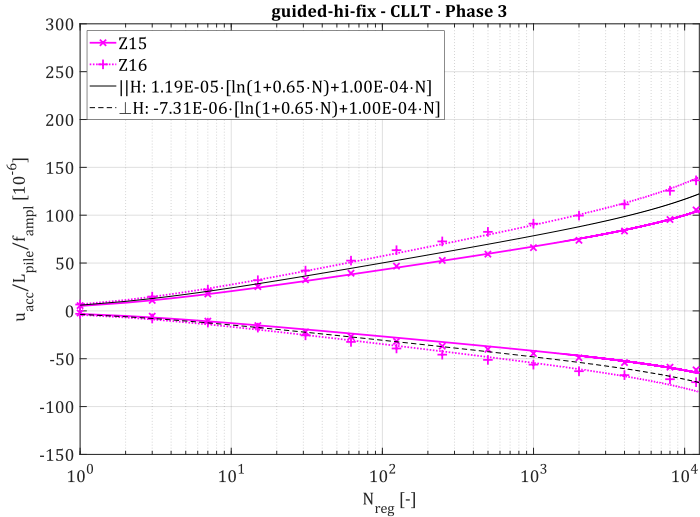


Figure F-26: Pile head displacement accumulation after first ('irregular') cycle of crane-guided vibratory driven piles with high eccentric moment during phase 3

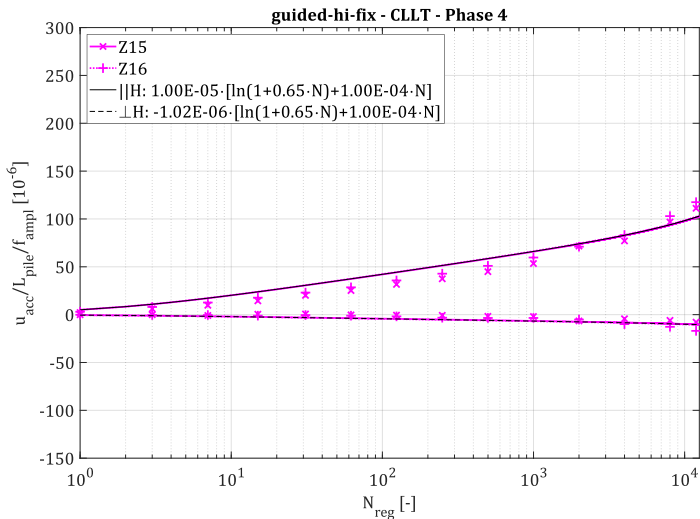


Figure F-27: Pile head displacement accumulation after first ('irregular') cycle of crane-guided vibratory driven piles with high eccentric moment during phase 4

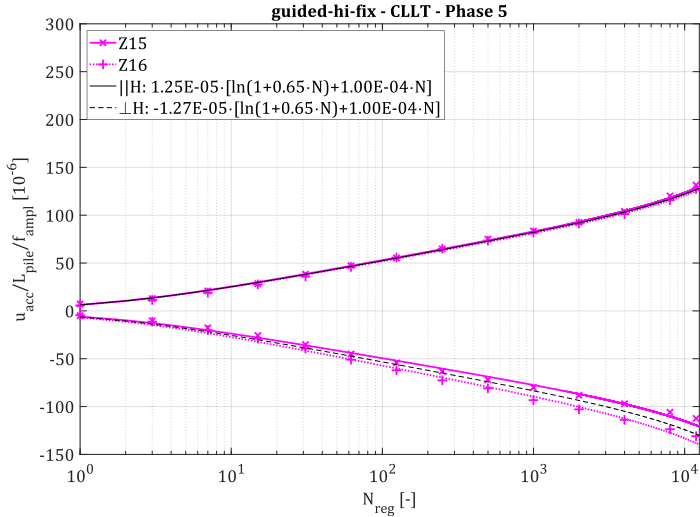


Figure F-28: Pile head displacement accumulation after first ('irregular') cycle of crane-guided vibratory driven piles with high eccentric moment during phase 5

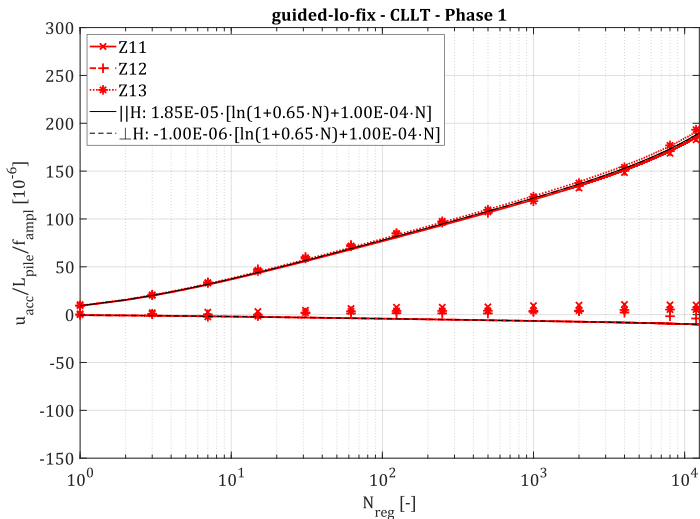


Figure F-29: Pile head displacement accumulation after first ('irregular') cycle of crane-guided vibratory driven piles with low eccentric moment during phase 1

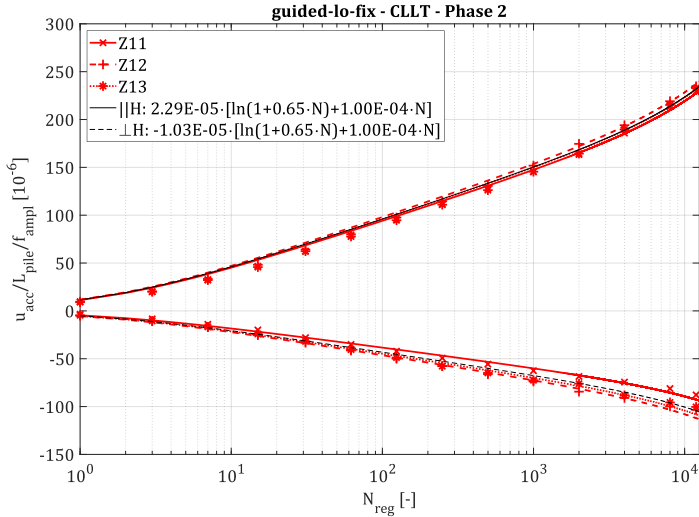


Figure F-30: Pile head displacement accumulation after first ('irregular') cycle of crane-guided vibratory driven piles with low eccentric moment during phase 2

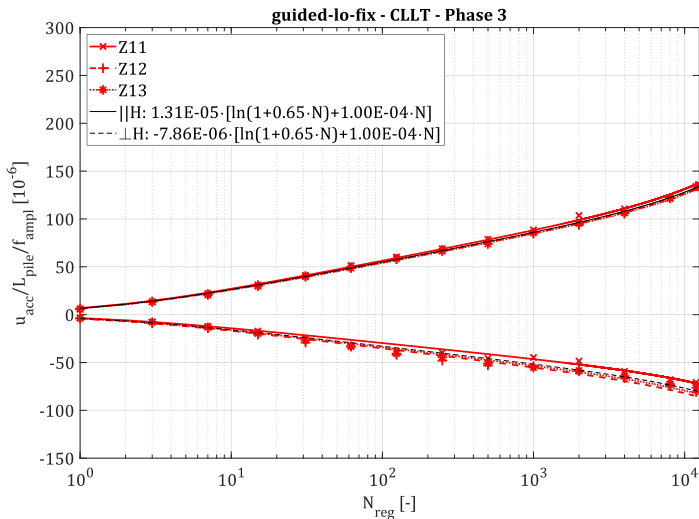


Figure F-31: Pile head displacement accumulation after first ('irregular') cycle of crane-guided vibratory driven piles with low eccentric moment during phase 3

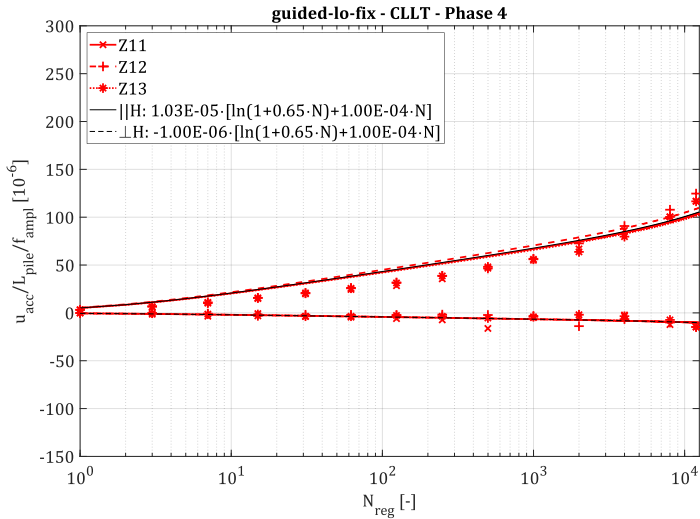


Figure F-32: Pile head displacement accumulation after first ('irregular') cycle of crane-guided vibratory driven piles with low eccentric moment during phase 4

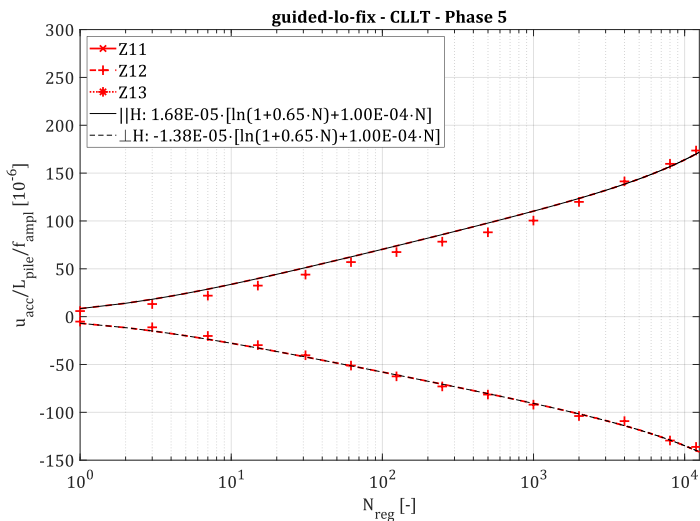


Figure F-33: Pile head displacement accumulation after first ('irregular') cycle of crane-guided vibratory driven piles with low eccentric moment during phase 5

To fit the measured values, soil constants $C_{N2} = 0,65$ and $C_{N3} = 10^{-4}$ according to Equation (6-13) were used in all cases. The strain accumulation differs in the 'biased' accumulation parameter \hat{C}_{N1} which is given in the following table:

Table F-1: Best fit parameters for pile head displacement accumulation described by HCA model (all tests, CLLT, phase 1)

		$\hat{C}_{N1} [10^{-6}]$				
	test/group	phase 1	phase 2	phase 3	phase 4	phase 5
	Z01	16.9	20.4	12.0	9.4	14.1
	Z02	14.7	15.6	10.5	10.0	--
	Z03	12.8	11.3	8.6	8.0	10.0
	Z04	11.8	12.7	8.7	7.9	9.5
	Z05	19.4	21.3	11.3	10.0	--
	Z06	15.2	16.4	10.0	10.0	12.0
	Z07	11.4	13.9	8.9	10.0	--
	Z08	13.1	16.0	10.0	8.7	--
	Z09	14.5	17.9	11.2	10.0	12.7
	Z10	12.0	11.8	9.4	8.8	--
	Z11	18.3	22.4	13.4	10.2	--
	Z12	18.5	23.4	13.0	10.7	16.8
	Z13	18.8	22.8	12.9	10.0	--
	Z14	11.1	15.0	9.0	9.5	--
	Z15	16.7	17.8	10.2	10.0	12.6
	Z16	16.2	15.1	13.6	10.1	12.3
	mean values					
	impact	12.2	11.9	8.9	8.2	9.8
	vibro (free-hi-aggr)	13.0	15.9	10.0	9.6	12.7
	vibro (free-lo)	11.1	15.0	9.0	9.5	--
	vibro (guided-hi-fix)	16.5	16.5	11.9	10.0	12.5
	vibro (guided-lo-fix)	18.5	22.9	13.1	10.3	16.8

Comparative diagrams of the accumulation behaviour for all tests and test groups and each phase are given in the following figures.

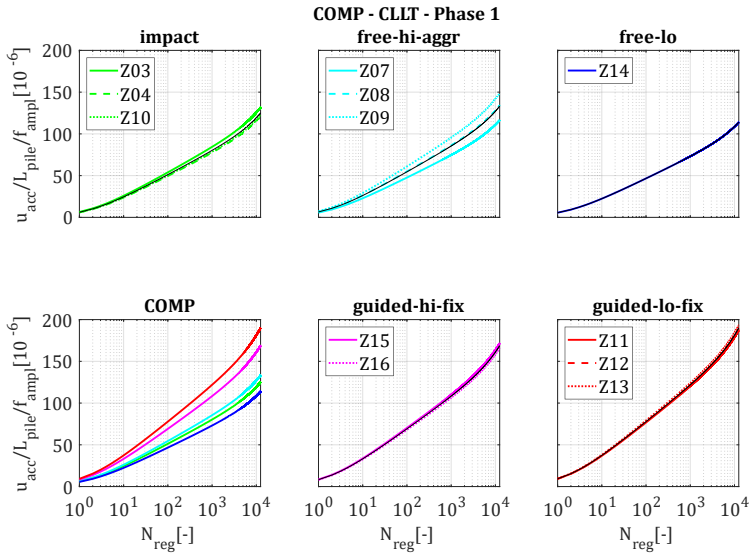


Figure F-34: Comparison of accumulation behaviour of tests and tests groups during phase 1

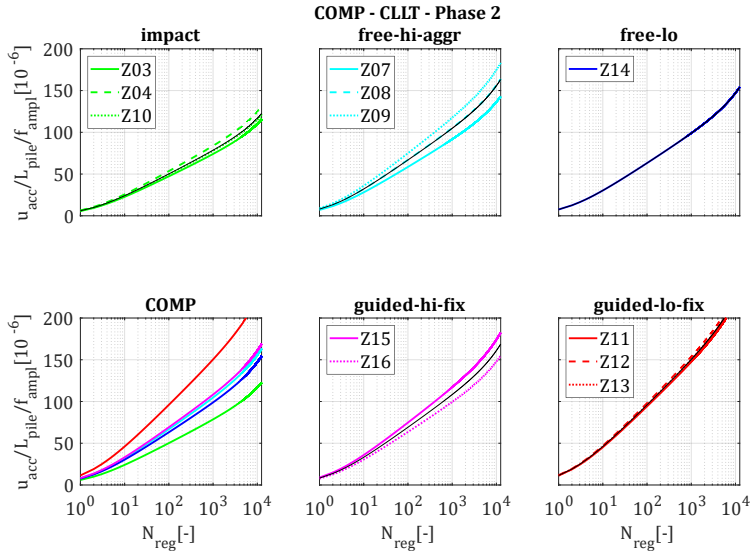


Figure F-35: Comparison of accumulation behaviour of tests and tests groups during phase 2

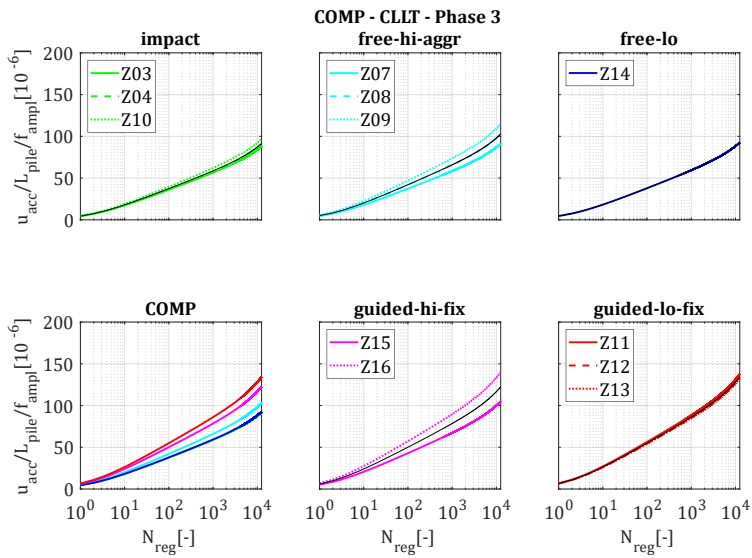


Figure F-36: Comparison of accumulation behaviour of tests and tests groups during phase 3

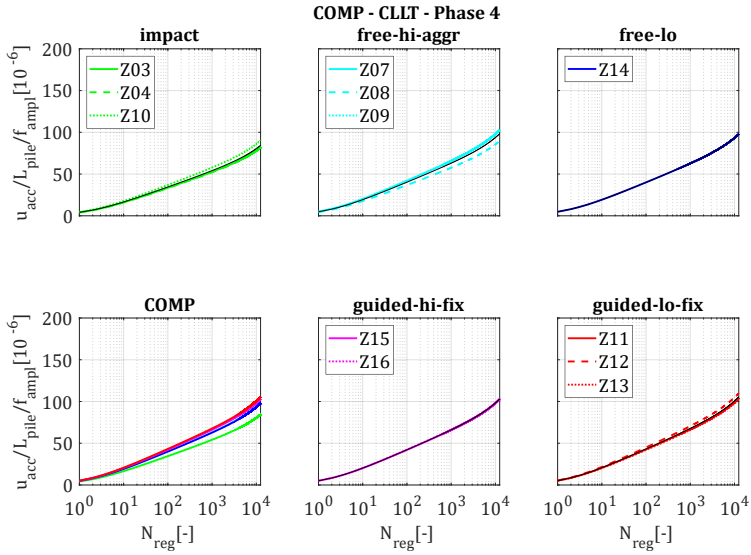


Figure F-37: Comparison of accumulation behaviour of tests and tests groups during phase 4

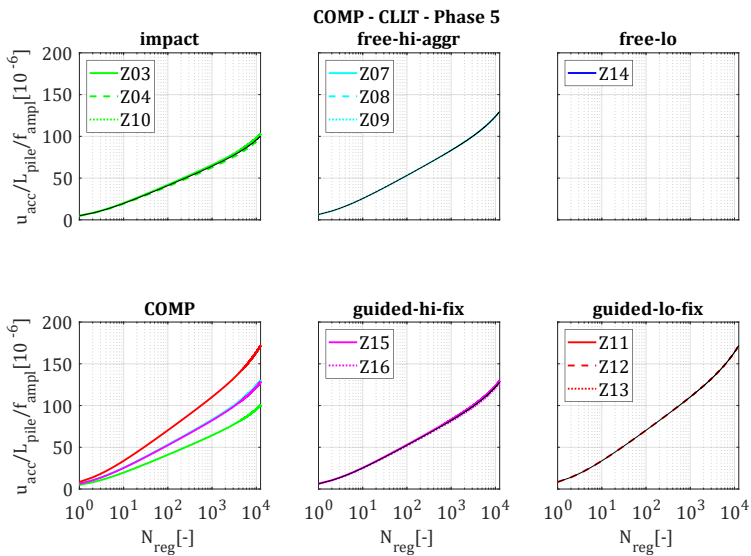


Figure F-38: Comparison of accumulation behaviour of tests and tests groups during phase 5

The following figures show the 'biased' accumulation parameter \hat{C}_{N1} versus the first cycles permanent fictional strain $u_{perm,N=1}/L_{pile}$ for all tests and test phases. Accumulation parameters $C_{N2} = 0,65$ and $C_{N3} = 10^{-4}$ according to Equation (6-13) were used in all cases.

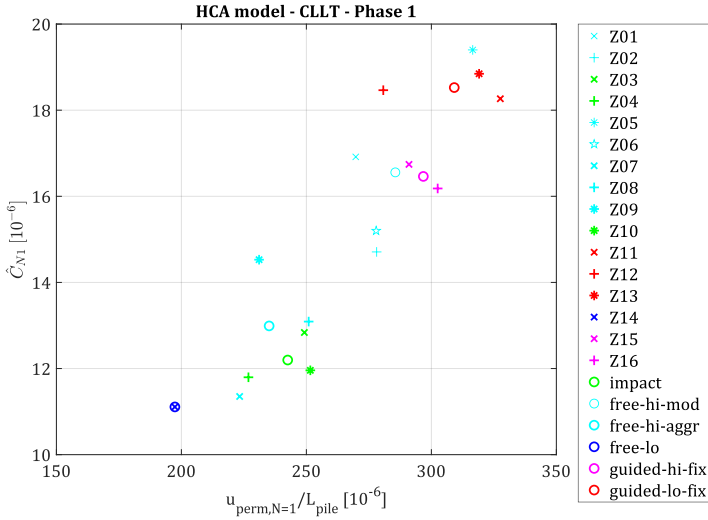


Figure F-39: Biased accumulation parameter over permanent fictional strain of first cycle of phase 1

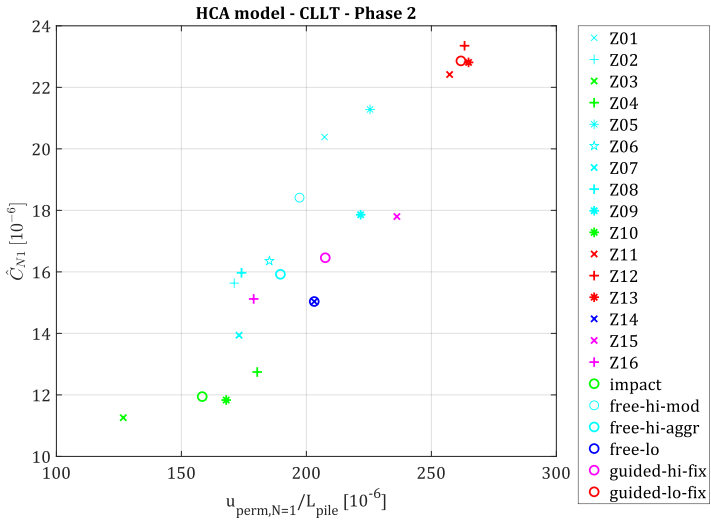


Figure F-40: Biased accumulation parameter over permanent fictional strain of first cycle of phase 2

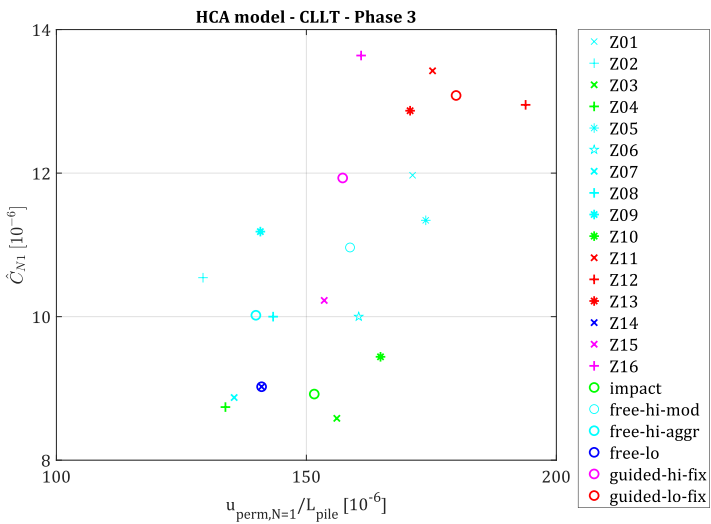


Figure F-41: Biased accumulation parameter over permanent fictional strain of first cycle of phase 3

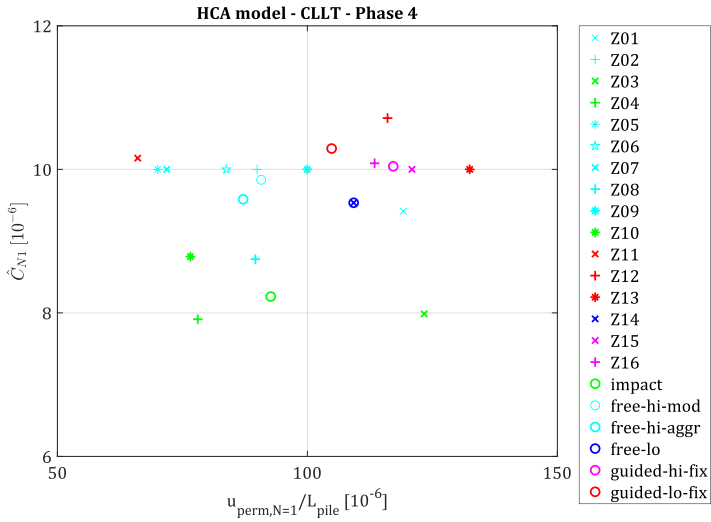


Figure F-42: Biased accumulation parameter over permanent fictional strain of first cycle of phase 4

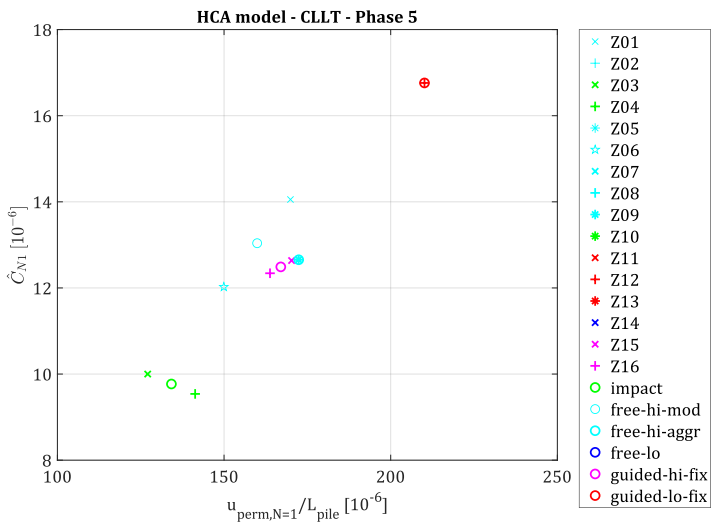


Figure F-43: Biased accumulation parameter over permanent fictional strain of first cycle of phase 5

Back-accumulation

The following figures show detailed plots of the load displacement behaviour in loading direction and in transverse direction for specific cycles of phases 2, 3, and 5 of all tests.

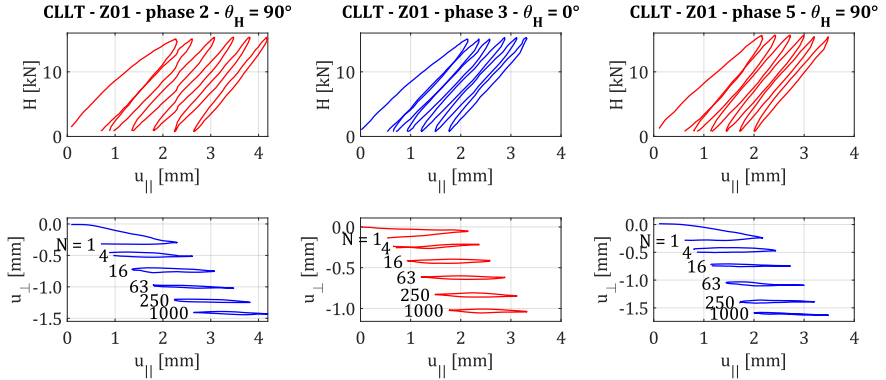


Figure F-44: Hysteresis loops (top) and pile head movement on cycle level in horizontal plane (bottom) for phases 2, 3 and 5 of test Z01

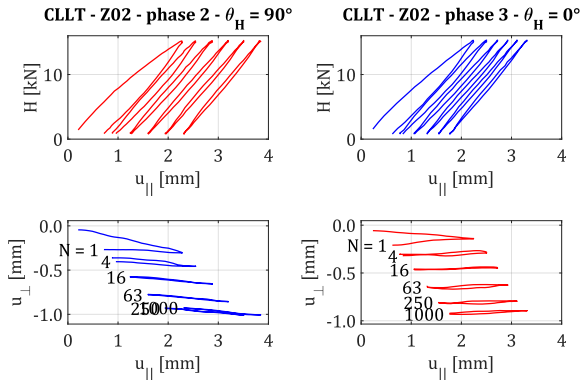


Figure F-45: Hysteresis loops (top) and pile head movement on cycle level in horizontal plane (bottom) for phases 2 and 3 of test Z02

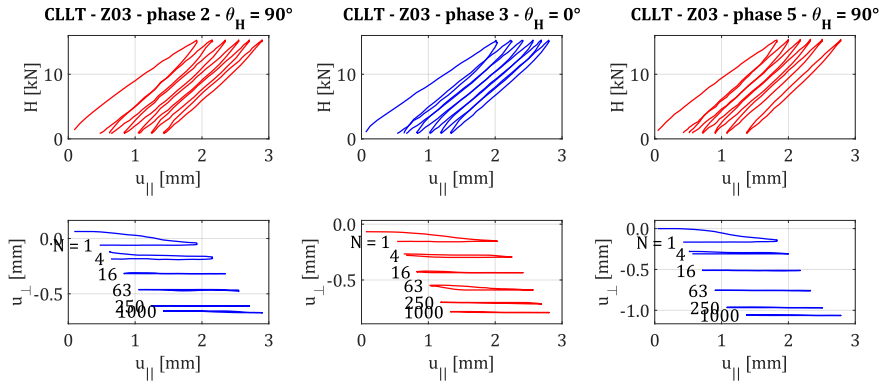


Figure F-46: Hysteresis loops (top) and pile head movement on cycle level in horizontal plane (bottom) for phases 2, 3 and 5 of test Z03

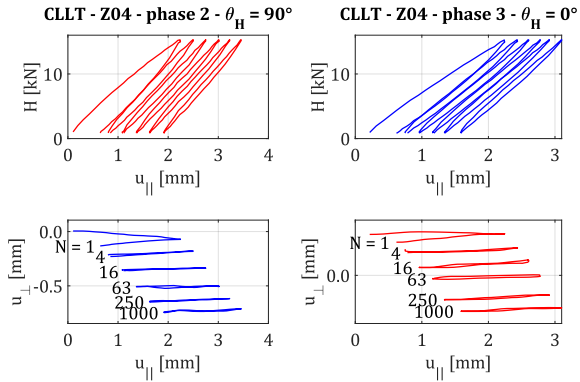


Figure F-47: Hysteresis loops (top) and pile head movement on cycle level in horizontal plane (bottom) for phases 2 and 3 of test Z04

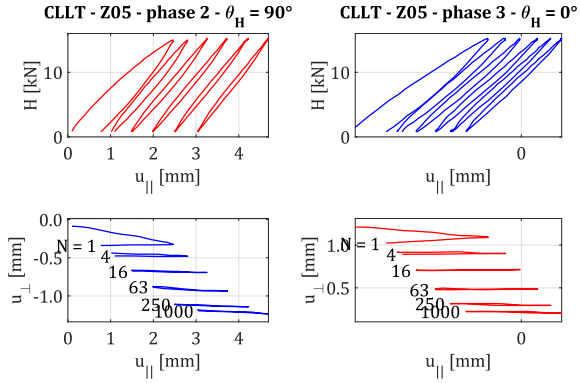


Figure F-48: Hysteresis loops (top) and pile head movement on cycle level in horizontal plane (bottom) for phases 2 and 3 of test Z05

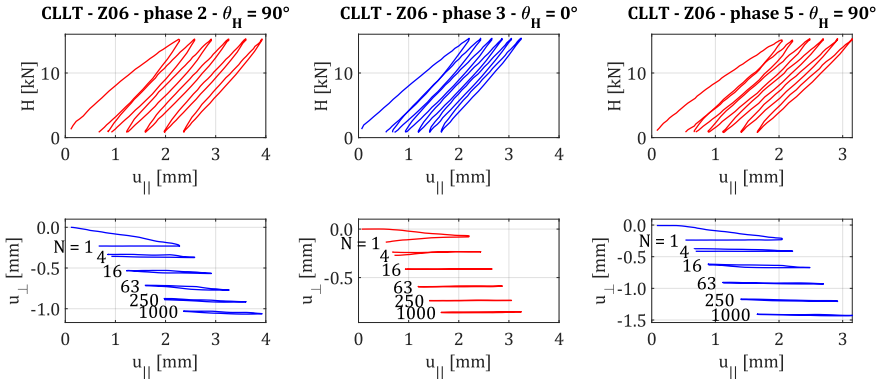


Figure F-49: Hysteresis loops (top) and pile head movement on cycle level in horizontal plane (bottom) for phases 2, 3 and 5 of test Z06

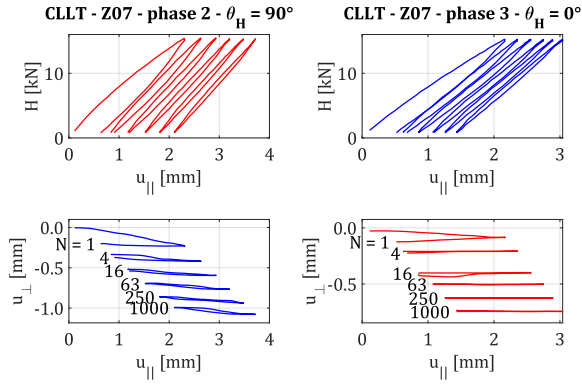


Figure F-50: Hysteresis loops (top) and pile head movement on cycle level in horizontal plane (bottom) for phases 2 and 3 of test Z07

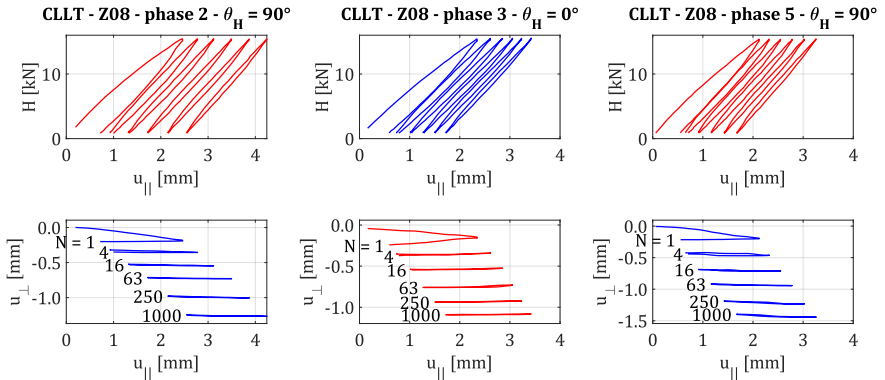


Figure F-51: Hysteresis loops (top) and pile head movement on cycle level in horizontal plane (bottom) for phases 2, 3 and 5 of test Z08

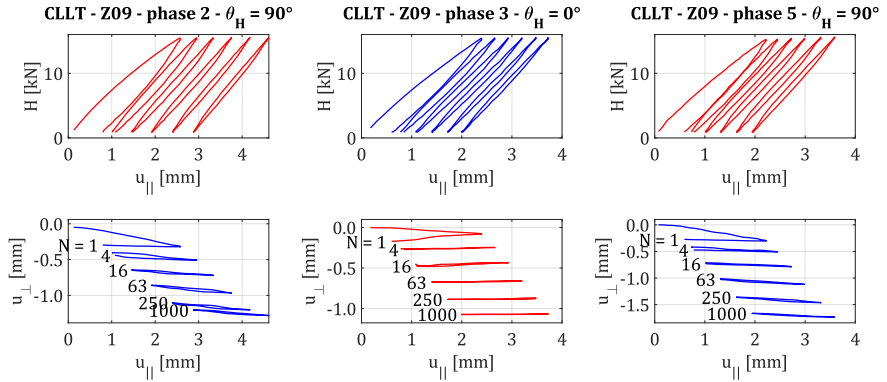


Figure F-52: Hysteresis loops (top) and pile head movement on cycle level in horizontal plane (bottom) for phases 2, 3 and 5 of test Z09

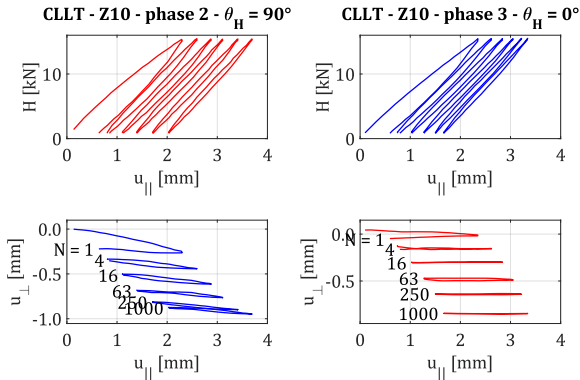


Figure F-53: Hysteresis loops (top) and pile head movement on cycle level in horizontal plane (bottom) for phases 2 and 3 of test Z10

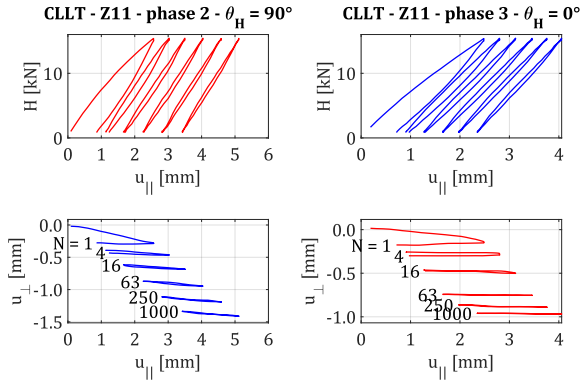


Figure F-54: Hysteresis loops (top) and pile head movement on cycle level in horizontal plane (bottom) for phases 2 and 3 of test Z11

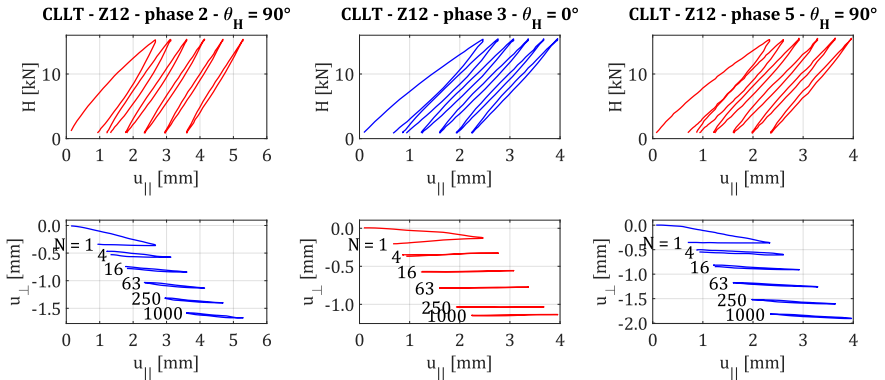


Figure F-55: Hysteresis loops (top) and pile head movement on cycle level in horizontal plane (bottom) for phases 2, 3 and 5 of test Z12

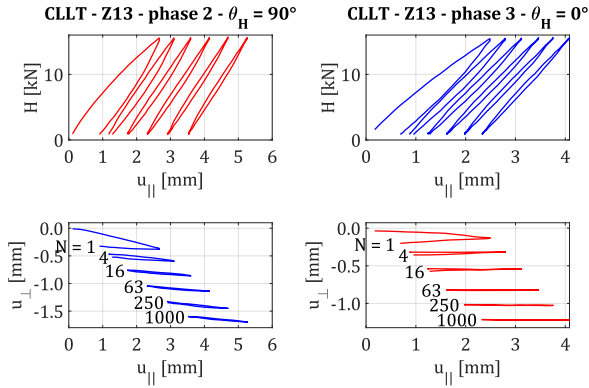


Figure F-56: Hysteresis loops (top) and pile head movement on cycle level in horizontal plane (bottom) for phases 2 and 3 of test Z13

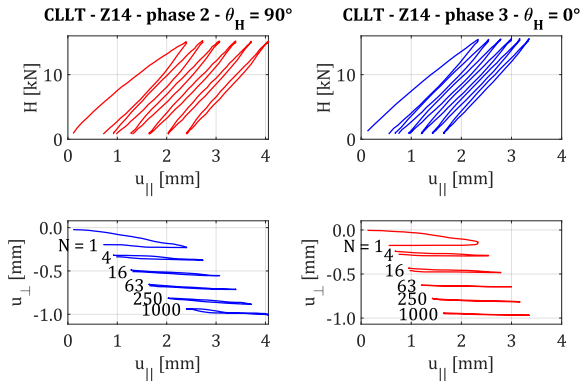


Figure F-57: Hysteresis loops (top) and pile head movement on cycle level in horizontal plane (bottom) for phases 2 and 3 of test Z14

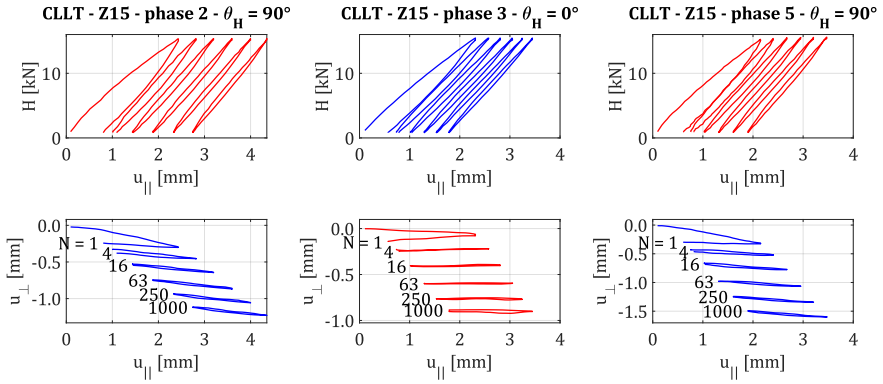


Figure F-58: Hysteresis loops (top) and pile head movement on cycle level in horizontal plane (bottom) for phases 2, 3 and 5 of test Z15

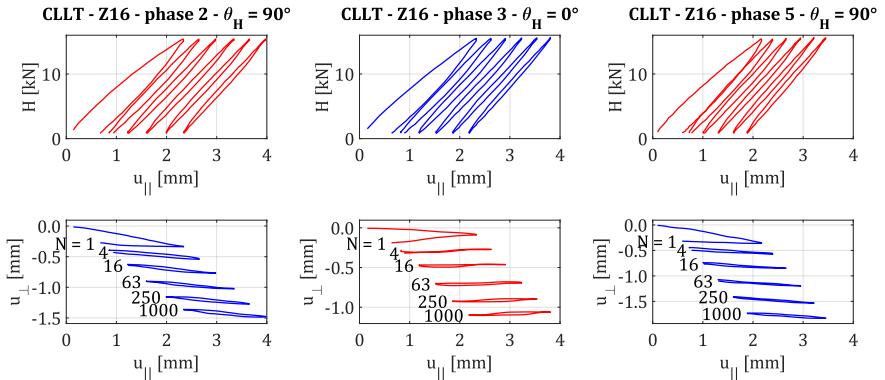


Figure F-59: Hysteresis loops (top) and pile head movement on cycle level in horizontal plane (bottom) for phases 2, 3 and 5 of test Z16

Mudline subsidence

The following figures show the soil subsidence measured around the pile (cf. Figure 5-19) after each loading phase for different tests.

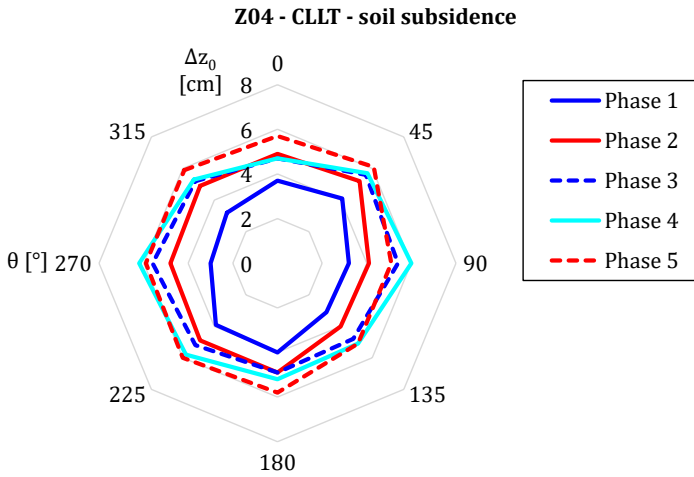


Figure F-60: Soil subsidence around pile Z04 after end of each loading phase

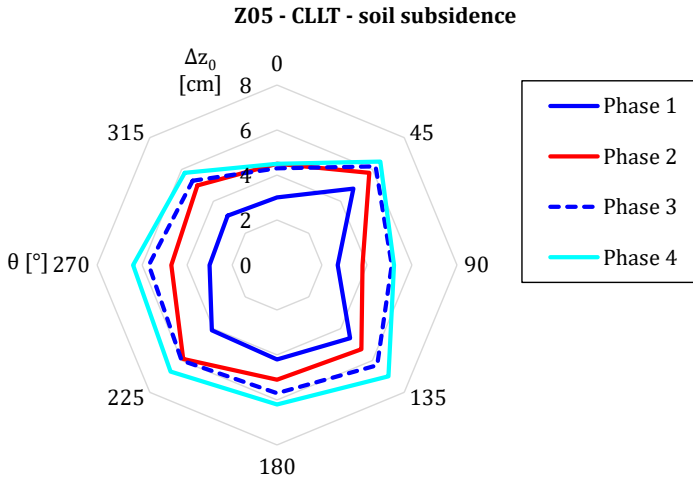


Figure F-61: Soil subsidence around pile Z05 after end of each loading phase

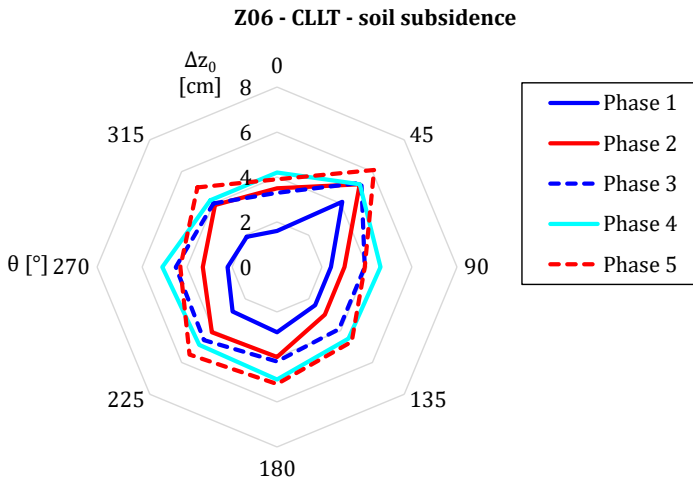


Figure F-62: Soil subsidence around pile Z06 after end of each loading phase

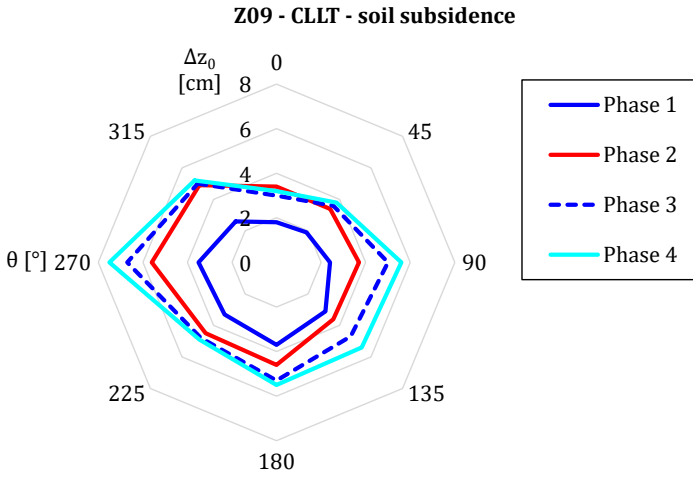


Figure F-63: Soil subsidence around pile Z09 after end of each loading phase

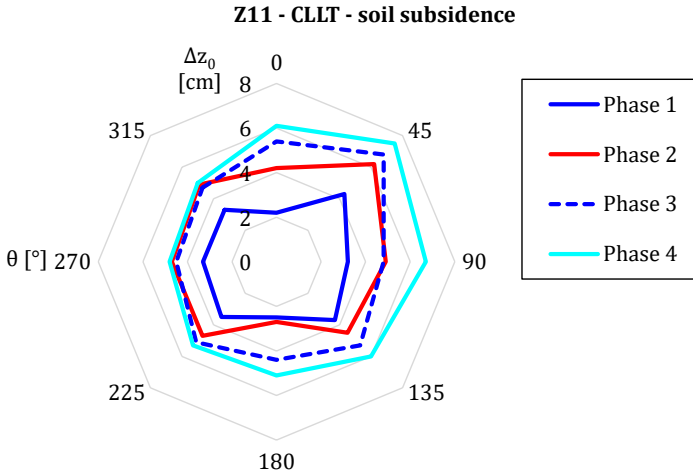


Figure F-64: Soil subsidence around pile Z11 after end of each loading phase

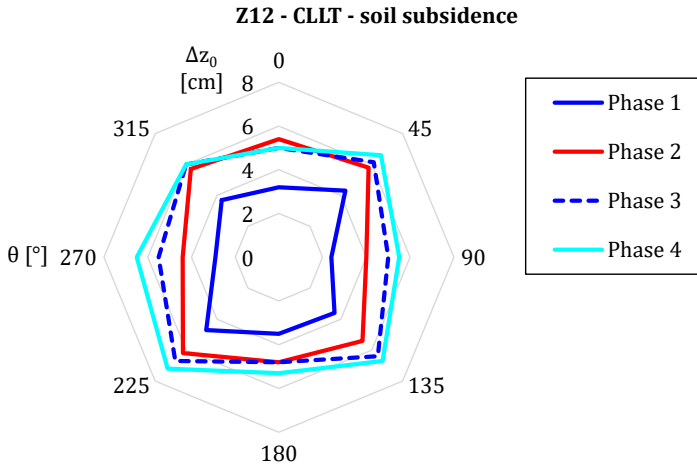


Figure F-65: Soil subsidence around pile Z12 after end of each loading phase

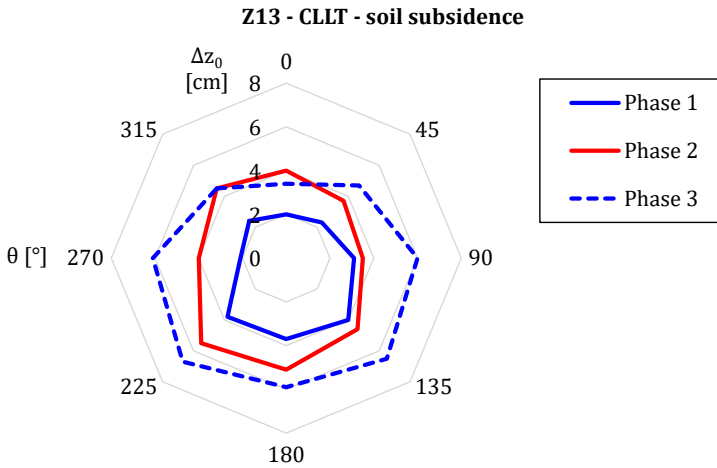


Figure F-66: Soil subsidence around pile Z13 after end of each loading phase

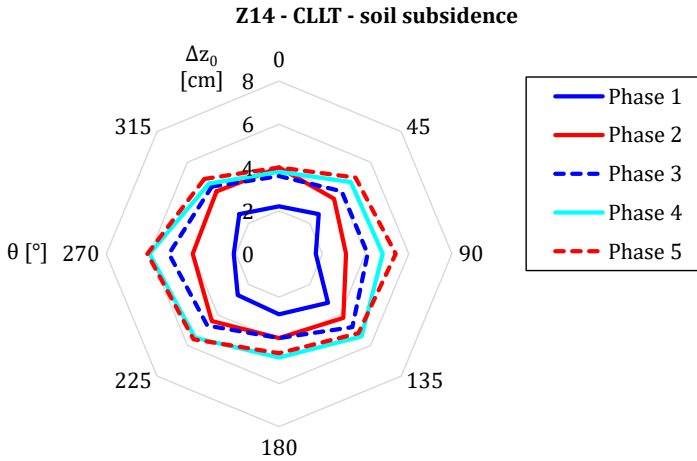


Figure F-67: Soil subsidence around pile Z14 after end of each loading phase

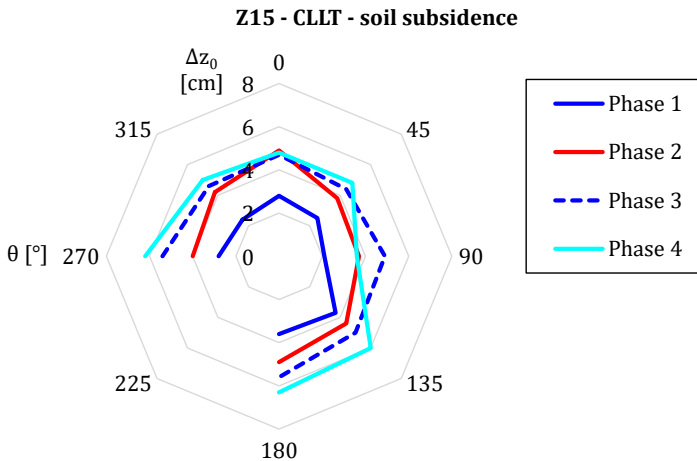


Figure F-68: Soil subsidence around pile Z15 after end of each loading phase

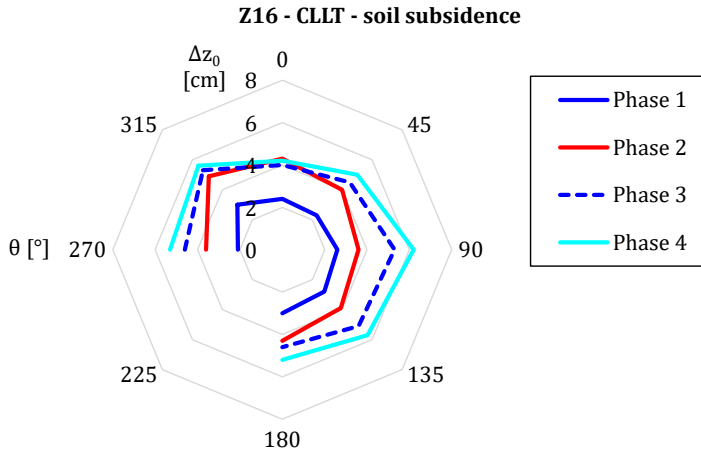


Figure F-69: Soil subsidence around pile Z16 after end of each loading phase

Pile head displacement accumulation ('classical' formulation)

The following diagrams show the displacement accumulation function f_N for all pile groups. Markers indicate measured values, lines indicate fits according to Equation (2-31). The increasing courses in the positive domain show the accumulation in loading direction (\parallel). The decreasing courses in the negative domain show back-accumulation in direction transverse to the loading direction (\perp). For accumulation in loading direction, the accumulation function is defined as $f_N = u_{perm,\parallel}(N)/u_{perm,\parallel}(1)$, for back-accumulation, the accumulation function is defined as $f_N = u_{perm,\perp}(N)/u_{perm,\parallel}(1)$. For test phases 1, 2, 3 and 5, the log-linear accumulation formulation was fitted to the measured data, for phase 4 a power law was used.

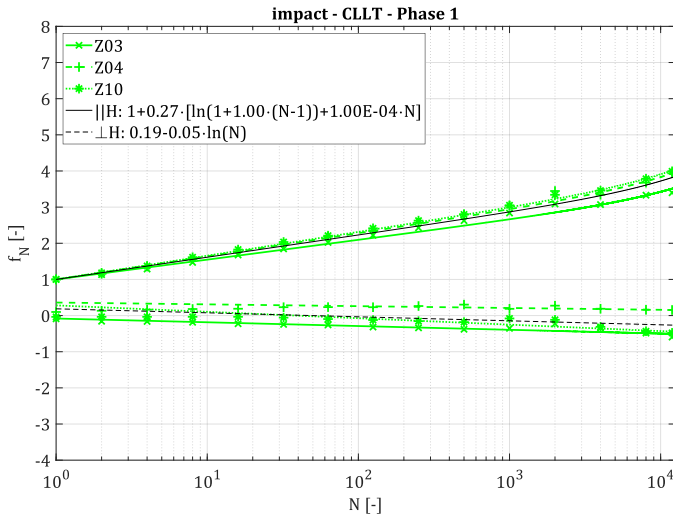


Figure F-70: Pile head displacement accumulation of impact driven piles during phase 1 after 'classical' formulation

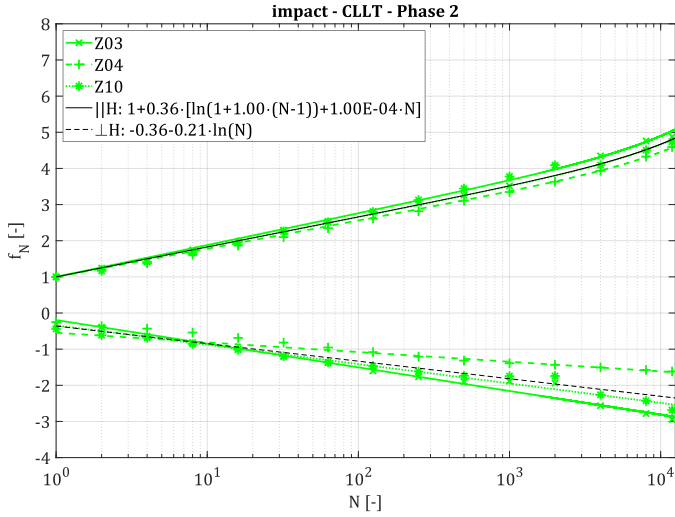


Figure F-71: Pile head displacement accumulation of impact driven piles during phase 2 after 'classical' formulation

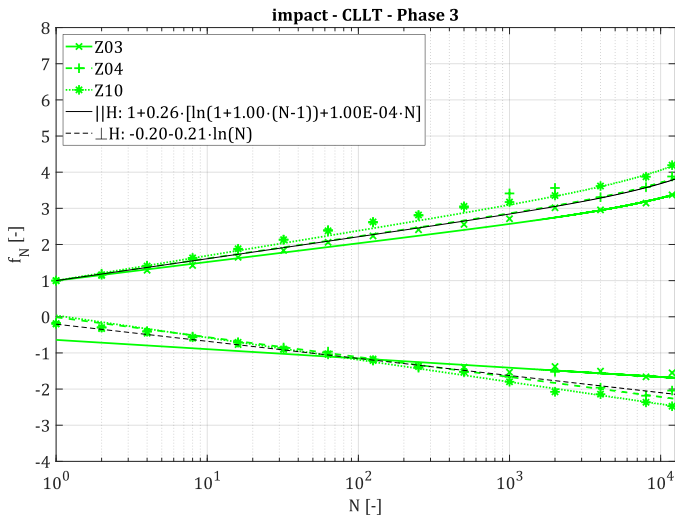


Figure F-72: Pile head displacement accumulation of impact driven piles during phase 3 after 'classical' formulation

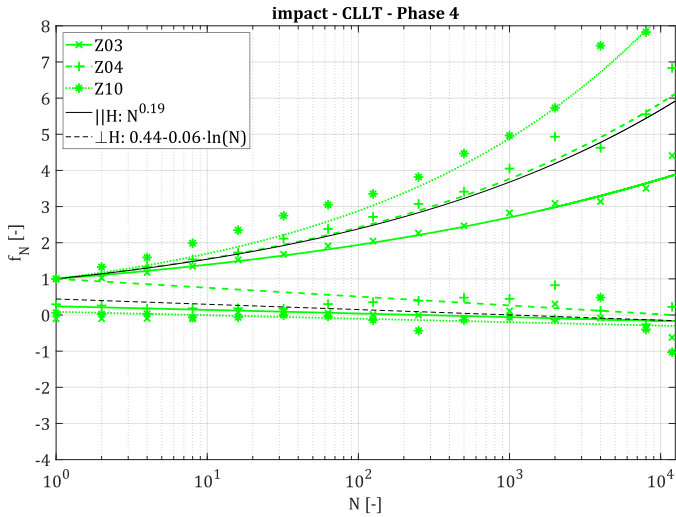


Figure F-73: Pile head displacement accumulation of impact driven piles during phase 4 after 'classical' formulation

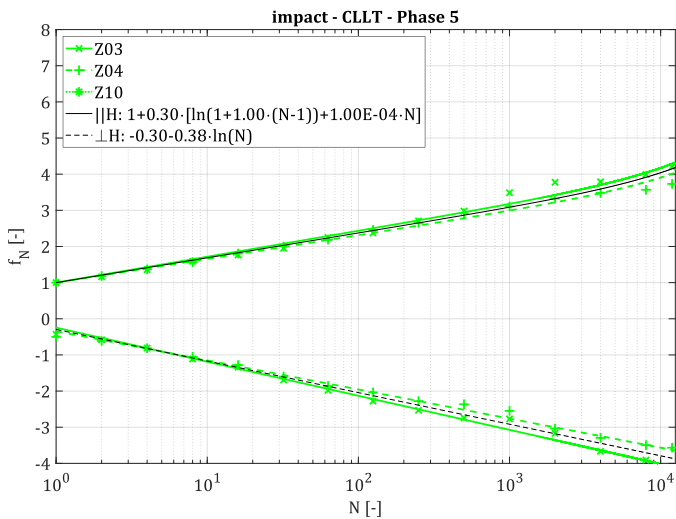


Figure F-74: Pile head displacement accumulation of impact driven piles during phase 5 after 'classical' formulation

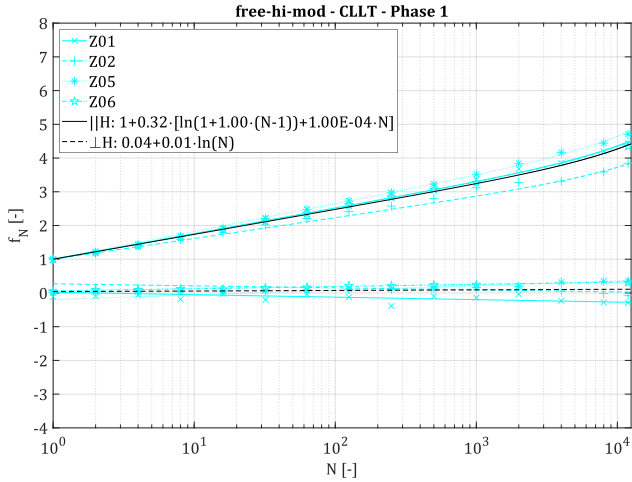


Figure F-75: Pile head displacement accumulation of free vibratory driven piles with high eccentric moment and 'aggressive' frequency control during phase 1 after 'classical' formulation

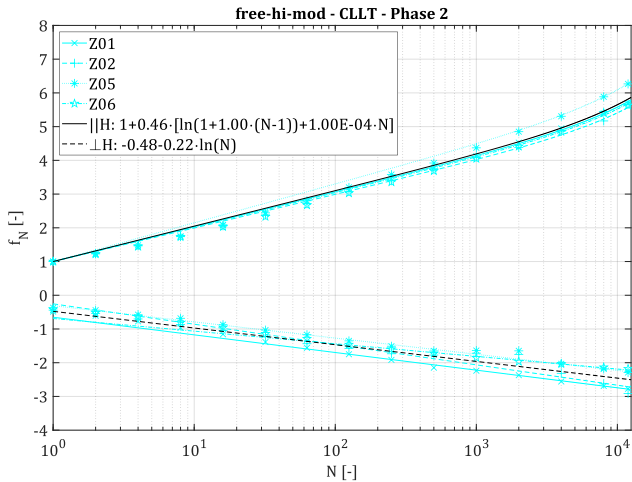


Figure F-76: Pile head displacement accumulation of free vibratory driven piles with high eccentric moment and 'aggressive' frequency control during phase 1 after 'classical' formulation

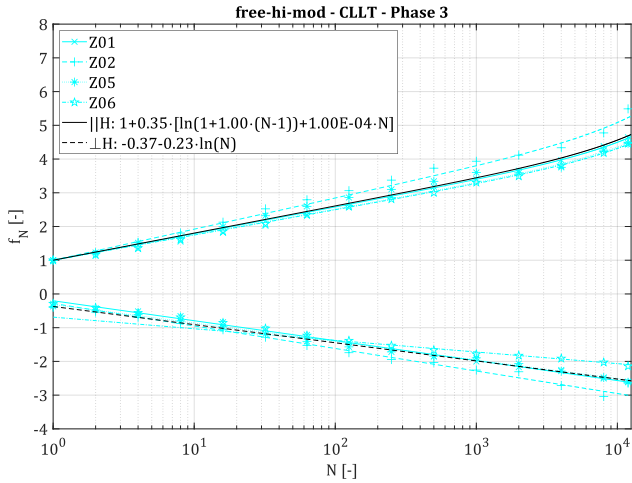


Figure F-77: Pile head displacement accumulation of free vibratory driven piles with high eccentric moment and 'aggressive' frequency control during phase 1 after 'classical' formulation

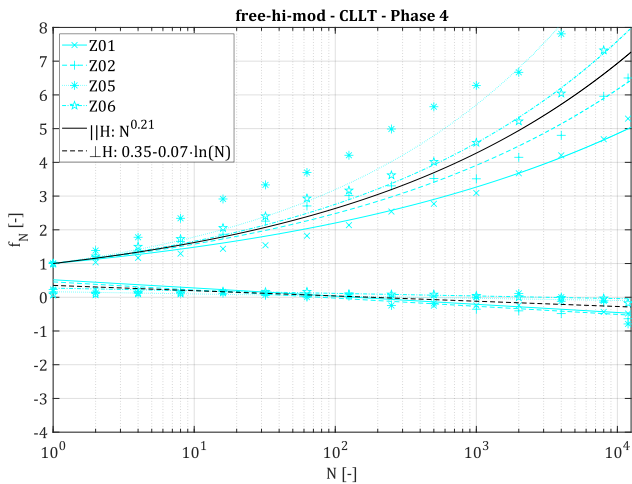


Figure F-78: Pile head displacement accumulation of free vibratory driven piles with high eccentric moment and 'aggressive' frequency control during phase 1 after 'classical' formulation

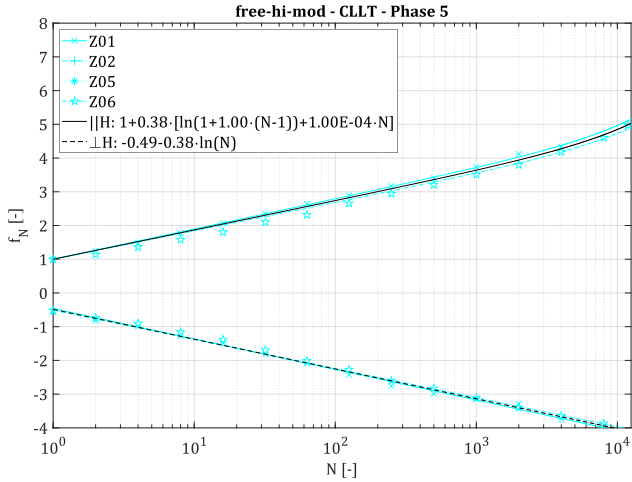


Figure F-79: Pile head displacement accumulation of free vibratory driven piles with high eccentric moment and 'aggressive' frequency control during phase 1 after 'classical' formulation

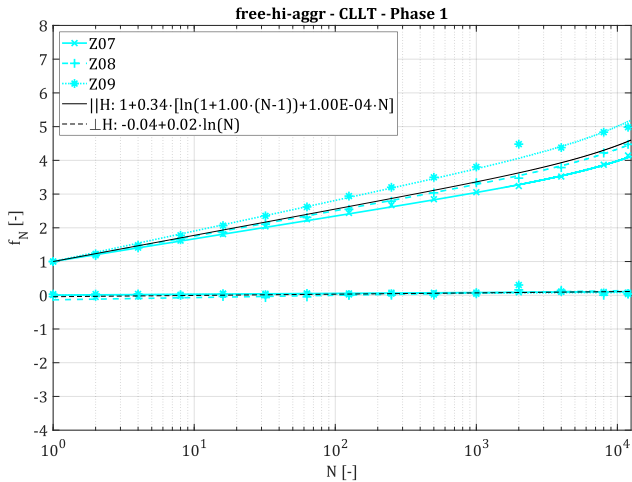


Figure F-80: Pile head displacement accumulation of free vibratory driven piles with high eccentric moment and 'aggressive' frequency control during phase 1 after 'classical' formulation

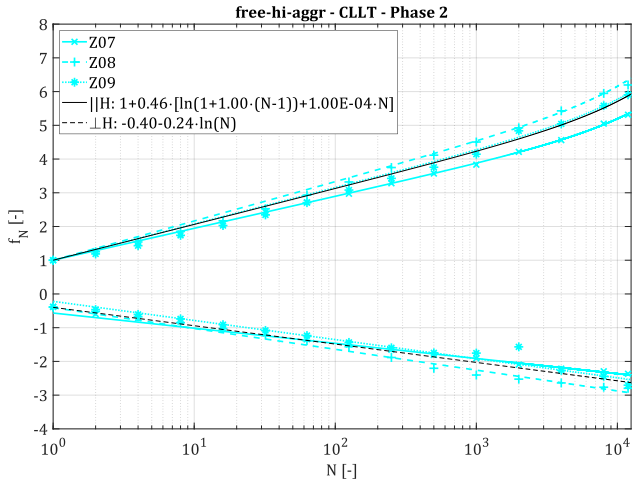


Figure F-81: Pile head displacement accumulation of free vibratory driven piles with high eccentric moment and 'aggressive' frequency control during phase 2 after 'classical' formulation

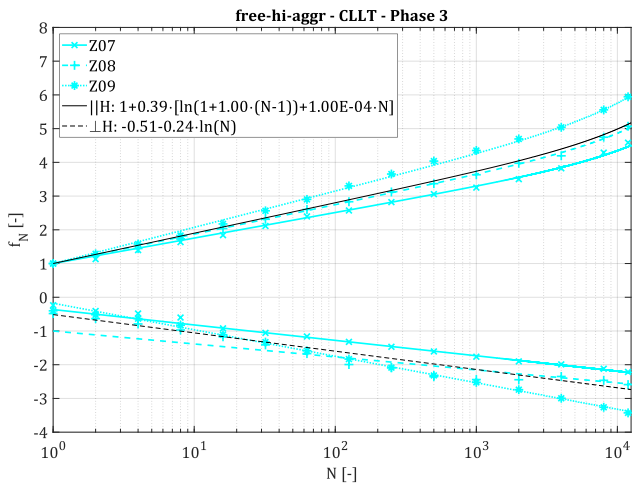


Figure F-82: Pile head displacement accumulation of free vibratory driven piles with high eccentric moment and 'aggressive' frequency control during phase 3 after 'classical' formulation

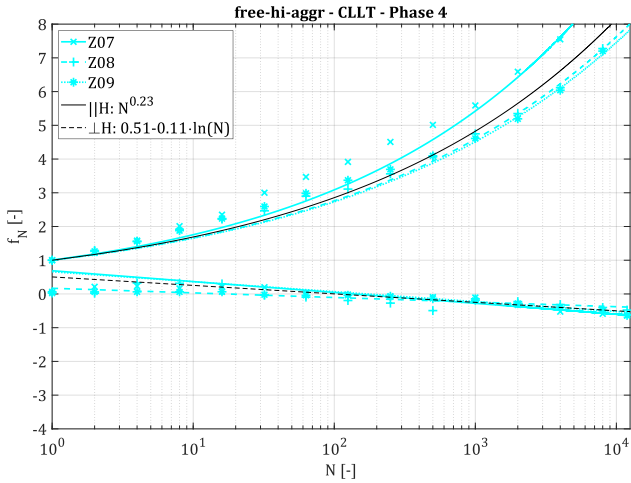


Figure F-83: Pile head displacement accumulation of free vibratory driven piles with high eccentric moment and 'aggressive' frequency control during phase 4 after 'classical' formulation

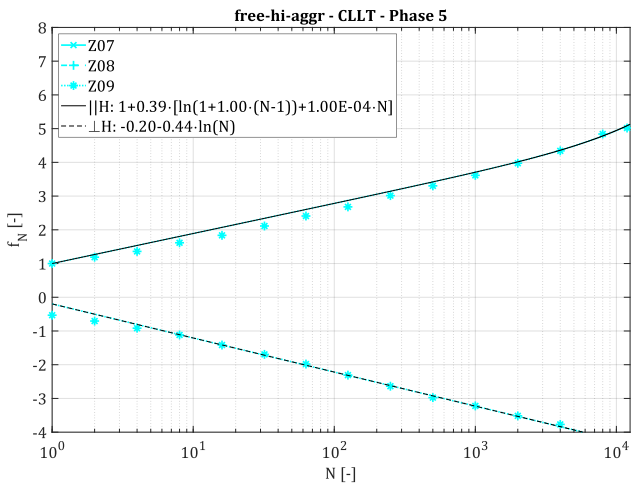


Figure F-84: Pile head displacement accumulation of free vibratory driven piles with high eccentric moment and 'aggressive' frequency control during phase 5 after 'classical' formulation

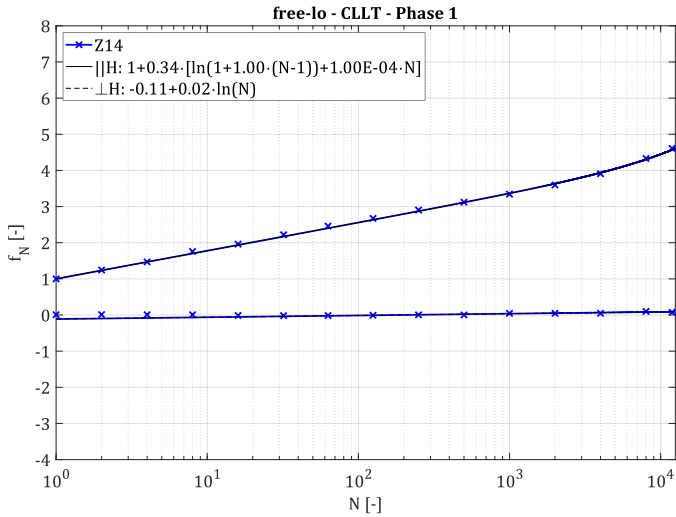


Figure F-85: Pile head displacement accumulation of free vibratory driven piles with low eccentric moment during phase 1 after 'classical' formulation

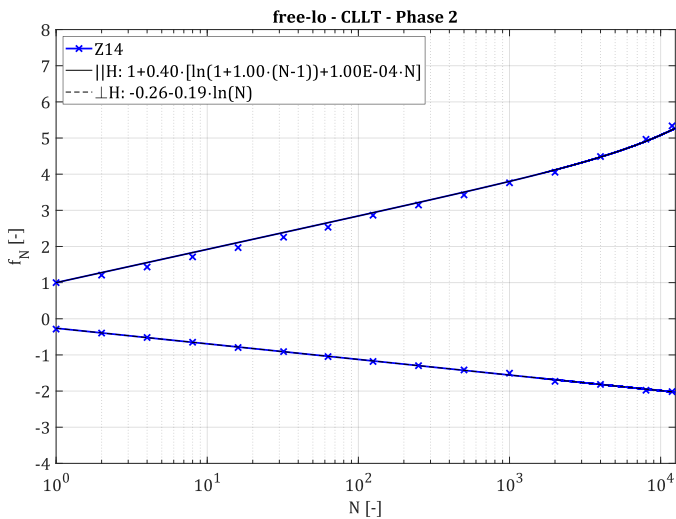


Figure F-86: Pile head displacement accumulation of free vibratory driven piles with low eccentric moment during phase 2 after 'classical' formulation

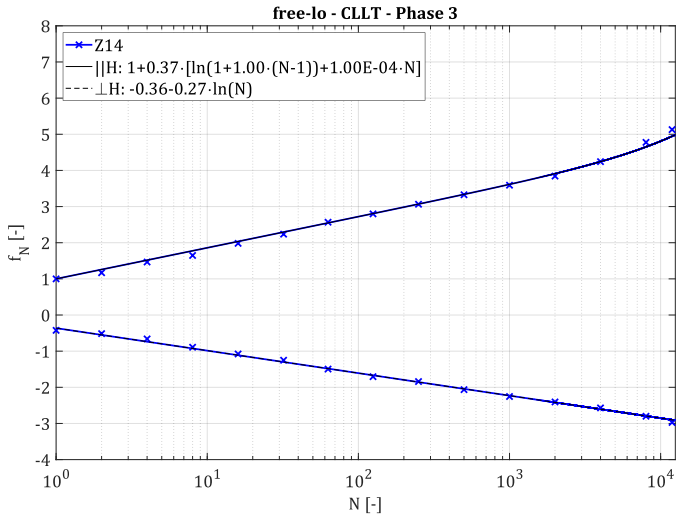


Figure F-87: Pile head displacement accumulation of free vibratory driven piles with low eccentric moment during phase 3 after 'classical' formulation

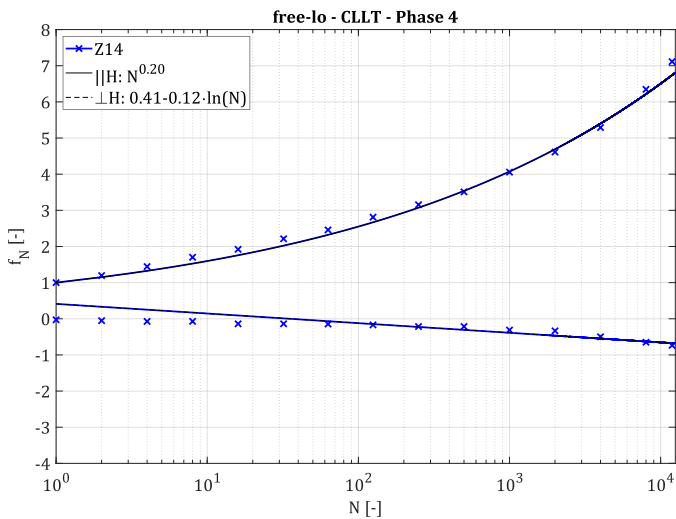


Figure F-88: Pile head displacement accumulation of free vibratory driven piles with low eccentric moment during phase 4 after 'classical' formulation

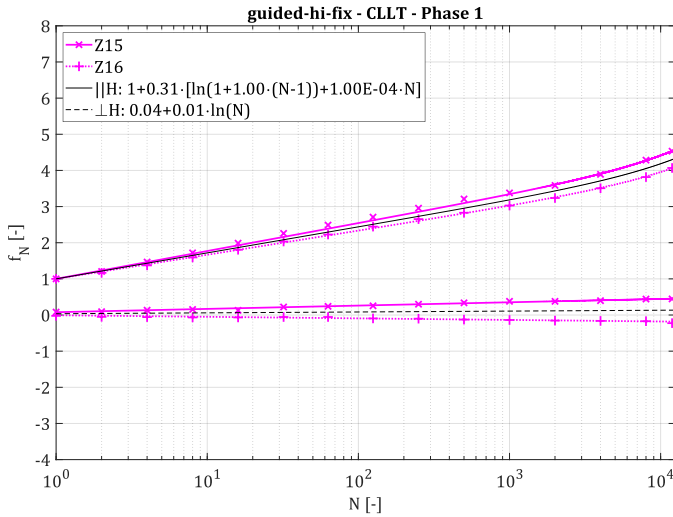


Figure F-89: Pile head displacement accumulation of crane-guided vibratory driven piles with high eccentric moment during phase 1 after 'classical' formulation

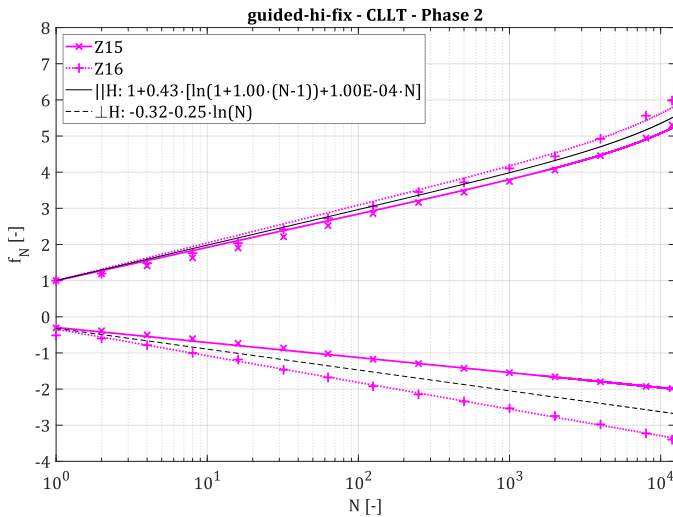


Figure F-90: Pile head displacement accumulation of crane-guided vibratory driven piles with high eccentric moment during phase 2 after 'classical' formulation

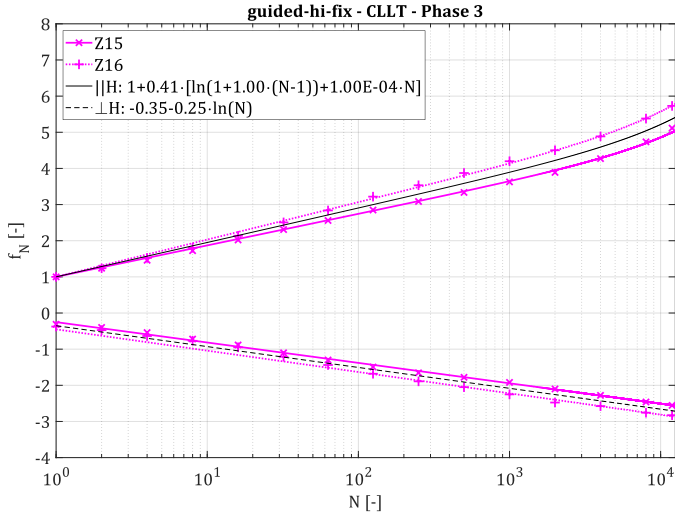


Figure F-91: Pile head displacement accumulation of crane-guided vibratory driven piles with high eccentric moment during phase 3 after 'classical' formulation

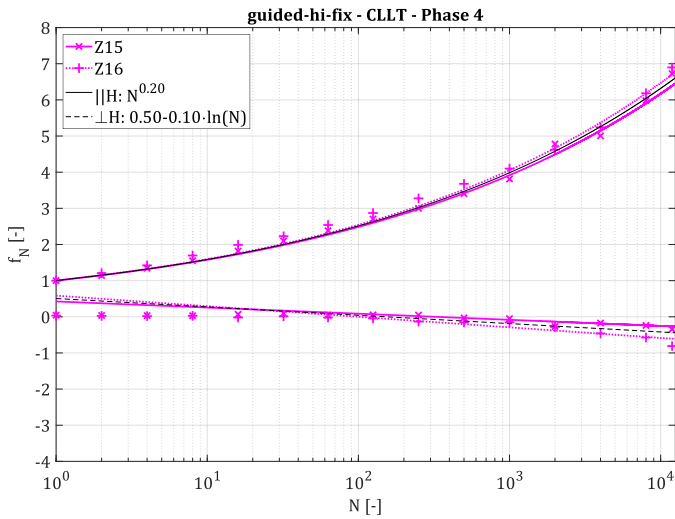


Figure F-92: Pile head displacement accumulation of crane-guided vibratory driven piles with high eccentric moment during phase 4 after 'classical' formulation

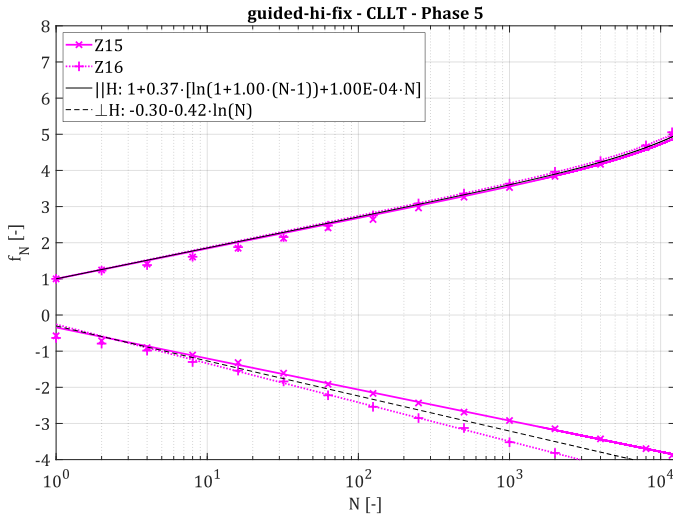


Figure F-93: Pile head displacement accumulation of crane-guided vibratory driven piles with high eccentric moment during phase 5 after 'classical' formulation

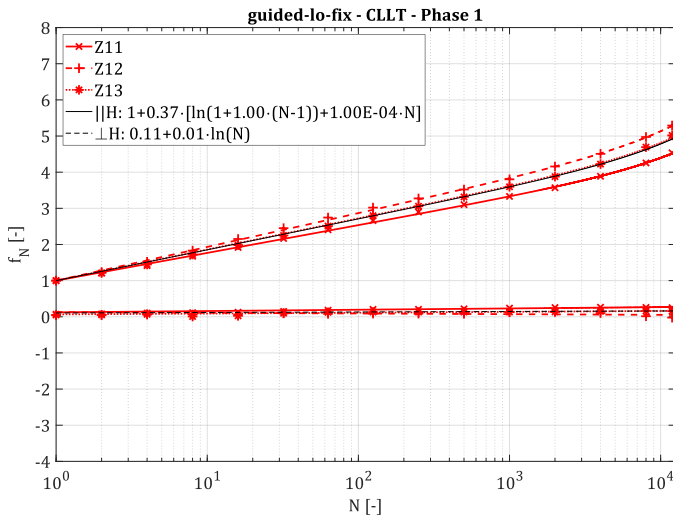


Figure F-94: Pile head displacement accumulation of crane-guided vibratory driven piles with low eccentric moment during phase 1 after 'classical' formulation

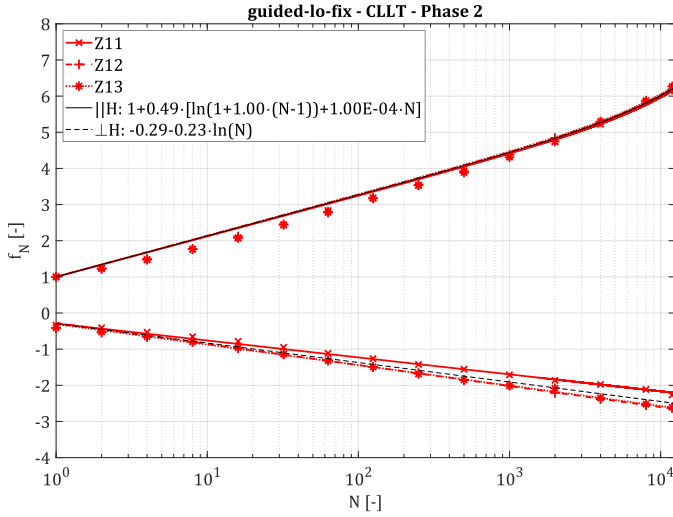


Figure F-95: Pile head displacement accumulation of crane-guided vibratory driven piles with low eccentric moment during phase 2 after 'classical' formulation

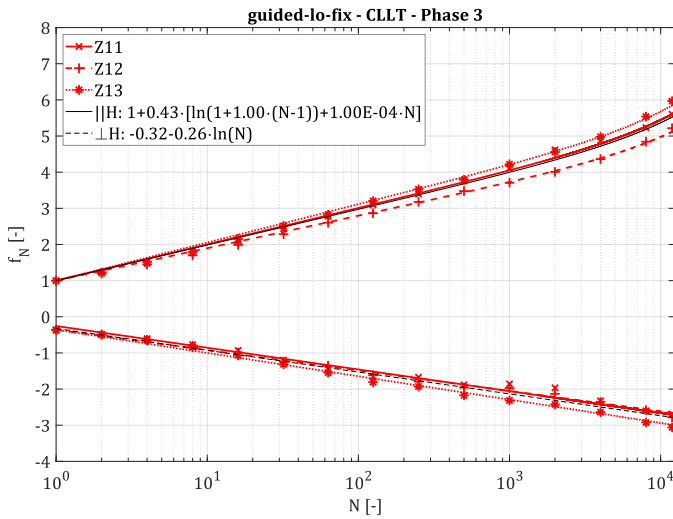


Figure F-96: Pile head displacement accumulation of crane-guided vibratory driven piles with low eccentric moment during phase 3 after 'classical' formulation

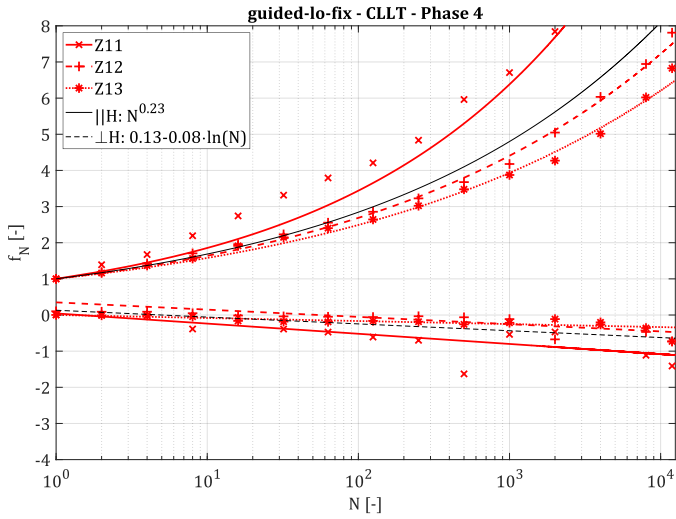


Figure F-97: Pile head displacement accumulation of crane-guided vibratory driven piles with low eccentric moment during phase 4 after 'classical' formulation

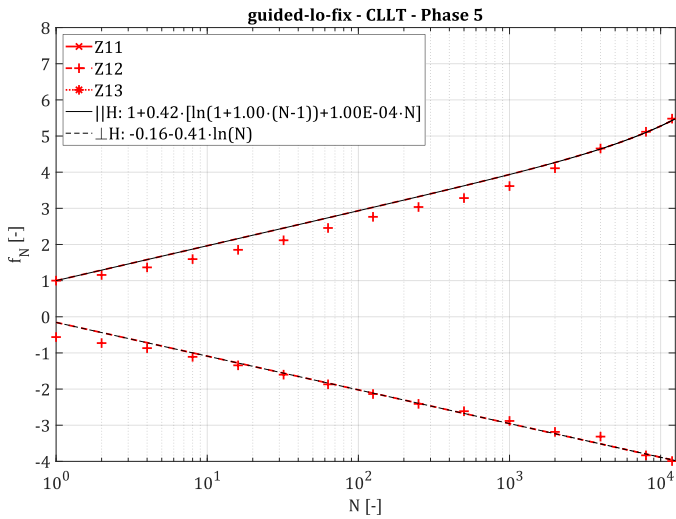


Figure F-98: Pile head displacement accumulation of crane-guided vibratory driven piles with low eccentric moment during phase 5 after 'classical' formulation

Cyclic secant stiffness

The following diagrams show the measured pile head secant stiffness during loading cycles $E_{lat,sec,load}$ related to the secant loading stiffness of the first 'regular' cycle ($N = 2$) for all pile groups and test phases. Markers indicate measured values, lines indicate logarithmic fits.

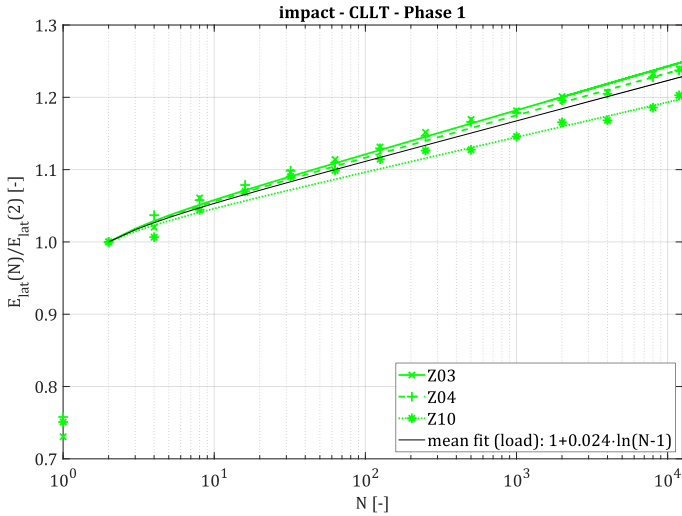


Figure F-99: Development of pile head secant stiffness of impact driven piles during phase 1

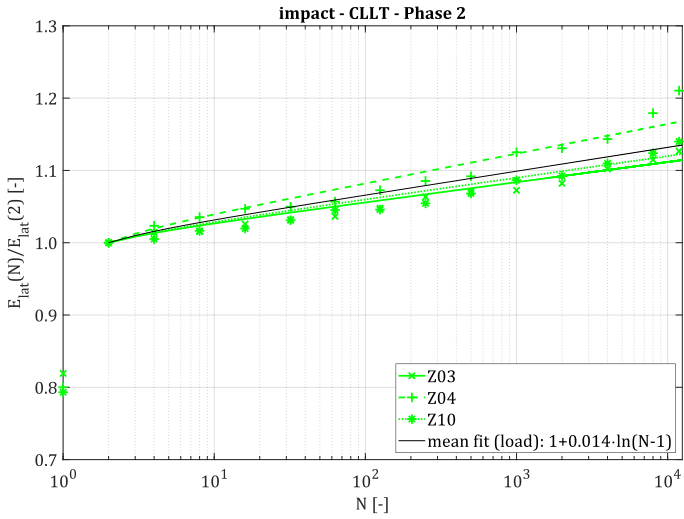


Figure F-100: Development of pile head secant stiffness of impact driven piles during phase 2

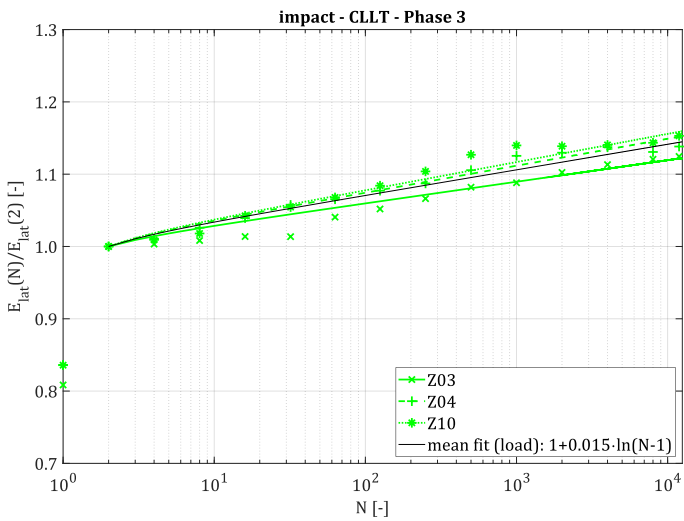


Figure F-101: Development of pile head secant stiffness of impact driven piles during phase 3

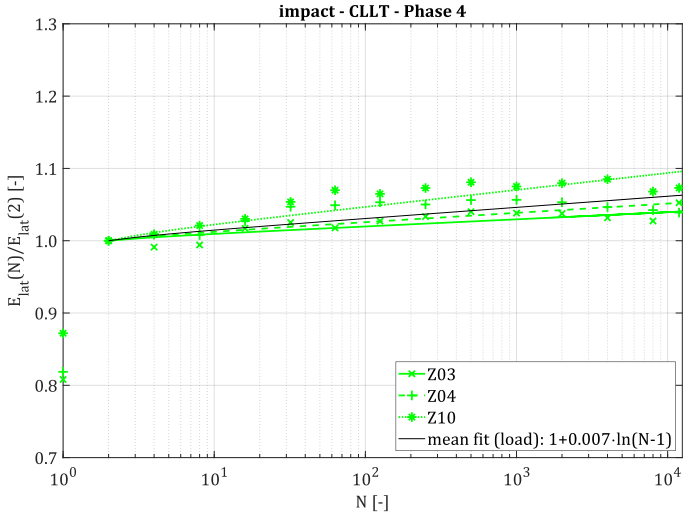


Figure F-102: Development of pile head secant stiffness of impact driven piles during phase 4

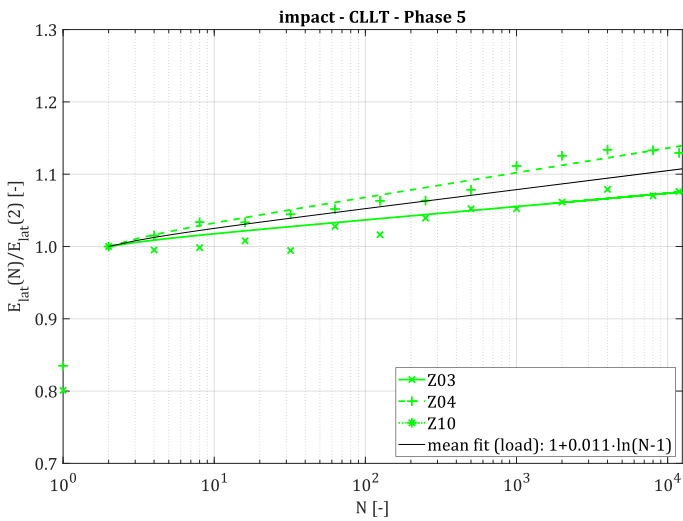


Figure F-103: Development of pile head secant stiffness of impact driven piles during phase 5

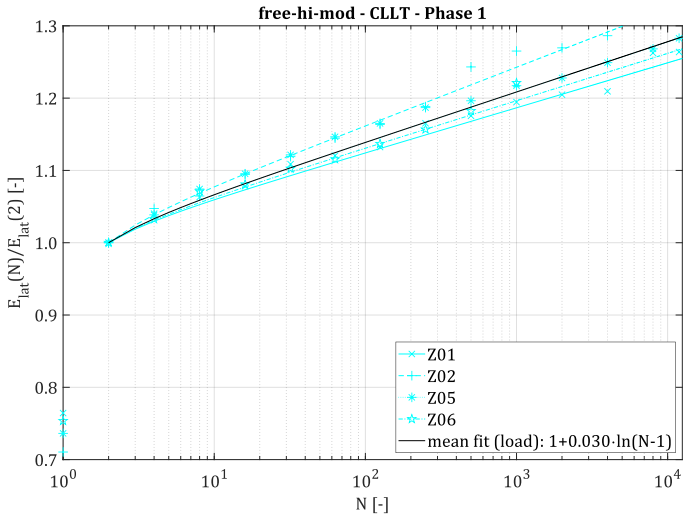


Figure F-104: Development of pile head secant stiffness of free vibratory driven piles with high eccentric moment and 'moderate' frequency control during phase 1

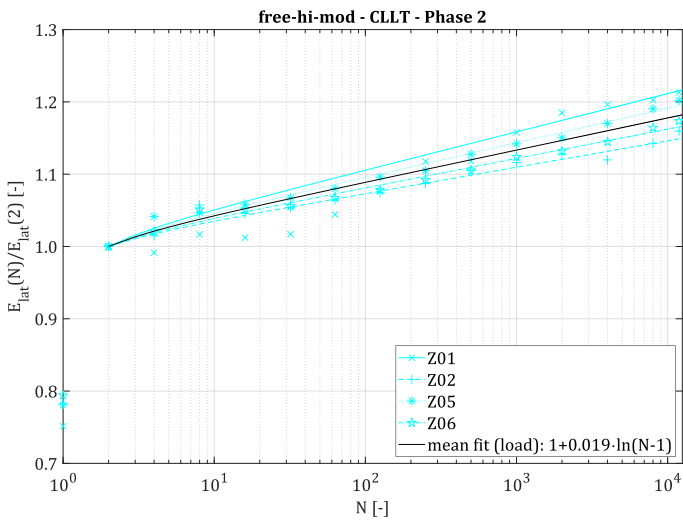


Figure F-105: Development of pile head secant stiffness of free vibratory driven piles with high eccentric moment and 'moderate' frequency control during phase 2

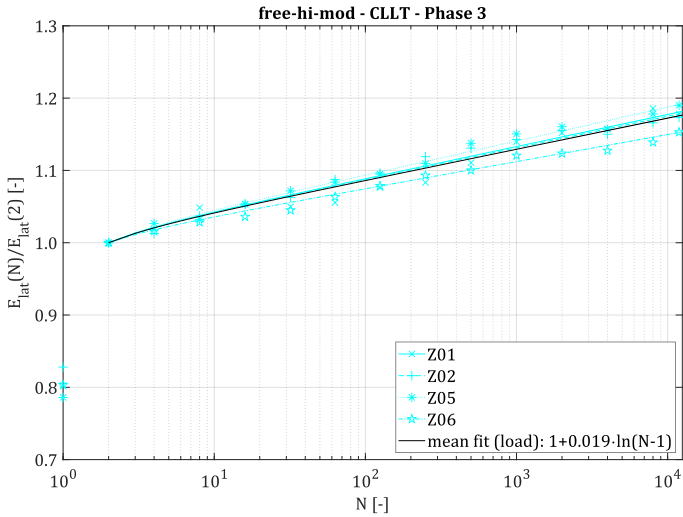


Figure F-106: Development of pile head secant stiffness of free vibratory driven piles with high eccentric moment and 'moderate' frequency control during phase 3

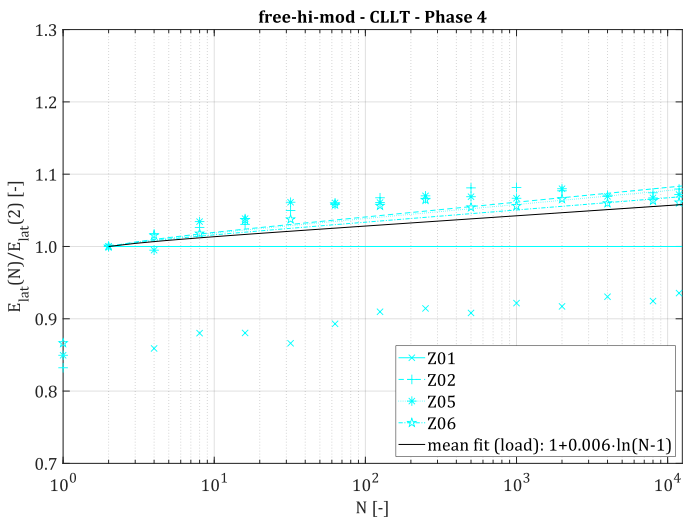


Figure F-107: Development of pile head secant stiffness of free vibratory driven piles with high eccentric moment and 'moderate' frequency control during phase 4

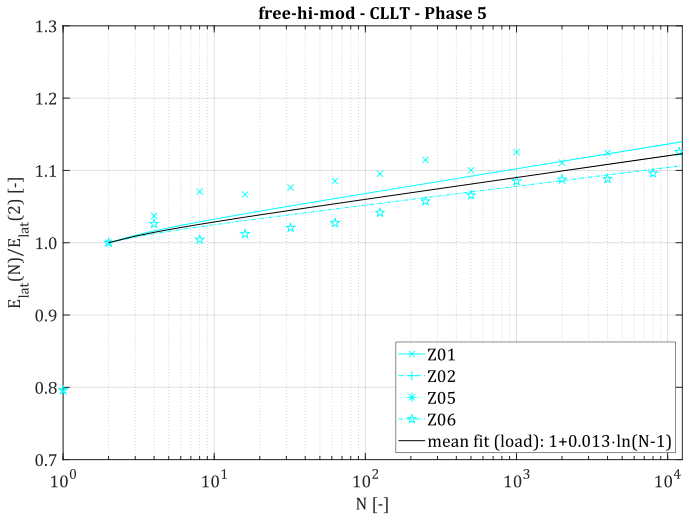


Figure F-108: Development of pile head secant stiffness of free vibratory driven piles with high eccentric moment and 'moderate' frequency control during phase 5

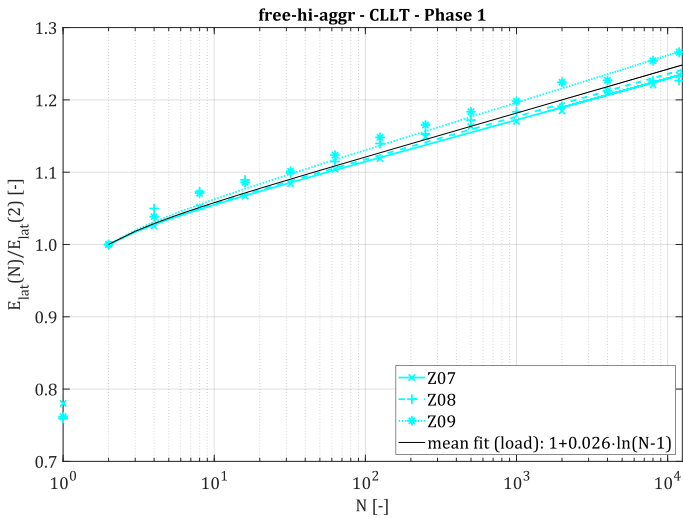


Figure F-109: Development of pile head secant stiffness of free vibratory driven piles with high eccentric moment and 'aggressive' frequency control during phase 1

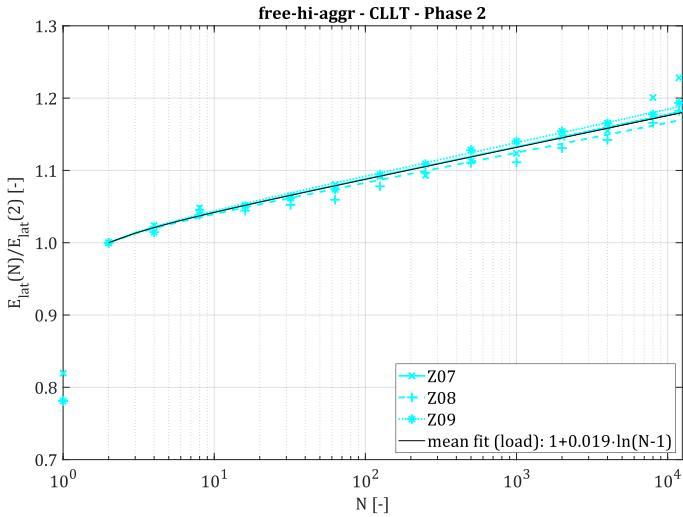


Figure F-110: Development of pile head secant stiffness of free vibratory driven piles with high eccentric moment and 'aggressive' frequency control during phase 2

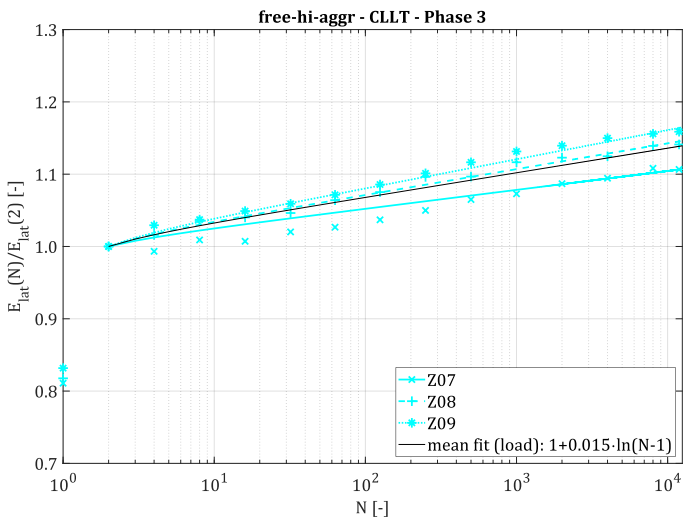


Figure F-111: Development of pile head secant stiffness of free vibratory driven piles with high eccentric moment and 'aggressive' frequency control during phase 3

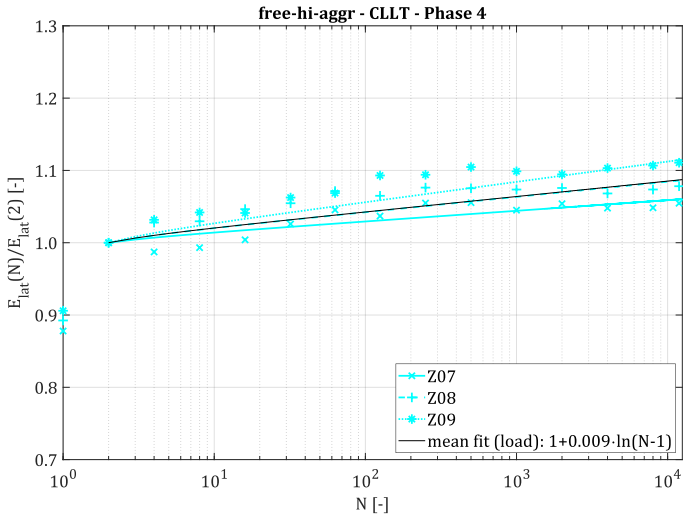


Figure F-112: Development of pile head secant stiffness of free vibratory driven piles with high eccentric moment and 'aggressive' frequency control during phase 4

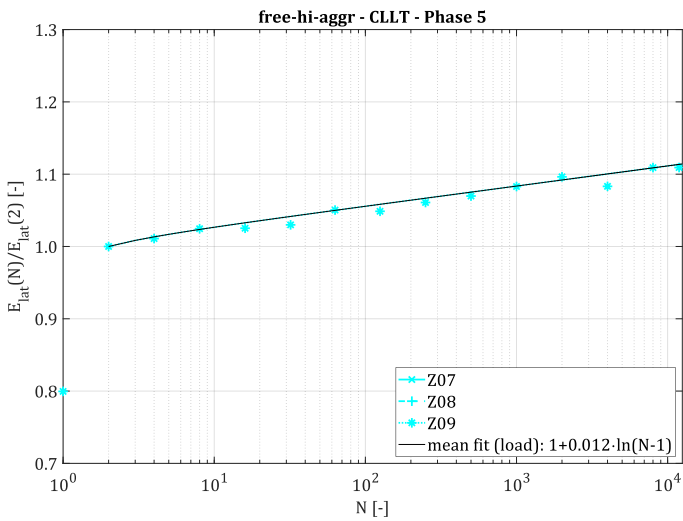


Figure F-113: Development of pile head secant stiffness of free vibratory driven piles with high eccentric moment and 'aggressive' frequency control during phase 5

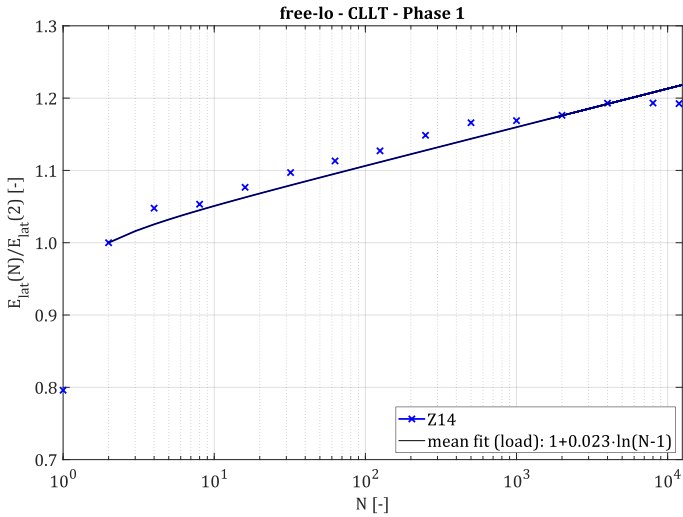


Figure F-114: Development of pile head secant stiffness of free vibratory driven pile with low eccentric moment during phase 1

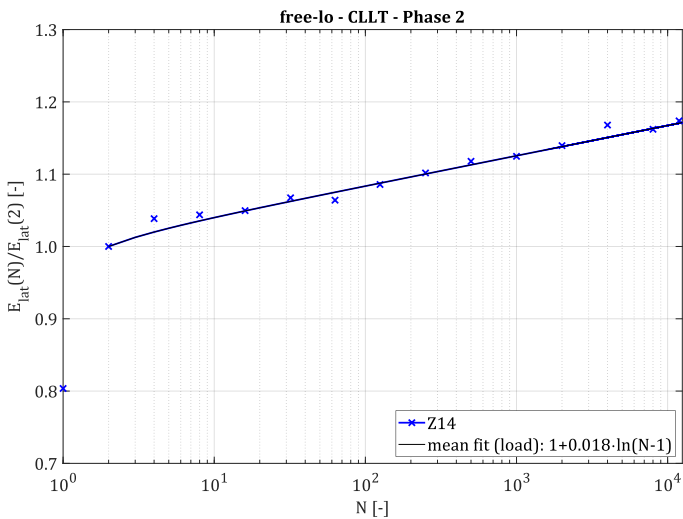


Figure F-115: Development of pile head secant stiffness of free vibratory driven pile with low eccentric moment during phase 2

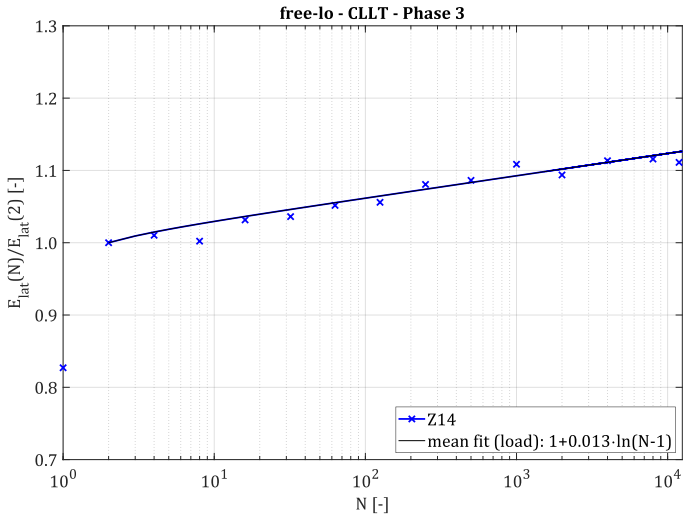


Figure F-116: Development of pile head secant stiffness of free vibratory driven pile with low eccentric moment during phase 3

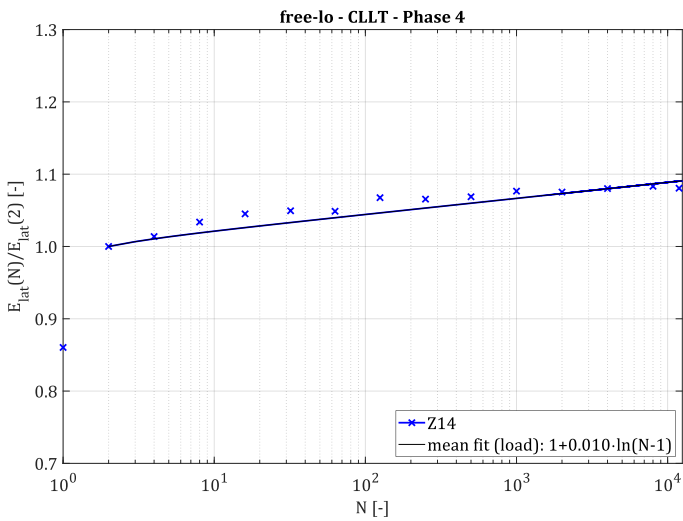


Figure F-117: Development of pile head secant stiffness of free vibratory driven pile with low eccentric moment during phase 4

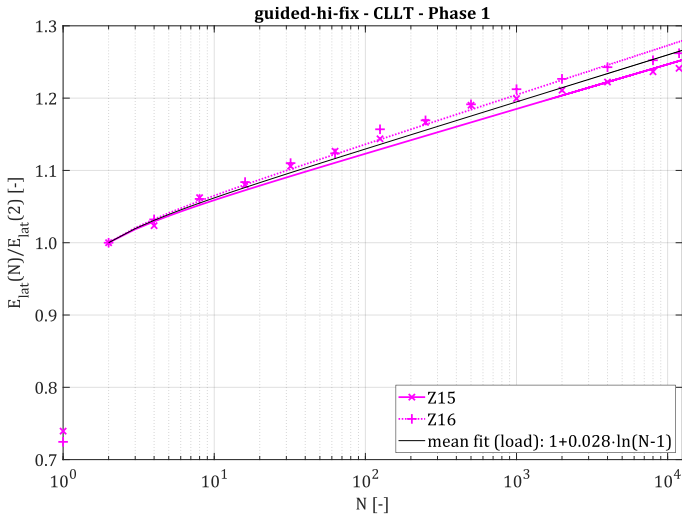


Figure F-118: Development of pile head secant stiffness of crane-guided vibratory driven piles with high eccentric moment during phase 1

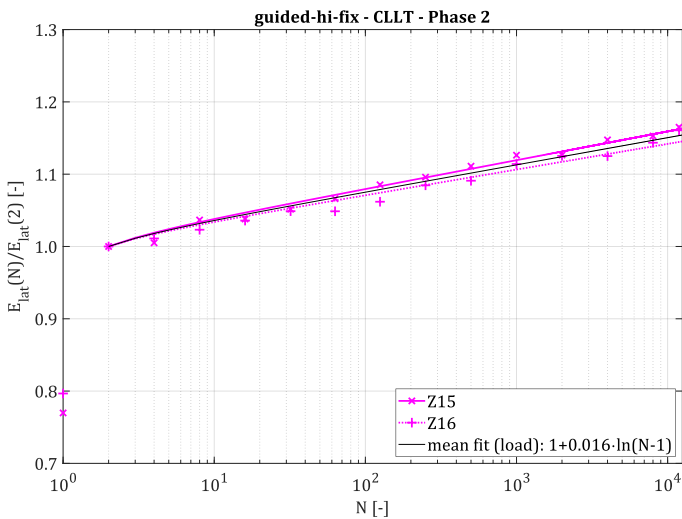


Figure F-119: Development of pile head secant stiffness of crane-guided vibratory driven piles with high eccentric moment during phase 2

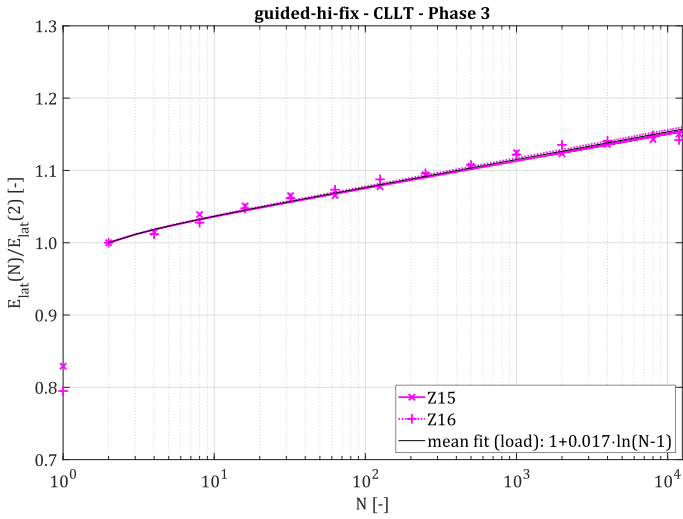


Figure F-120: Development of pile head secant stiffness of crane-guided vibratory driven piles with high eccentric moment during phase 3

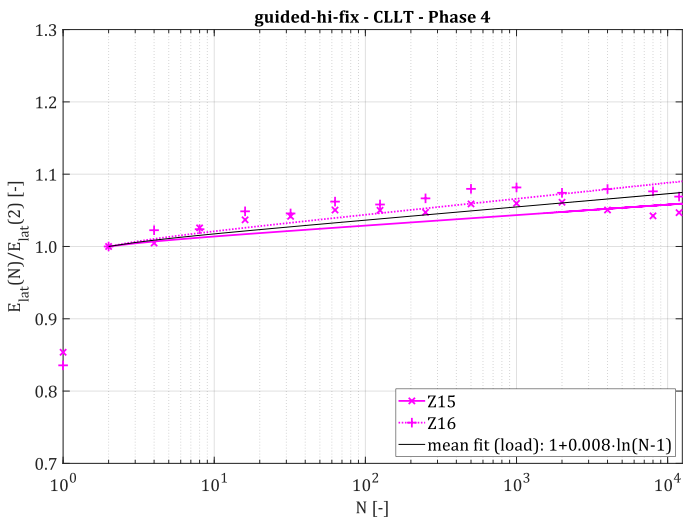


Figure F-121: Development of pile head secant stiffness of crane-guided vibratory driven piles with high eccentric moment during phase 4

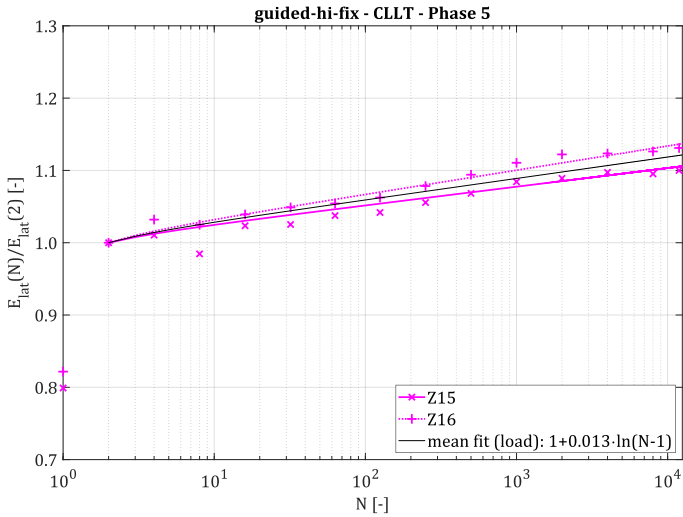


Figure F-122: Development of pile head secant stiffness of crane-guided vibratory driven piles with high eccentric moment during phase 5

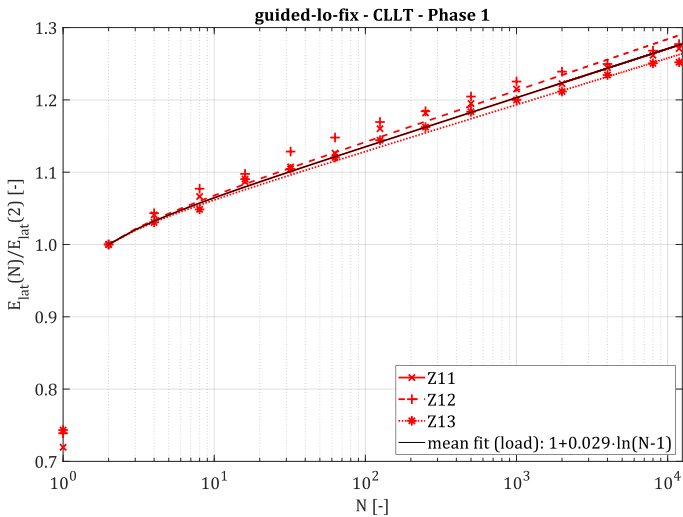


Figure F-123: Development of pile head secant stiffness of crane-guided vibratory driven piles with low eccentric moment during phase 1

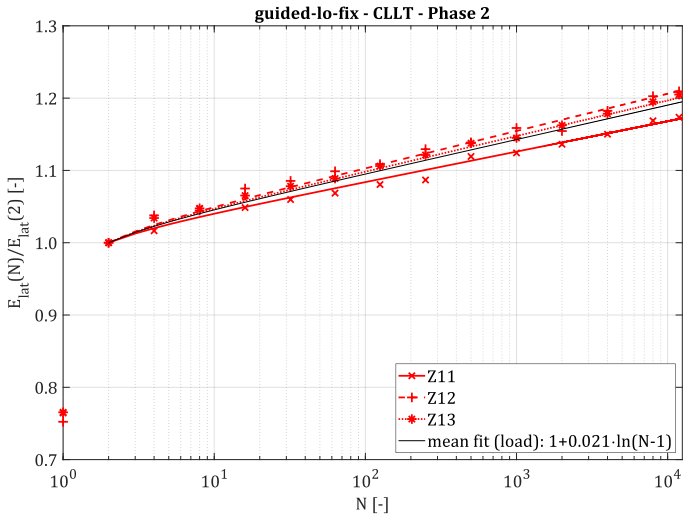


Figure F-124: Development of pile head secant stiffness of crane-guided vibratory driven piles with low eccentric moment during phase 2

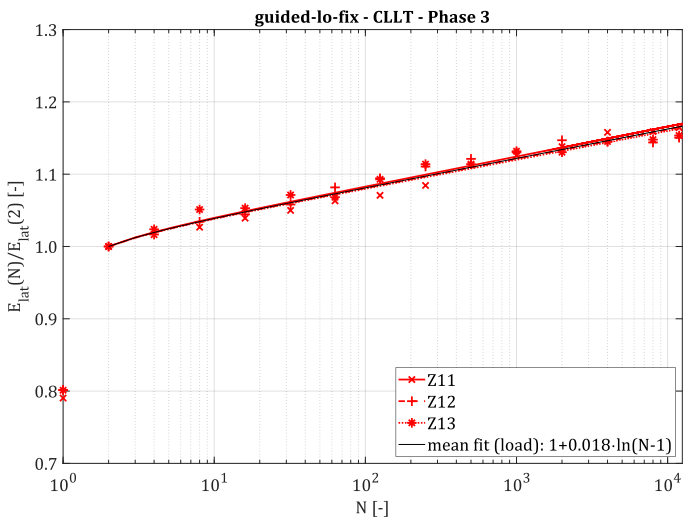


Figure F-125: Development of pile head secant stiffness of crane-guided vibratory driven piles with low eccentric moment during phase 3

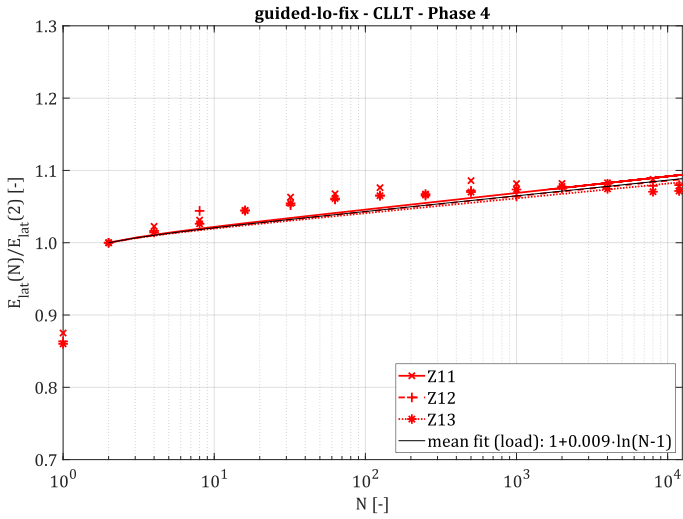


Figure F-126: Development of pile head secant stiffness of crane-guided vibratory driven piles with low eccentric moment during phase 4

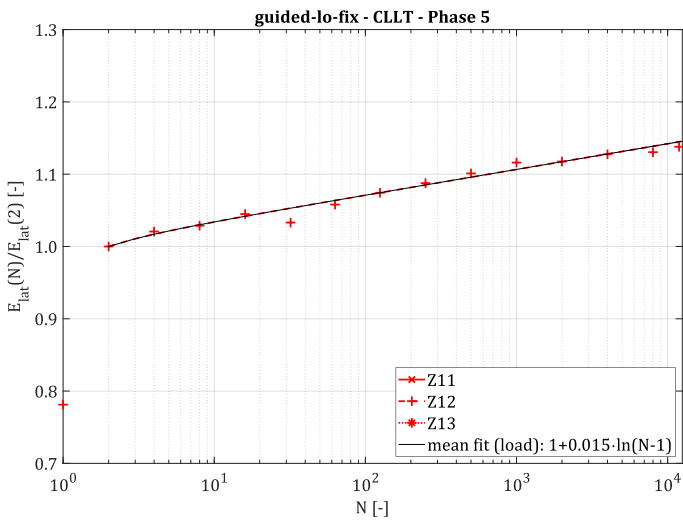


Figure F-127: Development of pile head secant stiffness of crane-guided vibratory driven piles with low eccentric moment during phase 5

Dynamic stiffness

The following figures show the pile's bending mode eigenfrequency determined by lateral frequency response tests (LFRT) after pile installation and after each phase of cyclic lateral loading. The horizontal axis indicates the test phase (0 indicates undisturbed system before start of lateral loading) and also gives the corresponding loading direction. For each test cluster (grouped according to installation parameters) two diagram are given for eigenfrequencies determined in directions of 0° and 90° .

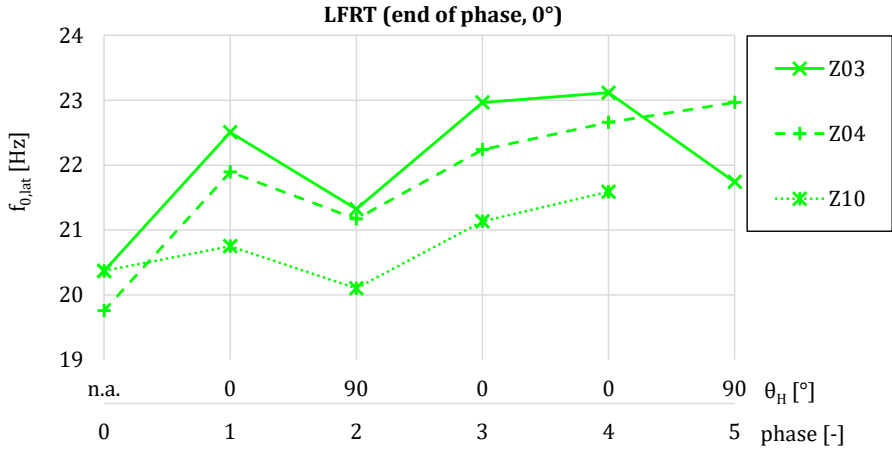


Figure F-128: Measured bending mode eigenfrequencies of impact driven piles over test phases in direction of 0°

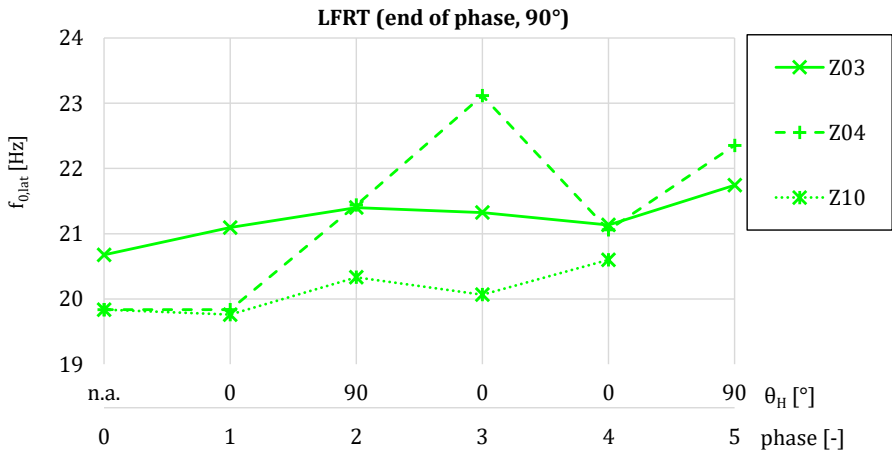


Figure F-129: Measured bending mode eigenfrequencies of impact driven piles over test phases in direction of 90°

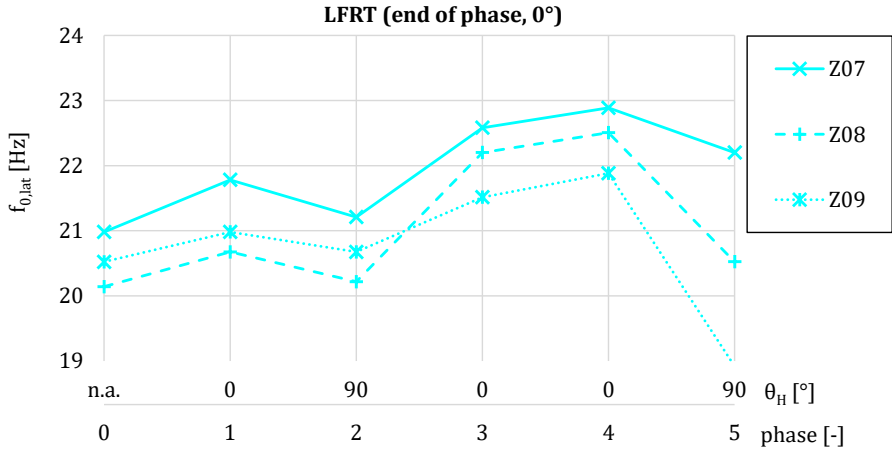


Figure F-130: Measured bending mode eigenfrequencies of free vibratory driven piles with high eccentric moment and 'aggressive' frequency control over test phases in direction of 0°

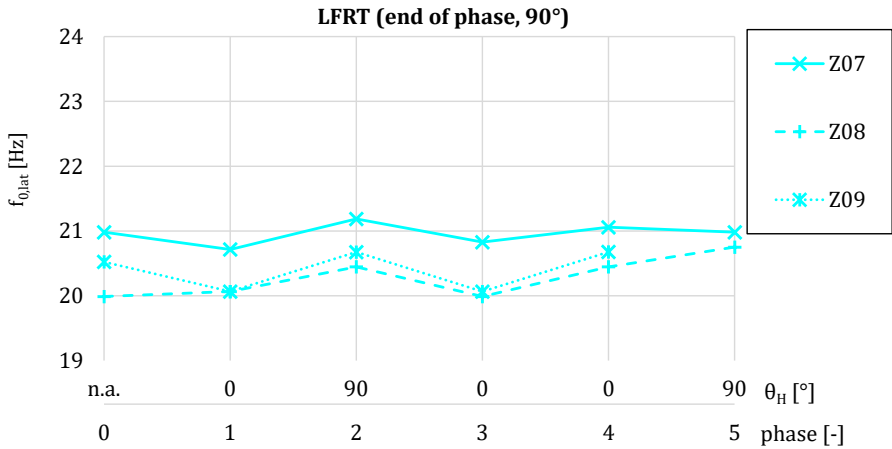


Figure F-131: Measured bending mode eigenfrequencies of free vibratory driven piles with high eccentric moment and 'aggressive' frequency control over test phases in direction of 90°

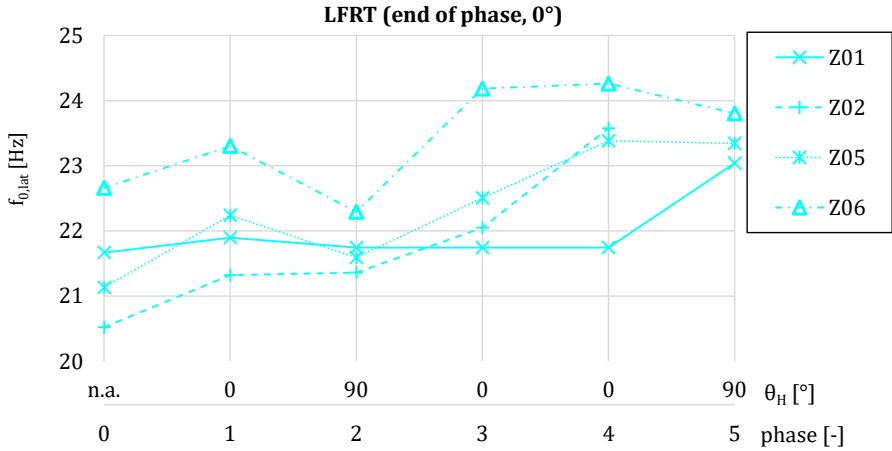


Figure F-132: Measured bending mode eigenfrequencies of free vibratory driven piles with high eccentric moment and 'moderate' frequency control over test phases in direction of 0°

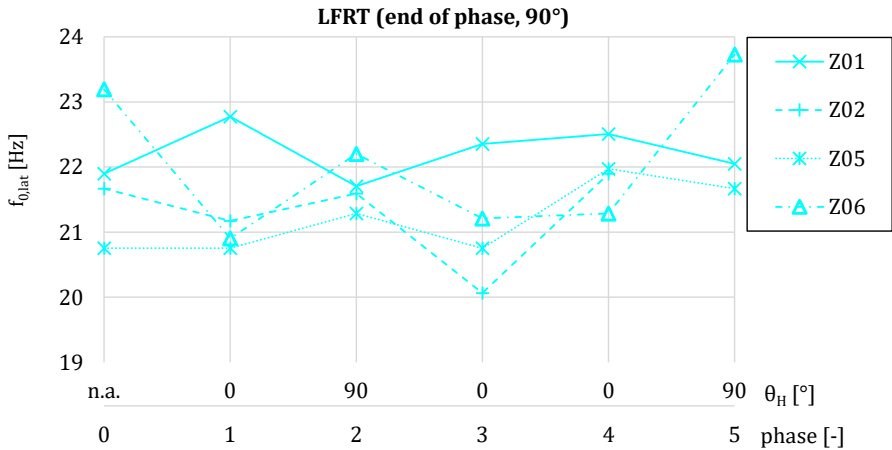


Figure F-133: Measured bending mode eigenfrequencies of free vibratory driven piles with high eccentric moment and 'moderate' frequency control over test phases in direction of 0°

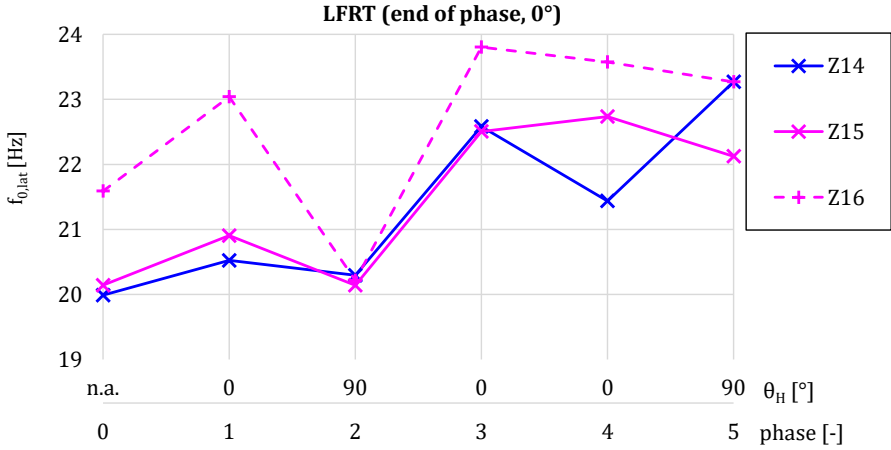


Figure F-134: Measured bending mode eigenfrequencies of free vibratory driven pile with low eccentric moment (blue) and crane-guided vibratory driven piles with high eccentric moment (magenta) over test phases in direction of 0°

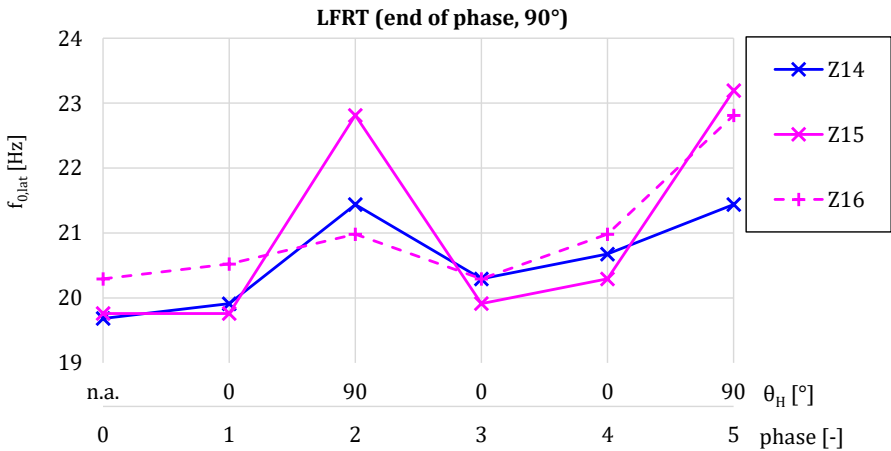


Figure F-135: Measured bending mode eigenfrequencies of free vibratory driven pile with low eccentric moment (blue) and crane-guided vibratory driven piles with high eccentric moment (magenta) over test phases in direction of 90°

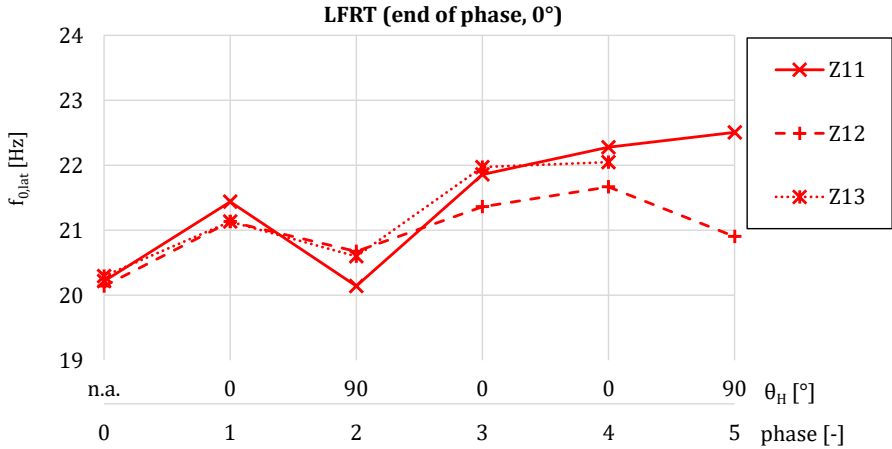


Figure F-136: Measured bending mode eigenfrequencies of crane-guided vibratory driven piles with low eccentric moment over test phases in direction of 0°

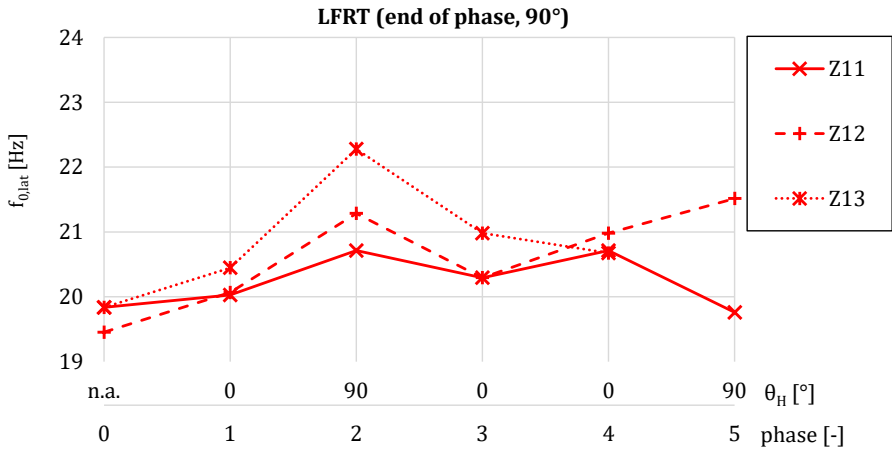


Figure F-137: Measured bending mode eigenfrequencies of crane-guided vibratory driven piles with low eccentric moment over test phases in direction of 90°

Soil stress developments

The following figures show the development of radial effective soil stress profiles over several phases of cyclic lateral loading from changing directions for all tests.

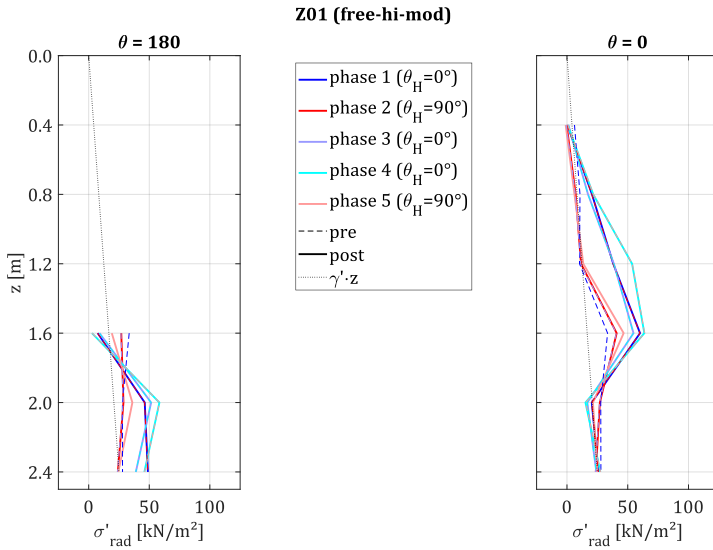


Figure F-138: Development of radial effective soil stress profiles over tests phases for pile Z01

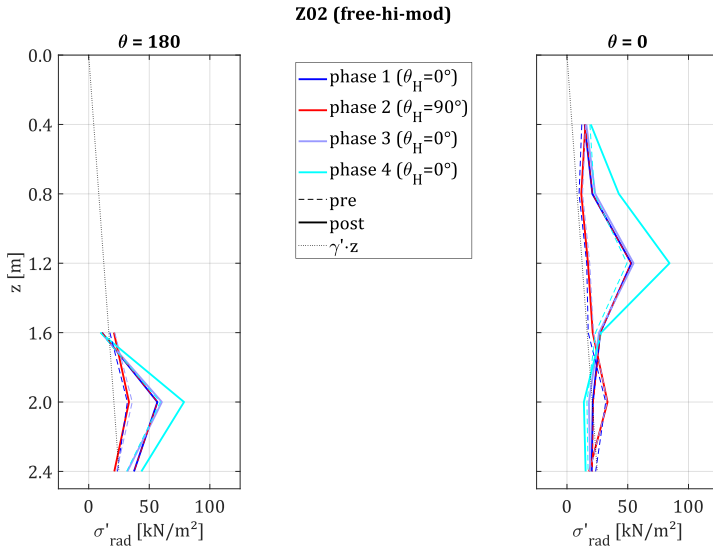
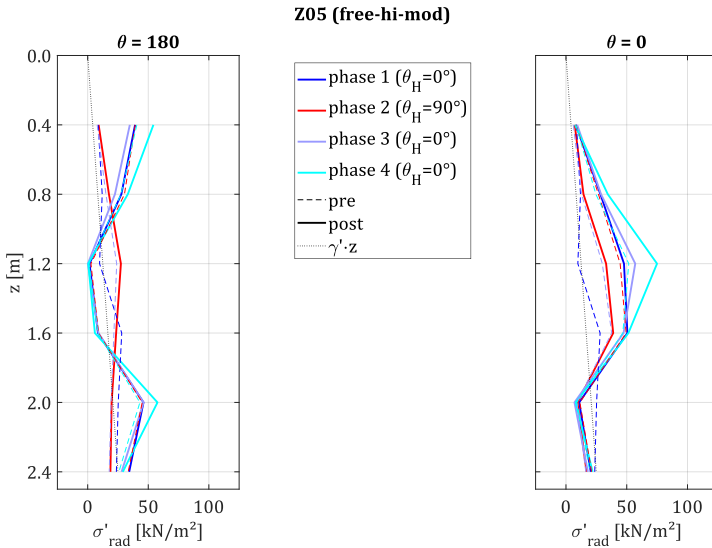
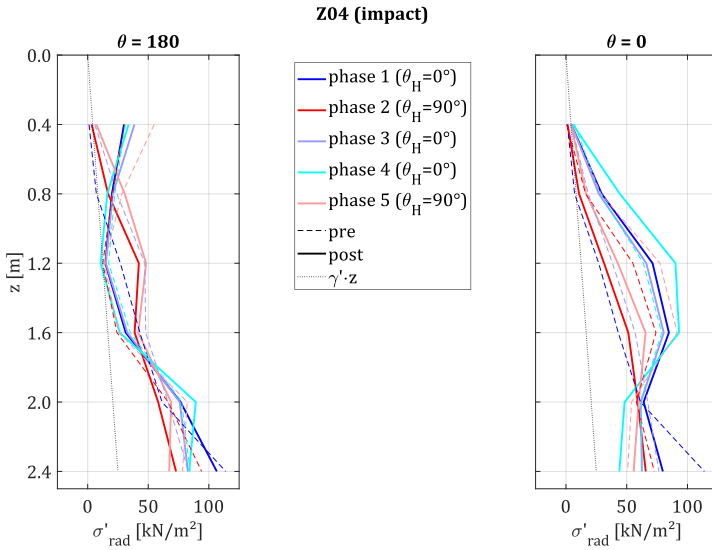


Figure F-139: Development of radial effective soil stress profiles over tests phases for pile Z02

Figure F-140: Development of radial effective soil stress profiles over tests phases for pile Z03



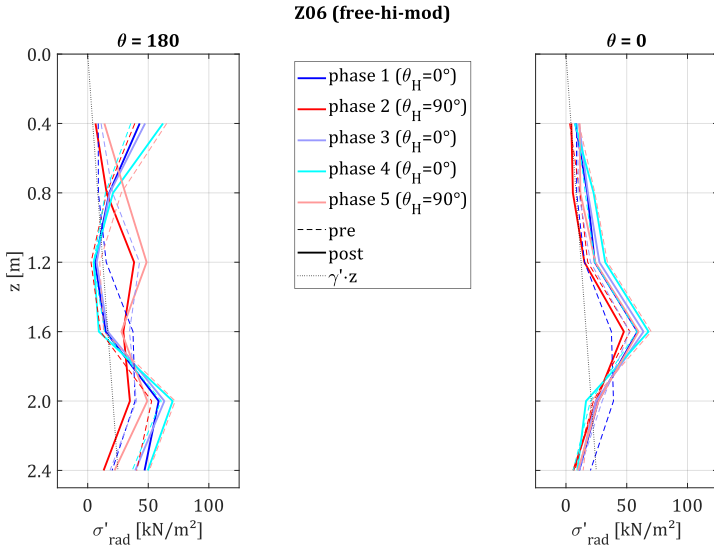


Figure F-143: Development of radial effective soil stress profiles over tests phases for pile Z06

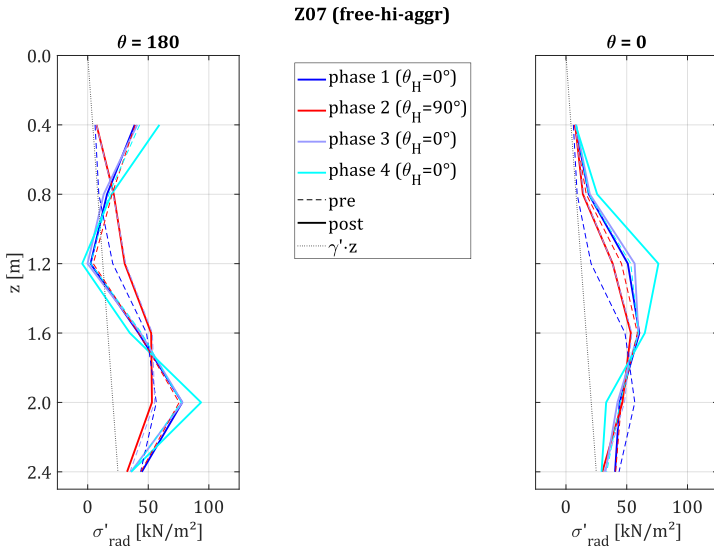
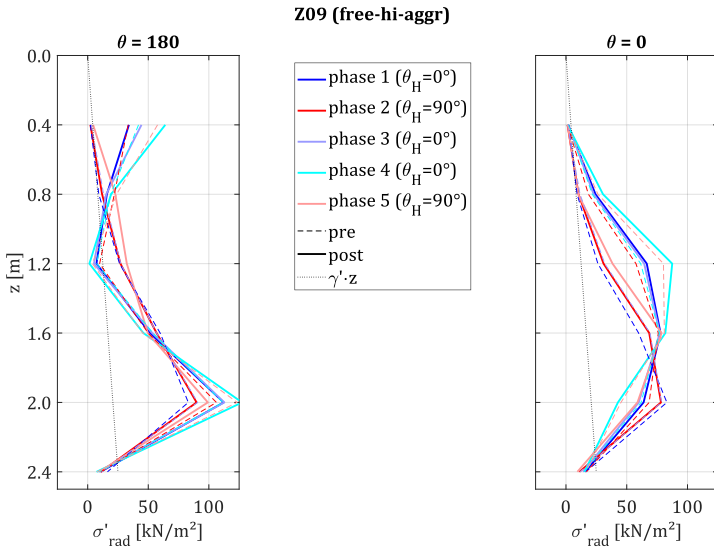
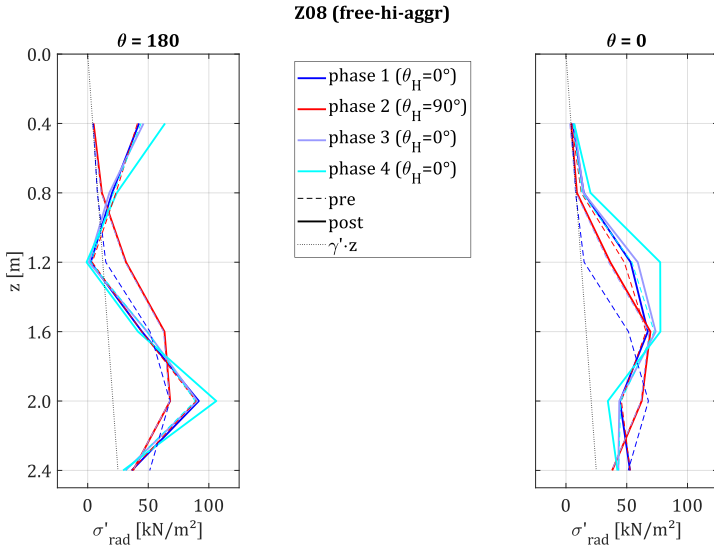


Figure F-144: Development of radial effective soil stress profiles over tests phases for pile Z07



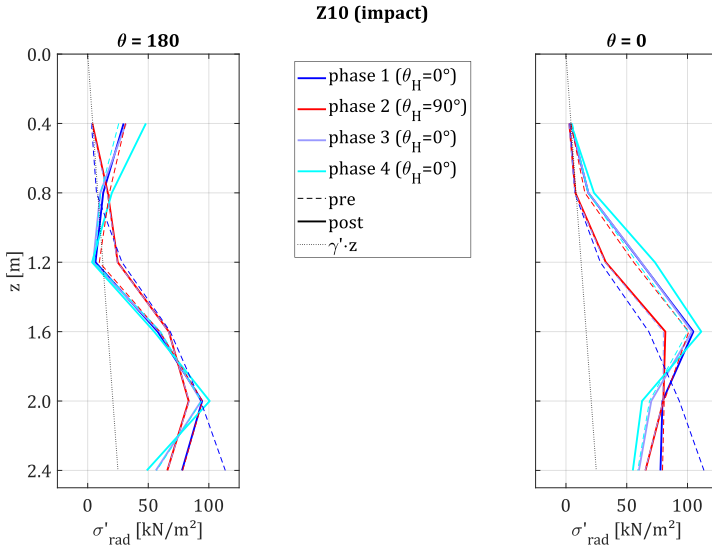


Figure F-147: Development of radial effective soil stress profiles over tests phases for pile Z10

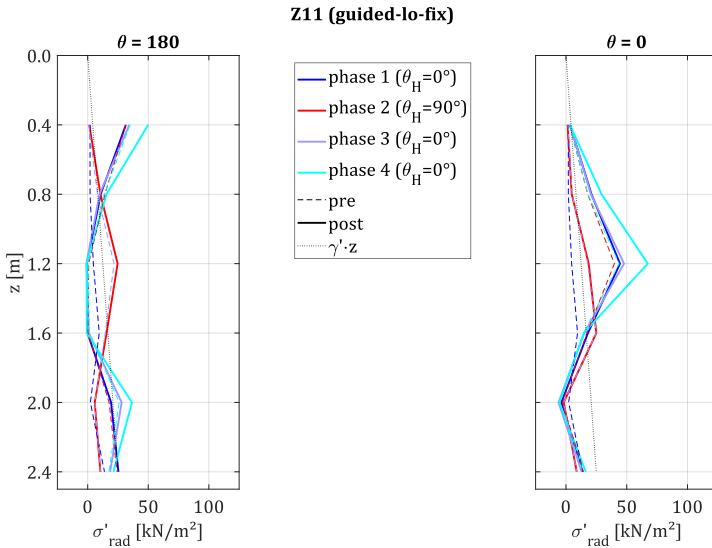


Figure F-148: Development of radial effective soil stress profiles over tests phases for pile Z11

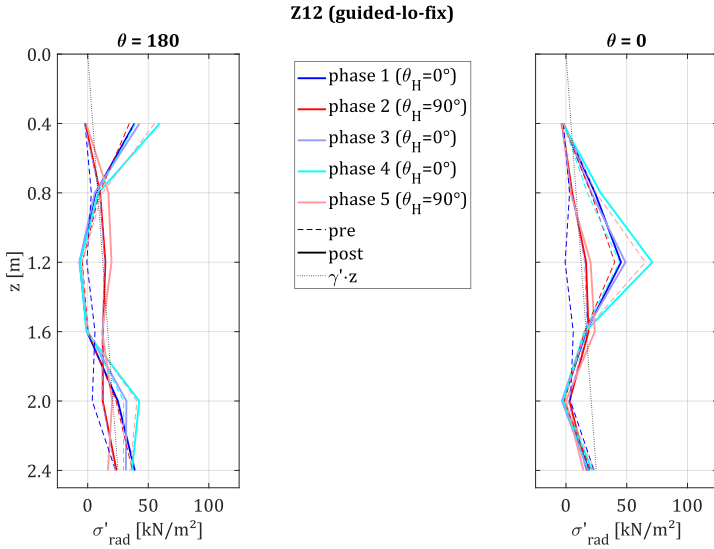


Figure F-149: Development of radial effective soil stress profiles over tests phases for pile Z12

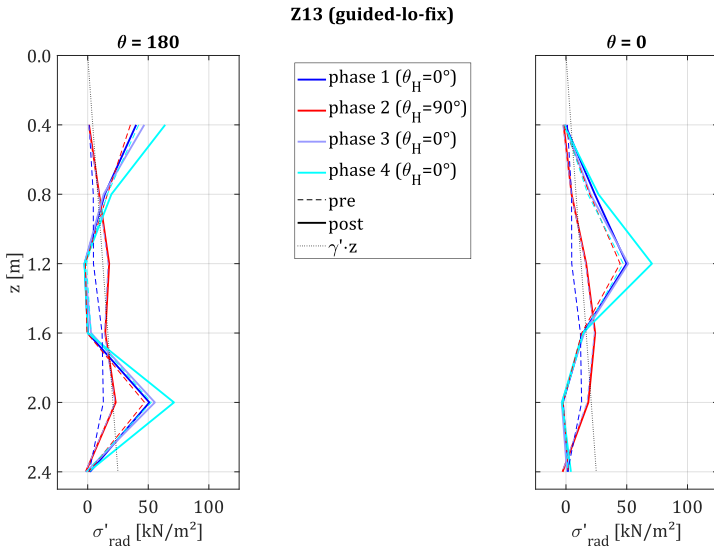


Figure F-150: Development of radial effective soil stress profiles over tests phases for pile Z13

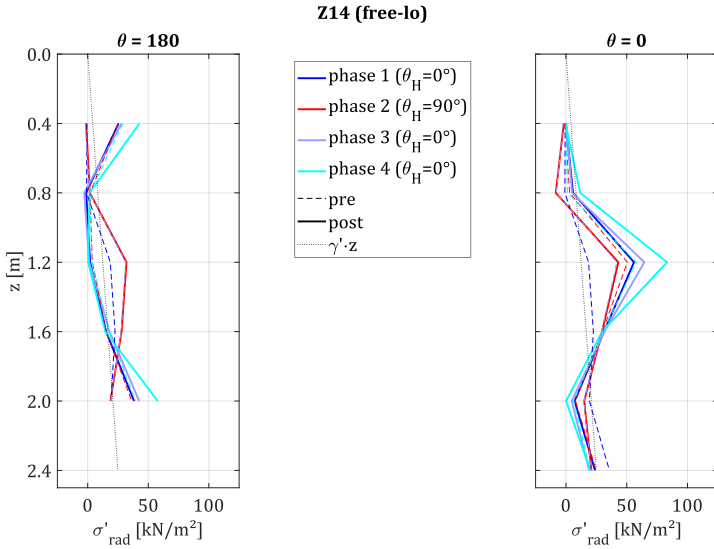


Figure F-151: Development of radial effective soil stress profiles over tests phases for pile Z14

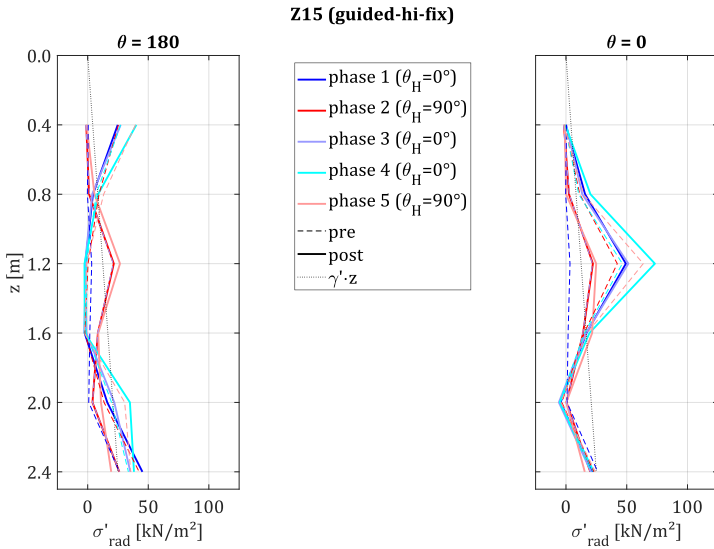


Figure F-152: Development of radial effective soil stress profiles over tests phases for pile Z15

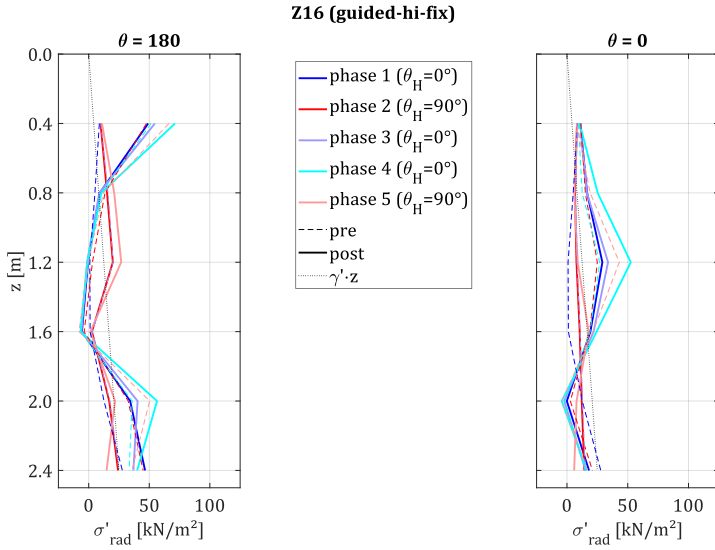


Figure F-153: Development of radial effective soil stress profiles over tests phases for pile Z16

Appendix G HCA model formulation and parameters

The accumulated strain γ^{acc} (after the first, irregular cycle, see Figure 2-15) is described by the flow rule m multiplied with a number of empirical functions f_j whose coefficients C_j may be calibrated by cyclic laboratory tests or taken from empirical correlations with the grain distribution (WICHTMANN & TRIANTAFYLIDIS 2011):

$$\gamma^{\text{acc}}(N_{\text{reg}}) = m \cdot f_{\text{ampl}} \cdot f_p \cdot f_Y \cdot f_e \cdot f_N \quad (\text{G-1})$$

The function for the mean strain amplitude $\gamma_{\text{ampl,mean}}$ yields

$$f_{\text{ampl}} = \left(\frac{\gamma_{\text{ampl,mean}}}{\gamma_{\text{ref}}} \right)^{C_{\text{ampl}}} \quad (\text{G-2})$$

with the reference strain $\gamma_{\text{ref}} = 10^{-4}$ and the constant $C_{\text{ampl}} = 1.7$.

The function for the mean stress state p_{av} [kN/m²] is described by

$$f_p = \exp \left[-C_p \cdot \left(\frac{p_{\text{av}}}{p_{\text{ref}}} - 1 \right) \right] \quad (\text{G-3})$$

with the atmospheric pressure $p_{\text{ref}} = 100$ kPa and

$$C_p = 0.41 \cdot [1 - 0.34 \cdot (d_{50} - 0.6)] \quad (\text{G-4})$$

with the mean grain size d_{50} [mm].

The function for the void ratio e [-] is described by

$$f_e = \frac{(C_e - e)^2}{1 + e} \cdot \frac{1 + e_{\text{max}}}{(C_e - e_{\text{max}})^2} \quad (\text{G-5})$$

with the min and max void ratios e_{min} and e_{max} [-] and

$$C_e = 0.95 \cdot e_{\text{min}} \quad (\text{G-6})$$

The function for the stress ratio is described by

$$f_Y = \exp[C_Y \cdot \bar{Y}] \quad (\text{G-7})$$

with

$$C_Y = 2.60 \cdot [1 + 0.12 \cdot \ln(d_{50}/0.6)] \quad (\text{G-8})$$

$$\bar{Y} = \frac{Y - 9}{Y_c - 9} \quad (\text{G-9})$$

with

$$Y = \frac{27 \cdot (3 + \eta_{av})}{(3 + 2\eta_{av})(3 - \eta_{av})} \quad (G-10)$$

$$\eta_{av} = q_{av}/p_{av} \quad (G-11)$$

$$Y_c = \frac{9 - \sin^2 \varphi_c}{1 - \sin^2 \varphi_c} \quad (G-12)$$

The function for the number of cycles is described by

$$f_N = C_{N1} \cdot [\ln(C_{N2} \cdot (N_{reg}) + 1) + C_{N3} \cdot N_{reg}] \quad (G-13)$$

WICHTMANN & TRIANTAFYLIDIS (2011) suggest to calibrate at least the parameters C_{N1} , C_{N2} and C_{N3} on cyclic tests. The following table gives coefficients for the HCA model based on empirical correlations with e_{min} , d_{50} , and C_u (WICHTMANN & TRIANTAFYLIDIS 2011) as well as coefficients calibrated on cyclic triaxial tests by NAWABI (2021).

Table G-1: Coefficients for HCA model

coefficient	empirical correlation (WICHTMANN & TRIANTAFYLIDIS 2011)	calibration on laboratory tests (NAWABI 2021)
C_{amp1}	1.70	1.68
C_e	0.452	0.45
C_p	0.439	0.50
C_Y	2.47	3.34
C_{N1}	$1.95 \cdot 10^{-3}$	$2.55 \cdot 10^{-4}$
C_{N2}	0.041	0.35
C_{N3}	$7.28 \cdot 10^{-5}$	$1.2 \cdot 10^{-6}$

The HCA model uses a soil state parameter g^A to describe the soil's loading history based on the function f_{amp1} considering the amplitude of cyclic loading, the number of cycles N_{reg} and the (cyclic) soil constants C_{N1} and C_{N2} :

$$g^A = f_{amp1} \cdot f_N^A = f_{amp1} \cdot C_{N1} \cdot \ln(1 + C_{N2} \cdot N_{reg}) \quad (G-14)$$

For an incremental procedure to calculate g^A for load packages with different amplitudes see WICHTMANN & TRIANTAFYLIDIS (2011).

Appendix H Numerical calculations

Numerical model

The lateral pile behaviour is described by a one-dimensional bedded beam model. The general formulation is

$$\mathbf{P}(t) = \mathbf{K} \cdot \mathbf{y}(t) + \mathbf{C} \cdot \dot{\mathbf{y}}(t) + \mathbf{M} \cdot \ddot{\mathbf{y}}(t) \quad (\text{H-1})$$

for the dynamic case (cf. Sections 2.3.2 and 7.3.1). For the static case (cf. Sections 2.3.1 and 7.2.1), time-dependent effects (damping and inertia) can be ignored and Equation (H-1) simplifies to

$$\mathbf{P} = \mathbf{K} \cdot \mathbf{y} \quad (\text{H-2})$$

The load vector \mathbf{P} consists of the lateral load H and bending moment M applied at the top node:

$$\mathbf{P} = \begin{pmatrix} H \\ M \\ 0 \\ \vdots \\ 0 \end{pmatrix} \quad (\text{H-3})$$

The deformation vector \mathbf{y} consists of the local lateral displacements y_i and local inclinations ψ_i at node i :

$$\mathbf{y} = \begin{pmatrix} y_1 \\ \psi_1 \\ \vdots \\ y_{nel+1} \\ \psi_{nel+1} \end{pmatrix} \quad (\text{H-4})$$

Stiffness, damping and mass matrices \mathbf{K} , \mathbf{C} and \mathbf{M} are composed of pile and soil parts, e.g.:

$$\mathbf{K} = \mathbf{K}_{\text{pile}} + \mathbf{K}_{\text{soil}} \quad (\text{H-5})$$

Pile and soil matrices are assembled of element matrices. For the pile, the formulation of the Euler-Bernoulli beam is used:

$$\mathbf{K}_{\text{pile},i} = \frac{EI}{dL^3} \cdot \begin{bmatrix} 12 & 6 \cdot dL & -12 & 6 \cdot dL \\ 6 \cdot dL & 4 \cdot dL^2 & -6 \cdot dL & 2 \cdot dL^2 \\ -12 & -6 \cdot dL & 12 & -6 \cdot dL \\ 6 \cdot dL & 2 \cdot dL^2 & -6 \cdot dL & 4 \cdot dL^2 \end{bmatrix} \quad (\text{H-6})$$

$$\mathbf{M}_{\text{pile},i} = \frac{A_{\text{pile}} \cdot \rho \cdot dL}{420} \begin{bmatrix} 156 & 22 \cdot dL & 54 & -13 \cdot dL \\ 22 \cdot dL & 4 \cdot dL^2 & 13 \cdot dL & -3 \cdot dL^2 \\ 54 & 13 \cdot dL & 156 & -22 \cdot dL \\ -13 \cdot dL & -3 \cdot dL^2 & -22 \cdot dL & 4 \cdot dL^2 \end{bmatrix} \quad (\text{H-7})$$

dL is the pile element length. Pile damping is neglected ($\mathbf{C}_{\text{pile}} = 0$). The soil springs only apply shear forces on the nodes:

$$\mathbf{K}_{\text{soil},i} = E_{py} \cdot dL \cdot \begin{bmatrix} 0.5 & 0 & 0 & 0 \\ 0 & 0 & 0 & 0 \\ 0 & 0 & 0.5 & 0 \\ 0 & 0 & 0 & 0 \end{bmatrix} \quad (\text{H-8})$$

with E_{py} depending on the formulation of the lateral bedding (e.g. p-y curves, cf. Sections 2.3.1, 2.3.3, 7.2.2, and 7.3.1).

The damping matrix is equivalent to the stiffness matrix with the damping coefficient C_{py} used instead of the spring stiffness E_{py} . Damping is assumed to act on the full circumference of the pile $\pi \cdot D_{\text{pile}}$:

$$\mathbf{C}_{\text{soil},i} = C_{py} \cdot dL \cdot \pi \cdot D_{\text{pile}} \cdot \begin{bmatrix} 0.5 & 0 & 0 & 0 \\ 0 & 0 & 0 & 0 \\ 0 & 0 & 0.5 & 0 \\ 0 & 0 & 0 & 0 \end{bmatrix} \quad (\text{H-9})$$

with

$$C_{py} = \sqrt{G_d \cdot \rho_{\text{soil}}} \quad (\text{H-10})$$

The mass matrix of the soil is equivalent to that of the pile but with the soil unit weight ρ_{soil} applied to the volume of the soil plug $A_{\text{plug}} \cdot dL$:

$$\mathbf{M}_{\text{soil},i} = \frac{A_{\text{plug}} \cdot \rho_{\text{soil}} \cdot dL}{420} \begin{bmatrix} 156 & 22 \cdot dL & 54 & -13 \cdot dL \\ 22 \cdot dL & 4 \cdot dL^2 & 13 \cdot dL & -3 \cdot dL^2 \\ 54 & 13 \cdot dL & 156 & -22 \cdot dL \\ -13 \cdot dL & -3 \cdot dL^2 & -22 \cdot dL & 4 \cdot dL^2 \end{bmatrix} \quad (\text{H-11})$$

The full matrices consist of n_{el} element matrices with $n_{el}+1$ nodes. In the assembly procedure, the four upper left entries of an element matrix are added to the four lower right entries of the prior element matrix:

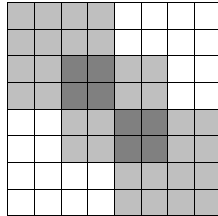


Figure H-1: Matrix assembly

Prediction of static lateral behaviour of model pile

The following figures show the calculated lateral pile behaviour. Lateral load H and pile head stiffness E_{lat} are plotted over pile head displacement u . Pile head displacement is extrapolated to 0.6 m above mudline to allow for comparison with measurements (coloured lines). To represent the measurements, load-displacement curves according to Equation (6-7) with parameters from Table 6-3 are plotted. Bending line y , inclination ψ , bending moment M , shear force Q , mobilised bedding reaction p_{py} together with yield bedding resistance $p_{py,ult}$ (grey), and underlying stress profile σ are plotted over depth z .

The following table gives the resulting pile head displacements at 0.6 m above mudline at maximum load level and the mobilised shear forces at the pile base.

Table H-1: Pile head displacements and mobilised base shear forces for model pile

variant	u [mm]	$u/\max u$ [-]	$Q_{base,mob}$ [kN]
<i>with base shear</i>			
no installation effect	3.33	1.00	-4.5
installation effect ($\alpha_{pen} = 1.6$)	2.53	0.76	-14.6
<i>without base shear</i>			
no installation effect	3.53	1.00	0
installation effect ($\alpha_{pen} = 1.6$)	2.85	0.81	0

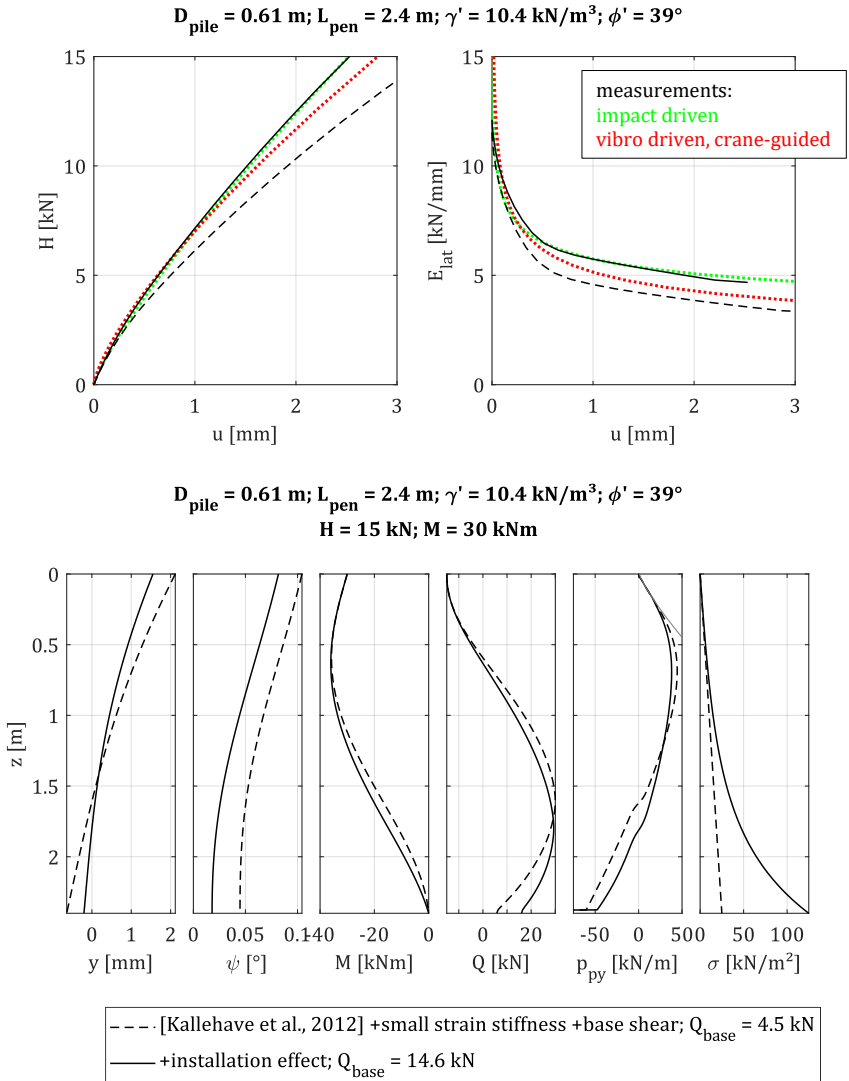


Figure H-2: Pile head results (top) and stress resultants (bottom) of model pile with base shear and variation of installation effect

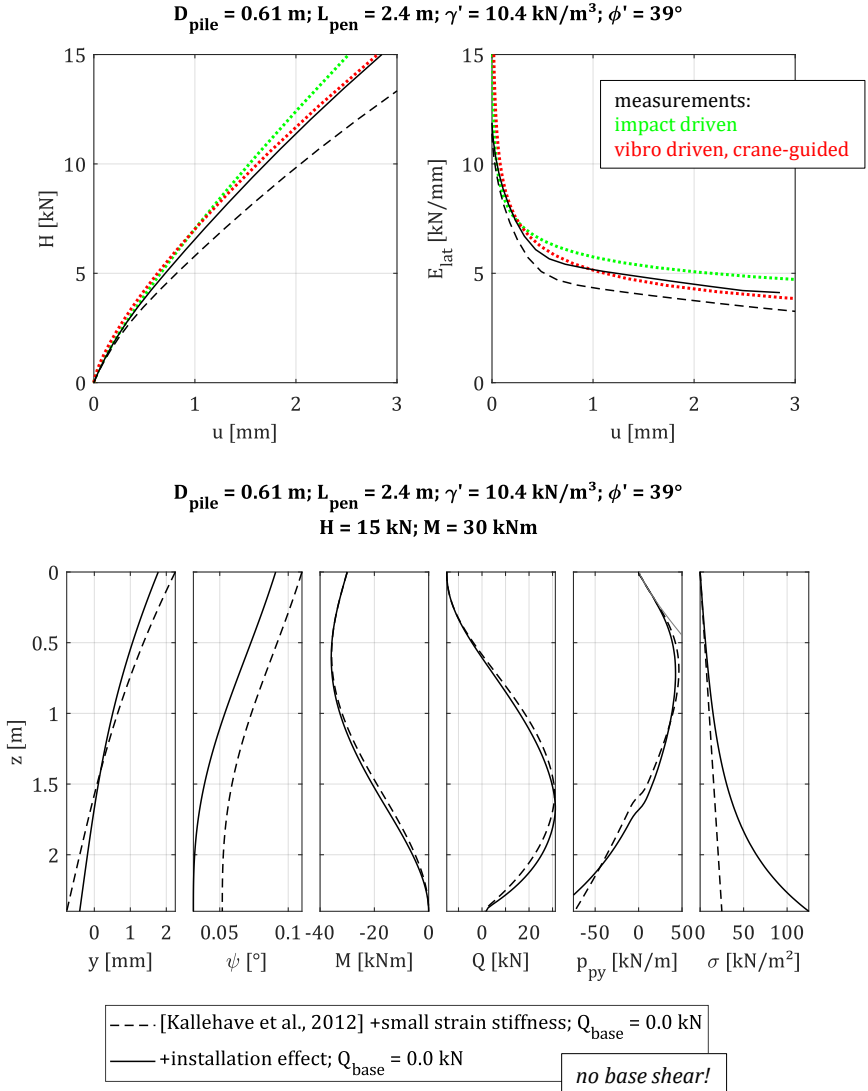


Figure H-3: Pile head results (top) and stress resultants (bottom) of model pile without base shear and variation of installation effect

Prediction of static lateral behaviour of generic monopile

The following figures show the calculated lateral pile behaviour. Lateral load H and pile head stiffness E_{lat} are plotted over pile head displacement u . Bending line y , inclination ψ , bending moment M , shear force Q , mobilised bedding reaction p_{py} together with yield bedding resistance $p_{py,ult}$ (grey), and underlying stress profile σ are plotted over depth z .

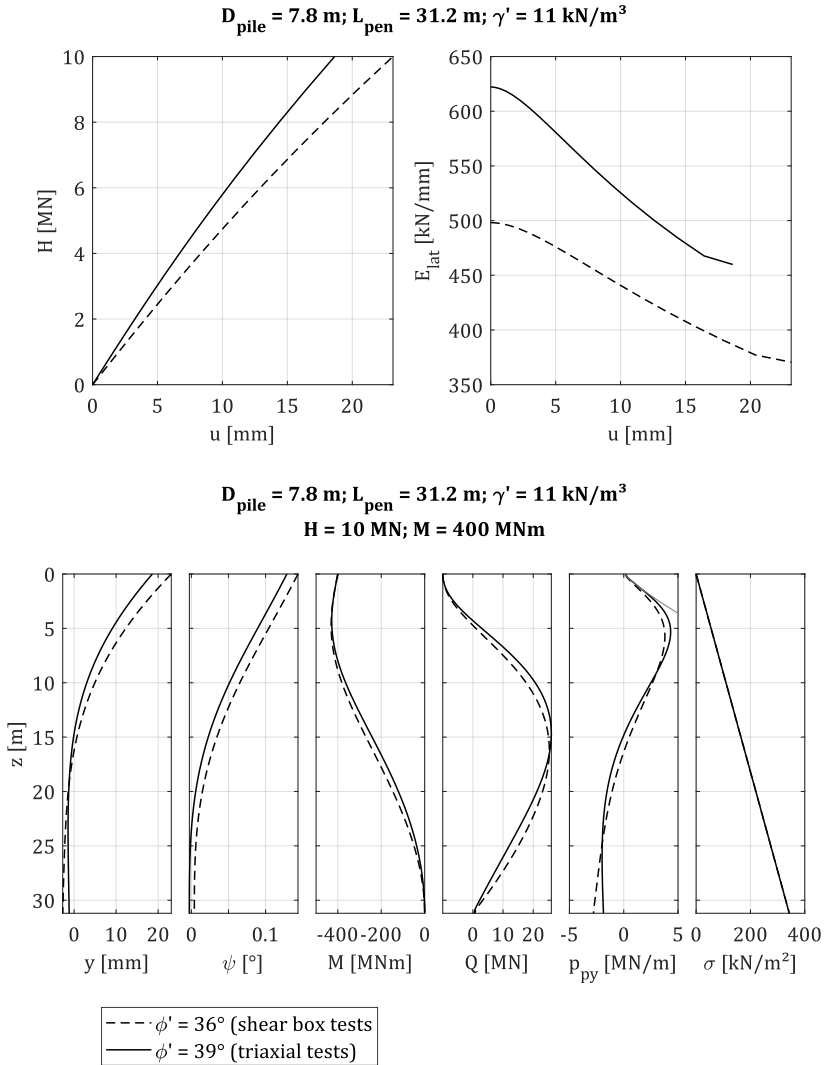


Figure H-4: Pile head results (top) and stress resultants (bottom) of 7.8 m monopile at different soil friction angles

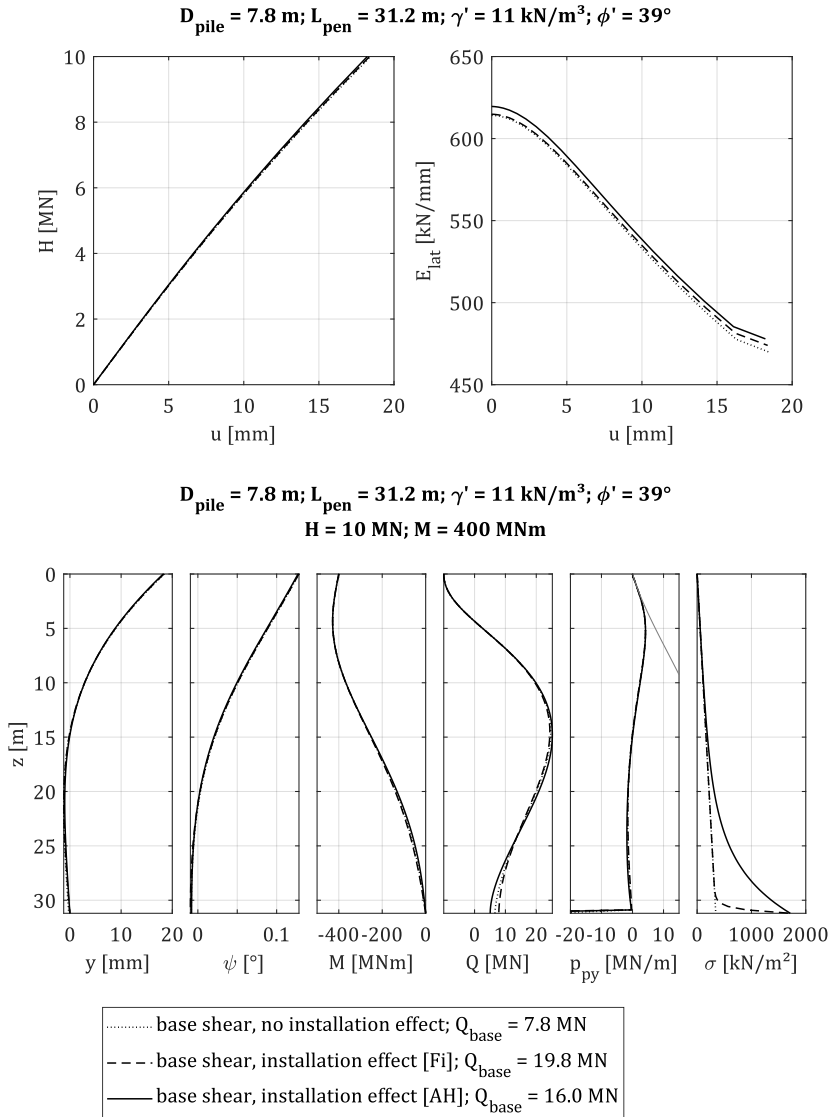


Figure H-5: Pile head results (top) and stress resultants (bottom) of 7.8 m monopile with base shear and variants of installation effect

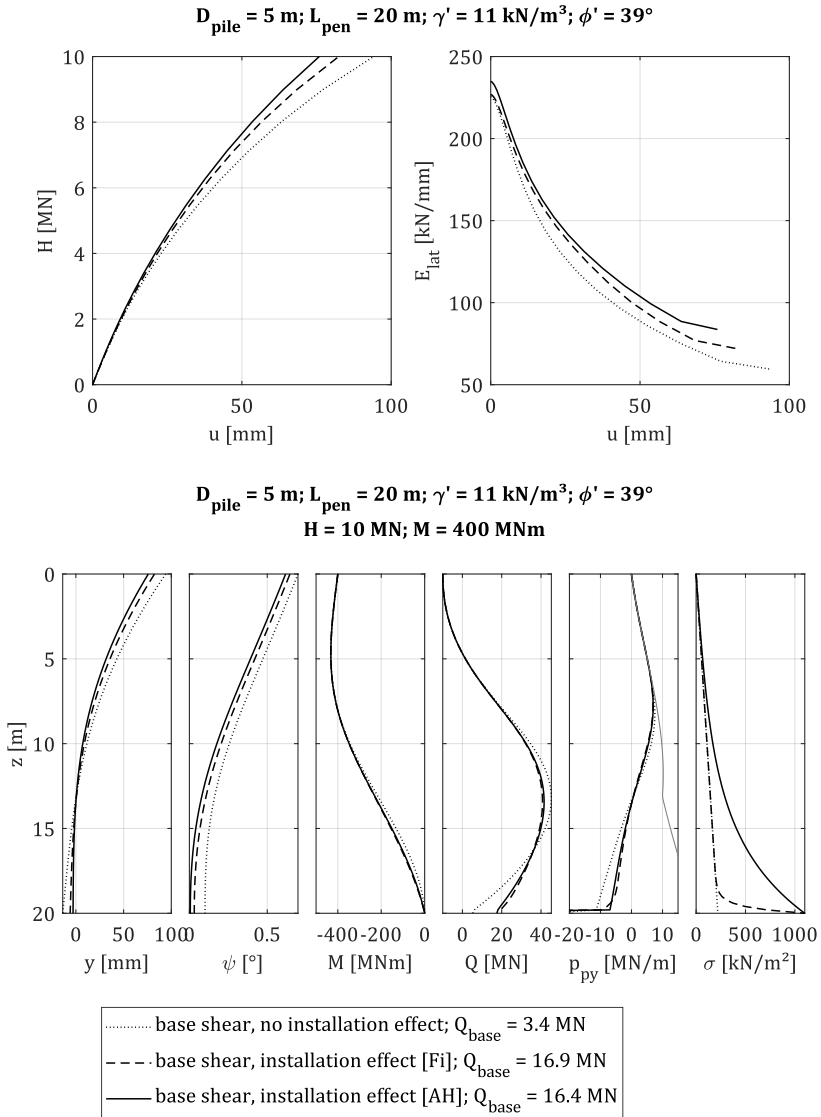


Figure H-6: Pile head results (top) and stress resultants (bottom) of 5 m monopile with base shear and variants of installation effect

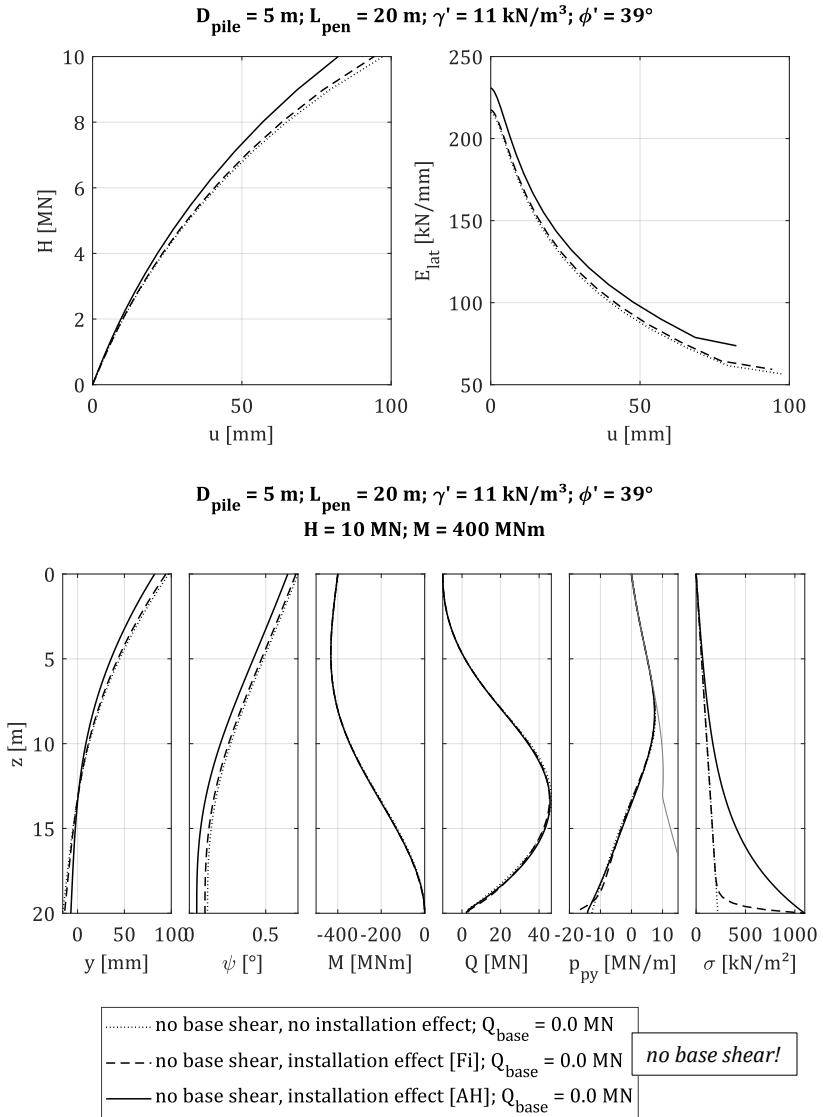


Figure H-7: Pile head results (top) and stress resultants (bottom) of 5 m monopile without base shear and variants of installation effect

Sensitivity of shape factor according to ALM & HAMRE (2002)

The following figure shows the influence of different CPT profiles (left) on the shape factor α_{pen} according to ALM & HAMRE (2002) (middle) and the decay function of soil stresses β_z (right). Note that low CPT values (thin, grey) lead to low absolute values of the shape factor and thus a more moderate decay function, resulting in higher overall soil stresses.

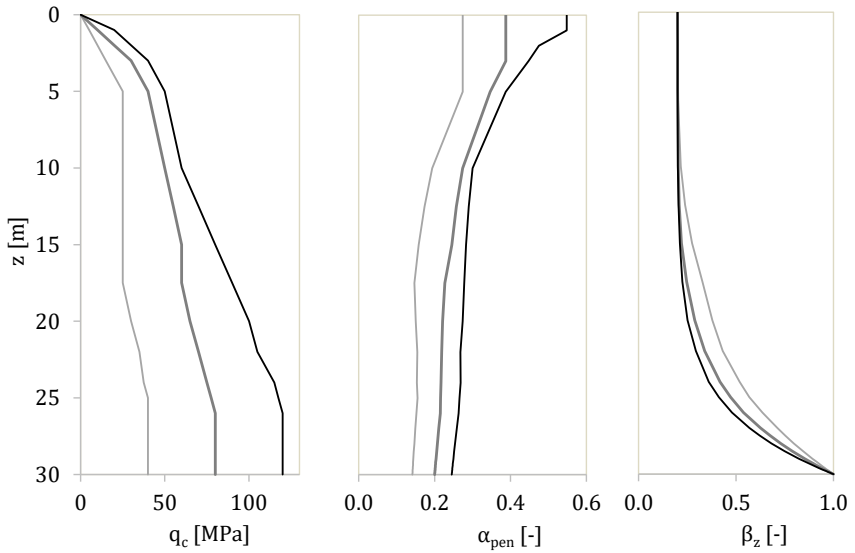


Figure H-8: Typical CPT readings from offshore locations in the German North Sea (left), resulting shape factors (middle) and soil strength reduction profiles (right)

*Bisher erschienene Mitteilungshefte
des Instituts für Geomechanik und Geotechnik
(vormals Grundbau und Bodenmechanik)*

**Die meisten Hefte können kostenfrei
auf unserer Homepage www.IGG-TUBS.de
als PDF heruntergeladen werden!**

- | | | |
|--------|------------------------------|---|
| Nr. 1 | Scheffler, E. | Die abgesteifte Baugrube berechnet mit nichtlinearen Stoffgesetzen für Wand und Boden , Dissertation, 1976 |
| Nr. 2 | Frank, H. | Formänderungsverhalten von Bewehrter Erde – untersucht mit Finiten Elementen , Dissertation, 1978 |
| Nr. 3 | Schnell, W. | Spannungen und Verformungen bei Fangedämmen
Dissertation, 1979 |
| Nr. 4 | Ruppert, F.-R. | Bodenmechanische Eigenschaften der Lauenburger Serie - Ein Beispiel für Statistik in der Bodenmechanik
Dissertation, 1980 |
| Nr. 5 | Schuppener, B. | Porenwasserüberdrücke im Sand unter Wellenbelastung auf Offshore-Bauwerken , Dissertation, 1981 |
| Nr. 6 | Wolff, F. | Spannungen und Verformungen bei Asphaltstraßen mit ungebundenen Tragschichten , Dissertation, 1981 |
| Nr. 7 | Bätcke, W. | Tragfähigkeit gedrungener Körper im geneigten Halbraum , Dissertation, 1982 |
| Nr. 8 | Meseck, H.
Schnell, W. | Dichtungswände und -sohlen , 1982 |
| Nr. 9 | Simons, H.
Ruppert, F.-R. | Entwicklung geeigneter Verfahren zum Messen der physikalischen Eigenschaften von Bentonitsuspensionen auf Baustellen , 1982 |
| Nr. 10 | Beckmann, U. | Einflußgrößen für den Einsatz von Tunnelbohrmaschinen
Dissertation, 1982 |
| Nr. 11 | Papakyriakopoulos | Verhalten von Erd- und Steinschüttdämmen unter Erdbeben , Dissertation, 1983 |
| Nr. 12 | Sondermann, W. | Spannungen und Verformungen bei Bewehrter Erde
Dissertation, 1983 |
| Nr. 13 | Meseck, H. | Sonderheft zum 10-jährigen Bestehen des Instituts
1984 |

- Nr. 14 Raabe, W. **Spannungs-Verformungsverhalten überkonsolidierter Tone und dessen Abhängigkeit von ingenieur-geologischen Merkmalen**, Dissertation, 1984
- Nr. 15 Fruchtenicht, H. **Zum Verhalten nichtbindigen Bodens bei Baugruben mit Schlitzwänden**, Dissertation, 1984
- Nr. 16 Knüpfer, J.
Meseck, H. **Schildvortrieb bei flüssigkeitsgestützter Ortsbrust**
1984
- Nr. 17 N.N. **Ablagerung umweltbelastender Stoffe**
Fachseminar in Braunschweig am 6. und 7. Februar 1985
- Nr. 18 Simons, H.
Reuter, E. **Entwicklung von Prüfverfahren und Regeln zur Herstellung von Deponieabdichtungen aus Ton zum Schutz des Grundwassers**, 1985
- Nr. 19 Meseck, H. **Dynamische Pfahltests** - Fachseminar in Braunschweig
am 23. und 24. Oktober 1985
- Nr. 20 Meseck, H. **Abdichten von Deponien, Altlasten und kontaminierten Standorten** - Fachseminar in Braunschweig
am 6. und 7. November 1986
- Nr. 21 Balthaus, H. **Zur Bestimmung der Tragfähigkeit von Pfählen mit dynamischen Pfahlprüfmethoden**, Dissertation, 1986
- Nr. 22 Kayser, R.
Meseck, H.
Rösch, A.,
Hermanns, R. **Untersuchungen zur Deponierung von Braunkohlenaschen**, 1986
- Nr. 23 Meseck, H. **Dichtwände und Dichtsohlen**
Fachseminar in Braunschweig am 2. und 3. Juni 1987
- Nr. 24 Krause, Th. **Schildvortrieb mit erd- und flüssigkeitsgestützter Ortsbrust**, Dissertation, 1987
- Nr. 25 Meseck, H. **Mechanische Eigenschaften mineralischer Dichtwandmassen**, Dissertation, 1987
- Nr. 26 Reuter, E. **Durchlässigkeitsverhalten von Tonen gegenüber anorganischen und organischen Säuren**
Dissertation, 1988
- Nr. 27 Wichert, H.-W. **Der Einfluß der Alterung auf die Tragfähigkeit historischer Spick-Pfahl-Gründungen**, Dissertation, 1988
- Nr. 28 Geil, M. **Untersuchungen der physikalischen und chemischen Eigenschaften von Bentonit-Zement-Suspensionen im frischen und erhärteten Zustand**, Dissertation, 1989

- Nr. 29 Kruse, T. **Standsicherheit von Kombinationsabdichtungen auf Deponieböschungen**, Dissertation, 1989
- Nr. 30 Rodatz, W. **Sonderheft zum 15jährigen Bestehen des Institutes für Grundbau und Bodenmechanik**, 1989
- Nr. 31 Rodatz, W.
Beckefeld, P.
Sehrbrock, U. **Standsicherheiten im Deponiebau / Schadstoffeinbindung durch Verfestigung von Abfällen**
- Fachseminar in Braunschweig am 19. u. 20. März 1990
- Nr. 32 Knüpfer, J. **Schnellverfahren für die Güteüberwachung mineralischer Deponiebasisabdichtungen**, Dissertation, 1990
- Nr. 33 Beckefeld, P. **Schadstoffaustrag aus abgebundenen Reststoffen der Rauchgasreinigung von Kraftwerken**
- Entwicklung eines Testverfahrens, Dissertation, 1991
- Nr. 34 He, G. **Standsicherheitsberechnungen von Böschungen**
Dissertation, 1991
- Nr. 35 Rodatz, W.
Sehrbrock, U. **Probenentnahme bei der Erkundung von Verdachtsflächen (Altlasten)**
Fachseminar in Braunschweig am 13. September 1991
- Nr. 36 Kahl, M. **Primär- und Sekundärspannungszustände in überkonsolidiertem Ton - Am Beispiel eines im Hamburger Glimmerton aufgefahrenen Tiefdükers**, Diss., 1991
- Nr. 37 Rodatz, W.
Hemker, O.
Voigt, Th. **Standsicherheiten im Deponiebau**
Fachseminar in Braunschweig am 30. und 31. März 1992
- Nr. 38 Rodatz, W.
Meier, K. **Dynamische Pfahltests**
Fachseminar in Braunschweig am 21. und 22. Januar 1991
- Nr. 39 Rösch, A. **Die Bestimmung der hydraulischen Leitfähigkeit im Gelände - Entwicklung von Meßsystemen und Vergleich verschiedener Auswerteverfahren**, Dissertation, 1992
- Nr. 40 Sehrbrock, U. **Prüfung von Schutzlagen für Deponieabdichtungen aus Kunststoff**, Dissertation, 1993
- Nr. 41 Rodatz, W.
Hartung, M.
Wienholz, B. **Pfahl-Symposium 1993**
Fachseminar in Braunschweig am 18. und 19. März 1993
- Nr. 42 Gattermann, J.
Hartung, M. **IGB-TUBS Lexikon** - Sammlung ca. 5500 geotechnischer Ausdrücke in Deutsch, Englisch, Französisch und Spanisch zusammengestellt in 4 Bänden, 4. überarbeitete Auflage 2002

- Nr. 43 Rodatz, W.
Hemker, O.
Horst, M.,
Kayser, J. **Deponieseminar 1994, Geotechnische Probleme im Deponie- und Dichtwandbau -**
Fachseminar in Braunschweig am 17. und 18. März 1994
- Nr. 44 Rodatz, W.
Gattermann, J.
Wienholz, B. **Messen in der Geotechnik 1994**
Fachseminar in Braunschweig am 26. und 27. Mai 1994
- Nr. 45 Hartung, M. **Einflüsse der Herstellung auf die Pfahltragfähigkeit in Sand**, Dissertation, 1994
- Nr. 46 Hemker, O. **Zerstörungsfreie Meßverfahren zur Qualitätsprüfung mineralischer Dichtungen**, Dissertation, 1994
- Nr. 47 Voigt, Th. **Frosteinwirkung auf mineralische Deponieabdichtungen**, Dissertation, 1994
- Nr. 48 Rodatz, W.
Ernst, U.
Wienholz, B. **Pfahl-Symposium 1995**
Fachseminar in Braunschweig am 23. und 24. Februar 1995
- Nr. 49 Kayser, J. **Spannungs-Verformungs-Verhalten von Einphasen-Dichtwandmassen**, Dissertation, 1995
- Nr. 50 Rodatz, W.
Gattermann, J.
Wienholz, B. **Messen in der Geotechnik 1996**
Fachseminar in Braunschweig am 22. und 23. Februar 1996
- Nr. 51 Rodatz, W.
Knoll, A. **Deponieseminar 1996 - Konstruktion, Bemessung und Qualitätssicherung bei Abdichtungssystemen -**
Fachseminar in Braunschweig am 22. und 23. März 1996
- Nr. 52 Maybaum, G. **Erddruckentwicklung auf eine in Schlitzwandbauweise hergestellte Kaimauer**, Dissertation, 1996
- Nr. 53 Rodatz, W.
Ernst, U.
Wienholz, B. **Pfahl-Symposium 1997**
Fachseminar in Braunschweig am 20. und 21. Februar 1997
- Nr. 54 Horst, M. **Wasserdurchlässigkeitsbestimmungen zur Qualitätssicherung mineralischer Abdichtungen**, Dissertation, 1997
- Nr. 55 Rodatz, W.
Gattermann, J.
Stahlhut, O. **Messen in der Geotechnik 1998**
Fachseminar in Braunschweig am 19. und 20. Februar 1998
- Nr. 56 Rodatz, W.
Bachmann, M.
Rosenberg, M. **Deponieseminar 1998 - Entwicklungen im Deponie- und Dichtwandbau**
Fachseminar in Braunschweig am 12. und 13. März 1998

- Nr. 71 Stahlmann, J.
 Fritsch, M.
 Kirsch, F.;
 Schallert, M. **Pfahl-Symposium 2003**
 Fachseminar in Braunschweig am 20. und 21. Februar 2003
- Nr. 72 Vittinghoff, T. **Analyse des Langzeitverhaltens einer Spundwandkonstruktion in einem überkonsolidierten Ton**, Diss., 2002
- Nr. 73 Witte, M. **Veränderung des Festigkeits- und Verformungsverhaltens bei bindigen Böden aufgrund von Porenwasserspannungen**, Dissertation, 2003
- Nr. 74 Stahlmann, J.
 Rosenberg, M.
 Nendza, M. **11. Braunschweiger Deponie und Dichtwandseminar 2004**
 Fachseminar in Braunschweig am 11. und 12. März 2004
- Nr. 75 Kirsch, F. **Experimentelle und numerische Untersuchungen zum Tragverhalten von Rüttelstopfsäulengruppen**, Diss., 2004
- Nr. 76 Stahlmann, J.
 Gattermann, J.
 Fritsch, M. **Geotechnik-Kolloquium 30 Jahre IGB·TUBS**
 Fachseminar in Braunschweig am 25. und 26. Mai 2004
- Nr. 77 Stahlmann, J.
 Gattermann, J.
 Kuhn, C. **Messen in der Geotechnik 2004**
 Fachseminar in Braunschweig am 09. und 10. September 2004
- Nr. 78 Bergs, T. **Untersuchungen zum Verformungs- und Lastabtragungsverhalten einer Kaikonstruktion**, Dissertation, 2004
- Nr. 79 Scholz, C. **Integrität von Einphasen-Dichtwänden - Untersuchungen zum rheologischen und mechanisch-hydraulischen Verhalten faserbewehrter Einphasen-Dichtwandmassen**
Dissertation, 2004
- Nr. 80 Stahlmann, J.
 Gattermann, J.
 Fritsch, M. **Pfahl-Symposium 2005**
 Fachseminar in Braunschweig am 24. und 25. Februar 2005
- Nr. 81 Nendza, M. **Untersuchungen zu den Mechanismen der dynamischen Bodenverdichtung bei Anwendung des Rütteldruckverfahrens**, Dissertation, 2006
- Nr. 82 Stahlmann, J.
 Gattermann, J.
 Kuhn, C. **Messen in der Geotechnik 2006**
 Fachseminar in Braunschweig am 23. und 24. Februar 2006
- Nr. 83 Stahlmann, J.
 Rosenberg, M. **geotechnische Aspekte im Umweltschutz**
 Fachseminar in Braunschweig am 23. und 24. März 2006

- Nr. 84 Stahlmann, J.
 Gattermann, J.
 Fritsch, M.;
 Fischer, J. **Pfahl-Symposium 2007**
 Fachseminar in Braunschweig
 am 22. und 23. Februar 2007
- Nr. 85 Kluge, K. **Soil Liquefaction around Offshore Pile Foundations
– Scale Model Investigations**, Dissertation, 2007
- Nr. 86 Fritsch, M. **Zur Modellbildung der Wellenausbreitung in
dynamisch belasteten Pfählen**, Dissertation, 2008
- Nr. 87 Stahlmann, J.
 Gattermann, J.
 Bruns, B. **Messen in der Geotechnik 2008**
 Fachseminar in Braunschweig am 23. und 24. Oktober 2008
- Nr. 88 Stahlmann, J.
 Gattermann, J.
 Fischer, J. **Pfahl-Symposium 2009**
 Fachseminar in Braunschweig am 19. und 20. Februar 2009
- Nr. 89 Schmitt, J. **Spannungsverformungsverhalten des Gebirges
beim Vortrieb mit Tunnelbohrmaschinen mit Schild**
Dissertation, 2009
- Nr. 90 Stahlmann, J.
 Rosenberg, M. **Stahl im Wasserbau 2009**
 Fachseminar in Braunschweig am 15. und 16. Oktober 2009
- Nr. 91 Kimme, N. **Prefailure Behaviour of Rock at Rockburst Hazard Areas
– Laboratory Investigations on Microacoustic Emissions**
Dissertation, 2009
- Nr. 92 Stahlmann, J.
 Gattermann, J.
 Bruns, B. **Messen in der Geotechnik 2010**
 Fachseminar in Braunschweig am 18. und 19. Februar 2010
- Nr. 93 Schallert, M. **Faseroptische Mikrodehnungsaufnehmer für die
Bewertung der Struktur von Betonpfählen**, Diss., 2010
- Nr. 94 Stahlmann, J.
 Fischer, J.
 Zahlmann, J. **Pfahl-Symposium 2011**
 Fachseminar in Braunschweig
 am 17. und 18. Februar 2011
- Nr. 95 Stahlmann, J.
 Rosenberg, M. **Stahl im Wasserbau 2011**
 Fachseminar in Braunschweig am 29. und 30. September 2011
- Nr. 96 Stahlmann, J.
 Zahlmann, J.
 Sychla, H. **Pfahl-Symposium 2013**
 Fachseminar in Braunschweig
 am 21. und 22. Februar 2013
- Nr. 97 Stahlmann, J.
 Rosenberg, M. **Stahl im Wasserbau 2013**
 Fachseminar in Braunschweig am 26. und 27. September 2013

- Nr. 98 Stahlmann, J.
Gattermann, J.
Bruns, B.;
Kuhn, C. **Messen in der Geotechnik 2014**
Fachseminar in Braunschweig
am 20. und 21. Februar 2014
- Nr. 99 Stahlmann, J.
Gattermann, J.
Stein, P.;
Sychla, H.;
Zahlmann, J. **Pfahl-Symposium 2015**
Fachseminar in Braunschweig
am 19. und 20. Februar 2015
- Nr. 100 Stahlmann, J.
Rosenberg, M. **Stahl im Wasserbau 2015**
Fachseminar in Braunschweig
am 30. September und 1. Oktober 2015
- Nr. 101 Stahlmann, J.
Gattermann, J.
Stein, P. **Messen in der Geotechnik 2016**
Fachseminar in Braunschweig
am 17. und 18. März 2016
- Nr. 102 Stahlmann, J.
Hinzmann, N.
Stein, P. **Pfahl-Symposium 2017**
Fachseminar in Braunschweig am
23. und 24. Februar 2017
- Nr. 103 Stahlmann, J.
Rosenberg, M. **Stahl im Wasserbau 2017**
Fachseminar in Braunschweig am 28. und 29. September 2017
- Nr. 104 Stahlmann, J.
Hinzmann, N.
Stein, P. **Messen in der Geotechnik 2018**
Fachseminar in Braunschweig
am 22. und 23. Februar 2018
- Nr. 105 Gährken, A. **Untersuchungen zum Einfluss der Spannungsgeometrie
auf das Verformungs- und Schädigungsverhalten von
Steinsalz, Dissertation, 2018**
- Nr. 106 Stahlmann, J.
Mintzlaff, V.
León Vargas, R.P.
Epkenhans, I. **Normalszenarien und Monitoringkonzepte
für Tiefenlager mit der Option Rückholung,**
ENTRIA-Arbeitsbericht-15, 2019
- Nr. 107 Stahlmann, J.
Hinzmann, N.
Stein, P. **Pfahl-Symposium 2019**
Fachseminar in Braunschweig
am 21. und 22. Februar 2019
- Nr. 108 Missal, C. **Numerisches Modell zur Entwicklung der Permeabilität
von Steinsalz in Abhängigkeit von Schädigung,
Fluiddruck und Spannungszustand, Dissertation, 2019**
- Nr. 109 Stahlmann, J.
Rosenberg, M.
Daumlechner, E. **Stahl im Wasserbau 2019**
Fachseminar in Braunschweig am 19. und 20. September 2019

- Nr. 110 Stahlmann, J.
Hinzmann, N.
Stein, P.
Gattermann, J. **Messen in der Geotechnik 2020**
Fachseminar in Braunschweig
am 20. und 21. Februar 2020
- Nr. 111 Fischer, J. **Ramminduzierte Spannungsfeldänderungen
im Nahbereich von Rohrprofilen großen Durchmessers,**
Dissertation, 2021
- Nr. 112 Stein, P. **Stress state developments during the installation of pipe
piles in sand and their influence on the lateral load-bearing
behaviour,** Dissertation, 2023
- Nr. 113 Stahlmann, J.
Gattermann, J. **Pfahl-Symposium 2023**
Fachseminar in Braunschweig am 16. und 17. Februar 2023

ISBN - Nr: 978-3-948141-04-2